Special Paper 477

THE GEOLOGICAL SOCIETY OF AMERICA®

Recent Advances and Current Research Issues in Lunar Stratigraphy

Edited by William A. Ambrose and David A. Williams

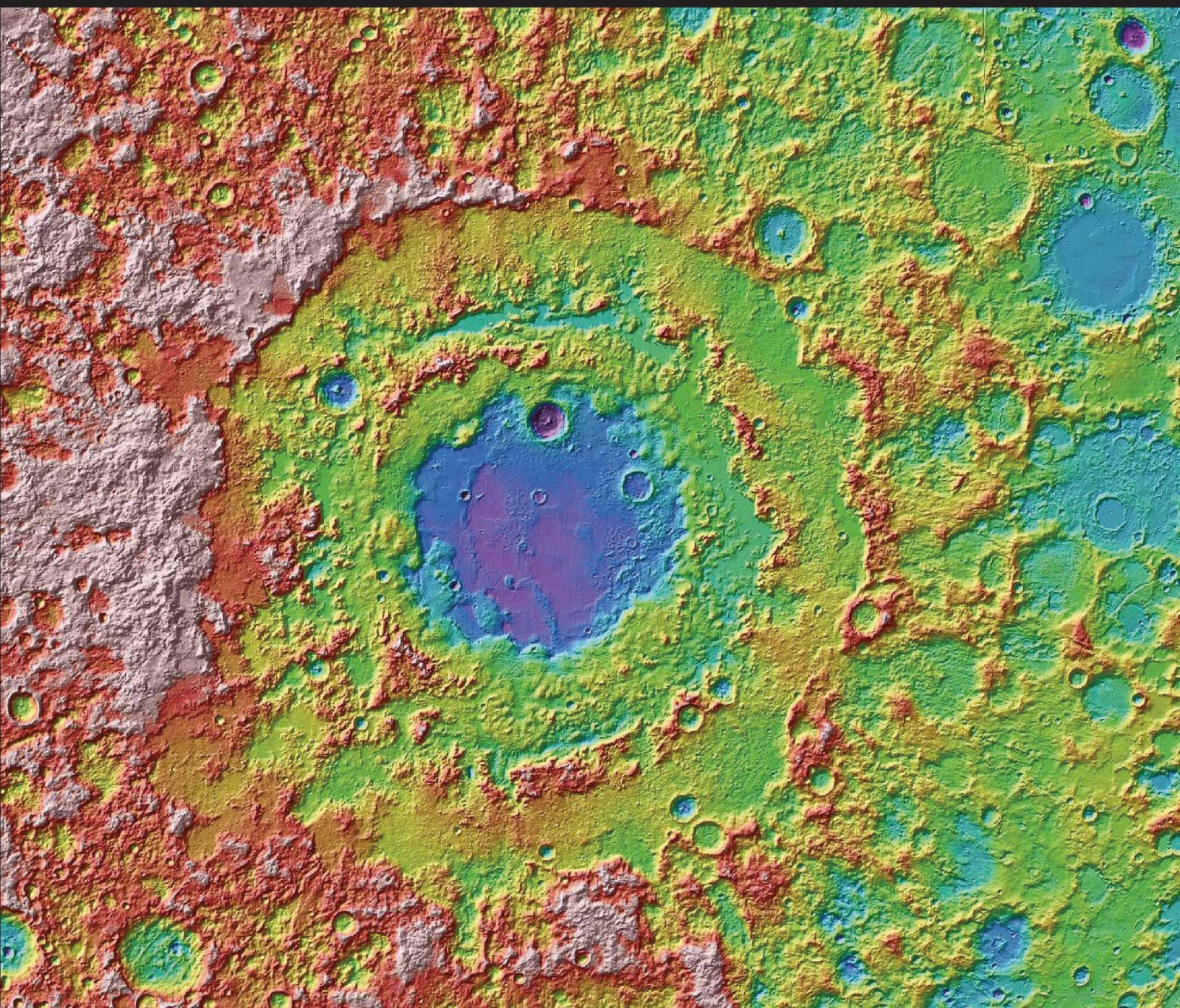

Recent Advances and Current Research Issues in Lunar Stratigraphy

edited by

William A. Ambrose
Bureau of Economic Geology
John A. and Katherine G. Jackson School of Geosciences
The University of Texas at Austin
University Station, Box X
Austin, Texas 78713-8924
USA

David A. Williams
School of Earth and Space Exploration
Arizona State University
Bateman Physical Sciences F506B
Tempe, Arizona 85287-1404
USA

THE
GEOLOGICAL
SOCIETY
OF AMERICA®

Special Paper 477

3300 Penrose Place, P.O. Box 9140 ▪ Boulder, Colorado 80301-9140, USA

2011

Published by The Geological Society of America, Inc.
3300 Penrose Place, P.O. Box 9140, Boulder, Colorado 80301-9140, USA
www.geosociety.org

Printed in U.S.A.

GSA Books Science Editors: Marion E. Bickford and Donald I. Siegel

Library of Congress Cataloging-in-Publication Data

Recent advances and current research issues in lunar stratigraphy / edited by William A. Ambrose and David A. Williams.
p. cm. — (Special paper ; 477)
Includes bibliographical references.
ISBN 978-0-8137-2477-5 (pbk. : alk. paper)
1. Lunar stratigraphy. I. Ambrose, William A. II. Williams, D. A. (David Andrew), 1951–.
QB592.R43 2011
559.9′1—dc22

2010051807

Cover: Lunar topographic map depicting the Orientale basin (930 km diameter), a multi-ringed basin that formed approximately 3.8 b.y. ago. The impact that formed the Orientale basin penetrated deeply into the lunar crust, ejecting millions of km^3 of material into surrounding areas. The topography is derived from more than 2.4 billion shots made by the Lunar Orbiter Laser Altimeter instrument on board the NASA *Lunar Reconnaissance Orbiter*. The inner basin floor, shown in purple, is more than 8 km deep with respect to the outer western basin rim shown in light pink. *Credit:* NASA, Goddard Space Flight Center, Massachusetts Institute of Technology, and Brown University, 2010.

10 9 8 7 6 5 4 3 2 1

Contents

The Geological Society of America
Special Paper 477
2011

Introduction

William A. Ambrose*
Bureau of Economic Geology, John A. and Katherine G. Jackson School of Geosciences, The University of Texas at Austin, University Station, Box X, Austin, Texas 78713-8924, USA

David A. Williams*
School of Earth and Space Exploration, Arizona State University, Bateman Physical Sciences F506B, Tempe, Arizona 85287-1404, USA

A succession of lunar missions in the previous 15 years—*Clementine* (NASA), *Lunar Prospector* (NASA), *SMART-1* (ESA), *SELENE/Kaguya* (JAXA), *Chang'e-1* (CNSA), Chandrayaan-1 (ISRO), and the *Lunar Reconnaissance Orbiter* (NASA)—are resulting in a greatly improved knowledge of lunar stratigraphy. These missions have targeted a variety of basins, highlands terrains, mare deposits, as well as the lunar poles, where current efforts are focused on detection and characterization of suspected deposits of water ice. This improved knowledge base will be valuable in supporting the return to the Moon in the upcoming decade, as well as leading to efficient development of lunar resources through a more precise characterization of their stratigraphic occurrence. Many planetary geologists are currently involved in seeking answers to problems in lunar stratigraphy, and their application to the current program of lunar exploration promises to be of great interest to the general scientific community.

Spacecraft observations have been key to understanding lunar stratigraphy. The first stratigraphic sequences and photogeologic maps of the Moon were developed based upon the pioneering work of Shoemaker and Hackman (1962), using telescopic images. Later maps made using *Lunar Orbiter* photographs provided a context for other geological and geophysical studies (e.g., the *Surveyor* program) in the 1960s, leading to the first geologic map of the whole nearside (Wilhelms and McCauley, 1971). This map and the lunar geologic timescale were developed by correlating relative ages from planetary mapping with absolute ages obtained from samples returned by the *Apollo*-manned landings. In fact, landing sites for the *Apollo*-manned missions were selected to verify the lunar stratigraphy and the nearside map. Wilhelms (1972) "codified" the techniques developed for geologic mapping of the Moon, which have been adapted to Mars, Venus, and the Galilean satellites of Jupiter in later systematic mapping programs.

Post-*Apollo* robotic missions have been designed either to fill data gaps in the Apollo data records (e.g., *Lunar Prospector*), or to apply existing ground-based techniques via new instruments to the previously unstudied lunar farside (e.g., *Clementine*), or to use more capable (i.e., higher spatial and spectral resolution) instruments to study the whole Moon, often as a measure of national prestige for new space-faring nations or unions: *SMART-1* (the European Union, via the European Space Agency [ESA]), *SELENE/Kaguya* (Japan), *Chang'e-1* (China), and *Chandrayaan-1* (India). As of this writing new insights into the Moon are just being published based on the data obtained by this international flotilla of lunar orbiters. For example, Haruyama et al. (2009) report, using crater counts performed on *SELENE/Kaguya's* Terrain Camera images of farside

*E-mails: william.ambrose@beg.utexas.edu, David.Williams@asu.edu.

Ambrose, W.A., and Williams, D.A., 2011, Introduction, *in* Ambrose, W.A., and Williams, D.A., eds., Recent Advances and Current Research Issues in Lunar Stratigraphy: Geological Society of America Special Paper 477, p. v–viii, doi:10.1130/2011.2477(00).

mare deposits, that most lunar mare farside volcanism ceased by ca. 3.0 Ga, but with a few areas of continued mare eruptions extending to ca. 2.5 Ga, lasting longer than previously considered.

The purpose of this Geological Society of America Special Paper is to highlight some of these key issues in lunar stratigraphy through presentation of chapters on several topical studies. Lunar stratigraphic relationships and issues relating to their resolution occur at a wide variety of scales—from the very largest scale (basins), to smaller scales (small basins, large craters, discrete highlands, and volcanogenic terrains), where detailed mapping of structural, volcanic, and impact-related features has led to a better understanding of three-dimensional (3-D) lunar stratigraphic relationships in areas where the chronological history has either been unknown or incomplete. Many of the investigations in this volume address at least six major questions regarding the Moon's origin and basin history, including (1) the lunar cataclysm hypothesis, (2) the timing and relative age of major basins such as the South Pole–Aitken basin versus the Procellarum system, (3) stratigraphic relationships of basins and mare-fill units within South Pole–Aitken, (4) recognition of cryptic basins from recent topographic data, leading to a more comprehensive lunar stratigraphic sequence, (5) internal mare stratigraphy and history of emplacement of volcanic strata in major basins, and (6) understanding the formation of lunar rilles through analysis of their final morphology, providing insight into both lunar volcanic processes and local stratigraphy.

This volume is highlighted by a comprehensive review of lunar mare stratigraphy by H. Hiesinger et al. Their review includes a discussion of the current status of age-dating issues in lunar mare stratigraphy, together with outstanding problems involving calibrating crater-frequency data with currently sparse radiometric age dates of mare-fill units. Their work concludes that maps of many homogeneous-count areas are not detailed enough or need to be based on spectral image criteria rather than poorly defined albedo criteria to yield accurate age estimates. Specifically, robust definitions of map units should be based on multispectral data combined with high-resolution photogeologic data (albedo-based mare-fill units) obtained from recent and current missions such as *SELENE* and *LRO (Lunar Reconnaissance Orbiter)*. Moreover, crater-count data should be reconciled with crater-degradation data. Another outstanding problem involves the ages of youngest basalt flows on the Moon that are still in need of better clarification, as with, for example, the suspected young (ca. 1 Ga or younger) mare-fill unit that may overlap crater Lichtenberg in Oceanus Procellarum.

A comprehensive study by Herbert Frey of large lunar basins from recent topographic data from the Unified Lunar Control Net 2005, based on *Clementine* laser altimetry and stereo imaging, suggests that several large basins exist on the Moon that have not been previously recognized by photogeologic mapping. These data indicate that the population of large basins >300 km in diameter could be at least two to three times greater than previously thought. Nearly all the new candidate basins are pre-Imbrium and many are likely pre-Nectarian. If these previously unrecognized basins occur in great numbers, one major implication from lunar stratigraphy is that the pre-Nectarian cratering flux should be revised upward. However, interpretations of previously unrecognized basins on the Moon, based on recognition of quasi-circular rims, are limited by the possibility of these topographic features having been molded and sculpted by ejecta from multiple impacts during the heavy bombardment phase, resulting in some of these circular-rim features in fact being spurious. This study concludes that the existence of these large basins should be tested with new topographic data from current missions including *SELENE/Kaguya*'s Terrain Camera and the LOLA (Lunar Orbiter Laser Altimeter) instrument package on *LRO*.

A series of three papers focuses on stratigraphic investigations in the South Pole–Aitken basin, including age relationships between this Pre-Nectarian basin and smaller, younger basins such as the Imbrian-age Schrödinger basin, as well as the stratigraphy of volcanic units in the extensive basin floor. Katie M. O'Sullivan et al. present a study that documents spatial and age relationships between the Schrödinger and South Pole–Aitken basins. This study addresses several important issues, including testing the lunar cataclysm hypothesis, refining age constraints on the beginning of basin-forming epoch on the Moon, as well as selecting specific sites in the South Pole–Aitken basin to assess both young and old areas to establish robust age dates.

Scott C. Mest also addresses major topics in stratigraphy in the Schrödinger basin and adjacent areas in a detailed mapping study using post–*Lunar Orbiter* data. By characterizing geologic units, recognizing contacts and structures, and identifying impact craters (D [diameter] > 2 km) for age-dating, he seeks to constrain ages of significant events in the geologic history of the lunar South Pole, to determine the timing and effects of major basin-forming impacts on crustal structure and stratigraphy, leading to an assessment of hydrogen and metal resources (e.g., H, Fe, Th) and their relationships to surface materials.

Noah E. Petro et al., in a third paper on the South Pole–Aitken basin, define and map a variety of geomorphic terrains in the northeastern region of South Pole–Aitken. This study concludes that cryptomare units in this region have a greater areal extent (by as much as a factor of three) than previously believed. This study also shows that, based on the cumulative number of craters within plains units, the cryptomare unit is older than other mare and plains units within South Pole–Aitken and is of a comparable age as a similar cryptomare deposit in Schickard crater. The study also concludes that the Plains South of Apollo may be the oldest basalts in the South Pole–Aitken basin, representing a unique locale within the basin.

The relationship between the South Pole–Aitken basin and structural and geochemical anomalies in the putative "nearside megabasin" in the Procellarum system is explored in a paper by Peter H. Schultz and David A. Crawford. Although the nearside megabasin could account for a sub-concentric and radial system of graben and ridges and geochemical anomalies associated with young features such as Ina, an alternative hypothesis is offered by Schultz and Crawford. They propose that an oblique collision for the South Pole–Aitken basin on the farside created the initial conditions that localized deep-seated and long-lasting weaknesses on the nearside. Their laboratory and computational experiments demonstrate that large oblique collisions generate asymmetric shock waves that converge in regions offset from a basin-center antipode. Damage from the collision that formed the South Pole–Aitken basin could have provided pathways for deep magma to reach shallow reservoirs, accounting for KREEP (potassium–rare earth elements–phosphorous) concentrations and anomalous, late-stage magmatic products. Their study concludes that future lunar missions should be designed to the proposed trajectory for South Pole–Aitken, its chronologic relationship with neighboring pre-Nectarian basins such as the Australe basin, and the consequences of focused seismic energy in antipodal regions through much higher-resolution topographic, geophysical, and geochemical data.

In addition to characterizing the stratigraphy and chronology of impact basins, important issues have yet to be resolved to unravel the complex stratigraphy of large sinuous rilles and the genesis of lunar volcanic provinces. The paper by W. Brent Garry and Jacob E. Bleacher in this volume addresses a variety of research topics regarding Vallis Schröteri in the Aristarchus Plateau. These topics include the need to (1) better understand the history of emplacement, involving multiple episodes; (2) determine more accurately the relation of volcanic units to pre-volcanic stratigraphy; and (3) evaluate the influences of structural framework as well as the substrate on rille morphology.

The chapters in this volume by no means address all the remaining problems that currently exist in lunar stratigraphy. For example, a recent study by Thomson et al. (2009) of mare stratigraphy in the Imbrium basin, based on observing relationships between crater types and depths of excavated substrate, suggests that the thickness of mare fill in the Imbrium basin is greater than previously inferred, with consequences for revising current estimates of thickness of mare-fill units in other lunar basins. Moreover, recognition of cryptomare with radar data suggests that late-stage extrusives are more widespread than previously believed (Campbell and Hawke, 2005; Campbell et al., 2007). Examples from the western margins of Oceanus Procellarum illustrate the need to re-define the limits of mare-fill units in large impact basins and therefore having to refine interpretations of age relationships between highlands and mare units, as well as having to adjust estimates of volumes of emplaced magmatic material.

Investigations continue in detailed mapping of lunar terrains with the goal of improving the differentiation of small secondary craters from primary craters, from which the lunar cratering flux can be re-calibrated. Both high-resolution photography with the LROC camera and radar data are crucial in these investigations. Related work is in progress in mapping crater rays in more detail, as well as observing asymmetries in their distribution, from which impact type and trajectory can be deduced. Recent work by Schultz et al. (2009) suggests that crater-ray morphometrics can be used to differentiate between asteroidal and cometary impacts, as well as reconstructing original impact velocities. Other work by Ambrose (2008) in recognizing and mapping large asymmetric secondary craters associated with large lunar basins has led to reinterpreting the ages of numerous extrabasinal landforms on the basis of superposition of these features and these secondaries, with consequences for locally refining chronostratigraphic relationships between Pre-Nectarian and Nectarian systems across a variety of lunar terrains.

Investigations are also currently underway in characterizing potential lunar resources such as polar water ice, volatiles and pyroclastic deposits with an array of instruments on *Chang'e-1*, *Chandrayaan-1*, and the *Lunar Reconnaissance Orbiter*. An important component of these investigations is to delineate the stratigraphic occurrence of water ice deposits. For example, mechanisms for stratigraphic entrapment and subsurface sequestration of water ice are incompletely understood. Moreover, a detailed knowledge of the form

of water ice (disseminated or layered), as well as its 3-D distribution, will have significant implications for resource development as well as optimizing future facilities and human settlements. These and other issues in lunar stratigraphy await presentation in upcoming volumes dedicated to lunar stratigraphy, a testimonial to the dynamic and ever-evolving nature of this scientific discipline.

References Cited

Ambrose, W.A., 2008, Origin, distribution and chronostratigraphy of asymmetric secondary craters associated with nearside lunar basins: Houston, Texas, Lunar and Planetary Institute, Lunar and Planetary Science Conference XXXIX, CD-ROM, abstract 1019.

Campbell, B.A., and Hawke, B.R., 2005, Radar mapping of lunar cryptomaria east of Orientale Basin: Journal of Geophysical Research, v. 110, E09002, doi:10.1029/2005JE002425, 12 p.

Campbell, B.A., Campbell, D.B., Margot, J.L., Ghent, R.R., Nolan, M., Chandler, C., Carter, L.M., and Stacy, N.J.S., 2007, Focused 70-cm wavelength radar mapping of the Moon: IEEE Transactions on Geoscience and Remote Sensing, v. 45, no. 12, p. 4032–4042.

Haruyama, J., Othake, M., Matsunaga, T., Honda, C., Yokota, Y., Abe, M., Ogawa, Y., Miyamoto, H., Iwasaki, A., Pieters, C.M., Asada, N., Demura, H., Hirata, N., Terazono, J., Sasaki, S., Saiki, K., Yamaji, A., Torii, M., and Josset, J.-L., 2009, Long-lived volcanism on the lunar farside revealed by SELENE Terrain Camera: Science, v. 323, p. 905–908, doi:10.1126/science.1163382.

Schultz, P.H., Anderson, J.B.L., and Hermalyn, B., 2009, Origin and significance of uprange ray patterns: Houston, Texas, Lunar and Planetary Institute, Lunar and Planetary Science Conference XL, CD-ROM, abstract 2496.

Shoemaker, E.M., and Hackman, R.J., 1962, Stratigraphic basis for lunar time scale, *in* Zopal, Z., and Mikhailov, K.Z., eds., The Moon: San Diego, California, Academic, p. 289–300.

Thomson, B.J., Grosfils, E.B., Bussey, D.B.J., and Spudis, P.D., 2009, A new technique for estimating the thickness of mare basalts in Imbrium Basin: Geophysical Research Letters, v. 36, L12201, doi:10.1029/2009GL037600, 5 p.

Wilhelms, D.E., 1972, Geologic mapping of the second planet: U.S. Geological Survey Interagency Report, Astrogeology 55, 36 p.

Wilhelms, D.E., and McCauley, J.F., 1971, Geologic map of the near side of the Moon: U.S. Geological Survey Map I-703, scale 1:5,000,000.

Printed in the USA

The Geological Society of America
Special Paper 477
2011

Ages and stratigraphy of lunar mare basalts: A synthesis

H. Hiesinger*
Institut für Planetologie, Westfälische Wilhelms-Universität, 48149 Münster, Germany, and
Department of Geological Sciences, Brown University, Providence, Rhode Island 02912, USA

J.W. Head III
Department of Geological Sciences, Brown University, Providence, Rhode Island 02912, USA

U. Wolf
R. Jaumann
Institute of Planetary Exploration, German Aerospace Center (DLR), 12489 Berlin, Germany

G. Neukum
Institut für Geologie, Geophysik, und Geoinformatik, Freie Universität Berlin, 12249 Berlin, Germany

ABSTRACT

The chronology of lunar volcanism is based on radiometric ages determined from *Apollo* and *Luna* landing site samples, regional stratigraphic relationships, and crater degradation and size-frequency distribution data for units largely defined prior to the end of the *Apollo* program. Accurate estimates of mare basalt ages are necessary to place constraints on the duration and the flux of lunar volcanism, as well as on the petrogenesis of lunar mare basalts and their relationship to the thermal evolution of the Moon. Here, we report on ages derived from crater size-frequency distribution measurements for exposed mare basalt units on the lunar nearside hemisphere. Crater size-frequency distribution measurements provide a statistically robust and accurate method to derive absolute model ages of unsampled regions on the Moon and other planetary surfaces. This paper summarizes and synthesizes results from our crater-counting efforts over more than 10 yr. We have dated basalts in Oceanus Procellarum, Imbrium, Serenitatis, Tranquillitatis, Humboldtianum, Australe, Humorum, Nubium, Cognitum, Nectaris, Frigoris, and numerous smaller occurrences like impact craters and sinus and lacus areas. Our investigations show that (1) in the investigated basins, lunar volcanism was active for almost 3 b.y., starting at ~3.9–4.0 b.y. ago and ceasing at ~1.2 b.y. ago, (2) most basalts erupted during the late Imbrian Period at ~3.6–3.8 b.y. ago, (3) significantly fewer basalts were emplaced during the Eratosthenian Period, and (4) basalts of possible Copernican age have been found only in limited areas in Oceanus Procellarum. Our results confirm and extend the general distribution of ages of mare basalt volcanism and further underscore the

*Hiesinger@uni-muenster.de

Hiesinger, H., Head, J.W., III, Wolf, U., Jaumann, R., and Neukum, G., 2011, Ages and stratigraphy of lunar mare basalts: A synthesis, *in* Ambrose, W.A., and Williams, D.A., eds., Recent Advances and Current Research Issues in Lunar Stratigraphy: Geological Society of America Special Paper 477, p. 1–51, doi:10.1130/2011.2477(01).

predominance of older mare basalt ages in the eastern and southern nearside and in patches of maria peripheral to the larger maria, in contrast to the younger basalt ages on the western nearside, i.e., in Oceanus Procellarum. New data from the recent international armada of lunar spacecraft will provide mineralogical, geochemical, morphological, topographic, and age data that will further refine our understanding of the flux of lunar mare basalts and their relation to petrogenetic trends and lunar thermal evolution.

INTRODUCTION

One of the major goals of stratigraphic investigations is to date geologic units, integrate them into a stratigraphic column that is applicable over the whole planet, and to calibrate this column with absolute ages. In preparation for and following the American and Russian lunar missions, extensive work on the lunar stratigraphy was conducted, for example, by Wilhelms (1970, 1987), Shoemaker and Hackman (1962), and Wilhelms and McCauley (1971). Based on this early work, we know that the lunar highlands are generally older than the mare regions (e.g., Wilhelms, 1987), that mare volcanism did not occur within a short time interval but instead shows a substantial range in ages (e.g., Shoemaker and Hackman, 1962; Carr, 1966), and that there is significant variation in the mineralogy of basalts of different ages (e.g., Soderblom et al., 1977; Pieters et al., 1980). Compared to Earth, we only have a small number of samples of the Moon that can help us to decipher its geologic history and evolution. For example, accurate radiometric ages for lunar mare basalts, which cover ~17% of the lunar surface (Head, 1976; Head and Wilson, 1992), are available only for the spatially very limited regions around the *Apollo* and *Luna* landing sites (e.g., BVSP, 1981; Stöffler and Ryder, 2001, and references therein). Because most lunar mare basalts remain unsampled, even after the *Apollo* and *Luna* missions (e.g., Pieters, 1978; Giguere et al., 2000), absolute radiometric age data for the majority of basalts are still lacking. Consequently, on the basis of the samples alone, the onset and extent of mare volcanism are not well understood (summarized by Nyquist et al., 2001). The returned samples indicate that mare volcanism was active at least between ca. 3.9 and 3.1 Ga (Head, 1976; Nyquist and Shih, 1992). Ages of some basaltic clasts in older breccias point to an onset of mare volcanism prior to 3.9 Ga (Ryder and Spudis, 1980), perhaps as early as 4.2–4.3 Ga in the *Apollo 14* region (Nyquist et al., 2001; Taylor et al., 1983; Dasch et al., 1987). Fortunately, we can derive relative and absolute model ages for unsampled regions with remote-sensing techniques. For example, inspection and interpretation of superposition of geologic units onto each other, embayment, and cross-cutting relationships within high-resolution *Apollo* and *Lunar Orbiter* images have been used to obtain relative ages for lunar surface units (e.g., Shoemaker and Hackman, 1962). In addition, it has been shown that crater degradation stages and crater size-frequency distribution measurements, calibrated to the landing sites, are useful to derive relative and absolute model ages (e.g., Hartmann, 1966; Greeley and Gault, 1970; Neukum et al., 1975a; Neukum and Horn, 1976; Boyce, 1976; Boyce and Johnson, 1978; Wilhelms, 1987; Neukum and Ivanov, 1994; Hiesinger et al., 2000, 2001, 2002, 2003, 2010; Morota et al., 2008; Haruyama et al., 2009).

The internal thermal history and evolution of a planetary body are reflected in the timing and extent of volcanism on its surface (Head and Wilson, 1992). Thus, investigations of the ages and compositions of volcanic products on the surface provide clues to the geologic and thermal evolution of a planet. Samples, remote-sensing data, and lunar meteorites indicate that volcanism was active early in lunar history. For example, dark-halo craters have been interpreted as impacts into basaltic deposits that are now buried underneath a veneer of basin or crater ejecta (e.g., Schultz and Spudis, 1979; Hawke and Bell, 1981; Antonenko et al., 1995). These underlying cryptomare basalts might be among the oldest basalts on the Moon, implying that volcanism was active prior to ~3.9 b.y. ago. Terada et al. (2007) argued that the lunar meteorite Kalahari 009 might represent a very low-Ti cryptomare basalt. Radiometric U-Pb age dating of phosphate grains associated with basaltic clasts in the lunar meteorite Kalahari 009 revealed that volcanism was already active at least 4.35 b.y. ago (Terada et al., 2007).

On the basis of crater degradation stages, Boyce (1976) and Boyce and Johnson (1978) derived absolute model ages that indicate volcanism might have lasted from 3.85 ± 0.05 b.y. until 2.5 ± 0.5 b.y. ago. Support for such young basalt ages comes from the lunar meteorite Northwest Africa (NWA) 032, which shows an Ar-Ar whole-rock age of ca. 2.8 Ga (Borg et al., 2007; Fagan et al., 2002). In addition, similar young ages for basaltic meteorites NWA 479 and several fragments of Lapaz Icefield (LAP) (02205, 02224, 02226, 02436, 03632, 04841) have been reported by Fernandes and Burgess (2006) and Fernandes et al. (2003). The ^{40}Ar-^{39}Ar plateau dating for NWA 479 yielded ages of 2.734 Ga (Fernandes and Burgess, 2006). Various techniques (Ar-Ar, Rb-Sr, Sm-Nd, U-Pb) applied to radiometrically date the LAP meteorites have revealed ages of 2.915–3.02 Ga (Shih et al., 2005; Fernandes and Burgess, 2006; Anand et al., 2006; Rankenburg et al., 2007), indicating that lunar volcanism was active later in lunar history than is documented in the *Apollo* and *Luna* sample collection.

Schultz and Spudis (1983) performed crater size-frequency distribution measurements for basalts embaying the Copernican crater Lichtenberg and concluded that these basalts might even

be younger than 1 b.y. old. However, on the basis of crater counts on *Lunar Orbiter IV* images, Hiesinger et al. (2003) derived older ages for the Lichtenberg basalts of 1.68 Ga, and even older ages of 2.20 Ga resulted from crater counts on *SELENE* Terrain Camera images (Morota et al., 2008).

Crater size-frequency ages for mare basalts on the lunar farside were derived, for example, by Haruyama et al. (2009). Haruyama et al. (2009) concluded that the majority of mare volcanism on the lunar farside ceased ~3.0 b.y. ago. However, they also identified mare deposits in several locations on the lunar farside (i.e., Antoniadi, Apollo N, Apollo S, Nishina, Mare Moscoviense) that show much younger ages, clustering at ca. 2.5 b.y. ago. Haruyama et al. (2009) argued that these young ages indicate that mare volcanism on the lunar farside lasted longer than was previously considered (e.g., Stuart-Alexander, 1978; Wilhelms et al., 1979; Walker and El-Baz, 1982; Wilhelms, 1987) and may have occurred episodically.

Here, we summarize and synthesize our ages for the majority of lunar nearside mare basalts exposed at the surface (Hiesinger et al., 2000, 2001, 2002, 2003, 2010). We have dated basalts in Oceanus Procellarum, Imbrium, Serenitatis, Tranquillitatis, Humboldtianum, Australe, Humorum, Nubium, Cognitum, Nectaris, Frigoris, and numerous smaller occurrences like impact craters and sinus and lacus areas (Fig. 1). Compared to previous studies (e.g., Hartmann, 1966; Greeley and Gault, 1970; Neukum et al., 1975a), we performed crater size-frequency distribution measurements for basalt units that are, to a first order, spectrally homogeneous. A major goal of this study is to provide absolute model ages of lunar nearside mare basalts in order to investigate their stratigraphy and to better understand the nature and evolution of lunar mare basalt volcanism.

On the basis of our crater size-frequency model ages, we address the following questions: (1) What was the time period of active lunar volcanism, i.e., when did volcanism start and when did it end? (2) Was lunar volcanism continuously active or are there distinctive periods of volcanic activity? (3) Is there a trend in the spatial distribution of basalt ages on the lunar surface? (4) What do the temporal distribution and abundance of mare basalts tell us about the role of mare volcanism in the crustal and thermal evolution of the Moon?

Figure 1. Map of the lunar surface showing the location of the investigated basins, the *Apollo* and *Luna* landing sites, and the location of selected features mentioned in the text. MV—Mare Vaporum, SM—Sinus Medii, PP—Palus Putredinis. Latitude, longitude grid is 30° × 30° wide; simple cylindrical projection. (from Hiesinger et al., 2010.)

TECHNIQUE, APPROACH, AND THE DEFINITION OF UNITS

Four methods have been used to derive the ages of lunar mare basalts, (1) radiometric investigations of lunar samples (e.g., Papanastassiou and Wasserburg, 1971; Tera and Wasserburg, 1974a, 1974b; Husain, 1974; Nunes et al., 1974; Schaefer and Husain, 1974; Maurer et al., 1978; Guggisberg et al., 1979; Ryder and Spudis, 1980; BVSP, 1981; Taylor et al., 1983; Dasch et al., 1987; Nyquist and Shih, 1992; Nyquist et al., 2001; Gaffney et al., 2008), (2) studies of crater degradation stages (e.g., Soderblom, 1972; Boyce, 1976; Boyce and Johnson, 1978), (3) stratigraphic approaches (e.g., Shoemaker and Hackman, 1962; Wilhelms, 1970; Wilhelms, 1987), and (4) crater size-frequency distribution measurements (e.g., Hartmann, 1966; Greeley and Gault, 1970; Neukum et al., 1975b; Neukum, 1977; Hiesinger et al., 2000, 2003, 2010).

Radiometric investigations of lunar rocks in the laboratory are restricted to a relatively small number of returned samples and provide ages only for the close vicinity of the *Luna* and *Apollo* landing sites. Data derived from crater degradation stages can give us ages for the entire lunar surface, but numerous endogenic and exogenic processes can influence the appearance of lunar impact craters, decreasing the certainty of age assignments. In addition, there are some discrepancies between crater degradation ages and radiometric ages for specific landing sites. Burgess and Turner (1998), for example, reported young radiometric ^{40}Ar -^{39}Ar ages (3.2–3.3 Ga) for the *Luna 24* landing site, which are in disagreement with ages derived from crater degradation measurements (3.5 ± 0.1 Ga) by Boyce and Johnson (1978). For the *Luna 24* landing site, Burgess and Turner (1998) concluded that crater degradation ages have to be reassessed in light of the new expanded radiometric age data. Using the ejecta blankets of impact craters as a stratigraphic marker horizon, Wilhelms (1987) was able to construct a moonwide relative stratigraphy by investigating superposition of ejecta blankets on each other. Additional application of the superposition criteria to mare basalt units (e.g., Head, 1976; Whitford-Stark, 1979; Whitford-Stark and Head, 1980) provided relative ages for the entire lunar surface and is one of the most important tools in geologic mapping and the interpretation of geologic processes on the Moon.

Crater size-frequency distribution measurements are a powerful remote-sensing technique to derive relative and absolute model ages of unsampled planetary surfaces. Since this technique is described elsewhere (e.g., Neukum and Ivanov, 1994; Hiesinger et al., 2000, 2003, 2010; Stöffler and Ryder, 2001; Neukum et al., 2001; Ivanov, 2001; Hartmann and Neukum, 2001; Stöffler et al., 2006; and references therein), we will only briefly outline how crater size-frequency distribution measurements can be used to date surfaces. The technique of crater size-frequency distribution measurements on spectrally homogeneous regions, including a discussion of model assumptions, strengths, and shortcomings, and an error analysis, has been described in detail by Hiesinger et al. (2000). In short, in order to obtain the age of a photogeological unit, one has to (1) measure the surface area of the unit, and (2) measure the diameters of each primary impact crater within this unit. Obtained crater diameters are sorted into 18 bins per diameter decade (i.e., in the interval $1 \le D \le 10$, we have the steps 1.0, 1.1, 1.2, 1.3, 1.4, 1.5, 1.7, 2.0, 2.5, 3.0, 3.5, 4.0, 4.5, 5.0, 6.0, 7.0, 8.0, 9.0, 10.0) and plotted as cumulative distributions (e.g., Arvidson et al., 1979), which give the number of craters larger than or equal to a certain diameter per area measured.

It has been shown that lunar crater distributions measured on geologic units of different ages and in overlapping crater diameter ranges can be aligned along a complex continuous curve, the lunar production function (e.g., Neukum, 1983; Neukum and Ivanov, 1994; Neukum et al., 2001). The lunar production function is given by an eleventh-degree polynomial

$$\log(N_{\mathrm{cum}}) = a_0 + \sum_{k=1}^{11} a_k \, (\log(D))^k, \qquad (1)$$

where a_0 represents the amount of time over which the unit has been exposed to the meteorite bombardment (Neukum, 1983; Neukum and Ivanov, 1994; Neukum et al., 2001). Compared to the production function of Neukum (1983), which we used for our previous age determinations (Hiesinger et al., 2000, 2001, 2002, 2003), Neukum et al. (2001) slightly reworked their production function for the larger-crater part. This resulted in a new set of coefficients for Equation 1, which are given in Table 1. The cumulative crater density of a geologic unit taken at a fixed reference diameter (usually 1 or 10 km) is directly related to the time the unit has been exposed to the meteorite flux and therefore gives a relative age of this unit.

One of the major geologic goals of the *Apollo* missions was to return lunar samples that could be dated in the laboratory with radiometric techniques (e.g., Rb-Sr, Sm-Nd, Ar-Ar). To obtain absolute model ages from crater size-frequency distribution measurements, one has to link the radiometric ages from the returned *Apollo* and *Luna* samples to crater counts of these landing sites

TABLE 1. COEFFICIENTS IN EQUATION 1*

Coefficient	"Old" *N*(D) (Neukum, 1983)	"New" *N*(D) (Ivanov et al., 2001; Neukum et al., 2001)
a0	–3.0768	–3.0876
a1	–3.6269	–3.557528
a2	+0.4366	+0.781027
a3	+0.7935	+1.021521
a4	+0.0865	–0.156012
a5	–0.2649	–0.444058
a6	–0.0664	+0.019977
a7	+0.0379	+0.086850
a8	+0.0106	–0.005874
a9	–0.0022	–0.006809
a10	-5.18×10^{-4}	$+8.25 \times 10^{-4}$
a11	$+3.97 \times 10^{-5}$	$+5.54 \times 10^{-5}$

*From Neukum et al. (2001).

in order to establish the lunar cratering chronology (e.g., BVSP, 1981; Neukum, 1983; Strom and Neukum, 1988; Neukum and Ivanov, 1994; Stöffler and Ryder, 2001). For this purpose, crater counts for the *Apollo 11*, *12*, *14*, *15*, *16*, *17*, and the *Luna 16* and *24* landing sites were performed and correlated with the corresponding radiometric ages of these sites (e.g., BVSP, 1981; Neukum, 1983; Strom and Neukum, 1988; Neukum and Ivanov, 1994; Stöffler and Ryder, 2001). However, this is not a trivial task and has led to several more or less different chronologies (e.g., BVSP, 1981; Neukum, 1983; Neukum and Ivanov, 1994; Stöffler and Ryder, 2001; Stöffler et al., 2006; and references therein). It is well known that lunar samples of each landing site show a range of radiometric ages, which is due to an unknown combination of vertical and horizontal mixing (BVSP, 1981). For example, if the investigated sample is a breccia, the individual particles can reflect very different geologic histories and reset ages. For breccia 73215, Jessberger et al. (1977) reported variations in the K-Ar ages of up to 300 m.y., and this raises the issue of which radiometric age should be assigned to the corresponding crater size-frequency distribution. In principle, there are two possibilities for correlating crater size-frequency distributions with radiometric ages, i.e., the correlation with the most frequently measured age (e.g., Neukum and Ivanov, 1994; Neukum, 1983; Neukum et al., 1975a) or with the youngest age (e.g., Jessberger et al., 1974; BVSP, 1981; Wilhelms, 1987). Neukum (1983) and Neukum and Ivanov (1994) argued that the "peak age" is the age that most likely reflects the major event/impact that reset the radiometric clocks of most samples, whereas the youngest age might only represent smaller local impacts that occurred after the main impact. The reasoning for adopting the peak age is discussed in greater detail by Neukum and Ivanov (1994).

For the discussion of the basalt stratigraphy, it is not crucial whether the peak age or the youngest radiometric age is used for the correlation with the crater counts of the landing sites. To a first order, this will only result in a shift of all absolute model ages; the relative stratigraphy of the basalt units is not affected. However, the laterally extensive ejecta deposits of Nectaris, Imbrium, Eratosthenes, and Copernicus have been used for the definition of the lunar stratigraphic systems (e.g., Wilhelms, 1987). Based on assumptions about the particular sample of a certain *Apollo* landing site that represents the ejecta material of these basins and craters, absolute ages have been assigned to the chronostratigraphic systems (e.g., Wilhelms, 1987; Neukum, 1983; Neukum and Ivanov, 1994). Therefore, for the discussion of absolute model ages of basalt units and the application of terms like "Eratosthenian" or "Imbrian," the reader must be aware of the differences in the definition of the chronostratigraphic systems (e.g., Wilhelms, 1987; Neukum and Ivanov, 1994) (Fig. 2). In our papers (Hiesinger et al., 2000, 2003, 2010), we adopted the system of Neukum and Ivanov (1994), with Nectaris having an age of 4.1 ± 0.1 Ga ($N[D = 1\text{ km}] = [1.2 \pm 0.4] \times 10^{-1}$), and the Imbrium basin being 3.91 ± 0.1 b.y. old ($N[D = 1\text{ km}] = [3.5 \pm 0.5] \times 10^{-2}$). According to Neukum (1983), the Eratosthenian System started ~3.2 b.y. ago ($N[D = 1\text{ km}] = 3.0 \times 10^{-3}$) and the Copernican System began at 1.5 b.y. ago ($N[D = 1\text{ km}] = [1.3 \pm 0.3] \times 10^{-3}$), while radiometric dating of samples, which are thought to represent Copernicus ejecta, indicates an age of 0.85 ± 0.1 Ga (Silver, 1971) or even 0.80 Ga (Eberhardt et al., 1973; Alexander et al., 1976) (Fig. 2).

The linkage of lunar sample ages to discreet basin-forming events is still subject to discussion (e.g., Wilhelms, 1987; Spudis, 1993; Neukum and Ivanov, 1994; Stöffler and Ryder, 2001). For example, based on their reevaluation of lunar samples, Stöffler and Ryder (2001) concluded that the Nectaris basin is 3.92 ± 0.03 b.y. old, and hence younger than in the Neukum and Ivanov (1994) chronology. This interpretation by Stöffler and Ryder (2001) is consistent with the conclusions of Spudis (1993). For the Imbrium basin, Stöffler and Ryder (2001) discussed two ages, ranging from 3.85 ± 0.02 Ga to 3.77 ± 0.02 Ga, the latter age being inconsistent with previously published ages of 3.80–3.85 Ga for the Orientale basin (e.g., Wilhelms, 1987; Schaefer and Husain, 1974). From this discussion, we conclude that the ages of individual lunar impact basins are still under discussion (e.g., James, 1981; Wetherill, 1981; Deutsch and Stöffler, 1987; Wilhelms, 1987; Stadermann et al., 1991; Neukum and Ivanov, 1994; Stöffler and Ryder, 2001; Stöffler et al., 2006). From a literature search for ages of specific lunar basins, we conclude that the basin ages derived with the lunar chronology of Neukum (1983) and Neukum and Ivanov (1994) are well within the range of previously published ages (Table 2), and we adopt these ages for the present paper.

The empirically derived chronology of Neukum and Ivanov (1994) and Neukum et al. (2001), which we use for our studies, is given by

$$N_{cum}(D \geq 1\text{ km}) = 5.44 \times 10^{-14} [\exp(6.93 \times t) - 1] + 8.38 \times 10^{-4}\, t. \quad (2)$$

A variety of techniques have been applied in order to correlate crater frequencies with radiometric ages. Neukum and Wise (1976) and Neukum and Ivanov (1994) compared the impact chronologies of several authors (Baldwin, 1971, 1974, 1987; Soderblom and Boyce, 1972; Hartmann, 1972; Soderblom et al., 1974; Neukum, 1971, 1977, 1983; Neukum and Ivanov, 1994) and found that the interpretations of these authors all coincide within a factor of 2–3. Once the lunar chronology is established, we can derive absolute model ages for the entire lunar surface from crater size-frequency distribution measurements by solving Equation 2 for time t for $N_{cum}(D \geq 1\text{ km})$ measured on the geologic unit to be dated.

A crucial prerequisite for reliable age determinations using crater size-frequency distribution measurements is the mapping of homogeneous count areas. The mare regions of the Moon have been previously geologically mapped by several authors (e.g., Wilhelms and McCauley, 1971; Wilhelms, 1968, 1987; Wilhelms and El-Baz, 1977; Holt, 1974; McCauley, 1967, 1973; Howard and Masursky, 1968; Schmitt et al., 1967; Eggleton, 1965; Trask and Titley, 1966; Hackman, 1962, 1966; Marshall, 1963; Moore, 1965, 1967; M'Gonigle and Schleicher, 1972; Wilshire, 1973; Scott et al., 1977; Titley, 1967; Schaber, 1969;

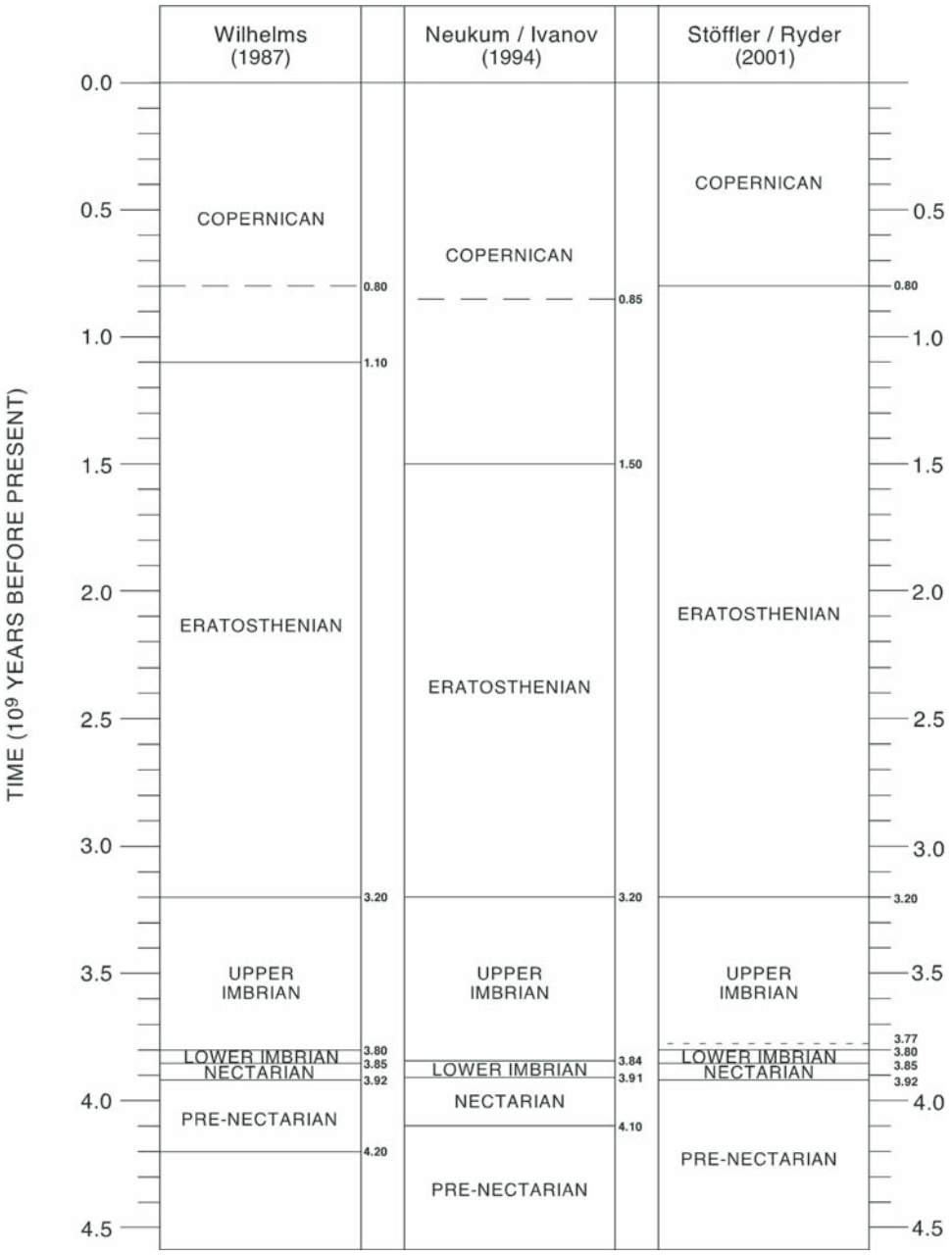

Figure 2. Comparison of stratigraphies of Wilhelms (1987), Neukum and Ivanov (1994), and Stöffler and Ryder (2001). Dashed lines in the stratigraphies of Wilhelms (1987) and Neukum and Ivanov (1994) indicate radiometric ages, which these authors attribute to the formation of the crater Copernicus. In Stöffler and Ryder (2001), two formation ages for the Imbrium basin have been proposed, that is, 3.85 Ga and 3.77 Ga (dashed line). (from Hiesinger et al., 2010.)

TABLE 2. ABSOLUTE MODEL AGES OF LUNAR IMPACT BASINS IN BILLION YEARS (Ga)*

Basin	Baldwin (1974)	Baldwin (1987)	Jessberger et al. (1974)	Maurer et al. (1978)	Schaefer and Husain (1974)	Nunes et al. (1974)	Wilhelms (1987)	Neukum (1983)	Stöffler and Ryder (2001)
Orientale	3.80	3.82	–	–	3.85	3.85	3.80	3.84	–
Imbrium	3.95	3.85	3.87–3.90	3.88	4.00	3.99	3.85	3.92	3.85 (3.77)
Crisium	4.05	4.00	3.90	†	4.13	4.13	3.84	–	3.89 (3.84)
Nectaris	4.21	4.07	3.98	3.98	4.20	4.2	3.92	4.10	3.92 (3.85)
Serenitatis	4.25	4.14	3.97	§	–	4.45?	3.87	3.98	3.89 (3.87)
Humorum	4.25	4.23	3.92–3.95	–	4.13–4.20	4.13–4.2	#	3.99	–

*Modified from Baldwin (1987).
†Between Imbrium and Nectaris.
§Older than Nectaris.
#Between Nubium and Imbrium.

Ulrich, 1969; Scott and Eggleton, 1973; Lucchitta, 1972, 1978; Karlstrom, 1974; Scott et al., 1977). However, because the definition of geologic units in these maps was based mainly on albedo differences, morphology, and qualitative crater densities on telescopic and *Lunar Orbiter* images, these maps are not detailed enough to ensure homogeneity of the investigated basalts. It is known that regional spectral differences of surface materials can be mapped by using ratios of various spectral bands to bring out diagnostic spectral features (e.g., Whitaker, 1972; McCord et al., 1976; Johnson et al., 1977a, 1977b; Pieters, 1978; Head et al., 1993). Regions where the spectral signature is homogeneous can be interpreted as surface mare units that are relatively uniform in surface composition, and thus may plausibly be interpreted to represent single eruptive episodes. Thus, we used a multispectral high-resolution *Clementine* color ratio composite (e.g., 750/415 ratio as red, 750/950 ratio as green, and 415/750 ratio as blue) in order to map the distribution of distinctive basalt units (Fig. 3A). In this color scheme, variations in the extended visible continuum slope are shown as red (high 750/415) to blue (high 415/750) variations. These ratios are interpreted to reflect variations in soil or surface material maturity (e.g., Pieters, 1993, and references therein). Variations in the 1 μm region of the electromagnetic spectrum add yellow and green hues for larger 750/950 values. This implies stronger 1 μm absorptions, flatter continuum slope, or both. The depth of the 1 μm absorption band is correlated with the Fe abundance (e.g., Pieters, 1993, and references therein). Thus, most of the spectral variation within an image is captured by this color ratio composite (Pieters et al., 1994). Because this color ratio emphasizes subtle spectral differences, it was used to visually determine the boundaries of our spectrally homogeneous units. We did not apply stringent statistical techniques to ensure accurate outlines of these spectral units because this is not too critical for our study since our count areas are usually only subsets of each spectral unit, i.e., the count areas are located somewhere within the spectral units. For our count areas, we selected only regions with visually homogeneous color. For the definition of our spectral units, we also used the information from U.S. Geological Survey (USGS) geologic maps (e.g., Wilhelms and McCauley, 1971), as well as other previously published maps (e.g., Schaber, 1973; Schaber et al., 1976; Pieters, 1978; Whitford-Stark and Head, 1980; Whitford-Stark, 1990), in order to incorporate all relevant information for our unit definition. Visually, these older morphologic and spectral maps correlate well with our definition of spectral units. However, we expanded on these previous studies by defining many more units in previously uncharted regions. We assume that because of the spectral homogeneity, each of our spectrally defined units represents a single eruptive phase. We define "single eruptive phase" as consisting of all deposits that were emplaced within a reasonably short period of time with similar composition. Such a single eruptive phase may consist of a single basalt flow or of several breakout flows forming during the same eruption. Having defined such units in *Clementine* images, we transferred the unit boundaries to high-resolution *Lunar Orbiter IV* images in order to measure the crater size-frequency distribution. This was necessary because *Clementine* images are not very well suited for crater counts due to their high sun angles. Figure 4 is a comparison of a *Lunar Orbiter* image and a *Clementine* image, and it illustrates the differences in the ability to detect small craters in these two data sets. The detailed views show that some craters that are clearly visible in the *Lunar Orbiter* image are barely detectable and certainly not countable in the *Clementine* image. Because miscounting certain craters has profound effects on the quality of the crater size-frequency distribution measurement, and hence the age of an investigated unit, we chose not to perform crater counts on *Clementine* material. Despite their excellent quality, we also chose not to count on *Apollo* metric camera or panoramic images because only *Lunar Orbiter* images provide a systematic coverage of all investigated mare areas. Compared to previous age determinations, our data fit spectral and lithological units and represent a major improvement in accuracy.

The method of crater size-frequency measurements is generally dependent on the quality, i.e., the spatial resolution and the illumination conditions, of the images on which the crater counts are performed. Contrast, brightness, and resolution of the images used for crater counts are important parameters because all can have influence on the detectability of craters, especially on dark mantle deposits. In our studies, we relied on high-resolution imaging data provided by the *Lunar Orbiter IV* mission in 1967 to determine lunar surface ages. Even more than 40 years after the *Lunar Orbiter IV* mission, its images, with a spatial resolution of 60–150 m, an incidence angle of 10°–30°, and excellent contrast, are still extremely well suited and useful for the acquisition of crater size-frequency distributions. However, new images from the American *Lunar Reconnaissance Orbiter*, the Chinese *Chang'e*, the Japanese *SELENE/Kaguya*, and the Indian *Chandrayaan* missions will soon supersede the *Lunar Orbiter* images in spatial resolution, coverage, and illumination geometry, allowing us to globally perform highly accurate crater counts.

Potential errors in the determination of relative ages using crater size-frequency distribution measurements can be caused by several factors. Errors in the determination of the size of the measured area, errors in the determination of crater diameters on monoscopic images, and errors caused by volcanic craters are negligible (Neukum et al., 1975b; Engel, 1986). Errors introduced by different crater sizes due to differences in target material are irrelevant because we dated only lunar mare basalts. Therefore, it is reasonable to assume that the physical properties (i.e., density) that might influence the crater size are very similar for all these basalts. Neukum et al. (1975b) discussed the influence of factors such as flooding, blanketing, secondary cratering, superposition, infilling, abrasion, mass wasting, and volcanic craters in great detail. Secondary craters form from ejected material of a primary crater and hence are not correlated to the impact rate. Most of those secondary craters can be readily identified and excluded from crater counts by their appearance in clusters, crater chains, elongated or irregular outline, and the herringbone pattern of their ejecta (Oberbeck and Morrison, 1973; Pike, 1980; Melosh,

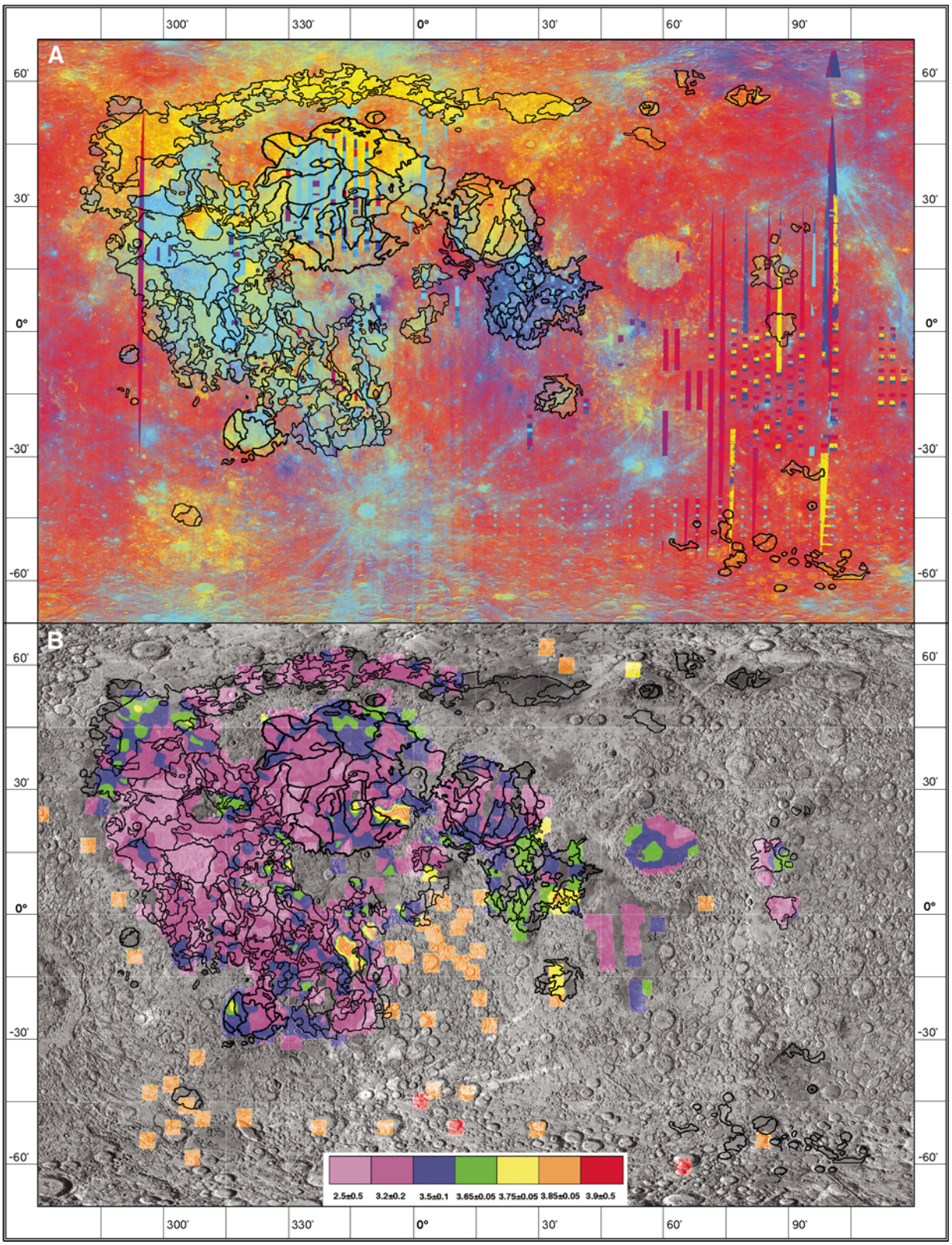

Figure 3. (A) Color ratio composite image based on three spectral ratios of *Clementine* imaging data (750/415 on red, 750/950 on green, 415/750 on blue). Black lines define spectral units. We have performed crater size-frequency distribution measurements for most of these units. Map coverage: ~90°W–120°E, ~75°S–75°N; latitude, longitude grid is 15° × 15° wide. (B) Crater degradation ages of lunar nearside surface units (Boyce, 1976; Boyce and Johnson, 1978). Ages are in billion years. Black lines outline spectrally homogeneous units (also see part A). Map coverage: ~90°W–120°E, ~75°S–75°N; latitude, longitude grid is 15° × 15° wide. (from Hiesinger et al., 2010.)

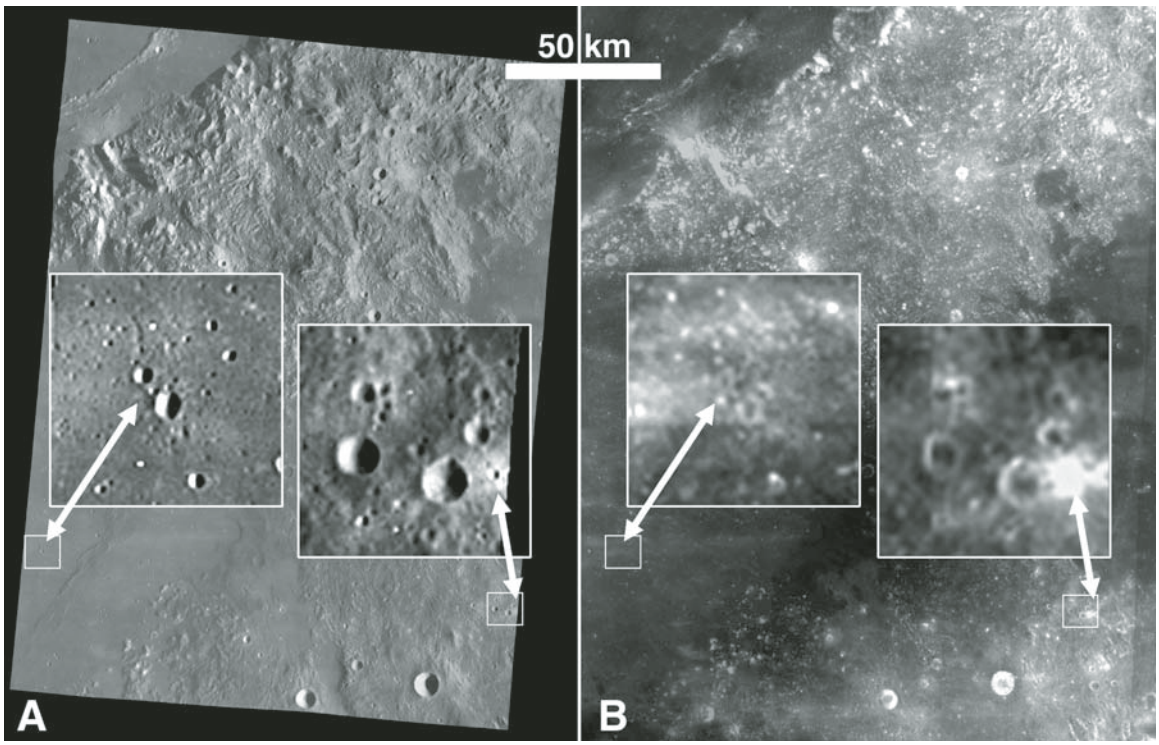

Figure 4. Comparison between *Lunar Orbiter IV* 109H2 (A) and *Clementine* (B) image of the Rima Bode area for the purpose of crater size-frequency distribution measurements (Hiesinger et al., 2003). Two examples of craters clearly measurable in the lower-sun *Lunar Orbiter* image are either barely visible or saturated in the high-sun *Clementine* image. This would yield incorrect crater statistics and less reliable ages. The *Lunar Orbiter* image has been subjected to a Fast Fourier transformation in order to remove the stripes and has been map-projected. A detailed description of the image processing of the *Lunar Orbiter* data is given by Gaddis et al. (2001).

1989). However, Bierhaus et al. (2005) raised concerns about the influence of secondary craters on the dating of the surface of the Jovian moon Europa, and based on findings for the Martian crater Zunil, McEwen (2003) and McEwen et al. (2005) discussed the effects of secondary cratering on crater size-frequency age determinations. McEwen et al. (2005) and Preblich et al. (2007) studied the 10-km-diameter Martian crater Zunil and found that this crater produced ~10^7 secondary craters in the size range of 10–200 m that extend up to 1600 km away from crater. McEwen et al. (2005) concluded that the production functions of Hartmann and Neukum (2001) overpredict primary craters smaller than a few hundred meters in diameter by a factor of 2000, similar to the conclusions of McEwen and Bierhaus (2006). McEwen et al. (2005) concluded that crater counts for craters <1 km in diameter are dominated by secondary craters and therefore do not yield reliable age determinations.

A solid argument that the observed steep −3 to −3.5 distribution of small craters results from small primary projectiles stems from observations of the Main Belt asteroid 951 Gaspra, which shows such a steep distribution down to the smallest measureable crater diameters (Neukum and Ivanov, 1994; Chapman et al., 1996a, 1996b). Secondary impact craters are less likely to occur on Gaspra because, due to its low gravity, ejected material will not re-impact the surface but will leave the body. In addition, observations of near-Earth asteroids (NEA) yield steep size distributions very similar to lunar crater size distributions (Werner et al., 2002). Finally, observations by Malin et al. (2006) indicate that the number of newly formed Martian craters agrees within a factor of 2–3 with the cratering rate of Hartmann and Neukum (2001). Malin et al. (2006) reported on 20 Martian impacts 2–150 m in diameter created between May 1999 and March 2006. They concluded that the values predicted by models that scale the lunar cratering rate to Mars are close to the observed rate (Malin et al., 2006). Therefore, Hartmann (2007a) argued that the new observations of Malin et al. (2006), if correct, are inconsistent with suggestions by McEwen (2003), McEwen et al. (2005), Bierhaus et al. (2005), and McEwen and Bierhaus (2006) that small craters must be dominated by secondary craters by factors of ~10^2–10^3. Werner et al. (2006) and Neukum et al. (2006) argued that less than 5% of craters smaller than 1 km in diameter are secondary craters and hence do not have a significant effect on the ages derived with crater counts. König (1977), Hartmann (2005), Werner (2006), Werner et al. (2006), Neukum et al. (2006), Hartmann et al. (2008), and Wagner et al. (2010) discussed the issue of secondary cratering and its influence on crater size-frequency ages in more detail and came to the conclusion

that secondary cratering does not pose a significant problem for dating of planetary surfaces using crater size-frequency distribution measurements. While the effect of secondary impact cratering on the production function of small craters is a matter of ongoing debate (e.g., Hartmann, 2007a, 2007b), it is of lesser importance for our crater counts because the spatial resolution of the *Lunar Orbiter IV* images of 60–100 m (Wilhelms, 1987) only allowed us to count craters larger than ~300–400 m, and these smallest craters were not even used for the determination of our ages.

The level of uncertainty of the crater retention age of a given count is given by the following equation:

$$\pm\sigma_N = \log\left[\frac{N(1)\pm\sqrt{N(1)}}{A}\right], \quad (3)$$

in which $N(1)$ is the crater retention age calculated for craters of 1 km diameter, and A is the size of the counted area. The $\pm\sigma_N$ value gives the upper and lower limits of the error bar of the crater retention age, which are used for estimating the uncertainty of the absolute crater model age from the cratering chronology. We principally assumed that the cratering chronology is free of errors. Therefore, errors in our absolute model ages are only caused by errors in the determination of crater frequencies (Neukum, 1983). Neukum et al. (1975a) estimated the systematic uncertainty of the standard distribution curve or the measurement to be <10% for 0.8 km ≤ D ≤ 3 km (this is the diameter range of most of our crater counts) and up to 25% for 0.8 km ≤ D ≤ 10 km.

In order to facilitate the discussion of our model ages, we avoided assigning type locality names to each unit. Instead, we rely on a simple letter/number system. The letter indicates the basin (A—Australe, H—Humorum, Hu—Humboldtianum, I—Imbrium, S—Serenitatis, T—Tranquillitatis, P—Oceanus Procellarum, N—Mare Nubium, C—Mare Cognitum, IN—Mare Insularum, F—Mare Frigoris, V—Mare Vaporum, Ma—Mare Marginis, Sy—Mare Smythii, SM—Sinus Medii, LT—Lacus Temporis, LA—Lacus Aestatis, PP—Palus Putredinis, CGr—Grimaldi, CCr—Crüger, CRo—Rocca A, CSc—Schickard, CHu—Hubble, CJo—Joliot, CGo—Goddard), and the number describes the unit within a basin. In a style similar to the geologic maps of the Moon, lower numbers reflect older units, and higher numbers indicate a younger age.

RESULTS

Oceanus Procellarum

Based on our crater size-frequency distributions, we conclude that basalt model ages in Oceanus Procellarum range from ca. 1.2 to ca. 3.93 Ga (Hiesinger et al., 2003) (Fig. 5; Table 3). Sixteen units, that is ~25% of all dated units, show characteristic kinks in their crater size-frequency distributions, which have been interpreted by Neukum and Horn (1976) to indicate resurfacing, i.e., flooding with subsequent lavas.

In Oceanus Procellarum, we dated 60 units. Using the chronostratigraphic system of Neukum and Ivanov (1994), basalts of 19 units are Imbrian in age. For three of these 19 units, we were able to detect late-stage flooding events during the Imbrian Period. Thirty-six units in Oceanus Procellarum are Eratosthenian in age, and 13 of them also show older Imbrian ages. Finally, if we apply the chronostratigraphic system of Neukum and Ivanov (1994), five basalt units are of Copernican age. If one uses the chronostratigraphic system of Wilhelms (1987) or Stöffler and Ryder (2001), these basalts would be of Eratosthenian age (Fig. 2).

Earlier attempts to measure the ages of surface units relied on crater degradation stages (e.g., Boyce, 1976; Boyce and Johnson, 1978). Crater degradation ages of Boyce (1976) and Boyce and Johnson (1978) were performed for 1/4° squares (~8 km), were interpolated by spatial filtering into a continuous image, and do not necessarily fit lithological or spectral units (Fig. 3B). While units P1, P18, P20, P21, P22, P23, P29, P30, P31, P32, P36, P38, P41, P44, P48, P50, and P59 exhibit a single degradation age, all other units show at least two, and some units (P10, P13) show up to four different ages in the map of Boyce and Johnson (1978). The implication is that ages derived from the map of Boyce and Johnson (1978) can vary up to 1.25 b.y. for a single spectral unit. In numerous cases (P2, P3, P4, P8, P9, P11, P13, P14, P17, P24, P26, P27, P34, P35), the ages of Boyce (1976) and Boyce and Johnson (1978) give us an upper and lower boundary, and our ages are either right in between or close to one or the other boundary (Table 3). In other cases (P1, P5, P7, P10, P15, P16, P19, P33), the spatially most abundant age of Boyce (1976) and Boyce and Johnson (1978) is similar to our age of a particular unit. Generally, we find a good agreement of our ages with ages of Boyce (1976) and Boyce and Johnson (1978) for units of Imbrian age. Only units P6 and P12 appear to be older than in the maps of Boyce (1976) and Boyce and Johnson (1978). Ages of units that are young according to our data are systematically overestimated in age (older) in the Boyce map (P25, P28, P39, P43, P46, P47, P49, P51, P55, P56, P57, P58, P60), and we find less agreement for younger units, i.e., late Eratosthenian and Copernican units. Units P40, P45, P52, and P53 show evidence for resurfacing, with both ages bracketing or being similar to the Boyce ages. Finally, units P37, P42, and P54 are not covered in the Boyce map.

Units P1, P2, P3, P4, P5, and P7 were mapped as Imbrian in age in the geologic maps of Wilhelms and McCauley (1971), Moore (1965), McCauley (1967), and Lucchitta (1978). Our data confirm an Imbrian age for these units and also confirm Wilhelms and McCauley's Imbrian ages for units P10, P14, and P16. Lucchitta (1978) mapped unit P6 as Eratosthenian, and Scott et al. (1977) mapped several units (P3, P9, P10, P12, P14, P15, P16, P18, P19) as Imbrian and/or Eratosthenian in age. Our data only show Imbrian ages and no Eratosthenian ages for these units. For unit P8, P9, P11, P12, P14, P15, P17, P18, and P19, Eratosthenian

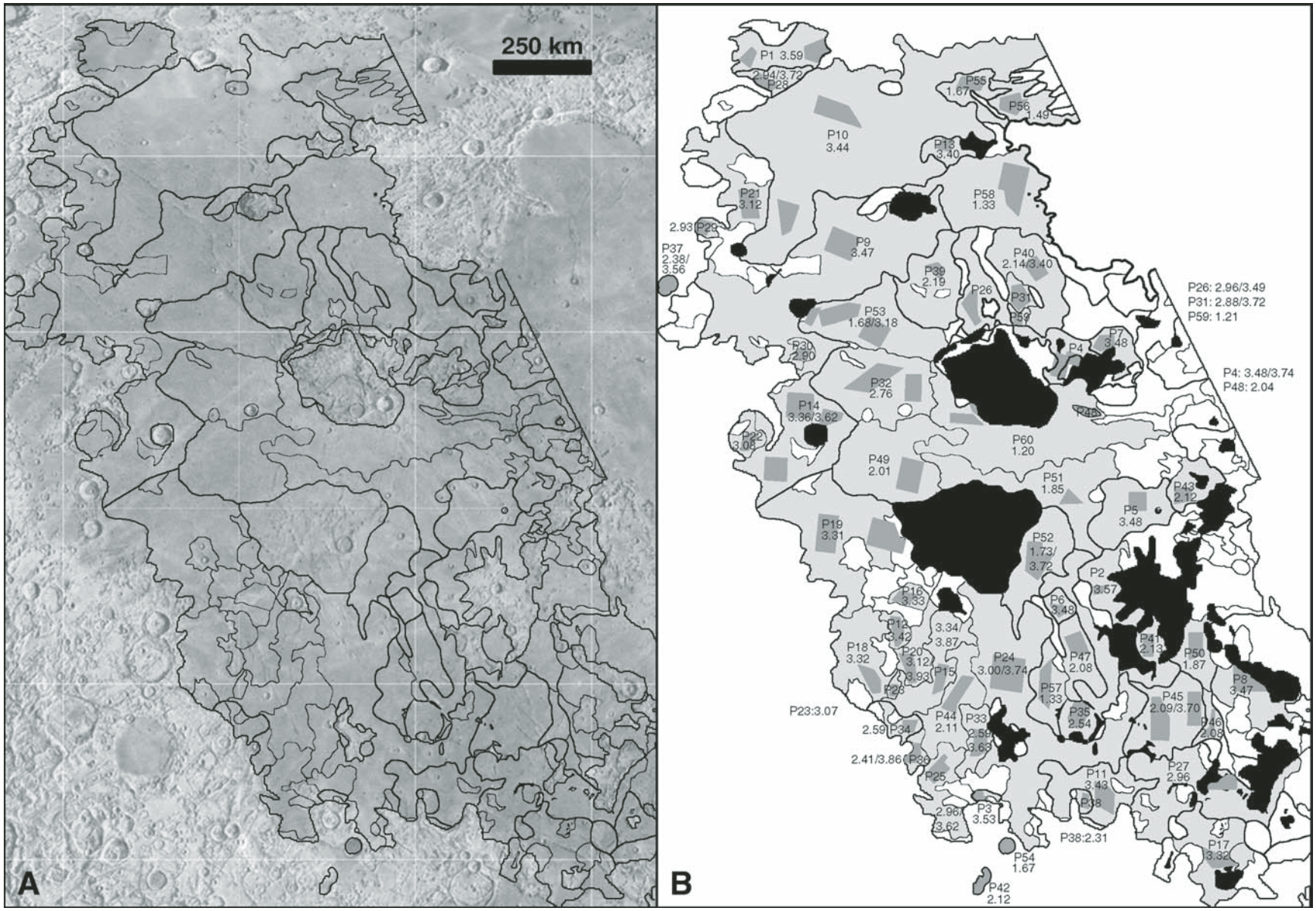

Figure 5. Spatial distribution of model ages for spectrally defined units in Oceanus Procellarum (Hiesinger et al., 2003). (A) U.S. Geological Survey shaded relief map, simple cylindrical map projection. Spectral units are outlined in black. (B) Sketch map of Oceanus Procellarum showing unit numbers and model ages in billion years (also see Table 3). Crater size-frequency distribution measurements were performed for the areas highlighted in dark gray. Black areas are non-mare materials or have been excluded from this investigation.

TABLE 3. COMPARISON OF AGES FOR BASALTS IN OCEANUS PROCELLARUM*

Unit	*Lunar Orbiter* image	Area (km^2)	Crater retention age *N*(1)	Error	Model age (Ga)	Error (b.y.)	Boyce (1976)	Wilhelms and McCauley (1971)	Moore (1965)	Moore (1967)	Marshall (1963)	Hackman (1962)	McCauley (1967)	McCauley (1973)	Wilshire (1973)	Titley (1967)	Scott and Eggleton (1973)	Ulrich (1969)	Scott et al. (1977)	Lucchitta (1978)
P60	IV157H3	1429	1.01E–03	+0.26E–03/ –0.30E–03	1.2	+0.32/ –0.35	3.2, 2.5, 3.5	Im	Ipm	Ipm									Elm	
P59	IV158H1	789	1.01E–03	+0.34E–03/ –0.35E–03	1.21	+0.40/ –0.42	3.2	Im	Ipm	Ipm							Im			
P58	IV158H2	2551	1.11E–03	+0.17E–03/ –0.21E–03	1.33	+0.19/ –0.25	3.2, 3.5, 3.65	Em, Im									Em, Im		Elm	
P57	IV150H1	2631	1.12E–03	+0.41E–03/ –0.08E–03	1.33	+0.49/ –0.08	2.5, 3.2, 3.5													
P56	IV170H3	1765	1.25E–03	+0.41E–03/ –0.46E–03	1.49	+0.49/ –0.55	2.5, 3.2	Em, Im										Elm		Em
P55	IV170H3	1057	1.40E–03	+0.44E–03/ –0.46E–03	1.67	+0.52/ –0.55	3.2, 3.5													
P54	IV149H2	1118	1.40E–03	+0.49E–03/ –0.50E–03	1.67	+0.58/ –0.59	no age	Em			Pm			Em						
P53	IV170H1	5886	1.40E–03/ 2.88E–03	+0.26E–03/ –0.09E–03 +0.20E–03/ –0.20E–03	1.68/ 3.18	+0.30/ –0.12 +0.08/ –0.10	2.5, 3.2	Em, Im		Cmd, Ipm, Ipmd							Em, Im		Elm	
P52	IV150H2	4075	1.45E–03/ 1.17E–02	+0.23E–03/ –0.26E–03 +0.67E–03/ –2.57E–03	1.73/ 3.72	+0.29/ –0.31 +0.08/ –0.05	2.5, 3.2	Em, Im				Pm								
P51	IV144H2	1357	1.55E–03	+0.31E–03/ –0.29E–03	1.85	+0.37/ –0.34	3.2, 2.5	Im, Em	Ipm										Elm	
P50	IV133H1	2000	1.56E–03	+0.48E–03/ –0.20E–03	1.87	+0.56/ –0.25	2.5	Em, Im				Pm								
P49	IV157H2	4822	1.63E–03	+0.31E–03/ –0.36E–03	2.01	+0.37/ –0.43	2.5, 3.2, 3.5	Im, Em		Ipmd, Ipm									Elm	
P48	IV144H3	1091	1.71E–03	+0.39E–03/ –0.45E–03	2.04	+0.46/ –0.54	3.5	Im	Ipm											
P47	IV144H1	1665	1.74E–03	+0.55E–03/ –0.32E–03	2.08	+0.65/ –0.39	2.5, 3.2	Im			Pm	Pm								
P46	IV132H3	1076	1.74E–03	+0.50E–03/ –0.56E–03	2.08	+0.58/ –0.67	3.2, 2.5	Im			Pm									
P45	IV137H3	5666	1.75E–03/ 1.03E–02	+0.24E–03/ –0.11E–03 +0.54 E–02/ –0.20E–02	2.09/ 3.70	+0.28/ –0.14 +0.08/ –0.05	2.5, 3.2	Im, Em			Pm									
P44	IV156H3	3245	1.77E–03	+0.39E–03/ –0.39E–03	2.11	+0.47/ –0.47	3.2	Im					Ipm, Ipmd	Im					Elm	
P43	IV138H2	1426	1.78E–03	+0.72E–03/ –0.77E–03	2.12	+0.82/ –0.91	2.5, 3.2, 3.5	Im, Em	Ipm											
P42	IV156H2	698	1.78E–03	+0.49E–03/ –0.53E–03	2.12	+0.58/ –0.63	no age	Em							Em					
P41	IV138H1	1786	1.79E–03	+0.64E–03/ –0.72E–03	2.13	+0.75/ –0.85	2.5	Im				Pm								
P40	IV158H1	3266	1.79E–03/ 3.80E–03	+0.48E–03/ –0.50E–03 +0.56E–03/ –0.66E–03	2.14/ 3.40	+0.56/ –0.60 +0.07/ –0.12	3.2, 2.5, 3.5	Im	Ipm								Im			

(*Continued*)

TABLE 3. COMPARISON OF AGES FOR BASALTS IN OCEANUS PROCELLARUM* (*Continued*)

Unit	*Lunar Orbiter* image	Area (km^2)	Crater retention age *N*(1)	Error	Model age (Ga)	Error (b.y.)	Boyce (1976)	Wilhelms and McCauley (1971)	Moore (1965)	Moore (1967)	Marshall (1963)	Hackman (1962)	McCauley (1967)	McCauley (1973)	Wilshire (1973)	Titley (1967)	Scott and Eggleton (1973)	Ulrich (1969)	Scott et al. (1977)	Lucchitta (1978)
P39	IV163H2	2298	1.83E–03	+0.46E–03/ –0.52E–03	2.19	+0.53/ –0.62	2.5, 3.2, 3.5	Em, Im		Ipm							Im, Em		Elm	
P38	IV143H2	1127	1.93E–03	+0.47E–03/ –0.49E–03	2.31	+0.53/ –0.60	3.2	Im, Em			Pm									
P37	IV183H1	1091	1.99E–03/ 5.82E–03	+0.30E–03/ –0.25E–03 +0.86E–03/ –0.75E–03	2.38/ 3.56	+0.34/ –0.31 +0.04/ –0.04	no age												Elm	
P36	IV156H3	1082	2.02E–03/ 2.54E–02	+0.38E–03/ –0.39E–03 +1.94E–02/ –0.47E–02	2.41/ 3.86	+0.43/ –0.46 +0.09/ –0.04	3.2	Im						Im					Elm	
P35	IV143H3	3441	2.13E–03	+0.26E–03/ –0.14E–03	2.54	+0.29/ –0.17	3.2, 2.5	Im, Em			Pm	Pm								
P34	IV156H3	1118	2.17E–03	+0.69E–03/ –0.71E–03	2.59	+0.59/ –0.85	3.2, 2.5	Em						Em					Elm	
P33	IV156H3	1855	2.18E–03/ 7.51E–03	+0.15E–03/ –0.15E–03 +1.73E–03/ –1.40E–03	2.59/ 3.63	+0.18/ –0.17 +0.04/ –0.06	2.5, 3.2	Im						Im					Elm	
P32	IV157H3 IV162H3	6475	2.32E–03	+0.33E–03/ –0.15E–03	2.76	+0.30/ –0.18	2.5	Im		Ipm, Ipmd									Elm	
P31	IV158H1	1719	2.44E–03/ 1.17E–02	+0.69E–03/ –0.16E–03 +0.58E–02/ –0.22E–02	2.88/ 3.72	+0.39/ –0.17 +0.08/ –0.04	3.2	Im									Im			
P30	IV169H3	583	2.46E–03	+0.36E–03/ –0.32E–03	2.9	+0.26/ –0.35	2.5	Im		Ipm									Elm	
P29	IV183H2	1546	2.49E–03	+0.37E–03/ –0.32E–03	2.93	+0.25/ –0.34	3.2												Elm	
P28	IV183H3	840	2.51E–03/ 1.14E–02	+0.66E–03/ –0.33E–03 +0.66E–02/ –0.21E–02	2.94/ 3.72	+0.34/ –0.34 +0.08/ –0.05	3.65, 3.5													Im
P27	IV132H3	2135	2.52E–03	+0.88E–03/ –0.17E–03	2.96	+0.38/ –0.17	3.2, 2.5, 3.5	Im, Em			Pm									
P26	IV158H1	2309	2.53E–03/ 4.62E–03	+0.61E–03/ –0.33E–03 +1.06E–03/ –0.69E–03	2.96/ 3.49	+0.32/ –0.34 +0.06/ –0.07	2.5, 3.2	Im		Ipm, Ipmd									Elm	
P25	IV156H3	2176	2.52E–03/ 7.46E–03	+0.77E–03/ –0.16E–03 +1.11E–03/ –1.39E–03	2.96/ 3.62	+0.35/ –0.17 +0.04/ –0.05	3.5, 3.2	Im, Em						Im, Em					Elm	
P24	IV150H1	6330	2.58E–03/ 1.27E–02	+0.58E–03/ –0.17E–03 +0.84E–02/ –0.18E–02	3.00/ 3.74	+0.28/ –0.15 +0.09/ –0.04	3.2, 2.5; 3.5	Im, Em					Ipm, Ipmd	Im						
P23	IV157H1	513	2.67E–03	+0.19E–03/ –0.18E–03	3.07	+0.11/ –0.14	2.5	Em						Em, Im					Elm	
P22	IV169H3	925	2.68E–03	+0.40E–03/ –0.18E–03	3.08	+0.18/ –0.14	2.5			Ipmd, Ipm									Elm	
P21	IV183H2	2725	2.75E–03	+0.40E–03/ –0.19E–03	3.12	+0.16/ –0.13	3.5												Elm	

(*Continued*)

TABLE 3. COMPARISON OF AGES FOR BASALTS IN OCEANUS PROCELLARUM* (*Continued*)

Unit	*Lunar Orbiter* image	Area (km^2)	Crater retention age *N*(1)	Error	Model age (Ga)	Error (b.y.)	Boyce (1976)	Wilhelms and McCauley (1971)	Moore (1965)	Moore (1967)	Marshall (1963)	Hackman (1962)	McCauley (1967)	McCauley (1973)	Wilshire (1973)	Titley (1967)	Scott and Eggleton (1973)	Ulrich (1969)	Scott et al. (1977)	Lucchitta (1978)
P20	IV157H1	1702	2.74E–03/ 3.94E–02	+0.50E–03/ –0.50E–03 +2.61E–02/ –0.74E–02	3.12/ 3.93	+0.18/ –0.45 +0.08/ –0.03	3.2	Em, Im					lpm, lpmd						Elm	
P19	IV162H2 IV169H2	8051	3.27E–03	+0.23E–03/ –0.22E–03	3.31	+0.05/ –0.06	3.2, 3.5, 2.5	Em, Im					lpmd, lpm, Cca						Elm	
P18	IV162H1	1874	3.31E–03	+0.49E–03/ –0.23E–03	3.32	+0.08/ –0.06	2.5	Em					lpmd, Cca	Em, Im					Elm	
P17	IV132H2	2909	3.30E–03	+0.79E–03/ –0.42E–03	3.32	+0.08/ –0.14	3.5, 3.2	Em			Pm					lpm3, lpm4				
P16	IV157H1	1108	3.36E–03	+0.60E–03/ –0.13E–03	3.33	+0.08/ –0.05	3.2, 3.5, 2.5	Im					lpm, Cre						Elm	
P15	IV156H3	1662	3.43E–03/ 2.75E–02	+0.51E–03/ –0.44E–03 +0.41E–02/ –0.51E–02	3.34/ 3.87	+0.08/ –0.11 +0.02/ –0.03	3.2, 3.5	Em, Im					lpm, lpmd	Im					Elm	
P14	IV162H3 IV169H2 IV169H3	7939	3.50E–03/ 7.35E–03	+0.37E–03/ –0.39E–03 +2.85E–03/ –1.38E–03	3.36/ 3.62	+0.05/ –0.09 +0.07/ –0.05	2.5, 3.2, 3.5	Em, Im		lpmd, lpm									Elm	
P13	IV163H2	1120	3.76E–03	+1.19E–03/ –0.70E–03	3.4	+0.11/ –0.15	3.65, 3.5, 3.2, 3.75	Im									Im			Im
P12	IV157H1	1807	3.97E–03	+1.09E–03/ –0.51E–03	3.42	+0.10/ –0.07	2.5, 3.2	Em					lpmd, lpm, Cca						Elm	
P11	IV143H2	2383	4.00E–03	+1.12E–03/ –0.52E–03	3.43	+0.09/ –0.08	3.2, 3.5	Im, Em			Pm									
P10	IV175H3	8419	4.08E–03	+0.83E–03/ –0.52E–03	3.44	+0.07/ –0.07	3.5, 3.2, 3.65, 2.5	Im									Im		Elm	Im
P9	IV170H2	3808	4.45E–03	+0.71E–03/ –0.56E–03	3.47	+0.08/ –0.06	3.2, 3.5	Em, Im									Em, Im		Elm	
P8	IV132H3	2525	4.44E–03	+1.32E–03/ –0.83E–03	3.47	+0.08/ –0.09	2.5, 3.5, 3.2	Em			Pm									
P7	IV144H3	1774	4.48E–03	+1.20E–03/ –1.08E–03	3.48	+0.07/ –0.14	3.5, 3.2	Im	lpm											
P6	IV144H1	884	4.52E–03	+1.68E–03/ –1.09E–03	3.48	+0.10/ –0.14	3.2, 2.5	Im				Pm								Em
P5	IV138H2	1792	4.57E–03	+1.30E–03/ –0.67E–03	3.48	+0.08/ –0.06	3.5, 3.2, 2.5	Im	lpm			Pm								
P4	IV151H1	1327	4.49E–03/ 1.29E–02	+1.19E–03/ –0.84E–03 +0.67E–02/ –0.39E–02	3.48/ 3.74	+0.07/ –0.10 +0.07/ –0.07	3.65, 3.5, 3.2	Im	lpm											
P3	IV149H3	718	5.26E–03	+1.97E–03/ –0.98E–03	3.53	+0.09/ –0.07	3.2, 3.5, 2.5	Im						Im					Elm	
P2	IV144H1	862	6.10E–03	+2.10E–03/ –1.47E–03	3.57	+0.08/ –0.08	3.2, 3.5, 2.5	Im				Pm								
P1	IV183H3	2269	6.47E–03	+1.53E–03/ –1.62E–03	3.59	+0.05/ –0.09	3.5													Im

*See text for details. Read 2.68E–03 as 2.68×10^{-3}.

or Eratosthenian/Imbrian ages are shown in the map of Wilhelms and McCauley (1971). However, our data indicate that these units are Imbrian in age, consistent with the mapping of McCauley (1967, 1973), Moore (1967), Titley (1967), Scott and Eggleton (1973), and Lucchitta (1978). Our crater counts do not confirm an Eratosthenian age for parts of unit P9, as shown in the map of Scott and Eggleton (1973). Our data do not agree with the map of McCauley (1967) that units P12, P16, P18, and P19 are partially of Copernican age, nor with the map of McCauley (1973), which shows that unit P18 is partially of Eratosthenian age.

Several units for which we determined an Eratosthenian age (P23, P34, P42, P54) are also mapped as Eratosthenian in age in the map of Wilhelms and McCauley (1971). Numerous units exhibit Eratosthenian and Imbrian ages in this map, and using our crater size-frequency distribution measurements, we obtained Eratosthenian ages for all these units (P20, P24, P25, P27, P35, P38, P39, P43, P45, P49, P50, P51, P52, P53). Wilhelms and McCauley (1971) mapped 12 units as Imbrian in age, but our data indicate an Eratosthenian age for these units (P26, P30, P31, P32, P33, P36, P40, P41, P44, P46, P47, P48). The geologic map of Scott et al. (1977) attributes Eratosthenian and/or Imbrian ages to units that we found to be of Eratosthenian age (P20, P21, P22, P23, P25, P26, P29, P30, P32, P33, P34, P36, P37, P39, P44, P49, P51, P53). Several other geologic maps show Imbrian ages for the units that, according to our crater counts, are Eratosthenian in age, i.e., units P20–P55. For example, Moore (1965) found Imbrian ages for units P40, P43, P48, and P51, and in the map of Moore (1967), six units (P22, P26, P30, P32, P39, P49) show Imbrian ages, and one unit (P53) is partially Imbrian and Copernican in age. Imbrian ages are also indicated for units P20, P24, and P44 in the map of McCauley (1967), and for unit P28 (Lucchitta, 1978), as well as for units P31, P39, P40, and P53 (Scott and Eggleton, 1973). However, significant parts of units P39 and P53 were also mapped as Eratosthenian in age, consistent with our dating. Finally, in the map of McCauley (1973), units P24, P33, P36, and P44 are Imbrian and units P23 and P25 are Imbrian and Eratosthenian in age. Our crater counts confirm an Eratosthenian age for unit P34 and unit P54. The map of Wilshire (1973) indicates an Eratosthenian age for unit P42, consistent with our age for this unit.

As mentioned earlier, for the application of terms like "Copernican" or "Eratosthenian" in an absolute sense, the reader must be aware that there is no formal definition of the Copernican system (Wilhelms, 1987) and that the chronostratigraphic systems of different authors vary in the beginning of the Copernican system (e.g., Wilhelms, 1987; Neukum and Ivanov, 1994; Stöffler and Ryder, 2001; Hawke et al., 2004). These differences are reviewed elsewhere (e.g., Hiesinger et al., 2000; Stöffler and Ryder, 2001). For our studies, we adopted the chronostratigraphic system of Neukum and Ivanov (1994). According to this chronostratigraphic system, our crater counts revealed Copernican ages for five units (P56, P57, P58, P59, P60). Application of the Wilhelms (1987) and the Stöffler and Ryder (2001) models would indicate Eratosthenian ages for these units. These units were mapped partially as Eratosthenian and Imbrian (P56, P58) or as Imbrian (P59, P60) by Wilhelms and McCauley (1971). Imbrian ages for units P59 and P60 are also shown in the maps of Moore (1965, 1967) and for units P58 and P59 in the map of Scott and Eggleton (1973). This map also shows an Eratosthenian age for unit P58. Ulrich (1969) and Lucchitta (1978) found Eratosthenian ages for unit P56, and Scott et al. (1977) mapped units P58 and P60 as Eratosthenian and/or Imbrian in age. A summary of this discussion of our units in the context of the geological maps of the U.S. Geological Survey and the Boyce ages is given in Table 3.

Mare Imbrium

In the Imbrium basin (1160 km in diameter; Spudis, 1993), we dated 30 spectrally defined units showing basalt ages between 2.01 and 3.57 Ga (Hiesinger et al., 2000). In our data, we observed a trend showing western basalts in Mare Imbrium slightly younger than eastern basalts. As in Mare Serenitatis, we observed a broad range of ages varying at least 1.5 Ga, which indicates an extremely long period of volcanic activity in these two basins (Fig. 6). On the basis of their crater size-frequency counts (for diameters >500 m), Bugiolacchi and Guest (2008) reported that for most of their mare basalts, crater count ages range between 3.5 and 5.5×10^{-2} per km^2, or 2.3–3.3 Ga.

In our data, ~52% of all units in Mare Imbrium exhibit ages of 3.3–3.6 Ga, with all other units younger than 3.3 Ga but older than 2.6 Ga, except unit I29, which is 2.26 Ga, and unit I30, which is 2.01 Ga. We conclude that the largest number of basalts erupted in the period 3.3–3.6 b.y. ago and that volcanism went on with a significantly lower intensity until ca. 2.6 Ga. We observed a weak bimodal distribution of basalt ages with peaks at 3.3–3.4 Ga and 3.5–3.6 Ga, thus indicating that volcanism was not continuously active with equal intensity over longer periods of time but shows phases with higher and lower levels of activity. During each of those periods with intensified volcanic activity, 20% of the dated basalt units were emplaced.

Young lava flows, originating near Euler β and flowing northward across the Imbrium basin for 1200 km, were studied by Schaber (1973). These youngest lava flows in central Imbrium consist of three distinctive phases and were previously mapped as Eratosthenian in age by Schaber (1973). However, our data show that at least one of those basalts (unit I7) is of Imbrian age, consistent with observations of Wilhelms (1987).

Table 4 shows that for a single spectrally defined unit, a broad variety of crater degradation ages (Boyce, 1976; Boyce and Johnson, 1978) can be extracted. Only three units (I23, I24, I27) exhibit only one age in the Boyce data, whereas all other units are characterized by two or more ages. In four units (I5, I6, I8, I17), our data match the most abundant Boyce ages. In 12 other units (I3, I7, I9, I10, I11, I12, I13, I15, I19, I20, I26, I28), the crater degradation ages of Boyce and Johnson (1978) mark an upper and lower boundary, with our data in between. Unit I28, mapped by Schaber (1969), and units I19, I20, I29, and

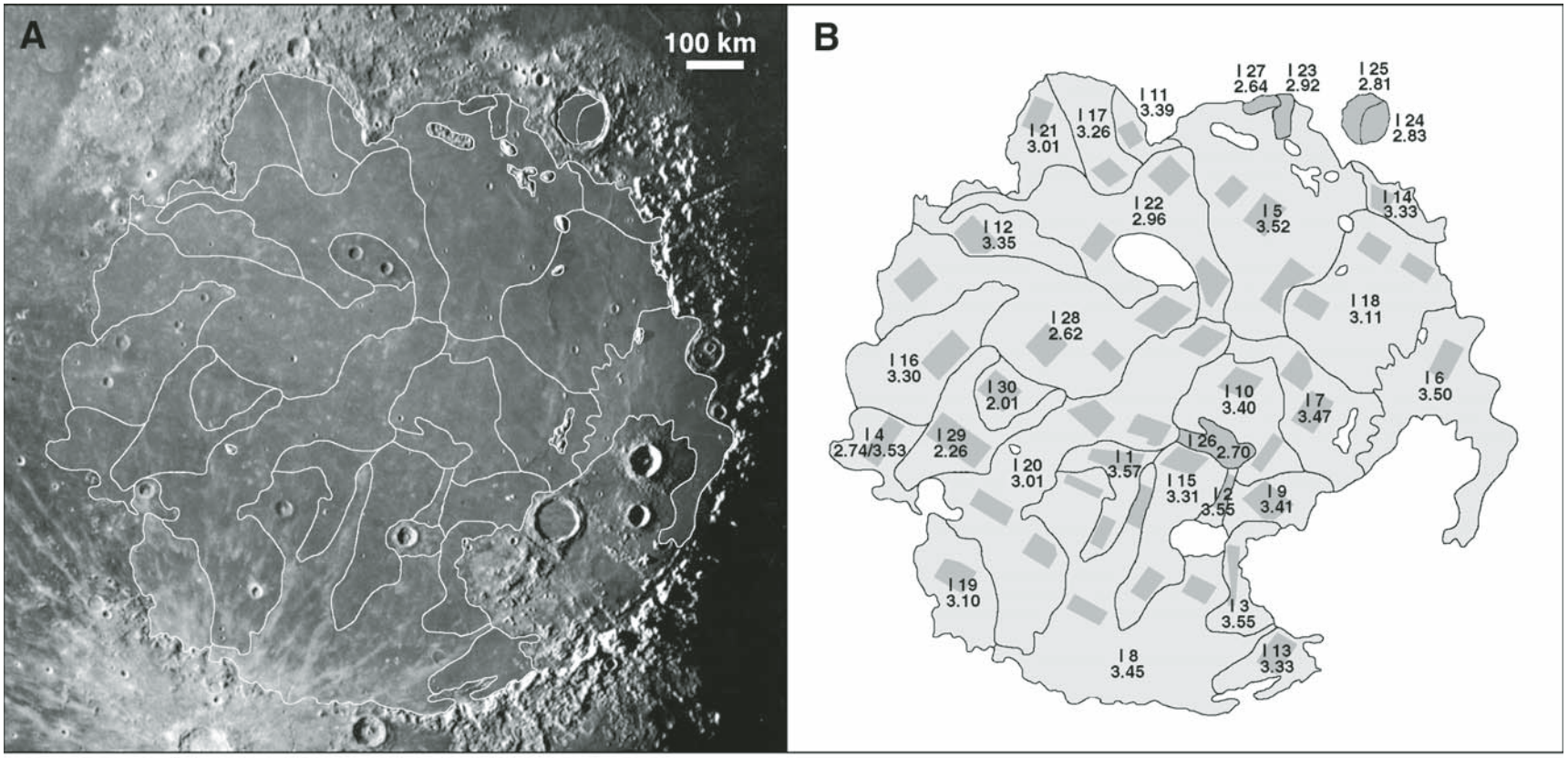

Figure 6. Spatial distribution of model ages for spectrally defined units in Mare Imbrium (Hiesinger et al., 2000). (A) Telescopic view (detail of Mount Wilson Observatory photograph 257). Spectral units are outlined in white. (B) Sketch map of Mare Imbrium showing unit numbers and model ages in billion years (also see Table 4). Crater size-frequency distribution measurements were performed for the areas highlighted in dark gray.

TABLE 4. COMPARISON OF AGES FOR BASALTS IN MARE IMBRIUM*

Unit	*Lunar Orbiter* image	Area (km^2)	Crater retention age *N*(1)	Error	Model age (Ga)	Error (b.y.)	Boyce (1976)	M'Gonigle and Schleicher (1972)	Schaber (1969)	Carr (1965)	Moore (1965)	Hackman (1966)	Page (1970)
I30	IV-134H1	3108	1.68E–03	+0.12E–03/ –0.11E–03	2.01	+0.14/ –0.14	2.5/3.2			Ipm			
I29	IV-134H1	5093	1.89E–03	+0.14E–03/ –0.12E–03	2.26	+0.16/ –0.15	2.5/3.2			Ipm			
I28	IV-127H2 IV-134H1 IV-145H1	11,035	2.20E–03	+0.15E–03/ –0.15E–03	2.62	+0.17/ –0.17	3.2/2.5/3.5		Im2 Im3				
I27	IV-134H3	1127	2.22E–03	+0.16E–03/ –0.15E–03	2.64	+0.18/ –0.17	3.5	Elm					
I26	IV-122H1	7837	2.27E–03	+0.16E–03/ –0.15E–03	2.70	+0.17/ –0.17	3.2/2.5		Elm				
I25	IV-127H3	3132	2.37E–03	+0.17E–03/ –0.16E–03	2.81	+0.16/ –0.17	n.d.	Elm					
I24	IV-127H3	2978	2.39E–03	+0.16E–03/ –0.17E–03	2.83	+0.15/ –0.18	3.2	Elm					
I23	IV-134H3	3470	2.48E–03	+0.18E–03/ –0.16E–03	2.92	+0.15/ –0.16	3.5	Im, Elm					
I22	IV-127H2 IV-134H2	8117	2.52E–03	+0.18E–03/ –0.17E–03	2.96	+0.13/ –0.17	3.2/3.5/2.5		Elm				
I21	IV-145H2	2323	2.58E–03	+0.19E–03/ –0.17E–03	3.01	+0.12/ –0.16	3.2/3.5		Im1, Im2				
I20	IV-126H3 IV-127H1 IV-127H2 IV-133H3 IV-134H1	13,948	2.58E–03	+0.19E–03/ –0.17E–03	3.01	+0.12/ –0.16	3.2/2.5/3.5		Elm	Ipm			
I19	IV-133H3	2723	2.71E–03	+0.19E–03/ –0.18E–03	3.10	+0.09/ –0.14	3.2/2.5			Ipm			
I18	IV-122H2	5604	2.74E–03	+0.19E–03/ –0.19E–03	3.11	+0.10/ –0.13	3.2/3.5/3.65						Im
I17	IV-139H2	1463	3.09E–03	+0.22E–03/ –0.21E–03	3.26	+0.08/ –0.07	3.2/3.5/3.65		Im1				
I16	IV-139H1	3108	3.24E–03	+0.23E–03/ –0.22E–03	3.30	+0.05/ –0.06	3.2/2.5		Im2, Im3		Ipm		
I15	IV-121H3 IV-127H1	4422	3.28E–03	+0.24E–03/ –0.22E–03	3.31	+0.05/ –0.06	3.5/3.2/2.5			Ipm			
I14	IV-122H3	1855	3.36E–03	+0.24E–03/ –0.22E–03	3.33	+0.04/ –0.05	3.5/3.65/3.2						Im, Elm
I13	IV-114H3	1962	3.38E–03	+0.24E–03/ –0.22E–03	3.33	+0.05/ –0.05	3.2/3.5					Ipm	
I12	IV-139H1	2618	3.47E–03	+0.51E–03/ –0.23E–03	3.35	+0.08/ –0.05	3.5/3.2		Im2				
I11	IV-139H2	1820	3.74E–03	+0.56E–03/ –0.48E–03	3.39	+0.07/ –0.08	3.5/3.2		Im1, Im2				
I10	IV-122H1 IV-127H2	4792	3.77E–03	+0.56E–03/ –0.25E–03	3.40	+0.06/ –0.04	3.2/3.5/2.5		Im1				Im

(*Continued*)

TABLE 4. COMPARISON OF AGES FOR BASALTS IN MARE IMBRIUM* (*Continued*)

Unit	*Lunar Orbiter* image	Area (km^2)	Crater retention age *N*(1)	Error	Model Age (Ga)	Error (b.y.)	Boyce (1976)	M'Gonigle and Schleicher (1972)	Schaber (1969)	Carr (1965)	Moore (1965)	Hackman (1966)	Page (1970)
I9	IV-122H1	3646	3.88E–03	+0.57E–03/ –0.50E–03	3.41	+0.06/ –0.08	3.5/3.2/2.5					lpm	
I8	IV-121H3 IV-122H1 IV-127H1	6621	4.23E–03	+0.63E–03/ –0.54E–03	3.45	+0.05/ –0.06	3.5/3.2/2.5/3.65			lpm			
I7	IV-115H1 IV-122H2	6491	4.39E–03	+0.65E–03/ –0.57E–03	3.47	+0.05/ –0.06	3.5/3.2						EIm
I6	IV-115H2	2155	4.76E–03	+1.10E–03/ –0.61E–03	3.50	+0.06/ –0.06	3.5/3.2						Im, Ccrg
I5	IV-122H2 IV-127H2 IV-134H2	7531	5.07E–03	+1.17E–03/ –0.95E–03	3.52	+0.06/ –0.08	3.5/3.65/3.2		Im1				Im
I4	IV-138H3	1719	5.21E–03	+1.20E–03/ –0.97E–03	3.53	+0.06/ –0.08	3.2/2.5				lpm		
			2.31E–03	+0.16E–03/ –0.16E–03	2.74	+0.17/ –0.18							
I3	IV-122H1	3106	5.55E–03	+1.28E–03/ –1.04E–03	3.55	+0.05/ –0.07	3.5/3.2/3.65/2.5					lpm	
I2	IV-122H1	1933	5.60E–03	+0.83E–03/ –0.72E–03	3.55	+0.04/ –0.04	3.2/2.5			lpm			
I1	IV-127H1	4397	5.99E–03	+1.90E–03/ –0.40E–03	3.57	+0.07/ –0.02	3.2/2.5/3.5			lpm			

*See text for details.

I30, mapped by Carr (1965) as Imbrian in age, could be shown to be of Eratosthenian age in our data as well as in the data of Boyce (1976) and Boyce and Johnson (1978).

Unit I30 is the youngest unit in Mare Imbrium. The young age of this unit is supported by the crater degradation age of Boyce and Johnson (1978). However, there are also units for which the ages derived from crater degradation and our data differ significantly from each other. Units I1, I2, I4, and I16 are Eratosthenian/Imbrian in age in the Boyce data but Imbrian in age in our data. We find that our ages are consistent with the previous mapping of Moore (1965), Schaber (1969), and Carr (1965). Units I18 and I21 are of Imbrian/Eratosthenian age in the Boyce data and Imbrian in the geologic maps of Schaber (1969) and Page (1970), but our data indicate Eratosthenian ages for these units. Ages for unit I14 show a broad variety in the Boyce data (3.2–3.65 Ga) and also in the map of Page (1970) (Im, EIm). For this unit, we derived an Imbrian age of 3.33 Ga. Eratosthenian and/or Imbrian ages (EIm) were reported for units I23, I24, I25, and I27 by M'Gonigle and Schleicher (1972), and we can confirm Eratosthenian ages for these units. We can also confirm Eratosthenian ages for unit I22 and I26, which were mapped as Eratosthenian and/or Imbrian in age (EIm) by Schaber (1969). Compared to crater size-frequency ages, crater degradation ages are often older and assign mostly Imbrian ages to these units in Mare Imbrium.

Mare Serenitatis

In Mare Serenitatis (920 km in diameter; Spudis, 1993), we identified and dated 29 spectral units, showing ages of 2.44–3.81 Ga (Hiesinger et al., 2000) (Fig. 7). This indicates that volcanism in this basin was active over an extremely long period of at least 1.4 Ga. As with the Humorum basin, we observed a bimodal distribution of ages, with the largest number of units formed at 3.4–3.5 b.y. ago and a second weaker maximum at 3.6–3.8 b.y. ago.

For the *Apollo 17* landing site, we found an age of 3.70 Ga, which is in excellent agreement with radiometric ages of returned samples (Table 5). Radiometric investigations of 17 returned *Apollo 17* samples revealed ages of 3.7–3.8 Ga (see primary references in Heiken et al.'s *Lunar Source Book*, 1991), 3.56–3.84 Ga (summarized in BVSP, 1981), and 3.59–3.79 Ga (summarized in Taylor, 1982). Ages for the *Apollo 17* landing site derived from crater degradation yielded ages of 3.65–3.75 Ga (Boyce, 1976; Boyce and Johnson, 1978). According to Nyquist et al. (1974), the ages of sample 70035 and other *Apollo 17* mare basalts indicate flooding of the Taurus-Littrow Valley ~3.7–3.8 b.y. ago. Dasch et al. (1998) found a Rb-Sr age of 3.92 ± 0.1 Ga for the most ancient *Apollo 17* high-titanium drive tube sample 79001,2175.

Our data show that large parts of the center of Mare Serenitatis are younger than the concentric area of lower albedo at the southern border of the mare (Hiesinger et al., 2000). The oldest units in Mare Serenitatis, which also exhibit an unusual low

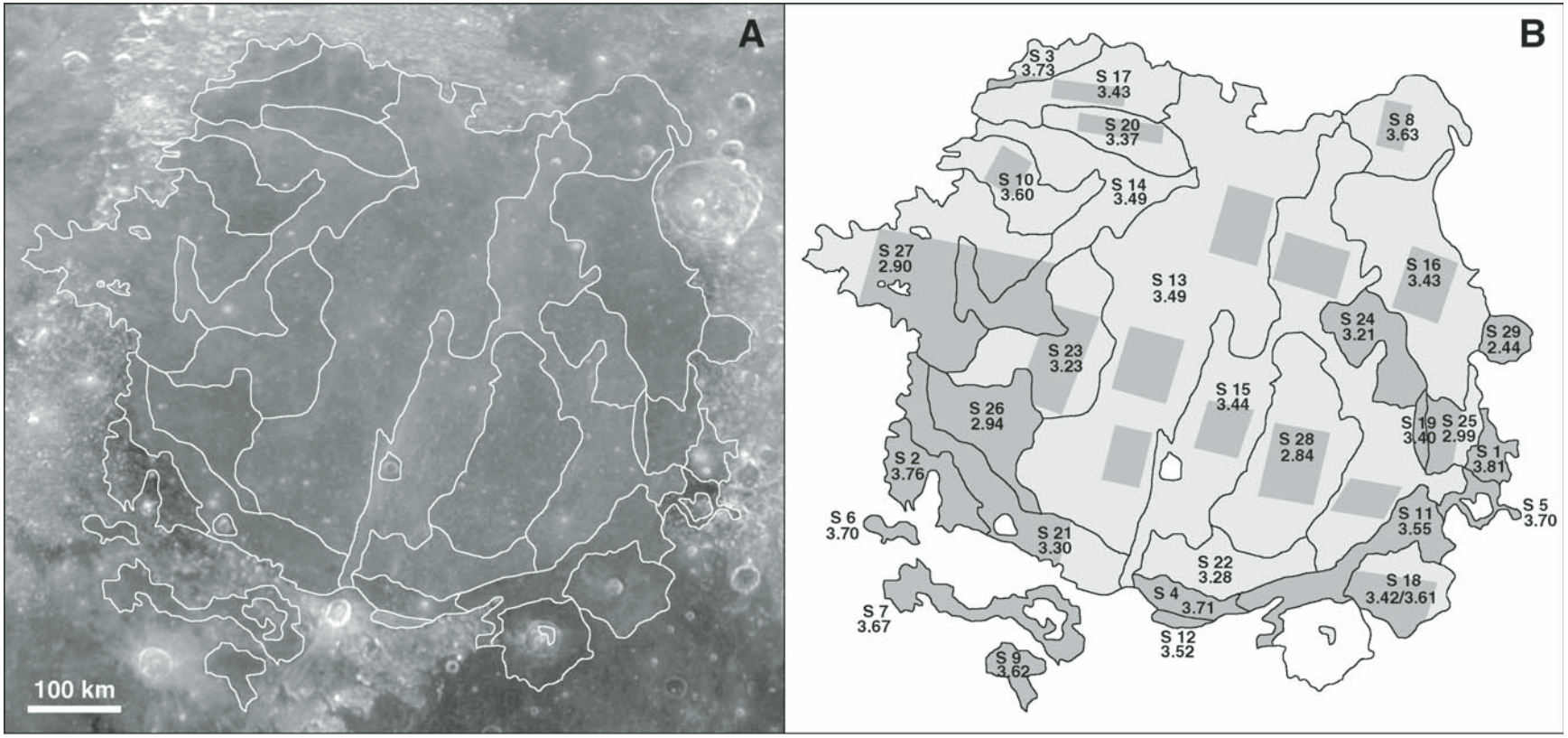

Figure 7. Spatial distribution of model ages for spectrally defined units in Mare Serenitatis (Hiesinger et al., 2000). (A) *Galileo* EM2 data (green filter), simple cylindrical map projection. Spectral units are outlined in white. (B) Sketch map of Mare Serenitatis showing unit numbers and model ages in billion years (also see Table 6). Crater size-frequency distribution measurements were performed for the areas highlighted in dark gray.

TABLE 5. COMPARISON OF RADIOMETRIC AGES AND CRATERING MODEL AGES OF THE *APOLLO* AND *LUNA* LANDING SITES

Landing site	Basalt type*	Radiometric ages[1] (Ga)	Cratering model ages[2,3,4,5] (Ga)
Apollo 11	Group A	3.85 ± 0.01	3.63 +0.03/–0.10
	Group B1–B3	3.70 ± 0.02	
	Group B2	3.80 ± 0.02	
	Group D	3.85 ± 0.01	
Apollo 12	Ol-basalt	3.22 ± 0.04	3.32 +0.10/–0.14
	Pig-basalt	3.15 ± 0.04	
	Ilm-basalt	3.17 ± 0.02	
	Fsp-basalt	3.20 ± 0.08	
Apollo 14	Fra Mauro F.	3.77 ± 0.02	3.85
		3.85 ± 0.02	
Apollo 15	Ol-normative	3.30 ± 0.02	3.35 +0.07/–0.11
	Qz-normative	3.35 ± 0.01	
	Picritic basalt	3.25 ± 0.05	
	Ilm-basalt	3.35 ± 0.04	
Apollo 17	Group A	3.75 ± 0.01	3.70 +0.04/–0.04
	Group B1/2	3.70 ± 0.02	
	Group C	3.75 ± 0.07	
	Group D	3.85 ± 0.04	
Luna 16	Al-basalt	3.41 ± 0.04	3.36

Note: References: 1—Stöffler and Ryder (2001); 2—Hiesinger et al. (2000); 3—Hiesinger et al. (2003); 4—Hiesinger et al. (2006); 5—Hiesinger et al. (2010).

*The most dominant basalt type is listed first; the least frequent basalt type is listed last at each landing site.

albedo, are often exposed directly at the mare/highland contact. As in Humorum, these dark deposits exhibit relatively old ages. In the Serenitatis basin, these deposits are ~3.76 Ga.

Our data confirm previous maps (Wilhelms, 1987), which show young Eratosthenian basalts in the western parts of Serenitatis and in the crater Le Monnier. Several authors, i.e., Carr (1966), Hackman (1966), Morris and Wilhelms (1967), and Scott (1972), geologically mapped Mare Serenitatis. Units S3 and S17 were previously mapped as Eratosthenian in age (Scott, 1972), but our data clearly show that these units are of Imbrian age and are 3.73 Ga and 3.43 Ga old. This is confirmed by crater degradation ages of Boyce (1976) and Boyce and Johnson (1978). According to Carr (1966), units S1, S2, S4, and S5 are at least partly of Eratosthenian age (Table 6). As these units show a very low albedo, they were interpreted to be dark mantle deposits mantling some preexisting topography and/or lithology and therefore to be younger than the adjacent mare basalts. However, our data yield Imbrian ages of 3.70–3.81 Ga for these units, demonstrating that the dark mantle deposits are older than most of the mare basalts. This is consistent with observations on high-resolution imaging data, which show the mare basalts to embay the dark mantle deposits (Wilhelms, 1987). Whitford-Stark and Head (1980) also reported old ages of pyroclastic deposits in Oceanus Procellarum, and we find old ages for dark mantle deposits in the Humorum region. Crater degradation ages for the dark mantle units are significantly younger than ours and yield ages for the formation of dark mantle deposits close to the Imbrian-Eratosthenian boundary (Boyce, 1976; Boyce and Johnson, 1978).

In Mare Serenitatis, ages derived from crater degradation (Boyce, 1976; Boyce and Johnson, 1978) and from crater size-frequency distributions are in most cases very similar to each other, but there are also units (S3, S10, S16, S19, S25, S28) for which the ages differ significantly. In other parts of Mare Serenitatis (S5, S20, S21, S26, S27), where two or more ages can be extracted from the Boyce data for a single spectral unit, our ages often lie between the upper and lower boundary given by the Boyce crater degradation ages. Young Eratosthenian ages, which we obtained for units S25, S26, S27, S28, and S29, are mostly consistent with the Boyce data (except unit S28). All these units were previously mapped by Carr (1966) and Hackman (1966) as Imbrian in age. Two units (S8, S9) are not covered in the Boyce data set. Our data, which yield Imbrian ages (3.62 Ga and 3.63 Ga) for these two units, confirm the mapping of Scott (1972) and Morris and Wilhelms (1967). In the Boyce data, the ages of unit S14 vary from 2.5 Ga up to 3.5 Ga, and we found an age of 3.49 Ga. For unit S6, our data are older (3.70 Ga) than the ages derived from the Boyce data (3.5–3.65 Ga).

TABLE 6. COMPARISON OF AGES FOR BASALTS IN MARE SERENITATIS*

Unit	*Lunar Orbiter* image	Area (km^2)	Crater retention age *N*(1)	Error	Model age (Ga)	Error (b.y.)	Boyce (1976)	Carr (1966)	Hackman (1966)	Scott (1972)	Morris and Wilhelms (1967)
S29	IV-78H3	2196	2.04E–03	+0.15E–03/ –0.13E–03	2.44	+0.17/ –0.17	2.5	Ipm4			
S28	IV-85H3	3927	2.40E–03	+0.17E–03/ –0.16E–03	2.84	+0.16/ –0.18	3.5/3.2	Ipm2, Ipm3			
S27	IV-97H3	11,882	2.46E–03	+0.18E–03/ –0.16E–03	2.90	+0.15/ –0.18	3.2/2.5		Ipm		
S26	IV-97H3	8928	2.51E–03	+0.17E–03/ –0.18E–03	2.94	+0.13/ –0.17	3.2/2.5/3.5	Ipm2, Ipm3			
S25	IV-85H3	3245	2.56E–03	+0.18E–03/ –0.18E–03	2.99	+0.12/ –0.16	3.2	Ipm3, Ipm4			
S24	IV-86H1	6201	2.95E–03	+0.21E–03/ –0.20E–03	3.21	+0.07/ –0.09	3.2/2.5	Ipm2			
S23	IV-97H3	7132	3.00E–03	+0.45E–03/ –0.38E–03	3.23	+0.12/ –0.20	3.2/2.5/3.5	Ipm1, Ipm2			
S22	IV-85H2	3415	3.13E–03	+0.47E–03/ –0.40E–03	3.28	+0.09/ –0.17	3.2/3.5	Ipm2			
S21	IV-97H3	9800	3.24E–03	+0.23E–03/ –0.42E–03	3.30	+0.05/ –0.14	3.5/3.2	Ipm3, Ipm4			
S20	IV-98H1	3213	3.57E–03	+0.25E–03/ –0.46E–03	3.37	+0.04/ –0.10	3.2/3.5			Im1, Em	
S19	IV-86H1	1255	3.81E–03	+0.88E–03/ –0.71E–03	3.40	+0.09/ –0.14	3.2	Ipm1			
S18	IV-85H2	5139	3.96E–03	+1.13E–03/ –0.53E–03	3.42	+0.10/ –0.08	3.65/3.5	Ipm1			
			6.93E–03	+1.59E–03/ –0.90E–03	3.61	+0.05 –0.04					
S17	IV-98H1	2780	4.06E–03	+0.60E–03/ –0.76E–03	3.43	+0.06/ –0.11	3.5				
S16	IV-86H1	4363	4.06E–03	+0.97E–03/ –0.63E–03	3.43	+0.09/ –0.09	2.5/3.2	Ipm3, Ipm4		Im2, Em	
S15	IV-90H3 IV-91H1 IV-85H3	9089	4.15E–03	+0.29E–03/ –0.54E–03	3.44	+0.03/ –0.06	3.5/3.2	Ipm1, Ipm2		Im1	
S14	IV-97H3	4998	4.73E–03	+0.71E–03/ –0.88E–03	3.49	+0.05/ –0.08	2.5/3.2/3.5	Ipm1		Im1, Em	
S13	IV-90H3 IV-91H1	10,173	4.60E–03	+1.44E–03/ –0.47E–03	3.49	+0.08/ –0.05	3.5/3.2/2.5	Ipm1, Ipm2		Im1, Im2	
S12	IV-90H2	529	5.08E–03	+1.61E–03/ –0.66E–03	3.52	+0.08/ –0.05	3.5/3.2	Ipm4			
S11	IV-85H3	5386	5.55E–03	+1.14E–03/ –1.27E–03	3.55	+0.05/ –0.09	3.5/3.2/3.65	Ipm2, Ipm3, Ipm4			
S10	IV-98H1	2557	6.66E–03	+1.65E–03/ –1.92E–03	3.60	+0.05/ –0.10	3.2	Ipm4		Em	
S9	IV-97H2	2896	7.33E–03	+1.84E–03/ –2.09E–03	3.62	+0.05/ –0.09	n.d.				Ipm3, Ipm4
S8	IV-86H1	1792	7.65E–03	+1.94E–03/ –1.20E–03	3.63	+0.05/ –0.04	n.d.			Im2	
S7	IV-97H2	6206	9.27E–03	+1.10E–03/ –2.36E–03	3.67	+0.03/ –0.06	3.65/3.5	Ipm4			Ipm4
S6	IV-97H3	1041	1.05E–02	+2.80E–03/ –2.90E–03	3.70	+0.04/ –0.07	3.5/3.65		Ipm		
S5	IV-78H3	2008	1.07E–02	+2.40E–03/ –2.00E–03	3.70	+0.04/ –0.04	3.5/3.75/3.65	Emd			
S4	IV-90H2	3704	1.14E–02	+0.70E–03/ –2.80E–03	3.71	+0.02/ –0.05	3.2/3.5	Ipm4, Etd			
S3	IV-98H1	424	1.24E–02	+3.50E–03/ –3.60E–03	3.73	+0.05/ –0.07	3.5			Em	
S2	IV-97H3	5945	1.44E–02	+2.90E–03/ –5.40E–03	3.76	+0.03/ –0.09	3.2/3.5	Els			
S1	IV-78H3	2310	1.94E–02	+3.10E–03/ –5.20E–03	3.81	+0.03/ –0.05	3.2/3.5/3.65	Emd			

*See text for details.

Mare Australe

In the geologic map of Wilhelms and El-Baz (1977), the basalt fillings of lava ponds in Mare Australe (880 km in diameter; Spudis, 1993) were mapped as middle Imbrian (Im1) to late Imbrian (Im2) in age. Compared to the geologic map of Wilhelms et al. (1979), our new crater counts yield different ages for a number of units. Unit A30 seems to be of early Eratosthenian age (Table 7) and therefore younger than indicated in the geologic map (Im2). According to Whitford-Stark (1979), ponds A8, A12, A19, A21, A24, and A29 are filled with basalts. In the geologic map of Wilhelms et al. (1979), these units are mapped as nonbasaltic (NpNt, Ntp, Nbl, Nc) and of Nectarian age, so older than the Imbrian basalts exposed in the other lava ponds. Our data show that all these units are of Imbrian age.

We dated 30 lava ponds along a NW-SE profile and a N-S profile crossing the Australe basin structure (Hiesinger et al., 2000) (Fig. 8). We used these profiles in order to investigate a possible relationship between the age of a pond and its position relative to the basin structure. Such a relation was originally proposed by Whitford-Stark (1979). The concentric distribution of ages with younger basalts toward the center of the basin, as mentioned by Whitford-Stark (1979), does not show up in our data. In our data, the dated lava ponds of the inner part of the basin show a broad variety of ages and seem to have been filled in a more or less random way. However, due to the poor quality of some of the available images (e.g., low contrast, unfavorable illumination) and the lack of high-resolution images, we dated less than 15% of all 248 lava ponds, and there may be a trend that basalts of lava ponds outside the 880 km ring structure (Spudis, 1993) are older than the basalts inside the basin structure. Because we have not dated a sufficiently large number of ponds outside the basin, this has to be left to future investigation.

The ages acquired in the study of Hiesinger et al. (2000) vary between 3.08 and 3.91 Ga (Fig. 8; Table 7). The largest number of lava ponds was formed in the late Imbrian Period at 3.6–3.8 Ga. About 51% of all dated basalts were erupted during this period of time, and 70% were erupted between 3.5 Ga and 3.8 Ga. The crater populations of 23% of the investigated ponds show hints of resurfacing events, i.e., older basalt flows underlying the basalts exposed at the surface.

Mare Smythii and Mare Marginis

Our results indicate that basalts in Mare Smythii (740 km in diameter; Spudis, 1993) are significantly younger than basalts in Mare Marginis, and that they might be of Eratosthenian age. On the basis of our crater counts, we also find evidence for resurfacing within Mare Smythii at 3.14 b.y. ago, affecting an underlying 3.48 b.y. old surface. For Mare Marginis basalts, we found late Imbrian ages, which vary from 3.38 to 3.88 Ga. Again, we see evidence for resurfacing of two units (Ma1, Ma2) at 3.80 and 3.62 Ga, which affected older surfaces of 3.88 and 3.81 Ga in age, respectively (Fig. 9; Table 8). Compared to crater degradation ages of Boyce (1976) and Boyce and Johnson (1978), we find a reasonably good agreement. According to our age determinations, the surface age of unit Ma1 is 3.80 Ga; in the Boyce data, it is 3.65 Ga (Boyce, 1976; Boyce and Johnson, 1978). Crater degradation ages for unit Ma2 vary between 3.20 and 3.65 Ga (Boyce, 1976; Boyce and Johnson, 1978), and we determined a surface age of 3.62 Ga. Similarly, crater degradation ages of 3.65 Ga for unit Ma3 are in excellent agreement with our ages (3.60 Ga). Finally, unit Ma4 exhibits a crater degradation age of 3.20 Ga (Boyce, 1976; Boyce and Johnson, 1978) compared to crater size-frequency ages of 3.38 Ga.

Mare Tranquillitatis

In Mare Tranquillitatis, we dated 27 spectral units (Hiesinger et al., 2000). The ages for the basalts in Mare Tranquillitatis in our age determinations vary from 3.39 to 4.23 Ga and show a very narrow distribution (Fig. 10). Most of the basalts in the Tranquillitatis basin (700 km in diameter; Spudis, 1993) that are still visible at the surface were erupted in the late Imbrian Period at 3.6–3.7 b.y. ago. We found that in Mare Tranquillitatis, 37% of the basalt units were formed 3.6–3.7 b.y. ago, and 89% of the eruptions took place between 3.5 Ga and 3.8 b.y. ago. Concerning the spatial distribution of these ages, we found a weak trend, showing older ages in the west (<30°E longitude) and younger ages in the east of Mare Tranquillitatis (Fig. 10). This would imply that volcanism lasted longer in the eastern parts of the basin compared to the western parts.

Our crater size-frequency distribution measurements reveal Imbrian ages for all the Tranquillitatis basalts, which is in principle consistent with the ages of Boyce (1976) and Boyce and Johnson (1978). However, the distribution of the Boyce ages does not necessarily fit the outline of spectrally defined units. Therefore, for some spectral units, it is possible to extract several ages from the Boyce data set, showing a variation of up to 500 m.y. In these cases, the most abundant "Boyce age" is often more or less identical with our ages for this unit. Unit T18 may serve as an example to show this (Table 9). In some other cases, the ages derived by Boyce (1976) and Boyce and Johnson (1978) give us an upper and lower boundary, with our ages either right between or close to one boundary. This is the case for units T7, T12, T15, and T25 (Table 9). However, there are also units (T3, T4, T13, T22, T27) for which the ages are significantly different in each of the two data sets (Table 9). As the ages vary in a nonsystematic way between the two methods, neither method yields systematically older or younger ages.

An independent verification of crater size-frequency ages was obtained by deriving the age of the *Apollo 11* landing site and comparing it with the radiometric ages of the returned samples. According to our age determination, the unit containing the *Apollo 11* landing site is 3.63 b.y. old. This is in excellent agreement with radiometric ages of the returned lunar samples, which

TABLE 7. COMPARISON OF AGES FOR BASALTS IN MARE AUSTRALE*

Unit	*Lunar Orbiter* image	Area (km^2)	Crater retention age $N(1)$	Error	Model age (Ga)	Error (b.y.)	Wilhelms and El-Baz (1977)	Wilhelms et al. (1979)
A30	IV-11H1	5763	2.68E–03	+1.10E–03/–0.78E–03	3.08	+0.32/–0.82	Im2	
A29	IV-5H1	428	3.11E–03	+0.71E–03/–0.40E–03	3.27	+0.13/–0.18		NpNt
			1.54E–02	+3.50E–03/–3.70E–03	3.77	+0.04/–0.05		
A28	IV-11H3	1173	3.12E–03	+0.46E–03/–0.40E–03	3.27	+0.10/–0.17		Im2
A27	IV-11H1	4409	3.46E–03	+0.51E–03/–1.01E–03	3.35	+0.07/–0.46	Im2	
	IV-11H2							
A26	IV-52H1	555	3.63E–03	+0.84E–03/–0.24E–03	3.38	+0.10/–0.04	Im2	Im2
A25	IV-38H2	3138	5.00E–03	+1.15E–03/–1.70E–03	3.51	+0.07/–0.19	Im2	Im2
A24	IV-5H1	1279	5.28E–03	+1.22E–03/–0.98E–03	3.53	+0.06/–0.07		NpNt, Ntp
			1.08E–02	+4.40E–03/–3.20E–03	3.70	+0.07/–0.07		
A23	IV-11H3	548	5.44E–03	+2.80E–03/–1.59E–03	3.54	+0.11/–0.13		Im2
A22	IV-38H1	6792	5.98E–03	+1.38E–03/–1.12E–03	3.57	+0.05/–0.07	Im2	Im2
A21	IV-5H1	576	6.42E–03	+2.04E–03/–2.46E–03	3.59	+0.06/–0.17		Nc
			3.48E–02	+2.57E–02/–2.33E–02	3.91	+0.09/–0.19		
A20	IV-5H1	1162	6.34E–03	+2.01E–03/–2.43E–03	3.59	+0.06/–0.17		Im2
A19	IV-5H1	773	7.74E–03	+3.20E–03/–2.97E–03	3.63	+0.08/–0.13		Nbl
			2.72E–03	+0.62E–03/–0.51E–03	3.10	+0.23/–0.47		
A18	IV-11H3	1788	7.89E–03	+1.16E–03/–3.00E–03	3.64	+0.03/–0.14		Im2
A17	IV-11H3	3608	7.96E–03	+1.83E–03/–2.70E–03	3.64	+0.05/–0.11		Im2, Imd
A16	IV-5H1	751	8.84E–03	+1.30E–03/–1.65E–03	3.66	+0.03/–0.04		Im2
A15	IV-11H3	482	8.87E–03	+2.00E–03/–1.15E–03	3.66	+0.05/–0.03		Im2
A14	IV-52H1	6960	9.20E–03	+1.40E–03/–0.62E–03	3.67	+0.03/–0.01	Im2	Im2
	IV-38H2		2.93E–02	+0.68E–02/–0.85E–02	3.88	+0.03/–0.06		
A13	IV-5H1	2672	9.12E–03	+2.10E–03/–1.71E–03	3.67	+0.04/–0.05		Im2
	IV-11H3		2.51E–02	+5.70E–03/–4.70E–03	3.86	+0.03/–0.04		
A12	IV-5H1	868	9.49E–03	+3.90E–03/–3.64E–03	3.68	+0.07/–0.12		Ntp
A11	IV-52H1	1494	1.02E–02	+4.10E–03/–3.00E–03	3.69	+0.07/–0.07		Im2
A10	IV-11H2	1988	1.03E–02	+1.90E–03/–3.30E–03	3.70	+0.05/–0.05	Im2	
A9	IV-52H1	3514	1.06E–02	+3.30E–03/–1.29E–03	3.70	+0.05/–0.06		Im1
A8	IV-5H1	523	1.13E–02	+0.80E–03/–3.30E–03	3.71	+0.02/–0.07		Ntp
A7	IV-11H3	368	1.16E–02	+1.70E–03/–3.40E–03	3.72	+0.03/–0.07		Im1
A6	IV-52H1	6793	1.16E–02	+3.70E–03/–3.90E–03	3.72	+0.05/–0.09		Im2, Im1
			5.05E–03	+1.16E–03/–1.22E–03	3.52	+0.06/–0.09		
A5	IV-5H1	1747	1.21E–02	+3.90E–03/–2.90E–03	3.73	+0.05/–0.06		Im1
A4	IV-5H1	1243	1.39E–02	+3.20E–03/–0.90E–03	3.75	+0.04/–0.01		Im1
A3	IV-52H1	939	1.59E–02	+2.30E–03/–3.90E–03	3.78	+0.02/–0.05	Ip, Nt	Ntp
A2	IV-5H1	3093	1.82E–02	+3.50E–03/–3.40E–03	3.80	+0.03/–0.05		Im1
A1	IV-52H1	2592	1.63E–02	+6.80E–03/–7.20E–03	3.88	+0.04/–0.04		Im1, Im2

*See text for details. Read 2.68E–03 as 2.68×10^{-3}.

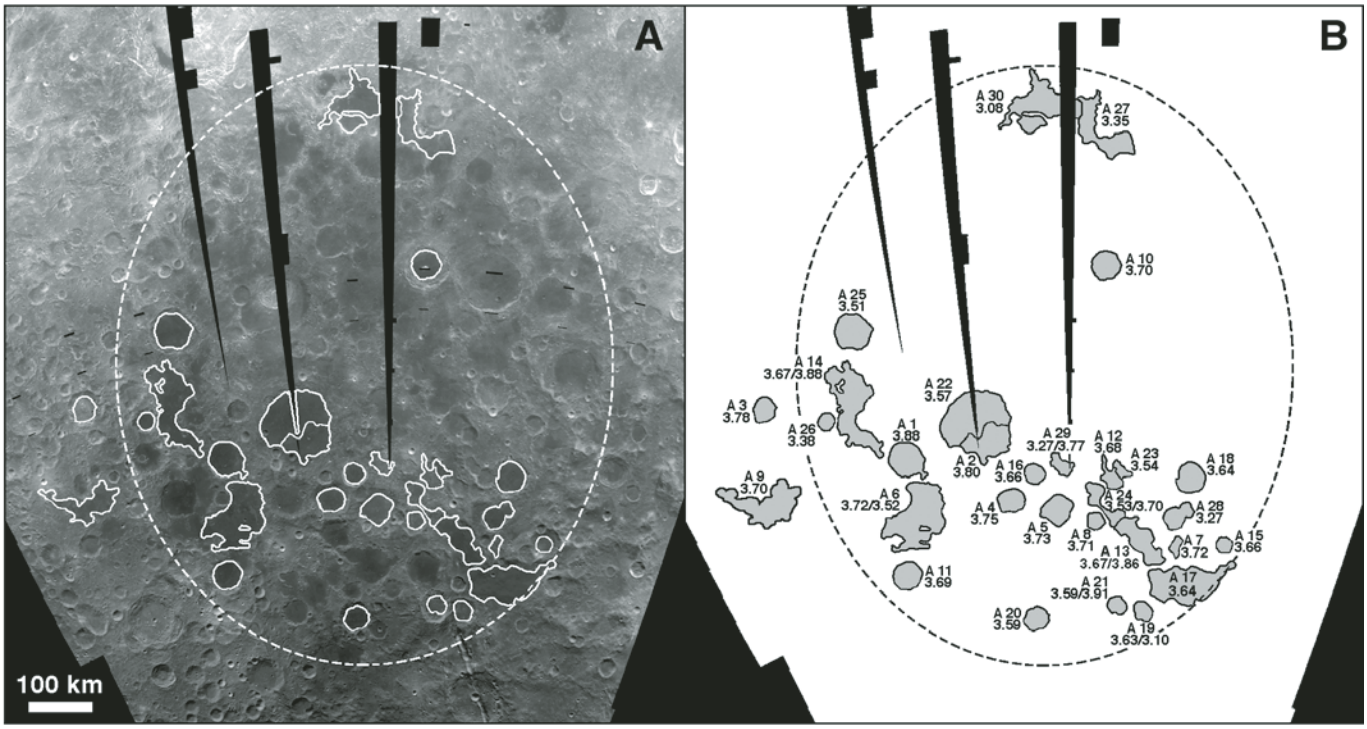

Figure 8. Spatial distribution of model ages in selected lava ponds of Mare Australe (Hiesinger et al., 2000). (A) Mosaic of *Clementine* data ($\lambda = 0.9$ μm), sinusoidal map projection. Investigated units are outlined in white; dashed line shows approximate location/size of Mare Australe. (B) Sketch map of Mare Australe showing unit numbers and model ages in billion years (also see Table 7). Crater size-frequency distribution measurements were performed for the entire surface of each individual pond.

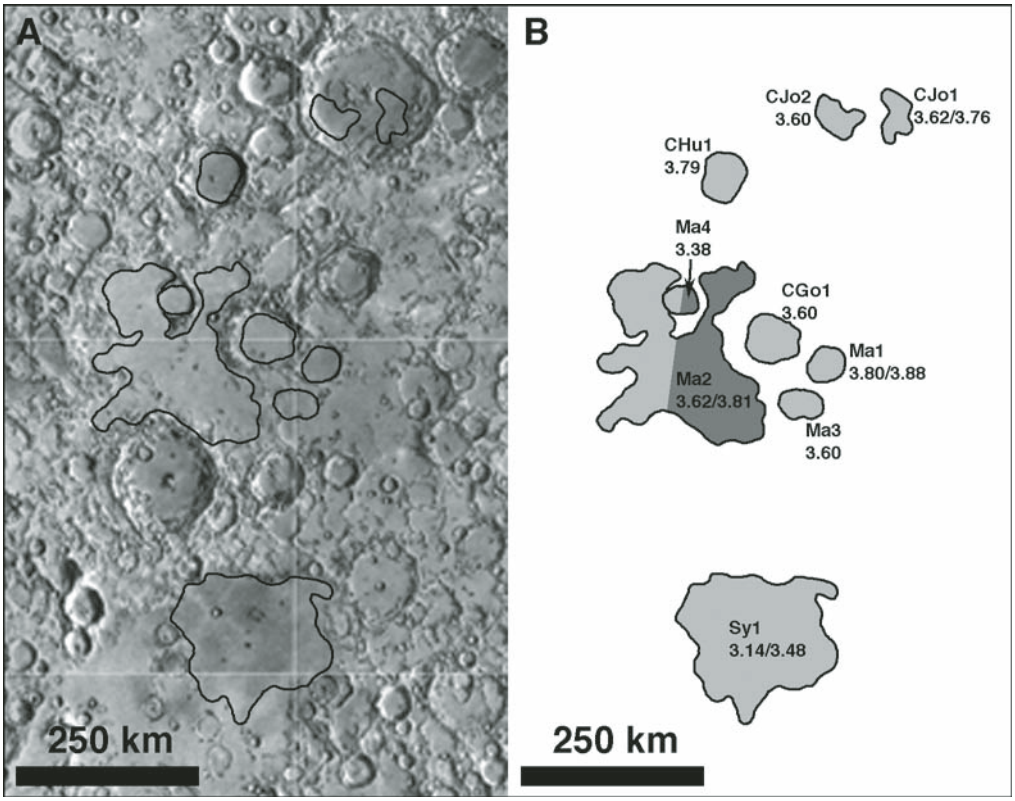

Figure 9. Spatial distribution of model ages for spectrally defined units in Mare Smythii, Mare Marginis, and the craters Hubble, Joliot, and Goddard (Hiesinger et al., 2010). (A) U.S. Geological Survey shaded relief map, simple cylindrical map projection. Spectral units are outlined in black. (B) Sketch map of Mare Smythii, Mare Marginis, and the craters Hubble, Joliot, and Goddard showing unit numbers and model ages in billion years (also see Tables 8 and 13). Sy—Mare Smythii, Ma—Mare Marginis, CHu—Hubble, CJo—Joliot, CGo—Goddard. Crater size-frequency distribution measurements were performed for the areas highlighted in gray. For unit Ma2, the count area is represented by the dark-gray area.

TABLE 8. COMPARISON OF AGES FOR BASALTS IN MARE SMYTHII (Sy), MARE MARGINIS (Ma), SINUS MEDII (SM), PALUS PUTREDINIS (PP), LACUS AESTATIS (LA), AND LACUS TEMPORIS (LT)*

Unit	*Lunar Orbiter* image	Area (km^2)	Crater retention age *N*(1)	Error	Model age (Ga)	Error (b.y.)	Boyce (1976); Boyce and Johnson (1978)	Wilhelms and McCauley (1971)	Wilhelms (1968)	Wilhelms and El-Baz (1977)	McCauley (1973)	Hackman (1966)	Howard and Masursky (1968)	Lucchitta (1978)	Scott et al. (1977)
Sy1	IV17H1	26,363	2.79E–03 / 4.53E–03	+2.00E–04/ –1.90E–04 +1.04E–03/ –5.90E–04	3.14/3.48	+0.09/ –0.12 +0.07/ –0.06	2.50/3.20			Im2					
Ma4	IV17H2	824	3.65E–03	+5.40E–04/ –4.70E–04	3.38	+0.07/ –0.09	3.20			Im2					
Ma3	IV17H2	1935	6.81E–03	+1.70E–03/ –1.78E–03	3.60	+0.06/ –0.08	3.65			Im2					
Ma2	IV17H2	14,599	7.35E–03 / 1.88E–02	+1.01E–03/ –1.07E–03 +1.01E–02/ –3.50E–03	3.62/3.81	+0.03/ –0.04 +0.07/ –0.04	3.20/3.50 3.65			Im2					
Ma1	IV17H2	2133	1.77E–02 / 2.99E–02	+4.20E–03/ –4.20E–03 +1.47E–02/ –7.20E–03	3.80/3.88	+0.03/ –0.05 +0.07/ –0.04	3.65			Im1					
SM4	IV102H1	8999	7.76E–03	+1.31E–03/ –1.42E–03	3.63	+0.04/ –0.05	3.50	Im	Ipm1, Ipm2						
SM3	IV102H1, IV102H2	8876	1.26E–02	+1.33E–02/ –1.19E–02	3.74	+0.01/ –0.01	3.75	Ip	Ica, Icah						
SM2	IV102H1	7260	1.41E–02	+2.20E–03/ –2.50E–03	3.76	+0.02/ –0.04	No age	Ip					Ica		
SM1	IV102H1	3515	1.70E–02	+3.50E–03/ –4.00E–03	3.79	+0.03/ –0.05	3.85	Ip	Ica						
PP2	IV109H3	492	2.67E–03	+3.06E–03/ –2.32E–03	3.07	+0.18/ –0.31	3.50	Em				Ipm			
PP1	IV102H3, IV109H3	9196	3.64E–03	+4.09E–03/ –3.19E–03	3.35	+0.07/ –0.11	3.50	Im, Em				Ipm			
LA1	IV168H2	400	4.84E–03	+1.20E–03/ –9.00E–04	3.50	+0.07/ –0.08	No age	Em			Em				Elm
LT2	IV74H3	1007	7.31E–03	+2.44E–03/ –1.76E–03	3.62	+0.06/ –0.07	No age							Im	
LT1	IV67H2, IV67H3, IV74H3	13,328	9.37E–03 / 1.45E–02	+1.01E–02/ –8.65E–03 +1.78E–02/ –1.12E–02	3.68/3.76	+0.01/ –0.02 +0.04/ –0.05	No age	Im						Im	

*See text for details.

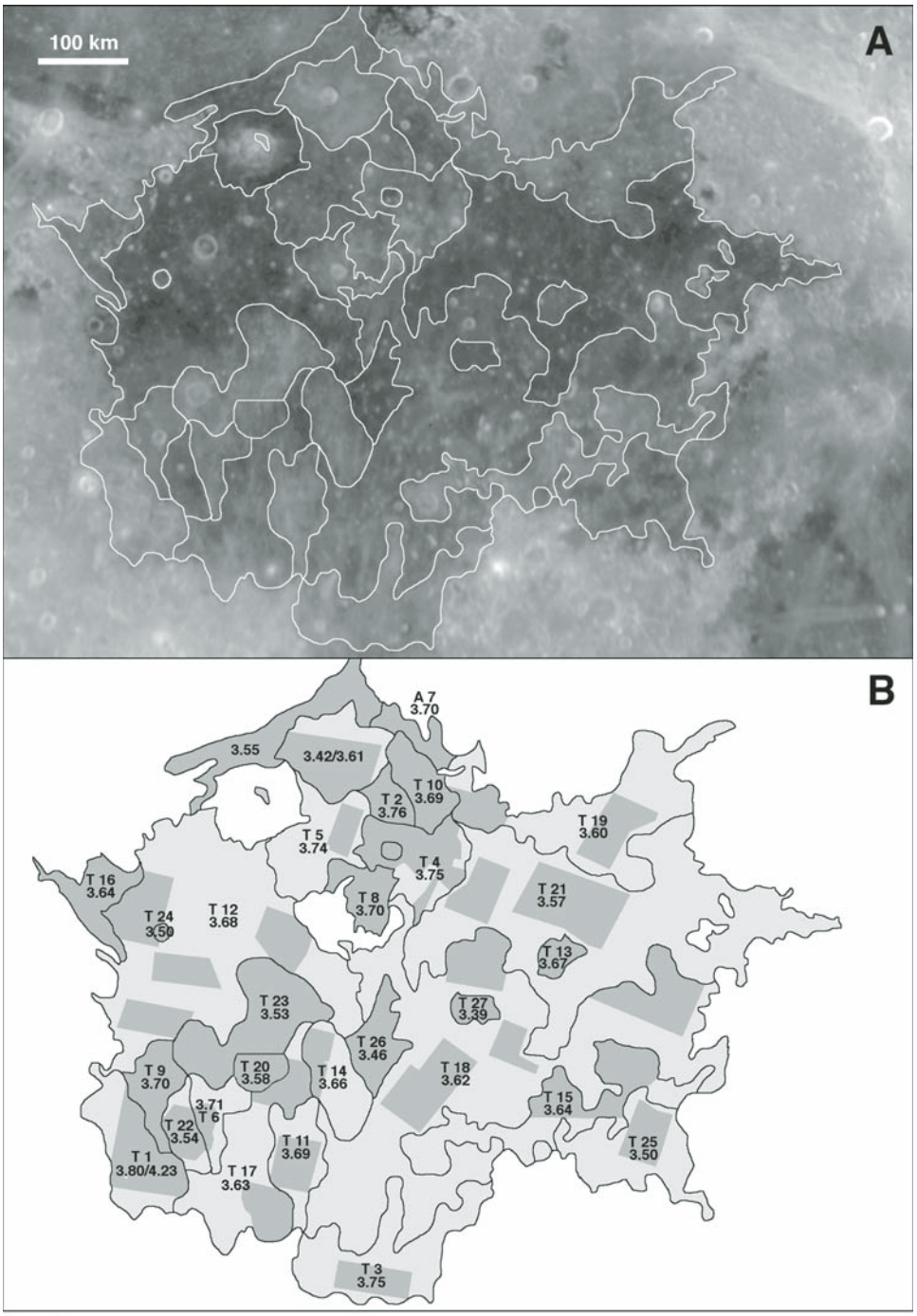

Figure 10. Spatial distribution of model ages for spectrally defined units in Mare Tranquillitatis (Hiesinger et al., 2000). (A) *Galileo* EM2 data (green filter), simple cylindrical map projection. Spectral units are outlined in white. (B) Sketch map of Mare Tranquillitatis showing unit numbers and model ages in billion years (also see Table 9). Crater size-frequency distribution measurements were performed for the areas highlighted in dark gray.

are dated to be 3.67 b.y. (summarized by Wilhelms, 1987), 3.47–3.86 b.y. (BVSP, 1981), and 3.56–3.92 b.y. old (summarized by Taylor, 1982) (Table 5).

Most workers (Morris and Wilhelms, 1967; Wilhelms, 1972; Milton, 1968; Carr, 1966) have mapped the Tranquillitatis basalts as Imbrian in age. These ages are generally confirmed by our age determinations. However, Scott and Pohn (1972) mapped units T7 and T10 as Eratosthenian in age, whereas Carr (1966) mapped these units as Imbrian. Our data are consistent with an Imbrian age of these units. Also, according to Scott and Pohn (1972), unit T19 exhibits at least partly an Eratosthenian age. Wilhelms (1972) mapped this unit as Imbrian in age, and, again, we can confirm an Imbrian age of unit T19. Ages from Boyce (1976) and Boyce and Johnson (1978) for these units are very similar to our ages (Table 9), so Imbrian ages for these units seem to be very likely.

TABLE 9. COMPARISON OF AGES FOR BASALTS IN MARE TRANQUILLITATIS*

Unit	*Lunar Orbiter* image	Area (km^2)	Crater retention age *N*(1)	Error	Model age (Ga)	Error (b.y.)	Boyce (1976)	Morris and Wilhelms (1967)	Wilhelms (1972)	Milton (1968)	Carr (1966)	Scott and Pohn (1972)	Staid et al. (1996)
T27	IV-78H2	876	3.74E–03	+0.56E–03/ –0.70E–03	3.39	+0.07/ –0.14	3.65/3.5		Im3				T_{vh-B}
T26	IV-78H1	3214	4.30E–03	+0.99E–03 –0.80E–03	3.46	+0.07/ –0.10	3.5/3.65	Ipm2					T_h, T_{vh-B}
T25	IV-73H1	4018	4.87E–03	+0.73E–03/ –0.63E–03	3.50	+0.05/ –0.05	3.75/3.5/3.65		Im2, Im3				T_{vh-B}
T24	IV-85H2	209	4.83E–03	+1.54E–03/ –0.62E–03	3.50	+0.09/ –0.05	3.65	Ipm3					T_{vh-B}
T23	IV-85H1 IV-85H2	8589	5.25E–03	+1.08E–03/ –1.19E–03	3.53	+0.06/ –0.10	3.5	Ipm1 Ipm2					T_h, T_{vh-B}
T22	IV-85H1	1670	5.48E–03	+1.26E–03/ –1.02E–03	3.54	+0.06/ –0.07	3.65	Ipm2					T_{vh-A}
T21	IV-73H2 IV-78H2	11,074	5.95E–03	+0.76E–03/ –0.78E–03	3.57	+0.03/ –0.05	3.5/3.65/3.2		Im3				T_{vh-B}
T20	IV-85H1	2393	6.32E–03	+1.46E–03/ –1.84E–03	3.58	+0.05/ –0.10	3.65	Ipm2					T_{vh-A}
T19	IV-73H2 IV-78H2	7232	6.88E–03	+2.69E–03/ –0.84E–03	3.60	+0.08/ –0.03	3.65/3.5		Im1 Im2			Im1, Im2, Em	T_l
T18	IV-73H1, 2 IV-78H1, 2	21,122	7.20E–03	+0.85E–03/ –0.90E–03	3.62	+0.02/ –0.04	3.65/3.2/3.75/3.5	Ipm1 Ipm2	Im3				T_{vh-B}, T_{vh-A}, T_l
T17	IV-85H1	3754	7.60E–03	+0.97E–03/ –1.77E–03	3.63	+0.03/ –0.10	3.65	Ipm2					T_{vh-A}, T_h, T_{vh-B}
T16	IV-90H2	5744	7.94E–03	+1.63E–03/ –1.87E–03	3.64	+0.04/ –0.07	3.65/3.5	Ipm3, Ipm4					n.d.
T15	IV-73H1	5232	7.98E–03	+1.37E–03/ –1.53E–03	3.64	+0.04/ –0.05	3.75/3.65/3.85		Em, Im1, Im2 Im3				T_{vh-B}, T_l
T14	IV-85H1	1708	8.87E–03	+2.50E–03/ –2.76E–03	3.66	+0.06/ –0.08	3.65/3.5	Ipm1					T_h
T13	IV-73H2	1835	9.20E–03	+2.10E–03/ –2.22E–03	3.67	+0.04/ –0.06	3.5/3.2		Im2				T_{vh-B}
T12	IV-85H1, 2 IV-90H2	11,252	9.66E–03	+1.50E–03/ –1.61E–03	3.68	+0.03/ –0.04	3.5/3.65/3.2	Ipm1 Ipm2, Ipm3					T_{vh-A}, T_{vh-B}, Cf
T11	IV-85H1	2178	1.01E–02	+2.00E–03/ –2.50E–03	3.69	+0.04/ –0.06	3.65	Ipm1					T_{vh-A}, T_h, T_{vh-B}
T10	IV-78H2	4837	1.01E–02	+1.00E–03/ –3.00E–03	3.69	+0.02/ –0.08	3.65				Ipm3	Em	T_{vh-B}
T9	IV-85H1	4778	1.07E–02	+2.20E–03/ –2.60E–03	3.70	+0.04/ –0.06	3.65/3.5	Ipm2					T_{vh-A}
T8	IV-78H2	3132	1.08E–02	+2.10E–03/ –2.70E–03	3.70	+0.04/ –0.06	3.65	Ipm1, Ipm2					T_{vh-B}
T7	IV-78H2	2186	1.06E–02	+0.16E–03/ –2.00E–03	3.70	+0.03/ –0.04	3.65/3.75				Ipm2 Ipm3	Em, Im1, Im2	T_h
T6	IV-85H1	895	1.12E–02	+3.30E–03/ –4.10E–03	3.71	+0.05/ –0.10	3.65	Ipm2					T_{vh-A}, T_{vh-B}
T5	IV-85H2	3122	1.31E–02	+2.10E–03/ –3.20E–03	3.74	+0.03/ –0.05	3.65	Ipm2					T_{vh-B}
T4	IV-78H2	5507	1.39E–02	+3.40E–03/ –2.30E–03	3.75	+0.04/ –0.03	3.65/3.5	Ipm2					T_h
T3	IV-78H1	3335	1.35E–02	+2.70E–03/ –3.40E–03	3.75	+0.03/ –0.06	3.65/3.5			Ipm			T_{vh-B}, T_{vh-A}
T2	IV-78H2	2455	1.42E–02	+2.10E–03/ –4.10E–03	3.76	+0.02/ –0.07	3.65	Ipm3					T_{vh-B}
T1	IV-85H1	6259	1.79E–02	+4.10E–03/ –3.40E–03	3.80	+0.03/ –0.04	3.65/3.5/3.75	Ipm2					T_{vh-A}, Cf
			3.02E–01	+1.25E–01/ –0.88E–01	4.23	+0.05/ –0.05							

*See text for details.

Mare Nubium

On the basis of our crater size-frequency distribution (Hiesinger et al., 2003), we identified 14 Imbrian and three Eratosthenian units in Mare Nubium (690 km in diameter; Spudis, 1993) (Fig. 11; Table 10). Compared to the crater degradation ages of Boyce (1976) and Boyce and Johnson (1978), we find a good agreement for several units (Table 10). We measured Imbrian ages for units N1–N14, and these ages are generally similar to the degradation ages. However, there are some discrepancies in the details. According to the map of Boyce (1976) and Boyce and Johnson (1978), unit N2 is 2.5 ± 0.5 b.y. old, but our data indicate that this unit is significantly older, i.e., 3.63/3.85 Ga. Similarly, very young ages (2.5 ± 0.5 Ga) have been measured for parts of units N6, N10, and N11. In all these cases, our ages are older than the degradation ages. Very often, the most abundant degradation age or at least one of the degradation ages that can be assigned to a particular unit is similar to our age for this unit (N1, N4, N5, N6, N7, N8, N10, N11, N12, N13, N16, N17). For unit N14, we derived an age of 3.76 Ga, with a resurfacing event taking place at 3.25 b.y. ago. Crater degradation ages of Boyce (1976) and Boyce and Johnson (1978) do not resolve this resurfacing event and indicate ages of 3.75, 3.65, and 3.85 Ga, with 3.75 Ga. being the most abundant age of this unit. Unit N9 is significantly older in the Boyce data (3.85 Ga) compared to our data (3.48 Ga), as is unit N15 (3.50 Ga, compared to our age of 3.16 Ga). Unit N3 is considerably younger (3.2 Ga) than our age (3.63 Ga). Eratosthenian ages of unit N16 and probably N17 in the maps of Boyce (1976) and Boyce and Johnson (1978) are consistent with our findings. On the basis of crater size-frequency distribution measurements, Bugiolacchi et al. (2006) reported ages of 2.34 (±0.4) to 3.55 (±0.08) b.y. for the basalts in Mare Nubium.

The geologic map of the nearside of the Moon indicates that units N1, N8, N11, and N12 are Imbrian in age, consistent with our ages (Wilhelms and McCauley, 1971). Several units (N3, N4, N7, N10, N13) were mapped as Imbrian and Eratosthenian in age, but we derived Imbrian ages based on our crater counts. Eratosthenian ages for units N2, N5, N6, and N9 are not consistent with our data. Unit N14 is shown as Eratosthenian in the geologic map, and we obtained an age of 3.25 Ga, i.e., very close to the border of the Eratosthenian and Imbrian Systems. Finally, units N15, N16, and N17 were mapped as Imbrian and Eratosthenian

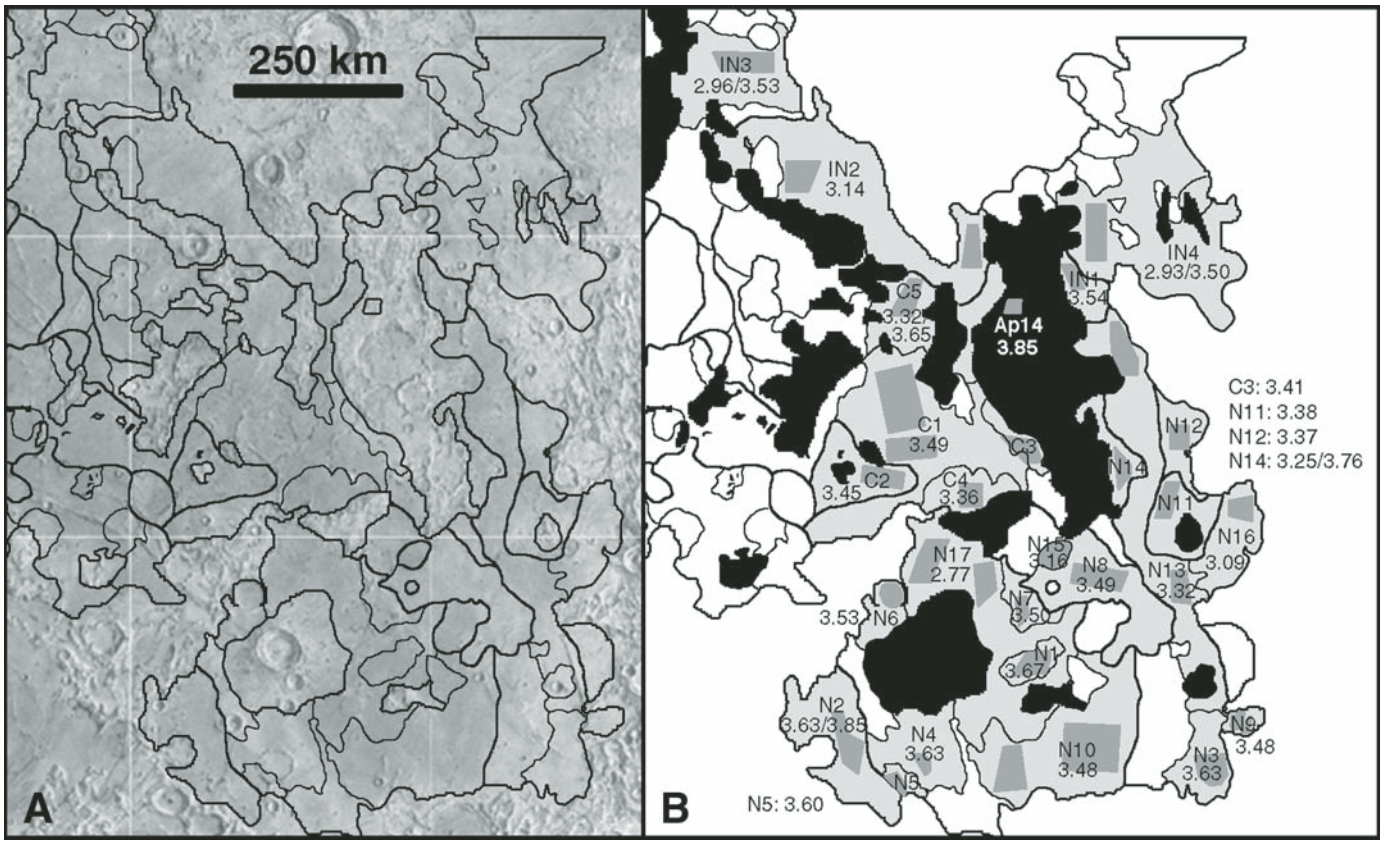

Figure 11. Spatial distribution of model ages for spectrally defined units in Mare Nubium, Mare Insularum, and Mare Cognitum (Hiesinger et al., 2003). (A) U.S. Geological Survey shaded relief map, simple cylindrical map projection. Spectral units are outlined in black. (B) Sketch map of Mare Nubium, Mare Insularum, and Mare Cognitum showing unit numbers and model ages in billion years (also see Tables 10, 12, and 16). Crater size-frequency distribution measurements were performed for the areas highlighted in dark gray. Black areas are non-mare materials or have been excluded from this investigation.

TABLE 10. COMPARISON OF AGES FOR BASALTS IN MARE NUBIUM*

Unit	*Lunar Orbiter* image	Area (km^2)	Crater retention age *N*(1)	Error	Model age (Ga)	Error (b.y.)	Boyce (1976)	Wilhelms and McCauley (1971)	Howard and Masursky (1968)	Eggleton (1965)	Trask and Titley (1966)	Holt (1974)
N17	IV120H2 IV125H2	3540	2.34E–03	+0.34E–03/ –0.16E–03	2.77	+0.31/ –0.17	3.2, 2.5, 3.5	Im, Em		Ipm	Ipm, Ipm1, Ipm2	
N16	IV113H2	865	2.70E–03	+0.19E–03/ –0.18E–03	3.09	+0.10/ –0.14	3.2	Im, Em	Ipm, Ipmd			Im2, Em
N15	IV120H2	1696	2.83E–03	+0.20E–03/ –0.19E–03	3.16	+0.08/ –0.11	3.5	Im, Em			Ipm1, Ipm2, Ipm3	
N14	IV113H2	963	3.06E–03/ 1.46E–02	+0.46E–03/ –0.39E–03 +0.34E–02/ –0.66E–02	3.25/3.76	+0.11/ –0.18 +0.04/ –0.09	3.75, 3.65, 3.85	Em		Ipm		
N13	IV113H2 IV113H3	3855	3.33E–03	+0.49E–03/ –0.43E–03	3.32	+0.09/ –0.13	3.2, 3.5	Em, Im		Ipm		Im1, Im2, Em
N12	IV113H2	522	3.60E–03	+0.54E–03/ –0.46E–03	3.37	+0.07/ –0.09	3.5, 3.2	Im	Ipm			
N11	IV113H2	1299	3.62E–03	+0.54E–03/ –0.46E–03	3.38	+0.07/ –0.10	2.5, 3.2	Im	Ipm, Ipmd			Em
N10	IV120H1 IV125H1	6992	4.49E–03	+0.91E–03/ –0.58E–03	3.48	+0.06/ –0.06	3.2, 2.5	Em, Im			Ipm, Ipm2	
N9	IV113H1	1048	4.54E–03	+1.09E–03/ –0.85E–03	3.48	+0.07/ –0.09	3.85	Em				Im2
N8	IV120H2	3016	4.62E–03	+1.26E–03/ –0.86E–03	3.49	+0.07/ –0.09	3.2, 3.5	Im			Ipm1, Ipm2, Ipm3	
N7	IV120H2	695	4.83E–03	+1.82E–03/ –1.16E–03	3.5	+0.10/ –0.12	3.5	Im, Em			Ipm2	
N6	IV125H2	1166	5.20E–03	+1.67E–03/ –0.97E–03	3.53	+0.07/ –0.08	3.2, 2.5	Em			Ipm, Ipm3	
N5	IV125H1	863	6.85E–03	+1.57E–03/ –0.89E–03	3.6	+0.05/ –0.03	3.5	Em			Ipm	
N4	IV125H1	686	7.75E–03	+1.78E–03/ –1.45E–03	3.63	+0.05/ –0.05	3.5, 3.2	Im, Em			Ipm	
N3	IV113H1	1639	7.58E–03	+2.09E–03/ –2.34E–03	3.63	+0.05/ –0.10	3.2	Im, Em				Em, Ip, Im2, Im1
N2	IV132H1	2332	7.50E–03/ 2.49E–02	+1.30E–03/ –1.31E–03 +1.00E–02/ –0.73E–02	3.63/3.85	+0.03/ –0.05 +0.06/ –0.05	2.5	Em			Ipm2, Ipm4	
N1	IV120H1	1528	9.26E–03	+2.89E–03/ –2.09E–03	3.67	+0.05/ –0.06	3.5	Im			Ipm, Ipm1, Ipm2	

*See text for details.

in age (Wilhelms and McCauley, 1971; Holt, 1974), and our data confirm an Eratosthenian age of these units. In addition, our data are consistent with Imbrian ages of units N11 and N12 (Howard and Masursky, 1968), N1, N2, N4, N5, N6, N7, N8, and N10 (Trask and Titley, 1966), N13 and N14 (Eggleton, 1965), and N3, N9, and N13 (Holt, 1974). However, we cannot confirm Eratosthenian ages of units N3, N11, and N13 as shown in the map of Holt (1974). In addition, our data are not consistent with Imbrian ages of units N15, N16, and N17, as indicated by various maps (Eggleton, 1965; Trask and Titley, 1966; Howard and Masursky, 1968; Holt, 1974). Based on our crater counts, we see that these units are Eratosthenian in age. A summary of the data of Hiesinger et al. (2003) and a comparison between geological maps and the Boyce ages are shown in Table 10.

Mare Humboldtianum

We mapped and dated 11 basalt units in the Humboldtianum basin (650 km in diameter; Spudis, 1993), and our results show that volcanism lasted ~200 m.y. longer in the basin center than

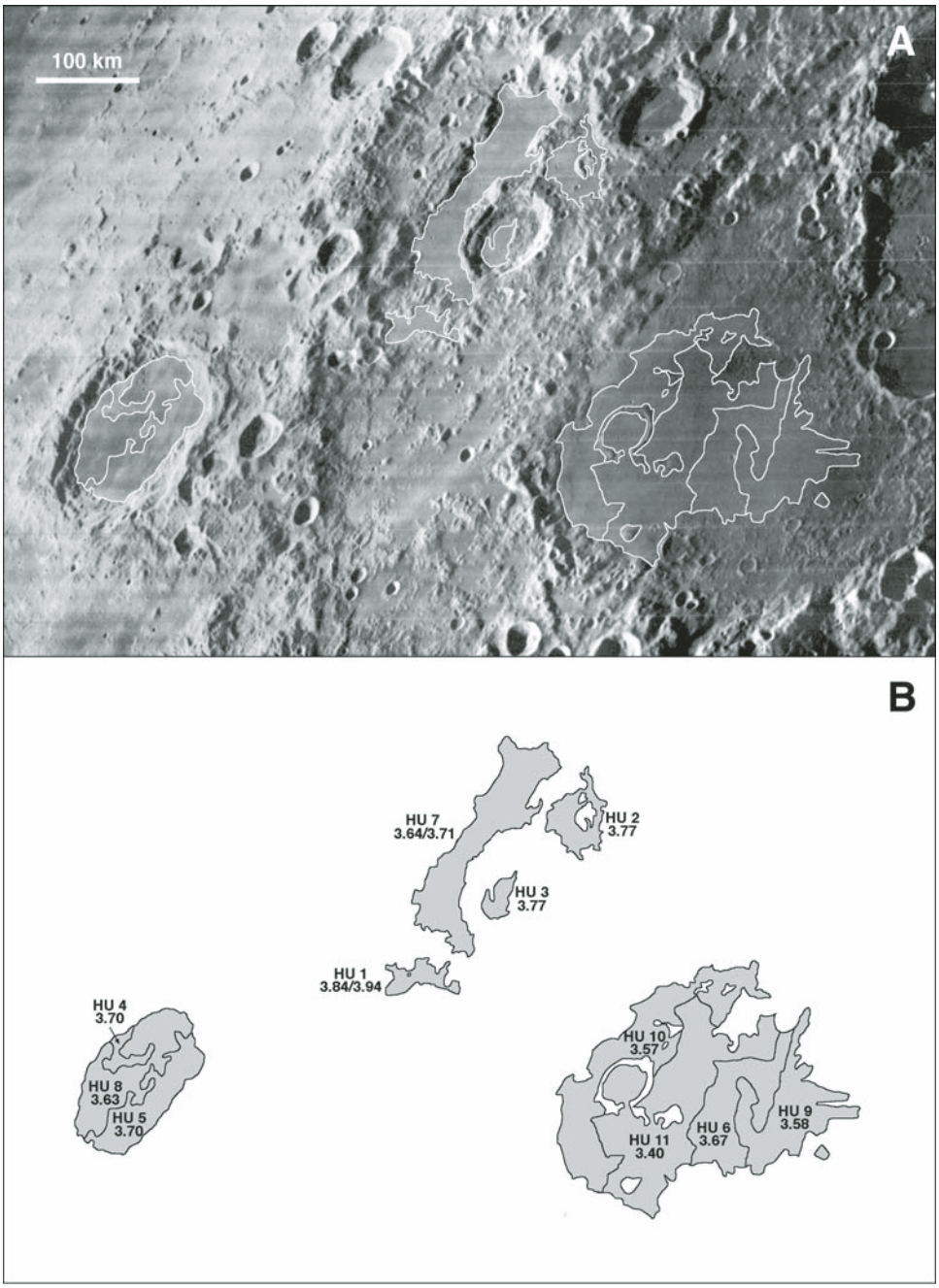

Figure 12. Spatial distribution of model ages of basalts in Mare Humboldtianum (Hiesinger et al., 2000). (A) Units are based on mapping *Lunar Orbiter* image IV-165H1. Investigated units are outlined in white. (B) Sketch map of Mare Humboldtianum showing unit numbers and model ages in billion years (also see Table 11). Crater size-frequency distribution measurements were performed for the entire surface of each individual unit.

outside the basin center (Hiesinger et al., 2000). The ages of the investigated basalts in the center vary between 3.40 and 3.67 Ga (Fig. 12). In the region between the two most prominent rings, outside the basin center, the basalts exhibit ages of 3.64–3.94 Ga. Endymion, a crater in the close vicinity of the Humboldtianum basin, was flooded by basalt lavas ca. 3.63–3.70 b.y. ago.

Our data generally confirm the previous mapping by Lucchitta (1978), which shows the Humboldtianum basalts to be of Imbrian age (Table 11). However, our data also reveal additional detail, as we can demonstrate that the surface ages of the basalts in the basin center are younger than the basalts in the interring area. What are the implications of this age distribution within the Humboldtianum basin? According to a model of Head and Wilson (1992), crustal thickness is a major factor that controls the eruption of basalt onto the surface. *Clementine* data (Zuber et al., 1994) show a significantly thinner crust for the center of the Humboldtianum basin, surrounded by an annulus of relatively thicker crust in the interring area. This finding is consistent with *Apollo* seismic data (e.g., Chenet et al., 2006; Wieczorek et al., 2008), *Clementine* data (e.g., Wieczorek and Phillips, 1998; Hikida and Wieczorek, 2007), and *SELENE/Kaguya* data (e.g., Ishihara et al., 2009). Based on our observations, we conclude that in regions with thinner crust, volcanism could last longer because dikes were still able to reach the surface at times, whereas in other lunar regions, the crust was already too thick for the propagation of dikes to the surface.

As in other basins, the largest numbers of basalt units were formed in the late Imbrian Period at 3.6–3.8 b.y. ago; 38% of the basalt units in Mare Humboldtianum were formed 3.7–3.8 b.y. ago, and we see a gradual decline in volcanic activity after 3.7 b.y. ago.

TABLE 11. COMPARISON OF AGES FOR BASALTS IN MARE HUMBOLDTIANUM*

Unit	*Lunar Orbiter* image	Area (km^2)	Crater retention age $N(1)$	Error	Model age (Ga)	Error (b.y.)	Lucchitta (1978)
HU11	IV-165H3	9888	3.75E–03	+1.20E–03/–1.10E–03	3.40	+0.11/–0.23	Im
HU10	IV-165H3	7631	6.06E–03	+1.93E–03/–1.46E–03	3.57	+0.07/–0.08	Im
HU9	IV-165H3	4836	6.29E–03	+1.80E–03/–1.92E–03	3.58	+0.06/–0.11	Im
HU8	IV-74H3	3977	7.68E–03	+0.55E–03/–0.51E–03	3.63	+0.02/–0.22	Im
HU7	IV-165H	6035	7.92E–03	+2.48E–03/–1.91E–03	3.64	+0.06/–0.07	Im
			1.10E–02	+3.40E–03/–2.70E–03	3.71	+0.05/–0.06	
HU6	IV-165H3	4996	8.92E–03	+3.68E–03/–2.16E–03	3.67	+0.06/–0.07	Im
HU5†	IV-74H3	2851	1.02E–02	+3.20E–03/–1.30E–03	3.70	+0.05/–0.03	Im
HU4†	IV-74H3	2851	1.02E–02	+3.20E–03/–1.30E–03	3.70	+0.05/–0.03	Im
HU3§	IV-165H	2073	1.55E–02	+3.60E–03/–3.70E–03	3.77	+0.04/–0.05	Im
HU2§	IV-165H	2073	1.55E–02	+3.60E–03/–3.70E–03	3.77	+0.04/–0.05	Ip
HU1	IV-165H	2508	2.32E–02	+5.30E–03/–5.60E–03	3.84	+0.04/–0.04	Im
			4.26E–02	+1.75E–02/–1.45E–02	3.94	+0.05/–0.07	

*See text for details.
†Units Hu5 and Hu4 were dated together. See text for details.
§Units Hu3 and Hu2 were dated together. See text for details.

Mare Insularum

In the Insularum basin (600 km in diameter; Spudis, 1993), mare basalt ages based on crater counts vary from 2.93 to 3.54 b.y. ago (Hiesinger et al., 2003) (Fig. 11; Table 12). Three of our four units are Eratosthenian in age, one unit is of Imbrian age, and two units show signs of resurfacing at about the same time (2.93/3.50 Ga; 2.96/3.53 Ga). Ages based on crater degradation stages (Boyce, 1976; Boyce and Johnson, 1978) show a wide range with up to four (IN3: 2.5–3.65 Ga) or five ages assigned to a single unit (IN4: 2.5–3.75 Ga). The geologic maps generally show Imbrian ages (Eggleton, 1965; Schmitt et al., 1967; Wilhelms and McCauley, 1971), and only unit IN2 was partially mapped as Eratosthenian in age in the map of Wilhelms and McCauley (1971).

Grimaldi

Grimaldi is a 440 km large pre-Nectarian multiring impact basin on the western nearside (Spudis, 1993). For the basalt unit in Grimaldi (CGr1), our crater size-frequency distribution measurements yielded a model age of 3.48 Ga, with a resurfacing

TABLE 12. COMPARISON OF AGES FOR BASALTS IN MARE INSULARUM*

Unit	*Lunar Orbiter* image	Area (km^2)	Crater retention age *N*(1)	Error	Model age (Ga)	Error (b.y.)	Boyce (1976)	Wilhelms and McCauley (1971)	Hackman (1962)	Schmitt et al. (1967)	Eggleton (1965)
IN4	IV120H3	1614	2.40E–03/ 4.71E–03	+0.18E–03/ –0.17E–03 +1.11E–03/ –0.90E–03	2.93/3.50	+0.14/–0.17 +0.07/–0.08	3.2, 3.5, 3.65, 2.5, 3.75	Im		Ipm	
IN3	IV133H1	1885	2.53E–03/ 5.18E–03	+0.18E–03/ –0.17E–03 +1.20E–03/ –0.66E–03	2.96/3.53	+0.13/–0.16 +0.06/–0.05	3.2, 2.5, 3.5, 3.65	Im	Pm	Ipm	
IN2	IV120H3 IV133H1	2861	2.79E–03	+0.41E–03/ –0.19E–03	3.14	+0.15/–0.12	3.2, 3.5, 3.65	Im; Em	Pm	Ipm	Ipm
IN1	IV120H3	712	5.34E–03	+1.78E–03/ –1.35E–03	3.54	+0.07/–0.11	3.2, 3.5	Im		Ipm	

*See text for details.

event at 3.16 b.y. ago (Hiesinger et al., 2010) (Fig. 13; Table 13). Greeley et al. (1993) found the eastern part of Grimaldi to be 2.49 Ga (+0.51/–0.46) in age and the western part to be 3.25 Ga (+0.11/–0.33) in age. The sum of larger craters revealed an age of 3.58 Ga (+0.03/–0.06). For Grimaldi, no crater degradation ages are available (Boyce, 1976; Boyce and Johnson, 1978). The geologic maps of Wilhelms and McCauley (1971) and McCauley (1973) indicate an Eratosthenian (Em) age for these basalts. In the geologic map of Scott et al. (1977), the basalts in Grimaldi are of Eratosthenian and/or Imbrian age (EIm).

Mare Humorum

In the Humorum basin (425 km; Spudis, 1993), we were able to distinguish 12 units, which exhibit ages of 2.93–3.94 Ga, including three units at the basin rim and one unit in Gassendi A (Hiesinger et al., 2000) (Fig. 14). This unit exhibits low FeO values and is likely not a mare basalt. From our crater counts, we see that numerous units in Mare Humorum show evidence for resurfacing, i.e., flooding of older basalts with younger basalts. Because most units of Mare Humorum have at least one age near 3.45 Ga, we conclude that a possible flooding (resurfacing) of Mare Humorum with lavas from Oceanus Procellarum, as proposed by Johnson et al. (1973), occurred at this time. These authors suggested that the source region of the Oceanus Procellarum basalts that flooded Mare Humorum can be located in the Sharp Formation near the crater Herigonius. According to the stratigraphy of basalts in Oceanus Procellarum (Whitford-Stark and Head, 1980), based on ages of Boyce and Johnson (1978), the Sharp Formation is 2.7 ± 0.7 b.y. old. However, the Humorum basalt member of this formation, which is supposed to have actually flooded the Humorum basin, is 3.2 Ga (Boyce and Johnson, 1978), and thus slightly younger than our ages. From careful examination of high-resolution *Lunar Orbiter* images, Whitford-Stark and Head (1980) concluded that the Humorum basalt member of Oceanus Procellarum overlies older basalts in Mare Humorum. This stratigraphic sequence is consistent with crater size-frequency ages derived for both the Humorum basalts in Oceanus Procellarum and the Humorum basalts in Mare Humorum.

Out of eight mare basalt units in Mare Humorum, five show additional ages older than 3.45 Ga. These ages, between 3.45 and 3.94 Ga, result from older surfaces that were not completely covered by younger basalts. The unit, which shows just one well-defined age of 3.45 Ga, is restricted to the northeastern part of the basin, i.e., to the vicinity of the passage to Oceanus Procellarum and the possible source region. This observation supports the idea of flooding of Mare Humorum with lavas from Oceanus Procellarum at 3.45 Ga. In this interpretation, the thickness of these lavas from Oceanus Procellarum would be large enough to completely cover craters exposed on older surfaces, but in other parts of the basin, the thickness of these lavas thins so that older craters are still visible. This causes the second, older age of the underlying substrate in the crater

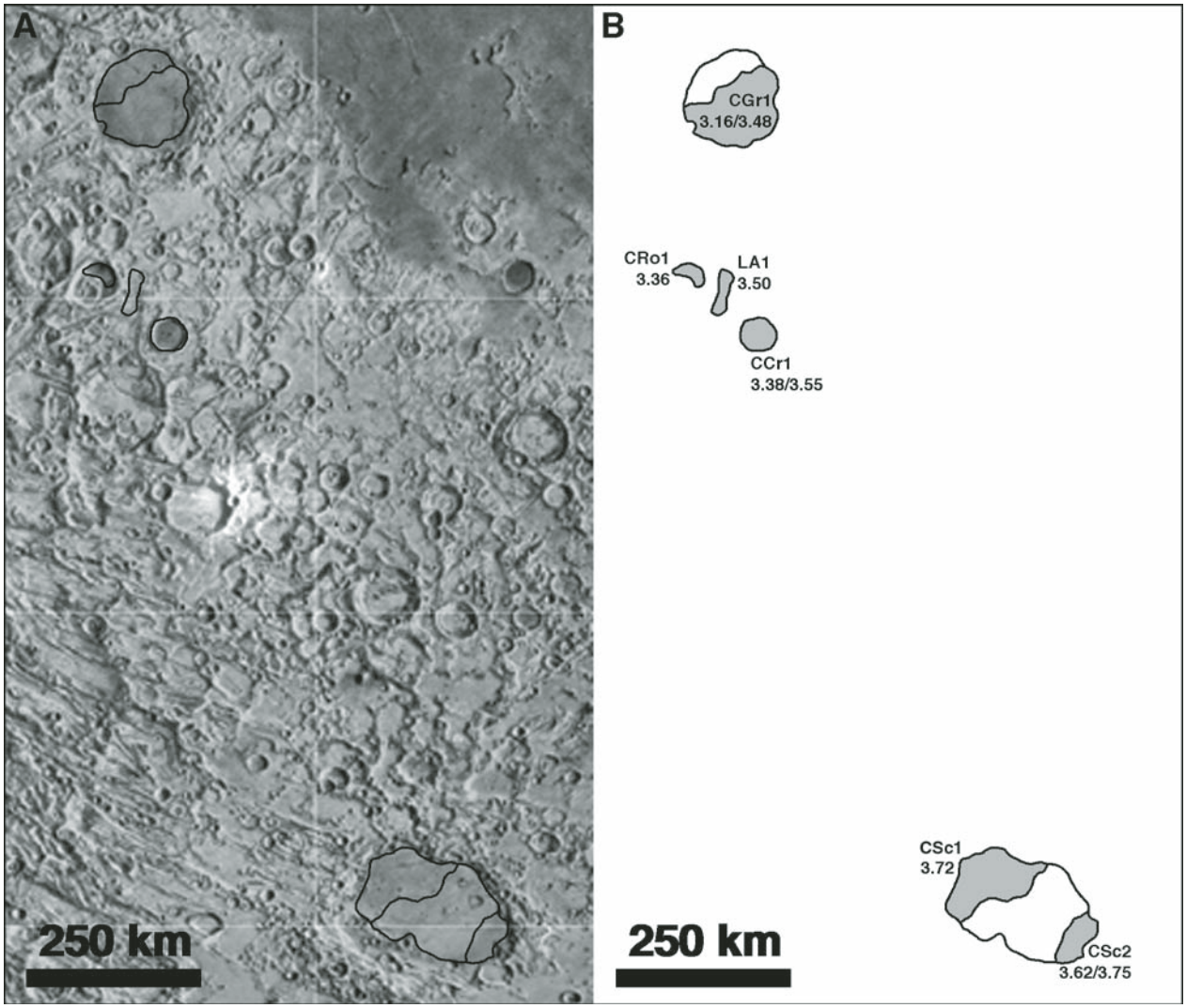

Figure 13. Spatial distribution of model ages for spectrally defined units in the craters Schickard, Grimaldi, Crüger, Rocca A, and Lacus Aestatis (Hiesinger et al., 2010). (A) U.S. Geological Survey shaded relief map, simple cylindrical map projection. Spectral units are outlined in black. (B) Sketch map of Schickard, Grimaldi, Crüger, Rocca A, and Lacus Aestatis showing unit numbers and model ages in billion years (also see Tables 8 and 13). CSc—Schickard, CGr—Grimaldi, CCr—Crüger, CRo—Rocca A, and LA—Lacus Aestatis. Crater size-frequency distribution measurements were performed for the areas highlighted in gray.

counts. In other words, these ages represent an older volcanic episode in the basin, which was terminated before the flooding with Oceanus Procellarum lavas occurred.

Dark mantle deposits in the south of Mare Humorum are older than ca. 3.62 Ga. Data from the *Clementine* altimeter show that these dark mantle deposits are located on a slightly higher topographic level than the basalts of Mare Humorum. From both the ages and the topographic position, we conclude that dark mantle deposits in the Humorum basin were not completely covered with lavas from Oceanus Procellarum (e.g., Head, 1974).

At the eastern edge of Mare Humorum, we identified a unit exhibiting two ages of 3.10 and 3.45 Ga. We interpret this as a hint of young volcanism, which was probably triggered by extensional tectonism occurring at the basin edge due to subsidence of the basin center. However, Head and Wilson (1992) demonstrated that dike propagation from great depths is in principle independent of near-surface extensional tectonism, but the near-surface orientation of dikes may be controlled by the shallow crustal stress field.

In Mare Humorum, our data reveal a bimodal distribution of surface ages, with a first maximum at 3.6–3.7 b.y. ago and a second maximum at 3.4–3.5 b.y. ago. In numbers, 24% of the basalt units exposed in Mare Humorum were formed during the first period, and 29% were formed during the second period. Our data indicate that the largest number of units was produced in the late Imbrian Period.

Hackwill et al. (2006) also performed crater counts for Mare Humorum. Their unit 111 (3.38 Ga) and 117 (3.37 Ga) roughly

TABLE 13. COMPARISON OF AGES FOR BASALTS IN SELECTED CRATERS
(SCHICKARD [CSc], GRIMALDI [CGr], CRÜGER [CCr], ROCCA A [CRo1], HUBBLE [CHu], JOLIOT [CJo], GODDARD [CGo])*

Unit	*Lunar Orbiter* image	Area (km^2)	Crater retention age *N*(1)	Error	Model age (Ga)	Error (b.y.)	Boyce (1976); Boyce and Johnson (1978)	Wilhelms and McCauley (1971)	Wilshire (1973)	Wilhelms and El-Baz (1977)	McCauley (1973)	Karlstrom (1974)	Scott et al. (1977)
CSc2	IV160H2	1801	7.25E–03/ 1.34E–02	+8.74E–02/ –5.73E–03 +1.93E–02/ –1.02E–02	3.62/3.75	+0.04/ –0.06 +0.06/ –0.06	3.85	Em				Em	Elm
CSc1	IV160H2	6516	1.15E–02	+1.36E–02/ –9.36E–03	3.72	+0.03/ –0.04	3.85	Em				Em	Elm
CGr1	IV168H3	14,201	2.81E–03/ 4.58E–03	+3.02E–03/ –2.63E–03 +5.63E–03/ –3.72E–03	3.16/3.48	+0.08/ –0.12 +0.07/ –0.09	No age	Em			Em		Elm
CCr1	IV168H2	1271	3.62E–03/ 5.69E–03	+4.13E–03/ –3.15E–03 +8.01E–03/ –4.63E–03	3.38/3.55	+0.06/ –0.10 +0.09/ –0.06	No age	Em	Em		Em		Elm
CRo1	IV168H2	392	3.51E–03	+4.32E–03/ –2.86E–03	3.36	+0.10/ –0.18	No age	Em			Em		Elm
CHu1	IV17H3	2543	1.66E–02	+2.03E–02/ –1.24E–02	3.79	+0.03/ –0.06	No age			Im1			
CJo2	IV17H3	2081	6.65E–03	+8.99E–03/ –5.41E–03	3.60	+0.07/ –0.06	No age			Im1			
CJo1	IV17H3	1494	7.43E–03/ 1.47E–02	+9.08E–03/ –5.72E–03 +2.37E–02/ –1.19E–02	3.62/3.76	+0.05/ –0.06 +0.09/ –0.04	No age			Im1			
CGo1	IV17H2	3817	6.68E–03	+8.29E–03/ –4.92E–03	3.60	+0.05/ –0.09	3.5/3.65			Im2			

*See text for details.

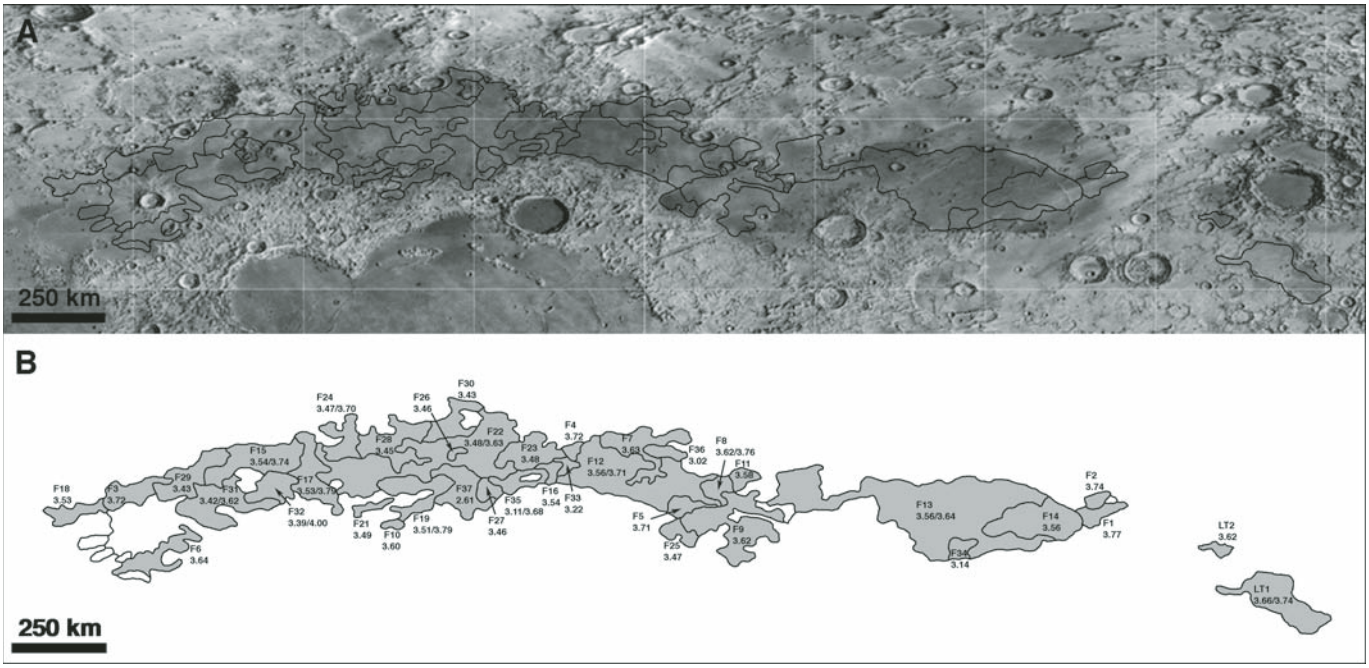

Figure 14. Spatial distribution of model ages for spectrally defined units in Mare Humorum (Hiesinger et al., 2000). (A) Image mosaic of Fourier-transformed *Lunar Orbiter* images IV-137H1, IV-137H2, IV-143H1, and IV-143H2. Spectral units are outlined in black. (B) Sketch map of Mare Humorum showing unit numbers and model ages in billion years (also see Table 14). Crater size-frequency distribution measurements were performed for the entire surface of each individual unit.

correspond to our unit H9 (3.42/3.52 Ga), their unit 136 (3.51 Ga) roughly corresponds to our unit H6 (3.46/3.75 Ga), and their unit 84 (3.41 Ga) roughly corresponds to our unit H7 (3.45/3.94 Ga). For their unit 85, they determined an age of 3.25 Ga, but our counts revealed model ages of 3.53/3.65 Ga. Interestingly, like us, Hackwill et al. (2006) also found relatively young ages (their unit 119; 2.79 Ga.) at the eastern edge of Mare Humorum, where we found basalts of 3.10 Ga, in some areas resurfacing older basalts of 3.45 Ga.

Mare Humorum was mapped by Titley (1967), and this map indicates that almost all basalts are of Imbrian age (Table 14). Units H3 and H4, which show very low albedo, were mapped as "Imbrian and/or Eratosthenian" (EId). For those units, our data reveal Imbrian ages of 3.62 Ga and 3.64 Ga, respectively. Unit H11 was mapped as Imbrian in age, which is consistent with our data, but we also see a younger age of 3.10 Ga, indicating a resurfacing event in the early Eratosthenian Period. Data from Boyce (1976) and Boyce and Johnson (1978) are generally consistent with our measurements but are not available for all of our spectral units in the Humorum region, i.e., H1, H2, H3, and H12. However, for two units (H4, H8), the differences in ages between the Boyce data and our data are significant. For all those units, our data exhibit older ages compared to the Boyce data.

Mare Frigoris

We performed crater counts for 37 spectrally homogeneous basalt units within Mare Frigoris (Hiesinger et al., 2010). Our data indicate that surface ages of Frigoris basalts range from 2.61 to 4.00 Ga (Fig. 15; Table 15). This is a wider range of ages compared to Whitford-Stark (1990), who argued that his blue, low-albedo unit with a strong 1 μm absorption band is 3.2 Ga (±0.2) in age, and his oldest red, high-albedo unit with an average to strong 1 μm absorption band is 3.6 (±0.2) b.y. old. Most of our units were formed in the late Imbrian Period between ca. 3.4 and ca. 3.8 Ga. This is consistent with observations made for other lunar nearside basalts in Oceanus Procellarum, Imbrium, Serenitatis, Tranquillitatis, Cognitum, Nubium, Insularum, Humorum, Humboldtianum, and Australe (Hiesinger et al., 2000, 2002, 2003). In detail, of our 37 units, six units (~16%) are younger than 3.4 Ga, 12 units (~32%) were formed between 3.4 and 3.5 b.y. ago, nine units (~24%) were formed between 3.5 and 3.6 b.y. ago, five units

TABLE 14. COMPARISON OF AGES FOR BASALTS IN MARE HUMORUM*

Unit	*Lunar Orbiter* image	Area (km^2)	Crater retention age *N*(1)	Error	Model age (Ga)	Error (b.y.)	Boyce (1976)	Titley (1967)	Marshall (1963)
H12	V-179M	20	2.50E–03	+0.17E–03/–0.17E–03	2.93	+0.14/–0.17	n.d.		Elf
H11	IV-137H1	4729	2.72E–03/ 4.24E–03	+0.20E–03/–0.18E–03 +1.35E–03/–0.79E–03	3.10 3.45	+0.10/–0.13 +0.10/–0.06	3.2	lpm4	
H10	IV-137H1	1755	3.35E–03	+0.47E–03/–0.45E–03	3.33	+0.08/–0.13	3.2	lpm3	
H9	IV-137H1 IV-143H1	12,619	3.91E–03/ 5.12E–03	+0.28E–03/–0.26E–03 +0.36E–03/–0.34E–03	3.42 3.52	+0.03/–0.04 +0.02/–0.02	3.5/3.2	lpm2	
H8	IV-137H1 IV-143H1	6296	4.17E–03	+0.62E–03/–0.20E–03	3.45	+0.05/–0.04	3.2	lpm3, lpm4	
H7	IV-143H1	8496	4.16E–03/ 4.37E–02	+0.29E–03/–0.28E–03 +1.81E–02/–1.27E–03	3.45 3.94	+0.02/–0.04 +0.06/–0.05	3.5	lpm3	
H6	IV-137H1 IV-143H1	30,222	4.30E–03/ 1.35E–02	+0.20E–03/–0.31E–03 +3.10E–03/–3.30E–03	3.46 3.75	+0.02/–0.03 +0.04/–0.06	3.2/3.5	lpm3	
H5	IV-143H1	12,676	5.18E–03/ 8.45E–03	+0.37E–03/–0.35E–03 +2.70E–03/–2.04E–03	3.53 3.65	+0.02/–0.03 +0.06/–0.06	3.5/3.65/3.75	lpm1, lpm3	
H4	IV-143H1	2291	7.34E–03	+0.52E–03/–0.49E–03	3.62	+0.02/–0.02	3.5	Eld	
H3	IV-143H1	298	7.99E–03	+1.84E–03/–1.49E–03	3.64	+0.05/–0.06	n.d.	Eld	
H2	IV-143H1	1116	1.01E–02	+1.40E–03/–1.30E–03	3.69	+0.03/–0.03	n.d.	lpm2, Eld	
H1	IV-143H1	668	1.08E–02	+0.70E–03/–2.60E–03	3.70	+0.02/–0.05	n.d.	lpm3	

*See text for details; n.d.—no data.

(~14%) were formed between 3.6 and 3.7 b.y. ago, and five units (~14%) are older than 3.7 Ga (Table 15).

Among the 37 units dated in this study, there are 12 units that show evidence for resurfacing (F8, F12, F13, F15, F17, F19, F20, F22, F24, F31, F32, F35). These resurfacing events occurred between 3.62 (F8) and 3.11 b.y. ago (F35) and affected older surfaces of 4.0 (F32) to 3.62 Ga (F31).

If we look at the spatial distribution of basalt ages in Mare Frigoris, it appears that older basalts (3.5–3.8 Ga) occur east of 0° longitude, and younger basalts (3.4–3.6 Ga) are exposed between 0° and 40°W. We also found evidence that basalts west of 40°W are older (3.5–3.8 Ga) and similar in age to the eastern basalts of Mare Frigoris.

Crater degradation ages are available only for western and central Mare Frigoris (Boyce, 1976; Boyce and Johnson, 1978). Units F1, F2, F3, F10, F13, F14, F20, F21, F25, and F34 are not covered in the maps of Boyce (1976) and Boyce and Johnson (1978). We found the best agreement between the two techniques for unit F33, for which the crater degradation age (3.20 Ga) and our crater model age (3.22 Ga) are basically identical, and the least agreement for unit F6 (2.50 vs. 3.64 Ga), for which the ages differ by 1.14 b.y. The crater size-frequency model age of unit F28 (3.45 Ga) is consistent with the crater degradation ages (3.20/3.50 Ga) of Boyce (1976) and Boyce and Johnson (1978). Similarly, for our unit F35, we derived an old age of 3.68 Ga and a resurfacing age of 3.11 Ga, which is in the range of the crater degradation age of 3.20 Ga (Boyce, 1976; Boyce and Johnson, 1978). The same is true for unit F37, for which the crater size-frequency model age of 2.61 Ga lies in between the crater degradation ages (2.50/3.20 Ga) of Boyce (1976) and Boyce and Johnson (1978). A comparison of the ages derived by the two techniques reveals that crater size-frequency ages of 22 units (F4, F5, F6, F7, F8, F9, F11, F12, F15, F16, F17, F18, F19, F22, F23, F24, F26, F27, F29, F30, F31, F32) are systematically older compared to crater degradation ages. Only unit F36 has a crater size-frequency model age that is younger than the crater degradation age (Table 15).

Mare Cognitum

Based on our crater counts, we see that all units in Mare Cognitum are of Imbrian age (3.32–3.65 Ga; Hiesinger et al., 2003) (Fig. 11; Table 16). Boyce (1976) and Boyce and Johnson (1978) found similar ages (3.2–3.5 Ga), and there is an excellent agreement between the two data sets for these units. Only unit C2 appears a little younger in the Boyce (1976) data (3.2 ± 0.2 Ga) compared to our age (3.45 Ga). For unit C5, we found evidence for a resurfacing event (3.32/3.65 Ga), but this is not resolved in the Boyce data (3.2 ± 0.2 Ga).

Imbrian ages for the units in Mare Cognitum are consistent with the mapping of Eggleton (1965) and Wilhelms and McCauley (1971). However, Wilhelms and McCauley (1971) also mapped units C1, C2, and C5 to consist, at least partially, of Eratosthenian basalts. These Eratosthenian ages are not consistent

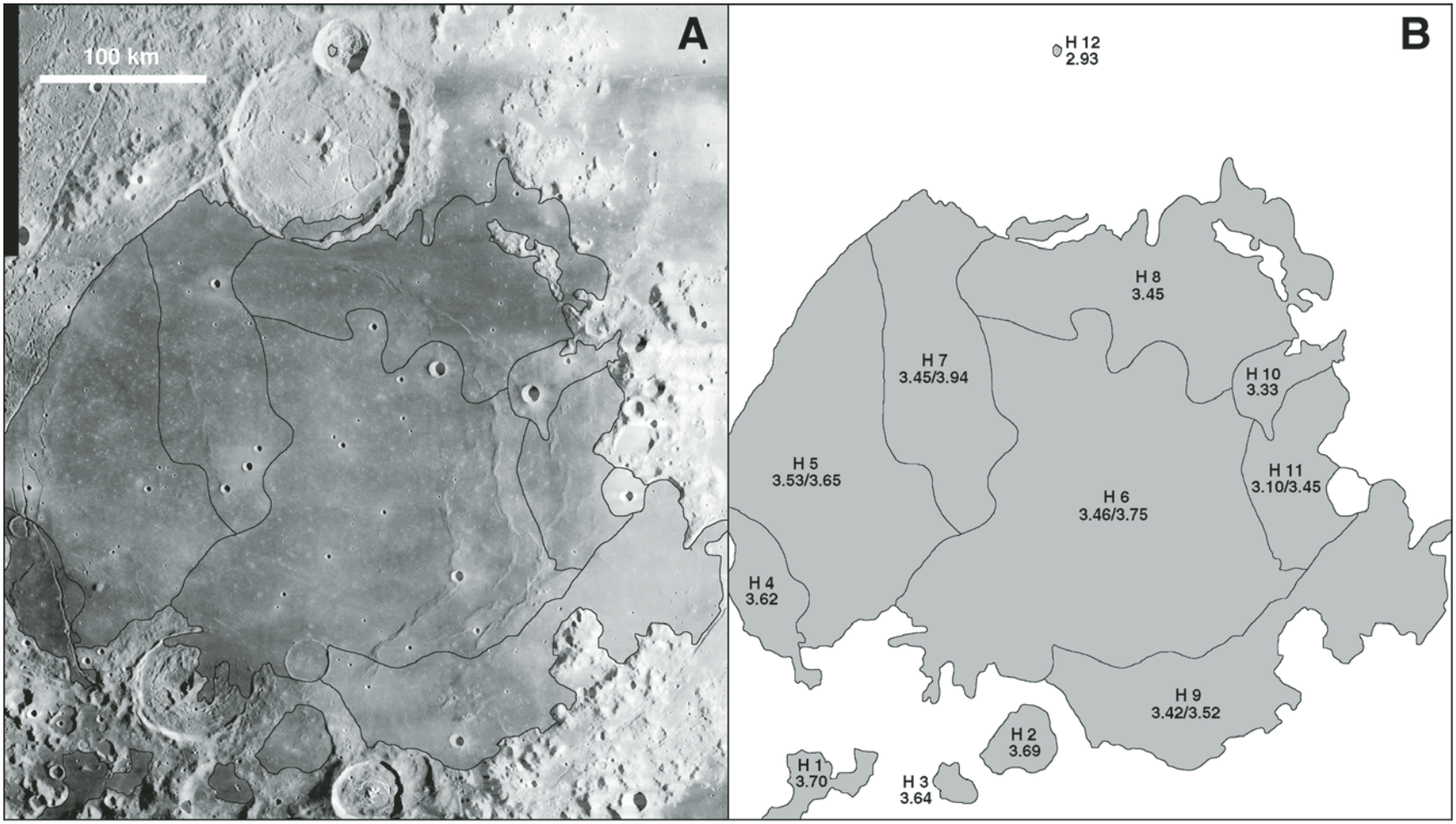

Figure 15. Spatial distribution of model ages for spectrally defined units in Mare Frigoris and Lacus Temporis (Hiesinger et al., 2010). (A) U.S. Geological Survey shaded relief map, simple cylindrical map projection. Spectral units are outlined in black. (B) Sketch map of Mare Frigoris (F) showing unit numbers and model ages in billion years (also see Tables 8 and 15). Crater size-frequency distribution measurements were performed for the areas highlighted in gray.

TABLE 15. COMPARISON OF AGES FOR BASALTS IN MARE FRIGORIS*

Unit	*Lunar Orbiter* image	Area (km^2)	Crater retention age *N*(1)	Error	Model age (Ga)	Error (b.y.)	Boyce (1976); Boyce and Johnson (1978)	Wilhelms and McCauley (1971)	Lucchitta (1978)	Ulrich (1969)	M'Gonigle and Schleicher (1972)	Lucchitta (1972)
F37	IV140H1	6728	2.19E–03	+0.54E–03/–0.29E–03	2.61	+0.50/–0.34	2.50/3.20	Im	Im, Em, Ip1		Im,Elm	
F36	IV116H1	1455	2.60E–03	+0.18E–03/–0.34E–03	3.02	+0.12/–0.33	3.20/3.50	Im	Im		Im	
F35	IV140H1	2520	2.74E–03/	+0.40E–03/–0.18E–03	3.11/3.68	+0.17/–0.12	3.20	Im	Im		Im	
	IV128H1		9.41E–03	+6.29E–03/–1.76E–03		+0.10/–0.05						
F34	IV92H1	1875	2.85E–03	+0.80E–03/–0.19E–03	3.17	+0.21/–0.11	No age	Im	Im			Im
F33	IV128H1	741	2.98E–03	+1.03E–03/–0.39E–03	3.22	+0.21/–0.20	3.20	Em	Im		Elm, Im	
F32	IV152H1	3301	3.70E–03/	+0.92E–03/–0.69E–03	3.39/4.00	+0.10/–0.16	2.50	Im	Im, Em	Im		
			6.22E–02	+3.88E–02/–1.50E–02		+0.07/–0.04						
F31	IV164H1	8642	3.90E–03/	+0.60E–03/–0.50E–03	3.42/3.62	+0.06/–0.08	2.50/3.20	Em	Em	Elm, Im		
	IV152H1		7.32E–03	+3.38E–03/–1.76E–03		+0.08/–0.07						
F30	IV140H1	3654	4.05E–03	+1.11E–03/–0.76E–03	3.43	+0.09/–0.12	3.20	Im	Im, Em		Im	
F29	IV164H1	4047	3.98E–03	+1.07E–03/–0.51E–03	3.43	+0.09/–0.08	2.50/3.20	Im, Em	Em	Im, Elm		
F28	IV152H1	6763	4.21E–03	+0.94E–03/–0.78E–03	3.45	+0.07/–0.11	3.20/3.50	Im	Em, Im	Im		
	IV140H1											
F27	IV140H1	1520	4.29E–03	+0.89E–03/–0.81E–03	3.46	+0.07/–0.11	3.20	Im	Im, Em		Im	
F26	IV140H1	350	4.30E–03	+1.78E–03/–0.80E–03	3.46	+0.11/–0.10	3.20	Im	Im		Im	
F25	IV116H1	1668	4.41E–03	+1.39E–03/–0.82E–03	3.47	+0.09/–0.10	No age	Em	Im		Elm, Im	
F24	IV152H1	4475	4.38E–03/	+0.90E–03/–0.81E–03	3.47/3.70	+0.06/–0.10	3.20	Im	Em	Im		
			1.04E–02	+4.30E–03/–1.97E–03		+0.06/–0.05						
F23	IV140H1	5279	4.49E–03	+1.04E–03/–0.84E–03	3.48	+0.07/–0.10	3.20	Im	Im		Im	
	IV128H1											
F22	IV140H1	21,713	4.51E–03/	+0.80E–03/–0.89E–03	3.48/3.63	+0.05/–0.10	2.50/3.20	Im	Im, Em	Im	Im	
	IV152H1		7.72E–03	+2.95E–02/–1.86E–03		+0.09/–0.07						
F21	IV140H1	1149	4.69E–03	+1.30E–03/–0.88E–03	3.49	+0.08/–0.09	No age	Im	Im	Im		
F20	IV79H3	159	4.68E–03/	+1.39E–03/–0.88E–03	3.49/3.80	+0.08/–0.09	No age		Ip2			
			1.78E–02	+1.04E–02/–0.43E–03		+0.07/–0.05						
F19	IV140H1	5305	4.89E–03/	+1.07E–03/–0.92E–03	3.51/3.79	+0.06/–0.09	2.50/3.20	Im	Im		Im, Elm	
			1.69E–02	+1.01E–02/–4.10E–03		+0.08/–0.05						
F18	IV164H1	2306	5.32E–03	+1.43E–03/–1.28E–03	3.53	+0.07/–0.10	2.50	Em	Im	Elm		
F17	IV152H1	6558	5.25E–03/	+1.10E–03/–0.98E–03	3.53/3.79	+0.05/–0.07	2.50/3.20	Im	Im	Im		
			1.67E–02	+1.06E–02/–3.10E–03		+0.08/–0.04						
F16	IV128H1	1298	5.35E–03	+1.49E–03/–1.00E–03	3.54	+0.06/–0.08	3.20	Im	Im		Im	
F15	IV164H1	8329	5.48E–03/	+1.16E–03/–0.78E–03	3.54/3.74	+0.06/–0.05	2.50	Im	Im, Em	Im		
	IV152H1		1.31E–02	+1.47E–02/–4.35E–03		+0.13/–0.08						
F14	IV92H1	11,046	5.85E–03	+1.00E–03/–1.09E–03	3.56	+0.04/–0.06	No age	Im, Ip	Im			Im
	IV80H1											
	IV79H3											
F13	IV104H1	42,044	5.76E–03/	+0.61E–03/–0.66E–03	3.56/3.64	+0.03/–0.04	No age	Im	Im			Im
	IV92H1		7.94E–03	+4.76E–03/–1.48E–03		+0.10/–0.05						
F12	IV128H1	17,652	5.77E–03/	+0.75E–03/–0.78E–03	3.56/3.71	+0.03/–0.05	3.20/2.50	Im	Im		Im	
	IV116H1		1.12E–02	+5.10E–03/–2.73E–03		+0.07/–0.06						
F11	IV116H1	1272	6.18E–03	+1.67E–03/–1.15E–03	3.58	+0.06/–0.06	3.20	Im	Im		Im, Elm	
F10	IV140H1	649	6.79E–03	+2.31E–03/–2.38E–03	3.60	+0.07/–0.13	No age	Em	Im	Elm		
F9	IV104H1	12,037	7.35E–03	+1.32E–03/–1.55E–03	3.62	+0.04/–0.06	3.50/3.20	Im	Im		Im	
	IV116H1											
F8	IV116H1	2226	7.33E–03/	+1.20E–03/–0.95E–03	3.62/3.76	+0.04/–0.03	3.50/3.20	Im	Im		Im	
			1.42E–02	+5.80E–03/–2.60E–03		+0.06/–0.04						
F7	IV128H1	7340	7.78E–03	+1.00E–03/–1.04E–03	3.63	+0.03/–0.03	3.50/2.50	Im	Im		Im	
	IV116H1											
F6	IV164H1	4015	7.81E–03	+1.72E–03/–1.46E–03	3.64	+0.04/–0.06	2.50	Em, Im	Em	Im		
F5	IV116H1	1591	1.12E–02	+3.00E–03/–3.36E–03	3.71	+0.05/–0.07	3.20	Im	Ip2, Im		Ip1, Im	
F4	IV128H1	550	1.15E–02	+3.80E–03/–4.24E–03	3.72	+0.05/–0.10	3.20	Im	Im		Elm, Im	
F3	IV164H1	4170	1.16E–02	+2.60E–03/–2.88E–03	3.72	+0.04/–0.06	No age	Im	Im	Im, Elm		
F2	IV79H3	721	1.29E–02	+2.50E–03/–3.12E–03	3.74	+0.03/–0.06	No age	Ip	Ip2			Ip
F1	IV79H3	2741	1.54E–02	+2.70E–03/–3.20E–03	3.77	+0.03/–0.04	No age	Ip	Ip2			Ip

*See text for details.

TABLE 16. COMPARISON OF AGES FOR BASALTS IN MARE COGNITUM*

Unit	*Lunar Orbiter* image	Area (km^2)	Crater retention age *N*(1)	Error	Model age (Ga)	Error (b.y.)	Boyce (1976)	Wilhelms and McCauley (1971)	Eggleton (1965)
C5	IV125H3	1597	3.30E–03/ 8.38E–03	+0.65E–03/ –0.43E–03 +4.22E–03/ –2.45E–03	3.32/3.65	+0.10/–0.14 +0.08/–0.08	3.2	Im, Em	Ipm
C4	IV125H2	1359	3.50E–03	+0.83E–03/ –0.45E–03	3.36	+0.10/–0.11	3.5, 3.2	Im	Ipm
C3	IV120H2	1621	3.88E–03	+0.79E–03/ –0.50E–03	3.41	+0.08/–0.08	3.5	Im	Ipm
C2	IV125H2	1325	4.23E–03	+1.24E–03/ –0.55E–03	3.45	+0.09/–0.06	3.2	Em, Im	Ipm
C1	IV125H2, IV125H3	6051	4.64E–03	+1.45E–03/ –0.92E–03	3.49	+0.08/–0.10	3.5, 3.2	Im, Em	Ipm

*See text for details.

with our ages, but they are within the error bars of the degradation ages (3.2 ± 0.2 Ga).

Mare Vaporum

In Mare Vaporum, we dated six spectrally defined basalt units (Hiesinger et al., 2010). On the basis of our crater counts, we found that our unit V6 is 3.10 b.y. old, hence Eratosthenian in age. Two units, V4 and V5, are 3.22 and 3.23 Ga in age, all other units (V1, V2, V3) are clearly Imbrian in age, with ages ranging from 3.44 to 3.61 Ga. Only unit V3 shows evidence of resurfacing of a 3.84 b.y. old surface at 3.44 Ga (Fig. 16; Table 17). A comparison between crater degradation ages of Boyce (1976) and Boyce and Johnson (1978) and our model ages revealed an excellent agreement for some units and substantial differences for other units. We found consistent ages for units V4, V5, and V6. For unit V4, our model age of 3.23 Ga compares favorably to the crater degradation ages of 3.20–2.50 Ga (Boyce, 1976; Boyce and Johnson, 1978). Similarly, the model age for unit V5 (3.22 Ga) is in the same range as the crater degradation age of 3.20–2.50 Ga (Boyce, 1976; Boyce and Johnson, 1978). For unit V6, our model age is 3.10 Ga; the Boyce age is 3.20–2.50 Ga (Boyce, 1976; Boyce and Johnson, 1978). For unit V3, several crater degradation ages can be extracted from the map of Boyce and Johnson (1978), ranging from 3.20 to 3.75 Ga. For this unit, we were able to constrain the age to 3.44 Ga. The largest differences were detected for units V1 and V2. For unit V1, the ages differ by 0.41 b.y. (crater degradation age of 3.20 Ga; crater count model age of 3.61 Ga), and for unit V2, there is a difference of 0.25 b.y. (crater degradation age of 3.20 Ga; crater count model age of 3.45 Ga).

Sinus Medii

Our crater size-frequency measurements revealed model ages of 3.63 (SM4), 3.74 (SM3), 3.76 (SM2), and 3.79 Ga (SM1) (Hiesinger et al., 2010) (Fig. 16; Table 8). Crater degradation ages of Sinus Medii correspond very well with our model ages. For example, according to Boyce (1976) and Boyce and Johnson (1978), unit SM1 is 3.85 Ga, i.e., within 0.06 b.y. of our derived model age. For unit SM3, both techniques basically yield identical ages of 3.74 and 3.75 Ga. A somewhat larger discrepancy was found for unit SM4. The crater degradation age (3.50 Ga) is significantly younger than our crater size-frequency model age (3.63 Ga). Despite the relatively large area of Sinus Medii (~300 × 150 km), our model ages are extremely similar, which is surprising considering the variety of geologic units exposed within this lunar region. On the basis of our crater counts, mare basalts and Cayley plains were emplaced more or less contemporaneously. Together with the fact that our model ages do not correspond to either the Imbrium (3.92 Ga; Neukum, 1983) or the Orientale (3.84 Ga; Neukum, 1983) event, we interpret this to be more consistent with a volcanic origin of the studied light plains in Sinus Medii, an interpretation already put

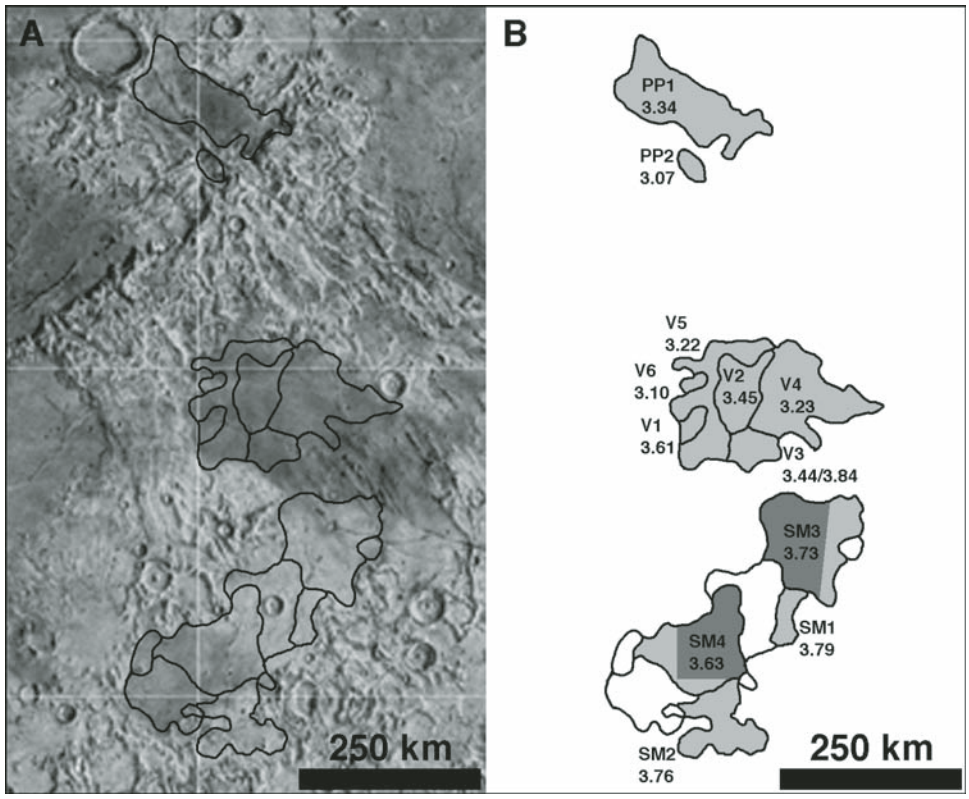

Figure 16. Spatial distribution of model ages for spectrally defined units in Mare Vaporum, Sinus Medii, and Palus Putredinis (Hiesinger et al., 2010). (A) U.S. Geological Survey shaded relief map, simple cylindrical map projection. Spectral units are outlined in black. (B) Sketch map of Mare Vaporum, Sinus Medii, and Palus Putredinis showing unit numbers and model ages in billion years (also see Tables 8 and 17). V—Mare Vaporum, SM—Sinus Medii, and PP—Palus Putredinis. Crater size-frequency distribution measurements were performed for the areas highlighted in gray. For units SM3 and SM4, the count area is represented by the dark-gray area.

forward by Neukum (1977) and Köhler et al. (1999, 2000) for light plains at northern latitudes. However, our ages (3.74, 3.76, 3.79 Ga) are in agreement with the age of the Imbrium basin (3.77 Ga) proposed by Stöffler in Stöffler and Ryder (2001). In the same paper, Ryder argued that the Imbrium basin is 3.85 Ga in age (Stöffler and Ryder, 2001), and hence is older than the dated light plains in Sinus Medii. Spudis (1978) and Hawke and Head (1978) suggested that some light plains might be related to KREEP (rocks rich in K, REE, and P) volcanism. Hawke and Bell (1981), Antonenko et al. (1995), and Robinson and Jolliff (2002) presented evidence that ancient lava plains (cryptomare) might be present beneath some light plains. In summary, these studies suggest that light plains may have formed by a variety of processes and that the interpretation of their origin should be addressed on a case-by-case basis. We conclude that the issue whether light plains are formed by impact or volcanic processes needs further investigation (also see discussion in Mustard and Head, 1996).

Palus Putredinis

For Palus Putredinis unit PP1, which contains the *Apollo 15* landing site, we determined an Imbrian basalt model age of 3.35 Ga (Hiesinger et al., 2010) (Fig. 16; Table 8). This is in excellent agreement with radiometric ages of basalt samples returned from the *Apollo 15* mission, which indicate ages from 3.30 to 3.35 Ga (Stöffler and Ryder, 2001) or 3.20–3.40 Ga (Nyquist and Shih, 1992). Our second unit PP2 is slightly younger (3.07 Ga) and of Eratosthenian age. Crater degradation ages of Palus Putredinis indicate older ages of 3.50 Ga for both of our count areas (Boyce, 1976; Boyce and Johnson, 1978) and are less consistent with the ages in the geologic maps (Hackman, 1966; Wilhelms and McCauley, 1971) and the radiometric ages of the *Apollo 15* samples (Stöffler and Ryder, 2001; Nyquist and Shih, 1992).

Lacus Aestatis

Our crater size-frequency measurements revealed a model age of 3.50 Ga for the Lacus Aestatis basalt, i.e., an Imbrian age (Hiesinger et al., 2010). Also based on crater size-frequency distribution measurements, Williams et al. (1995) found a similar age for this unit of 3.46 Ga. Crater degradation ages for this part of the Moon are not available (Boyce, 1976; Boyce and Johnson, 1978) (Fig. 13; Table 8).

Lacus Temporis

Based on our crater counts, we determined late Imbrian ages for the basalts in the Lacus Temporis region (Hiesinger et al., 2010). According to our crater size-frequency distribution measurements, unit LT1 shows an old model age of 3.76 Ga and a resurfacing model age of 3.68 Ga (Fig. 15; Table 8). Our

TABLE 17. COMPARISON OF AGES FOR BASALTS IN MARE VAPORUM*

Unit	*Lunar Orbiter* image	Area (km^2)	Crater retention age *N*(1)	Error	Model age (Ga)	Error (b.y.)	Boyce (1976); Boyce and Johnson (1978)	Wilhelms and McCauley (1971)	Hackman (1966)	Wilhelms (1968)
V6	IV102H2	463	2.72E–03	+1.90E–04/–3.60E–04	3.10	+0.10/–0.30	3.20/2.50	Em, Im		CEm2
V5	IV102H2	10,846	2.96E–03	+6.20E–04/–3.80E–04	3.22	+0.15/–0.21	3.20/2.50	Im	Ipm	Ipm1, Ipm2, CEm1, CEm2
V4	IV102H2	12,814	2.99E–03	+4.50E–04/–2.00E–04	3.23	+0.11/–0.09	3.20/2.50	Im	Ipm	Ipm1, Ipm2, CEm1
V3	IV102H2	3102	4.13E–03	+1.07E–03/–7.70E–04	3.44	+0.09/–0.11	3.75/3.65/ 3.50/3.20	Em, Im		CEm1, Ipm2, Ipm1
V2	IV102H2	6324	4.23E–03	+1.11E–03/–7.90E–04	3.45	+0.09/–0.11	3.20	Im		Ipm1, Ipm2
V1	IV102H2	1044	6.89E–03	+2.24E–03/–1.66E–03	3.61	+0.06/–0.08	3.20	Em		CEm1

*See text for details. Read 2.72E–03 as 2.72×10^{-3}.

unit LT2, located south of crater Endymion, has a model age of 3.62 Ga. There are no crater degradation ages available for these basalts (Boyce, 1976; Boyce and Johnson, 1978).

Basalts in Schickard, Crüger, Rocca A, Goddard, Joliot, and Hubble

For the larger northern mare basalt in Schickard crater (CSc1), we derived an Imbrian model age of 3.72 Ga (Hiesinger et al., 2010). The smaller southern mare basalt (CSc2) shows evidence for resurfacing of an older 3.75 b.y. old surface at 3.62 b.y. ago. Because the two model ages of 3.75 and 3.72 Ga are extremely similar, this could imply that both regions were flooded with mare basalts at the same time. However, while volcanism stopped in the northern part at 3.72 Ga, it continued at least to 3.62 Ga in the southern part, as demonstrated by the resurfacing event at this time (Fig. 13; Table 13). Greeley et al. (1993) reported an age of 3.80 Ga (+0.02/–0.04) for both mare occurrences in Schickard. Crater degradation ages are older (3.85 Ga) and show the same age for both mare basalt deposits (Boyce, 1976; Boyce and Johnson, 1978).

According to our crater counts, the basalts in Crüger crater (CCr1) also show evidence for resurfacing (Hiesinger et al., 2010). In this crater, we found that a 3.55 b.y. old surface was resurfaced at 3.38 b.y. ago (Fig. 13; Table 13). This age is similar to the 3.57 Ga age found by Williams et al. (1995). We derived a similar age of 3.36 Ga for the basalt in adjacent Rocca A crater (CRo1) (Hiesinger et al., 2010) (Fig. 13; Table 13). For this unit, Williams et al. (1995) found an age of 3.18 Ga. As with Crüger crater, there are no crater degradation ages available (Boyce, 1976; Boyce and Johnson, 1978).

In the northeastern hemisphere, we dated the basalts in the craters Hubble, Joliot, and Goddard (Hiesinger et al., 2010). We found a model age of 3.79 Ga for the basalts in Hubble crater (CHu1), and a model age of 3.60 Ga for the basalts in Goddard crater (CGo1) (Fig. 9; Table 13). In Joliot crater, we mapped and dated two basalt units. Unit CJo1 shows evidence of resurfacing of a 3.76 b.y. old surface at 3.62 b.y. ago. The second unit (CJo2) exhibits only one age of 3.60 Ga (Fig. 9; Table 13). Crater degradation ages (3.50/3.65 Ga) are only available for Goddard crater, and these ages are in good agreement with our crater size-frequency ages (3.60 Ga) (Boyce, 1976; Boyce and Johnson, 1978). Generally, we found that all basalt ages within the studied craters in the northeastern hemisphere are substantially older than the basalts of the craters in the southwestern hemisphere (Fig. 17).

SYNOPTIC VIEW OF THE INVESTIGATED BASINS

Based on our age data, Figure 17 shows the spatial distribution of basalt ages in the investigated mare regions on the lunar near- and farside. Figure 18 shows the temporal distribution of basalt ages found in the investigated areas.

In the investigated regions, the largest numbers of basalt units per time bin were formed in the late Imbrian Period at

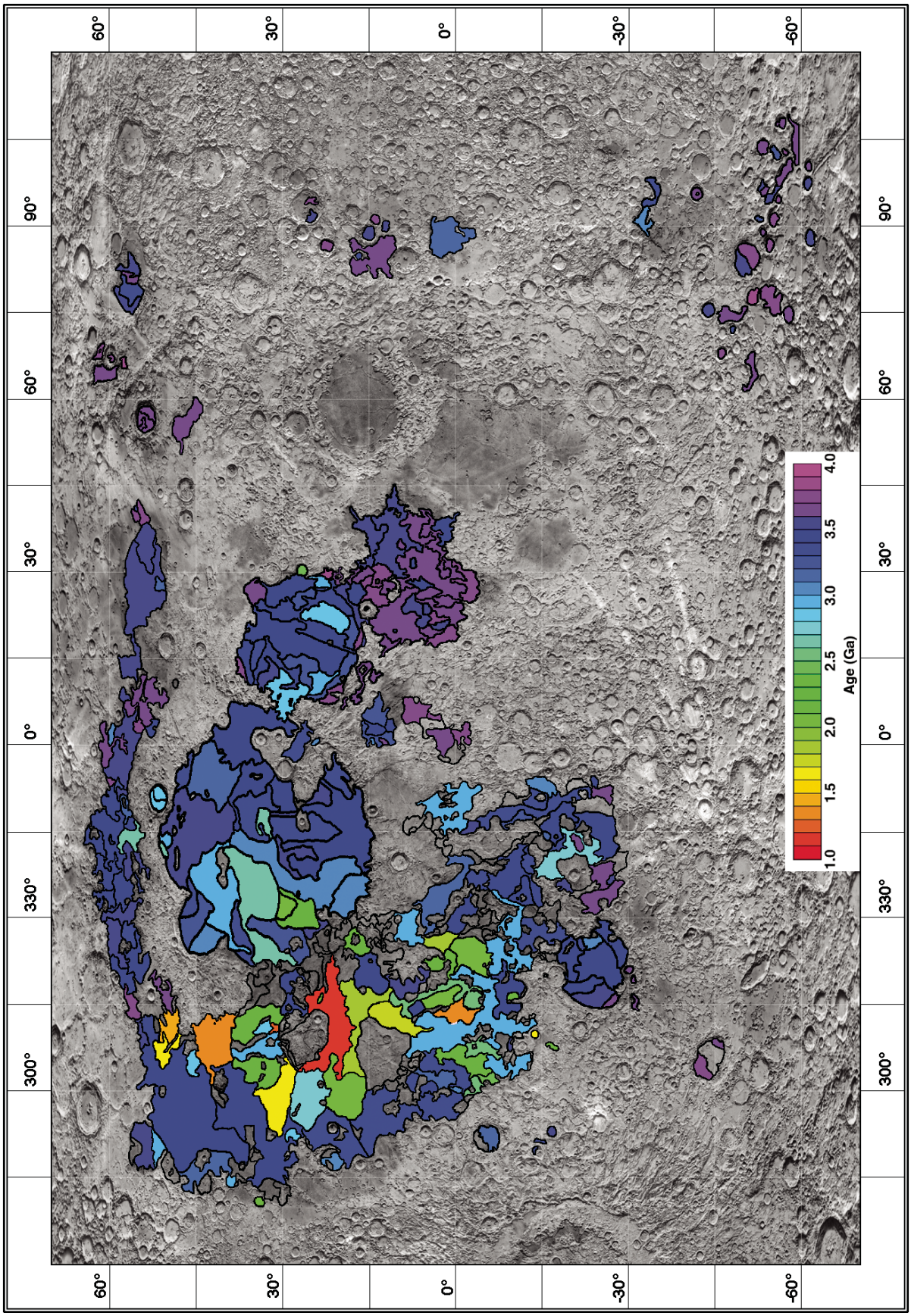

Figure 17. Spatial distribution of model ages for spectrally defined units on the lunar nearside and farside. U.S. Geological Survey shaded relief map, simple cylindrical map projection. Spectral units are outlined in black.

ca. 3.3–3.8 Ga. The general distribution can be described as asymmetrical, with the peak toward older ages. Beginning at ca. 4 Ga, the frequency rapidly increased to a peak at ca. 3.6–3.7 Ga, and then declined generally, but perhaps episodically, to ca. 1.2 Ga. Our crater size-frequency distribution data of the mapped basalt units indicate that the ages of basalts on the Moon range from ca. 1.20 to ca. 4.0 Ga, for a total duration of ~2.8 b.y. There are 58 units that show evidence for resurfacing by later flows, 16 of which occur in Oceanus Procellarum, 12 in Frigoris, 7 in Australe, 5 in Humorum, 2 each in Nubium, Marginis, Insularum, and Humboldtianum, and 1 in Imbrium, Serenitatis, Tranquillitatis, Cognitum, Smythii, Lacus Temporis, and craters Crüger, Grimaldi, Joliot, and Schickard. Ages in Oceanus Procellarum vary from 1.2 to 3.93 Ga, in Imbrium from 2.01 to 3.57 Ga, in Serenitatis from 2.44 to 3.81 Ga, and in Australe from 3.08 to 3.91 Ga. In Mare Smythii, we observed ages from 3.14 to 3.48 Ga, in Marginis from 3.38 to 3.88 Ga, in Tranquillitatis from 3.39 to 4.23 Ga, and in Nubium from 2.77 to 3.85 Ga. Basalts exhibit a range of ages between 3.40 and 3.94 Ga in Humboldtianum, 2.93–3.54 Ga in Insularum, 3.16–3.48 Ga in Grimaldi, 2.93–3.94 Ga in Humorum, 2.61–4.00 Ga in Frigoris, 3.32–3.65 Ga in Cognitum, and 3.10–3.61 Ga in Vaporum, We observed ages of 3.63–3.79 Ga in Sinus Medii, 3.07–3.35 Ga in Palus Putredinis, 3.50 Ga in Lacus Aestatis, and 3.62–3.76 Ga in Lacus Temporis. Finally, basalts in Schickard crater show ages of 3.62–3.75 Ga, basalts in Crüger crater have ages of 3.38–3.55 Ga, basalts in Rocca A crater have ages of 3.36 Ga, basalts in Hubble crater have ages of 3.79 Ga, basalts in Goddard crater have ages of 3.60 Ga, and basalts in Joliot crater have ages of 3.60–3.76 Ga.

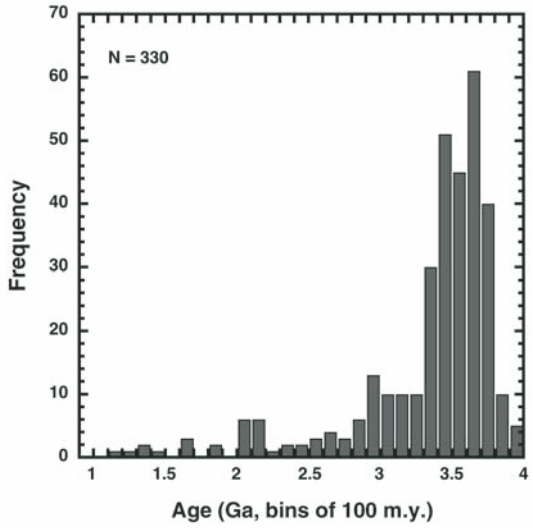

Figure 18. Histogram showing the temporal distribution of model ages for all investigated basalts in Oceanus Procellarum, Mare Imbrium, Mare Serenitatis, Mare Australe, Mare Smythii, Mare Marginis, Mare Tranquillitatis, Mare Nubium, Mare Humboldtianum, Mare Insularum, Mare Humorum, Mare Frigoris, Mare Cognitum, Mare Vaporum, Sinus Medii, Palus Putredinis, Lacus Aestatis, Lacus Temporis, Grimaldi, Schickard, Crüger, Rocca A, Goddard, Joliot, and Hubble (Hiesinger et al., 2000, 2003, 2010).

Figures 17 and 18 show the distribution of model ages of ~330 basalt units of the investigated regions. The data indicate that mare volcanism on the Moon started at least ~4 b.y. ago and ended at ca. 1.2 Ga. Most of the investigated basalts on the lunar nearside erupted during the late Imbrian Period, fewer basalts erupted during the Eratosthenian Period, and even fewer basalts are of Copernican age (Fig. 18).

In the past, extensive work has been done on cryptomaria, i.e., maria that were subsequently buried by the ejecta blankets of large craters or impact basins (e.g., Schultz and Spudis, 1979, 1983; Hawke and Bell, 1981; Bell and Hawke, 1984; Head and Wilson, 1992; Antonenko et al., 1995; Antonenko and Yingst, 2002). Due to the nature of cryptomare, one cannot directly date the emplacement of the mare units with crater counts. However, based on stratigraphic relationships, previous studies have interpreted cryptomare as evidence for early mare volcanism that was already active before the formation of the large lunar impact basins and the volcanism that filled these basins (e.g., Schultz and Spudis, 1979, 1983; Hawke and Bell, 1981; Bell and Hawke, 1984; Head and Wilson, 1992; Antonenko et al., 1995; Antonenko and Yingst, 2002). The existence of these cryptomaria implies that mare volcanism likely started prior to the emplacement of the oldest dated basalts at ca. 4 Ga, possibly expanding the total duration of active volcanism on the Moon to more than ~3 b.y. The lunar meteorite Kalahari 009 might represent a very low-Ti cryptomare basalt (Terada et al., 2007). Radiometric U-Pb age dating of phosphate grains associated with basaltic clasts in this meteorite revealed that lunar volcanism was already active at least at 4.35 b.y. ago (Terada et al., 2007).

Young ages of some basalts on the lunar surface are supported by crater degradation ages of Boyce (1976) and Boyce and Johnson (1978), crater counts by Schultz and Spudis (1983), several lunar meteorites that have ages of ca. 2.7–3.0 Ga (Fagan et al., 2002; Fernandes et al., 2003; Fernandes and Burgess, 2006; Anand et al., 2006; Rankenburg et al., 2007; Borg et al., 2007), and geophysical models of the thermal history of the Moon (Ziethe et al., 2009). For example, the youngest age group of Boyce (1976) and Boyce and Johnson (1978) represents an age of 2.5 ± 0.5 Ga, and the Lichtenberg basalt might be as young as 900 Ma (Schultz and Spudis, 1983).

The spatial distribution of model ages indicates that younger (Eratosthenian/Copernican) basalts occur preferentially in the Oceanus Procellarum region and in the vicinity of volcanic centers such as the Aristarchus Plateau (Fig. 17). In general, we find young basalts associated with the Procellarum KREEP Terrane (PKT), which contains enhanced concentrations of heat-producing elements such as thorium (e.g., Lawrence et al., 1998, 1999, 2000; Jolliff et al., 2000; Haskin et al., 2000; Feldman et al., 1998, 2000, 2002). Ziethe et al. (2009) presented several thermal evolution models in which they varied the boundary conditions at the model surface in order to evaluate the influence

on the extent and lifetime of a molten layer in the lunar interior, i.e., the source region of the mare basalts. In their model, the rapid growth of an insulating lithosphere kept the Moon's interior warm and prevented the melt zone from rapidly freezing. Their modeled lifetimes of the melt zones are consistent with basalt ages obtained from crater chronology, implying that the Moon remained warm enough to produce basaltic eruptions until at least 2.0 b.y. ago. Ziethe et al. (2009) argued that in order to explain the very youngest basalts (ca. 1.0 Ga), an additional heat source in the form of concentrated heat-producing elements within the PKT might be required.

LUNAR MARE BASALT FLUX

Establishing the volume of mare basalts emplaced on the surface as a function of time (the flux) is important in order to place constraints on the petrogenesis of lunar mare basalts and the thermal evolution of the Moon (Head and Wilson, 1992; Zhong et al., 1999; Wieczorek and Phillips, 2000; Parmentier et al., 2000; Wilson and Head, 2001). Head and Wilson (1992) reviewed and summarized different approaches to determine the extent and flux of mare basalts and found that based only on returned lunar samples, one would obtain a more or less Gaussian flux curve with a peak flux prior to ca. 3.5 Ga (Fig. 19A). Looking at the surface exposure of basalt units, one would derive a similar flux curve that is somewhat wider and shifted toward younger ages (ca. 3–3.5 Ga) (Fig. 19B). Investigation of the stratigraphy of mare basalt volumes would yield an asymmetric flux curve with the peak at older ages at ca. 3.8 Ga (Fig. 19C). Figure 19D shows a flux curve that accounts for probable volcanism in the period of early impact bombardment, which is now obscured. Finally, a flux curve based on the combination of approaches is shown in Figure 19E. Based on their investigation, Head and Wilson (1992) argued that the flux in the last half of lunar history has been characterized by episodic rather than continuous eruptions.

In order to calculate the flux, we need accurate information on (1) the age, (2) the surface extent, and (3) the thickness of a basalt flow. Early work mostly focused on estimating the total thickness of mare basalt fill in the mare basins (e.g., DeHon, 1974; DeHon and Waskom, 1976; Hörz, 1978, DeHon, 1979). These studies used a variety of techniques, which are summarized elsewhere (e.g., Head, 1982; Budney and Lucey, 1998). Results from crater geometry techniques using pristine crater morphometric relationships and the diameter of partially to almost completely flooded craters showed that lunar impact basins are filled with up to 2 km of basalts, with 200–400 m on average (DeHon and Waskom, 1976). Hörz (1978) reviewed the assumptions that underlie the thickness estimates of DeHon and Waskom (1976) and concluded that such values were overestimates. Similarly, Budney and Lucey (1998) concluded that basalts in Mare Humorum are generally less thick than estimated by DeHon (1979). In a recent study, Thomson et al. (2009) reinvestigated the thickness of Mare Imbrium basalts and found that their new thickness estimates are in excess of 0.5 km greater than the thickness determined by DeHon (1979) from partially flooded craters alone. Head (1982) flooded existing basin and crater terrain and showed the sensitivity of flooding thickness estimates to details of preexisting topography. Head (1982) pointed out that two stages of filling a basin can be distinguished: Stage 1 is characterized by flooding the interior and thick deposits (~6 km) of small to intermediate volumes covering small areas; stage 2 is characterized by flooding outward to the basin-defining scarp and thin deposits (~2 km) of large volume covering large areas. Estimated thicknesses of mare basalts in Oceanus Procellarum are on the order of 0–500 m for most regions, with some areas having basalts up to >1500 m thick (DeHon, 1979; DeHon and Waskom, 1976). Recent studies based on new *Clementine* data are consistent with these estimates (Dunkin et al., 2000; Boroughs and Spudis, 2001; Heather and

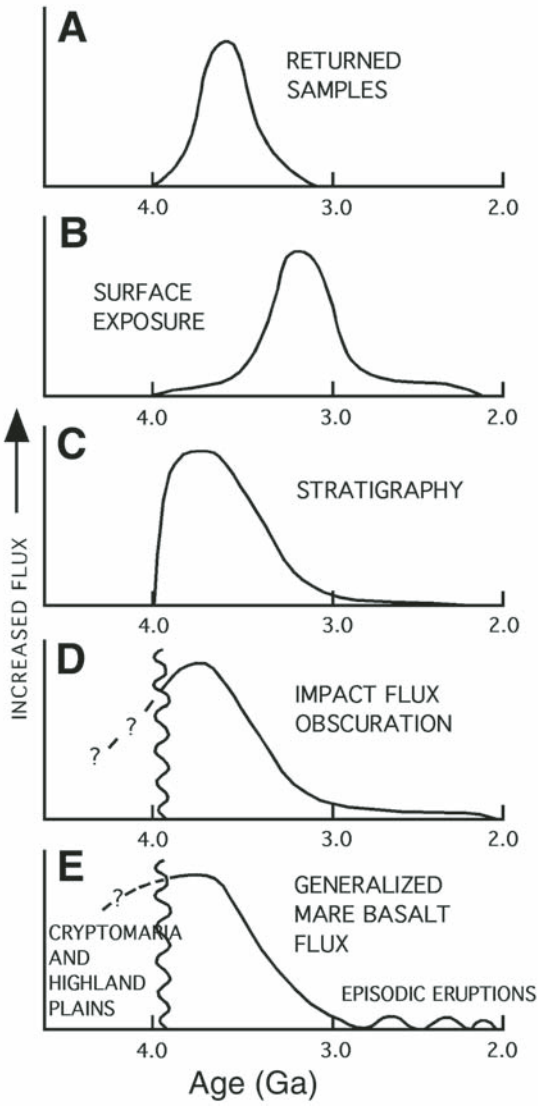

Figure 19. Diagram of the flux of lunar mare basalts based on different approaches (Head and Wilson, 1992).

Dunkin, 2002). Using craters that excavated highland material from beneath the mare basalts in Oceanus Procellarum, Heather and Dunkin (2002) estimated that the basalts are 160–625 m thick, with thicknesses ranging from tens to hundreds of meters near the mare/highland boundaries and several hundreds of meters closer to the center of the mare. Based on the exposure of highland islands and crater rims such as Flamsteed, Wilhelms and McCauley (1971) concluded that the thickness of mare basalts within Oceanus Procellarum is relatively thin. All these estimates, which are based on flooded impact craters or impact craters that penetrated the mare basalts and excavated underlying highland material, provide the total thickness of basalts in a particular basin, but not the thickness of individual basalt flow units.

To place better constraints on the flux of lunar mare basalt volcanism, we need to know the thicknesses of individual mare flow units. In the past, extensive work has been done to estimate the thicknesses of individual flow units (e.g., Howard et al., 1972; Schaber, 1973; Brett, 1975; Schaber et al., 1976; Gifford and El-Baz, 1978, 1981). Gifford and El-Baz (1978, 1981) noted that despite the wide acceptance of the idea of multiple flow units filling the basins, morphometric characteristics of individual flow units have not been extensively studied. Measurements of flow unit thicknesses are complicated by (1) the limited availability of suitable data necessary for the recognition of flow fronts, i.e., high-resolution topography and near-terminator low-sun images, (2) regolith formation processes, i.e., impact cratering, which can obliterate flow fronts of up to 15 m (Head, 1976), and (3) the composition and the eruption style of lunar lavas, which are thought to be responsible for the sparseness of mare flow features (Schultz et al., 1976; Head, 1976).

Numerous techniques have been applied to estimate the thicknesses of individual flow units. Such techniques included: (1) shadow measurements in high-resolution low-sun images (e.g., Schaber, 1973; Schaber et al., 1976; Gifford and El-Baz, 1978, 1981); (2) in situ observations of flow units by the *Apollo* astronauts, e.g., within the walls of Hadley Rille at the *Apollo 15* landing site (Howard et al., 1972); and (3) studies of the chemical kinetic aspects of lava emplacement and cooling (Brett, 1975).

On the basis of *Apollo 14* and *15* near-terminator images of the region southeast of Kunowsky crater, Lloyd and Head (1972) determined a flow front height of 3–5 m for a single flow unit. Reporting on a much larger number of units, Gifford and El-Baz (1981) found flow heights of 1–96 m, with an average thickness of ~21 m. These results are similar to thicknesses of 10–20 m observed in the wall of Hadley Rille (Howard et al., 1972). Gifford and El-Baz (1981) argued that a few flow units might even have actual thicknesses in excess of 100 m because only the shadowed portions of the flow fronts were measured. Schaber (1973) found that the average thickness of the Eratosthenian flows in Mare Imbrium is 30–35 m. However, they considered these Eratosthenian flows as atypical because their thickness (10–63 m) is much larger compared to other lunar flow fronts that could be identified in imaging data (5–10 m) (Schaber et al., 1976). Finally, chemical kinetic considerations based on *Apollo* samples suggest that lunar lava flow units are no thicker than ~8–10 m at the *Apollo 11*, *12*, and *15* sites (Brett, 1975).

A fourth technique was applied by Neukum and Horn (1976). They showed that endogenic lava flow processes could be identified by their characteristic effects on crater size-frequency distributions, even if these individual flows were not visible in the images. This is an important result because photogeologic and morphologic recognition of individual flow fronts on the Moon is difficult and is mostly restricted to thicker flows and areas where low-sun images or samples have been obtained. Based on deflections (knees) in crater size-frequency distribution curves, Neukum and Horn (1976) estimated the thickness of Imbrian-age flow units in Mare Imbrium. They found that these flows are ~200 m thick, and they reported Eratosthenian flows to be ~60 m thick. The latter value is consistent with photogeologic estimates of the same flow unit by Schaber (1973), Schaber et al. (1976), and Gifford and El-Baz (1981). Hiesinger et al. (2002) applied this technique to a much larger number of their crater counts and found that the average thickness of 58 of their investigated individual basalt flow units is ~30–60 m, with a range of flow unit thickness of ~20–200 m. A comparison with previously published thickness estimates (e.g., Howard et al., 1972; Schaber, 1973; Brett, 1975; Schaber et al., 1976; Gifford and El-Baz, 1978, 1981) showed that crater size-frequency distribution measurements yield thicknesses that are in excellent agreement with results from these other techniques and allow one to obtain thicknesses of additional flow units that have not been detected in low-sun images. Based on their thickness estimates, Hiesinger et al. (2002) also reported that the volumes of individual basalt flows range from 30 to 7700 km^3, with an average of 590–940 km^3. Yingst and Head (1997) estimated the volumes of lava ponds thought to represent single eruptive phases and found that pond volumes range from 35 to 8745 km^3, with a mean value of 860 km^3 for South Pole–Aitken, and 10–1280 km^3, with a mean value of 240 km^3 for the Orientale region.

For our flux estimates, we used ages and thicknesses derived from crater size-frequency distribution measurements and surface extents of mare basalt units measured in imaging data. We have already demonstrated that crater size-frequency distribution measurements constitute an adequate method to derive the surface age of the uppermost basalt unit with sufficient accuracy (Hiesinger et al., 2000, 2003, 2010). We have also demonstrated that crater size-frequency distribution measurements can be used to estimate the thickness of mare flow units (Hiesinger et al., 2002).

Using this approach, we have to consider potential caveats. First, because older units might have been covered by younger flows, the measured surface area of older basalt flow units might be too small. Consequently, volumes estimated for these flow units must be considered as minimum estimates. Secondly, we also have to consider variations of flow unit thicknesses with time, i.e., older flow units might be thicker than younger flow units, as indicated by the work of Head (1982). Again, this implies that volumes estimates of early flow units are minimum estimates.

As discussed already, craters that penetrate the entire stack of basalts have been used to estimate the thicknesses of basalts within individual basin structures (e.g., DeHon, 1979). These studies indicate that basalt thicknesses are up to 2 km, with 200–400 m on average. If we assume a thickness of 30–60 m for the uppermost basalt flow unit (e.g., Hiesinger et al., 2002), this would imply that at least ~150 m or up to ~1900 m of basalts are covered by the youngest flow units. Similarly, thickness estimates by Heather and Dunkin (2002) would imply that at least ~100–550 m of basalts are buried beneath the youngest flow units. Using the Orientale basin as an example, Head (1982) argued that the basalt thickness in the central parts of lunar basins can be up to 8 km. From the comparison of this maximum total thickness of mare basalts in a basin with the thickness of the uppermost flow units, we conclude that a large number of flow units must have filled the lunar impact basins.

Figure 20 shows a cumulative plot of the flux of basalts in some investigated areas, e.g., Imbrium, Serenitatis, Tranquillitatis, Humorum, Humboldtianum, Australe, Oceanus Procellarum, Cognitum, Nubium, and Insularum. We plotted the flux curves of four scenarios, each of which assumed a different average thickness of the flow units. The thicknesses were chosen to be within reasonable limits given by the previous discussion, i.e., 10 m, 25 m, 50 m, and 100 m. For comparison, we also plotted a flux curve for linearly increasing thicknesses with increasing age. In this model, we assumed a thickness of 10 m for flows of 1.0 Ga age, which increases to 100 m for flows of 4.0 Ga age. If it is true that the thickness of early flow units was larger (Head, 1982), and that the surface exposure of older units is underestimated, the implication is that the flux curve should be steeper at older ages, and this is what we observe for our flux curve based on increasing flow unit thicknesses. While the actual amount of increase in thickness is not known to date, the model illustrates several effects on the flux curve. First, even with a tenfold linear increase in thickness with increasing age, the overall shape of the flux curve remains similar, and phases of higher and lower volcanic activity are detectable. Second, by assuming a larger thickness of older flow units, the model indirectly offsets effects introduced by the fact that older units are covered to a larger extent with subsequent units than younger units. While the models provide a qualitative basis for discussions of the lunar volcanic flux, exact quantitative measurements are left for future studies.

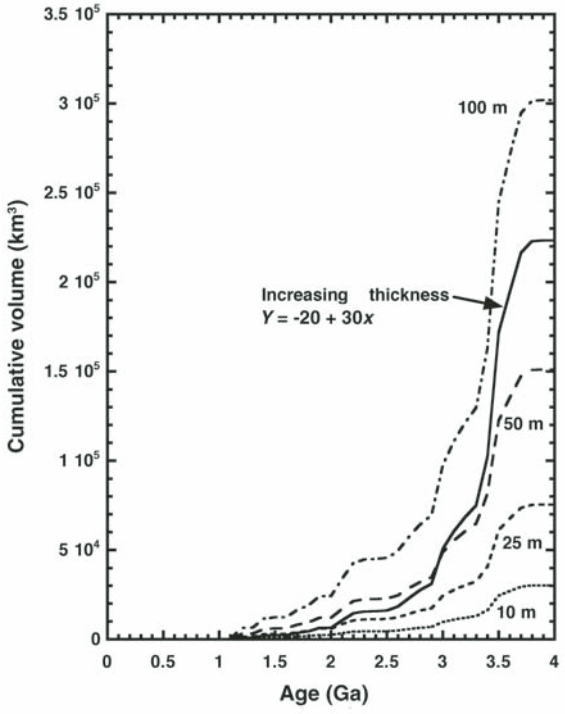

Figure 20. Flux of mare basalts for four estimated flow unit thicknesses (10, 25, 50, 100 m). The solid line is the flux curve for linearly increasing thicknesses of basalt flow units with time, i.e., older units are thicker than younger units. For this case, it was assumed that the thickness of a 1.0-b.y.-old flow is 10 m and that this thickness increases linearly to 100 m for flows of 4.0 Ga age (Hiesinger et al., 2003).

Our data indicate that the flux of mare basalts was highest in the late Imbrian ~3.3–3.7 b.y. ago. Based on our data, we observe a decreased flux during the Eratosthenian and Copernican Period. The decrease in flux was not continuous but was interrupted by brief phases of relatively higher volcanic activity, as indicated by the steeper segments of our flux curve (Fig. 20). This is consistent with predictions of Head and Wilson (1992), who argued for episodic eruptions during the later half of lunar history (Fig. 19E). Flattening of the curve at ages older than 3.7 Ga might be a combination of covering older units by younger units and/or a probably lower flux.

CONCLUSIONS

Based on our age determinations for basalts that are exposed in mare regions on the lunar near- and farside, we conclude that (1) volcanism on the Moon was active for a very long period of time of almost 3 b.y., from 4.0 to 1.2. Ga. (2) The investigated impact basins are mostly filled with Imbrian basalts, but there are a few areas that are covered with Eratosthenian and possibly Copernican basalts. (3) Most basalts exposed on the surface today were erupted between 3.3 and 3.8 b.y. ago. (4) Only small numbers of basalts are identified to be older than 3.8 Ga, and this might be an effect of these basalts being covered by younger basalts. (5) At ages younger than 3.3 Ga, there is a steep decline in volcanic activity. (6) Episodically, there might have been intervals with increased volcanic activity, for example, at ca. 2.0–2.2 Ga. (7) The youngest basalts are associated with the PKT; the enhanced concentration in heat-producing elements probably allowed this area to remain warm enough for such young basaltic eruptions. (8) Basalts in craters of the southwestern hemisphere (Schickard, Grimaldi, Crüger, Rocca A) are systematically younger than the basalts exposed in the craters of the northeastern hemisphere (Goddard, Hubble, Joliot). (9) All dark

mantle deposits are Imbrian in age and often older than adjacent mare basalts. (10) Thickness estimates for 58 basalt units based on crater size-frequency measurements revealed average thicknesses of 30–60 m. (11) Volume estimates in combination with ages of individual basalt units indicate a steep decline in erupted basalt volumes since ca. 3.6 Ga.

ACKNOWLEDGMENTS

We would like to thank the National Aeronautics and Space Administration (NASA) Planetary Geology and Geophysics Program, which provided support for this analysis to Head and Hiesinger while at Brown University. Figures 1–17, and 20 are reproduced by permission of the American Geophysical Union.

REFERENCES CITED

Alexander, E.C., Jr., Bates, A., Coscio, M.R., Jr., Dragon, J.C., Murthy, V.R., Pepin, R.O., and Venkatesan, T.R., 1976, K/Ar dating of lunar soils II: Houston, Texas, Lunar and Planetary Institute, Lunar and Planetary Science Conference VII, p. 625–648.

Anand, M., Taylor, L.A., Floss, C., Neal, C.R., Terada, K., and Tanikawa, S., 2006, Petrology and geochemistry of LaPaz Icefield 02205: A new unique low-Ti mare-basalt meteorite: Geochimica et Cosmochimica Acta, v. 70, p. 246–264, doi:10.1016/j.gca.2005.08.018.

Antonenko, I., and Yingst, R.A., 2002, Mare and cryptomare deposits in the Schickard region of the Moon: New measurements using *Clementine* FeO data: Houston, Texas, Lunar and Planetary Institute, Lunar and Planetary Science Conference XXXIII, CD-ROM, abstract 1438.

Antonenko, I., Head, J.W., III, Mustard, J.F., and Hawke, B.R., 1995, Criteria for the detection of lunar cryptomaria: Earth, Moon, and Planets, v. 69, p. 141–172, doi:10.1007/BF00613096.

Arvidson, R., Boyce, J., Chapman, C., Cintala, M., Fulchignoni, M., Moore, H., Neukum, G., Schultz, P., Soderblom, L., Strom, R., Woronow, A., and Young, R., 1979, Standard techniques for presentation and analysis of crater size-frequency data: Icarus, v. 37, p. 467–474, doi:10.1016/0019-1035(79)90009-5.

Baldwin, R.B., 1971, On the history of lunar impact cratering: The absolute time scale and the origin of planetesimals: Icarus, v. 14, p. 36–52, doi:10.1016/0019-1035(71)90100-X.

Baldwin, R.B., 1974, Was there a "terminal lunar cataclysm" 3.9–4.0 × 10^9 years ago?: Icarus, v. 23, p. 157–166, doi:10.1016/0019-1035(74)90003-7.

Baldwin, R.B., 1987, On the relative and absolute ages of seven lunar front face basins: II. From crater counts: Icarus, v. 71, p. 19–29, doi:10.1016/0019-1035(87)90159-X.

Basaltic Volcanism Study Project (BVSP), 1981, Basaltic Volcanism on the Terrestrial Planets: New York, Pergamon, 1286 p.

Bell, J.F., and Hawke, B.R., 1984, Lunar dark-haloed impact craters: Origins and implications for early mare volcanism: Journal of Geophysical Research, v. 89, p. 6899–6910, doi:10.1029/JB089iB08p06899.

Bierhaus, E.B., Chapman, C.R., and Merline, W.J., 2005, Secondary craters on Europa and implications for cratered surfaces: Nature, v. 437, p. 1125–1127, doi:10.1038/nature04069.

Borg, L.E., Gaffney, A., and DePaolo, D., 2007, Rb-Sr and Sm-Nd isotopic systematics of NWA 032, *in* 70th Annual Meteoritical Society Meeting Abstracts, 13–17 August 2007, Tucson, Arizona: Meteoritics and Planetary Science Supplement, v. 42, p. 5232.

Boroughs, L.L., and Spudis, P.D., 2001, The stratigraphy of lava flows in northern Oceanus Procellarum, Moon: Houston, Texas, Lunar and Planetary Institute, Lunar and Planetary Science Conference XXXII, CD-ROM, abstract 1192.

Boyce, J.M., 1976, Ages of flow units in the lunar nearside maria based on *Lunar Orbiter IV* photographs: Houston, Texas, Lunar and Planetary Institute, Lunar and Planetary Science Conference VII, p. 2717–2728.

Boyce, J.M., and Johnson, D.A., 1978, Ages of flow units in the far eastern maria and implications for basin-filling history: Houston, Texas, Lunar and Planetary Institute, Lunar and Planetary Science Conference IX, p. 3275–3283.

Brett, R., 1975, Thicknesses of some lunar mare basalt flows and ejecta blankets based on chemical kinetic data: Geochimica et Cosmochimica Acta, v. 39, p. 1135–1141, doi:10.1016/0016-7037(75)90055-1.

Budney, C.J., and Lucey, P.G., 1998, Basalt thickness in Mare Humorum: The crater excavation method: Journal of Geophysical Research, v. 103, no. E7, p. 16,855–16,870, doi:10.1029/98JE01602.

Bugiolacchi, R., and Guest, J.E., 2008, Compositional and temporal investigation of exposed lunar basalts in the Mare Imbrium region: Icarus, v. 197, p. 1–18, doi:10.1016/j.icarus.2008.04.001.

Bugiolacchi, R., Spudis, P.D., and Guest, J.E., 2006, Stratigraphy and composition of lava flows in Mare Nubium and Mare Cognitum: Meteoritics & Planetary Science, v. 41, p. 285–304, doi:10.1111/j.1945-5100.2006.tb00210.x.

Burgess, R., and Turner, G., 1998, Laser ^{40}Ar-^{39}Ar age determinations of *Luna 24* mare basalts: Meteoritics and Space Science, v. 33, no. 4, p. 921–935, doi:10.1111/j.1945-5100.1998.tb01697.x.

Carr, M.H., 1965, Geologic Map of the Timocharis Region of the Moon (LAC-40): U.S. Geological Survey I-462, scale 1:1,000,000.

Carr, M.H., 1966, Geologic Map of the Mare Serenitatis Region of the Moon (LAC-42): U.S. Geological Survey I-489, scale 1:1,000,000.

Chapman, C.R., Ryan, E.V., Merline, W.J., Neukum, G., Wagner, R., Thomas, P.C., Veverka, J., and Sullivan, R.J., 1996a, Cratering on Ida: Icarus, v. 120, p. 77–86, doi:10.1006/icar.1996.0038.

Chapman, C.R., Veverka, J., Belton, M.J.S., Neukum, G., and Morrison, D., 1996b, Cratering on Gaspra: Icarus, v. 120, p. 231–245, doi:10.1006/icar.1996.0048.

Chenet, H., Lognonné, P., Wieczorek, M., and Mizutani, H., 2006, Lateral variations of lunar crustal thickness from the *Apollo* seismic data set: Earth and Planetary Science Letters, v. 243, p. 1–14, doi:10.1016/j.epsl.2005.12.017.

Dasch, E., Shih, C.-Y., Bansal, B.M., Wiesmann, H., and Nyquist, L.E., 1987, Isotopic analysis of basaltic fragments from lunar breccia 14321: Chronology and petrogenesis of pre-Imbrium mare volcanism: Geochimica et Cosmochimica Acta, v. 51, p. 3241–3254, doi:10.1016/0016-7037(87)90132-3.

Dasch, J., Ryder, G., Reese, Y., Wiesmann, H., Shih, C.-Y., and Nyquist, L., 1998, Old age of formation for a distinct variety of A17 high-titanium mare basalts: Houston, Texas, Lunar and Planetary Institute, Lunar and Planetary Science Conference XXIX, CD-ROM, abstract 1750.

DeHon, R.A., 1974, Thickness of mare material in the Tranquillitatis and Nectaris basins: Houston, Texas, Lunar and Planetary Institute, Lunar and Planetary Science Conference V, p. 53–59.

DeHon, R.A., 1979, Thickness of the western mare basalts: Houston, Texas, Lunar and Planetary Institute, Lunar and Planetary Science Conference X, p. 2935–2955.

DeHon, R.A., and Waskom, J.D., 1976, Geologic structure of the eastern mare basins: Houston, Texas, Lunar and Planetary Institute, Lunar and Planetary Science Conference VII, p. 2729–2746.

Deutsch, A., and Stöffler, D., 1987, Rb-Sr-analyses of *Apollo 16* melt rocks and a new age estimate for the Imbrium basin: Lunar basin chronology and the early heavy bombardment of the moon: Geochimica et Cosmochimica Acta, v. 51, p. 1951–1964, doi:10.1016/0016-7037(87)90184-0.

Dunkin, S.K., Heather, D.J., Dandy, C.L., Spudis, P.D., and Bussey, D.B.J., 2000, Stratigraphy of the mare flows in southern Oceanus Procellarum: Houston, Texas, Lunar and Planetary Institute, Lunar and Planetary Science Conference XXXI, CD-ROM, abstract 1357.

Eberhardt, P., Geiss, J., Grögler, N., and Stettler, A., 1973, How old is the crater Copernicus?: The Moon, v. 8, p. 104–114, doi:10.1007/BF00562752.

Eggleton, R.E., 1965, Geologic Map of the Riphaeus Mountains Region of the Moon (LAC-76): U.S. Geological Survey I-458, scale 1:1,000,000.

Engel, S., 1986, Genese der lunaren hellen Ebenen: Impakt oder Vulkanismus? [Diploma thesis]: München, Germany, Universität München, 75 p.

Fagan, T.J., Taylor, G.J., Keil, K., Bunch, T.E., Wittke, J.H., Korotev, R.L., Jolliff, B.L., Gillis, J.J., Haskin, L.A., Jarosewich, E., Clayton, R.N., Mayeda, T.K., Fernandes, V.A., Burgess, R., Turner, G., Eugster, O., and Lorenzetti, S.S., 2002, Northwest Africa 032: Product of lunar volcanism: Meteoritics and Planetary Science, v. 37, p. 371–394.

Feldman, W.C., Barraclough, B.L., Maurice, S., Elphic, R.C., Lawrence, D.J., Thomsen, D.R., and Binder, A.B., 1998, Major compositional units of the Moon: *Lunar Prospector* thermal and fast neutrons: Science, v. 281, p. 1489, doi:10.1126/science.281.5382.1489.

Feldman, W.C., Lawrence, D.J., Elphic, R.C., Vaniman, D.T., Thomsen, D.R., Barraclough, B.L., Maurice, S., and Binder, A.B., 2000, Chemical information

content of lunar thermal and epithermal neutrons: Journal of Geophysical Research, v. 105, p. 20,347–20,363, doi:10.1029/1999JE001183.

Feldman, W.C., Gasnault, O., Maurice, S., Lawrence, D.J., Elphic, R.C., Lucey, P.G., and Binder, A.B., 2002, Global distribution of lunar composition: New results from *Lunar Prospector*: Journal of Geophysical Research, v. 107, doi:10.1029/2001JE001506.

Fernandes, V.A., and Burgess, R., 2006, Lunar volcanism during the Eratosthenian II: NWA479, *in* 69th Annual Meteoritical Society Meeting Abstracts, 6–11 August 2006, Zurich, Switzerland: Meteoritical Society, abstract 5312.

Fernandes, V.A., Burgess, R., and Turner, G., 2003, ^{40}Ar-^{39}Ar chronology of lunar meteorites Northwest Africa 032 and 773: Meteoritics & Planetary Science, v. 38, p. 555–564, doi:10.1111/j.1945-5100.2003.tb00026.x.

Gaddis, L.R., Sucharski, T., Becker, T., and Gitlin, A., 2001, Cartographic processing of digital lunar orbiter data: Houston, Texas, Lunar and Planetary Institute, Lunar and Planetary Science Conference XXXII, CD-ROM, abstract 1892.

Gaffney, A.M., Borg, L.E., Depaolo, D.J., and Irving, A.J., 2008, Age and isotope systematics of Northwest Africa 4898, a new type of highly-depleted mare basalt: Houston, Texas, Lunar and Planetary Institute, Lunar and Planetary Science Conference XXXIX, CD-ROM, abstract 1877.

Gifford, A.W., and El-Baz, F., 1978, Thickness of mare flow fronts: Houston, Texas, Lunar and Planetary Institute, Lunar and Planetary Science Conference IX, p. 382–384.

Gifford, A.W., and El-Baz, F., 1981, Thicknesses of lunar mare flow fronts: The Moon and the Planets, v. 24, p. 391–398, doi:10.1007/BF00896904.

Giguere, T.A., Taylor, G.J., Hawke, B.R., and Lucey, P.G., 2000, The titanium content of lunar mare basalts: Meteoritics & Planetary Science, v. 35, p. 193–200, doi:10.1111/j.1945-5100.2000.tb01985.x.

Greeley, R., and Gault, D.E., 1970, Precision size-frequency distributions for craters for 12 selected areas of the lunar surface: The Moon, v. 2, p. 10–77, doi:10.1007/BF00561875.

Greeley, R., Kadel, S.D., Williams, D.A., Gaddis, L.R., Head, J.W., III, McEwen, A.S., Murchie, S.L., Nagel, E., Neukum, G., Pieters, C.M., Sunshine, J.M., Wagner, R., and Belton, M.J.S., 1993, *Galileo* imaging observations of lunar maria and related deposits: Journal of Geophysical Research, v. 98, p. 17,183–17,205, doi:10.1029/93JE01000.

Guggisberg, S., Eberhardt, P., Geiss, J., Grögler, N., Stettler, A., Brown, G.M., and Peckett, A., 1979, Classification of the *Apollo-11* mare basalts according to Ar^{39}-Ar^{40} ages and petrological properties: Houston, Texas, Lunar and Planetary Institute, Lunar and Planetary Science Conference X, p. 1–39.

Hackman, R.J., 1962, Geologic Map and Sections of the Kepler Region of the Moon (LAC-57): U.S. Geological Survey I-355, scale 1:1,000,000.

Hackman, R.J., 1966, Geologic Map of the Montes Apenninus Region of the Moon (LAC-41): U.S. Geological Survey I-463, scale 1:1,000,000.

Hackwill, T., Guest, J., and Spudis, P.D., 2006, Stratigraphy and evolution of basalts in Mare Humorum and southeastern Procellarum: Meteoritics & Planetary Science, v. 41, p. 479–488, doi:10.1111/j.1945-5100.2006.tb00475.x.

Hartmann, W.K., 1966, Early lunar cratering: Icarus, v. 5, p. 406–418, doi:10.1016/0019-1035(66)90054-6.

Hartmann, W.K., 1972, Interplanet variations in scale of crater morphology—Earth, Mars, Moon: Icarus, v. 17, p. 707–713, doi:10.1016/0019-1035(72)90036-X.

Hartmann, W.K., 2005, Martian cratering 8: Isochron refinement and the chronology of Mars: Icarus, v. 174, p. 294–320, doi:10.1016/j.icarus.2004.11.023.

Hartmann, W.K., 2007a, Martian cratering 9: Toward resolution of the controversy about small craters: Icarus, v. 189, p. 274–278, doi:10.1016/j.icarus.2007.02.011.

Hartmann, W.K., 2007b, Martian chronology: Toward resolution of the 2005 "controversy" and evidence for obliquity-driven resurfacing processes, *in* 7th International Conference on Mars: Houston, Texas, Lunar and Planetary Institute, Lunar and Planetary Institute Contribution 1320, abstract 3318.

Hartmann, W.K., and Neukum, G., 2001, Cratering chronology and the evolution of Mars: Space Science Reviews, v. 96, p. 165–194, doi:10.1023/A:1011945222010.

Hartmann, W.K., Neukum, G., and Werner, S.C., 2008, Confirmation and utilization of the "production function" size-frequency distributions of Martian impact craters: Geophysical Research Letters, v. 35, doi:10.1029/2007GL031557.

Haruyama, J., Othake, M., Matsunaga, T., Honda, C., Yokota, Y., Abe, M., Ogawa, Y., Miyamoto, H., Iwasaki, A., Pieters, C.M., Asada, N., Demura, H., Hirata, N., Terazono, J., Sasaki, S., Saiki, K., Yamaji, A., Torii, M., and Josset, J.-L., 2009, Long-lived volcanism on the lunar farside revealed by *SELENE* Terrain Camera: Science, v. 323, p. 905–908, doi:10.1126/science.1163382.

Haskin, L.A., Gillis, J.J., Korotev, R.L., and Jolliff, B.L., 2000, The materials of the lunar Procellarum KREEP terrane: A synthesis of data from geomorphological mapping, remote sensing, and sample analyses: Journal of Geophysical Research, v. 105, p. 20,403–20,415, doi:10.1029/1999JE001128.

Hawke, B.R., and Bell, J.F., 1981, Remote sensing studies of lunar dark-halo impact craters: Preliminary results and implications for early volcanism: Houston, Texas, Lunar and Planetary Institute, Lunar and Planetary Science Conference XII, p. 665–678.

Hawke, B.R., and Head, J.W., 1978, Lunar KREEP volcanism—Geologic evidence for history and mode of emplacement: Houston, Texas, Lunar and Planetary Institute, Lunar and Planetary Science Conference IX, p. 3285–3309.

Hawke, B.R., Blewett, D.T., Lucey, P.G., Smith, G.A., Bell, J.F., III, Campbell, B.A., and Robinson, M.S., 2004, The origin of lunar crater rays: Icarus, v. 170, p. 1–16, doi:10.1016/j.icarus.2004.02.013.

Head, J.W., III, 1974, Lunar dark-mantle deposits: Possible clues to the distribution of early mare deposits: Houston, Texas, Lunar and Planetary Institute, Lunar and Planetary Science Conference V, p. 207–222.

Head, J.W., III, 1976, Lunar volcanism in space and time: Reviews of Geophysics, v. 14, p. 265–300, doi:10.1029/RG014i002p00265.

Head, J.W., III, 1982, Lava flooding of ancient planetary crusts: Geometry, thickness, and volumes of flooded lunar impact basins: The Moon and the Planets, v. 26, p. 61–88, doi:10.1007/BF00941369.

Head, J.W., III, and Wilson, L., 1992, Lunar mare volcanism: Stratigraphy, eruption conditions, and the evolution of secondary crusts: Geochimica et Cosmochimica Acta, v. 56, p. 2155–2175, doi:10.1016/0016-7037(92)90183-J.

Head, J.W., III, Murchie, S., Mustard, J.F., Pieters, C.M., Neukum, G., McEwen, A., Greeley, R., Nagel, E., and Belton, M.J.S., 1993, Lunar impact basins: New data for the western limb and far side (Orientale and South Pole–Aitken basins) from the first *Galileo* flyby: Journal of Geophysical Research, v. 98, no. E9, p. 17,149–17,181, doi:10.1029/93JE01278.

Heather, D.J., and Dunkin, S.K., 2002, A stratigraphic study of southern Oceanus Procellarum using *Clementine* multispectral data: Planetary and Space Science, v. 50, p. 1299–1309, doi:10.1016/S0032-0633(02)00124-1.

Heiken, G.H., Vaniman, D.T., and French, B.M., eds., 1991, Lunar Source Book—A User's Guide to the Moon: Cambridge, UK, Cambridge University Press, 736 p.

Hiesinger, H., Jaumann, R., Neukum, G., and Head, J.W., III, 2000, Ages of mare basalts on the lunar nearside: Journal of Geophysical Research, v. 105, p. 29,239–29,275, doi:10.1029/2000JE001244.

Hiesinger, H., Head, J.W., III, Wolf, U., and Neukum, G., 2001, New age determinations of lunar mare basalts in Mare Cognitum, Mare Nubium, Oceanus Procellarum, and other nearside mare: Houston, Texas, Lunar and Planetary Institute, Lunar and Planetary Science Conference XXXII, CD-ROM, abstract 1815.

Hiesinger, H., Head, J.W., III, Wolf, U., Jaumann, R., and Neukum, G., 2002, Lunar mare basalt flow thicknesses determined from crater size-frequency distributions: Geophysical Research Letters, v. 29, doi:10.1029/2002GL014847.

Hiesinger, H., Head, J.W., III, Wolf, U., Jaumann, R., and Neukum, G., 2003, Ages and stratigraphy of mare basalts in Oceanus Procellarum, Mare Nubium, Mare Cognitum, and Mare Insularum: Journal of Geophysical Research, v. 108, doi:10.1029/2002JE001985.

Hiesinger, H., Head, J.W., III, Wolf, U., Jaumann, R., and Neukum, G., 2006, New ages for basalts in Mare Fecunditatis based on crater size-frequency measurements: Houston, Texas, Lunar and Planetary Institute, Lunar and Planetary Science Conference IX, p. 382–384.

Hiesinger, H., Head, J.W., III, Wolf, U., Jaumann, R., and Neukum, G., 2010, Ages and stratigraphy of lunar mare basalts in Mare Frigoris and other nearside maria based on crater size-frequency distribution measurements: Journal of Geophysical Research, v. 115, E03003, doi:10.1029/2009JE003380.

Hikida, H., and Wieczorek, M.A., 2007, Crustal thickness of the Moon: New constraints from gravity inversions using polyhedral shape models: Icarus, v. 192, p. 150–166, doi:10.1016/j.icarus.2007.06.015.

Holt, H.E., 1974, Geologic Map of the Purbach Quadrangle of the Moon (LAC-95): U.S. Geological Survey I-822, scale 1:1,000,000.

Hörz, F., 1978, How thick are lunar mare basalts?: Houston, Texas, Lunar and Planetary Institute, Lunar and Planetary Science Conference IV, p. 3311–3331.

Howard, K.A., and Masursky, H., 1968, Geologic Map of the Ptolemaeus Quadrangle of the Moon (LAC-77): U.S. Geological Survey I-566, scale 1:1,000,000.

Howard, K.A., Head, J.W., III, and Swann, G.A., 1972, Geology of Hadley Rille: Houston, Texas, Lunar and Planetary Institute, Lunar and Planetary Science Conference III, p. 1–14.

Husain, L., 1974, ^{40}Ar-^{39}Ar chronology and cosmic ray exposure ages of the *Apollo 15* samples: Journal of Geophysical Research, v. 79, no. 17, p. 2588–2606, doi:10.1029/JB079i017p02588.

Ishihara, Y., Goossens, S., Matsumoto, K., Noda, H., Araki, H., Namiki, N., Hanada, H., Iwata, T., Tazawa, S., and Sasaki, S., 2009, Crustal thickness of the Moon: Implications for farside basin structures: Geophysical Research Letters, v. 36, doi:10.1029/2009GL039708.

Ivanov, B.A., 2001, Moon cratering rate ratio estimates: Space Science Reviews, v. 96, p. 87–104, doi:10.1023/A:1011941121102.

Ivanov, B.A., Neukum, G., and Wagner, R., 2001, Size-frequency distributions of planetary impact craters and asteroids, *in* Rickmann, H., and Marov, M., eds., Collisional Processes in the Solar System: Dordrecht, the Netherlands, ASSL Kluwer Academic Publishers, 357 p.

James, O.B., 1981, Petrologic and age relations of the *Apollo 16* rocks: Implications for subsurface geology and the age of the Nectaris Basin: Houston, Texas, Lunar and Planetary Institute, Lunar and Planetary Science Conference XII, p. 209–233.

Jessberger, E.K., Huneke, J.C., Podosek, F.A., and Wasserburg, G.J., 1974, High resolution argon analysis of neutron irradiated *Apollo* rocks and separated minerals: Houston, Texas, Lunar and Planetary Institute, Lunar and Planetary Science Conference V, p. 1419–1449.

Jessberger, E.K., Kirsten, T., and Staudacher, T., 1977, One rock and many ages—Further K-Ar data on consortium breccia 73215: Houston, Texas, Lunar and Planetary Institute, Lunar and Planetary Science Conference VIII, p. 2567–2580.

Johnson, T.V., Pieters, C.M., and McCord, T.B., 1973, Mare Humorum: An integrated study of spectral reflectivity: Icarus, v. 19, p. 224–229, doi:10.1016/0019-1035(73)90125-5.

Johnson, T.V., Mosher, J.A., and Matson, D.L., 1977a, Lunar spectral units: A northern hemispheric mosaic: Houston, Texas, Lunar and Planetary Institute, Lunar and Planetary Science Conference VIII, p. 1013–1028.

Johnson, T.V., Saunders, R.S., Matson, D.L., and Mosher, J.A., 1977b, A TiO_2 abundance map for the northern maria: Houston, Texas, Lunar and Planetary Institute, Lunar and Planetary Science Conference VIII, p. 1029–1036.

Jolliff, B.L., Gillis, J.J., Haskin, L.A., Korotev, R.L., and Wieczorek, M.A., 2000, Major lunar crustal terranes: Surface expressions and crust-mantle origins: Journal of Geophysical Research, v. 105, p. 4197–4216, doi:10.1029/1999JE001103.

Karlstrom, T.N.V., 1974, Geologic Map of the Schickard Quadrangle of the Moon (LAC-110): U.S. Geological Survey I-823, scale 1:1,000,000.

Köhler, U., Head, J.W., Neukum, G., and Wolf, U., 1999, North-polar lunar light plains: Ages and compositional observations, *in* Workshop on New Views of the Moon II: Understanding the Moon through the Integration of Diverse Datasets, 22–24 September 1999, Flagstaff, Airzona, abstract 8050.

Köhler, U., Head, J.W., III, Neukum, G., and Wolf, U., 2000, Lunar light plains in the northern latitudes: Latest results on age distributions, surface composition, nature, and possible origin: Houston, Texas, Lunar and Planetary Institute, Lunar and Planetary Science Conference XXXI, CD-ROM, abstract 1822.

König, B., 1977, Investigations of Primary and Secondary Impact Structures on the Moon and Laboratory Experiments to Study the Ejecta of Secondary Particles [Ph.D. dissertation]: Heidelberg, Germany, Ruprecht-Karls University, 88 p. (in German).

Lawrence, D.J., Feldman, W.C., Barraclough, B.L., Binder, A.B., Elphic, R.C., Maurice, S., and Thomsen, D.R., 1998, Global elemental maps of the Moon: The *Lunar Prospector* gamma-ray spectrometer: Science, v. 281, p. 1484, doi:10.1126/science.281.5382.1484.

Lawrence, D.J., Feldman, W.C., Barraclough, B.L., Binder, A.B., Elphic, R.C., Maurice, S., Miller, M.C., and Prettyman, T.H., 1999, High resolution measurements of absolute thorium abundances on the lunar surface: Geophysical Research Letters, v. 26, p. 2681–2684, doi:10.1029/1999GL008361.

Lawrence, D.J., Feldman, W.C., Barraclough, B.L., Binder, A.B., Elphic, R.C., Maurice, S., Miller, M.C., and Prettyman, T.H., 2000, Thorium abundances on the lunar surface: Journal of Geophysical Research, v. 105, p. 20,307–20,331, doi:10.1029/1999JE001177.

Lloyd, D.D., and Head, J.W., III, 1972, Lunar surface properties as determined from earthshine and near-terminator photography: Houston, Texas, Lunar and Planetary Institute, Lunar and Planetary Science Conference III, p. 3127–3142.

Lucchitta, B.K., 1972, Geologic Map of the Aristoteles Quadrangle of the Moon (LAC-13): U.S. Geological Survey I-725, scale 1:1,000,000.

Lucchitta, B.K., 1978, Geologic Map of the North Side of the Moon: U.S. Geological Survey I-1062, scale 1:5,000,000.

Malin, M.C., Edgett, K., Posiolova, L., McColley, S., and Noe Dobrea, E., 2006, Present-day impact cratering rate and contemporary gully activity on Mars: Science, v. 314, p. 1573–1577, doi:10.1126/science.1135156.

Marshall, C.H., 1963, Geologic Map and Sections of the Letronne Region of the Moon (LAC-75): U.S. Geological Survey I-385, scale 1:1,000,000.

Maurer, P., Eberhardt, P., Geiss, J., Grögler, N., and Stettler, A., 1978, Pre-Imbrium craters and basins: Ages, compositions and excavation depths of *Apollo 16* breccias: Geochimica et Cosmochimica Acta, v. 42, p. 1687–1720, doi:10.1016/0016-7037(78)90257-0.

McCauley, J.F., 1967, Geologic Map of the Hevelius Region of the Moon (LAC-56): U.S. Geological Survey I-491, scale 1:1,000,000.

McCauley, J.F., 1973, Geologic Map of the Grimaldi Quadrangle of the Moon (LAC-74): U.S. Geological Survey I-740, scale 1:1,000,000.

McCord, T.B., Pieters, C.M., and Feierberg, M.A., 1976, Multi-spectral mapping of the lunar surface using ground-based telescopes: Icarus, v. 29, p. 1–34, doi:10.1016/0019-1035(76)90099-3.

McEwen, A.S., 2003, Secondary cratering on Mars: Implications for age dating and surface properties, *in* 6th International Conference on Mars: Pasadena, California, Lunar and Planetary Institute, abstract 3268.

McEwen, A.S., and Bierhaus, E.B., 2006, The importance of secondary cratering to age constraints on planetary surfaces: Annual Review of Earth and Planetary Sciences, v. 34, p. 535–567, doi:10.1146/annurev.earth.34.031405.125018.

McEwen, A.S., Preblich, B.S., Turtle, E.P., Artemieva, N.A., Golombek, M.P., Hurst, M., Kirk, R.L., Burr, D.M., and Christensen, P.R., 2005, The rayed crater Zunil and interpretations of small impact craters on Mars: Icarus, v. 176, p. 351–381, doi:10.1016/j.icarus.2005.02.009.

Melosh, H.J., 1989, Impact Cratering: A Geologic Process: Oxford Monographs on Geology and Geophysics, no. 11, 245 p.

M'Gonigle, J.W., and Schleicher, D., 1972, Geologic Map of the Plato Quadrangle of the Moon (LAC-12): U.S. Geological Survey I-701, scale 1:1,000,000.

Milton, D.J., 1968, Geologic Map of the Theophilus Quadrangle of the Moon (LAC-78): U.S. Geological Survey I-546, scale 1:1,000,000.

Moore, H.J., 1965, Geologic Map of the Aristarchus Region of the Moon (LAC-39): U.S. Geological Survey I-465, scale 1:1,000,000.

Moore, H.J., 1967, Geologic Map of the Seleucus Quadrangle of the Moon (LAC-38): U.S. Geological Survey I-527, scale 1:1,000,000.

Morota, T., Haruyama, J., Ohtake, M., Matsunaga, T., Yokota, Y., Honda, C., Torii, M., Ogawa, Y., Abe, M., and the LISM Working Group, 2008, Age determination of mare basalts surrounding the crater Lichtenberg: Preliminary results using *SELENE*(*Kaguya*)/Terrain Camera data: Houston, Texas, Lunar and Planetary Institute, Lunar and Planetary Science Conference XXXIX, CD-ROM, abstract 1513.

Morris, E.C., and Wilhelms, D.E., 1967, Geologic Map of the Julius Caesar Quadrangle of the Moon (LAC-60): U.S. Geological Survey I-510, scale 1:1,000,000.

Mustard, J.F., and Head, J.W., 1996, Buried stratigraphic relationships along the southwestern shores of Oceanus Procellarum: Implications for early lunar volcanism: Journal of Geophysical Research, v. 101, p. 18,913–18,925, doi:10.1029/96JE01826.

Neukum, G., 1971, Untersuchungen über Einschlagskrater auf dem Mond [Dissertation]: Heidelberg, Germany, Ruprecht-Karls Universität, 74 p.

Neukum, G., 1977, Lunar cratering: Philosophical Transactions of the Royal Society of London, ser. A, v. 285, p. 267–272.

Neukum, G., 1983, Meteoritenbombardement und Datierung planetarer Oberflächen, Habilitationsschrift: München, Germany, Universität München, 186 p.

Neukum, G., and Horn, P., 1976, Effects of lava flows on lunar crater populations: The Moon, v. 15, p. 205–222, doi:10.1007/BF00562238.

Neukum, G., and Ivanov, B.A., 1994, Crater size distributions and impact probabilities on Earth from lunar, terrestrial-planet, and asteroid cratering data, *in* Gehrels, T., ed., Hazards Due to Comets and Asteroids: Tucson, University of Arizona Press, p. 359–416.

Neukum, G., and Wise, D.U., 1976, A standard crater curve and possible new time scale: Science, v. 194, p. 1381–1387, doi:10.1126/science.194.4272.1381.

Neukum, G., Koenig, B., Fechtig, H., and Storzer, D., 1975a, Cratering in the Earth-Moon system: Consequences for age determination by crater counting: Houston, Texas, Lunar and Planetary Institute, Lunar and Planetary Science Conference VI, p. 2597–2620.

Neukum, G., Koenig, B., and Arkani-Hamed, J., 1975b, A study of lunar impact crater size-distributions: The Moon, v. 12, p. 201–229, doi:10.1007/BF00577878.

Neukum, G., Ivanov, B.A., and Hartmann, W.K., 2001, Cratering records in the inner solar system in relation to the lunar reference system: Space Science Reviews, v. 96, p. 55–86, doi:10.1023/A:1011989004263.

Neukum, G., Werner, S.C., and Ivanov, B.A., 2006, The characteristics of the impact crater production size-frequency distributions on the solar system planetary bodies, their relationships to asteroidal and cometary impacts, and the question of secondary-cratering contributions, *in* Workshop on Surface Ages and Histories: Issues in Planetary Chronology: Houston, Texas, Lunar and Planetary Institute, Lunar and Planetary Institute Contribution 1320, p. 38–39.

Nunes, P.D., Tatsumoto, M., and Unruh, D.M., 1974, U-Th-Pb systematics of some *Apollo 17* lunar samples and implications for a lunar basin excavation chronology: Houston, Texas, Lunar and Planetary Institute, Lunar and Planetary Science Conference V, p. 1487–1514.

Nyquist, L.E., and Shih, C.-Y., 1992, The isotopic record of lunar volcanism: Geochimica et Cosmochimica Acta, v. 56, p. 2213–2234, doi:10.1016/0016-7037(92)90185-L.

Nyquist, L.E., Bansal, B.M., Wiesmann, H., and Jahn, B.-M., 1974, Taurus-Littrow chronology: Some constraints on early lunar crustal development: Houston, Texas, Lunar and Planetary Institute, Lunar and Planetary Science Conference V, p. 1515–1539.

Nyquist, L.E., Bogard, D.D., and Shih, C.-Y., 2001, Radiometric chronology of the Moon and Mars, *in* Bleeker, J.A.M., Geiss, J., and Huber, M.C.E., eds., The Century of Space Science: Dordrecht, Netherlands, Kluwer Academic Publishers, p. 1325–1376.

Oberbeck, V.R., and Morrison, R.H., 1973, On the formation of the lunar herringbone pattern: Houston, Texas, Lunar and Planetary Institute, Lunar and Planetary Science Conference IV, p. 107–123.

Page, N.J., 1970, Geologic Map of the Cassini Quadrangle of the Moon (LAC-25): U.S. Geological Survey I-666, scale 1:1,000,000.

Papanastassiou, D.A., and Wasserburg, G.J., 1971, Lunar chronology and evolution from Rb-Sr studies of *Apollo 11* and *12* samples: Earth and Planetary Science Letters, v. 11, p. 37–62, doi:10.1016/0012-821X(71)90139-7.

Parmentier, E.M., Zhong, S., and Zuber, M.T., 2000, On the relationship between chemical differentiation and the origin of lunar asymmetries: Houston, Texas, Lunar and Planetary Institute, Lunar and Planetary Science Conference XXXI, CD-ROM, abstract 1614.

Pieters, C.M., 1978, Mare basalt types on the front side of the Moon: Houston, Texas, Lunar and Planetary Institute, Lunar and Planetary Science Conference IX, p. 2825–2849.

Pieters, C.M., 1993, Compositional diversity and stratigraphy of the lunar crust derived from reflectance spectroscopy, *in* Pieters, C.M., and Englert, P.A.J., eds., Topics in Remote Sensing—Remote Geochemical Analysis: Elemental and Mineralogical Composition: Cambridge, UK, Cambridge University Press, p. 309–339.

Pieters, C.M., Head, J.W., Adams, J.B., McCord, T.B., Zisk, S.H., and Whitford-Stark, J.L., 1980, Late high-titanium basalts of the western maria: Geology of the Flamsteed region of Oceanus Procellarum: Journal of Geophysical Research, v. 85, p. 3913–3938, doi:10.1029/JB085iB07p03913.

Pieters, C.M., Staid, M.I., Fischer, E.M., Tompkins, S., and He, G., 1994, A sharper view of impact craters from *Clementine* data: Science, v. 266, p. 1844–1848, doi:10.1126/science.266.5192.1844.

Pike, R.J., 1980, Geometric Interpretation of Lunar Craters: U.S. Geological Survey Professional Paper 1046-C, 77 p.

Preblich, B.S., McEwen, A.S., and Studer, D.M., 2007, Mapping rays and secondary craters from the Martian crater Zunil: Journal of Geophysical Research, v. 112, doi:10.1029/2006JE002817.

Rankenburg, K., Brandon, A.D., and Norman, M.D., 2007, A Rb-Sr and Sm-Nd isotope geochronology and trace element study of lunar meteorite LaPaz Icefield 02205: Geochimica et Cosmochimica Acta, v. 71, p. 2120–2135, doi:10.1016/j.gca.2007.01.014.

Robinson, M.S., and Jolliff, B.L., 2002, *Apollo 17* landing site: Topography, photometric corrections, and heterogeneity of the surrounding highland massifs: Journal of Geophysical Research, v. 107, doi:10.1029/2001JE001614.

Ryder, G., and Spudis, P.D., 1980, Volcanic rocks in the lunar highlands, *in* Proceedings of the Conference on the Lunar Highlands Crust: New York and Oxford, Pergamon Press, p. 353–375.

Schaber, G.G., 1969, Geologic Map of the Sinus Iridum Quadrangle of the Moon (LAC-24): U.S. Geological Survey I-602, scale 1:1,000,000.

Schaber, G.G., 1973, Lava flows in Mare Imbrium: Geologic evaluation from *Apollo* orbital photography: Houston, Texas, Lunar and Planetary Institute, Lunar and Planetary Science Conference IV, p. 73–92.

Schaber, G.G., Boyce, J.M., and Moore, H.J., 1976, The scarcity of mappable flow lobes on the lunar maria: Unique morphology of the Imbrium flows: Houston, Texas, Lunar and Planetary Institute, Lunar and Planetary Science Conference VII, p. 2783–2800.

Schaefer, O.A., and Husain, L., 1974, Chronology of lunar basin formation and ages of lunar anorthositic rocks: Houston, Texas, Lunar and Planetary Institute, Lunar and Planetary Science Conference V, p. 663–665.

Schmitt, H.H., Trask, N.J., and Shoemaker, E.M., 1967, Geologic Map of the Copernicus Quadrangle of the Moon (LAC-58): U.S. Geological Survey I-515, scale 1:1,000,000.

Schultz, P.H., and Spudis, P.D., 1979, Evidence for ancient mare volcanism: Houston, Texas, Lunar and Planetary Institute, Lunar and Planetary Science Conference X, p. 2899–2918.

Schultz, P.H., and Spudis, P.D., 1983, Beginning and end of lunar mare volcanism: Nature, v. 302, p. 233–236, doi:10.1038/302233a0.

Schultz, P.H., Greeley, R., and Gault, D.E., 1976, Degradation of small mare surface features: Houston, Texas, Lunar and Planetary Institute, Lunar and Planetary Science Conference VII, p. 985–1003.

Scott, D.H., 1972, Geologic Map of the Eudoxus Quadrangle of the Moon (LAC-26): U.S. Geological Survey I-705, scale 1:1,000,000.

Scott, D.H., and Eggleton, R.E., 1973, Geologic Map of the Rümker Quadrangle of the Moon (LAC-23): U.S. Geological Survey I-805, scale 1:1,000,000.

Scott, D.H., and Pohn, H.A., 1972, Geologic Map of the Macrobius Quadrangle of the Moon (LAC-43): U.S. Geological Survey I-799, scale 1:1,000,000.

Scott, D.H., McCauley, J.F., and West, M.N., 1977, Geologic Map of the West Side of the Moon: U.S. Geological Survey I-1034, scale 1:5,000,000.

Shih, C.-Y., Nyquist, L.E., Reese, Y., Yamaguchi, A., and Takeda, H., 2005, Rb-Sr and Sm-Nd isotopic studies of lunar highland meteorite Y86032 and lunar ferroan anorthosites 60025 and 67075: Houston, Texas, Lunar and Planetary Institute, Lunar and Planetary Science Conference XXXVI, CD-ROM, abstract 1433.

Shoemaker, E.M., and Hackman, R., 1962, Stratigraphic basis for a lunar time scale, *in* Kopal, Z., and Mikhailov, Z.K., eds., The Moon: Symposium 14 of the International Astronomical Union: San Diego, California, Academic Press, p. 289–300.

Silver, L.T., 1971, U-Th-Pb isotope systems in *Apollo 11* and *12* regolithic materials and a possible age for the Copernican impact: Eos (Transactions, American Geophysical Union), v. 52, no. 7, 534 p.

Soderblom, L.A., 1972, The process of crater removal in the lunar maria, *in* *Apollo 15* Preliminary Science Report: National Aeronautics and Space Administration Report SP-289, p. 25-87–25-91.

Soderblom, L.A., and Boyce, J.M., 1972, Relative ages of some near-side and far-side terra plains based on *Apollo 16* metric photography, *in Apollo 16* Preliminary Science Report: National Aeronautics and Space Administration Report SP-315, p. 29-3–29-6.

Soderblom, L.A., Condit, C.D., West, R.A., Herman, B.M., and Kreidler, T.J., 1974, Martian planetwide crater distributions: Implications for geologic history and surface processes: Icarus, v. 22, p. 239–263, doi:10.1016/0019-1035(74)90175-4.

Soderblom, L.A., Arnold, J.R., Boyce, J.M., and Lin, R.P., 1977, Regional variations in the lunar maria: Age, remanent magnetism, and chemistry: Houston, Texas, Lunar and Planetary Institute, Lunar and Planetary Science Conference VIII, p. 1191–1199.

Spudis, P.D., 1978, Composition and origin of the Apennine Bench Formation: Houston, Texas, Lunar and Planetary Institute, Lunar and Planetary Science Conference IX, p. 1086–1088.

Spudis, P.D., 1993, The Geology of Multi-Ring Impact Basins: Cambridge Planetary Science Series, Volume 8: New York, Cambridge University Press, 263 p.

Stadermann, F.J., Heusser, E., Jessberger, E.K., Lingner, S., and Stöffler, D., 1991, The case for a young Imbrium basin: New ^{40}Ar-^{39}Ar ages of *Apollo 14* rocks: Geochimica et Cosmochimica Acta, v. 55, p. 2339–2349, doi:10.1016/0016-7037(91)90108-H.

Staid, M.I., Pieters, C.M., and Head, J.W., III, 1996, Mare Tranquillitatis: Basalt emplacement history and relation to lunar samples: Journal of Geophysical Research, v. 101, no. E10, p. 23,213–23,228.

Stöffler, D., and Ryder, G., 2001, Stratigraphy and isotope ages of lunar geologic units: Chronological standard for the inner solar system: Space Science Reviews, v. 96, p. 9–54, doi:10.1023/A:1011937020193.

Stöffler, D., Ryder, G., Ivanov, B.A., Artemieva, N.A., Cintala, M.J., and Grieve, R.A.F., 2006, Cratering history and lunar chronology, *in* Jolliff, B.L., Wieczorek, M.A., Shearer, C.K., and Neal, C.R., eds., New Views of the Moon: Reviews in Mineralogy and Geochemistry, v. 60, p. 519–596.

Strom, R.G., and Neukum, G., 1988, The cratering record on Mercury and the origin of impacting objects, *in* Vilas, F., Chapman, C.R., and Matthews, M.S., eds., Mercury: Tucson, University of Arizona Press, p. 336–373.

Stuart-Alexander, D.E., 1978, Geologic Map of the Central Far Side of the Moon: U.S. Geological Survey I-1047, scale 1:5,000,000.

Taylor, L.A., Shervais, J.W., Hunter, R.H., Shih, C.-Y., Bansal, B.M., Wooden, J., Nyquist, L.E., and Laul, L.C., 1983, Pre–4.2 AE mare-basalt volcanism in the lunar highlands: Earth and Planetary Science Letters, v. 66, p. 33–47, doi:10.1016/0012-821X(83)90124-3.

Taylor, S.R., 1982, Planetary Science: A Lunar Perspective: Houston, Lunar and Planetary Institute, 481 p.

Tera, F., and Wasserburg, G.J., 1974a, The evolution and history of mare basalts as inferred from U-Th-Pb systematics: Houston, Texas, Lunar and Planetary Institute, Lunar and Planetary Science Conference VI, p. 807–809.

Tera, F., and Wasserburg, G.J., 1974b, U-Th-Pb systematics on lunar rocks and interferences about lunar evolution and the age of the Moon: Houston, Texas, Lunar and Planetary Institute, Lunar and Planetary Science Conference V, p. 1571–1599.

Terada, K., Anand, M., Sokol, A., Bischoff, A., and Sano, Y., 2007, Cryptomare magmatism 4.35 Gyr ago recorded in lunar meteorite Kalahari 009: Nature, v. 450, doi:10.1038/nature06356.

Thomson, B.J., Grosfils, E.B., Bussey, D.B.J., and Spudis, P.D., 2009, A new technique for estimating the thickness of mare basalts in Imbrium Basin: Geophysical Research Letters, v. 36, doi:10.1029/2009GL037600.

Titley, S.R., 1967, Geologic Map of the Mare Humorum Region of the Moon (LAC-93): U.S. Geological Survey I-495, scale 1:1,000,000.

Trask, N.J., and Titley, S.R., 1966, Geologic Map of the Pitatus Region of the Moon (LAC-94): U.S. Geological Survey I-485, scale 1:1,000,000.

Ulrich, G.E., 1969, Geologic Map of the J. Herschel Quadrangle of the Moon (LAC-11): U.S. Geological Survey I-604, scale 1:1,000,000.

Wagner, R., Head, J.W., III, Wolf, U., and Neukum, G., 2010, Lunar red spots: Stratigraphic sequence and ages of domes and plains in the Hansteen and Helmet regions on the lunar near-side: Journal of Geophysical Research, v. 115, no. E6, E06015, doi:10.1029/2009JE003359.

Walker, A.S., and El-Baz, F., 1982, Analysis of crater distributions in mare units on the lunar far side: The Moon and the Planets, v. 27, p. 91–106, doi:10.1007/BF00941559.

Werner, S.C., 2006, Major Aspects of the Chronostratigraphy and Geologic Evolutionary History of Mars [Ph.D. dissertation]: Berlin, Germany, Freie Universität, http://www.diss.fu-berlin.de/2006/33/indexe.html, 226 p.

Werner, S.C., Harris, A.W., Neukum, G., and Ivanov, B.A., 2002, The near-Earth asteroid size-frequency distribution: Note to Icarus, v. 156, p. 287–290, doi:10.1006/icar.2001.6789.

Werner, S.C., Ivanov, B.A., and Neukum, G., 2006, Mars: Secondary cratering—Implications for age determination: Houston, Texas, Lunar and Planetary Institute, Lunar and Planetary Science Conference XXXVII, CD-ROM, abstract 1595.

Wetherill, G.W., 1981, Nature and origin of basin-forming projectiles, *in* Schultz, P.H., and Merrill, R.B., eds., Multi-Ring Basins: Houston, Texas, Lunar and Planetary Institute, Lunar and Planetary Science Conference XII, p. 1–18.

Whitaker, E.A., 1972, Lunar color boundaries and their relationship to topographic features: A preliminary survey: The Moon, v. 4, p. 348–355, doi:10.1007/BF00562002.

Whitford-Stark, J.L., 1979, Charting the southern seas: The evolution of the lunar Mare Australe: Houston, Texas, Lunar and Planetary Institute, Lunar and Planetary Science Conference X, p. 2975–2994.

Whitford-Stark, J.L., 1990, The volcanotectonic evolution of Mare Frigoris: Houston, Texas, Lunar and Planetary Institute, Lunar and Planetary Science Conference XX, p. 175–185.

Whitford-Stark, J.L., and Head, J.W., III, 1980, Stratigraphy of Oceanus Procellarum basalts: Sources and styles of emplacement: Journal of Geophysical Research, v. 85, p. 6579–6609, doi:10.1029/JB085iB11p06579.

Wieczorek, M.A., and Phillips, R.J., 1998, Potential anomalies on a sphere: Applications to the thickness of the lunar crust: Journal of Geophysical Research, v. 103, p. 1715–1724, doi:10.1029/97JE03136.

Wieczorek, M.A., and Phillips, R.J., 2000, The "Procellarum KREEP terrane": Implications for mare volcanism and lunar evolution: Journal of Geophysical Research, v. 105, p. 20,417–20,430, doi:10.1029/1999JE001092.

Wieczorek, M.A., Cahill, J.T.S., Lucey, P.G., and Shearer, C.K., 2008, The mantle of the Moon: Exposed or sampled?: Houston, Texas, Lunar and Planetary Institute, Lunar and Planetary Science Conference XXXIX, CD-ROM, abstract 1271.

Wilhelms, D.E., 1968, Geologic Map of the Mare Vaporum Quadrangle of the Moon (LAC-59): U.S. Geological Survey I-548, scale 1:1,000,000.

Wilhelms, D.E., 1970, Summary of telescopic lunar stratigraphy: U.S. Geological Survey Professional Paper 599-F, p. 235–305.

Wilhelms, D.E., 1972, Geologic Map of the Taruntius Quadrangle of the Moon (LAC-61): U.S. Geological Survey I-722, scale 1:1,000,000.

Wilhelms, D.E., 1987, The Geologic History of the Moon: U.S. Geological Survey Professional Paper 1348, 302 p.

Wilhelms, D.E., and El-Baz, F., 1977, Geologic Map of the East Side of the Moon: U.S. Geological Survey I-948, scale 1:1,000,000.

Wilhelms, D.E., and McCauley, J.F., 1971, Geologic Map of the Nearside of the Moon: U.S. Geological Survey I-703, scale 1:1,000,000.

Wilhelms, D.E., Howard, K.A., and Wilshire, H.G., 1979, Geologic Map of the South Side of the Moon: U.S. Geological Survey I-1162, scale 1:1,000,000.

Williams, D.A., Greeley, R., Neukum, G., Wagner, R., and Kadel, S.D., 1995, Multispectral studies of western limb and farside maria from *Galileo* Earth-Moon Encounter 1: Journal of Geophysical Research, v. 100, p. 23,291–23,299, doi:10.1029/94JE01863.

Wilshire, H.G., 1973, Geologic Map of the Byrgius Quadrangle of the Moon (LAC-92): U.S. Geological Survey I-755, scale 1:1,000,000.

Wilson, L., and Head, J.W., III, 2001, Ascent and eruption of mare basalts on the Moon: Houston, Texas, Lunar and Planetary Institute, Lunar and Planetary Science Conference XXXII, CD-ROM, abstract 1297.

Yingst, R.A., and Head, J.W., III, 1997, Volumes of lunar lava ponds in South Pole–Aitken and Orientale Basins: Implications for eruption conditions, transport mechanisms, and magma source regions: Journal of Geophysical Research, v. 102, no. E5, p. 10,909–10,931, doi:10.1029/97JE00717.

Zhong, S., Parmentier, E.M., and Zuber, M.T., 1999, Early lunar evolution and the origin of asymmetric distribution of mare basalts: Houston, Texas, Lunar and Planetary Institute, Lunar and Planetary Science Conference XXX, CD-ROM, abstract 1789.

Ziethe, R., Seiferlein, K., and Hiesinger, H., 2009, Duration and extent of lunar volcanism: Comparison of 3D convection models to mare basalt ages: Planetary and Space Science, v. 57, p. 784–796, doi:10.1016/j.pss.2009.02.002.

Zuber, M.T., Smith, D.E., Lemoine, F.G., and Neumann, G.A., 1994, The shape and internal structure of the Moon from the *Clementine* mission: Science, v. 266, p. 1839–1843, doi:10.1126/science.266.5192.1839.

Manuscript Accepted by the Society 26 August 2010

Printed in the USA

The Geological Society of America
Special Paper 477
2011

Previously unknown large impact basins on the Moon: Implications for lunar stratigraphy

Herbert Frey
Goddard Space Flight Center, Greenbelt, Maryland 20771, USA

ABSTRACT

Lunar topographic and model crustal thickness data provide evidence for large basins on the Moon not previously recognized by photogeologic mapping. The number of these basins larger than 300 km diameter suggests that the total population may be 2–3 times greater than previously thought. Some previously proposed named basins have little to no basin-like topographic character; most of those that do also have pronounced crustal thickness signatures in the form of circular thin areas (CTAs). There also exist CTAs that lack a pronounced quasi-circular depression (QCD) signature in the available topographic data. Newly recognized candidate basins contribute significantly to a total population in which there are more large basins on the lunar farside than on the nearside. The North Pole region appears remarkably devoid of large basins, with only three larger than 300 km diameter and only one at >70°N. Disruption of the topographic and/or crustal thickness structure can be used to establish overlap relationships between QCDs and CTAs and thus relative ages (and a relative local stratigraphy) for those features not visible in images. If large basins have the ability to significantly modify the surface out to twice their diameter, there are likely no parts of the Moon that remain unaffected by the total population shown here. If such effects extend out to only 1.5 basin diameters, there may be 1.8 million km^2 of lunar surface where rocks predating most basin formation may still exist. The early history of the Moon likely involved much greater large-diameter impact cratering than previously thought, and therefore much greater global mixing and redistribution of surface materials. Early lunar stratigraphy is likely far more complex than previously appreciated.

INTRODUCTION

A large population of previously unrecognized, likely buried, impact basins exists on Mars (Frey et al., 2002) that are not obvious in image data. Revealed first as "quasi-circular depressions" (QCDs) in MOLA (Mars Orbiter Laser Altimeter) topographic data (Frey et al., 1999, 2002; Frey 2006a), and more recently as "circular thin areas" (CTAs) (Edgar and Frey, 2008; Frey 2009a) in crustal thickness data (Neumann et al., 2004, 2008), the non-visible population greatly outnumbers the visible impact basin population everywhere on Mars. It is an obvious question to ask whether a previously unrecognized population of large impact features also exists on the Moon.

Mars has more ways to bury or degrade impact craters than does the Moon because it had a much more active and long-lived geologic history. Perhaps it is not surprising that 90% of the

Frey, H., 2011, Previously unknown large impact basins on the Moon: Implications for lunar stratigraphy, *in* Ambrose, W.A., and Williams, D.A., eds., Recent Advances and Current Research Issues in Lunar Stratigraphy: Geological Society of America Special Paper 477, p. 53–75, doi:10.1130/2011.2477(02).

craters and basins suggesting that the Mars lowland basement is actually extremely old are part of the buried population, hidden below the younger lowland plains (Frey et al., 2002; Frey, 2006b). However, even the highlands of Mars have a large population of impact basins not previously recognized through photogeologic mapping that appear to have been buried by early resurfacing processes. Impact ejecta from large basins likely contributed to this burial (Morrison and Frey, 2007), and this process also occurred on the Moon.

Martian QCDs were mapped using an interactive graphics program called GRIDVIEW (Roark et al., 2000) designed to stretch, contour, and analyze MOLA data to reveal subtle topographic features. The same approach can be used on gridded lunar topographic data. This paper addresses the issue of whether or not there is a population of large lunar impact basins not previously recognized that can be identified using topographic and crustal thickness data.

Large multiring impact basins are well-established on the Moon. Classic compilations of those mapped photogeologically have been provided by Wilhelms (1987) and Spudis (1993). Wood (2004) presented a catalog including new candidate basins not listed by Wilhelms and Spudis. *Clementine* laser altimetry (Zuber et al., 1994; Neumann et al., 1996) showed that many of the named features, including some of the most degraded, had the pronounced multiring topographic structure expected for large impact basins (Spudis et al., 1994; Zuber et al., 1994). That altimetry data and derived crustal thickness models (Zuber et al., 1994; Neumann et al., 1996, 1998) also revealed several previously unrecognized features that were likely additional large impact basins (Spudis et al., 1994; Zuber et al., 1994; Cook et al., 2000). Though limited in horizontal and vertical resolution, the altimetry demonstrated the utility of topography for mapping large impact basins on the Moon, as MOLA did for Mars (Frey et al., 1999, 2002; Frey, 2006a, 2006b).

The state-of-the-art topography for the Moon available for this study was the Unified Lunar Control Net 2005 (ULCN2005; Archinal et al., 2006), based on *Clementine* laser altimetry and stereo imaging. The digital elevation models derived from this have a stated horizontal resolution of ~2 km (ranging from ~100 m to a few kilometers) and a vertical accuracy of a few hundred meters. Though low in resolution compared with data sets soon to be available, this is adequate for studying the topography of known large (≥300 km diameter) impact basins and for searching for large new candidate basins not previously known. This paper describes such a search and provides a list of new candidate basins ≥300 km in diameter that coming higher resolution topographic data from *Kaguya* and *LRO* (*Lunar Reconnaissance Orbiter*) should be able to verify or disqualify.

ULCN2005 data were examined using the same approach taken with the MOLA data, employing the GRIDVIEW software to identify sometimes subtle circular topographic lows (QCDs) (see Fig. 1). As with the Mars data, circles were fitted to identified QCDs in which at least 50% of a (not always continuous) topographic "ring" could be identified bounding a circular depression. An initial search revealed 92 QCDs ranging from 300 to over 2600 km (the South Pole–Aitken basin). These were first compared with named lunar impact basins ≥300 km (Wilhelms, 1987) in order to characterize the topographic structure of photogeologically identified and named features. Table 1 shows the results.

Not all the named basins listed by Wilhelms (1987) have obvious basin-like (circular) topographic structure. Wilhelms has 28 "definite" and another 17 "probable and possible" basins larger than 300 km diameter; of these 17, he described six as "probable," nine as "possible," and two as "doubtful" (see Table 1). Most prominent large named basins (Imbrium, Serenitatis, Crisium, Nectaris) and many of the obvious smaller basins (Humorum, Grimaldi) on the nearside and the farside (Mendeleev, Moscoviense, Korolev, Hertzsprung) have pronounced topographic structure that matches well the ring structure described by Wilhelms. However, the low-resolution ULCN2005 data showed no basin-like topographic structure associated with Wilhelms' "distinct" Australe Basin. The "probable" Tranquillitatis "basin" contains an interior topographic *high* (Frey, 2008a, 2008b) and lacks the overall circular topographic depression normally associated with a basin. Six of the nine "possible" basins listed by Wilhelms (Procellarum, Grissom-White, Insularum, Marginis, Flamsteed-Billy, and Pingre-Hausen), and both of the two he lists as "doubtful" (Al-Khwarismi-King and Werner-Airy) have no circular basin topography in the ULCN2005 data centered where Wilhelms lists the basin. Overall, 10 of the 45 basins listed by Wilhelms lack pronounced basin topographic structure. Another 10 having overall circular basin-like topography appear either offset or have different diameters (based on the topography) from those listed by Wilhelms.

The 10 basins from Wilhelms lacking obvious basin-like topography are excluded from the final compilation provided here (Table 2). Two others that the topography suggests may exist, but at much smaller diameter and with significant offset from the Wilhelms location (Keeler-Heaviside, Tsiolkovsky-Stark), are also excluded. Thirty-three basins listed by Wilhelms with pronounced circular basin topography are retained as "named features," but their diameters and centers are based on circular fits to the ULCN2005 topographic structure in order to have a consistent data set.

The initial search for QCDs ≥300 km diameter yielded 92 candidate basins. The number of new candidate topographic basins (not all of which survived more detailed study; see following) was substantially larger than the number of named basins with topographic structure. These new candidate basin QCDs were carefully reexamined as described next. In addition, model crustal thickness data were also used to search for possible additional basins.

APPROACH

Based on prior experience in searching for previously unknown large impact basins on Mars (Frey et al., 2002; Frey, 2006a, 2006b, 2008c, 2009a; Edgar and Frey, 2008), two related

kinds of information were used to search for possible new large basins on the Moon. The first was ULCN2005 topography, as described already. Figure 1 shows GRIDVIEW stretches of this topography for the lunar nearside, with and without contours and with impact basins 300 km from Wilhelms' (1987) complete list, including those lacking basin-like topographic structure.

Detailed study of the 92 QCDs originally found (Frey 2008a, 2008b) revealed that not all were viable as candidate impact basins. Comparisons of QCDs with image data or previous compilations of large (named) craters revealed a number of cases where the apparent single QCD in ULCN2005 topography was actually a known large crater <300 km diameter, or due to a cluster of craters in the 100–200-km-diameter range grouped closely enough that the low-resolution ULCN2005 data "saw" this as a single, roughly circular, low. After eliminating these obvious mistakes and other very weak cases, 38 good candidate basins remain that are not previously named features (compared with the 33 named basins that also were good topographic basins; see Table 2). Some of these QCDs are very obvious circular topographic lows. Others are not, even among named features (see following). To quantify the topographic "expression" of all identified QCDs, a numerical score was assigned using a range of 1 (weak) to 5 (very strong). Most (but not all) of the named basins have high expression scores (>3). Topographic expression scores are included in Table 2 and are discussed in more detail in the following discussion.

A second source for identifying possible previously unknown large lunar basins is crustal thickness data. Edgar and Frey (2008) showed there were on Mars a large number of circular thin areas (CTAs) ≥300 km diameter revealed in the Neumann et al. (2004) crustal thickness model. Many of these coincided with large impact basins revealed as QCDs (either visible or not), but a large number of CTAs did not correspond to known QCDs and yet still had the crustal thickness structure of large impact basins: a roughly circular area of thin crust surrounded by a (sometimes discontinuous) ring of thicker material. Edgar and Frey (2008) suggested these might be additional candidate impact basins, perhaps more deeply buried. The recent crustal thickness model

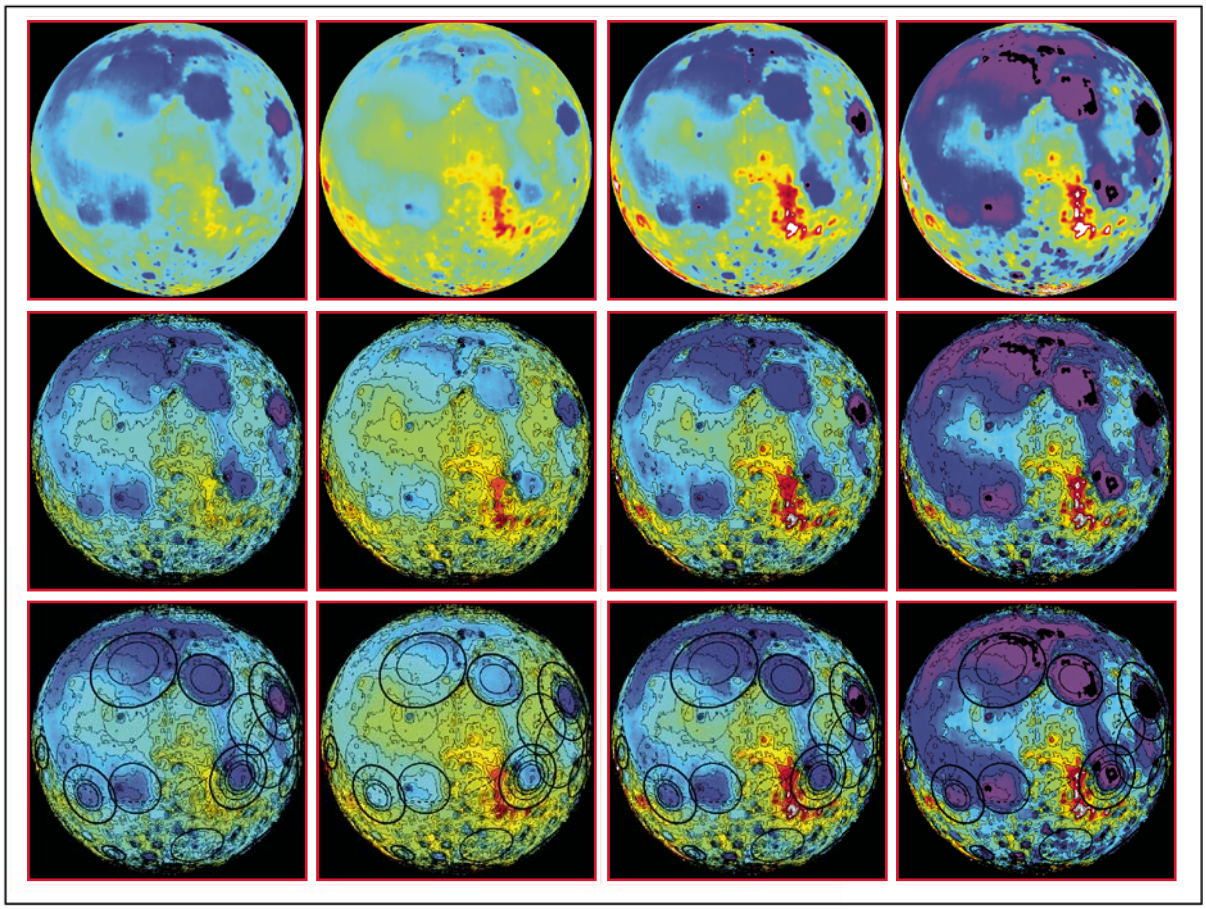

Figure 1. Stretched ULCN2005 lunar topography. Blues and purples are low elevations; yellows and reds are high elevations. Top row: Topography only. Middle row: 400 m contours added. Note how this accentuates the circularity of many quasi-circular depressions. Bottom row: Basins >300 km diameter from Wilhelms (1987) shown as black circles. "Probable and possible" basins are shown as thinner black circles. See text for discussion.

of Neumann et al. (2008), based on higher-resolution gravity data, confirms many of these CTAs and reveals even more, including some very large candidate basins (Frey, 2009a).

The Wieczorek et al. (2006) lunar crustal thickness model (downloaded from the Web site http://www.ipgp.fr/~wiecz0r/CrustalThicknessArchive/CrustalThickness.html) was searched for CTAs using the same approach employed with the ULCN2005 data (Frey, 2008b, 2008c, 2009b). Figure 2 shows GRIDVIEW stretches of this data with and without contours, and with Wilhelms' (1987) complete list of basins. Most (but not all) named and many additional candidate basins revealed as QCDs are also strong CTA features: Many known lunar basins have preserved a crustal thickness signature over lunar history. An initial search revealed 56 CTAs ≥300 km in diameter that are not coincident with QCDs, in addition to CTAs associated with most, but not all, of the QCDs described previously (Frey, 2009b). An expression score was assigned to the CTAs based on circularity and strength of the signature (the contrast between the interior and exterior of the CTA), using the same 1 (weak) to 5 (very strong) scale as for the QCDs.

Some of the candidate CTAs can be explained by clusters of smaller craters and basins for which the combined crustal thickness structure gives the appearance of a single large feature. After

TABLE 1. ULCN CHARACTER OF LUNAR BASINS IDENTIFIED BY WILHELMS (1987)

Type	Name	Sym	Lat	West long	Diam (km)	Topographic character
Distinct	South Pole–Aitken	SPA	–56.0	180.0	2500	Strong basin signature
Distinct	Imbrium	Im	33.0	18.0	1160	Strong basin signature
Distinct	Crisium	Cr	17.5	301.5	1060	Strong basin signature
Distinct	Orientale	Or	–20.0	95.0	930	Strong basin signature
Distinct	**Australe**	Au	–51.5	265.5	880	**NO TOPOGRAPHIC BASIN**
Distinct	Nectaris	Ne	–16.0	326.0	860	Strong basin signature
Distinct	Smythii	Sm	–2.0	273.0	840	Strong basin signature but smaller
Distinct	Humorum	Hu	–24.0	39.5	820	Strong basin signature
Distinct	**Keeler-Heaviside**	KH	–10.0	198.0	780	**Much smaller, offset**
Distinct	Serenitatis	Se	27.0	341.0	740	Strong basin signature
Distinct	**Mendel-Rydberg**	MR	–50.0	94.0	630	**Offset from Wilhelms (1987)**
Distinct	**Humboldtianum**	Hm	61.0	276.0	600	Strong basin signature but **larger**
Distinct	Freundlich-Sharonov	FS	18.5	185.0	600	Strong basin signature, inner rings
Distinct	Hertzsprung	He	1.5	128.5	570	Strong basin signature
Distinct	Ingenii	Ig	–34.0	197.0	560	Strong basin signature
Distinct	Coulomb-Sarton	CS	52.0	123.0	530	Strong basin signature
Distinct	Apollo	Ap	–36.0	151.0	505	Strong basin signature
Distinct	Moscoviense	Mo	25.0	213.0	445	Strong basin signature
Distinct	Korolev	Ko	–4.5	157.0	440	Strong basin signature
Distinct	**Grimaldi**	Gr	–5.0	68.0	430	Strong basin signature but **smaller**
Distinct	Lorentz	Lo	34.0	97.0	360	Strong basin signature
Distinct	Poincare	Po	–57.5	198.0	340	Strong basin signature
Distinct	Mendeleev	Me	6.0	219.0	330	Strong basin signature
Distinct	Birkhoff	Bi	59.0	147.0	330	Strong basin signature
Distinct	**Schiller-Zucchius**	SZ	–56.0	44.5	325	**Main is larger than DEW***
Distinct	**Planck**	Pl	–57.5	224.5	325	Strong basin signature but **offset**
Distinct	Schrödinger	Sc	–75.0	226.0	320	Strong basin signature
Distinct	Bailly	Ba	–67.0	68.0	300	Strong basin signature
Probable	**Fecunditatis**	Fe	–4.0	308.0	990	Strong basin signature but **offset**
Probable	**Tranquillitatis**	Tr	7.0	320.0	800	**NO TOPOGRAPHIC BASIN**
Probable	**Mutus-Vlacq**	MV	–51.5	339.0	690	**Offset from DEW, larger**
Probable	**Nubium**	Nu	–21.0	15.0	690	**Offset from DEW**
Probable	**Lomonosov-Fleming**	LF	19.0	255.0	620	**Slightly offset, smaller**
Probable	**Balmer-Kapteyn**	BK	–15.5	291.0	550	Strong basin signature but **offset**
Possible	**Procellarum**	Pr	26.0	15.0	3200	**NO TOPOGRAPHIC BASIN**
Possible	**Tsiolkovskiy-Stark**	TS	–15.0	232.0	700	**Much smaller, offset**
Possible	**Grissom-White**	GW	–44.0	161.0	600	**NO TOPOGRAPHIC BASIN**
Possible	**Insularum**	In	9.0	18.0	600	**NO TOPOGRAPHIC BASIN**
Possible	**Marginis**	Ma	20.0	276.0	580	**NO TOPOGRAPHIC BASIN**
Possible	**Flamsteed-Billy**	FB	–7.5	45.0	570	**NO TOPOGRAPHIC BASIN**
Possible	Amundsen-Ganswindt	AG	–81.0	240.0	355	Strong basin signature
Possible	Sikorsky-Rittenhouse	SR	–68.5	249.0	310	Moderate basin signature
Possible	**Pingre-Hausen**	PH	–56.0	82.0	300	**NO TOPOGRAPHIC BASIN**
Doubtful	**Al-Khwarismi-King**	AK	1.0	248.0	590	**NO TOPOGRAPHIC BASIN**
Doubtful	**Werner-Airy**	WA	–24.0	348.0	500	**NO TOPOGRAPHIC BASIN**

*DEW—Don E. Wilhelms, referenced as Wilhelms (1987).

TABLE 2. LUNAR IMPACT BASINS ≥300 km DIAMETER

Basins Identified in ULCN2005 Topography as Quasi-Circular Depressions										
Basin		Center		Ring diameters (km)			Scores			Likelihood
Name	Sym	Lat	W Long	Inner	Main	Outer	Topo	CrTh	Sum	
TOPO-1	T1	59.07	357.13	321	**438**	547	3	3	6	Likely
TOPO-2	T2	–15.62	353.03		**437**		4	3	7	Likely
Mutus Vlacq	MV	–52.35	342.22	466, 615	**864**		2	2	4	Likely
Serenitatis	Se	26.74	341.25	420	**725**	982	5	5	10	Likely
TOPO-3	T3	54.98	326.29	359	**510**	651, 822	3	4	7	Likely
Nectaris	Ne	–16.19	325.56	389, 495, 610	**884**	1320 (s)	5	5	10	Likely
Fecunditatis	Fe	–1.80	305.82	697	**849**	1060	3	4	7	Likely
Crisium	Cr	17.36	302.78	476, 590, 881	**1059**		4	5	9	Likely
TOPO-4	T4	–46.88	293.02	619	**942**	1500	3	3	6	Likely
TOPO-5	T5	16.65	292.02		**428**		1	3	4	Likely
Balmer-Kaptyen	BK	–14.63	289.78		**409**	644 (?)	1	4	5	Likely
Humboldtianum	Hm	58.01	276.63	377, 560	**696**		5	5	10	Likely
Smythii	Sm	–2.27	272.68		**502**	711 (?)	5	5	10	Likely
TOPO-6	T6	–32.80	272.50	273	**474**		3	3	6	Likely
TOPO-7	T7	–34.23	261.54		**389**		3	2	5	Likely
TOPO-8	T8	–26.87	256.65	182 (?)	**314**	413	3	3	6	Likely
Lomonosov-Fleming	LF	19.53	256.53		**565**		2	1	3	Possible
Sikorsky-Rittenhouse	SR	–67.93	249.06		**319**		2	–2	0	Possible
TOPO-9	T9	–50.80	243.33	256	**321**	435	3	4	7	Likely
TOPO-10	T10	57.80	242.60	328, 495	**603**		3	3	6	Likely
Aamundson-Ganswindt	AG	–81.53	238.04		**349**		4	0	4	Likely
TOPO-11	T11	50.14	235.26	466	**824**		2	3	5	Likely
Schrödinger	Sc	–74.75	225.96	175	**343**		5	2	7	Likely
Planck	Pl	–57.24	223.70	244	**365**		4	1	5	Likely
TOPO-12	T12	–16.34	221.23		**329**		5	4	9	Likely
Mendeleev	Me	4.98	218.35	240	**385**		5	5	10	Likely
Moscoviense	Mo	25.81	213.07	373	**507**		5	5	10	Likely
TOPO-13	T13	–35.78	211.86		**328**		4	4	8	Likely
TOPO-14	T14	–5.52	210.36	300	**446**		3	4	7	Likely
TOPO-15	T15	–64.80	209.71		**352**		3	1	4	Likely
TOPO-16	T16	27.14	209.69		**626**	760 (?)	4	2	6	Likely
TOPO-17	T17	14.43	203.54	254, 410	**600**		3	3	6	Likely
TOPO-18	T18	–19.18	199.06	340, 513	**805**		4	3	7	Likely
Poincare	Po	–57.52	197.74	203	**331**		3	1	4	Likely
Ingenii	Ig	–32.40	196.68	337	**465**	554	4	3	7	Likely
TOPO-19	T19	–0.19	189.26	261	**392**		3	2	5	Likely
Freundlich-Sharonov	FS	18.54	185.03	272, 402	**628**		4	4	8	Likely
South Pole–Aitken	SPA	–55.43	184.71		**2653**		3	3	6	Likely
TOPO-20	T20	39.61	183.57	252	**432**		2	4	6	Likely
TOPO-21	T21	–71.56	182.23	191, 280	**377**		2	1	3	Possible
TOPO-22	T22	50.00	180.18	219	**314**	429 (?)	4	2	6	Likely
TOPO-41	T41	24.75	168.14	172	**317**		5	3	8	Likely
TOPO-23	T23	–57.08	162.10	392, 557	**696**		3	2	5	Likely
TOPO-24 (1)	T24	13.85	158.29		**427**		4	4	8	Likely
Korolev	Ko	–4.10	157.29	208	**452**		5	3	8	Likely
Apollo	Ap	–35.47	150.82	242	**573**		5	3	8	Likely
Birchoff	Bi	59.01	147.00		**349**		4	3	7	Likely
TOPO-25	T25	–57.44	137.30		**688**		2	1	3	Possible
Hertzsprung	He	1.91	129.06	390	**619**		5	5	10	Likely
Coulomb-Sarton	CS	51.61	122.67	349	**518**		5	5	10	Likely
TOPO-26	T26	–14.89	119.23		**410**		1	2	3	Possible
TOPO-27	T27	–10.42	116.22		**325**		2	1	3	Possible

(*Continued*)

TABLE 2. LUNAR IMPACT BASINS ≥300 km DIAMETER (*Continued*)

Basins Identified in ULCN2005 Topography as Quasi-Circular Depressions

Basin		Center		Ring diameters (km)			Scores			Likelihood
Name	Sym	Lat	W Long	Inner	Main	Outer	Topo	CrTh	Sum	
TOPO-28	T28	29.58	114.26	277	**393**	523	3	4	7	Likely
Lorentz	Lo	34.22	97.14		**379**		4	1	5	Likely
Orientale	Or	–19.35	95.17	483, 683	**992**		4	4	8	Likely
Mendel-Rydberg	MR	–48.98	95.00	339, 528	**689**		5	4	9	Likely
Bailly	Ba	–66.76	69.23		**313**		4	2	6	Likely
Grimaldi	Gr	–5.29	68.38		**304**	420	4	4	8	Likely
TOPO-30 (2)	T30	–15.82	66.60	318	**380**		4	5	9	Likely
TOPO-31	T31	42.06	65.55	716	**973**	1294	3	3	6	Likely
TOPO-32	T32	20.45	62.14	735	**1253**	1702	3	2	5	Likely
TOPO-33	T33	–38.15	61.96		**500**		3	2	5	Likely
TOPO-34	T34	–43.98	56.19		**317**		3	1	4	Likely
Schiller-Zucchius	SZ	–56.29	44.80	182	**371**	531 (T)	3	4	7	Likely
Humorum	Hu	–24.36	39.06	492	**867**		3	4	7	Likely
TOPO-35	T35	–7.66	37.81	313	**451**		3	4	7	Likely
TOPO-37	T37	59.16	22.29	354	**470**	560 (CrTh)	4	2	6	Likely
TOPO-38 (3)	T38	37.85	18.77		**616**		1	5	6	Likely
Imbrium	Im	33.07	17.47		**1166**		2	3	5	Likely
Nubium	Nu	–22.42	14.78		**618**	809	3	3	6	Likely
TOPO-40	T40	15.76	12.55		**771**		2	2	4	Likely

Basins Identified in Lunar Crustal Thickness Data as Circular Thin Areas (CTAs)

Basin		Center		Ring diameters (km)			Scores			Likelihood
Name	Sym	Lat	W Long	Inner	Main	Outer	Topo	CrTh	Sum	
CTA-1	C1	1.52	358.81		**328**		2	5	7	Likely
CTA-2	C2	14.18	356.64	248, 350	**419**		3	5	8	Likely
CTA-3	C3	–24.58	355.73		**406**		1	3	4	Likely
CTA-4	C4	–83.37	327.10		**319**		0	3	3	Possible
CTA-5	C5	42.30	289.55		**309**		1	4	5	Likely
CTA-6	C6	29.08	279.50	333	**457**		2	4	6	Likely
CTA-7	C7	47.50	264.22		**389**		1	3	4	Likely
CTA-8	C8	19.89	253.22	918, 1300	**1764**		2	2	4	Likely
CTA-9	C9	23.18	241.81		**312**		1	3	4	Likely
CTA-10	C10	–25.20	237.66		**324**		2	5	7	Likely
CTA-11	C11	27.08	232.12	217	**313**		3	4	7	Likely
CTA-12	C12	–36.82	231.38	202	**360**		2	5	7	Likely
CTA-13	C13	15.91	224.87		**315**		1	4	5	Likely
CTA-14	C14	76.61	217.43	296	**744**		1	3	4	Likely
CTA-26	C26	26.51	171.48	401	**533**		2	5	7	Likely
CTA-15	C15	–15.34	169.39	189, 356	**490**		3	4	7	Likely
CTA-16	C16	50.79	164.49		**491**		1	3	4	Likely
CTA-17	C17	40.11	149.15		**362**		2	4	6	Likely
CTA-18	C18	18.60	123.38		**539**		2	2	4	Likely
CTA-19	C19	–34.66	114.25	354	**467**		2	2	4	Likely
CTA-20	C20	67.75	112.48		**501**		2	3	5	Likely
CTA-21	C21	61.89	74.04	334	**468**		3	3	6	Likely
CTA-22	C22	1.83	60.25		**401**		0	4	4	Likely
CTA-23	C23	12.58	53.35		**304**		0	3	3	Possible
CTA-24	C24	0.37	45.32		**323**		0	4	4	Likely
CTA-27	C27	18.42	18.44	286	**409**		2	5	7	Likely
CTA-25	C25	11.43	9.91		**330**		1	5	6	Likely

Note: Numbers in parentheses: 1—Dirichlet-Jackson; 2—south of Grimaldi; 3—inside Imbrium.

eliminating these cases, 27 CTAs appear to be good candidates for additional large lunar impact basins, over and above the previously found QCDs. Many CTAs find support in the ULCN2005 topography, such as overall bowl-like shape, or suggestions of partial rim structure. While generally not enough for the feature to be called a QCD, these topographic aspects add to the confidence that many of the CTAs are good candidates for being impact basins. The CTA topographic attributes are indicated by the topographic score in Table 2. A CTA score for all the previously identified QCDs, and a sum of the two scores are also found in Table 2.

Figures 3 and 4 show examples of QCDs (both named and unnamed features) and CTAs not identified first as QCDs. The very prominent and very obvious QCD (TOPO-24 in Table 2; single dashed circle in Fig. 3) north of Korolev (solid circles in Fig. 3) seems to have been previously identified, though it does not appear in the classic compilations by Wilhelms (1987) or Spudis (1993), nor was it described in early *Clementine* studies (Spudis et al., 1994). Byrne (2009, personal commun.) calls this "Raimond-Engelhardt." Wood (2004) listed this as "Dirichlet-Jackson" and referenced Cook et al. (2000). Though slightly less obvious than Korolev (a two-ring basin with ring diameters 208 and 452 km, based on the topography) to the south, the Dirichlet-Jackson QCD (TOPO-24) is almost as large (427 km; Wood gives 470 km). A second obvious QCD (TOPO-41) lies to the NW; it has a double ring structure with diameters 172 and 317 km.

Note features marked by "X." These are QCDs originally identified but later rejected as possible large basins when closer examination revealed a known crater <300 km in diameter or a cluster of smaller craters that appeared as a single feature in the low-resolution topographic data.

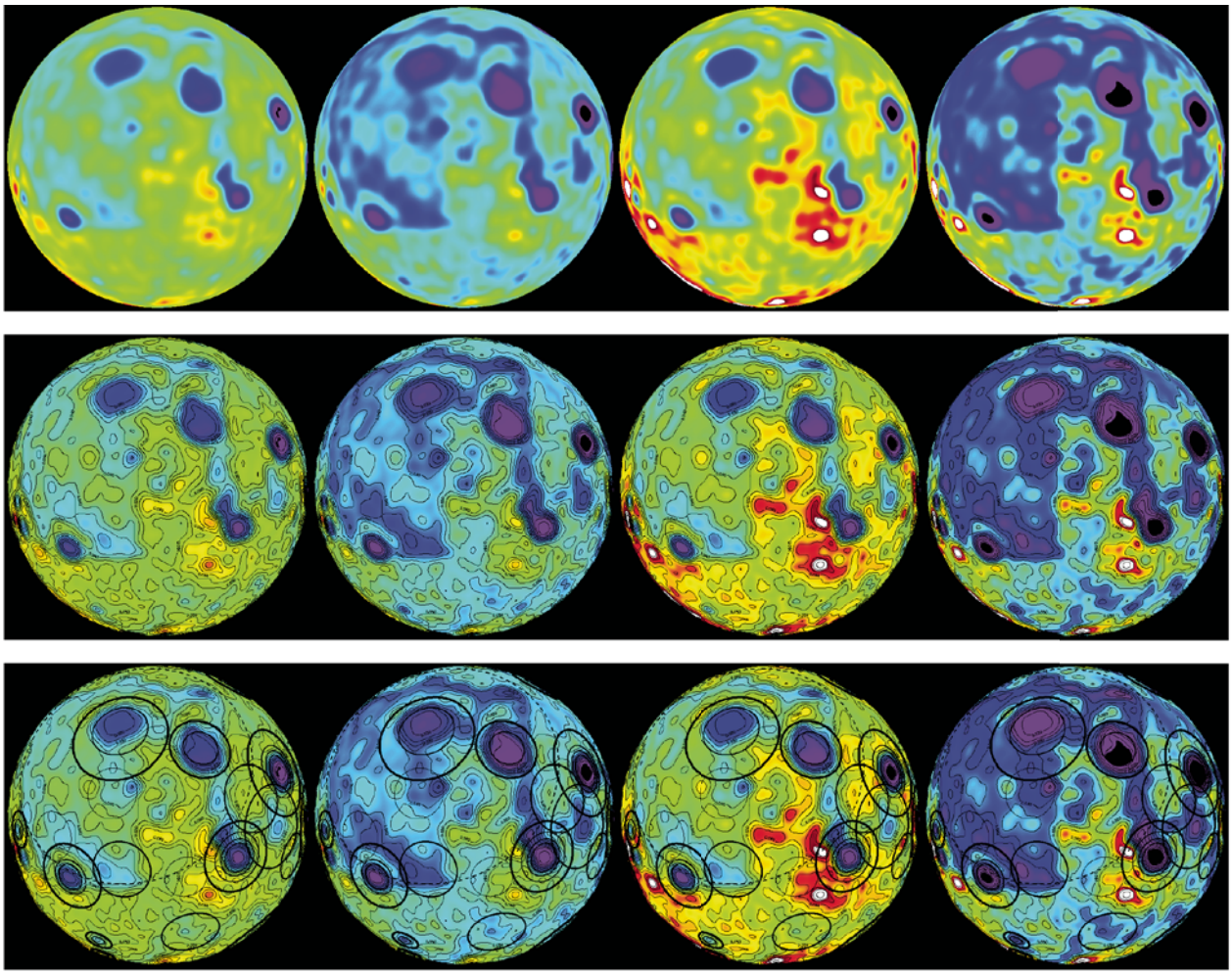

Figure 2. Stretched color versions of lunar crustal thickness (Wieczorek et al., 2006). Blues—thin crust, reds—thick crust. Top row: Different stretches reveal different circular thin areas (CTAs). Middle row: 5 km contours added. Bottom row: Basins identified by Wilhelms (1987). Thicker lines are more obvious basins. Most but not all prominent named basins have strong CTA signatures, but there are many additional CTAs that are not named features. Many, but not all, are also quasi-circular depressions. See text for discussion.

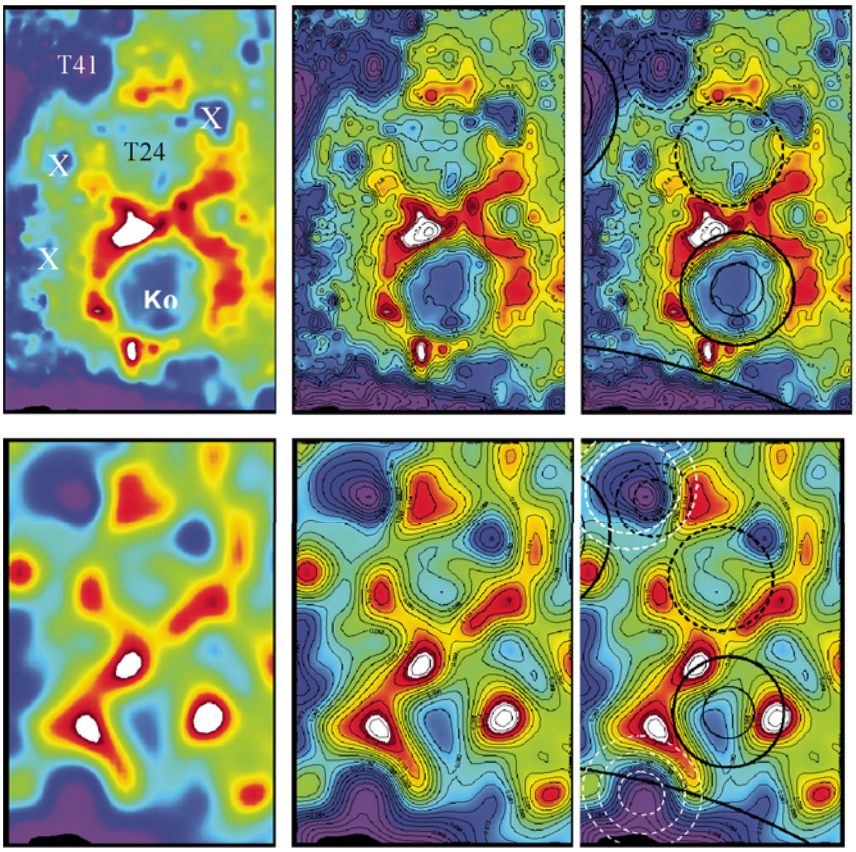

Figure 3. Lunar farside region centered at 33°N, 170°W. Top row: Stretched ULCN2005 data (left) with 400 m contours (middle) and quasi-circular depressions (QCDs) identified (right). Korolev (Ko) is shown by the two solid rings near lower center; the very obvious QCD (TOPO-24, Dirichlet-Jackson) above it is almost as large but was not identified by Wilhelms (1987). A second obvious but somewhat smaller QCD (TOPO-41) lies to the NW. Bottom row: Stretched lunar crustal thickness (left) with 4 km contours (middle) and both QCDs (black) and circular thin areas (CTAs) (white) identified. Korolev and Dirichlet-Jackson have clear CTA signatures; two additional CTAs are identified in this region. "X's" indicate QCDs originally identified but later rejected as likely candidate large basins. See text for discussion.

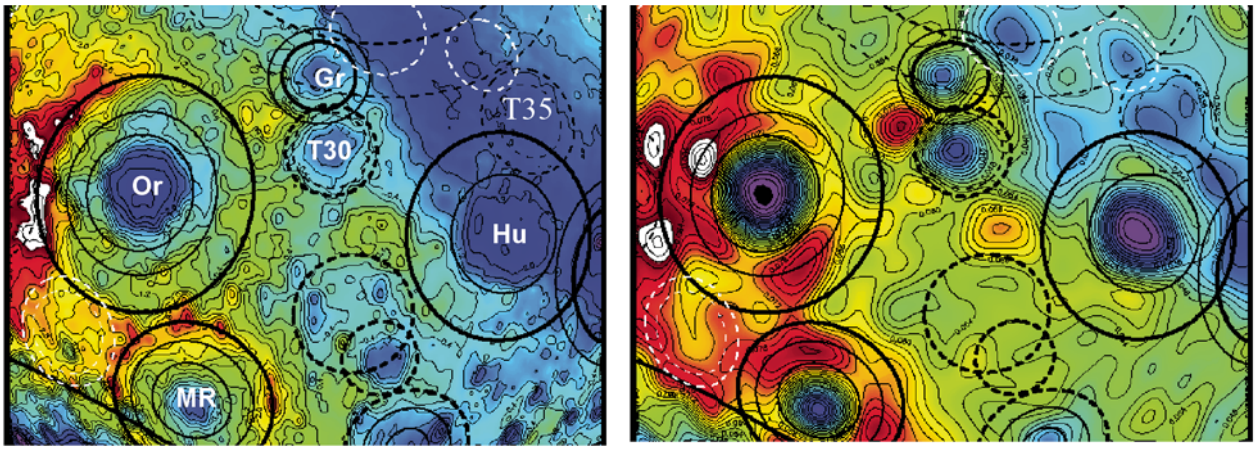

Figure 4. Stretched ULCN2005 topography (left) and crustal thickness (right) for the region including the large multiring basins (solid circles) Orientale (Or), Mendel-Rydberg (MR), and Humorum (Hu). Topography contour interval is 400 m; crustal thickness contour interval is 3 km. The black dashed quasi-circular depression (QCD) (T30) and circular thin area (CTA) just south of Grimaldi (Gr) is slightly larger than, and at least as obvious as, Grimaldi, but it is not listed in Wilhelms' (1987) or Spudis' (1993) inventory of large lunar basins. Several other QCDs are shown as dashed black lines (thicker lines mean stronger expression), and three CTAs that are good candidates for impact basins are shown as white dashed circles. See text for detailed discussion.

Figure 3 also shows crustal thickness (bottom row). The Dirichlet-Jackson (T24) CTA is actually better aligned with its topographic structure than is the equally obvious CTA associated with Korolev. In Table 2, both basins have an expression score of 8, but Korolev gets this with a 5 topography and a 3 crustal thickness score; Dirichlet-Jackson gets a 4 for both topography and crustal thickness. A strong CTA clearly larger than TOPO-41 is centered to the west of the QCD. This may be an older, 533-km-wide basin located at 26.5°N, 171.5°W (CTA-26 in Table 2; white dashed circle in Fig. 3) on which TOPO-41 may be superimposed. The CTA has a summary score of 7, and the QCD has a summary score of 8; both are very good individual candidates for impact basins. See further examples of nearly coincident CTAs and QCDs in the discussion on overlapping basins below.

Another example is shown in Figure 4. Topographically derived diameters for Orientale and Mendel-Rydberg, 992 and 689 km, respectively, are larger than those given by Wilhelms (930 and 630 km, respectively). Humorum has a diameter of 867 km compared with 820 km from Wilhelms. In the upper center of the figure, there is the two-ring basin Grimaldi. Wilhelms gives the diameter as 430 km; based on topography, the inner ring at 304 km is more prominent than the outer ring at 420 km. These named basins also have prominent CTA signatures and high crustal thickness as well as topography expression scores, leading to high summary scores for Orientale (8), Mendel-Rydberg (9), Humorum (7), and Grimaldi (8). See Table 2 for details.

Just south of Grimaldi, there is an unnamed QCD of nearly the same size (TOPO-30) that is also a very strong feature in crustal thickness (right in Fig. 4). This 380 km candidate basin has topography and crustal thickness scores (see Table 2) of 4 and 5, for a summary score of 9, compared with Grimaldi itself, which has scores of 4 and 4, and a total of 8. TOPO-30 appears to be a very strong candidate for a basin not previously identified.

Overlapping the northern part of Humorum, there is a 451 km QCD (TOPO-35) that is actually more weakly expressed in the topography (score = 3) than in the crustal thickness (score = 4). Both the circular topography and crustal thickness structure of Humorum are disrupted in this area; if an impact basin, TOPO-35 is likely superimposed on Humorum.

This area contains three CTAs (19, 22, and 24) (white dashed circles in the figure) that are moderate candidates for impact basins. All three have summary scores of 4, but the two more northerly CTAs are derived solely from their crustal thickness signatures, having no topographic attributes in the ULCN2005 data. The candidate two-ring basin south of Orientale (TOPO-19) is less obvious in crustal thickness (score 2) but has some support in the topography (score 2).

Expression scores for topography and crustal thickness (and their sum) are used herein to make judgments about the likelihood that a given CTA or QCD is a previously unknown large impact basin. There appears to be a group of candidate impact basins that are revealed only through their crustal thickness signature (i.e., they have essentially no or very little expression in the available low-resolution ULCN2005 topography).

It is not possible, of course, to prove that the QCDs and CTAs not associated with named basins are indeed impact basins, even though they have signatures expected for and clearly seen associated with such (named) features. The approach taken here is to treat these as *candidate* impact basins, and to explore the implications of a potentially larger population of large impact basins if these candidates are in fact the result of large impacts.

RESULTS AND DISCUSSION

Expression Scores

Table 2 shows possible impact basins ≥300 km diameter derived from both the ULCN2005 topography (Archinal et al., 2006) and a lunar crustal thickness model (Wieczorick et al., 2006). There are 98 features that appear to be good candidates. Most of these (71) were identified topographically, including 33 named features and 38 additional QCDs not recognized by Wilhelms (1987) or by Spudis (1993). Twenty-seven additional features were identified in crustal thickness data. This is a conservative list, much smaller than the original 148 (92 QCDs and 56 CTAs) originally mapped (Frey, 2008c, 2009b), but even in this list, the expression scores vary greatly; some candidates have much stronger signatures than do others. Figure 5 shows expression score distributions. These distributions have the following characteristics:

Named Features

For most named features, both topographic and crustal thickness scores are generally high (mostly 3–5), and the number increases from 3 to 5. However, there are low scores among the named features. Several have low (<3) topographic scores, including Mutus-Vlacq (2), Lomonosov-Fleming (2), Sikorsky-Rittenhouse (2), Imbrium (2), and Balmer-Kaptyen (1). Four named features have a crustal thickness score of 1 (Lomonosov-Fleming, Planck, Poincare, and Lorentz). One (Aamundson-Ganswindt) has a score of 0, indicating essentially no crustal thickness signature, and one was assigned a score of −2 (Sikorsky-Rittenhouse) because the QCD actually had a circular *thick* area associated with it. Some low crustal thickness scores associated with strong topographic features are to be expected. There are also some strong crustal thickness features with relatively low topographic scores. However, low scores in both topography and crustal thickness (e.g., Lomonosov-Fleming, Sikorsky-Rittenhouse) suggest a candidate basin is a weak case. A combined summary score of 3 (Lomonosov-Fleming) and especially a summary score of <3 (Sikorsky-Rittenhouse) for a named basin either calls into question the original identification of such a feature, or indicates a structural or geophysical nature that is substantially different from most other basins.

Additional QCDs

These features show a more normal distribution for both the topographic and the crustal thickness scores. Though both cover the full range of 1–5, the vast majority are in the 2–4 range. There

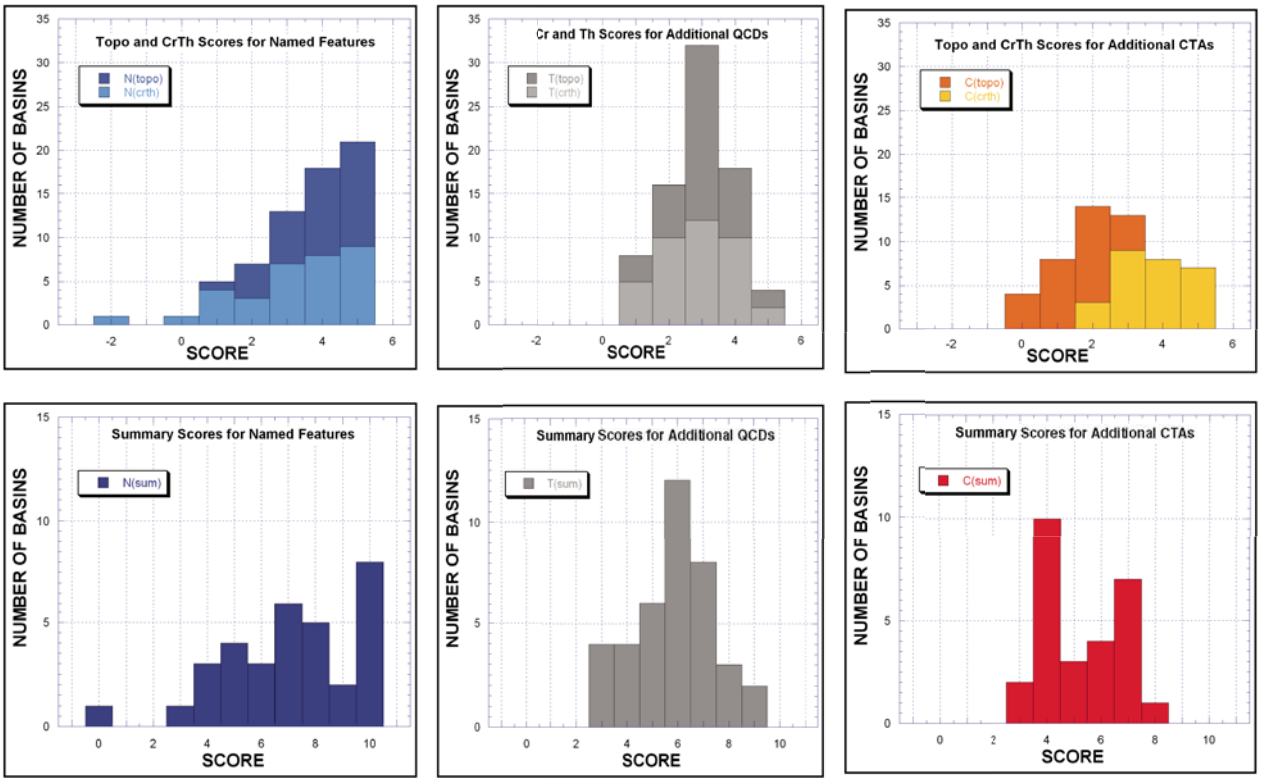

Figure 5. Expression scores for candidate basins in this study. Top row: Topography (darker color) and crustal thickness (lighter color) scores. Bottom row: Combined (summary) scores. Left panels: Named features. Middle panels: Additional quasi-circular depressions (QCDs). Right panels: Additional circular thin areas (CTAs). Note the difference in distribution for topography and crustal thickness scores for additional CTAs (upper-right panel) and corresponding bimodal summary scores (lower-right panel). There is a group of candidate basins with low topographic scores for which identification depends almost entirely on crustal thickness signatures. See text for discussion.

are three additional QCDs with a very low topographic score of 1 (TOPO-5, 26, and 38). These have crustal thickness scores of 3, 2, and 5, respectively (summary scores of 4, 3, and 6). CTA scores of 3 and 5 would be moderate and strong candidates on their own; the summary scores of 4 and 6 suggest these are plausible candidate impact basins. The one with a combined score of 3 (TOPO 26, topographic score 1, crustal thickness score 2) is considered a "possible basin" (see following). Five of the QCDs have crustal thickness scores of only 1 (TOPO-15, 21, 25, 27, and 34), and these have topographic scores of 3, 2, 2, 2, and 3 respectively, for summary scores of 4, 3, 3, 3, and 4. The 4's (TOPO-15 and 34) are probably good candidates; topographic scores of 3 would likely be retained even without any crustal thickness signature. The summary 3's (TOPO- 21, 25, 27) are considered "possible basins" in the following discussion.

Additional CTAs

The topography and crustal thickness distributions here are offset: The peak for the topographic scores lies at 1–2, but for the crustal thickness scores, the peak lies at 3–4. Of the 27 CTAs in the final list, only three have scores as low as 2 (CTA-8, 18, 19). These also have topographic scores of 2; all have summary scores of 4. The fact that these three were found in both data sets (topography and crustal thickness) suggests they may be real, though it is important to point out that the two data sets are not independent. The overall low topographic scores compared to the on-average higher crustal thickness scores suggest that the CTAs identified were done so on the strength of the gravity contribution to the crustal thickness signature (these candidates do not have much, if any, topographic expression). There is a group of objects with weak or very weak topographic expression for which their gravity signature identifies them as possible impact basins.

Overall Combined Scores

Figure 6 shows combined summary scores for all 98 candidate basins from Table 2. There appears to be a clear break between summary scores of 3 and 4. This is consistent with the previous descriptions for the named features, additional QCDs, and additional CTAs individually. The eight features with summary scores <4 are considered to be weak cases or "possible basins" compared with the much more likely basins, which have summary scores of 4 or greater. The eight possible basins include 4 QCDs (TOPO-21, 25, 26, and 27), 2 CTAs (CTA-4 and 23), and 2 named features (Lomonosov-Fleming

and Sikorsky-Rittenhouse). The named features are listed by Wilhelms as "probable" and "possible," respectively; both are included in Spudis' list of basins.

Global Distribution of Candidate Basins

Figure 7 shows the distribution of candidate basins listed in Table 2. Dashed circles show basins not identified by Wilhelms but revealed as QCDs in topography (black) or as CTAs from crustal thickness data (white). Thicker circles indicate higher confidence in identification (higher summary expression scores). Some named features (solid circles) have a dashed outer or inner ring where ULCN2005 topography suggests a ring even though that ring was not identified by Wilhelms. Humboldtianum is shown dashed because its topographically determined center and diameter are significantly different from that given by Wilhelms (compare Tables 1 and 2).

Candidate basin distribution is extensive but not uniform in either latitude or longitude. There is an apparent paucity of large lunar basins at the highest northern latitudes: In the North Pole region (>70°N), only a single CTA (no. 14) is shown, and this has a confidence summary score of only 4 based mostly on crustal thickness. No large QCDs were identified in the northern polar region, in contrast to the large number of both named and new QCDs in the south polar region inside South Pole–Aitken basin.

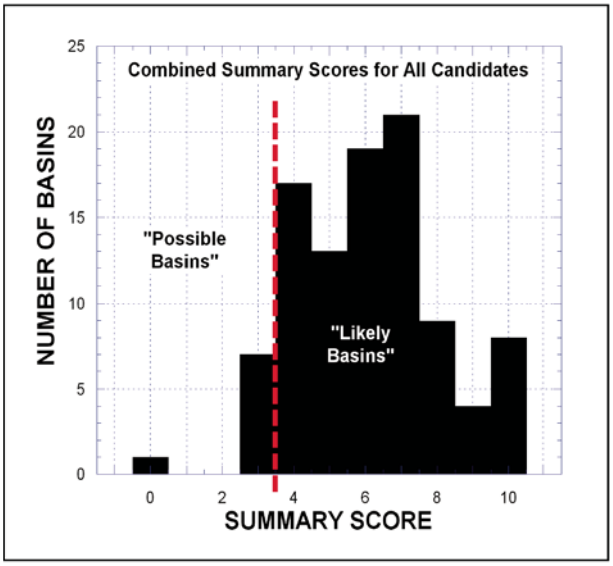

Figure 6. Distribution of combined summary (topography + crustal thickness) scores for all candidate basins (named features, additional quasi-circular depressions and additional circular thin areas). A clear break occurs at 3/4. Only eight candidates have scores less than 4. These are weak cases compared to the 90 other candidates and are called "possible" basins. Candidates with summary scores ≥4 are considered "likely" basins. "Possible basins" represent ~8% of the total; they are included in the analyses in this paper (including the cumulative frequency curves in Fig. 9) and are listed with the other 90 candidates in Table 2.

There appears to be a lower density of basins, especially very large basins, in the 120°W hemisphere than elsewhere, despite the abundance of non-mare crust. In terms of total number, there are more smaller basins (diameter <500 km) on the farside than the nearside, probably due to the presence of more recent large basins like Imbrium.

Figure 8 shows 98 candidate basins as black circles (solid—named features; dashed—additional QCDs or additional CTAs) compared with Wilhelms' full list (including those for which there is no basin-like topographic structure). In this figure, arranged like Figure 7, white basins are from Wilhelms' list.

Though having fewer overall basins than the other two longitudinal views, the 120°W hemisphere shows a significant number of new possible basins in this longitude range compared with those listed by Wilhelms. Nearly all of those listed by Wilhelms (or Spudis, 1993) in this longitude range have pronounced topographic structure and are included in Table 2.

In the 0°W hemisphere, the most notable differences are that examination of ULCN2005 topography and the Wieczorek et al. (2006) crustal thickness data revealed no evidence for the very large ("possible") Procellarum basin, and the ULCN2005 topography lacks a circular low associated with the ("probable") Tranquillitatis basin, as discussed already. Two other "possible" basins discussed by Wilhelms are shown by white circles with no corresponding black circles: the 500-km-wide Werner-Airy (24°S, 348°W) and the 570-km-wide Flamsteed-Billy (8°S, 45°W). We do find a smaller two-ring feature (TOPO-35) at 8°S, 38°W, with likely ring diameters of 313 and 451 km; if this is the named Flamsteed-Billy feature, the center (like that for Humboldtianum) is significantly offset, and the basin is significantly smaller than that suggested by Wilhelms.

The 240°W hemisphere may have the largest differences compared to basins listed by Wilhelms. Ring diameters for Smythii (2°S, 273°W) are slightly different: Wilhelms has two rings, 360 and 840 km (main ring). ULCN2005 data reveal two possible rings also, but the main basin ring diameter is assigned to the more prominent 502 km topographic ring and not the less pronounced 711 km ring. Differences for Humboldtianum are greater. Wilhelms lists two rings (275 and 600 km main ring) centered at 61°N, 276°W. ULCN2005 topography, which is very pronounced for this basin, indicates three possible rings (377, 560, and a 696 km main ring) centered at 58°N, 277°W. Also in this hemisphere, there is no evidence in the low-resolution ULCN2005 topography for the 580 km Marginis (20°N, 276°W), the 590 Al-Khwarizmi-King (1°N, 248°W), and the 700 km Tsiolkovsky-Stark (15°S, 232°W) basins, all listed as only "possible" by Wilhelms (see Table 1). More difficult to understand is the lack of circular topographic basin structure for two "distinct" Wilhelms basins, Keeler-Heaviside (10°S, 198°W, 780 km) and Australe (52°S, 266°W, 880 km).

In the North Pole view, there are a large number of new candidate basins, especially north of Imbrium (33°N, 17°W) and

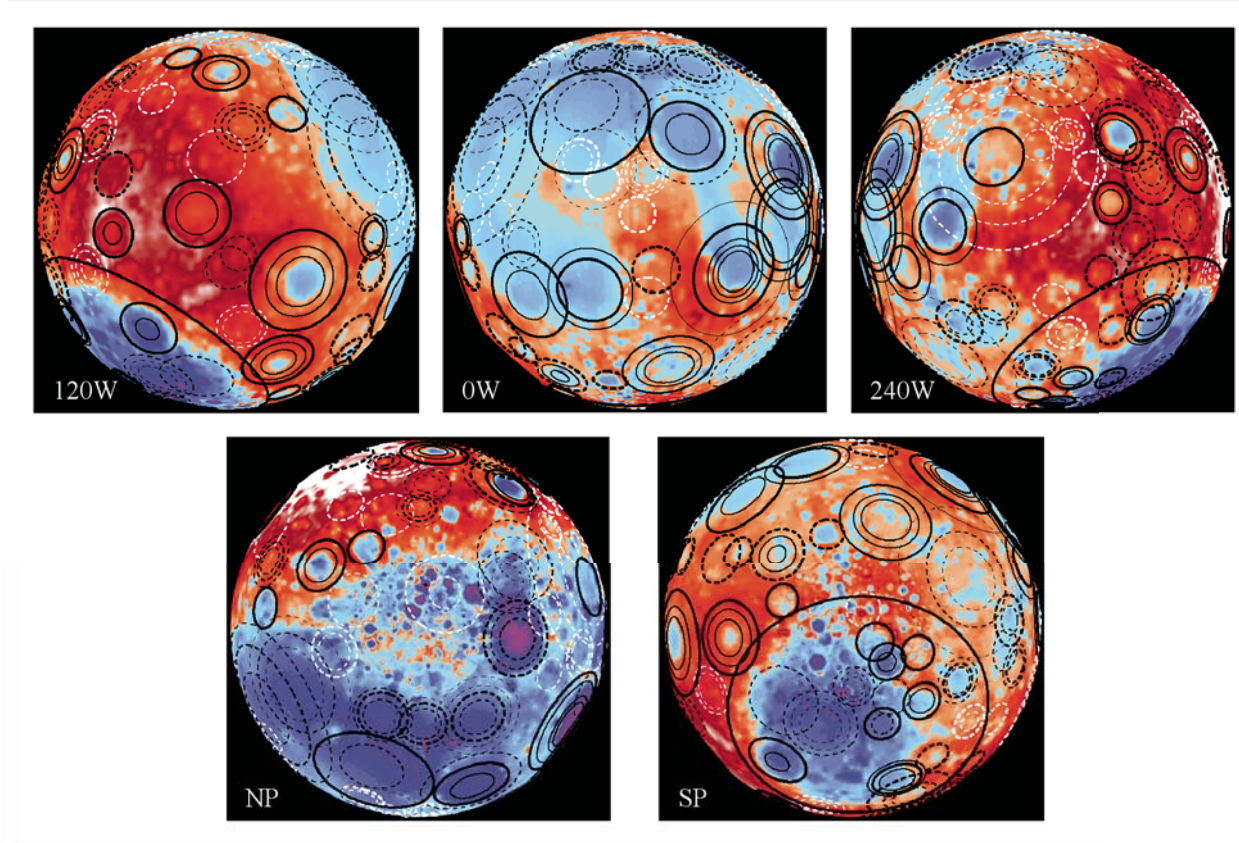

Figure 7. Distribution of large lunar basins derived from topography and crustal thickness data. Background is arbitrarily stretched ULCN2005 data (reds are high topography; blues are low topography). Solid black circles are named features (but using topographically derived basin centers and ring diameters). Dashed black circles are additional quasi-circular depressions derived from topography. White dashed circles are additional circular thin areas derived from the crustal thickness data. Note lack of many large basins in the north polar latitudes. See text for discussion. NP—North Pole; SP—South Pole.

Serenitatis (27°N, 341°W), and east of Humboldtianum (58°N, 277°W), that are not listed by Wilhelms. QCDs in these areas range from 400 and 500 km to over 800 km (inferred diameter), and the most northerly candidate basin and the only one lying above 70°N latitude (CTA-14), at 77°N, 217°W, has an estimated diameter of 744 km. The centers and rings for Imbrium and Serenitatis derived from topography are close to those given by Wilhelms, but there is also a suggestion of a possible outer ring for Serenitatis at 982 km.

In the South Pole region, there is no basin-like topography associated with the "possible" Grissom-White (44°S, 161°W, 600 km), the much smaller "possible" Pingre-Hausen (56°S, 82°W, 300 km), and the 880-km-wide "distinct" Australe (52°S, 266°W) basins. These features may exist, but they are not supported by the ULCN2005 topography. There are also significant differences for the Mutus-Vlacq feature. Wilhelms listed a single 690-km-diameter ring for this "probable" basin at 52°S, 339°W. Topography indicates instead a three-ring basin at 52°S, 342°W (possibly within the uncertainty of determination of a topographic center) with ring diameters 466, 615, and 864 (main ring). That is, this basin may be a substantially larger, possibly slightly offset, and multiring compared with that given by Wilhelms (compare Tables 1 and 2).

Cumulative Frequency Curves for Large Lunar Basins

Figure 9 (left) shows cumulative frequency curves (cumulative number >300 km diameter per million km^2) for the named features, additional QCDs, additional CTAs, and the combined total population of candidate basins given in Table 2. The combined population closely follows a –2 power-law curve (dashed line) over the diameter range ~900 km down to 300 km. At D >1000 km, the number of basins is small, so it is not surprising that these points fall off the –2 slope.

On the right side of Figure 9, cumulative frequency curves from the total inventory are compared to those from the lists of Wilhelms and Spudis. The Spudis' and Wilhelms' (total) curves differ mostly in diameter: Spudis tends to assign smaller diameters to the same feature, shifting his curve to the left. The Spudis' and Wilhelms' curves roughly follow a –2 power-law slope, but

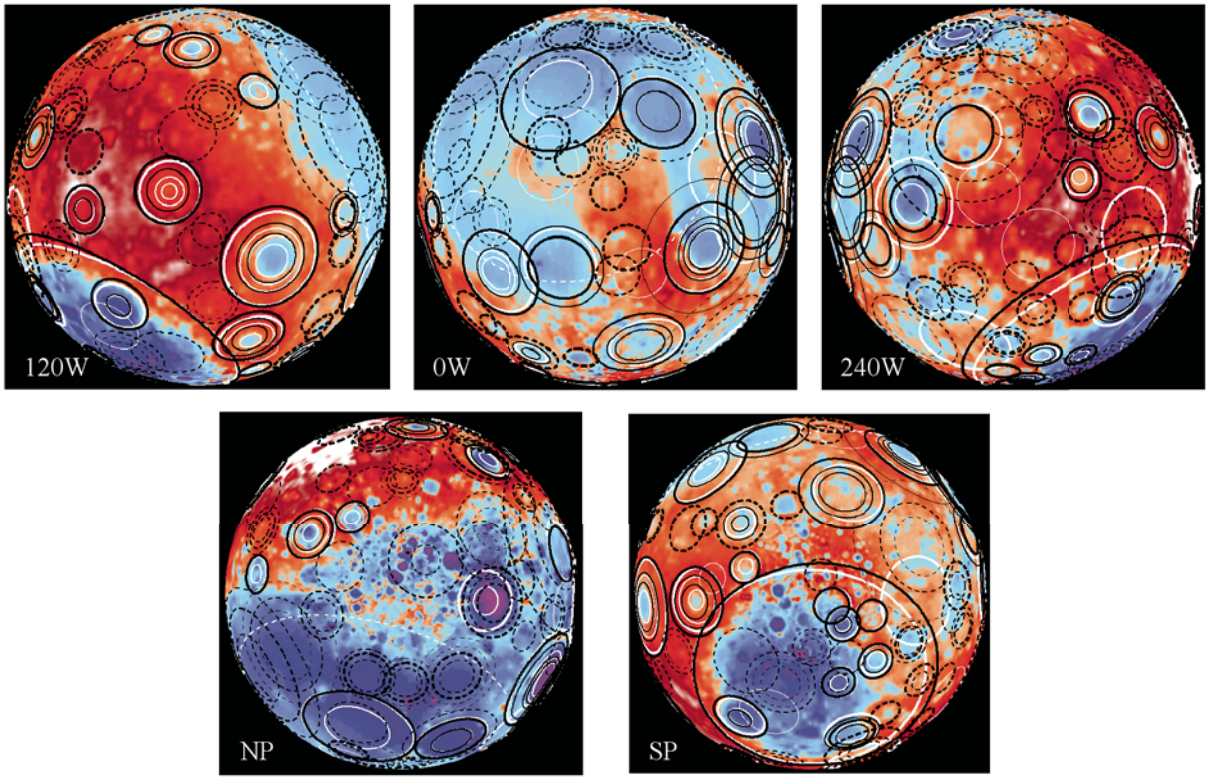

Figure 8. Basins derived from this study (black) compared with Wilhelms' (1987) list of basins (white), including basins listed by Wilhelms that have no obvious basin-like topography. Thicker lines show stronger candidates. Top row: Equatorial views at 120°W, 0°W, and 240°W. Bottom row: North Pole (NP) and South Pole (SP) views. Background is arbitrarily stretched ULCN2005 topography: high topography shown as reds; low topography shown as blues.

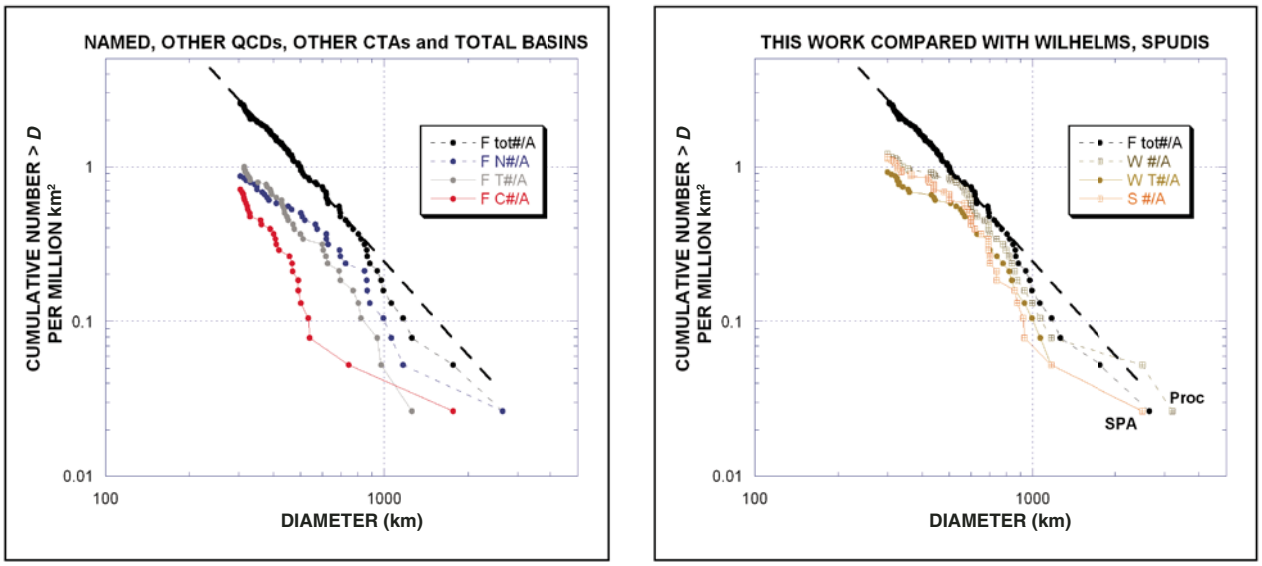

Figure 9. Cumulative frequency curves for candidate basins found in this study. Left: Named features (blue), additional quasi-circular depressions (QCDs; gray), and additional circular thin areas (CTAs; red) are combined into a total population (black). The total population of 98 basins ≥300 km diameter follows a −2 power law over the diameter range 300–900 km. Right: Total population from this work (black) compared with Wilhelms' total population (brown squares), Wilhelms' basins for which there is topographic basin structure (lighter brown circles), and Spudis' total population (orange squares). The $N(300)$ crater retention age from this work is 2.58 (basins ≥300 km diameter per million km^2), compared with 1.2 for the total populations given by Wilhelms and Spudis or 0.92 for the basins listed by Wilhelms that have basin-like topography. SPA—South Pole–Aitken; Proc—Procellarum.

only over the diameter range 500 to ~800 km. The curve for Wilhelms' basins with basin topography lies low because it has 25% fewer basins than his total curve. The Wilhelms' (total) and Spudis' curves fall off a –2 power law at D <500 km, suggesting significant observational loss among basins identified photogeologically. This may be due to unfavorable lighting conditions (lack of consistent low-angle lighting) in previously available imagery. Candidate basins mapped from the topography do not suffer this problem, so the population may be more complete down to the 300-km-diameter cutoff.

The largest basin found in this study is South Pole–Aitken. In agreement with Spudis (1993), there is no compelling evidence in the ULCN2005 topography for the giant "possible" Procellarum basin listed by Wilhelms (1987) as proposed by Whitaker (1981) and earlier by Cadogan (1974) as the Gargantuan Basin. Partial topographic structure on the western side of that proposed 3200-km-wide basin is likely associated with a number of smaller basins (see Fig. 7). There is also no compelling topographic or crustal thickness support for the large nearside megabasin proposed by Byrne (2008a, 2008b). This does not necessarily mean these two proposed basins do not exist. Lack of support for these giant features may be a shortcoming of the approach used here: It may be that such huge structures cannot be easily recognized when they are a large fraction of the hemisphere over which the stretched ULCN2005 or crustal thickness data are viewed. Higher-resolution data soon to be available may settle this issue.

Figure 10 shows histograms of basin diameters from Wilhelms (total list), Spudis, and the inventory in Table 2. This emphasizes the larger number of candidate basins in the 300–500-km-diameter range suggested here than were recognized by Wilhelms or Spudis. The distribution of basin diameters from this work more nearly matches the expectation that the number of impact basins should increase rapidly (exponentially) toward smaller diameters.

The large number of new candidate basins suggested here implies large-diameter impact cratering at the Moon was significantly greater than previously thought. For D ≥500 km, the older Wilhelms (total) and Spudis numbers are not that different from the inventory proposed here (~32 vs. 37 in Table 2). At 300 km, the difference is significant: at least a factor 2 (Wilhelms total list compared with this new inventory) and a factor 3 for features with basin topography (33 for Wilhelms vs. 98 in Table 2). The N(300) crater retention age (cumulative number ≥300 km per million km^2) from the proposed inventory is 2.58 compared with ~1.2 for Wilhelms (total) and Spudis (and 0.92 for Wilhelms' basins having basin-like topography). Implications for early cratering on the Moon (and Earth) are considered elsewhere; the implications of this possibly larger population of large basins for the stratigraphy of the Moon are discussed next.

STRATIGRAPHIC RELATIONS AND IMPLICATIONS

The implications of a possibly larger population of large basins for lunar stratigraphy are significant. Here, the spatial distribution of the candidate large basins is considered more closely, their overlapping and relative age relationships are discussed, and the extent to which the surface may have been significantly influenced by this population of large basins is shown.

Basin Size versus Location on the Moon

Figure 11 shows plots of basin diameter versus basin center locations (west longitude and latitude), with named features, additional QCDs, and additional CTAs indicated separately by color. The lunar farside is shown by the shaded region in the diameter versus center longitude plot on the left.

Somewhat greater numbers of large basins have their centers on the lunar farside (57% or 58%) than on the nearside (41% or 42%). There is no significant difference for basin center latitude: 50 basins have their centers in the northern hemisphere, and 48 are centered in the southern hemisphere. The larger total number of basins on the lunar farside is most likely due to the lack of recent very large impacts there; the relatively recent large

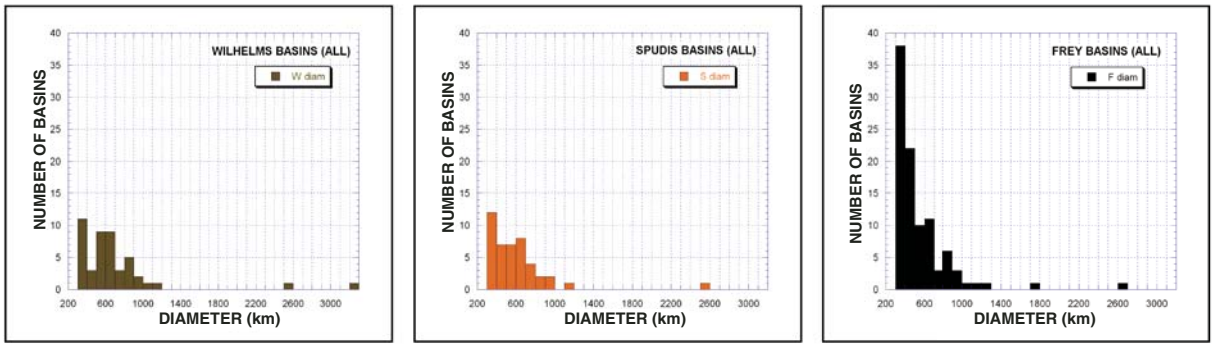

Figure 10. Histograms of basin diameters for Wilhelms' (1987) total inventory (left), Spudis' (1993) total inventory (middle), and the named, additional quasi-circular depressions, and additional circular thin areas listed in Table 2 (right). Bin size is 100 km.

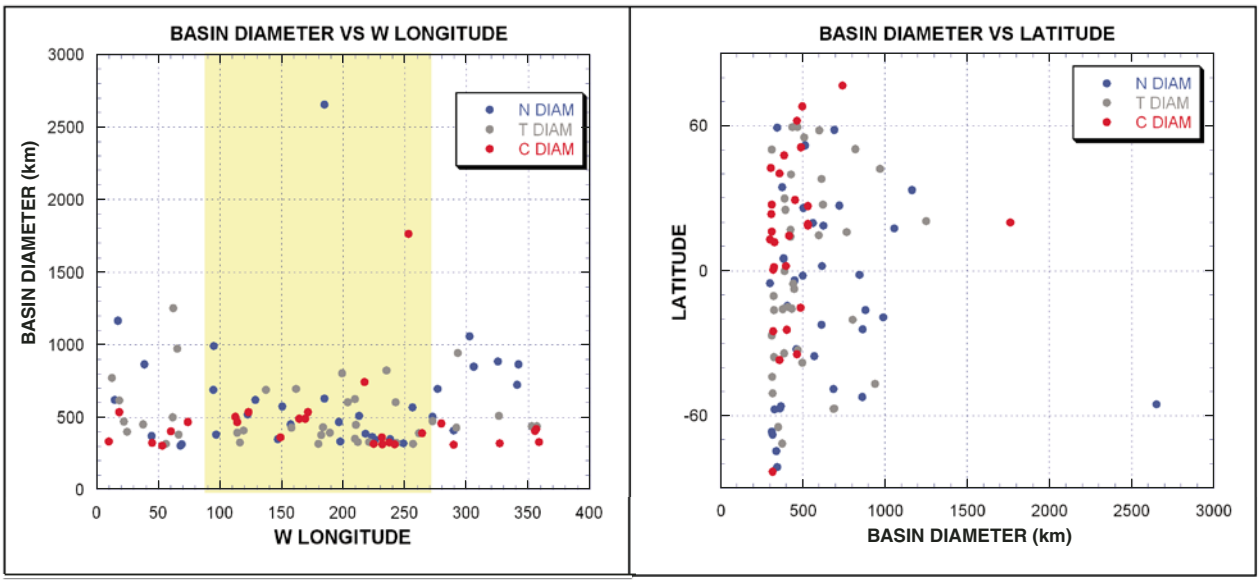

Figure 11. Basin diameter versus west longitude (left) and versus latitude (right) of the basin center. Named features are shown in blue, additional quasi-circular depressions are shown in gray, and additional circular thin areas are shown in red. In the longitude plot, the lunar farside is shown shaded. See text for discussion.

Imbrium impact has likely caused a depletion of smaller older basins on the nearside. Longitudinal distribution of basins by type is similar to that of the entire population: named features are 19 farside, 14 nearside; additional QCDs are 23 farside, 16 nearside; and additional CTAs are 15 farside, 11 nearside.

The two largest basins are centered on the farside (South Pole–Aitken and the 1800-km-wide candidate CTA-8; see following discussion); otherwise, the largest basins are concentrated on the nearside. For basins >800 km diameter, there are nine with centers on the nearside compared with only three on the farside. This likely contributes to the larger total number of basins, especially in the 300–500-km-diameter range, on the farside. For basins larger than 500 km, there are 15 on the nearside but 18 on the farside. Most of the basins larger than 500 km diameter are named features or additional QCDs. CTAs are concentrated in the 300–500-km-diameter range and, like named features and QCDs with the same diameters, are roughly evenly distributed in longitude.

Latitude distribution of centers of the largest basins is nearly uniform. For those >700 km, there are nine in the northern hemisphere and eight in the southern hemisphere. At D >500 km, there are more centered in the north (25) than in the south (15). At the highest southern latitudes (>60°S), there is a noticeable lack of basins larger than 400 km diameter; this is most likely due to the presence of South Pole–Aitken basin. In contrast, there are seven basins in the 300–400 km size range at high southern latitudes (mostly in South Pole–Aitken) compared to 0 in that size range at latitudes >60°N. As described before, there is a very obvious lack of large basins centered at the highest northern latitudes (see Fig. 7): In all sizes, they number only three at latitudes >60°N and only one at >70°N.

Overlapping Basins and Relative Ages

Relative ages for basins can be determined from superposition relations. Even in the case where the basin structure is based on topography and/or crustal thickness, it is often possible to determine where one basin has had its circular structure interrupted by another (likely superimposed) basin. An excellent example of how "disruption of structure" can be used to infer overlapping relations of large basins is shown in Figure 12.

Both topography and crustal thickness show the same overlap relationships in Figure 12: The high topography and thick crust of the South Pole–Aitken rim is broken by the large three-ring TOPO-18 basin, the circular but incomplete structure of which interrupts the South Pole–Aitken rim and likely is superimposed on it. TOPO-18 is likewise broken in its SE portion both by the multiring Ingenii basin (solid circles) and, on its western side, by the large crater (solid ring) Gargarin (265 km diameter). TOPO-18 is likely older than both of these more obvious, visible impact features (named features). Both of the named features are very clear in topography, as is the 233-km-wide Van de Graaff crater, which disrupts the topography of Ingenii on its eastern side, and therefore is younger than Ingenii. TOPO-18, Ingenii, and Van de Graaff are also well expressed in the crustal thickness data and show the same patterns of broken continuity described previously. Though not as clear, it is likely that Ingenii is also younger than the TOPO-13 basin to its western side at 36°S, 212°W, within which lies a 143-km-wide crater named Jules Verne. TOPO-13 and TOPO-18 both predate Ingenii, but from the topography and crustal thickness data set, it is not possible to determine which of the two is older since they do not quite overlap.

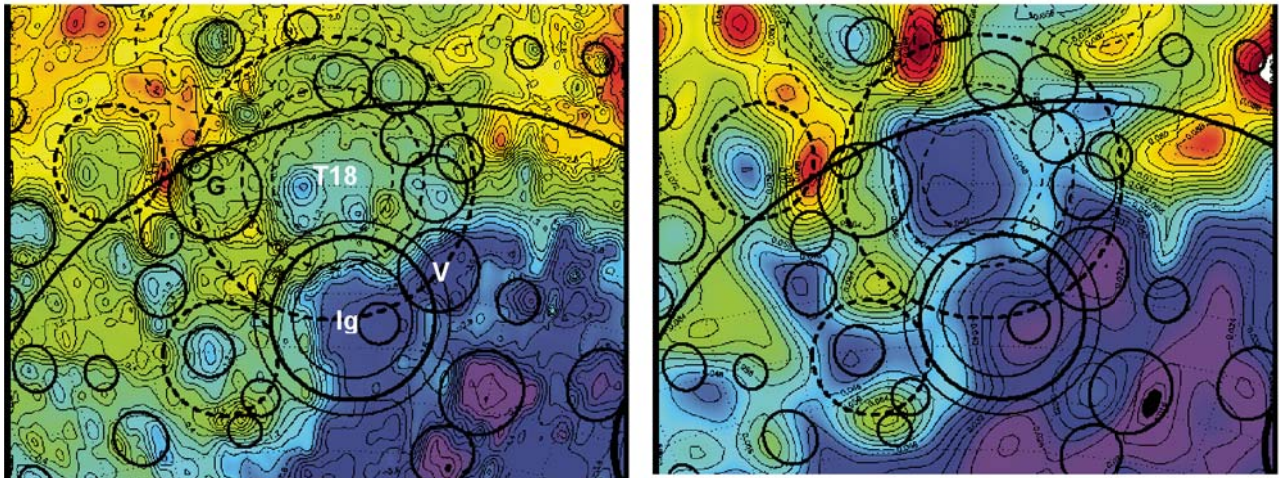

Figure 12. Overlapping basin relations show relative ages using stretched ULCN2005 topography (left) and crustal thickness data (right) for an area centered at 25°S, 200°W. Topography contour interval is 400 m; crustal thickness contour interval is 4 km. Solid circles are named craters and basins. The solid incomplete arc is an approximation of the South Pole–Aitken basin rim. The dashed three-ringed basin that disrupts this ring is the quasi-circular depression TOPO-18 (T18) in Table 2. The named three-ring basin Ingenii (Ig) likewise breaks the topographic and crustal thickness structure of TOPO-18. Note that Gargarin crater (G) on the western side of TOPO-18 also breaks the TOPO-18 topographic structure (but does not have an obvious crustal thickness signature). The Van de Graaff crater (V) disrupts the structure on the NE side of Ingenii. See text for discussion of relative age relationships based on "disruption of structure" superposition.

A second and far more complex set of overlapping relationships is shown in Figure 13, centered on 20°N, 198°W. This area includes three named features: the two-ringed Mendeleev (385 km diameter) and Moscoviense (507 km diameter) basins and the three-ring basin Freundlich-Sharonov (628 km diameter). These have very obvious topographic signatures and reasonably strong crustal thickness signatures, though the Mendeleev signature is not as strong as those for Moscoviense and Freundlich-Sharonov.

ULCN2005 topography reveals three strong candidate impact basins (from left to right TOPO-16, 17, and 41) and several weaker but still likely candidates (TOPO-20 near the top and TOPO-19 near the bottom). These also have compelling crustal thickness signatures. Another CTA (26) is identified on the far

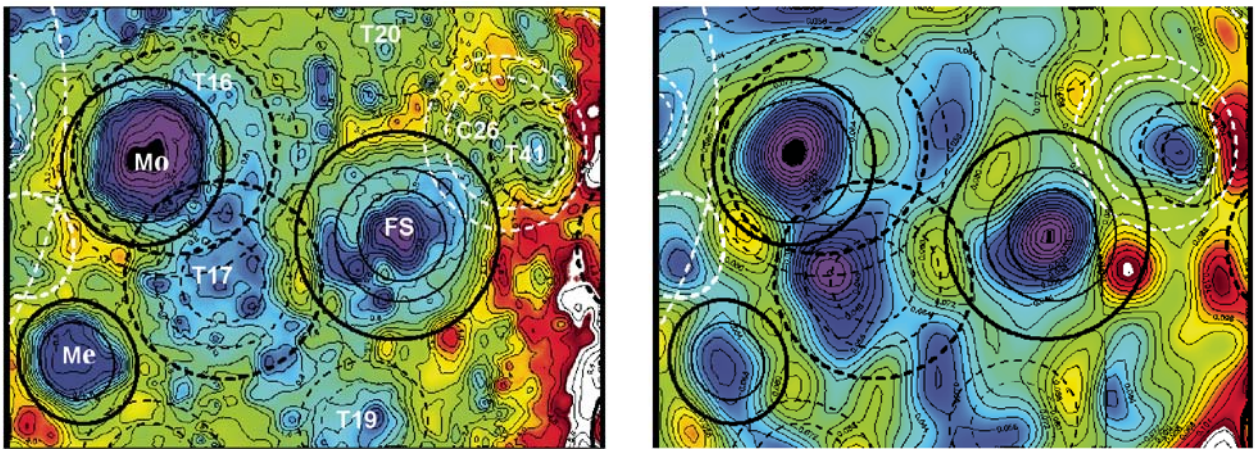

Figure 13. Stretched ULCN2005 topography and lunar crustal thickness for a region centered on 20°N, 198°W. Contour interval for the topography (left) is 400 m, and contour interval for the crustal thickness (right) is 4 km. The three named basins (solid circles) are (left to right) Mendeleev (Me), Moscoviense (Mo), and Freundlich-Sharonov (FS). Additional basins are revealed by both topography (black dashed circles T16, 17, 19, 20, 41 = TOPO 16, 17, 19, 20, and 41) and crustal thickness (white dashed circles, C26 = CTA 26). In most cases, the topographic basins have clear crustal thickness counterpart signatures. From the disruption of topographic or crustal thickness structure, it is possible to determine overlap relations and the relative sequence of basin formation. See text for details.

right (white dashed circles), on which TOPO-41 may be superimposed. There is weak topographic support for this CTA, which has a broad circular shape as outlined by the dashed rings; the more prominent portion of this signature corresponds with the topographic structure of TOPO-41. This is consistent with enhanced thinning due to the superposition of the smaller feature on the older and larger structure. The topography around Moscoviense suggests the presence of a possible larger and likely older feature (TOPO-16) on which the more obvious and younger basin may be superimposed. The older feature has its center somewhat eastward of Moscoviense, with a diameter of 626 km, compared with the 507-km-wide Moscoviense feature.

TOPO-16 topography slightly overlaps TOPO-17 on its NW side, so TOPO-17 is likely older than TOPO-16, and obviously older than Moscoviense, the circular topographic and crustal thickness structure of which is more intact and appears to overlap TOPO-17. On its eastern side, TOPO-17 appears overprinted by the more continuous structure of Freundlich-Sharonov, which therefore is likely younger than TOPO-17.

The relative age relations in this region appear to be fairly clear: Consistent with their stronger and more prominent topographic and crustal thickness signatures, Freundlich-Sharonov and Moscoviense are both younger than TOPO-17, Freundlich-Sharonov is younger than CTA-26, and TOPO-16 may lie stratigraphically between Moscoviense and TOPO-17.

Figure 14 shows the area centered on 20°N, 250°W, surrounded by prominent a number of multiringed named basins (Humboldtianum, Crisium, Smythii, Mendeleev, and Moscoviense).

The center of this area contains the named feature Lomonosov-Fleming. Wilhelms called this a "probable" basin; it is designated a "possible" basin in Table 2. Crustal thickness suggests a possible large CTA (8) centered at 20°N, 253°W, slightly offset from the center of Lomonosov-Fleming. Though the crustal thickness score is low (2), there is some support for this structure from topography (topographic score also 2), which suggests three possible rings with diameters 918, 1300, an 1764 km. If real, and if either the outer or the middle ring is taken as the diameter, CTA-8 is the second largest basin in this inventory (the next largest is TOPO-32 at 1253 km, followed by Imbrium at 1166 km). The poor expression of this basin may be due to ejecta from several surrounding younger and more prominent named multiringed basins.

It is likely that CTA-8, if real, is old. The named Smythii, Moscoviense, and Mendeleev basins are superimposed on its rim, and there several large QCDs (mostly on the northern side; note especially TOPO-11 = T11) and CTAs (in the interior) that appear superimposed on it (especially the large CTA-6 = C6 on the NW side). These include several features somewhat smaller than the 300-km-diameter cutoff (mostly 230–260 km diameter) that also may be impact basins, some of which correspond to named

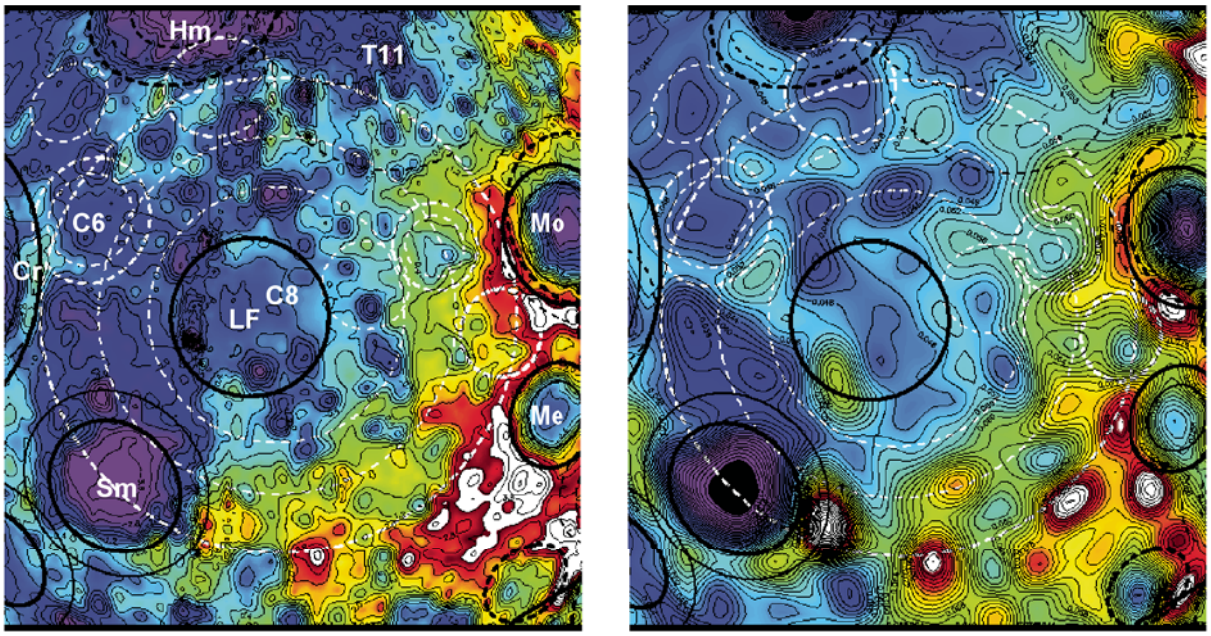

Figure 14. Stretched ULCN2005 and crustal thickness data centered on 20°N, 250°W. Topography contour interval is 400 m; crustal thickness contour interval is 2 km. Lomonosov-Fleming (LF; Wilhelms, 1987) is the single solid ring near the center. Smythii (Sm) is at lower left; Moscoviense (Mo) and Mendeleev (Me) are at far right. Crustal thickness suggests that a large basin (C8 = CTA-8) occupies this region (white dashed circles); topography provides some support. The basin is likely quite old, based on the number of superimposed basins revealed as circular thin areas (CTAs), both those >300 km diameter (dashed white circles) and a large number somewhat smaller than this (230–260 km diameter).

large craters. Smythii and Lomonosov-Fleming are pre-Nectarian basins, age groups 5 and 3, respectively (Stoffler et al., 2006); CTA-8 must be older, if these are in fact superimposed on it.

There is an alternative interpretation (S. Robinson, 2009, personal commun.). The large rings of CTA-8 might be outer rings of Lomonosov-Fleming, subdued by overprinting of ejecta from the named multiring basins surrounding it. If so, Lomonosov-Fleming would be much larger than previously thought, perhaps the second largest basin on the Moon. Offset of CTA-8 rings might be explained by a low-angle oblique impact.

Basin Formation Sequence and Stratigraphy

The relative sequence of basin-forming events can be determined using a combination of obvious superposition and the more subtle "disruption of structure" relationships, supported by crater counts. In this, it will be important to allow for craters buried by ejecta from the large basins (and, where possible, for mare infilling). Improved topography expected from modern spacecraft missions (e.g., *Kaguya*, LRO) should make it possible to determine accurate crater retention ages to smaller diameters and help establish the relative stratigraphy of these features. An example is shown in Figure 15.

From topography and crustal thickness, it is not possible to establish unambiguous overlap relations. The facts that Korolev was easily recognized in image data and TOPO-24 (Dirichlet-Jackson) was not suggests that Dirichlet-Jackson is likely older, perhaps buried by ejecta from Korolev (and maybe Freundlich-Sharonov to the west). Figure 15 shows a preliminary release of 1° gridded *Kaguya* data. Black dashed circles are QCDs >50 km diameter; these are much more numerous than named craters (white circles) on both basins. *N*(50) crater retention ages derived from counting all these likely craters are ~94 and ~119 (per million km^2) for Korolev and Dirichlet-Jackson, respectively. Dirichlet-Jackson is indeed older, as expected. It seems clear that improved topography should lead to more accurate total crater retention ages for large lunar basins, including those like Mendel-Rydberg and Dirichlet-Jackson, which appear to show through (at least topographically) ejecta of nearby large basins. Along with overlap relationships, it should be possible to determine the relative sequence of basin formation and establish the stratigraphic position of each of these basins with respect to Imbrium and Nectaris.

Possible Extent of Basin Formation Effects

It is interesting to consider that there may be parts of the Moon that might still have evidence for yet older basins not suggested by the current topography or crustal thickness information. That is, are there places where rocks predating the formation of these 98 candidate basins might still survive? This depends on the true extent of catastrophic effects away from large basins. Figure 16 shows some examples.

The total area of the 98 basins in Table 2 is ~30,715,000 km^2, ~81% of the lunar surface area. Given the considerable and obvious overlap of lunar basins, the actual area of the lunar surface occupied by these basins is significantly less, ~60% from Figure 16 (top row). Catastrophic effects of large impact basin formation likely extend well beyond the diameter of the basin. Figure 16 also shows masks of 1.5 and 2.0 times the diameter (*D*) of the basins. At 2*D*, essentially the entire lunar surface is covered; only one small patch of ~48,750 km^2 remains unaffected at ~24°N–34°N and 140°W–150°W. It might be interesting to consider this a potential location for crustal rocks predating most of lunar basin formation, and perhaps the source of the oldest material on the Moon.

A more interesting scenario is if the area severely affected by large impacts extends to only 1.5*D*. There might then be

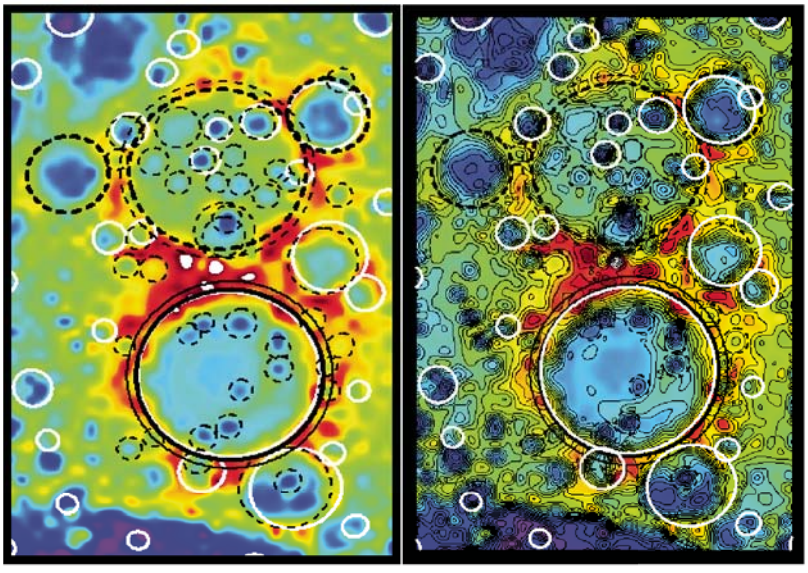

Figure 15. Stretched *Kaguya* 1° topography (left), with 500 m contours (right). Large solid and dashed circles are Korolev and Dirichlet-Jackson basins, respectively. Thinner solid and dashed circles indicate areas 10% larger than the basins. White circles are known impact craters from the "Principle Lunar Craters" database. Dashed circles represent quasi-circular depressions ≥50 km diameter (some of which are known craters).

several areas where prebasin crust might survive, or where yet (older) unrecognized basins may exist. On the nearside, there is an area of ~203,700 km^2 near Tranquillitatis, which is a mare region and may therefore not have much in the way of exposed prebasin rocks. This is also true for an additional smaller area in Oceanus Procellarum. On the lunar farside, there are a number of areas not masked by the 1.5*D* limits. The largest is ~456,300 km^2 between 5°N to 35°N and 125°W to 155°W. Another large area (~184,00 km^2) is at 40°N to 60°N, 145°W to 205°W. There is an even larger area (~342,750 km^2) north of Orientale stretching from 0°N to 25°N and 90°W to 115°W. The North Pole region has an unmasked region ~453,650 km^2 on the nearside at 70°N to 85°N and 82°W running through 0–305°W longitude. An area half as large (~234, 000 km^2) lies in the southern hemisphere at 40°S to 55°S and running from 0 to 40°W.

All together, these possibly "unaffected" areas outside the 1.5*D* limits total ~1,874,200 km^2. There may be a significant amount of surface area where future studies may find evidence for rocks that predate the formation of the 98 candidate lunar basins described here.

IMPLICATIONS

It is not possible to prove that the unnamed candidate basins identified in the topography and crustal thickness data are in fact large impact basins. The unnamed QCDs and CTAs do have topographic and crustal thickness signatures much like those of named basins, though sometimes more subdued as might be expected for buried basins. It is clear from named features that large basins can retain both a strong topographic and a crustal thickness signature over the history of the Moon. The approach taken here is to explore the possible consequences and implications of a significantly larger population of large impact basins, assuming the candidates listed in Table 2 are all in fact such basins.

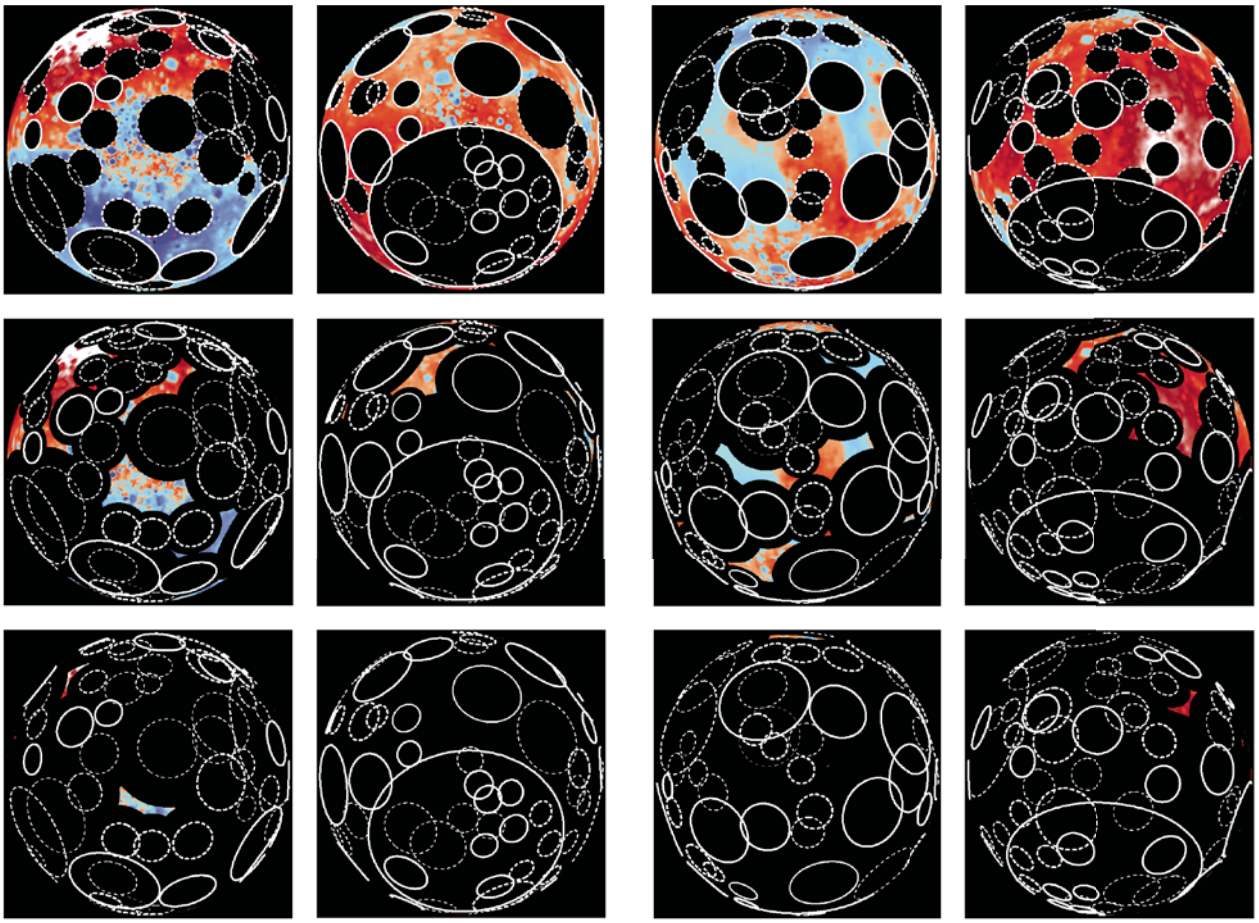

Figure 16. Areas significantly affected by large lunar basins, assuming effects extend as far as the basin diameter (top row), out to 1.5 times the basin diameter (middle row), and out to 2.0 times the basin diameter (bottom row). Hemispheres shown from left to right: North Pole, South Pole (both centered on 0°W), nearside (0°W), and farside (180°W) centered on the equator. The 98 candidate lunar basins total ~81% the lunar surface area, but overlap between basins substantially reduces the area actually occupied. If basin-forming impacts catastrophically affect an area out to 1.5 times the basin diameter or less, there may be parts of the Moon that preserve earlier rocks. See text for details.

How Complete Is the Current Search for Large Impact Basins?

The inventory of 98 candidate large impact basins provided here is conservative. Only the most viable candidates in this survey have been retained, and it is quite possible that some of those rejected may in fact turn out to be real when higher-quality topographic and higher resolution crustal thickness data are available. However, 98 is most likely a minimum estimate: If there is a substantial population of impact features that cannot be easily identified in image data and are revealed only in topographic or crustal thickness data, it becomes very unlikely that the true total population of all impacts that ever occurred on the Moon can ever be fully known. Even if the lunar surface were not completely saturated at these large diameters, obliterating and obscuring effects of later impacts could well hide earlier structures well enough that remote sensing will not find them (see Fig. 16).

Some candidate basins identified in the relatively low-resolution ULCN2005 topography and existing crustal thickness data may turn out to be bad. Better and higher-resolution data may show that some of the large features proposed here are actually clusters of smaller impact basins, or that what appeared to be a circular depression at low resolution is not really circular at all. However, better topography and higher-resolution gravity may also reveal more subtle features and add more candidates to the inventory. Data from *LRO* and *Kaguya* can test the reality of the basins proposed here and the suggestion that there is likely a large population of previously unrecognized large impact basins on the Moon.

It is reasonable to expect that there are craters at smaller diameters that will be found in higher-resolution topography that are not easily seen in current image data (for example, below impact basin ejecta blankets; see Fig. 16). It is not obvious that the roughly factor of 2 increase found here for large basins (and which is likely a minimum estimate) should apply at smaller diameters. Smaller craters are easier to "hide," and so the relative proportion of "hidden" smaller basins may in fact be even larger. There is also the issue of whether large-diameter basins and smaller craters are part of the same impacting population, and the actual size-frequency distribution of that population. It is possible that the large-diameter population is something special, perhaps unique, as could be the case if a Nice-type model of Late Heavy Bombardment (e.g., Gomes et al., 2005) were in fact true and responsible for the sometimes invoked "Terminal Lunar Cataclysm" (Tera et al., 1974; Ryder et al., 2000). ULCN2005 topography is not suitable to answer this question because it cannot reliably resolve QCDs much smaller than ~100 km, and often not always at this size. Higher-resolution, higher-quality data, which LOLA on *LRO* should produce, and which is in at least preliminary form available from *Kaguya*, will be needed to determine how large the population may be of previously unrecognized smaller lunar impact craters.

A more complete size-frequency distribution for lunar craters over a large diameter range is important for attempting to determine model absolute chronologies for all the bodies throughout the inner solar system. However, even the minimum twofold increase for just the large impact basins has important implications for lunar and inner solar system planetary history. Some of these are discussed next.

Implications for Lunar Stratigraphy and Early Lunar Evolution

Though reliable total population (both visible and not) crater retention ages are not yet available for all the new candidate basins, it seems clear that many are very old because many are overlain by large named basins which themselves are old and for which a stratigraphic age has been established (e.g., see Table 5.9 in the Stoffler et al. [2006] modification of Wilhelms [1987]). The very large CTA-8 shown in Figure 14, perhaps the second largest basin on the Moon, has the Nectarian age Moscoviense and Mendeleev basins, the pre-Nectarian Smythii (age group 5) and Lomonosov-Fleming (age group 3) basins superimposed on it. It is clearly pre-Nectarian and likely early pre-Nectarian. TOPO-17 in Figure 13 predates the named Freundlich-Sharonov basin that is pre-Nectarian (age group 8). The TOPO-18 candidate basin in Figure 12 is younger than South Pole–Aitken but older than the pre-Nectarian (age group 4) Ingenii basin. It is likely that the pre-Nectarian history of the Moon is far more complex than previously thought. Given the number of newly identified, likely very old candidate basins, it may be desirable to consider subdividing this earlier part of lunar history. This will, however, depend on developing an unambiguous and self-consistent stratigraphic sequence for the large basins, which in turn will depend on obtaining reliable crater retention ages based on more than just easily visible craters, to verify the observed overlap relationships and constrain the age of isolated basins.

Though nearly all the newly found basins are older than Imbrium, some may be younger than Nectaris. This means all of the pre-Imbrium history of the Moon is likely more complex than previously thought. For example, regolith development and mixing from large basins (e.g., Petro and Pieters, 2006, 2008) must now take into account that likely twice the number of basins (at least) may have contributed to those processes at almost every place on the lunar surface. From Figure 16 it is clear that most parts of the Moon likely suffered substantially from large basin formation and it may be that no part of the Moon entirely escaped being modified by impact basin ejecta.

Implications for Early Lunar and Inner Solar System Cratering

The early cratering for the Moon, at least for large objects, was likely higher by at least a factor 2 (and maybe more) than previously thought. This has important implications for the early bombardment history not only of the Moon and the Earth, but for calibrating the likely impact rate elsewhere in the inner solar system, especially if the increase in population extends to

smaller diameters. The list in Table 2 is conservative and almost certainly represents only a minimum number of impact basins ≥ 300 km diameter. For that reason, large diameter cratering and cratering rates on other planets inferred from it must also be considered a minimum. Even with improved counts based on better topographic and crustal thickness data (see below) extended to smaller diameters, the derived populations and inferred cratering rates should always be considered a minimum estimate.

The inventory presented here has 6 basins equal to or larger than 1000 km in diameter. On Mars there is evidence for ~30 > 1000 km diameter (Frey, 2009a). The 30 Mars basins do not include the recently re-proposed Borealis Basin (Andrews-Hanna et al., 2008), which is in a separate class in terms of its diameter and which most likely pre-dates all the other basins on Mars (Frey, 2010). Model absolute ages for more than two dozen of the large Mars basins are narrowly confined in time (Frey, 2008d, 2009a) and may be consistent with a Nice-type Late Heavy Bombardment (Gomes et al., 2005). It is important to determine whether or not the larger population of large lunar basins is also narrowly confined in time, and what is the relationship between these basins and the inferred oldest basin on the Moon, South Pole–Aitken. The Borealis Basin on Mars also bears on the question whether or not impact basins larger (and older) than South Pole–Aitken ever formed on the Moon. This includes the proposed Procellarum (Cadogan, 1974; Whitaker, 1981; Wilhelms, 1987) and Near Side Megabasin (Byrne, 2008a, 2008b).

At the very least it should be assumed that current estimates of the effects of the Late Heavy Bombardment on the early Earth derived from lunar crater counts underestimate the true effects, especially those due to large objects. This inventory includes two new basins larger than Imbrium, a number of basins ≥ 500 km diameter close to what Wilhelms (1987) suggested, but a substantial increase in the total number ≥ 300 km in diameter. It is possible, perhaps likely (given that smaller craters are easier to hide), that the difference between visible craters and all craters increases toward smaller diameters; if so, the number of craters 50–100 km in diameter may be much larger than previously thought. Abramov and Mojzsis (2009) showed that the sterilization effects of smaller impacts may be just as important as those of the largest impacts, but may be concentrated more in the upper habitable portions of the crust. A more complete inventory of craters to diameters smaller than 300 km is important for assessing the likely effects of the Late Heavy Bombardment on the habitability of the early Earth, and will provide a useful comparison for their impact model using the inferred fossil main asteroid belt size-frequency distribution.

Future Prospects

The approach adopted here will obviously benefit from improved lunar topography and crustal thickness data which should soon become available. It can equally well be applied to Mercury when MESSENGER provides high quality global digital elevation data from the Mercury Laser Altimeter. New, previously unknown (because they were not previously imaged) large impact basins have been discovered on Mercury with the on-board imaging system (Watters et al., 2009); it seems safe to predict that additional basins that are not obvious in image data will be revealed by altimetry as QCDs, as is the case with the Moon and Mars. Determining the population of such hidden basins will be important for assessing possible variation in large diameter impact bombardment across the inner solar system, and may help constrain scenarios such as the Nice Model (Gomes et al., 2005).

Searching for CTAs in other crustal thickness models would provide an additional test of the robustness of the candidate basins proposed here based on the Wieczorek et al. (2006) model. Hikida and Wieczorek (2007) employed a spatial domain approach that takes better advantage of the full resolution of nearside gravity data; this might reveal more subtle and perhaps smaller CTAs than those found here using the earlier model. Better crustal thickness models will also soon be available using new higher resolution topography and gravity data.

The distribution of large basins should be compared with crustal terrain units (e.g., Jolliff et al., 2000) and with the new global mineralogical data becoming available from the current armada of lunar spacecraft. It would be interesting to see, for example, if any of the "surviving" areas (those maybe not so much affected by large diameter impact) in Figure 16 have unique spectroscopic signatures compared with areas more likely severely affected by the overlapping effects of large impacts.

High priority must be given to establishing the relative sequence and crater retention ages of the candidate basins in Table 2. Overlap and "disruption of structure" relations provide insight into relative ages but they must really be verified by crater counts. Even more important, crater counts are needed to determine the relative age of isolated basins for which overlap relations are not available or where such relationships are ambiguous. Image data alone will likely not reveal all the impact craters at the smaller diameters needed for statistically meaningful counts; it will be important to use improved higher resolution topographic data to count QCDs superimposed on the basins. In the example of Figure 15 preliminary *Kaguya* data were used to derive an N(50) crater retention age for Korolev and its northern twin Dirichlet-Jackson. With final *Kaguya* data it should be possible to produce N(50) crater retention ages for basins ≥ 300 km diameter. When LRO/LOLA data becomes available it should be possible to push these CRAs down to the 20 km diameter range often used in counts of visible craters.

A more complete inventory of impact craters to smaller diameters will also be important for possibly improving not only the lunar cratering rate (Stoffler et al., 2006) but also the current model chronologies for the inner solar system (e.g., Hartmann and Neukum, 2001). If there is a large population of previously unknown lunar impact craters at diameters much smaller than basin size, then such chronologies, which are based on lunar cratering, may need revision.

CONCLUSIONS

Current lunar topography and crustal thickness provide evidence in the form of Quasi-Circular Depressions and Circular Thin Areas that suggest there may exist on the Moon a large number of previously unrecognized large impact basins. The minimum number of candidate basins ≥ 300 km diameter is 98, more than twice the number proposed earlier by Wilhelms (1987) or Spudis (1993) based on compilations from photogeologic and other imaging studies. The new candidate impact features include two larger than Imbrium but the approach used here does not provide any support for either the Procellarum basin (Whitaker, 1981) or the Near Side Megabasin (Byrne, 2008a). Ten of the basins listed by Wilhelms, including some designated as "distinct" or "probable," have no obvious basin structure in the current relatively low-resolution topography. Although reliable crater retention ages for all the basins do not yet exist, overlap relationships suggest that many are pre-Nectarian in age, and nearly all are pre-Imbrium in age. It may be desirable to subdivide the pre-Nectarian history of the Moon, if a reliable and self-consistent stratigraphy of the large basins can be developed from overlap relations supported by crater counts. Those counts should be done using QCDs derived from topography and not just visible craters from image data.

Known large (named) impact basins have clearly retained strong topographic and crustal thickness signatures that have persisted over the history of the Moon. Thus the use of these kinds of data to search for basins not easily visible on image data (e.g., basins partially covered by ejecta from nearby basins) is a viable approach to finding previously unknown large impact basins. Future higher resolution, higher quality versions of these kinds of data will be able to test the viability of the additional new candidate basins presented here, and may provide evidence for new more subtle candidates.

The surface evolution of the Moon was likely more complex than previously thought, and lunar stratigraphy may be more complicated than currently appreciated. A larger number of large basins would certainly contribute to more enhanced regolith development and greater mixing than were previously considered. The early history of the Moon was likely far more violent than previously believed; early cratering and the Late Heavy Bombardment, at least for large objects, were certainly more intense than previously estimated. This has important implications for the bombardment history and habitability of the early Earth, the possibility of a Nice-like Terminal Lunar (and Planetary) Cataclysm, and the cratering chronologies for other planets. If a similar large population of not-yet recognized smaller diameter impact craters also exists on the Moon, model chronologies for the planets of the inner solar system will need revision.

REFERENCES CITED

Abramov, O., and Mojzsis, S.J., 2009, Microbial habitability of the Hadean Earth during the Late Heavy Bombardment: Nature, v. 459, p. 419–422, doi:10.1038/nature08015.

Andrews-Hanna, J., Zuber, M.T., and Banerdt, W.B., 2008, The Borealis basin and the origin of the Martian crustal dichotomy: Nature, v. 453, p. 1212–1215, doi:10.1038/nature07011.

Archinal, B.A., Rosiek, M.R., Kirk, R.L., and Redding, B.L., The Unified Lunar Control Network 2005, 2006, U.S. Geological Survey Open-File Report 2006-1367, version 1.0, 21 p.

Byrne, C.J., 2008a, A large basin on the near side of the Moon: Earth, Moon, and Planets, v. 101, p. 153–188, doi:10.1007/s11038-007-9225-8.

Byrne, C.J., 2008b, The near side megabasin: Topography and crustal thickness: Houston, Texas, Lunar and Planetary Institute, Lunar and Planetary Science Conference XXXIX, CD-ROM, abstract 1302.

Cadogan, P.H., 1974, Oldest and largest lunar basin?: Nature, v. 250, p. 315–316, doi:10.1038/250315a0.

Cook, A.C., Robinson, M.S., and Watters, T.R., 2000, Planet-wide lunar digital elevation model: Houston, Texas, Lunar and Planetary Institute, Lunar and Planetary Science Conference XXXI, CD-ROM, abstract 1078.

Edgar, L.A., and Frey, H.V., 2008, Buried impact distribution on Mars: Contributions from crustal thickness data: Geophysical Research Letters, v. 35, p. L02201, doi:10.1029/2007GL031466.

Frey, H.V., 2006a, Impact constraints on, and a chronology for, major events in early Mars history: Journal of Geophysical Research–Planets, v. 111, p. E08S91, doi:10.1029/2005JE002449.

Frey, H.V., 2006b, Impact constraints on the age and origin of the lowlands of Mars: Journal of Geophysical Research, v. 33, p. L08S02, doi:10.1029/2005GL024484.

Frey, H.V., 2008a, Previously unrecognized large lunar impact basins revealed by topographic data: Houston, Texas, Lunar and Planetary Institute, Lunar and Planetary Science Conference XXXIX, CD-ROM, abstract 1344.

Frey, H.V., 2008b, Previously unknown large impact basins on the Moon revealed by lunar topographic data, 2008: Geological Society of America Abstracts with Programs, v. 40, no. 6, p. 519.

Frey, H.V., 2008c, Previously unrecognized large impact basins on Mars and the Moon: Implications for the Late Heavy Bombardment in the inner solar system, *in* Workshop on Early Solar System Impact Bombardment: Houston, Texas, abstract 3008.

Frey, H.V., 2008d, Ages of very large impact basins on Mars: Implications for the Late Heavy Bombardment in the inner solar system: Geophysical Research Letters, v. 35, p. L13203, doi:10.1029/2008GL033515.

Frey, H.V., 2009a, New large Late Heavy Bombardment impact basins on Mars revealed in crustal thickness data: Crater retention ages and implications: Houston, Texas, Lunar and Planetary Institute, Lunar and Planetary Science Conference XL, CD-ROM, abstract 1123.

Frey, H.V., 2009b, Crustal thickness evidence for more previously unrecognized large lunar basins: Houston, Texas, Lunar and Planetary Institute, Lunar and Planetary Science Conference XL, CD-ROM, abstract 1687.

Frey, H.V., 2010, A minimum crater retention age for the proposed "Borealis Basin" on Mars: Houston, Texas, Lunar and Planetary Institute, Lunar and Planetary Science Conference XLI, CD-ROM, abstract 1136.

Frey, H.V., Sakimoto, S.E.H., and Roark, J.H., 1999, Discovery of a 450 km diameter, multi-ring basin on Mars through analysis of MOLA data: Geophysical Research Letters, v. 26, p. 1657–1660, doi:10.1029/1999GL900357.

Frey, H.V., Roark, R.J., Schockey, K.M., Frey, E.L., and Sakimoto, S.E.H., 2002, Ancient lowlands on Mars: Geophysical Research Letters, v. 29, p. 1384, doi:10.1029/2001GL013832.

Gomes, R., Levison, H.F., Tsiganis, K., and Morbidelli, A., 2005, Origin of the cataclysmic Late Heavy Bombardment period of the terrestrial planets: Nature, v. 435, p. 466–469, doi:10.1038/nature03676.

Hartmann, W.K., and Neukum, G., 2001, Cratering chronology and the evolution of Mars: Space Science Reviews, v. 96, p. 165–194, doi:10.1023/A:1011945222010.

Hikida, H., and Wieczorek, M.A., 2007, Crustal thickness of the Moon: New constraints from gravity inversions using polyhedral shape models: Icarus, v. 192, p. 150–166, doi:10.1016/j.icarus.2007.06.015.

Jolliff, B.L., Gillis, J.J., Haskin, L.A., Korotev, R.L., and Wieczorek, M.A., 2000, Major lunar crustal terrains: Surface expressions and crust-mantle origins: Journal of Geophysical Research, v. 105, p. 4197–4216, doi:10.1029/1999JE001103.

Morrison, S.J., and Frey, H.V., 2007, Crater densities in Noachis Terra: Evidence for overlapping ejecta from Argyre and Hellas: Houston, Texas, Lunar and Planetary Institute, Lunar and Planetary Science Conference XXXVIII, CD-ROM, abstract 1355.

Neumann, G.A., Zuber, M.T., Smith, D.E., and Lemoine, F.G., 1996, The lunar crust: Global structure and signature of major basins: Journal of Geophysical Research, v. 101, p. 16,841–16,843, doi:10.1029/96JE01246.

Neumann, G.A., Lemoine, F.G., Smith, D.E., and Zuber, M.T., 1998, Lunar basins: New evidence from gravity for impact-formed mascons, *in* Jolliff, B., and Ryder, G., eds., Workshop on New Views of the Moon: Integrated Remotely Sensed, Geophysical, and Sample Datasets: Houston, Texas, Lunar and Planetary Institute, p. 59–60.

Neumann, G.A., Zuber, M.T., Wieczorek, M.A., McGovern, P.J., Lemoine, F.G., and Smith, D.E., 2004, Crustal structure of Mars from gravity and topography: Journal of Geophysical Research–Planets, v. 109, p. E08002, doi:10.1029/2004JE002262.

Neumann, G.A., Lemoine, F.G., Smith, D.E., and Zuber, M.T., 2008, MarsCrust3—A crustal thickness inversion from recent MRO gravity solutions, Houston, Texas, Lunar and Planetary Institute, Lunar and Planetary Science Conference XXXIX, CD-ROM, abstract 2167. Model data provided by author.

Petro, N.E., and Pieters, C.M., 2006, Modeling the provenance of the *Apollo 16* Regolith: Journal of Geophysical Research, v. 111, p. E09005, doi:10.1029/2005JE002559.

Petro, N.E., and Pieters, C.M., 2008, The lunar-wide effects of basin formation on the lunar crust: Meteoritics & Planetary Science, v. 43, no. 9, p. 1517–1529.

Roark, J.H., Frey, H.V., and Sakimoto, S.E.H., 2000, Interactive graphics tools for analysis of MOLA and other data: Houston, Texas, Lunar and Planetary Institute, Lunar and Planetary Science Conference XXXI, CD-ROM, abstract 2026.

Ryder, G., Koeberl, C., and Mojzsis, S.J., 2000, Heavy bombardment on the Earth at ~3.85 Ga: The search for petrographic and geochemical evidence, *in* Canup, R.N., and Righter, K., eds., Origin of the Earth and Moon: Tucson, University of Arizona Press, p. 475–492.

Spudis, P.D., 1993, The Geology of Multi-Ring Basins: Cambridge, UK, Cambridge University Press, 263 p.

Spudis, P.D., Reisse, R.A., and Gillis, J.J., 1994, Ancient multi-ring basins on the Moon revealed by *Clementine* laser altimetry: Science, v. 266, p. 1848–1851, doi:10.1126/science.266.5192.1848.

Stoffler, D., Ryder, G., Ivanov, B.A., Artemieva, N.A., Cintala, M.J., and Grieve, R.A.F., 2006, Cratering history and lunar chronology, *in* Jolliff, B.L., Wieczorek, M.A., Shearer, C.K., and Neal, C.R., eds., New Views of the Moon: Reviews in Mineralogy & Geochemistry, v. 60, p. 519–596.

Tera, F., Papanastassiou, D.A., and Wasserburg, G.J., 1974, Isotopic evidence for a terminal lunar cataclysm: Earth and Planetary Science Letters, v. 22, p. 1–21, doi:10.1016/0012-821X(74)90059-4.

Watters, T.R., Murchie, S.L., Robinson, M.S., Head, J.W., Chapman, C.R., Solomon, S.C., Denevi, B.W., Andre, S.L., Fassett, C.I., and the MESSENGER Team, 2009, A newly discovered impact basin on Mercury revealed by MESSENGER: Houston, Texas, Lunar and Planetary Institute, Lunar and Planetary Science Conference XL, CD-ROM, abstract 1817.

Whitaker, E.A., 1981, The lunar Procellarum basin, *in* Schultz, P.H., and Merrill, R.B., eds., Multi-Ring Basins: Houston, Texas, Lunar and Planetary Institute, Lunar and Planetary Science Conference XIIA, CD-ROM, abstract 105-11.

Wieczorek, M.A., Jolliff, B.A., Khan, A., Pritchard, M.E., Weiss, B.P., Williams, J.G., Hood, L.L., Righter, K., Neal, C.R., Shearer, C.K., McCallum, L.S., Tompkins, S., Hawke, B.R., Peterson, C., Gillis, J.J., and Bussey, B., 2006, The constitution and structure of the lunar interior, *in* Jolliff, B.L., Wieczorek, M.A., Shearer, C.K., and Neal, C.R., eds., New Views of the Moon: Reviews in Mineralogy & Geochemistry, v. 60, p. 221–364 (downloaded from http://www.ipgp.fr/~wiecz0r/CrustalThicknessArchive/CrustalThickness.html; accessed July 2009).

Wilhelms, D.E., 1987, The Geologic History of the Moon: U.S. Geological Survey Professional Paper 1348, 302 p.

Wood, C.A., 2004, Lunar Basin Database, originally compiled August 2004: http://www.lpod.org/cwm/DataStuff/Lunar%20Basins.htm (accessed July 2009).

Zuber, M.T., Smith, D.E., Lemoine, F.G., and Neumann, G.A., 1994, The shape and internal structure of the Moon from the *Clementine* mission: Science, v. 266, p. 1839–1843, doi:10.1126/science.266.5192.1839.

Manuscript Accepted by the Society 26 August 2010

Printed in the USA

The Geological Society of America
Special Paper 477
2011

Emplacement scenarios for Vallis Schröteri, Aristarchus Plateau, the Moon

W. Brent Garry
Center for Earth and Planetary Studies, Smithsonian Institution, National Air and Space Museum MRC 315, P.O. Box 37012, Washington, DC 20013-7012, USA

Jacob E. Bleacher
Planetary Geodynamics Laboratory, Code 698, National Aeronautics and Space Administration Goddard Space Flight Center, Greenbelt, Maryland 20771, USA

ABSTRACT

The volcanic processes that formed Vallis Schröteri are not well understood. Vallis Schröteri, located on the Aristarchus Plateau, is the largest rille on the Moon, and it displays three key morphologic components: the Cobra Head, the 155-km-long primary rille, and the 240-km-long inner rille. Observations of terrestrial eruptions are applied here to help explain the morphologic relationships observed for Vallis Schröteri. The Cobra Head, a 10-km-wide source vent surrounded by a 35-km-diameter and 900-m-high low shield, might have been constructed from flows, spatter, and pyroclastic deposits erupted during lava fountain events, similar to the early stages of the vent at Pu‘u ‘Ō‘ō in Hawaii and the final morphology of Bandera crater, a cinder cone in New Mexico. The vent fed an initial sheet flow controlled by pre-eruption topography. A channel formed within this sheet flow was the foundation for the primary rille, which deepened through construction and thermomechanical erosion by lava. The inner rille is confined to the flat floor of the primary rille and is characterized by tight gooseneck meanders. This rille crosscuts the distal scarp of the primary rille and extends toward Oceanus Procellarum. This enigmatic relationship can be explained through backup, overflow, and diversion of the lava into a new rille that eroded into the margin of the primary rille. Similar backup, overflow, and redirection of the lava flow were observed during the 1984 Mauna Loa eruption in Hawaii. Analysis of the final morphology of lunar rilles provides key information about lunar volcanic processes and insight into the local stratigraphy.

Garry, W.B., and Bleacher, J.E., 2011, Emplacement scenarios for Vallis Schröteri, Aristarchus Plateau, the Moon, *in* Ambrose, W.A., and Williams, D.A., eds., Recent Advances and Current Research Issues in Lunar Stratigraphy: Geological Society of America Special Paper 477, p. 77–93, doi:10.1130/2011.2477(03).

INTRODUCTION

Vallis Schröteri, the largest lunar rille (Wilhelms, 1987), originates on a topographic rise, the Aristarchus Plateau, which is one of the most diverse geologic locations on the Moon (Zisk et al., 1977; Lucey et al., 1986; McEwen et al., 1994; Le Mouélic et al., 2000; Chevrel et al., 2009) (Fig. 1). The formation of Vallis Schröteri remains enigmatic because the complex morphology and superposition relationships displayed by the rille cannot be explained by a single emplacement process (Fig. 2A). To understand this rille's formation, we need to consider the volcanic processes involved during the eruption(s) and the influence of local pre-eruption stratigraphy and structure on the final flow morphology. There is the possibility for both thermal and mechanical erosion processes to be influenced, in part, by the physical properties of the substrate (Hulme, 1982; Williams et al., 1998, 1999), and flow direction can be structurally controlled (Gornitz, 1973). Therefore, the final rille morphology can reveal information about the stratigraphy, structure, and volcanic evolution of the Aristarchus Plateau. The rille is divided into three distinct morphologic features: the Cobra Head, the primary rille, and the inner rille (Fig. 2A). Here, we take a qualitative look at the relationship of these features and compare them with observations and morphologies of terrestrial volcanic analogs to provide insight into eruption conditions and events that resulted in their formation. In this paper, we: (1) review the stratigraphy of the Aristarchus Plateau, (2) review lunar rille formation, (3) present emplacement scenarios for Vallis Schröteri based on terrestrial volcanic analogs, and (4) discuss future exploration opportunities with new and upcoming missions that might better constrain quantitative models of Vallis Schröteri's formation. Using data from past missions to the Moon, including *Lunar Orbiter* (LO), *Apollo*, and *Clementine*, combined with field observations of terrestrial volcanoes and lava flows, we present emplacement scenarios to account for the morphologic relationships observed among the Cobra Head, the primary rille, the inner rille, and the surrounding terrain.

BACKGROUND AND PREVIOUS WORK

Geologic Setting

Vallis Schröteri originates near the craters Aristarchus and Herodotus and trends through the central part of the Aristarchus Plateau (Fig. 1). The Aristarchus Plateau is an exotic topographic high on the nearside of the Moon, centered at 26°N and 51°W,

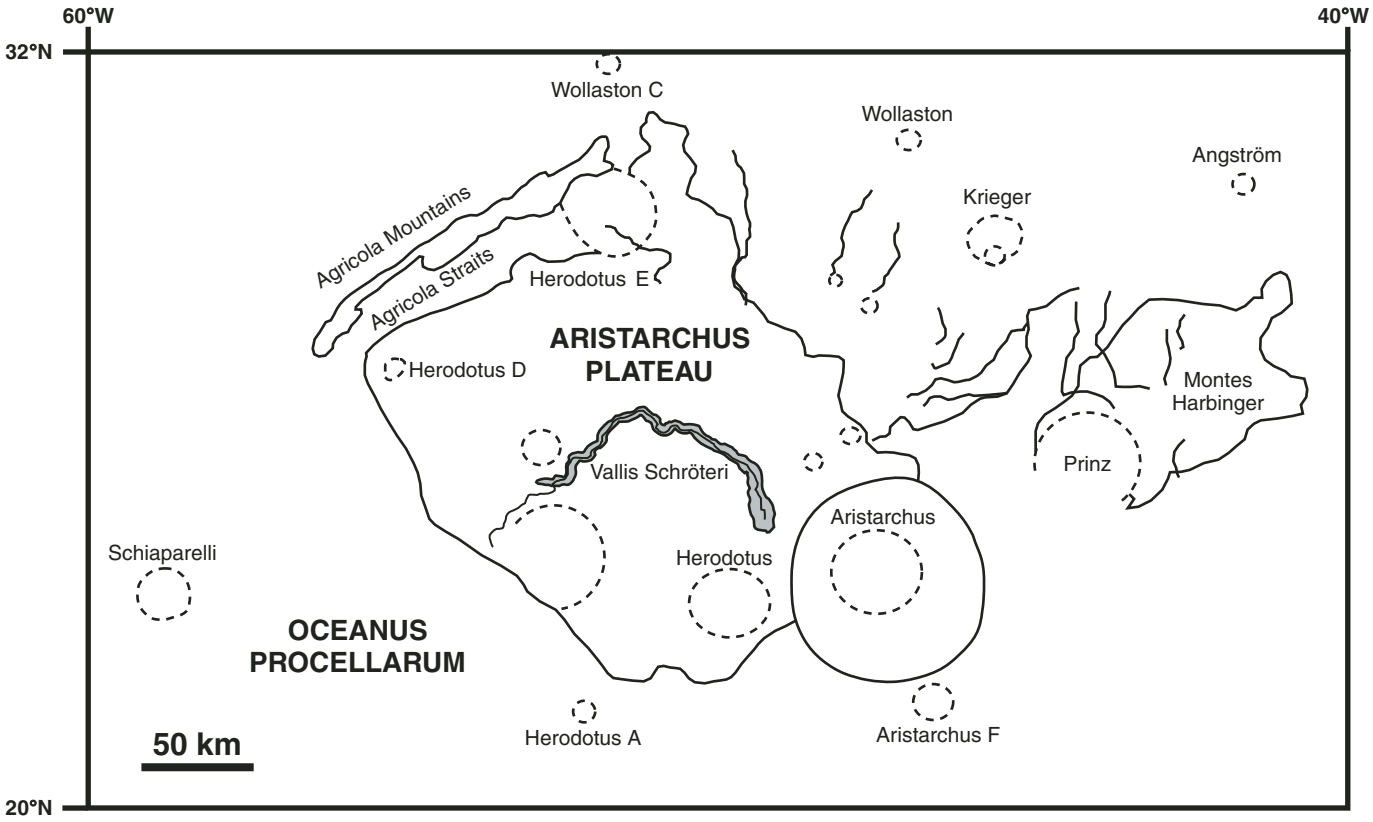

Figure 1. Map of the Aristarchus Plateau region. Vallis Schröteri is located at the center of the Aristarchus Plateau and originates near craters Herodotus and Aristarchus. The primary rille is shown in gray, and the inner rille is marked by a black line. Dashed lines mark the exposed rims of craters and partially buried craters. Figure was traced from the *Lunar Orbiter* mosaic in simple cylindrical projection.

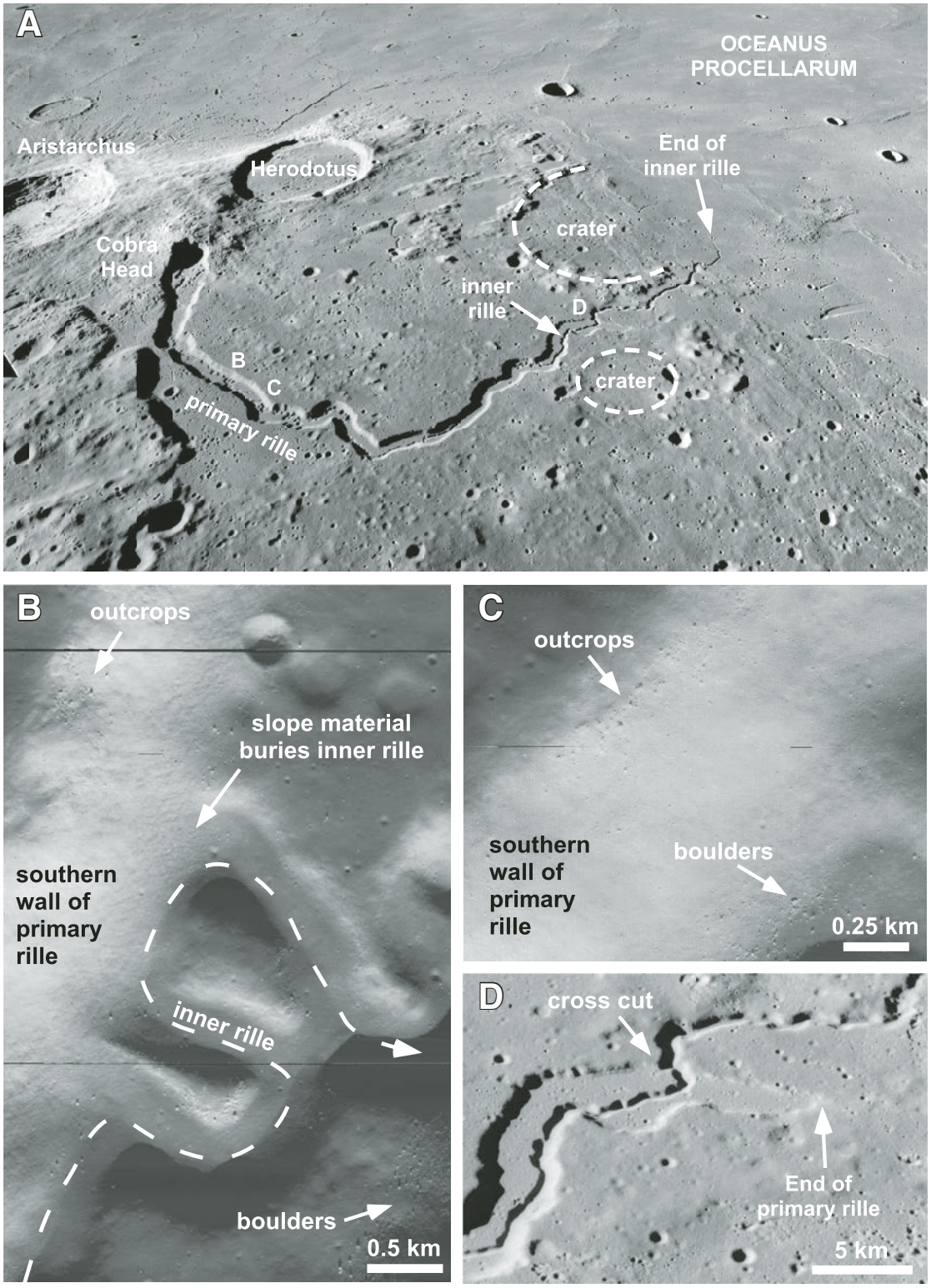

Figure 2. Geologic features of the Aristarchus Plateau and Vallis Schröteri. (A) Full view of Vallis Schröteri showing the Cobra Head, primary rille, and inner rille. Oblique view is toward the southeast. *Apollo 15* image AS15-M-2612 (National Aeronautics and Space Administration [NASA]/Johnson Space Center [JSC]/Arizona State University). Crater Herodotus is 35 km in diameter. (B) Dashed white line traces the gooseneck meanders of the inner rille, which are partially buried by slope material from the wall of the primary rille. Portion of *Lunar Orbiter* V LOV-5204 h3 (NASA). (C) Outcrops are exposed near the rim, and boulders are visible on the floor of the primary rille. Portion of *Lunar Orbiter* V LOV-5204 h3 (NASA). (D) The inner rille cuts the distal wall of the primary rille. Portion of *Apollo 15* image AS15-M-2612 (NASA/JSC/Arizona State University).

west of Mare Imbrium and north of the Marius Hills. The plateau, composed primarily of crustal material mantled by volcanic flows and pyroclastic deposits, rises ~2 km above the surrounding maria and slopes to the west (Zisk et al., 1977; Chevrel et al., 2009). The margins of the plateau are embayed by lavas from Oceanus Procellarum, including some of the youngest lava flows on the lunar surface dated at 1.2 Ga through crater size frequency distribution methods (Hiesinger et al., 2003). Two large impact craters dominate the plateau's southeastern margin. Crater Herodotus (35 km diameter) is a mare-filled Imbrian-aged impact crater (Moore, 1965), and crater Aristarchus (40 km diameter) formed from an impact along the eastern margin that exposed the cross-sectional stratigraphy of the plateau and surrounding lunar maria (e.g., Chevrel et al., 2009). Ejecta from crater Aristarchus blankets part of the Cobra Head (e.g., Guest, 1973; Guest and Spudis, 1985; Weitz et al., 1998; Campbell et al., 2008). Parallel to the northwest margin of the plateau, the Agricola Mountains are a 150-km-long, narrow, mountain range separated from the Aristarchus Plateau by the mare-filled Agricola Straits. Several rilles originate from or in the vicinity of the plateau. The Rimae Aristarchus, a series of rilles along the northern margin of the plateau, are up to ~120 km long, over a kilometer wide, and up to 100 m deep (Chen et al., 2008). To the northeast of the plateau, there lie the Montes Harbinger and crater Prinz (46 km diameter), which is partially buried by mare lava flows. The rilles near Montes Harbinger range in length from 12 to 79 km, have widths from 0.8 to 4.8 km, and have depths from 100 to 300 m (Strain and El-Baz, 1977). The other rilles in the Aristarchus region do not display significant topographic shields near their source areas as observed at Vallis Schröteri. However, these other rille source regions might have had different eruption parameters (McGetchin and Head, 1973) or have been significantly buried by younger lava flows, pyroclastic deposits, and/or impact ejecta (Zisk et al., 1977). The high concentration of rilles in this area indicates that a significant amount of volcanic activity was involved in the development of the Aristarchus region (Zisk et al., 1977).

Stratigraphy of the Aristarchus Plateau

The Aristarchus Plateau displays a complex stratigraphy composed of volcanic and impact-related deposits that have been detailed in several studies (Zisk et al., 1977; Whitford-Stark and Head, 1977; Lucey et al., 1986; McEwen et al., 1994; Hawke et al., 1995; Weitz et al., 1998; Le Mouélic et al., 2000; Campbell et al., 2008; Chevrel et al., 2009), and a new U.S. Geological Survey (USGS) mapping project, taking advantage of recent data sets, is currently under way (Yingst and Gregg, 2009). Four distinct geologic units are present on the plateau, including: (1) crustal-anorthositic material, (2) lava flows (basaltic unit), (3) pyroclastic materials, and (4) impact ejecta. Overall, the crustal-anorthositic material, exposed within crater Aristarchus and in a discrete section at the head of Vallis Schröteri (Lucey et al., 1986; McEwen et al., 1994; Chevrel et al., 2009), is overlain by basaltic material cropping out in the upper walls of the craters and rilles on the plateau (Zisk et al., 1977). Both units are mantled by an iron-rich pyroclastic glass (McEwen et al., 1994; Weitz et al., 1998; Campbell et al., 2008). The presence of mare-filled craters indicates that impact ejecta was present on the pre-eruption surface, and ejecta from fresh craters is also currently intermixed with the pyroclastic units at the surface (Lucey et al., 1986; McEwen et al., 1994; Chevrel et al., 2009). The geologic diversity and potential resources of this region make the Aristarchus Plateau a viable future landing site for both robotic and human missions (e.g., Coombs et al., 1989; Zhang and Jolliff, 2008). Here, we provide an overview of the characteristics of each unit from previous studies.

Unit 1: Crustal-Anorthositic Materials

The lowest stratigraphic unit of the Aristarchus Plateau is crustal-anorthositic material (Zisk et al., 1977; Lucey et al., 1986; McEwen et al., 1994; Chevrel et al., 2009). It is typically exposed in impact crater walls and ejecta blankets, namely of crater Aristarchus, as well as crater Herodotus, crater Raman (also known as Herodotus D, 10 km diameter), and a number of other impact craters >2 km diameter along the northwest side of the plateau. This unit is also observed on the slopes of hummocky mounds on the plateau, for example, Mons Herodotus (Herodotus c) (Moore, 1967; McEwen et al., 1994). Inside the vent area of Vallis Schröteri and along the walls of the primary rille, there are spots of an anomalous spectral signature that are consistent with anorthositic material, and that contrast with the exposure of basalt in the rille walls as seen in the *Clementine* data (750 nm and color ratio) (McEwen et al., 1994).

A variety of crustal-anorthositic materials are exposed in the walls and central peak of crater Aristarchus. The central peak of the crater is interpreted as a feldspar-rich (anorthositic) unit with an assemblage of clinopyroxene and olivine (unit 2C—Lucey et al., 1986; unit AP—Chevrel et al., 2009). Chevrel et al. (2009) interpreted the bulk of the substratum of the Aristarchus Plateau to be composed of this unit. Spectral characteristics of the northeast rim of crater Aristarchus suggest an anorthositic composition of clinopyroxene and orthopyroxene, while the southeastern outer rim displays olivine-rich materials (Lucey et al., 1986; McEwen et al., 1994; Chevrel et al., 2009). The rock type classifications associated with this unit are anorthosite, gabbroic rocks, troctolites, and dunites (Hawke et al., 1995).

Unit 2: Lava Flows

Mare-like lava flows cover and likely comprise a significant portion of the plateau, though their areal extent and thickness are still not well constrained due to burial by pyroclastic material and minimal cross-sectional exposures. This unit is most prominent along walls of rilles and craters and is present in impact ejecta (McEwen et al., 1994). Rock exposures in the upper walls of Vallis Schröteri are interpreted to be in situ layers of mare lava flows (Zisk et al., 1977) (Figs. 2B and 2C). The lower portions of the rille walls are buried by talus and debris that cover any additional

exposures of lava flows or bedrock. If the entire rille wall is assumed to be composed entirely of basalt, then, at a minimum, this unit is a 200–600-m-thick series of lava flows that accumulated over time and that overlie the crustal-anorthositic material (McEwen et al., 1994; Chevrel et al., 2009). Lava-flow emplacement began to resurface the plateau during the Imbrian period, possibly around 3.7 Ga (Zisk et al., 1977). The Aristarchus Plateau lava flows are of interest because they formed along a broad topographic rise opposed to impact basin–filling mare flows. As such, they possibly represent volcanic history that is unique from the majority of lunar basaltic magma production and lava-flow emplacement events.

Unit 3: Pyroclastic Materials

A low-albedo unit is inferred to mantle a majority of the plateau. This unit is interpreted to be ~90% pyroclastic material, predominantly glassy spheroids similar to *Apollo 17* orange and black glass samples (Zisk et al., 1977; Lucey et al., 1986; McEwen et al., 1994; Gaddis et al., 2003; Campbell et al., 2008; Chevrel et al., 2009; Hagerty et al., 2009). Zisk et al. (1977) interpreted the unit to be 50–100 m thick, but more recent studies of small impact craters and Earth-based radar data suggest that the pyroclastic deposits are ≤20 m thick across the plateau (McEwen et al., 1994; Campbell et al., 2008). The pyroclastic units were emplaced beginning in the Imbrian period, 3.7–3.6 Ga (Zisk et al., 1977; Chevrel et al., 2009), possibly by large lava fountain events at a few localized sources around the plateau associated with events that formed the sinuous rilles (Whitford-Stark and Head, 1977). *Lunar Prospector* data show that there are pyroclastic deposits on the plateau that have not been contaminated by thorium-rich ejecta from Aristarchus crater, as have most other units, and represent the incorporation of potassium (K), Rare Earth Elements (REE), and phosphorus (P) (KREEP) material into the parent magma sources (Hagerty et al., 2009).

Unit 4: Impact Ejecta

Mare-filled craters, including Herodotus and two unnamed craters (diameters: ~21 and ~45 km) (Fig. 2A), indicate that major impacts had occurred on the plateau prior to or contemporaneous with eruption of the plateau lava flows. Therefore, ejecta from at least these large craters mantled portions of the crustal-anorthositic unit and/or earliest basaltic units. The present surface displays abundant small craters and secondary craters, the result of which is a well-mixed regolith of mare and pyroclastic units. Ejecta derived from highland and mare units from the Copernican-aged crater Aristarchus is asymmetrically distributed across the plateau, with the continuous ejecta blanket extending ~48–50 km from the rim and discontinuous deposits appearing up to 240–300 km from the crater rim (Zisk et al., 1977; McEwen et al., 1994). Based on 70 cm Earth-based radar data, Campbell et al. (2008) suggested that deposition of fine-grained, rock-poor, ejecta from crater Aristarchus near and possibly on the Cobra Head of Vallis Schröteri is at the scale of several meters thick, covering and/or mixing with any pyroclastic materials.

Lunar Sinuous Rilles

Some researchers originally thought lunar sinuous rilles were formed as a result of flowing water (Urey, 1967; Peale et al., 1968), while others favored a volcanic origin (e.g., Oberbeck et al., 1969; Greeley, 1971a). The volcanic origin was proven based on results from the *Apollo* missions (e.g., Vaniman et al., 1991). The investigation of Hadley Rille by *Apollo 15* revealed layers of basalt exposed in the wall of the rille, indicating a lava-flow origin (Swann et al., 1972). Theories for the volcanic formation of lunar rilles involve erosion by ash flow (Cameron, 1964), fluidization of gas along fractures (McCall, 1970), lava tubes where the roof has collapsed, exposing the inside of the tube (Oberbeck et al., 1969; Greeley, 1971a; Gornitz, 1973), and erosion of the underlying bedrock by turbulent lava flow (Hulme, 1973; Carr, 1974; Hulme and Fielder, 1977; Hulme, 1982; Williams et al., 2000).

Lunar rilles are typically distributed around the margins of mare-filled impact basins and have a variety of well-developed meander patterns (Schubert et al., 1970; Oberbeck et al., 1972; Gornitz, 1973; Hulme, 1982) where the head is typically marked by a source depression that is generally interpreted to represent a volcanic vent (Head and Wilson, 1980). The floors of rilles are V-shaped, U-shaped, or flat and sometimes contain inner rilles (Gornitz, 1973). The observed V-shape is primarily interpreted as a result of debris covering the sides from mass wasting events, thereby suggesting a more vertical face for the rille walls during formation (e.g., Swann et al., 1972; Gornitz, 1973). Models have shown that lunar volcanic eruptions might have involved high effusion rates, lava fountain events, and turbulent flows (e.g., Hulme, 1982), possibly capable of mechanically or thermally eroding older units. However, a study of Hadley Rille shows that it coincides with the crest of a local ridge and also displays distributary channels from the main rille (Greeley, 1971a). These observations are not consistent with an origin related solely to erosion and suggest that the ridge and channel also formed through construction by overflow of lava along certain sections of the rille (Greeley, 1971a). Thus, an origin for lunar rilles that involves volcanic erosion, construction, or a combination of these processes needs to be considered. Identification of morphologic and topographic aspects of these two styles of rille formation would provide unique insight into lunar mare eruption and emplacement conditions, as well as for magma production and ascent models for the Moon. Observations from current and future lunar missions could provide new thoughts on the formation and development of lunar rilles.

MORPHOLOGY OF VALLIS SCHRÖTERI

Cobra Head

A low shield surrounds the 10-km-wide topographic depression that was the source vent of the Vallis Schröteri flow or flows, and it is informally referred to as the Cobra Head (Moore, 1965; Zisk et al., 1977) (Figs. 3A and 3B). The Cobra Head shield is a

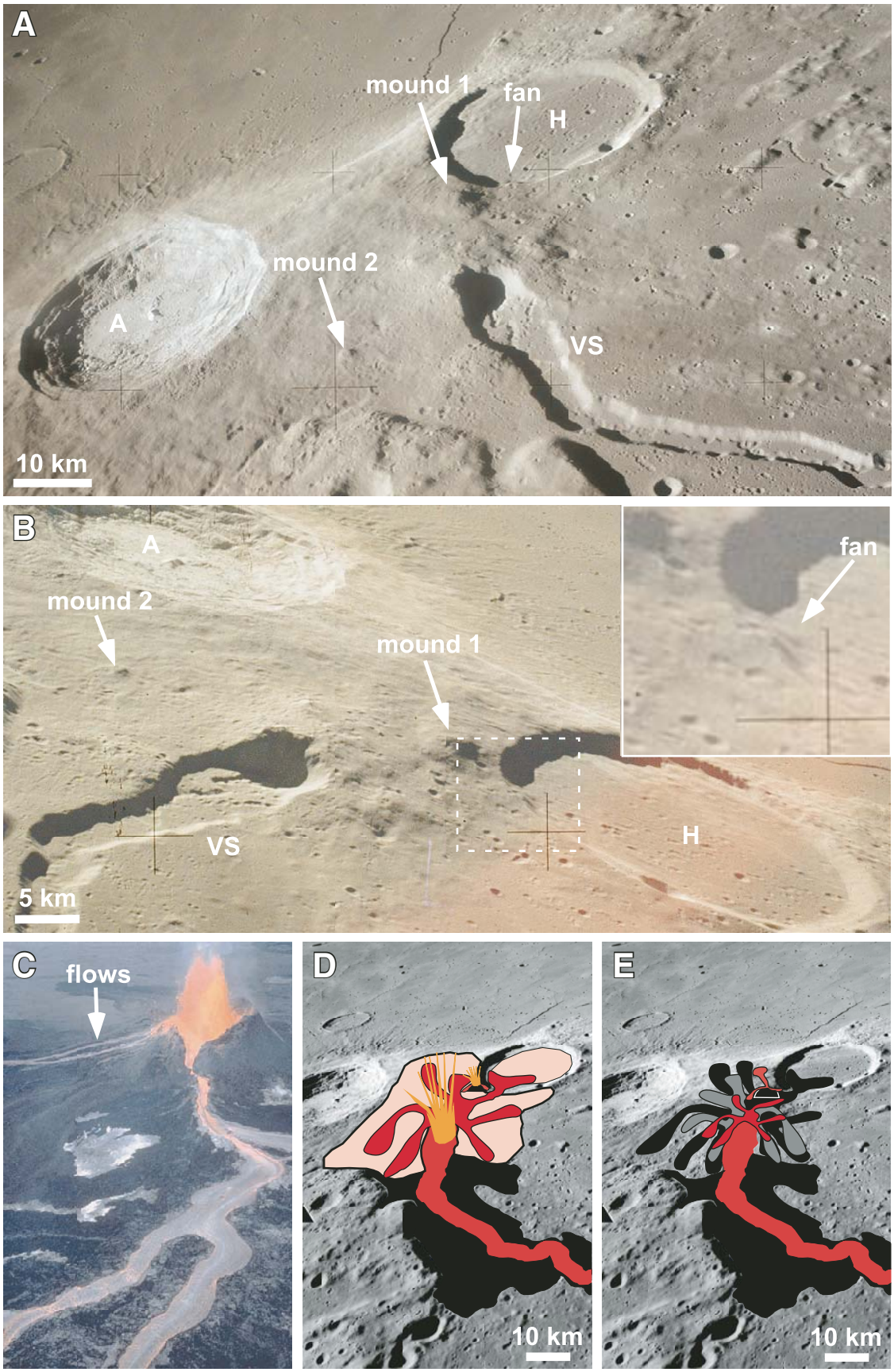
A
mound 1
fan
H
mound 2
A
VS
10 km
B
A
mound 2
mound 1
fan
VS
H
5 km
C
flows
D
10 km
E
10 km

key geologic component related to the origin and evolution of the rille. The shield spans ~35 km at the base, has a relief of ~900 m, and has flank slopes of ~2° to 2.5° as determined from lunar 1:1,000,000 topographic maps (Lunar Map, 1979). Topographic data from *Lunar Reconnaissance Orbiter* (*LRO*) and *Kaguya*, not available for this study, will provide more accurate measurements of the slopes, depths, and thicknesses of the shield and rille. The extent and volume of lavas erupted from the source vent are not well constrained, and it is unclear if the low shield extends past the eastern margin of the plateau. The flank of the shield is composed of a combination of smooth and hummocky terrain. The northern and eastern flanks are mantled by ejecta and secondary impacts from crater Aristarchus (e.g., Guest, 1973; Zisk et al., 1977). Three morphologic features, two mounds and a fan, of unknown, but possibly volcanic, origin are observed around the shield (Figs. 3A and 3B). The larger of the two mounds, located adjacent to the northern rim of Herodotus, is ~300–600 m in relief and ~8 km in length (Lunar Map, 1979) (mound 1 in Figs. 3A and 3B). On the northern flank of the shield, in the saddle between the Cobra Head and crater Aristarchus, there is a knob with a basal diameter of 2 km and ~100s m in relief (mound 2 in Figs. 3A and 3B). The third feature, which we refer to as a lava fan, occurs on the inner wall of crater Herodotus and extends to the crater floor (fan in Figs. 3A and 3B). This fan can be traced back to an irregular depression along the shield's southern flank. We do not observe any additional fans around the crater walls of crater Herodotus. We suggest that this fan feature is related to the formation of the Cobra Head, but it may also be an artifact from the degradation of the crater wall.

Primary Rille

The primary rille forms a distinctive arch pattern in map view as the trend of the rille changes from west-northwest to the southwest about halfway along the flow length (Fig. 2A). The length of the primary rille of Vallis Schröteri is 155 km (Honda et al., 2009) to 160 km (Zisk et al., 1977). The rille, including the vent region, is 6–10 km wide along the first 25 km of its length. However, the majority of the rille is 2.5–5 km wide. The depth of the vent as measured from the top of the shield to the bottom of the Cobra Head is ~1200 m, based on topographic maps (Lunar Map, 1979). The rille depth fluctuates between 200 and 500 m along its length, eventually reaching its shallowest depth of ~100 m at the distal end. The primary rille does not gradually transition to a negligible depth, as do many other rilles, but instead is bound by a distinct, enclosing scarp 100–200 m high (Fig. 2D). The floor of the rille is flat and confines a much more sinuous inner rille (Fig. 2B). Walls of the primary rille appear steep (slopes unknown), with outcrops exposed near the upper rims of the rille, and boulders are observed along the floor (Gornitz, 1973) (Figs. 2B and 2C). Distinct layers, as observed at Hadley Rille during *Apollo 15* (Swann et al., 1972), are not distinguishable in currently available remote-sensing data, but their possible presence should be the focus of future high-resolution image acquisition.

Inner Rille

Confined along the flat floor of the primary rille, there is a highly sinuous, inner rille. Originating at the Cobra Head, the length of the inner rille, measured along its center line, is ~240 km, and the width and depth are ~1 km and 150 m, respectively (Honda et al., 2009). The inner rille displays very tight, gooseneck-like meanders, some of which span from wall to wall entirely across the floor of the primary rille (Gornitz, 1973) (Fig. 2B). Slope materials from the primary rille walls bury portions of the inner rille (Fig. 2B). High-resolution *Lunar Orbiter V* images show outcrops and boulders exposed along the meanders (Fig. 2B). The inner rille crosscuts the southern, terminal wall at the distal end of the primary rille and extends for an additional 54 km along the degraded outer rim of a buried crater toward Oceanus Procellarum (Figs. 2A and 2D) (Zisk et al., 1977). The distal end of the inner rille narrows and grades out into a featureless mare deposit along the southwestern margin of the plateau (Fig. 2A). No flow margins or deposits extending from the inner rille are observed in the lunar maria.

Figure 3. Oblique views of the Cobra Head showing the morphology and volcanic features (mound 1, mound 2, fan). A—Aristarchus, H—Herodotus, VS—Vallis Schröteri. (A) Looking toward the southeast. *Apollo 15* 70 mm image AS15-88-12002 (National Aeronautics and Space Administration [NASA]). (B) Looking toward the northeast. *Apollo 15* 70 mm image AS15-88-12005 (NASA). (C) Eruption at the vent of Pu'u 'Ō'ō on Kilauea volcano, Hawaii, on 31 January 1984. The fountain is approximately 100 m high (U.S. Geological Survey/J.D. Griggs). The lava fountain feeds a primary lava channel that has breached the cone, as well as flows along the flank of the cone. The overall morphology of Pu'u 'Ō'ō at this stage is very similar to that of the Cobra Head, indicating possible eruption events that could have occurred at the vent of Vallis Schröteri. (D) Schematic drawing of the formation of the Cobra Head mound through lava fountain events, pyroclastic deposits, and lava flows. (E) Schematic drawing of the formation of the Cobra Head mound through lava flows only. Initial flows spread out farther and shorter-length flows build up the mound around the vent. Base image is a portion of AS15-M-2612 (National Aeronautics and Space Administration/Johnson Space Center/Arizona State University).

DISCUSSION: EMPLACEMENT OF THE VALLIS SCHRÖTERI FLOW

Emplacement processes observed in terrestrial analogs can help explain the complex relationships of the Cobra Head, primary rille, and inner rille of Vallis Schröteri. Our approach is primarily qualitative, and we understand that many factors of an eruption can influence the final flow morphology, including viscosity, temperature, composition, and volatile content of the lava, plus parameters like eruption duration, effusion rate, erupted volume, and repeated eruptions from a vent (e.g., Whitford-Stark and Head, 1977; Whitford-Stark, 1982). Here, we review

observations of terrestrial lava flows and the ways in which they relate to scenarios that can explain the final flow morphology of Vallis Schröteri. Quantitative assessments of this rille need to be completed in future studies with higher-resolution images and topography when they become available. The goal of our qualitative analysis is to identify the measurements that will help to constrain these types of quantitative models in the future.

Cobra Head

What Volcanic Processes Formed the Cobra Head Shield?

The topographic rise surrounding the vent implies the emplacement of layers of volcanic material as is seen in volcanic vent areas around the solar system. Two terrestrial volcanic features that show a similar morphology to the Cobra Head and rille relationship, although at a much smaller scale in both cases, are the early eruption stages (June 1983 through July 1986: episodes 1–48) of Pu‘u ‘Ō‘ō on Kilauea volcano, Hawaii (Wolfe, 1988; Heliker et al., 2003) (Fig. 3C), and Bandera crater, part of the Zuni-Bandera volcanic field in El Malpais National Monument, New Mexico (Laughlin et al., 1972). Both of these eruptions formed cones constructed from lava flows, agglutinated spatter, and tephra, opened on one side that fed a primary lava channel or tube (Figs. 3C and 4). A photograph of the Pu‘u ‘Ō‘ō vent in June 1984 shows how a lava fountain fed a primary lava channel that flowed from the amphitheater-shaped cone, while additional

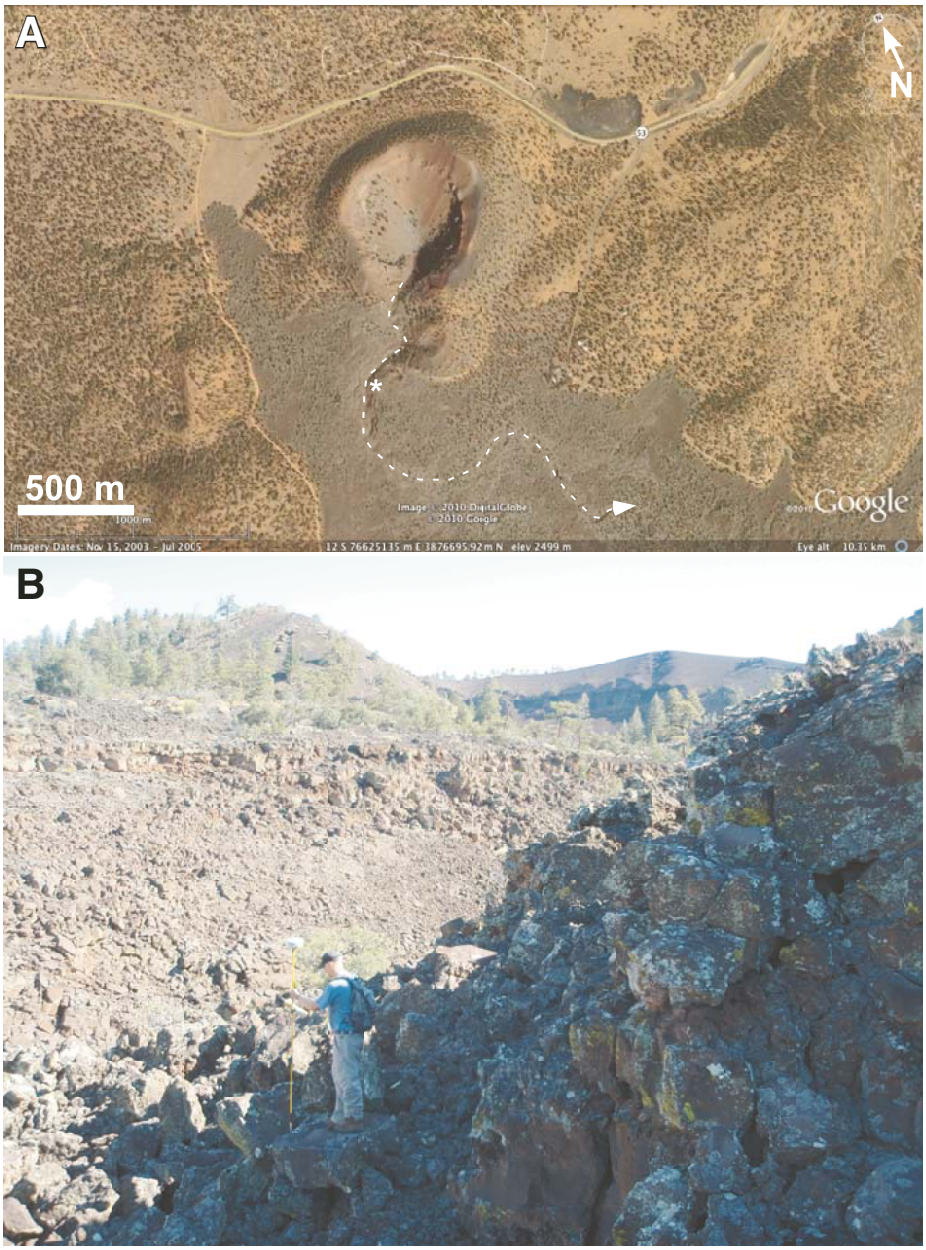

Figure 4. Bandera crater in New Mexico. (A) Remote-sensing image of Bandera crater. The cone opens to the south. Dashed white line shows the path of the lava tube. Asterisk marks location of photograph in B. Image is from Google Earth. (B) Photograph of the collapsed lava tube in the foreground with Bandera crater in the background, looking north toward the western flank of the cone. The depth of the collapsed lava tube is up to 26 m at this location based on a survey with a Trimble R8 Differential Global Positioning System.

lava flows fed by accumulated spatter on the rim (rootless spatter flows) occurred on the flanks of the cone (Fig. 3C). Although the morphology of the Pu‘u ‘Ō‘ō cone has changed dramatically through growth and collapse during more than 25 yr of eruption (a summary of which is given in Heliker et al., 2003), this early stage of the cone illustrates that the morphologic relationship between an amphitheater cone and a primary channel, as observed with Vallis Schröteri, can occur in effusive to mildly explosive terrestrial eruptions. In New Mexico, the ~10,000-yr-old Bandera crater is a basaltic cinder cone with a basal diameter of 1 km and a relief of 150 m. A breach on the southern flank of the cone feeds a 28.6-km-long, meandering lava tube, presently marked by an open trench formed by complete roof sag and collapse near the vent and by collapse pits within the lava flow throughout its distal reaches (Fig. 4A) (Hatheway and Herring, 1970; Laughlin et al., 1972).

Two possible eruption scenarios for the Cobra Head shield are: (1) eruption with a gas phase forming a composite of lava flows and pyroclastic deposits (ash, glass, spatter) (Fig. 3D) or (2) construction by lava flows from an eruption without a gas phase (Wilson and Head, 1981) (Fig. 3E). The final vent system displays a generally circular depression, suggesting a point source, at least in the waning stages of the eruption. However, we cannot rule out a scenario in which eruptions along a now-buried fissure became centralized at this point at the end of the eruptive phase.

The first scenario involves the eruption of gas-rich lava at the vent resulting in a lava fountain event. This style of eruption typically produces a composite shield around the vent area composed of a combination of lava flows, spatter, and ash fall (Fig. 3D). This scenario agrees with Moore's (1965) geologic map interpretation that the low shield is composed of ash falls, ash flows, and lava flows. The *Clementine* color ratio image shows that the shield surface is composed of dark mantle deposits and/or basaltic deposits. Unfortunately, the percentage of these geologic units, and their presence in the underlying stratigraphy are unknown. Based on the morphology and the relief of the Cobra Head, we suggest that the majority of the shield would be composed of thin lava flows and spatter if consistent with the first scenario. The majority of fine-grained glass deposits would likely be dispersed across the plateau (McGetchin and Head, 1973).

In the second scenario, the shield would have been constructed by repeated lava overflows at the vent due to a high hydraulic head and/or surges in the magma flux, possibly involving the eruption of minor amounts of spatter (Fig. 3E). The majority of the lava would have been directed down a primary conduit to form the rille. Intermittent, low- and/or high-volume fluctuations of lava might overflow at the vent in different directions, thereby contributing to the construction of a shield. Decreases in the volume of the overflows, flow velocity, and/or an increase in viscosity through time would shorten the flow lengths and build up the relief closer to the rim. We do not observe flow margins or channels on the flanks of the shield (Figs. 3A and 3B), suggesting low-velocity, nonchanneled flows on the shield (Rowland and Walker, 1990) or burial by regolith and/or crater ejecta to a depth that has obscured this morphology. High-resolution spectral and/or visible image data of the Cobra Head walls might better clarify the nature of these materials and differentiate between the two formation hypotheses.

We must point out the orders of magnitude difference in scale compared to the Vallis Schröteri Cobra Head height to basal diameter ratios (Cobra Head: 0.03; Pu‘u ‘Ō‘ō January 1984: 0.18; Bandera: 0.15). Wilson and Head (1981) showed that the lower gravity of the Moon would result in larger dispersion of pyroclasts and therefore a broader vent base and lower height if all other conditions were held equal. Therefore, this difference in height/diameter ratios is to be expected. Irrespective of each event's eruption environments, a reasonably similar volcanic morphology was produced. The broad shield morphology of the Cobra Head can be attributed to a fountain eruption in the low gravity and vacuum of the lunar environment, where material would be dispersed more evenly and not confined directly at the vent, or the emplacement of repeated, overlapping effusive flows that enabled their distribution away from the vent. Both scenarios can explain the differences between the lunar and terrestrial examples discussed here. Based on the composite nature of cones around the terrestrial vents and the significant presence of pyroclastic deposits on Aristarchus Plateau, we suggest that the first scenario, where volcanic deposition from a lava fountain event of volatile-rich lava as it reached the lunar surface combined with a buildup of lava flows, is the most likely scenario for the formation of the Cobra Head. This would have involved a fountain event that produced tiny pyroclastic glass beads dispersed across the plateau, likely concluding with more viscous spatter and flow accumulation around the edges of the vent in its later stages. Current issues surrounding the Cobra Head and pyroclastic deposits on the Aristarchus Plateau include: How high and how far would the lava fountain products have been dispersed? Why do other rilles around the Aristarchus Plateau not display well-developed shields around their vent areas? Are they sources for pyroclastic deposits on the plateau?

Are There Additional Volcanic Features at the Cobra Head?

The Cobra Head shield is a broad construct that can be explained through a generalized volcanic sequence, as stated previously. However, with such a broad volcanic feature, a detailed look at the morphology can provide insight into the evolution of the shield. Rootless vents and flows, satellite cones, and hornitos are just some of the smaller-scale features observed in the development of terrestrial shields. Their presence provides evidence of the dynamics of lava flows during eruptions. In the case of the Cobra Head, we suggest that two smaller morphologic mounds at the base of the shield and a fan along the wall of crater Herodotus are volcanic features related to the formation of the Cobra Head. The two mounds (hereafter referred to as mound 1 and mound 2), both over 100 m in relief and more than a kilometer wide, could have formed as the result of: (1) eruptions from satellite vents away from the primary Vallis Schröteri

vent, (2) construction from rootless vents fed by lava flows from the Vallis Schröteri vent, or (3) older impact ejecta for which the features have been either buried or degraded by volcanic activity and additional impacts.

A linear shadow along the crest of mound 1 may indicate a vent opening for an eruption (Figs. 3A and 3B), while mound 2, which is more conical in form, does not display such a feature. Mound 2 on the north side of the shield was most likely present prior to the Aristarchus impact event, since ejecta forms curved flow lines around the feature. Compared to the overall morphology of the Cobra Head, these features are just a minor aspect, but if they are volcanic in origin, they either indicate that multiple vents were present in the area or flows from the flanks were able to feed rootless eruptions at the base of the shield.

Lava fans are volcanic constructs that can form when lava piles up as it continuously flows over a steep slope, forming a delta-like structure along cliff faces. These features are observed in Hawaiian eruptions where lavas flowed into pit craters (Holcomb et al., 1974) and along lava tubes on the pali and coastal plain (e.g., Bleacher, 2007; Bleacher et al., 2009). On Mars, lava fans are observed on the steep slopes (in some places >10°) of the basal scarp of Olympus Mons (Bleacher et al., 2007; Richardson et al., 2009). Crater Herodotus is a mare-filled crater, which indicates that lava erupted from either now-buried vents along the crater floor and/or was filled in by lava flows originating outside the crater. We interpret the fan-like feature on the northern wall of crater Herodotus to be evidence of the latter, while we acknowledge that the majority of the lava in the crater could have originated within the crater floor. Assuming a volcanic origin for the fan, lava would have breached the crater rim, flowing onto the crater floor. A crescent-shaped deposit of basaltic material along the northern floor of crater Herodotus is observed in the *Clementine* color ratio image and might have been fed by the breached lavas. Stratigraphically, it is unclear if the crescent lava deposit is above or below pyroclastic deposits present on the floor of the crater (McEwen et al., 1994). If the flows are stratigraphically above the pyroclastic deposit, then that would indicate lava flows continued after major lava fountain events had ceased from Vallis Schröteri. The proximity to the Cobra Head, the deposit of basaltic material on the crater floor, and the lack of additional fan structures around the crater rim lead us to interpret this feature as a lava fan. An alternative interpretation that should be considered is that the fan is a morphologic artifact from the degradation and collapse of the crater wall. Additional images and topography data will be necessary to better characterize this feature in future studies, and might provide insight into the timing of eruptive events if the fan can be clearly determined to have been emplaced before or after pyroclastic deposition.

Primary Rille

Was the Primary Rille a Lava Tube or a Channel?

Arguments have been made for rilles originating as either open channels or collapsed lava tubes (Oberbeck et al., 1969; Greeley, 1971a; Gornitz et al., 1973; Hulme, 1982). While a quantitative analysis of eruption parameters and flow surface cooling is in order to discuss crust coverage and cooling within Vallis Schröteri, this is beyond the scope of our study. However, the current morphology of Vallis Schröteri can be used to qualitatively infer aspects that would contribute to a mobile crust or roofed-over channel origin. Cooling rates are a function of insulation, flow velocity, and channel geometry (Harris et al., 2005). Cashman et al. (2006) presented a thorough discussion on crust coverage in variable channel geometries. Irregular channel geometries (e.g., zigzag, meandering) can have variable crust coverage depending on effusion rates. Physical laboratory experiments show that flows with higher effusion rates form a laterally narrow section of crust within the channel that flows through the meanders with some extensional breaking, while lower effusion rates can promote solidification across the channel or collection of broken crust to form sections of tubes across the channel (Cashman et al., 2006). In one example of different crust coverage in an active Hawaiian lava channel, minimal crust coverage (20%) was observed on a hairpin turn (meander) in an active Hawaiian lava channel, while sections of the channel that were straight and places where the channel expanded or contracted in width had higher percentages of crust coverage (44%–69%) (Cashman et al., 2006).

The geometry of the primary rille can be classified as irregular by its broad arch shape, plus several meanders along its path (Fig. 2A). Due to the present open-channel form of the primary rille, we argue that the rille formed as a channel rather than a lava tube. Assuming "high" effusion rates within the rille, we assume that greater crust coverage would be observed along the straight sections of the rille and would be negligible or lower and disrupted along the meanders and major bends. This does not preclude the idea that crust could have connected across the rille during periods of lower effusion rates or if disrupted crust formed blockages along sections of the channel to create a tube-like form. A lava tube scenario that stretched the full length would require a significantly wide roof (kilometers) to span the rille, being disconnected from the active flow beneath (Greeley, 1971b). Lunar rilles have been compared to terrestrial lava channels in Hawaii (e.g., Cruikshank and Wood, 1972; Coombs and Hawke, 1989). Terrestrial channeled lava flows typically have solid or semidisrupted crust along the central part of the channel that flows with the active lava and is separated from the margins by shear zones (e.g., Lipman and Banks, 1987; Griffiths et al., 2003; Bailey et al., 2006; Cashman et al., 2006). Due to the incomplete coverage of crust, channeled flows are thermally inefficient compared to lava tubes (e.g., Kauahikaua et al., 1998; Harris et al., 2005). One scenario that would counter a lack of insulation in a channel origin is to consider a superheated lava flow that is ~200 °C above its liquidus, where the lava could remain crust-free for several kilometers from the vent (Williams et al., 2000). These concepts make the effusion rates, eruption duration, and cooling history of Vallis Schröteri in the lunar environment important issues to investigate.

How Was the Primary Rille Established and Influenced by Preflow Topography?

Terrestrial lava flows can form levees and evolve into channeled flows within hours of the eruption. Channels form within an active flow due to a velocity gradient perpendicular to the flow direction (Hulme, 1974). Lava-flow velocity is highest along the central, thickest part of the flow, quickly dropping toward the lateral, thinner margins, thereby producing a sharp velocity gradient between stagnated or slowly moving lava along the margins and lava in the central stream (e.g., Lipman and Banks, 1987). As the margins solidify to confine the lava into a central stream, the high velocity gradient at the boundary of the channel and levees forms uncrusted shear zones. While the proximal sections of a lava flow establish a well-defined channel in which the lateral margins are no longer advancing perpendicular to flow direction (or doing so sporadically during channel overflow), lava at the flow front tends to remain mobile and advance across the entire flow width, being dispersed radially from the end of the channel; therefore, the end of the developed channel can be set at some distance behind the active flow front (e.g., Lipman and Banks, 1987; Linneman and Borgia, 1993; Harris et al., 2002). As lava at the flow front spreads radially from the channel, it begins to stagnate along the margins, thereby continually establishing a velocity gradient across the flow and extending the developing channel as the entire flow field advances downslope. Typically, the defined channel in basaltic lava flows on Earth display are set back several tens to hundreds of meters up flow from the distal extend of the flow field (e.g., Lipman and Banks, 1987). The formation of the primary rille likely involved similar steps in flow development as a terrestrial channeled lava flow. We suggest that the initial eruption of the Vallis Schröteri flow began as a broad sheet flow, ~10–20 km wide, and spread away from the vent, primarily to the west. Based on the fluidity of lunar lavas (Murase and McBirney, 1970), the flow margins might have been confined by preexisting topographic barriers, including local topographic highs, cliff faces, older basalts, and ejecta material, which could also have influenced the direction of the preferred pathway or channel. A flow moving in this direction would have been confined by a 600–900-m-high scarp to the north and low-relief hummocky terrain to the southwest. The margins would have stagnated and cooled to create a velocity gradient that defined the active channel that was approximately the current width (5–10 km) of Vallis Schröteri. Terrestrial lava-flow channels begin to form between the stagnated flow margins within several hours of the onset of eruption (Lipman and Banks, 1987; Gregg and Fink, 2000; Garry, 2006; Glaze et al., 2009). Channeled (leveed) lava flows are typically established by high-effusion-rate eruptions of low-viscosity lavas, with increased slopes aiding in channel formation (e.g., Gregg and Fink, 2000). Higher-effusion-rate eruptions (>250 m^3/s) on Mauna Loa extend tens of kilometers from the vent in a matter of hours to days (Kauahikaua et al., 2003), implying that the Vallis Schröteri eruption could have extended a significant distance (tens of kilometers) over a brief period of time (hours to days). As such, the primary rille could have been established within hours of the eruption. The low viscosity of lunar lavas and observations of flow fronts imply that the initial sheet flow would have at least been a few meters thick (Murase and McBirney, 1970; Gifford and El Baz, 1981); therefore, the initial depth of the rille would also only have been a few meters, not the hundreds of meters of depth observed in the final morphology. Quantitative analysis of the eruption under different flow thicknesses will be necessary to constrain these characteristics. Final channel depth in terrestrial lava flows does not reflect initial flow thickness because levees are typically constructed through spatter and overflow, while flow field thickness continually increases, as does channel depth within the flow (Harris et al., 2009). This is important to consider for quantitative models based on morphologic parameters. Morphology measurements of Vallis Schröteri could help refine future models by (1) defining the distal margins to better constrain flow area and volumes, (2) identifying levees (width, height), (3) better characterizing volcanic features such as the mounds on the shield and outcrops in the rille walls, and (4) improving topographic control on morphometric properties of the shield height and slope and changes in the rille width and depth.

The path of the primary rille indicates that it was influenced by preexisting topography. Linear segments of the rille near the vent region follow the general trend of the plateau margins, suggesting the channel path was tectonically controlled (Gornitz, 1973; Whitford-Stark and Head, 1977). Preexisting fractures or faults could have helped establish the rille within a sheet flow by focusing the flow along an existing pathway. The distal half of the rille displays meanders around low-relief topographic mounds at several locations (Fig. 2A). For example, the flow could have been directed to the west by the scarp along the north side of the plateau and redirected to the southwest by an apparent subtle rise in elevation to the west associated with a more hummocky topography (Fig. 2A). Two impact craters, both partially buried by lava flows, possibly from the Vallis Schröteri eruption, also appear to have altered the path at the distal end of the rille (Figs. 2A, 2D, and 5). The distal end of the primary rille curves between the rims of these two partially buried craters (Fig. 5A). The outer wall of the 22 km crater on the western side is obscured. This suggests that lava flows were built up or inflated to the height of the crater rim, and possibly breached the top, flowing into the crater.

How Did the Primary Rille Achieve the Observed Depth?

In our previous scenario, we suggested that the initial depth of the rille was limited by the thickness of the lava flow during the early stages of the eruption, and therefore was probably only a few meters to tens of meters thick, which is a typical estimate for lunar flows (Gifford and El Baz, 1981), although we cannot discount any tectonic control on flow thickness (Gornitz, 1973). The current depth of the primary rille is hundreds of meters, indicating a significant increase in flow thickness and/or rille depth during the eruption. This change in depth can be attributed to thermal erosion, mechanical erosion, and/or flow field construction. We argue that some combination of these three processes

was likely responsible for the development of the Vallis Schröteri primary rille. *Clementine* color ratio images and albedo images show suspected crustal-anorthositic material exposed along the floor of the primary rille and the Cobra Head. If this material is assumed to be in situ crustal material, then lava must have eroded into the unit to expose it. Thermal erosion involves removal of substrate material through heating, partial melting, and incorporation into the flow material (e.g., Hulme, 1973, 1982; Carr, 1974; Greeley et al., 1998; Williams et al., 2000). Thermal erosion has been observed and documented in terrestrial lava tubes in basalt flows from Mount St. Helens in Washington, flows in Hawaii, and in komatiite flows (Greeley et al., 1998; Kauahikaua et al., 1998; Williams et al., 1998, 2000). The idea of thermal erosion by laminar flow alone in lunar lavas requires continued investigation (Kerr, 2001). Increasing flow thickness and/or eruption temperatures yields higher thermal erosion rates, and shorter durations are required to erode the rille (Williams et al., 2000). Stratigraphic relationships, compositions of the substrate material, and its physical properties can influence the erosion rate, which is why an understanding of the stratigraphy of the plateau is important for the quantitative models. Different geochemical stratigraphic units will have different melting temperatures, meaning some units could be easier to thermally erode than others. Further modeling of the thermal erosion of these different units by lava flows is needed. The stratigraphy of the Aristarchus Plateau suggests that the lava flow could have encountered crustal, basaltic lava, impact ejecta, and pyroclastic glass deposits to varying degrees and thicknesses. Strictly mechanical erosion models involve the removal of nonmelted material from the substrate. Highly fractured rock or layers of pyroclastic deposits or ejecta could provide easily removed substrate material. Regolith material was found to be tightly compacted during the *Apollo* missions (e.g., Wilhelms, 1987) and, therefore, these deposits might be dense, but erosion of them still requires modeling.

Outcrops, including multiple identifiable units observed in the upper primary rille wall, suggest that several lava flow units are present as opposed to one thick flow (Fig. 2B). Lava overflowing the rim of the rille could thicken the flow margins, thereby increasing the depth of the rille. Thinly mantled lava-flow deposits along the rim of Vallis Schröteri have been interpreted to be the result of overflow of lava above the rim, indicating the rille was flowing at and above full capacity at times during the eruption (Campbell et al., 2008). This interpretation fits with eruption scenarios we present here. Outcrops in the rille walls could be the result of overflow from the rille or older lava flows that were eroded through during the Vallis Schröteri emplacement

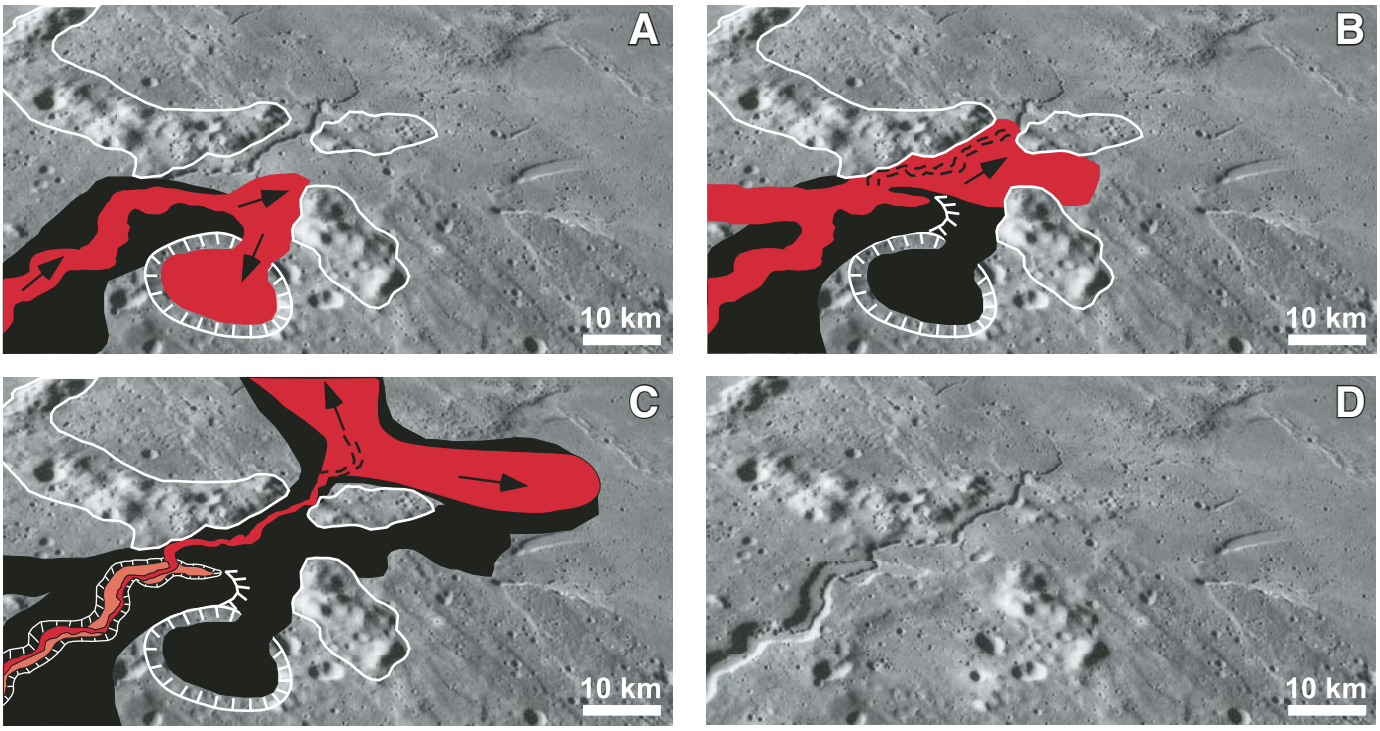

Figure 5. An eruption scenario that explains the formation of the scarp at the distal end of the primary rille and the breach in the wall by the inner rille. Portion of *Apollo 15* image AS15-M-2612 (National Aeronautics and Space Administration/Johnson Space Center/Arizona State University). (A) The front of the lava flow diverts between the rims of two craters and fills in one of them. Red indicates active lava, and black indicates stalled or solidified portions of the flow. Topographic highs are outlined by white lines. Hatches mark wall of the crater. (B) The lava flow stalls, ponds, backs up, and begins to overflow the margin of the primary rille. The inner rille begins as a preferred path established in the overflowing lava. (C) Lava is diverted toward Oceanus Procellarum through the inner rille. The level of the lava flow within the primary rille drops and creates the scarp along the distal end. (D) The final morphology at the distal end of the primary rille.

event. Basaltic deposits are estimated to be 200–600 m thick in the Aristarchus Plateau (e.g., McEwen et al., 1994). The extent to which the plateau had been covered by lava flows prior to the eruption that formed Vallis Schröteri is unknown, but we assume that if the rille was filled to capacity, some of these preexisting basaltic layers could have been eroded into while the flow field was thickened by periodic overflow of lava from the rille. The measured depth of Vallis Schröteri primary rille should be considered a minimum because the true depth might be obscured by late-stage lava-flow material that solidified within the channel, thereby forming a flat floor and inner rille.

Why Is the Distal Margin an Enclosing Scarp?

The distal end of the primary rille does not grade out evenly into the plateau. Instead, a scarp defines its terminus (Fig. 2D). This scarp might mark the full extent of the primary rille, but not the extent of the entire flow field. Terrestrial lava channels do not typically extend all the way to the flow front; they are preceded by a nonchanneled zone of dispersed flow (Lipman and Banks, 1987; Bailey et al., 2006; Garry, 2006; Glaze et al., 2009). Based on terrestrial observations, we suggest that the Vallis Schröteri lava flow developed the rille for at least the 155 km that are currently present, but that there was also an active, nonchanneled, dispersed zone of lava that extended beyond the end of the rille (Fig. 5A). Lava at the flow front began to back up, possibly due to confinement by previous topography (i.e., rims of impact craters) (Fig. 2B), stagnation of the flow front, and/or blockage of the channel. Lava would have likely ponded at the distal end (Fig. 5B), possibly overflowing the rille wall (Campbell et al., 2008), and flowing toward Oceanus Procellarum via a preferred pathway that established the inner rille, which will be discussed in the following section (Figs. 5B and 6). The walls of the rille were exposed as lava drained out of the channel, and the boundary between the rille and dispersed zone could have formed the enclosing scarp (Fig. 5C). In a terrestrial example, field observations and differential global positioning system (DGPS) topography of the eastern limb of the basaltic, 1907 ’a’ā flow on Mauna Loa volcano, Hawaii, show that there is a topographic boundary where the channel transitions into the zone of dispersed flow ~1 km from the distal margin (Zimbelman et al., 2008). Lava was diverted from the eastern limb of the 1907 flow before it could reach the ocean, preserving the flow front morphology. A scarp as distinct as the one on Vallis Schröteri is not present in the eastern limb of the 1907 flow, but change from a channeled to nonchanneled section of the flow is evident in the topography. High-resolution images of the distal end of the primary rille may reveal stratigraphic information within the scarp walls and insight into its formation.

Inner Rille

What Is the Origin of the Inner Rille?

To achieve the observed depth of the inner rille, either a deep channel was established in a (>100 m) lava flow confined by the walls of the primary rille or a thin flow (a few tens of meters thick) established a preferred path that eroded into the floor of the primary rille or underlying substrate material. Previous work suggests that the primary rille and inner rille formed during separate flow events (Zisk et al., 1977). We suggest that the inner rille could be the result of: (1) the final volume of lava draining out from a single, continuous eruptive event that formed the primary rille or (2) a flow that reoccupied the primary rille after a hiatus or pause in the initial eruption. Each scenario is viable, and we do not feel that observations distinguish one over the other. If the inner rille formed as part of a continuous eruption related to the primary rille, then this scenario would not require thermal erosion of the rille floor or substrate, because the inner rille could completely exist within the thickness of the

Figure 6. Blockage and overflow along the lava channel during the 1984 eruption on Mauna Loa volcano, Hawaii (U.S. Geological Survey/J.D. Griggs). Channel width is estimated to be ≤50 m based on measurements in remote-sensing images.

late-stage lava flow. If the inner rille formed as part of a secondary eruption, two considerations need to be made: Did the flow form a thin layer over the primary rille floor and then erode into it, or did the flow thicken, creating a new level for the rille floor, obscuring the true depth of the primary rille? If thermal erosion is assumed, then higher-resolution images of the walls of inner rille might reveal outcrops, the nature of which could help clarify if the inner rille involved erosion into basaltic material on the floor of the primary rille or erosion into the underlying anorthositic-crustal material.

The general path of the inner rille hugs the wall of the primary rille wall and alternates from one wall to the other along the flow length (Figs. 1 and 2A) (Gornitz, 1973). Physical models of wax flowing through a predefined irregular channel, representative of meanders, show that dye tracers along the centerline of the flow migrate toward the walls and alternate sides after each bend (Cashman et al., 2006). This occurs when there is no or minimal cooling within the wax flow and the surface remains crust free. The inner rille displays this same pattern, alternating to a different side of the primary rille after each major bend (Fig. 1), suggesting that the inner rille was a meandering preferred path within a flow that spread out to both walls of the primary rille.

How Did the Sinuous Gooseneck Morphology Form?

The gooseneck meanders of the inner rille (Fig. 2B) resemble terrestrial river channels (Schubert et al., 1970; Gornitz, 1973), but they were formed by volcanic processes. Formation of such tight meanders with extreme changes in direction requires: (1) a very fluid, low-viscosity lava, (2) establishment of a preferred path, but with easily modified margins, and (3) erosion (Murase and McBirney, 1970; Hulme, 1982), which could preclude the idea of the inner rille forming solely within a thick lava flow. Sections of levees in terrestrial channeled lava flows are modified during eruptions, with portions breaking off and being rafted downstream (Lipman and Banks, 1987), but a high frequency of gooseneck meanders is not observed in terrestrial lava flows. This suggests that the inner rille was not established in the typical way that terrestrial channeled lava flows are established (e.g., Lipman and Banks, 1987; Linneman and Borgia, 1993; Harris et al., 2009; Glaze et al., 2009). Since the goosenecks are well defined and relatively consistent in width, this would imply a steady and stable flow through the established inner rille. A thermal erosion mechanism requires time and an established channel (Greeley et al., 1998; Williams et al., 2000; Fagents and Greeley, 2001). Substrate material could also influence the rille morphology. A pyroclastic mantle deposit that accumulated on the rille floor between major flow events could be a potential substrate to facilitate tight meanders, but this has not yet been modeled. Issues to consider, which we cannot fully address at this time, are: What was the difference in rheologic properties of the stalled lava compared to the lava within the main inner rille conduit and how would this influence formation of the meanders? What were the differences in the emplacement parameters between the inner rille and primary rille?

How Did the Inner Rille Crosscut the Primary Rille?

Building on our previous discussion of the scarp at the distal end of the primary rille, we propose that this relationship is the result of lava overflowing and branching from the primary rille (Figs. 5 and 6). We present this scenario with the assumption that the same eruption formed both the primary and inner rille, but the basic premise still applies if the inner rille was formed by a later eruption that ponded at the distal end of the primary rille. Two key observations need to be explained in the scenario: the change in flow direction between the primary rille and inner rille and a mechanism for the lava to cut into the rille wall. A change in flow direction can occur if the lava in the primary rille becomes confined at the flow front, ponds, and backs up, and then overflows toward the southern margin of the plateau (Fig. 5A). A channel or preferred path forms within the overflowing lava, establishing the inner rille, and erodes down through the distal wall of the primary rille (Fig. 5B). A similar event occurred during the 1984 eruption on Mauna Loa, where lava was blocked in the original channel (flow 1) and was diverted to form a new, channeled flow lobe (flow 1A) (Lipman and Banks, 1987) (Fig. 6). The overflow lava was diverted around topographic barriers, including the degraded rim of a partially buried crater, and flowed into Oceanus Procellarum, and the inner rille continued to lengthen in this direction (Fig. 5C). Lava-flow parameters in this area did not facilitate continued channel growth, and the lava dispersed as a sheet flow beyond the plateau margin. As the lava eruption rate waned, the level of the lava in the primary rille subsided, and the inner rille became well established along the rille floor and continued to feed lava through the thermally eroded notch in the primary rille wall (Fig. 5C). As lava drained from the rille and the surface level of the lava lowered, it would have cut further into the primary rille wall, and the path of the inner rille would have been controlled by the primary rille walls.

This proposed mechanism also fits a scenario where the primary rille is reoccupied by a second eruption event, as suggested by previous work (e.g., Zisk et al., 1977). The lava from this new eruption would still have to become confined at the distal end, overflow the wall, and establish the inner rille as it drained out. Current issues with the inner rille include determining the flow parameters, eruption duration, and erosion rates. Higher-resolution images of the crosscut could yield clues to the stratigraphy of the inner rille and primary rille walls.

CONCLUSIONS

Our qualitative scenarios of the Vallis Schröteri eruption based on morphologic relationships reveal that current issues still remain in understanding the formation of this rille. The Vallis Schröteri eruption consisted of a possible point source eruption that constructed a low shield through lava fountain events and fed a sheet flow within which the primary rille developed. Based on the path of the primary rille and its relationship to older terrains, the influence of the pre-eruption topography becomes

very evident. The depth of the primary rille and exposure of anomalous crustal-anorthositic material at the base of the rille walls suggest that a combination of thermal erosion, mechanical erosion, and construction through overflow resulted in the rille's depth. The true depth of the rille is likely unknown due to remnant lava from the initial eruption remaining in the channel or a secondary flow that reoccupied the primary rille and formed the inner rille. The gooseneck meanders and alternation of its path between walls of the primary rille suggest that the lava was very fluid during emplacement of the inner rille. The scarp at the terminus of the primary rille and the crosscut of this margin by the inner rille is possibly due to backup, overflow, and erosion as lava was diverted to flow into Oceanus Procellarum through a newly established channel.

Stratigraphy on Aristarchus Plateau has been influenced by the volcanic activity and may also have affected rille formation. The thickness of basaltic materials is between 200 and 600 m, but the areal extent of this unit across the plateau is not well constrained. Future work through stratigraphic and compositional analysis of small craters and ejecta could be used to produce an isopach map of the thickness of the basaltic units around the plateau. Defining the extent of the Vallis Schröteri eruption is also important for quantitative models to calculate eruption volumes, effusion and flow rates, erosion rates, and eruption durations. Accounting for multiple processes versus a single process (e.g., thermal erosion, mechanical erosion, construction) in the formation of the primary rille will be important to address in future models. Constraints for the eruption and flow parameters that form the tight gooseneck meanders observed in the inner rille will require robust quantitative modeling.

Observations of terrestrial analogs provide information on the dynamics of lava flows. Volcanic features with similar morphologies on other planetary bodies, although at different scales, could be the result of a similar eruption process, but in different eruption environments. Processes and factors such as thermal erosion, overflows, construction, and pre-eruption topography need to be considered when explaining the complex morphology of lunar sinuous rilles. Current missions to the moon will provide new, high-resolution data sets of the surface and topography that can be applied to morphologic analysis and quantitative modeling of the lunar sinuous rilles.

ACKNOWLEDGMENTS

This research was funded through the Center for Earth and Planetary Studies Postdoctoral Fellowship at the Smithsonian National Air and Space Museum and a National Aeronautics and Space Administration (NASA) Postdoctoral Program Fellowship administered through Oak Ridge Associated Universities at NASA Goddard Space Flight Center. Fieldwork was supported by NASA Moon and Mars Analog Mission Activities grant NNX08AR76G. We would like to thank the Ice Caves Trading Co. for permission to conduct fieldwork at Bandera crater.

REFERENCES CITED

Bailey, J.E., Harris, A.J.L., Dehn, J., Calvari, S., and Rowland, S.K., 2006, The changing morphology of an open lava channel on Mt. Etna: Bulletin of Volcanology, v. 68, no. 6, p. 497–515, doi:10.1007/s00445-005-0025-6.

Bleacher, J.E., 2007, Observations of the campout tube-fed flow encountering a slope break, Kilauea, Hawai'i: An analogue to lava fans on Olympus Mons, Mars: Houston, Texas, Lunar and Planetary Institute, Lunar and Planetary Science Conference XXXVIII, CD-ROM, abstract 1886.

Bleacher, J.E., Greeley, R., Williams, D.A., Werner, S.C., Hauber, E., and Neukum, G., 2007, Olympus Mons, Mars: Inferred changes in late Amazonian aged effusive activity from lava flow mapping of Mars Express High Resolution Stereo Camera data: Journal of Geophysical Research, v. 112, p. E04003, doi:10.1029/2006JE002826.

Bleacher, J.E., Garry, W.B., Zimbelman, J.R., and Richardson, P.W., 2009, Field observations of rootless vents over the Pōhue Bay lava tube, Hawai'i: Comparisons with Olympus Mons lava fans, Mars: Houston, Texas, Lunar and Planetary Institute, Lunar and Planetary Science Conference XL, CD-ROM, abstract 1980.

Cameron, W.S., 1964, An interpretation of Schröter's Valley and other lunar sinuous rilles: Journal of Geophysical Research, v. 69, p. 2423–2430, doi:10.1029/JZ069i012p02423.

Campbell, B.A., Carter, L.M., Hawke, B.R., Campbell, D.B., and Ghent, R.R., 2008, Volcanic and impact deposits of the Moon's Aristarchus Plateau: A new view from Earth-based radar images: Geology, v. 36, no. 2, p. 135–138.

Carr, M.H., 1974, The role of lava erosion in the formation of lunar rilles and Martian channels: Icarus, v. 22, p. 1–23.

Cashman, K.V., Kerr, R.C., and Griffiths, R.W., 2006, A laboratory model for surface crust formation and disruption on lava flows through non-uniform channels: Bulletin of Volcanology, v. 68, p. 753–770, doi:10.1007/s00445-005-0048-z.

Chen, L.J., Bleacher, J.E., and Lowman, P.D., 2008, The sinuosity of lunar rilles in the Aristarchus Plateau: Houston, Texas, Lunar and Planetary Institute, Lunar and Planetary Science Conference XXXIX, CD-ROM, abstract 1713.

Chevrel, S.D., Pinet, P.C., Daydou, Y., Le Mouélic, S., Langevin, Y., Costard, F., and Erard, S., 2009, The Aristarchus Plateau on the Moon: Mineralogical and structural study from integrated Clementine UV-Vis-NIR spectral data: Icarus, v. 199, p. 9–24, doi:10.1016/j.icarus.2008.08.005.

Coombs, C.R., and Hawke, B.R., 1989, Kauhako crater and channel, Kalaupapa, Molokai, Hawaii: A terrestrial analogue to lunar sinuous rilles: Houston, Texas, Lunar and Planetary Institute, Lunar and Planetary Science Conference XX, CD-ROM, p. 183–184.

Cruikshank, D.P., and Wood, C.A., 1972, Lunar rilles and Hawaiian volcanic features: Possible analogues: The Moon, v. 3, p. 412–447, doi:10.1007/BF00562463.

Fagents, S.A., and Greeley, R., 2001, Factors influencing lava-substrate heat transfer and implications for thermomechanical erosion: Bulletin of Volcanology, v. 62, p. 519–532, doi:10.1007/s004450000113.

Gaddis, L.R., Staid, M.I., Tyburczy, J.A., Hawke, B.R., and Petro, N.E., 2003, Compositional analyses of lunar pyroclastic deposits: Icarus, v. 161, p. 262–280, doi:10.1016/S0019-1035(02)00036-2.

Garry, W.B., 2006, Emplacement of Channeled Flows in Subaerial, Submarine, Simulated, and Extraterrestrial Environments [Ph.D. thesis]: Buffalo, State University of New York, 256 p.

Gifford, A.W., and El-Baz, F., 1981, Thicknesses of lunar mare flow fronts: The Moon and the Planets, v. 24, p. 391–398, doi:10.1007/BF00896904.

Glaze, L.S., Baloga, S.M., Garry, W.B., Fagents, S.A., and Parcheta, C., 2009, A hybrid model for leveed lava flows: Implications for eruption styles on Mars: Journal of Geophysical Research, v. 114, p. E07001, doi:10.1029/2008JE003278.

Gornitz, V., 1973, The origin of sinuous rilles: The Moon, v. 6, p. 337–356.

Greeley, R., 1971a, Lunar Hadley Rille: Considerations of its origin: Science, v. 172, p. 722–725.

Greeley, R., 1971b, Observations of actively forming lava tubes and associated structures, Hawai'i (Lava tube formation in pāhoehoe basalt and flow activity in vent near Alae crater, Hawai'i): Modern Geology, v. 2, p. 207–223.

Greeley, R., 1971c, Lava tubes and channels in the lunar Marius Hills: Earth, Moon, and Planets, v. 3, no. 3, p. 289–314.

Greeley, R., Fagents, S.A., Harris, R.S., Kadel, S.D., and Williams, D.A., 1998, Erosion by flowing lava: Field evidence: Journal of Geophysical Research, v. 103, no. B11, p. 27,325–27,345, doi:10.1029/97JB03543.

Gregg, T.K.P., and Fink, J.H., 2000, A laboratory investigation into the effects of slope on lava flow morphology: Journal of Volcanology and Geothermal Research, v. 96, p. 145–159, doi:10.1016/S0377-0273(99)00148-1.

Griffiths, R.W., Kerr, R.C., and Cashman, K.V., 2003, Patterns of solidification in channel flows with surface cooling: Journal of Fluid Mechanics, v. 496, p. 33–62, doi:10.1017/S0022112003006517.

Guest, J.E., 1973, Stratigraphy of ejecta from the lunar crater Aristarchus: Geological Society of America Bulletin, v. 84, no. 9, p. 2873–2894, doi:10.1130/0016-7606(1973)84<2873:SOEFTL>2.0.CO;2.

Guest, J.E., and Spudis, P.D., 1985, The Aristarchus impact event and the effects of target material: Geological Magazine, v. 122, no. 4, p. 317–327, doi:10.1017/S0016756800031769.

Hagerty, J.J., Lawrence, D.J., Hawke, B.R., and Gaddis, L.R., 2009, Thorium abundances on the Aristarchus Plateau: Insights into the composition of the Aristarchus pyroclastic glass deposits: Journal of Geophysical Research, v. 114, p. E04002, doi:10.1029/2008JE003262.

Harris, A., Flynn, L.P., Matias, O., and Rose, W.I., 2002, The thermal stealth flows of Santiaguito dome, Guatemala: Implications for the cooling and emplacement of dacitic block-lava flows: Geological Society of America Bulletin, v. 114, no. 5, p. 533–546, doi:10.1130/0016-7606(2002)114<0533:TTSFOS>2.0.CO;2.

Harris, A., Bailey, J., Calvari, S., and Dehn, J., 2005, Heat loss measured at a lava channel and its implications for down-channel cooling and rheology, *in* Manga, M., and Ventura, G., eds., Kinematics and Dynamics of Lava Flows: Geological Society of America Special Paper 396, p. 124–146.

Harris, A., Favalli, M., Mazzarini, F., and Hamilton, C.W., 2009, Construction dynamics of a lava channel: Bulletin of Volcanology, v. 71, no. 4, p. 459–474, doi:10.1007/s00445-008-0238-6.

Hatheway, A.W., and Herring, A.K., 1970, Bandera lava tubes of New Mexico and lunar implications: University of Arizona, Communications of the Lunar and Planetary Lab, v. 8, no. 152, p. 299–327.

Hawke, B.R., Peterson, C.A., Coombs, C.R., Lucey, P.G., Smith, G.A., and Taylor, G.J., 1995, Remote sensing studies of the Aristarchus region of the Moon: Houston, Texas, Lunar and Planetary Institute, Lunar and Planetary Science Conference XXVI, p. 559–560.

Head, J.W., and Wilson, L., 1980, The formation of eroded depressions around the sources of lunar sinuous rilles: Observations: Houston, Texas, Lunar and Planetary Institute, Lunar and Planetary Science Conference XI, CD-ROM, p. 426–428.

Heliker, C., Kauahikaua, J., Sherrod, D.R., Lisowski, M., and Cervelli, P.F., 2003, The rise and fall of Pu‘u ‘Ō‘ō cone, 1983–2002: U.S. Geological Survey Professional Paper 1676, p. 29–51.

Hiesinger, H., Head, J.W., III, Wolf, U., Jaumann, R., and Neukum, G., 2003, Ages and stratigraphy of mare basalts in Oceanus Procellarum, Mare Nubium, Mare Cognitum, and Mare Insularum: Journal of Geophysical Research, v. 108, no. E7, p. 5065, doi:10.1029/2002JE001985.

Holcomb, R.T., Peterson, D.W., and Tilling, R.I., 1974, Recent landforms at Kilauea volcano: A selected photographic compilation, *in* Greeley, R., ed., Geologic Guide to the Island of Hawai’i: A Field Guide for Comparative Planetary Geology: National Aeronautics and Space Administration CR 152416, p. 49–86.

Honda, C., Morota, T., Yokota, Y., Ogawa, Y., Demura, H., Hirata, N., Matsunaga, T., Ohtake, M., and Haruyama, J., 2009, Morphologic characteristics of the Vallis Schröteri: Houston, Texas, Lunar and Planetary Institute, Lunar and Planetary Science Conference XL, CD-ROM, abstract 1524.

Hulme, G., 1973, Turbulent lava flow and the formation of lunar sinuous rilles: Modern Geology, v. 4, p. 107–117.

Hulme, G., 1974, The interpretation of lava flow morphology: Geophysical Journal of the Royal Astronomical Society, v. 39, p. 361–383.

Hulme, G., 1982, A review of lava flow processes related to the formation of lunar sinuous rilles: Geophysical Surveys, v. 5, p. 245–279, doi:10.1007/BF01454018.

Hulme, G., and Fielder, G., 1977, Effusion rates and rheology of lunar lavas: Philosophical Transactions of the Royal Society of London, ser. A, v. 285, p. 227–234.

Kauahikaua, J.K., Cashman, K., Hon, K., Mattox, T., Heliker, C., Mangan, M., and Thornber, C., 1998, Observations on basaltic lava streams in tubes from Kilauea volcano, Hawai’i: Journal of Geophysical Research, v. 103, p. 27,303–27,323, doi:10.1029/97JB03576.

Kauahikaua, J., Sherrod, D.R., Cashman, K.V., Heliker, C., Hon, K., Mattox, T.N., and Johnson, J.A., 2003, Hawaiian lava-flow dynamics during the Pu‘u ‘Ō‘ō-Kūpaianaha eruption: A tale of two decades: U.S. Geological Survey Professional Paper 1676, p. 63–87.

Kerr, R.C., 2001, Thermal erosion by laminar lava flows: Journal of Geophysical Research, v. 106, p. 26,453–26,465, doi:10.1029/2001JB000227.

Laughlin, A.W., Brookins, D.G., and Causey, J.D., 1972, Late Cenozoic basalts from the Bandera Lava Field, Valencia County, New Mexico: Geological Society of America Bulletin, v. 83, p. 1543–1552, doi:10.1130/0016-7606(1972)83[1543:LCBFTB]2.0.CO;2.

Le Mouélic, S., Langevin, Y., Erard, S., Pinet, P., Chevrel, S., and Daydou, Y., 2000, Discrimination between maturity and composition of lunar soils from integrated Clementine UV-visible/near-infrared data: Application to the Aristarchus Plateau: Journal of Geophysical Research, v. 105, p. 9445–9455, doi:10.1029/1999JE001196.

Linneman, S.R., and Borgia, A., 1993, The blocky andesitic lava flows of Arenal volcano, Costa Rica, *in* Kilburn, C.R.J., and Luongo, G., eds., Active Lavas: Monitoring and Modelling: London, University College London Press, p. 25–72.

Lipman, P.W., and Banks, N.G., 1987, A’a flow dynamics, *in* Decker, R.W., Wright, T.L., and Stauffer, P.H., eds., Volcanism in Hawaii: U.S. Geological Survey Professional Paper 1350, v. 2, p. 1527–1567.

Lucey, P.G., Hawke, B.R., Pieters, C.M., Head, J.W., and McCord, T.B., 1986, A compositional study of the Aristarchus region of the Moon using near-infrared reflectance spectroscopy: Proceedings of the 16th Lunar and Planetary Science Conference, Part 2: Journal of Geophysical Research, v. 91, no. B4, p. D344–D354.

Lunar Map, 1979, LM-39, Aristarchus: St. Louis Air Force Station, Missouri, Defense Mapping Agency, scale 1:1,000,000 (available at http://www.lpi.usra.edu/resources/mapcatalog/LM/lm39/72dpi.jpg).

McCall, G.H.J., 1970, Lunar rilles and a possible terrestrial analog: Nature, no. 225, p. 714–716, doi:10.1038/225714a0.

McEwen, A.L., Robinson, M.S., Eliason, E.M., Lucey, P.G., Duxbury, T.C., and Spudis, P.D., 1994, Clementine observations of the Aristarchus region of the Moon: Science, v. 266, p. 1858–1862.

McGetchin, T.R., and Head, J.W., 1973, Lunar cinder cones: Science, v. 180, p. 68–70.

Moore, H.J., 1965, Geologic Map of the Aristarchus Region of the Moon: U.S. Geological Survey Geology Investigation Map I-465 (LAC-39), scale 1:1,000,000, 1 sheet.

Moore, H.J., 1967, Geologic Map of the Seleucus Quadrangle of the Moon: U.S. Geological Survey Geology Investigation Map I-527 (LAC-38), scale 1:1,000,000, 1 sheet.

Murase, T., and McBirney, A.R., 1970, Viscosity of lunar lavas: Science, v. 167, p. 1491–1493.

Oberbeck, V.R., Quaide, W.L., and Greeley, R., 1969, On the origin of lunar sinuous rilles: Modern Geology, v. 1, p. 75–80.

Oberbeck, V.R., Michio, A., Greeley, R., and Lovas, M., 1972, Planimetric shapes of lunar rilles, *Apollo 16*: National Aeronautics and Space Administration Preliminary Science Report Special Publication 315, C-3, p. 29–80.

Peale, S.J., Schubert, G., and Lingenfelter, R.E., 1968, Distribution of sinuous rilles and water on the Moon: Nature, v. 220, p. 1222–1225.

Richardson, P.W., Bleacher, J.E., Glaze, L.S., and Baloga, S.M., 2009, The relationship between lava fans and tubes on Olympus Mons in the Tharsis region, Mars: Houston, Texas, Lunar and Planetary Institute, Lunar and Planetary Science Conference XL, CD-ROM, abstract 1527.

Rowland, S.K., and Walker, G.P.L., 1990, Pāhoehoe and ’a’ā in Hawaii: Volumetric flow rate controls the lava structure: Bulletin of Volcanology, v. 52, no. 8, p. 615–628, doi:10.1007/BF00301212.

Schubert, G., Lingenfelter, R.E., and Peale, S.J., 1970, The morphology, distribution, and origin of lunar sinuous rilles: Reviews of Geophysics and Space Physics, v. 8, no. 1, p. 199–224.

Strain, P.L., and El-Baz, F., 1977, Topography of sinuous rilles in the Harbinger Mountains region of the Moon: Earth, Moon, and Planets, v. 16, no. 2, p. 221–229.

Swann, G.A., Bailey, N.G., Batson, R.M., Freeman, V.L., Hait, M.H., Head, J.W., Holt, H.E., Howard, K.A., Irwin, J.B., Larson, K.B., Muehlberger,

W.R., Reed, V.S., Rennilson, J.J., Schaber, G.G., Scott, D.R., Silver, L.T., Sutton, R.L., Ulrich, G.E., Wilshire, H.G., and Wolfe, E.W., 1972, Preliminary geologic investigation of the *Apollo 15* landing site, *in Apollo 15* Preliminary Science Report: National Aeronautics and Space Administration Special Publication 289, p. 5-1–5-112.

Urey, H.C., 1967, Water on the Moon: Nature, v. 216, p. 1094–1095.

Vaniman, D., French, B., and Heiken, G., 1991, Afterword, *in* Heiken, G., Vaniman, D., and French, B., eds., Lunar Sourcebook: Cambridge, UK, Cambridge University Press, p. 633–643.

Weitz, C.M., Head, J.W., III, and Pieters, C.M., 1998, Lunar regional dark mantle deposits: Geologic, multispectral, and modeling studies: Journal of Geophysical Research, v. 103, no. E10, p. 22,725–22,759, doi:10.1029/98JE02027.

Whitford-Stark, J.L., 1982, Factors influencing the morphology of volcanic landforms: An Earth-Moon comparison: Earth-Science Reviews, v. 18, p. 109–168, doi:10.1016/0012-8252(82)90050-2.

Whitford-Stark, J.L., and Head, J.W., 1977, The Procellarum volcanic complexes: Contrasting styles of volcanism: Houston, Texas, Lunar and Planetary Institute, Lunar and Planetary Science Conference VIII, p. 2705–2724.

Wilhelms, D., 1987, The Geologic History of the Moon: U.S. Geological Survey Professional Paper 1348, 302 p.

Williams, D.A., Kerr, R.C., and Lesher, C.M., 1998, Emplacement and erosion by Archean komatiite lava flows at Kambalda: Revisited: Journal of Geophysical Research, v. 103, p. 27,533–27,549, doi:10.1029/97JB03538.

Williams, D.A., Kerr, R.C., and Lesher, C.M., 1999, Thermal and fluid dynamics of komatiitic lavas associated with magmatic Ni-Cu-(PGE) sulphide deposits, *in* Keays, R.R., Lesher, C.M., Lightfoot, P.C., and Farrow, C.E.G., eds., Dynamic Processes in Magmatic Ore Deposits and Their Application in Mineral Exploration: Geological Association of Canada Short Course, v. 13, p. 367–412.

Williams, D.A., Fagents, S.A., and Greeley, R., 2000, A reassessment of the emplacement and erosional potential of turbulent, low-viscosity lavas on the Moon: Journal of Geophysical Research, v. 105, p. 20,189–20,205, doi:10.1029/1999JE001220.

Wilson, L., and Head, J.W., III, 1981, Ascent and eruption of basaltic magma on the Earth and Moon: Journal of Geophysical Research, v. 86, no. B4, p. 2971–3001, doi:10.1029/JB086iB04p02971.

Wolfe, E.W., 1988, The Pu‘u ‘Ō‘ō eruptions of Kilauea volcano, Hawai’i: Episodes 1 through 20: U.S. Geological Survey Professional Paper 1463, p. 17–23.

Yingst, R.A., and Gregg, T.K.P., 2009, Lunar geologic mapping: A preliminary map of a portion of the Marius Quadrangle: Houston, Texas, Lunar and Planetary Institute, Lunar and Planetary Science Conference XL, CD-ROM, abstract 1319.

Zhang, J., and Jolliff, B.L., 2008, Aristarchus Region: A potential location for future surface exploration: Houston, Texas, Lunar and Planetary Institute, Lunar and Planetary Science Conference XXXIX, CD-ROM, abstract 2534.

Zimbelman, J.R., Garry, W.B., Johnston, A.K., and Williams, S.H., 2008, Emplacement of the 1907 Mauna Loa basalt flow as derived from precision topography and satellite imaging: Journal of Volcanology and Geothermal Research, v. 177, no. 4, p. 837–847, doi:10.1016/j.jvolgeores.2008.01.042.

Zisk, S.H., Hodges, C.A., Moore, H.J., Shorthill, R.W., Thompson, T.W., Whitaker, E.A., and Wilhelms, D.E., 1977, The Aristarchus-Harbinger region of the Moon: Surface geology and history from recent remote sensing observations: The Moon, v. 17, p. 59–99, doi:10.1007/BF00566853.

Manuscript Accepted by the Society 26 August 2010

Printed in the USA

The Geological Society of America
Special Paper 477
2011

*The geology of Schrödinger basin: Insights from post–*Lunar Orbiter *data*

Scott C. Mest
Planetary Science Institute, 1700 E. Ft. Lowell Road, Suite 106, Tucson, Arizona 85719-2395, USA, and
Planetary Geodynamics Laboratory (Code 698), National Aeronautics and Space Administration (NASA) Goddard Space Flight Center, Building 34, Room S288, Greenbelt, Maryland 20771, USA

ABSTRACT

The lunar south polar region (60°S–90°S) is being mapped at 1:2,500,000 scale using spacecraft data (*Lunar Reconnaissance Orbiter*, *Clementine*, *Lunar Prospector*, and *Lunar Orbiter*) to characterize geologic units, recognize contacts and structures, and identify impact craters (diameter [*D*] >2 km) for age dating. Most of the map area is located within the South Pole–Aitken basin, the largest (~2600 km) and oldest basin known on the Moon. At 18 km deep, South Pole–Aitken basin is believed to have exposed materials from the Moon's lower crust or upper mantle. Several large impact basins, such as Schrödinger basin (*D* = 334 km), are superposed on the floor of South Pole–Aitken and may have excavated through the floor of the basin. Thus, the materials that form the primary basin structures (rim and peak-ring) of Schrödinger, as well as the materials that cover its floor, may be used as proxies for the ancient lunar crustal and/or upper-mantle materials. Characterization of the materials that constitute Schrödinger and geologic mapping of the basin have identified nine units within the Schrödinger assemblage organized into three groups: basin materials, the plains formation, and the volcanic formation. The volcanic and plains materials found on the floor of Schrödinger exhibit flat expanses with smooth to rough surfaces and are dissected by floor fractures. These materials are interpreted to consist of impact melt and/or were emplaced by effusive eruptions of mafic materials, and they are some of the youngest materials in the basin, ranging from early Imbrian to early Eratosthenian in age.

INTRODUCTION

The lunar South Polar Highlands preserve a long and complex history of impact cratering that ranges from ancient basin-forming events to formation of geologically recent small-diameter craters. In addition, this terrain has been subjected to millions of years of impact gardening and regolith development, resulting in the muted appearance of most landforms that is common to the lunar landscape. The region surrounding the lunar south pole is contained within the South Pole–Aitken impact basin (Fig. 1), the largest recognizable impact basin on the Moon (~2600 km in diameter) (Stuart-Alexander, 1978; Wilhelms et al., 1979; Spudis et al., 1994). The entire basin exhibits ~18 km of relief, and it is believed that the South Pole–Aitken basin-forming event exposed deep crustal, and perhaps upper-mantle, material of the moon (Pieters et al., 2001). The unique material exposed within

Mest, S.C., 2011, The geology of Schrödinger basin: Insights from post–*Lunar Orbiter* data, *in* Ambrose, W.A., and Williams, D.A., eds., Recent Advances and Current Research Issues in Lunar Stratigraphy: Geological Society of America Special Paper 477, p. 95–115, doi:10.1130/2011.2477(04).

South Pole–Aitken was identified and classified as South Pole–Aitken terrane by Jolliff et al. (2000) and is characterized by high thorium and iron anomalies (e.g., Lawrence et al., 1998, 2000, 2002a, 2002b, 2003; Jolliff et al., 2000) relative to the surrounding feldspathic lunar highlands.

Numerous impact craters have subsequently formed on the floor of South Pole–Aitken basin, and many of them may have been large enough to penetrate the floor of South Pole–Aitken, thus exposing deep crustal materials. One impact basin located within South Pole–Aitken of particular interest is Schrödinger basin. Schrödinger basin (334 km in diameter), located at 76°S, 134°E, is believed to be an Imbrium-aged impact feature (Wilhelms et al., 1979; Shoemaker et al., 1994) that is part of a population of impact basins (including Orientale basin) that represent the last stages of multiring basin-forming events during the Late Heavy Bombardment on the Moon. Schrödinger basin is one of the best preserved impact features of its size and age, and it provides a unique opportunity for analysis.

Geologic mapping of the Schrödinger basin has revealed a number of plains units on its floor that likely consist of impact melt resulting from the Schrödinger impact event, and others interpreted to be volcanic in nature. The basin contains volcanically derived plains units that are unique to the South Pole region and could provide information about the thermal history of the

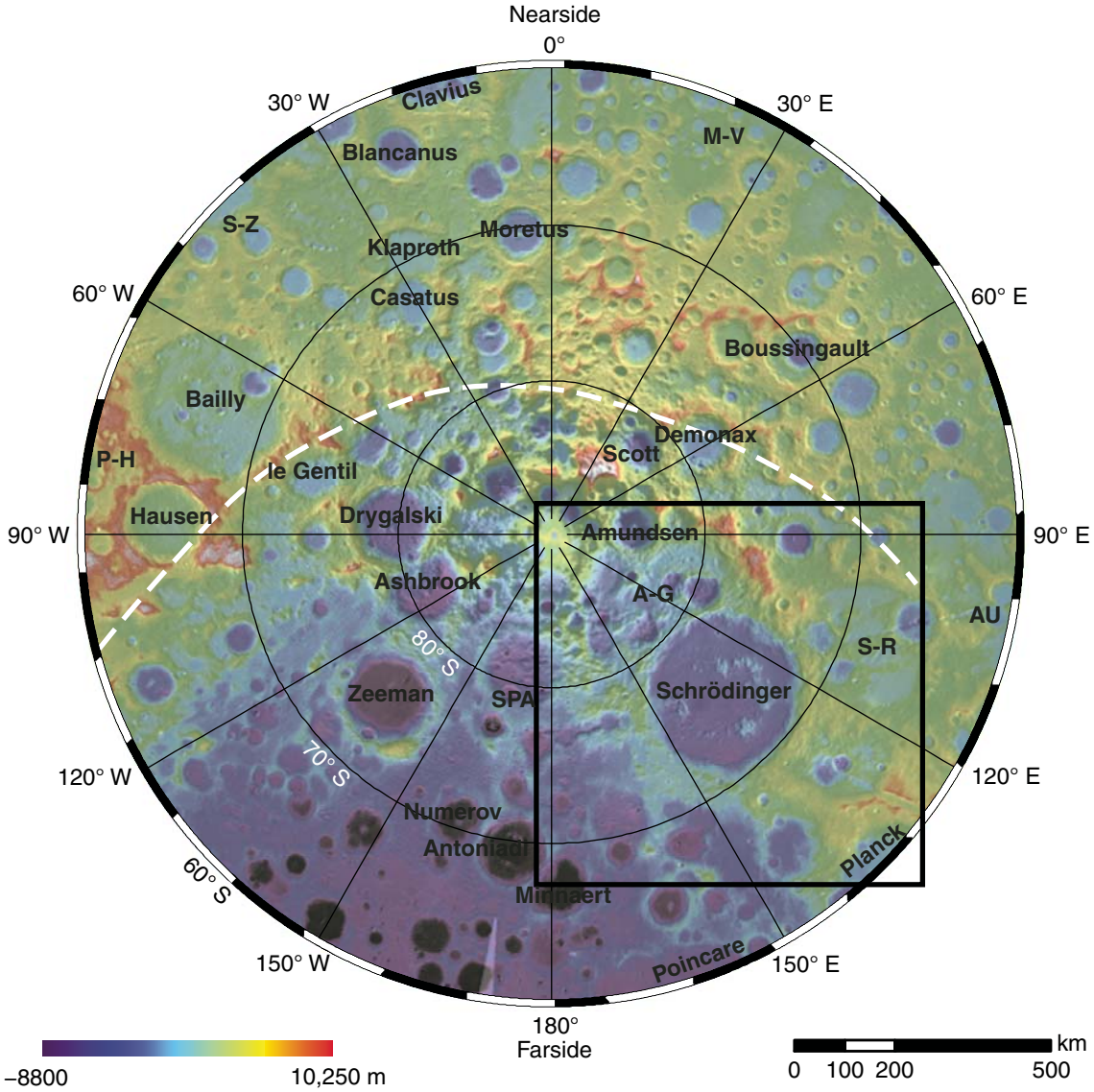

Figure 1. *Lunar Orbiter* Laser Altimeter gridded digital elevation model (DEM; 240 m/pixel) over *Clementine* Ultraviolet/Visible 750 nm mosaic of the lunar south polar area showing some of the larger basins (A-G—Amundsen-Ganswindt, AU—Australe, M-V—Mutus-Vlacq, P-H—Pingré-Hausen, S-R—Sikorsky-Rittenhouse, S-Z—Schiller-Zucchius, SPA—South Pole–Aitken) and craters, the rim of South Pole–Aitken (white dashed line), and the location of Figure 2 (black box). Projection is polar stereographic.

post–South Pole–Aitken and post-Schrödinger crust. Through geologic mapping and analysis of *Lunar Reconnaissance Orbiter* Camera (LROC) and *Clementine* Ultraviolet Visible (UVVIS 750 nm) images, Clementine UVVIS-derived color ratio data, and *Lunar Reconnaissance Orbiter* Lunar Orbiter Laser Altimeter (LOLA) topographic data, this paper provides insights into (1) the volcanic history within the basin and the nature of volcanism in this part of the south polar region, (2) the stratigraphy of the materials found on the basin floor, and (3) Schrödinger's relevance in the history of the South Pole–Aitken basin.

The Moon will likely play a key role in the development and targeting of robotic, and possibly human, exploration over the next decades. Schrödinger basin has been named as a National Aeronautics and Space Administration (NASA) Constellation region of interest for LROC targeting (Gruener and Joosten, 2009), and several groups have used Schrödinger basin as a planned destination for long-distance traverse analyses from a south polar outpost (Weisbin et al., 2010) or as a destination for a future landing site (Kohout et al., 2009). Recent interest in Schrödinger basin shows its geologic importance with respect to other lunar craters. Generation of a geologic map and characterization of the basin's geology, as shown in this paper, can be used by future studies as a resource for mission planning.

REGIONAL GEOLOGIC SETTING

Schrödinger basin, centered at 76°S, 134°E, is located on the lunar farside on the floor of the South Pole–Aitken (Fig. 1). Regionally, the highest elevations (~7 km) are located on the nearside and are associated with highland terrains, and the lowest elevations are located on the farside on the floor of Antoniadi crater (~–9 km). The nearside polar region consists predominantly of cratered highlands, is more heavily cratered, and displays generally higher elevations than the farside. This difference is due to the overwhelming presence of the South Pole–Aitken impact basin, which encompasses nearly all of the farside south polar region.

South Pole–Aitken is the largest (diameter [*D*] = 2600 km) and oldest (pre-Nectarian) impact basin identified on the Moon (Stuart-Alexander, 1978; Wilhelms et al., 1979; Spudis et al., 1994), and it exhibits nearly 18 km of relief. Scaling models (e.g., Melosh, 1989; Cintala and Grieve, 1998) suggest that the South Pole–Aitken impact event could have excavated materials down to the lower crust (~52–54 km deep), possibly exposing upper-mantle material (Wieczorek et al., 2006). Several remote-sensing studies support this hypothesis. *Galileo* and *Clementine* multispectral data show enrichment in mafic materials within South Pole–Aitken basin (Belton et al., 1992; Head et al., 1993; Lucey et al., 1995, 1998; Pieters et al., 1997, 2001), and *Lunar Prospector* Gamma Ray Spectometer data show enhancements in both iron and thorium within the basin relative to the surrounding highlands (Lawrence et al., 1998, 2002a, 2002b; Jolliff et al., 2000). It is believed that the South Pole–Aitken impact event, combined with subsequent local volcanism within the basin and reworking of basin floor materials by impacts, resulted in the compositionally unique terrane currently observed at the surface, which has been characterized as the South Pole–Aitken terrane by Jolliff et al. (2000). Although the composition of most of the exposed materials within South Pole–Aitken has likely been altered by billions of years of surface impacts and space weathering or buried by subsequent eruptions of localized mare and pyroclastic deposits, some materials exposed within South Pole–Aitken basin, such as crater walls, central peaks, peak-rings, impact melt, and volcanic deposits, could be used as proxies for estimating the composition of the lower crust and/or upper mantle.

Impact features within the south polar region range in size from the limits of image resolution (hundreds of meters) to 2600 km in diameter (South Pole–Aitken) and display a variety of morphologies, ranging from simple to complex craters, to central peak-ring, peak-ring, and multiring basins (Fig. 1) (Wood and Andersson, 1978; Wilhelms et al., 1979; Wilhelms, 1987). The south polar region hosts all or part of 46 impact features greater than 100 km in diameter, including Schrödinger basin, which would have significantly affected the structure of the crust and redistributed large amounts of material across the surface. Previous mapping by Wilhelms et al. (1979) showed that materials exposed at the surface in the south polar region consist predominantly of pre-Nectarian–aged (e.g., Australe, Poincaré, Amundsen-Ganswindt, and Planck basins), Nectarian-aged (e.g., Bailly basin), and early Imbrian–aged (e.g., Schrödinger basin; discussed in more detail in the following paragraphs) impact crater–derived materials (i.e., impact crater melt, and crater rim and ejecta materials). Based on mapping by Wilhelms et al. (1979), the western farside quadrant of the south polar region is largely covered by impact materials from Schrödinger, including the crater and its ejecta blanket, which were determined to be Nectarian in age. Only a small portion, the area in the center of Schrödinger and several small patches outside of Schrödinger's peak-ring, was characterized as Imbrian in age (Wilhelms et al., 1979).

METHODOLOGY

The Schrödinger basin, as part of the regional lunar south polar study, is being mapped in polar stereographic projection at 1:2,500,000 scale in accordance with standard principles for geologic mapping of planetary surfaces (Wilhelms, 1972, 1990; Tanaka, 1994). For this project, Arc Geographic Information System software (ArcGIS, v. 9.2) is utilized to map layers (e.g., image mosaics, topography, spectral maps), and the mapping is conducted using digital mapping techniques supported by the NASA Planetary Geologic Mapping Program.

A GIS database containing base maps—*Clementine* 5-band UVVIS and 6-band Near Infrared (NIR) mosaics, *Lunar Orbiter* photomosaic, and LOLA topographic data—as well as derived data (e.g., slope maps, *Clementine* color ratio and iron maps), and LROC images are being used to construct the geologic map of Schrödinger basin. The *Clementine* UVVIS 750 nm mosaic is being used as the primary base, but all data sets are being used

to characterize geologic units from surface texture and albedo, identify unit contacts, and identify impact craters (greater than 1 km in diameter) for calculation of crater size-frequency distribution statistics and unit age determination. The *Clementine* UVVIS 750 nm mosaic makes an ideal mapping base due to the consistency in image-to-image resolution and lighting.

Geologic mapping and surface analyses are based primarily on *Clementine* UVVIS 750 nm images (100–325 m/pixel) and the global UVVIS 750 nm mosaic (averaged to 100 m/pixel) (Eliason et al., 1999), the global NIR 1100 nm mosaic (Eliason et al., 2003; Gaddis et al., 2007), high-resolution camera (HIRES; 7–20 m/pixel) images, and wide-angle (100 m/pixel visible, 400 m/pixel ultraviolet [UV]) and narrow-angle (0.5 m/pixel) *Lunar Reconnaissance Orbiter* LROC images (Robinson et al., 2010a, 2010b). *Lunar Orbiter IV* and *V* data (images ~100 m/pixel) and the global mosaic (Becker et al., 2008) are used to complement the other image data sets.

Spectroscopic data provide some of the most unique views of the lunar surface. *Clementine* UVVIS-derived color ratio data are used to characterize geologic materials and assess their lateral distribution. The *Clementine* UVVIS and NIR wavelengths provide mineralogic information about lunar surface materials (Nozette et al., 1994). For this study, the *Clementine* UVVIS-derived color ratio map (e.g., Pieters et al., 1994, 2001), which uses the 750/415 nm (red), 750/950 nm (green), and 415/750 nm (blue) wavelengths, is used to provide first-order compositional information about the geologic materials exposed on the floor of Schrödinger basin. This combination of wavelengths has been shown to provide a relative assessment of mafic versus felsic composition, which appear orange-red to green-blue, respectively (e.g., Pieters et al., 1994, 2001). However, low sun angles near the lunar south pole yield poor data with regard to using the UVVIS-derived products, especially on steep slopes. Therefore, these data are only used to investigate materials where phase angle and topographic effects are less significant, such as on the floor of the basin.

Lastly, this study uses *Lunar Reconnaissance Orbiter* LOLA topographic data (Fig. 1) to characterize the topographic expression of the surface in and around Schrödinger basin. Currently, the basin is covered by ~470 LOLA tracks, and gridded topographic data provide coverage at a resolution of 240 m/pixel (e.g., Smith et al., 2010a, 2010b).

GEOLOGY OF SCHRÖDINGER BASIN

This section summarizes observations made for Schrödinger basin using the methodology described previously (data analysis and geologic mapping). The Schrödinger basin is morphologically one of the least modified lunar impact basins of its size (Fig. 2). Schrödinger is believed to be early Imbrian in age (Wilhelms et al., 1979; Shoemaker et al., 1994) and is likely one of the last major basin-forming impact events on the Moon, only slightly older than the Orientale impact, which emplaced secondary craters on Schrödinger's floor (Shoemaker et al., 1994).

Basin Morphometry

Morphometric parameters for Schrödinger basin were measured using LOLA topographic data. Diameters (basin rim and peak-ring) are measured from rim-crest to rim-crest (or peak-ring crest) along orthogonal north-south and east-west transects and are defined as the averages of these values. Basin depth is measured from the maximum elevation along the basin rim to the lowest point on the floor. Schrödinger (Fig. 3) exhibits a 334-km-diameter outer ring that defines its topographic rim, and a 168-km-diameter inner peak-ring represented by a discontinuous ring of mountains. The western and northern parts of the rim are ~2.6 km and 2.2 km in elevation, respectively, whereas the eastern and southern parts of the rim are ~–1.1 km and –1.7 km in elevation, respectively. The basin is ~8 km deep (2.6 km maximum rim elevation to –4.9 minimum floor elevation), and it exhibits a depth:diameter ratio of 0.024.

The interior wall of Schrödinger displays an average slope of ~0.2°. Terraces are found along all parts of the interior wall except for the eastern part, which shows the lowest rim relief. In general, the terraces start at the base of a scarp inside the rim and continue stepwise in a zone ~20–50 km wide to the floor of the basin. Schrödinger terraces likely consist of slump blocks formed by failure of wall material immediately after the basin-forming impact event (Melosh, 1989).

Geologic Materials

Mapping of Schrödinger basin has identified nine distinct units that constitute the Schrödinger assemblage and are organized into three groups: basin materials, plains formation, and volcanic formation. These materials include the rocks that constitute the rim, wall, and peak-ring materials, as well as the "plains"-forming materials that were emplaced on the basin floor subsequent to the basin's formation (Fig. 4).

Schrödinger Basin Materials

Schrödinger peak-ring material (unit INspr) and Schrödinger basin rim material (unit INsr) form the primary structure of Schrödinger basin. The peak-ring material forms an incomplete ring (~168 km in diameter) of mountainous terrain around the center of Schrödinger basin (Figs. 2 and 4). The peak-ring is continuous and most rugged along the southwestern to northern parts of the ring, is composed of discontinuous knobs along the northeastern arc of the ring, is mountainous again in the east, and is not found in the southeast. Schrödinger peak-ring material displays moderate albedo in *Clementine* images but is mottled in high-resolution LROC images, in which interpeak areas generally contain darker materials with hummocky surfaces (Fig. 5). LROC images also show that the regolith on peak-ring material is overprinted with "elephant-skin" or "tree bark" texture (Fig. 5), common to most surfaces on the Moon (Schultz, 1972), which shows patterns of small-scale hummocks separated by intersecting lineations that form parallel and perpendicular to local

slopes. This texture is interpreted to form by slow mass-wasting processes similar to soil creep (Crittenden, 1967; Greeley, 1971). Some peaks expose blocky outcrops of peak-ring material that shed boulders downslope. Peak-ring material is interpreted to consist of pre-Schrödinger crustal materials that were uplifted (Melosh, 1989; Spudis, 1993) following the impact event. Dark areas between peaks could contain impact melt emplaced after the impact event.

Portions of the peak-ring are intersected by fractures, which are the dominant structures within the basin (Figs. 2 and 4). These arcuate to linear features occur concentric and radial to the basin rim. The fractures predominantly bisect materials that are plains-forming units, but the fractures are also observed to cut the peak-ring in several locations. These features are only a few kilometers wide, and most are tens to a few hundred kilometers long. The fractures on the floor of Schrödinger basin appear similar to other floor-fractured craters (Schultz, 1976) that are interpreted to have formed as magma rises into fractures and ponds in the shallow subsurface; the resulting pressure lifts the crater floor and forms fractures at the surface. Shoemaker et al. (1994) suggested that these features reflect pre-Schrödinger faults and fractures in the lunar crust that propagated throughout the peak-ring and plains materials as the basin floor underwent rebound following basin formation.

Schrödinger basin rim material (unit INsr) includes the materials that form the topographic rim crest and the interior wall of Schrödinger basin (Figs. 2 and 4). The outer and inner boundaries of this unit are defined by relatively distinct slope breaks where

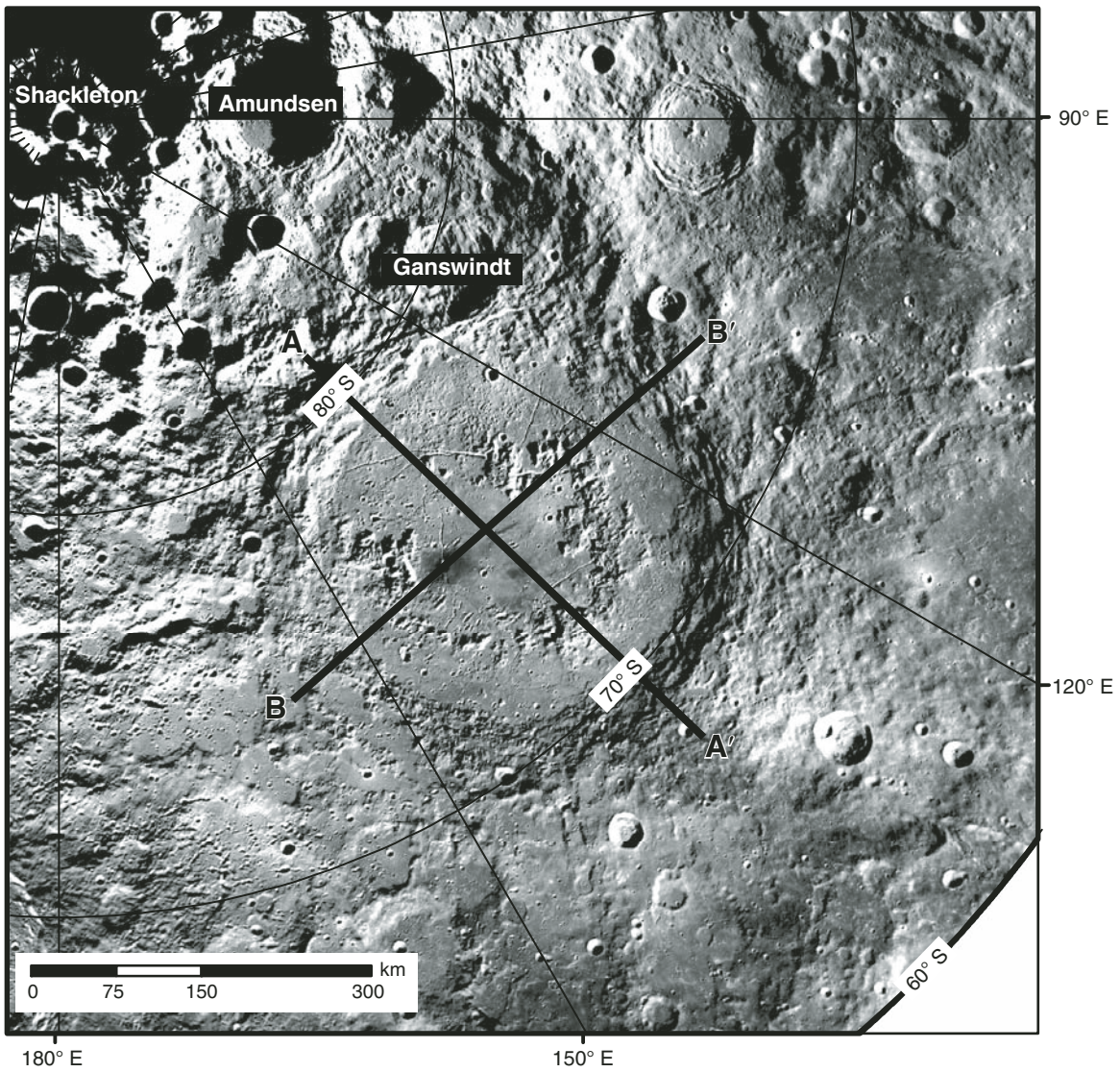

Figure 2. Part of the *Clementine* Ultraviolet/Visible 750 nm mosaic showing a close-up view of Schrödinger basin and surrounding terrain. The locations of profiles A and B (heavy black lines) across Schrödinger (Fig. 3) are shown. Projection is polar stereographic.

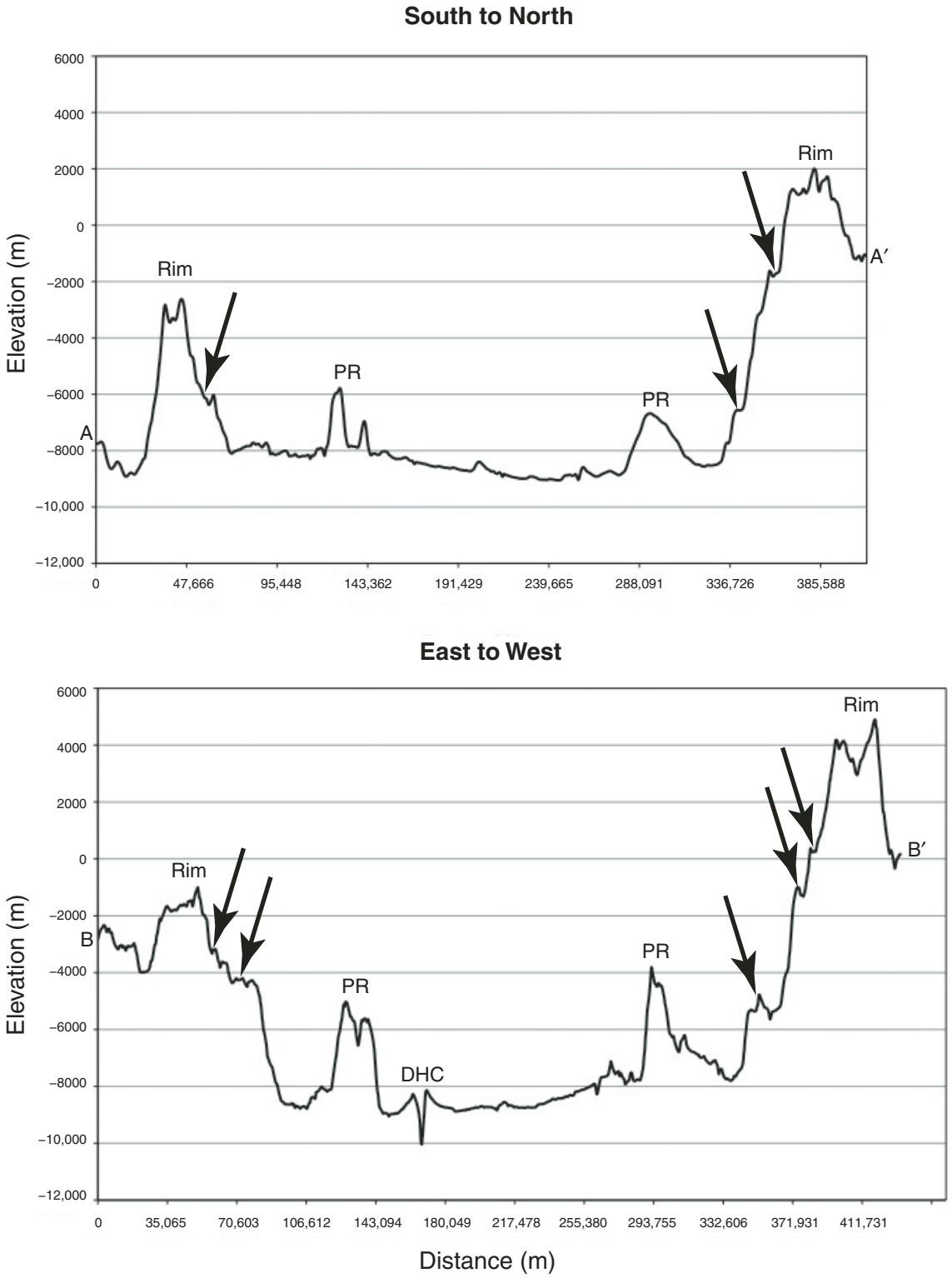

Figure 3. Topographic profiles A and B, generated from Lunar Orbiter Laser Altimeter gridded data, showing the differences in rim height between the south and north (A–A′) and east and west (B–B′) sides of Schrödinger's rim. Also note the differences in floor elevation throughout the basin, which are likely due to emplacement of wall materials on the basin's floor via slumping and mass wasting, as well as distribution of impact melt and emplacement of varying amounts of volcanic materials on the basin floor. Also shown are the peak-ring (PR), terraces (arrows), and the dark-halo crater (DHC).

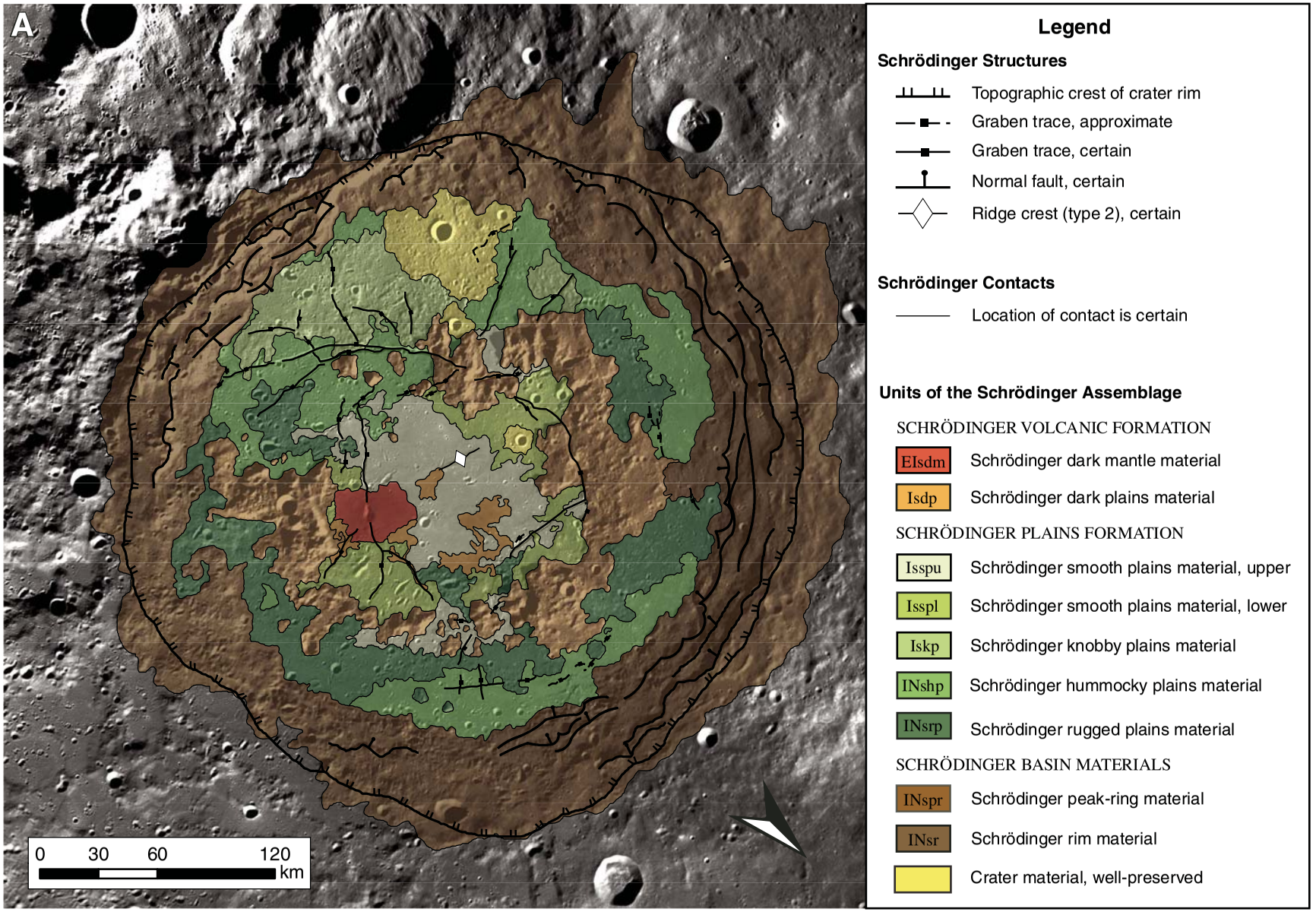

Figure 4 (*Continued on following page*). (A) Geologic map of Schrödinger basin. Projection is polar stereographic. Center latitude/longitude is 76°S, 134°E.

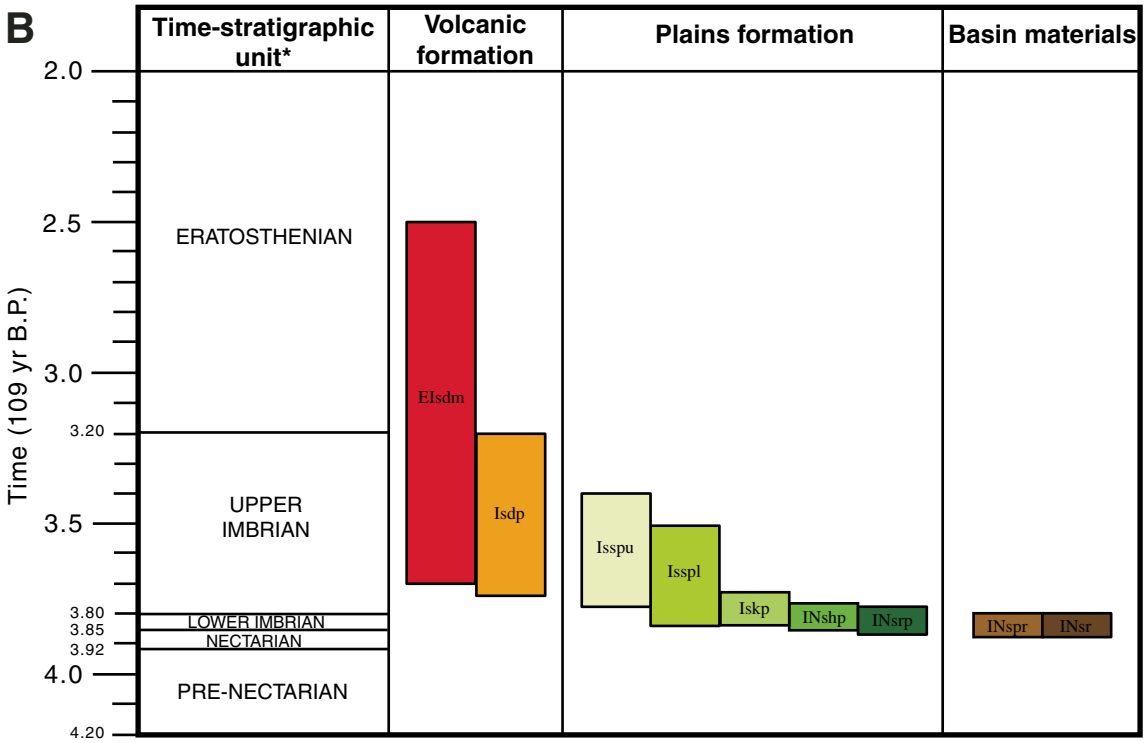

Figure 4 (*Continued*). (B) Correlation of map units. *—Wilhelms (1987). *Note:* Ages of units identified in this mapping effort of Schrödinger basin do not extend beyond the lower Eratosthenian, so the Copernican and upper part of the Eratosthenian Periods are not shown.

the "rim" meets the shallower slopes of the intercrater highland plains and the wall meets the basin floor, respectively. The interior walls of Schrödinger are deformed by a series of nested normal faults whereby rim material is faulted downward toward the center of the basin, resulting in a series of fault scarps and terraces. Formation of these features is due to slumping of material following formation of the transient basin of Schrödinger (Melosh, 1989; Spudis, 1993). Similar to peak-ring material, the regolith formed on basin rim material is overprinted with "elephant-skin" texture. Based on models of impact basin formation (e.g., Melosh, 1989; Spudis, 1993), the Schrödinger basin rim material is interpreted to consist of pre-Schrödinger materials overturned and uplifted during the Schrödinger impact event, as well ejecta emplaced on the basin's rim and wall, and postimpact wall materials that underwent mass wasting and were emplaced along the base of the wall via landslides (Shoemaker et al., 1994).

Schrödinger Plains Formation

The floor of Schrödinger basin is filled with relatively flat-laying plains-forming materials that display various surface textures and albedos. Five plains-forming units are identified on the floor of Schrödinger that form the Schrödinger plains formation. Superposition and crosscutting relationships with adjacent units and structures indicate that Schrödinger rugged plains material (unit INsrp) is stratigraphically the oldest plains material on the floor of Schrödinger basin. Exposures of INsrp (Figs. 4 and 6A) are found outside of the peak-ring and are generally higher in elevation than other plains units on the floor of Schrödinger (Fig. 3). In *Clementine* images, INsrp appears as knobby plateaus and massifs of moderately high albedo (Fig. 6A); however, in LROC images, the rugged plains appear rugged due in part to a relatively high density of superposed small-diameter impact craters (Fig. 6B), likely consisting of both primary and secondary populations. These materials embay peak-ring and basin wall materials, and most exposures are cut by floor fractures. Secondary craters, likely from the Orientale and Antoniadi impact events (Shoemaker et al., 1994), are dispersed within this unit in the eastern and northern parts of the basin. Surface textures, although muted by billions of years of regolith development and modification by impacts, and this unit's isolation between the peak-ring and basin wall suggest that the rugged plains material likely consists predominantly of impact melt that resulted from basin formation. In addition, the presence of secondary craters from both nearby (Antoniadi) and large (Orientale) impacts suggests that a portion of the rugged plains may contain ejecta from these impact events (Shoemaker et al., 1994).

Schrödinger hummocky plains material (unit INshp) occupies much of the floor along the northern and western walls

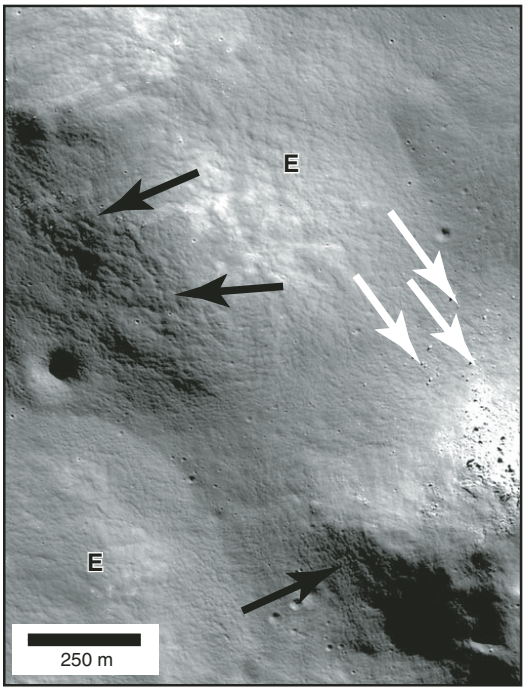

Figure 5. Part of *Lunar Reconnaissance Orbiter* Camera image (M106068472R) showing "elephant-skin" terrain (E) or "tree-bark" terrain that is common to many lunar surfaces and is believed to have formed by creep (Crittenden, 1967; Greeley, 1971; Schultz, 1972). Here, on the peak-ring, dark material (black arrows) fills between peaks, whereas on the opposite slope, the elephant terrain forms by hummocks separated by lineations perpendicular and parallel to the local slope. Outcrops of peak-ring material are observed to shed boulders downslope (white arrows). Image is centered at 73.8°S, 123.1°E; north is to the top; resolution is 0.786 m/pixel; National Aeronautics and Space Administration/Goddard Space Flight Center/Arizona State University.

within Schrödinger basin, and in the south where the peak-ring is the most discontinuous (Figs. 4 and 6A). At all scales, hummocky plains display moderately cratered, low albedo surfaces with gently rolling topography (Fig. 6C). These materials embay peak-ring and basin wall materials where they are in contact. Contacts between INshp and INsrp are difficult to discern in some places, but the differences in albedo, ruggedness, and density of superposed craters allow these materials to be mapped as separate units. The southern exposure of hummocky plains material is cut by floor fractures, and a few secondary craters believed to come from Antoniadi crater have been identified within all exposures (Shoemaker et al., 1994). The hummocky plains material is interpreted to consist of impact melt emplaced after basin formation and after emplacement of the rugged plains material. The location of these materials, primarily along the basin wall, suggests that these materials may be composed of impact melt that ran off the basin walls and collected at the base of the basin wall (Shoemaker et al., 1994). If INsrp is mantled by a thin layer of ejecta from Antoniadi and/or Orientale, lack of this mantle on INshp could explain the observed differences between these units despite their similar origin.

Schrödinger smooth plains material consists of an upper and lower member and forms most of the floor inside the peak-ring. These materials embay peak-ring and rugged plains materials where they are in contact. The lower member of Schrödinger smooth plains material (unit Isspl) is found just inside the peak-ring (Fig. 4); the unit displays moderate to high albedo and contains fewer superposed craters than the rugged and hummocky plains (Fig. 7A). Most of the secondary craters superposed on the floor of Schrödinger basin that are believed to be have originated from the Antoniadi crater are found primarily

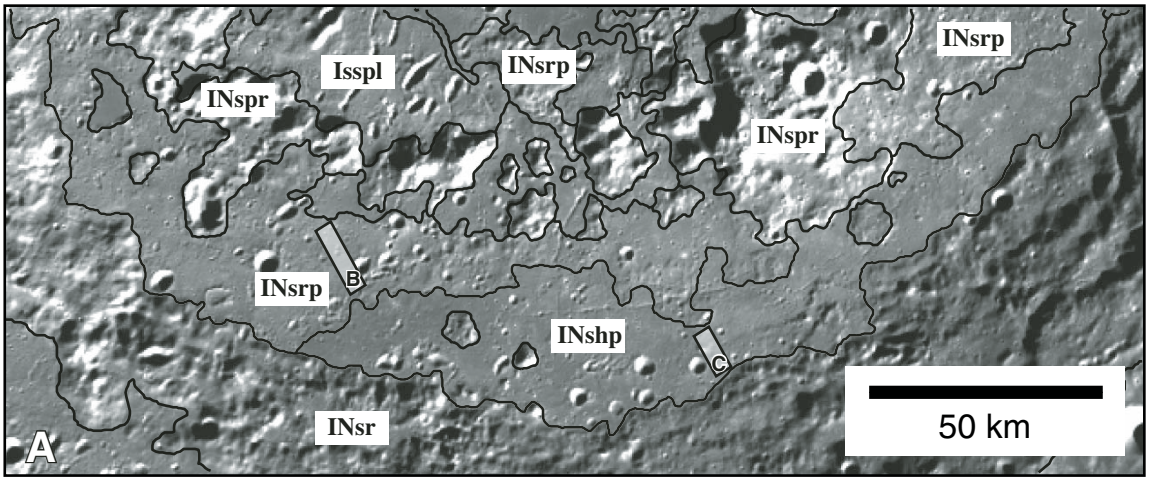

Figure 6 (*Continued on following page*). (A) Northern part of Schrödinger basin showing a closer view of contacts in this part of the basin. Here, rugged plains material (INsrp) appears topographically higher than hummocky plains material (INshp), but the hummocky plains superpose the rugged plains. *Clementine* Ultraviolet/Visible 750 nm mosaic; image centered at 72.7°S, 139.1°E; projection is polar stereographic. Rectangles B and C represent Figure 6B and Figure 6C, respectively.

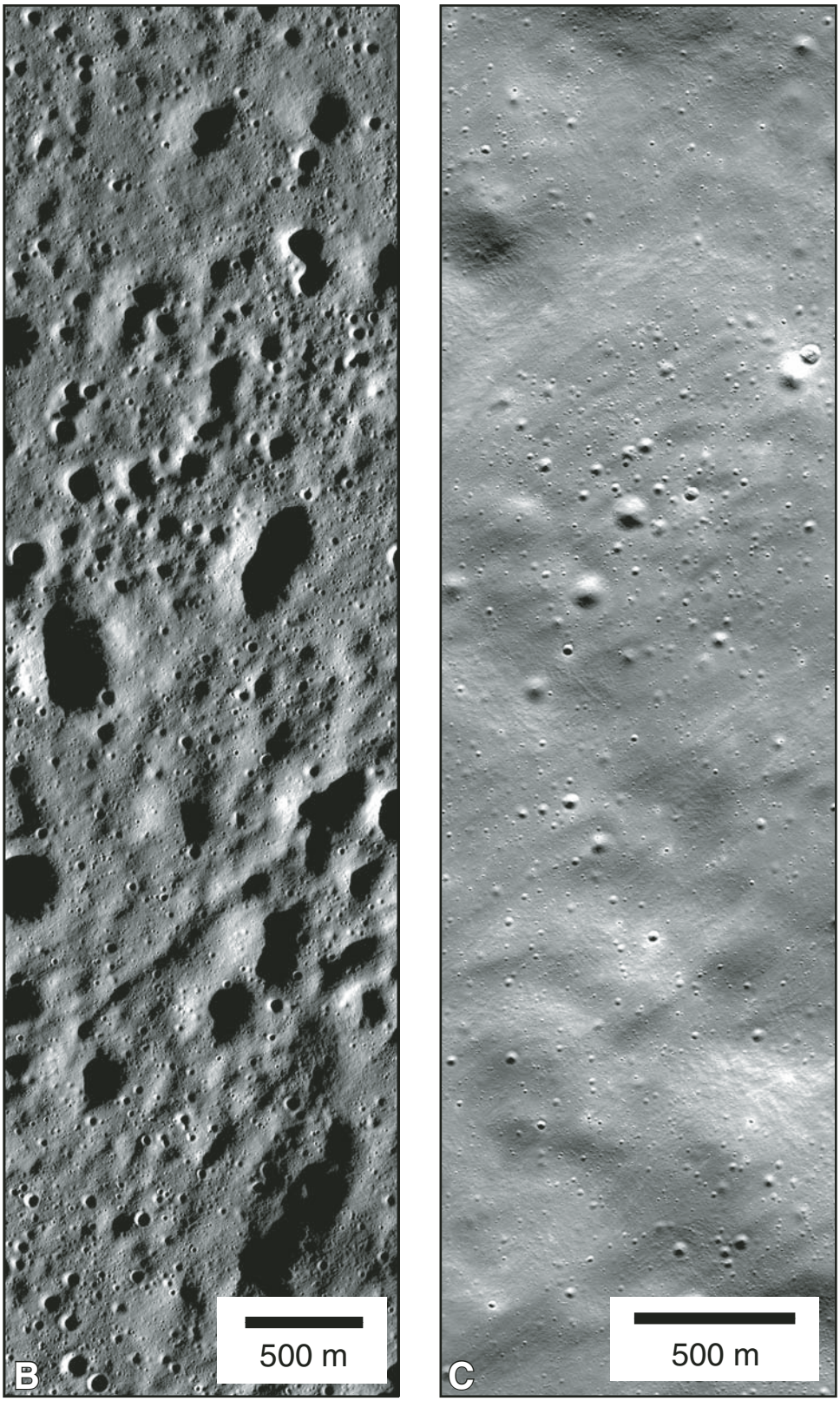

Figure 6 (*Continued*). Parts of *Lunar Reconnaissance Orbiter* Camera images (B) M115361568R (resolution is 1.01 m/pixel; image centered at 73.3°S, 144.4°E) and (C) M108320101R (resolution is 0.790 m/pixel; image centered at 71.2°S, 139.1°E) showing the Schrödinger rugged plains material and Schrödinger hummocky plains material, respectively. North is to the bottom in both images; National Aeronautics and Space Administration/Goddard Space Flight Center/Arizona State University.

within this lower member in the eastern part of the basin (Shoemaker et al., 1994). The upper member of Schrödinger smooth plains material (unit Isspu) is found primarily in the center of Schrödinger basin, but two small exposures are found among the peak-ring massifs in the southwestern and northeastern parts of the peak-ring (Fig. 4). The upper member displays an overall smooth surface that is lower in albedo and slightly less cratered than the lower member (Fig. 7A), and the upper member embays the lower member where they are in contact (Fig. 7B). Most exposures of the smooth plains are cut by floor fractures, but the fractures in the upper member are shallower and less defined than in the lower member and other plains materials within Schrödinger. Wilhelms et al. (1979) interpreted this material as Orientale and/or Imbrium impact ejecta; however, as Shoemaker et al. (1994) noted, if this material were a thin ejecta deposit, superposed craters could have excavated to the Schrödinger melt sheet, and thus an albedo contrast should be observed. This unit's smooth surface texture, or rather its lack of rugged or hummocky textures, allows it to be separated from these other units. Here, Schrödinger smooth plains are interpreted to consist of impact melt or early stage volcanic materials erupted, possibly via floor fractures, and emplaced after basin formation.

Based on the *Clementine* color ratio map, units INsrp, INshp, and Issp appear spectrally similar, exhibiting an orange-red signature (Fig. 8), suggesting a mafic composition. However, recent spectral measurements by Shankar et al. (2010) indicate that these plains (INsrp, INshp, Issp) are anorthositic in composition. This compositional ambiguity likely reflects (1) mixing of anorthositic highland country rock with underlying mafic materials at the time of impact, and/or (2) mafic materials, emplaced at the time of impact (as impact melt and/or volcanic eruptions), mixed with an overlying mantle of anorthositic ejecta from nearby impact craters.

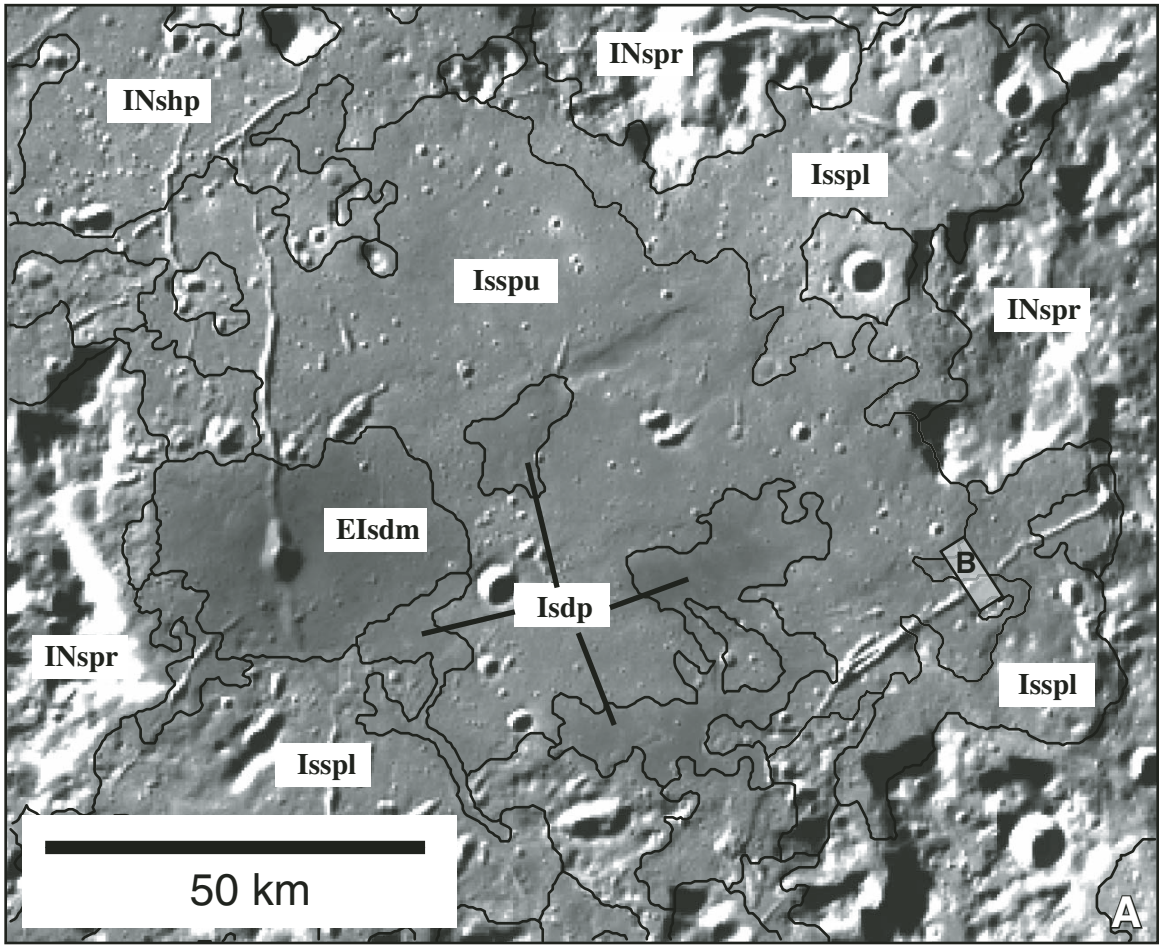

Figure 7 (*Continued on following page*). (A) Central part of Schrödinger basin showing a closer view of contacts in this part of the basin. Here, the floor inside the peak-ring is occupied predominantly by materials interpreted to be volcanic in origin, including the upper and lower members of the Schrödinger smooth plains material (Isspu and Isspl), Schrödinger dark plains material (Isdp), and Schrödinger dark mantle material (EIsdm). *Clementine* Ultraviolet/Visible 750 nm mosaic; image centered at 74.6°S, 133.0°E; projection is polar stereographic. Rectangle B represents Figure 7B.

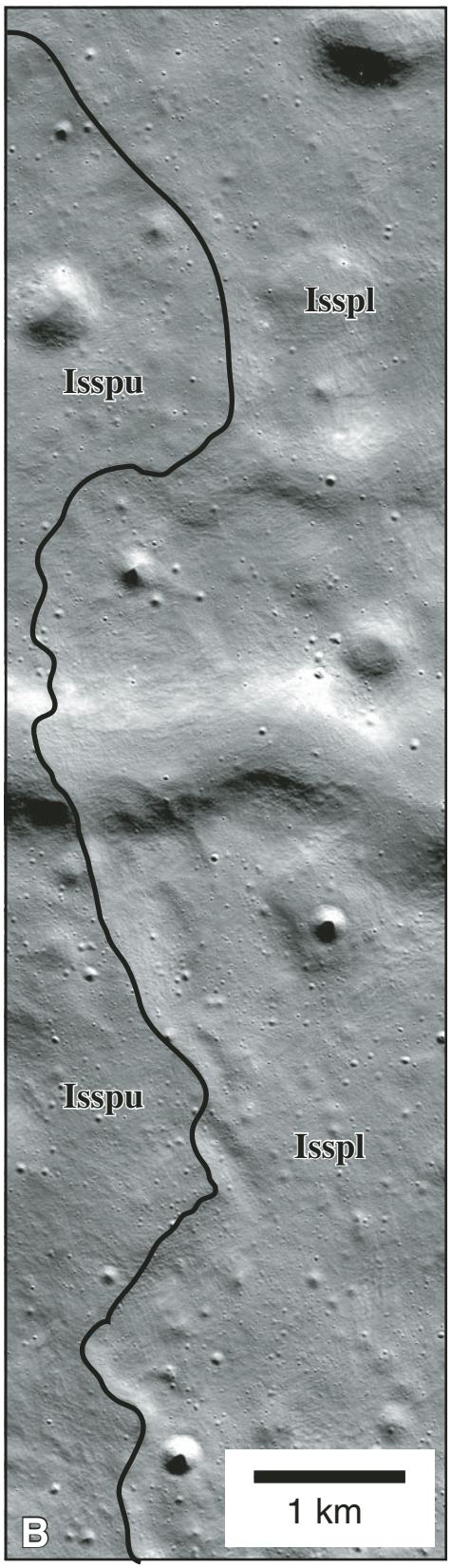

Lastly, the Schrödinger knobby plains material (unit Iskp) forms two fairly high-albedo deposits along the southern basin wall (Figs. 4 and 9). The edges of these deposits are lobate, and these materials embay peak-ring and basin wall materials where they are in contact. The knobby plains exhibit clusters of rounded and elongated knobs similar to the ejecta deposit surrounding a small (~8.5 km diameter) crater along the southern wall. Floor fractures within this unit are subdued relative to those that cut other Schrödinger plains units and suggest burial by this unit. The Schrödinger knobby plains material is interpreted to consist of ejecta from a nearby impact that was emplaced on the floor of Schrödinger, and/or wall material emplaced via mass wasting. If ejecta, Ganswindt or Amundsen craters appear to be two likely candidates. Ganswindt crater (D = 74 km) is located on or just outside of Schrödinger's southern rim; its proximity to Schrödinger makes assessing crosscutting relationships between these structures difficult. Furthermore, Ganswindt appears more degraded relative to other craters similar in size, as well as Schrödinger, suggesting Ganswindt may predate Schrödinger and could not have contributed ejecta to Schrödinger's floor. Amundsen crater (D = 101 km), located ~150 km to the south, is younger than Schrödinger, but Amundsen may be too far away for either its continuous or distal ejecta (Moore et al., 1974; Melosh, 1989) to be preserved within Schrödinger. Alternatively, these plains could be composed of basin wall materials that were emplaced by landslides due to failure of Schrödinger's southern wall.

Schrödinger Volcanic Formation

Volcanic materials are concentrated in the northern and eastern parts of the basin inside Schrödinger's peak-ring. Four patches of Schrödinger dark plains material (unit Isdp) are found on the basin floor: Three are located around the deposit of Schrödinger dark mantle material (unit EIsdm, discussed later herein), and the fourth, and largest exposure, is located along the northern part of the peak-ring (Fig. 4). In *Clementine* images, these deposits display smooth, relatively featureless, low-albedo surfaces (Fig. 10A); however, in LROC images, the low-albedo surface is peppered with a high density of small-diameter impact craters (Fig. 10B). Within the northern deposit, a 21-km-long sinuous rille emerges from the smooth plains (upper member) and terminates within the dark plains (Figs. 10A and 10B). This is the only clearly identifiable rille to be observed on the floor of Schrödinger. Some exposures of the dark plains, such as those

Figure 7 (*Continued*). (B) Part of *Lunar Reconnaissance Orbiter* Camera image M110731705R showing a close-up of the upper and lower members of the Schrödinger smooth plains formation. Here, the upper member embays the lower member; both members superpose the fracture in the center of the image. North is to the bottom; resolution is 0.598 m/pixel; image centered at 73.2°S, 131.0°E; National Aeronautics and Space Administration/Goddard Space Flight Center/Arizona State University.

around the Schrödinger dark mantle materials (discussed later herein), are cut by floor fractures, but the fractures appear subdued compared to those found in other plains unit. In *Clementine* UVVIS-derived color ratio data (Fig. 8), deposits of dark plains appear orange and are distinct from surrounding plains material, suggesting that these deposits are more mafic in composition relative to other Schrödinger plains materials (Pieters et al., 1994, 2001). In addition, spectral measurements from Shankar et al. (2010) indicate that these areas are mafic in composition. In some areas, these deposits display indistinct contacts with adjacent materials, suggesting that parts of the dark plains get extremely thin toward the edges and/or maturation due to impact gardening has obscured contacts with adjacent units. The morphology of the Schrödinger dark plains material, their spectral appearance, and the presence of the rille suggest that these plains were emplaced as basaltic lavas (Shoemaker et al., 1994; Mest, 2007, 2008; Shankar et al., 2010).

The eastern part of Schrödinger, just inside the peak-ring, contains a small (~5 km in diameter) well-preserved ovoidal cone with its long axis trending approximately north-south (Fig.

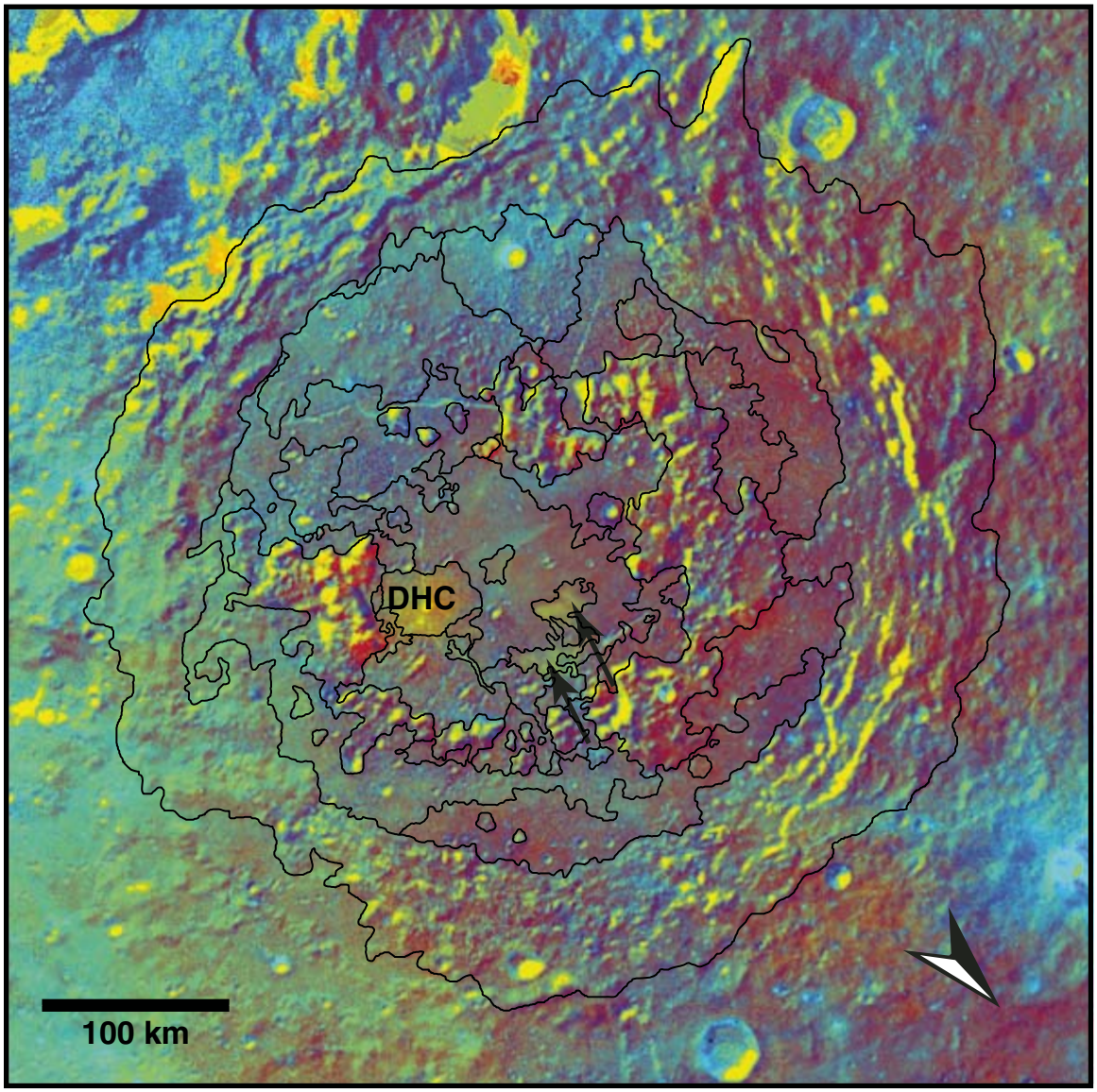

Figure 8. *Clementine*-derived color ratio map of Schrödinger basin with superposed contacts. This color ratio map, generated using the ratioed *Clementine* Ultraviolet/Visible data sets (R—750/415 nm; G—750/950 nm; and B—415/750 nm), was found to be the ideal combination to express mafic-rich (orange-red tones) and feldspathic (green-blue tones) materials (Pieters et al., 1994, 2001). In Schrödinger, the dark-halo crater (DHC) and surrounding dark mantle material appear yellow, and dark plains material (arrows) appears orange relative to the much redder surrounding basin floor materials. Image centered at 76°S, 134°E.

10A). The depression has been characterized as a "maar"-type crater (Shoemaker et al., 1994) and a "dark-halo crater" (Gaddis et al., 2003), and has been identified as the source of pyroclastic eruptions (Shoemaker et al., 1994; Gaddis et al., 2003). However, "maar" implies a specific endogenic process involving interactions between magma and significant amounts of water, which is unlikely given the lunar environment. Therefore, this conical feature is herein referred to as a dark-halo crater (DHC). This dark-halo crater displays ~500 m of relief above the surrounding plains and is ~400 m deep from floor to rim.

The dark-halo crater is surrounded by a deposit that exhibits a relatively smooth, lightly cratered surface with lower albedo than the surrounding plains materials (higher albedo compared to other lunar pyroclastic deposits; Gaddis et al., 2003), and it is mapped as Schrödinger dark mantle material (unit EIsdm; Figs. 4 and 10A). Schrödinger dark mantle material forms a small deposit that surrounds and forms the flank of the dark-halo crater and was previously mapped as mare by Wilhelms et al. (1979). The deposit is cut by floor fractures along a north-south trend that also intersect the dark-halo crater along its long axis; floor fractures within the deposit display subdued morphology, whereas outside of the deposit, the fractures are more pristine. Schrödinger dark mantle material is distinct from surrounding plains materials and Schrödinger dark plains material. The spectral signature of the deposit displays an unusually strong mafic band (950/750 nm vs. 750 nm) in *Clementine* UVVIS data, it but also displays similarities to lunar highland soils (Gaddis et al., 2003). Schrödinger dark mantle material appears yellow in

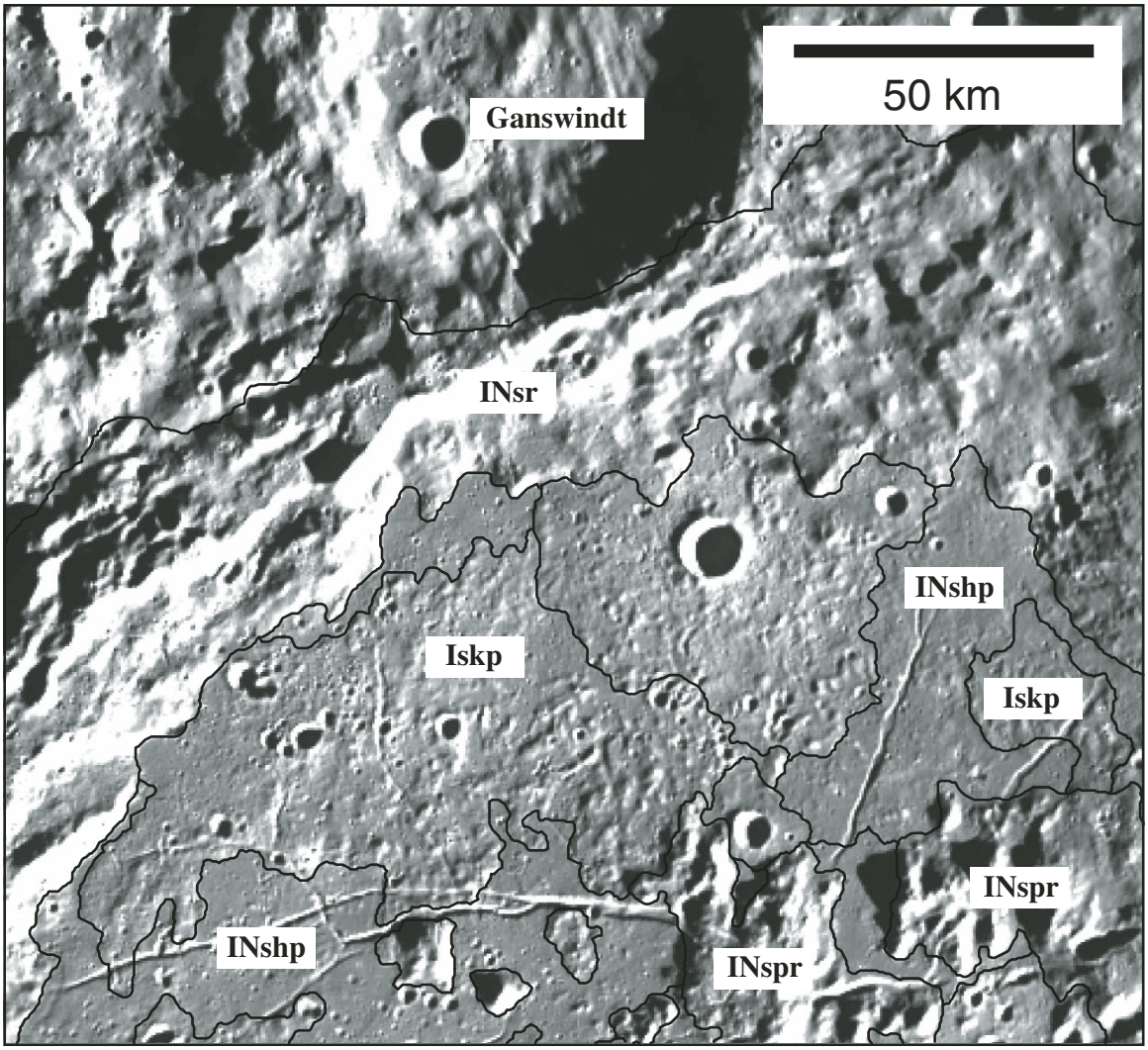

Figure 9. Southern part of Schrödinger basin showing a closer view of contacts in this part of the basin. Here, Schrödinger knobby plains material (Iskp) is similar in appearance to the ejecta deposit of an ~8.5-km-diameter crater, suggesting it may be composed of ejecta from a crater outside of Schrödinger, such as Ganswindt or Amundsen to the south. However, parts of the knobby plains are also similar in appearance to the rugged plains. *Clementine* Ultraviolet/Visible 750 nm mosaic; image centered at 77.9°S, 120.1°E; projection is polar stereographic.

Clementine UVVIS color ratio maps, suggesting mixed anorthositic and mafic materials. Lastly, recent spectra from the Selene Multi-band Imager and mixing models indicate that the dark mantle material exhibits properties of the underlying plains and ~15% TiO_2 pyroclastic glass (Kobayashi et al., 2010). Based on the unit's relationship with the dark-halo crater and its spectral information, Schrödinger dark mantle material is interpreted to consist of mafic materials emplaced via pyroclastic eruptions originating from the dark-halo crater. The deposit's spectral signature (strong mafic band relative to albedo, yellow color) suggests that it is not composed purely of mafic materials, but has been contaminated with feldspathic highland-type materials by either superposed crater materials and/or vertical mixing (Gaddis et al., 2003). Preliminary mapping of this feature (Van Arsdall and Mest, 2008; Mest and Van Arsdall, 2008; Mest, 2007, 2008) identified two potentially distinct deposits of dark mantle material (based on albedo differences) surrounding the dark-halo crater. However, due to the nature of this deposit, it likely consists of a single thin mantle of pyroclastic material; albedo differences are likely due to thinning of the deposit further from the dark-halo crater. Thus, this deposit is mapped as a single deposit, which is consistent with previous studies (Wilhelms et al., 1979; Shoemaker et al., 1994).

RELATIVE AGE DETERMINATIONS

Superposition and crosscutting relationships can be used to evaluate the stratigraphy of units defined in the Schrödinger basin. In addition, cumulative crater size-frequency distributions were determined for the geologic units identified within Schrödinger basin by counting all craters greater than 1 km in diameter (total population = 2360 craters) identified in *Clementine* UVVIS and NIR images and *Lunar Orbiter IV* and *V* images.

Crater size-frequency distributions represent an approximation of lunar chronology based on the crater production function (Neukum et al., 1975, 2001) because most lunar surfaces have an interrelated history of crater accumulation and degradation (e.g., Hartmann, 1995). The principle of using

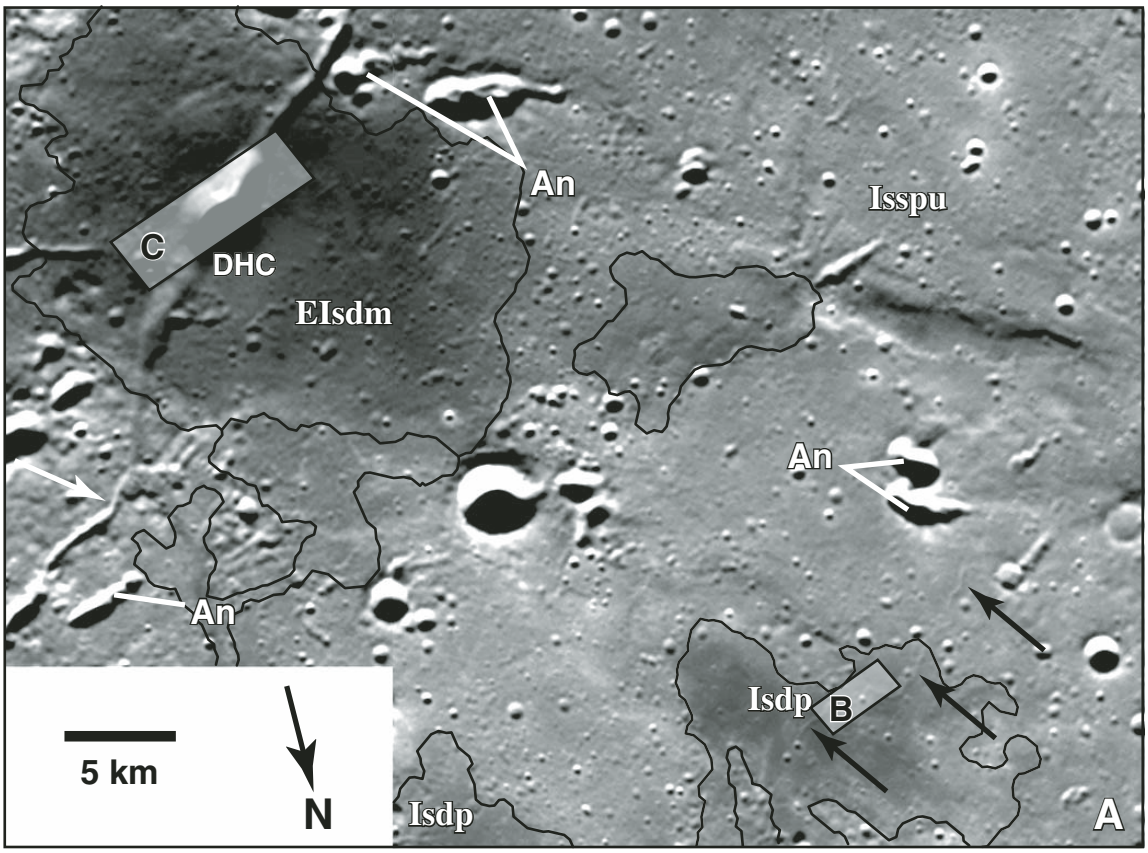

Figure 10 (*Continued on following page*). (A) Mosaic of four *Clementine* Ultraviolet/Visible 750 nm images (LUB0611b.118, LUB0580b.118, LUB0584b.116, and LUB0553b.116; 160–163 m/pixel) showing the dark-halo crater (DHC) on the eastern floor of Schrödinger basin. Schrödinger dark mantle material (EIsdm) surrounds the dark-halo crater and superposes the upper member of the Schrödinger smooth plains formation (Isspu). Schrödinger dark plains material (Isdp) shows few craters on its surface; a narrow, ~21-km-long rille (arrows) emerges from the smooth plains and terminates within the dark plains. Secondary craters from Antoniadi (An) crater are found on the floor of Schrödinger. Image is centered at 74°S, 138°E. Rectangles B and C represent Figure 10B and Figure 10C, respectively.

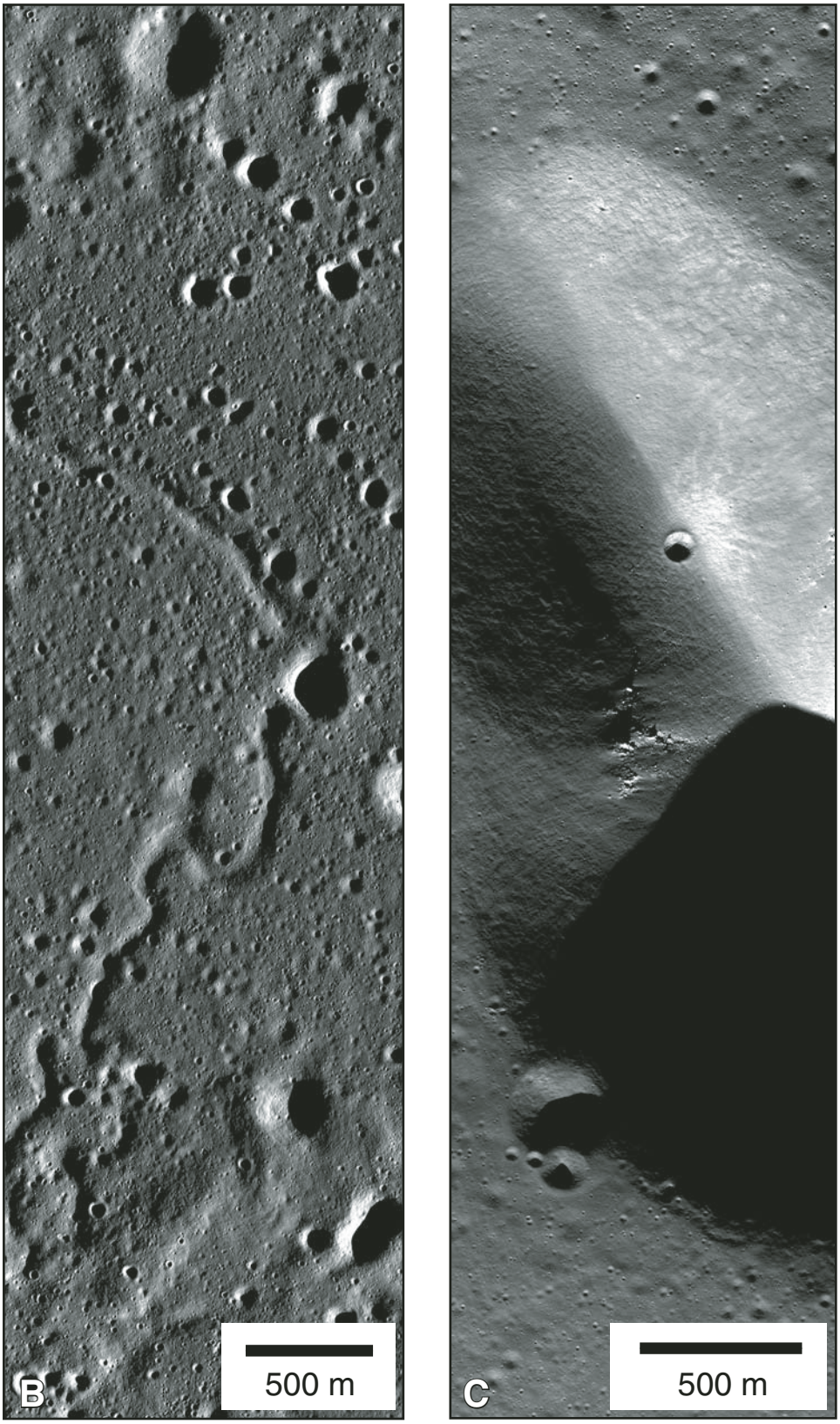

Figure 10 (*Continued*). (B) Part of *Lunar Reconnaissance Orbiter* Camera (LROC) image M115429448L (resolution is 0.970 m/pixel; image centered at 74.3°S, 134.0°E) showing a close-up of the dark plains and the sinuous rille that cuts through this deposit. (C) Part of LROC image M108313384L (resolution is 0.785 m/pixel; image centered at 75.4°S, 138.6°E) showing a close-up of the dark-halo crater. North is to the bottom in both images; National Aeronautics and Space Administration/Goddard Space Flight Center/Arizona State University.

crater size-frequency distributions as a proxy for relative age where superposition relationships are inadequate has long been established for the Moon (e.g., Neukum et al., 1975; Hartmann et al., 1981; Wilhelms, 1987). Here, we use the Hartmann production function (HPF) because it is a relatively reliable model approach because it is the result of averaging of crater counts in different lunar terrains (Hartmann et al., 2000; Hartmann and Neukum, 2001; Neukum et al., 2001; Stöffler et al., 2006). For the HPF, crater size-frequency distributions are represented by a standard bin size, where the number of craters per km^2 (N_H) is calculated for craters in diameter bin sizes that vary logarithmically by a factor of $\sqrt{2}$ (e.g., bins range from 1 to 1.4 km, 1.4–2 km, etc.) (Neukum et al., 2001; Stöffler et al., 2006), and the steep, moderate and shallow portions of the HPF are approximated by a three-segment power law (Hartmann and Neukum, 2001; Stöffler et al., 2006).

In this study, we are principally interested in statistical representations of the entire population of impact craters as a standard for age dating of discrete units. In using small-diameter craters, there is great potential that a portion of secondary craters might be included in the crater counts. This effect is considered to be noteworthy because an overwhelming number of secondary craters steepens the size-frequency distribution curve and provides artificially old ages (McEwen and Bierhaus, 2006). For example, recent mapping of Shackleton crater and the surrounding highlands by Spudis et al. (2008) using Arecibo radar and *Smart-1* Advanced Moon micro-Imager Experiment (AMIE) images (~20 m/pixel and ~50 m/pixel, respectively) found that Shackleton formed ca. 3.6 Ga, nearly 300 m.y. older than previous estimates (Wilhelms et al., 1979). Such discrepancies could be due to inclusion of secondary craters in the counts; conversely, the simple fact that better data allow more craters to be identified than in previous studies will result in older, but more constrained, ages. Where data allowed, craters were classified as either primary or secondary. For example, the obvious secondary craters believed to come from Orientale, Humboldt, and Antoniadi (Shoemaker et al., 1994) were excluded from calculation of the crater size-frequency distributions. However, it is likely that several less obvious secondary craters were counted, and as a result relative age estimates could be skewed toward older ages. These effects will be noted in the analysis, and, when possible, stratigraphic relationships (superposition and crosscutting relationships) will be used to constrain unit ages.

Crater size-frequency distributions for most of the units identified in Schrödinger yield surface ages of Imbrian to Nectarian. Previous studies have estimated Schrödinger to be early Imbrian in age (e.g., Wilhelms et al., 1979; Shoemaker et al., 1994). The basin's morphology indicates that it is similar to other early Imbrian–aged craters, and the population of craters with diameters >5 km suggests an early Imbrian age as well. However, crater size-frequency distributions calculated here for Schrödinger basin materials (e.g., rim and peak-ring materials; Fig. 11A) suggest that Schrödinger may be slightly older, perhaps closer to mid-Nectarian in age.

Crater size-frequency distributions calculated for materials of the Schrödinger plains material (Fig. 11B) all plot as Nectarian in age. Assuming an early Imbrian to mid-Nectarian age of the basin, and if these plains consist of impact melt and/or volcanic materials erupted within a short time after basin formation, then an early Imbrian to mid-Nectarian age for the rugged and hummocky plains and an early Imbrian age for the smooth and knobby plains seem likely. The presence of secondary craters from several other large impact basins and craters (e.g., Orientale, Humboldt, and Antoniadi) could also be skewing the plains to older ages. Based on crosscutting relationships, it also seems likely that the floor fractures formed after the plains were emplaced, or were active throughout plains emplacement.

Lastly, the materials of the Schrödinger volcanic formation appear to be some of the youngest on the basin floor. Crater size-frequency distributions suggest that the Schrödinger dark plains material is early Imbrian in age (Fig. 11C), but slightly younger than materials of the Schrödinger plains formation. Based on the crater size-frequency distributions and superposition relationships with other plains material, the dark plains material is interpreted to be mid–early Imbrian to late Imbrian in age. The Schrödinger dark mantle material contains few craters superposed on its surface, and some of those that have been identified (N = 19) could be mantled by the pyroclastic deposits, and thus this deposit could be younger than indicated. In addition, Shoemaker et al. (1994) showed that the pyroclastic materials forming the dark mantle material also superpose secondary craters from nearby Antoniadi crater, suggesting that these materials could be as young as Eratosthenian, or even Copernican, in age. Based on crater statistics and superposition relationships, this study considers the dark mantle material to be late Imbrian to early Eratosthenian in age.

DISCUSSION

Lunar scientific hypotheses have advanced significantly since the last major *Lunar Orbiter*–based geologic mapping effort was undertaken. Geologic mapping of the lunar surface, particularly of the lunar south polar region and Schrödinger basin, is required to address these advancements, as well as provide tools for future exploration of the Moon. A large amount of data has been acquired since *Lunar Orbiter* from recent (*Lunar Prospector*, *Clementine*, *Smart-1*, *Kaguya*, and *Chandrayaan-1*) and ongoing (*Lunar Reconnaissance Orbiter*) missions. Detailed and up-to-date geologic maps of the lunar surface are required at scales to reflect these recent and newly acquired data sets, as well as address important scientific issues about the history of the lunar surface and interior, especially as it relates to impact basin formation and distribution of impact-related materials, the emplacement of volcanic materials on the lunar surface, and the distribution of potentially useful resources on the surface. Lastly, geologic maps of the lunar surface can provide valuable tools for determining potential landing sites for future robotic and human missions to the Moon.

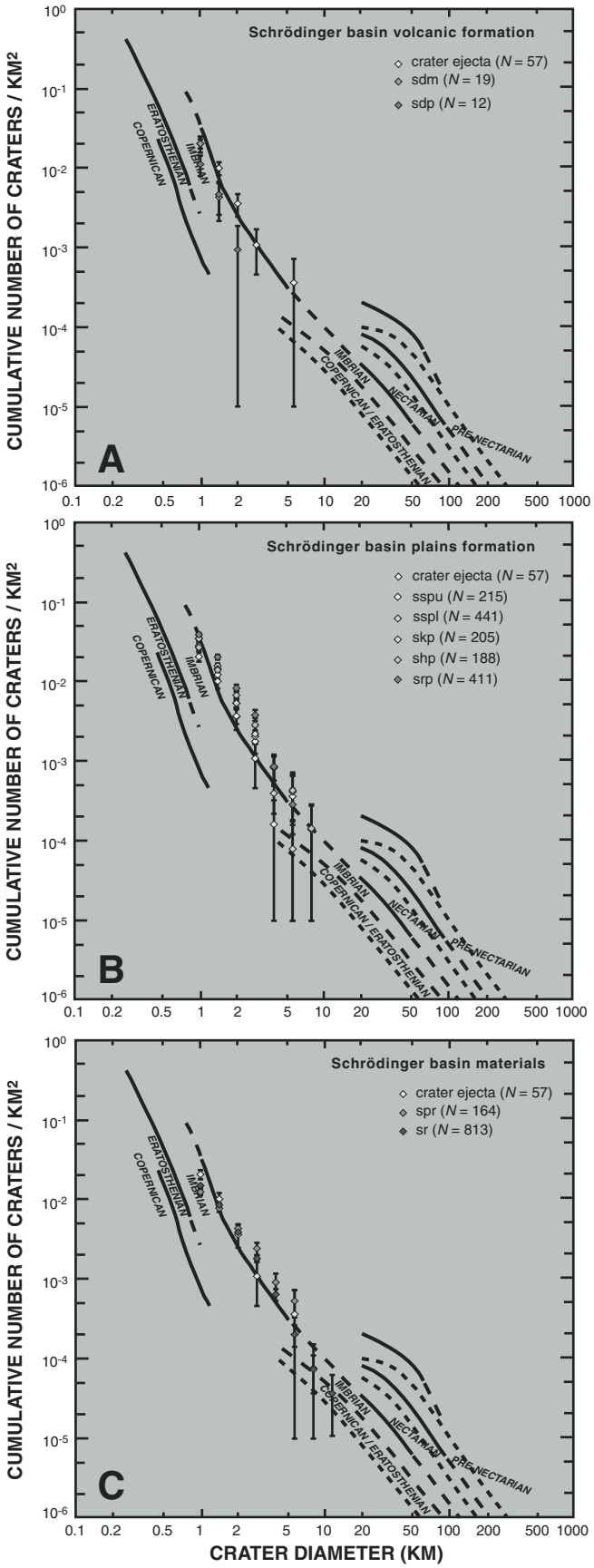

Geologic mapping of the lunar south polar region, which includes the Schrödinger basin, is being undertaken for several scientific reasons. The lunar south pole map area contains the lowest elevations on the Moon and a large portion of the South Pole–Aitken impact basin, which is believed to expose material from the lower lunar crust, and perhaps upper mantle. The thorium- and iron-rich basin floor materials (relative to the surrounding feldspathic lunar highlands), as well as volcanic deposits and central peaks (i.e., within Schrödinger), could be used as a proxy to estimate the composition of the lunar crust and mantle, and mapping the geology of these exposed materials using the most recent data sets available is providing significant insights into the structure and composition of this part of the South Pole–Aitken basin.

As part of this larger mapping effort, geologic mapping of Schrödinger basin is providing insights into the history of this unique impact basin, which is a member of a small population of large (>300 km in diameter) well-preserved multiring impact basins that represent the final stages of Late Heavy Bombardment on the Moon. Geologic mapping of Schrödinger basin has identified nine units organized into three groups within the Schrodinger assemblage, including Schrödinger basin materials (peak-ring and rim material), the Schrödinger plains formation (rugged, hummocky, upper and lower smooth, and knobby plains material), and the Schrödinger volcanic formation (dark material and dark plains material).

This work and previous studies (Wilhelms et al., 1979; Wilhelms, 1987; Shoemaker et al., 1994) indicate that Schrödinger basin formed during the early Imbrian (ca. 3.8–3.85 Ga; absolute ages from Stöffler and Ryder, 2001; Hiesinger and Head, 2006; Stöffler et al., 2006), or perhaps mid-Nectarian (ca. 3.85–3.89 Ga). The Schrödinger peak-ring and rim materials represent the oldest materials associated with the Schrödinger basin-forming event and are interpreted to be mid-Nectarian to early Imbrian in age, consistent with other studies (Wilhelms, 1987; Shoemaker et al., 1994). The Schrödinger basin impact event resulted in excavation and overturn of pre-Schrödinger crustal material to form the rim material and uplift of crustal material to form the peak-ring material.

Following basin formation, several plains units—rugged, hummocky, smooth, and knobby plains material—were emplaced on the floor of Schrödinger basin. These plains deposits display

Figure 11. Crater size-frequency distribution (CSFD) plots for geologic units mapped in the Schrödinger assemblage; CSFD data for crater ejecta deposits from superposed fresh-looking impact craters are included in each plot for reference. Plots are organized by groups of units including (A) Schrödinger volcanic formation: sdm—Schrödinger dark plains material, sdp—Schrödinger dark plains; (B) Schrödinger plains formation: sspu—Schrödinger smooth plains, upper member, sspl—Schrödinger smooth plains, lower member, skp—Schrödinger knobby plains, shp—Schrödinger hummocky plains, srp—Schrödinger rugged plains; (C) Schrödinger basin materials: spr—Schrödinger peak ring material, sr—Schrödinger rim material.

a variety of surface textures and albedos in *Clementine* UVVIS and *Lunar Orbiter* images. Crater size-frequency distribution plots show that the rugged and hummocky plains materials are the oldest plains deposits on Schrödinger's floor, late Nectarian (ca. 3.85–3.92 Ga) to early Imbrian (ca. 3.75–3.85 Ga) in age. Rugged plains material is topographically higher than other Schrödinger plains materials, but it is embayed by other plains material. The hummocky plains embay the rugged plains, and this unit is located primarily along the base of the basin wall. The rugged and hummocky plains are believed to consist of impact melt emplaced immediately following basin formation.

Crater size-frequency data suggest that the knobby plains range in age from late Nectarian (ca. 3.85–3.92 Ga) to early Imbrian (ca. 3.75–3.85 Ga). The knobby plains material superpose the rugged and hummocky plains, and possibly the smooth plains (lower member), but this relationship is unclear. The knobby plains exhibits surface textures consistent with emplacement as an ejecta deposit, but they could also consist of basin wall material emplaced via mass wasting. If this unit is composed of ejecta, a few likely candidate source craters are located nearby, including Ganswindt or Amundsen. The origin of the knobby plains, as well as its age, can be constrained by determining the ages of these potential source craters.

Origins of the smooth plains are less clear. Based on superposition relationships, both members of the smooth plains are younger than the hummocky and rugged plains, and the upper member clearly superposes the lower member where they are in contact. Crater size-frequency distributions suggest that these units are likely early Imbrian (ca. 3.75–3.85 Ga) to late Imbrian (ca. 3.8–3.2 Ga) in age. Their surfaces do not reflect an obvious mode of emplacement, but their generally lower albedos, smoother surfaces, and younger ages suggest emplacement by volcanic processes; however, obvious flows or source vents are not observed, and thus impact melt cannot be ruled out. The floor fractures that bisect the floor of Schrödinger basin could have been provided a conduit for the lava that formed these plains.

As a result of the Schrödinger basin-forming event, rebound of the floor caused uplift of floor materials, and stresses within the near surface caused a series of floor fractures (Schultz, 1976; Shoemaker et al., 1994), oriented parallel and radial to the basin walls, to form throughout the basin within both plains and peak-ring materials.

The youngest materials in Schrödinger basin are materials strongly believed to be volcanic in nature, including the Schrödinger dark plains and dark mantle materials. Deposits of dark plains material, exhibiting smooth, low-albedo surfaces and located at the termination of a narrow, ~21-km-long rille, are believed to be the products of late-stage (late Imbrian, ca. 3.8–3.2 Ga) eruptions and emplacement of mafic lavas in low-lying areas of the preexisting plains. The dark mantle material occurs as one deposit that surrounds an ovoidal cone, which is classified as a dark-halo crater and believed to be the site of pyroclastic eruptions (Shoemaker et al., 1994; Gaddis et al., 2003). This deposit, which consists of a thin mantle of low-albedo material, is believed to be the youngest material emplaced on the floor of Schrödinger basin, likely late Imbrian (ca. 3.8–3.2 Ga) to early Eratosthenian (ca. 2.5–3.2 Ga) in age, but some studies (e.g., Shoemaker et al., 1994) suggest that the dark material may even be as young as Copernican in age (younger than ca. 0.8 Ga).

ACKNOWLEDGMENTS

I wish to thank David Williams and William Ambrose for all of their hard work in forming this session at the 2008 Geological Society of America (GSA) Annual Meeting and in compiling this Special Paper. I would also like to thank GSA for their support of this volume. Many thanks are given to David Williams and James Skinner for their insightful reviews. Special thanks are due to David Shulman, Lauren Van Arsdall, and Erin Dominov for their tireless assistance in identifying and measuring impact craters. A portion of this work was previously supported by the National Aeronautics and Space Administration (NASA) Postdoctoral Program (Oak Ridge Associated Universities), and is currently supported by NASA's Planetary Geology and Geophysics Program.

REFERENCES CITED

Becker, T.L., Weller, L., Gaddis, L., Cook, D., Archinal, B., Rosiek, M., Isbell, C., Hare, T., and Kirk, R., 2008, *Lunar Orbiter* mosaic of the Moon: Houston, Lunar and Planetary Institute, Lunar and Planetary Science Conference XXXIX, CD-ROM, abstract 2357.

Belton, M.J.S., Head, J.W., Pieters, C.M., Greeley, R., McEwen, A.S., Neukum, G., Klaasen, K.P., Anger, C.D., Carr, M.H., and Chapman, C.R., 1992, Lunar impact basins and crustal heterogeneity—New western limb and far side data from *Galileo*: Science, v. 255, p. 570–576, doi:10.1126/science.255.5044.570.

Cintala, M.J., and Grieve, R.A.F., 1998, Scaling impact-melt and crater dimensions: Implications for the lunar cratering record: Meteoritics & Planetary Science, v. 33, p. 889–912, doi:10.1111/j.1945-5100.1998.tb01695.x.

Crittenden, M.D., 1967, Terrestrial analogues of lunar mass wasting, *in* Preliminary Geologic Evaluation and *Apollo* Landing Analysis of Areas Photographed by *Lunar Orbiter III*: Hampton, Virginia, Langley Research Center, Langley Working Paper 407, p. 125–127.

Eliason, E., McEwen, A., Robinson, M., Lee, E., Becker, T., Gaddis, L., Weller, L., Isbell, C., Shinaman, J., Duxbury, T., and Malaret, E., 1999, Digital processing for a global multispectral map of the Moon from the *Clementine* UVVIS imaging instrument: Houston, Lunar and Planetary Institute, Lunar and Planetary Science Conference XXX, abstract 1933.

Eliason, E.M., Lee, E.M., Becker, T.L., Weller, L.A., Isbell, C.E., Staid, M.L., Gaddis, L.R., McEwen, A.S., Robinson, M.S., Duxbury, T., Steutel, D., Blewett, D.T., and Lucey, P.G., 2003, A near-infrared (NIR) global multispectral map of the Moon from *Clementine*: Houston, Lunar and Planetary Institute, CD-ROM, Lunar and Planetary Science Conference XXXIV, abstract 2093.

Gaddis, L.R., Staid, M.I., Tyburczy, J.A., Hawke, B.R., and Petro, N.E., 2003, Compositional analyses of lunar pyroclastic deposits: Icarus, v. 161, p. 262–280, doi:10.1016/S0019-1035(02)00036-2.

Gaddis, L.R., Isbell, C., Staid, M., Eliason, E., Lee, E.M., Weller, L., Sucharski, T., Lucey, P., Blewett, D., Hinrichs, J., and Steutel, D., 2007, The *Clementine* NIR Global Lunar Mosaic, PDS Volumes USA_NASA_PDS_CL_5001 through 5078: Produced by the U.S. Geological Survey and distributed online (ftp://pdsimage2.wr.usgs.gov/cdroms/clementine/Clem_NIR_V0.1/ [accessed 2007]) and on DVD media by the Planetary Data System.

Greeley, R., 1971, Lava tubes and channels in the lunar Marius Hills: The Moon, v. 3, p. 289–314, doi:10.1007/BF00561842.

Gruener, J.E., and Joosten, B.K., 2009, NASA Constellation Program Office Regions of Interest on the Moon: A representative basis for scientific

exploration, resource potential, and mission operations: Tempe, Arizona, Lunar Reconnaissance Orbiter Science Targeting Meeting, abstract 036.

Hartmann, W.K., 1995, Planetary cratering I: Lunar highlands and tests of hypotheses on crater populations: Meteoritics, v. 30, p. 451–467.

Hartmann, W.K., and Neukum, G., 2001, Cratering chronology and evolution of Mars, *in* Altwegg, K., Ehrenfreund, P., Geiss, J., and Huebner, W.F., eds., Composition and Origin of Cometary Materials: Dordrecht, the Netherlands, Kluwer Academic Publishers, p. 165–194.

Hartmann, W.K., Strom, R.G., Weidenschilling, S.J., Balsius, K.R., Woronow, A., Dence, M.R., Grieve, R.A.F., Diaz, J., Chapman, C.R., Shoemaker, E.M., and Jones, K.L., 1981, Chronology of planetary volcanism by comparative studies of planetary cratering, *in* Basaltic Volcanism Study Project, eds., Basaltic Volcanism on the Terrestrial Planets: Basaltic Volcanism Study Project: New York, Pergamon Press, p. 1050–1129.

Hartmann, W.K., Ryder, G., Dones, L., and Grinspoon, D.H., 2000, The time-dependent intense bombardment of the primordial Earth-Moon system, *in* Righter, R.M., and Canup, R., eds., Origin of the Earth and Moon: Tucson, University of Arizona Press, p. 493–512.

Head, J.W., Murchie, S., Mustard, J.F., Pieters, C.M., Neukum, G., McEwen, A., Greeley, R., Nagel, E., and Belton, M.J.S., 1993, Lunar impact basins: New data from the western limb and the far side (Orientale and South Pole–Aitken basins) from the first *Galileo* flyby: Journal of Geophysical Research, v. 98, p. 17,149–17,181, doi:10.1029/93JE01278.

Hiesinger, H., and Head, J.W., 2006, New views of lunar geoscience: An introduction and overview, *in* Jolliff, B.L., Wieczorek, M.A., Shearer, C.K., and Neal, C.R., eds., New Views of the Moon: Mineralogical Society of America, Reviews in Mineralogy and Geochemistry, v. 60, p. 1–81.

Jolliff, B.L., Gillis, J.J., Haskin, L.A., Korotev, R.L., and Wieczorek, M.A., 2000, Major lunar crustal terranes: Surface expressions and crust-mantle origins: Journal of Geophysical Research, v. 105, p. 4197–4216, doi:10.1029/1999JE001103.

Kobayashi, Y., Ohtake, M., Haruyama, J., Matsunaga, T., Iwata, T., Morota, T., Yokota, Y., Yamamoto, S., and Kitazato, K., 2010, Estimating composition of dark mantle deposit in Schrödinger basin using *Selene* spectral data: Houston, Lunar and Planetary Institute, Lunar and Planetary Science Conference XLI, CD-ROM, abstract 1636.

Kohout, T.K., O'Sullivan, K.M., Losiak, A., Thaisen, K.G., Weider, S., and Kring, D.A., 2009, Scientific opportunities for human exploration of the Moon's Schrödinger basin: Houston, Lunar and Planetary Institute, Lunar and Planetary Science Conference XL, CD-ROM, abstract 1572.

Lawrence, D.J., Feldman, W.C., Barraclough, B.L., Binder, A.B., Elphic, R.C., Maurice, S., and Thomsen, D.R., 1998, Global elemental maps of the Moon: The *Lunar Prospector* gamma-ray spectrometer: Science, v. 281, p. 1484–1489, doi:10.1126/science.281.5382.1484.

Lawrence, D.J., Feldman, W.C., Barraclough, B.L., Elphic, R.C., Prettyman, T.H., Maurice, S., Binder, A.B., and Miller, M.C., 2000, Thorium abundances on the lunar surface: Journal of Geophysical Research, v. 105, p. 20,307–20,331, doi:10.1029/1999JE001177.

Lawrence, D.J., Elphic, R.C., Feldman, W.C., Gasnault, O., Genetay, I., Maurice, S., and Prettyman, T.H., 2002a, Optimizing the spatial resolution for gamma-ray measurements of thorium abundances on the lunar surface, *in* Jolliff, B.L., Wieczorek, M.A., Shearer, C.K., and Neal, C.R., eds., New Views of the Moon: Mineralogical Society of America, Reviews in Mineralogy and Geochemistry, v. 60, p. 12–14.

Lawrence, D.J., Feldman, W.C., Elphic, R.C., Little, R.C., Prettyman, T.H., Maurice, S., Lucey, P.G., and Binder, A.B., 2002b, Iron abundances on the lunar surface as measured by the *Lunar Prospector* gamma-ray and neutron spectrometers: Journal of Geophysical Research, v. 107, doi:10.1029/2001JE001530.

Lawrence, D.J., Elphic, R.C., Feldman, W.C., Gasnault, O., Genetay, I., Maurice, S., and Prettyman, T.H., 2003, Small-area thorium features on the lunar surface: Journal of Geophysical Research, v. 108, doi:10.1029/2003JE002050.

Lucey, P.G., Taylor, G.J., and Malaret, E., 1995, Abundance and distribution of iron on the Moon: Science, v. 268, p. 1150–1153, doi:10.1126/science.268.5214.1150.

Lucey, P.G., Taylor, G.J., Hawke, B.R., and Spudis, P.D., 1998, FeO and TiO_2 concentrations in the South Pole–Aitken basin: Implications for mantle composition and basin formation: Journal of Geophysical Research, v. 103, no. E2, p. 3701–3708, doi:10.1029/97JE03146.

McEwen, A.S., and Bierhaus, E.B., 2006, The importance of secondary cratering to age constraints on planetary surfaces: Annual Review of Earth and Planetary Sciences, v. 34, p. 535–567, doi:10.1146/annurev.earth.34.031405.125018.

Melosh, H.J., 1989, Impact Cratering—A Geologic Process: Oxford, UK, Oxford University Press, 245 p.

Mest, S.C., 2007, Updated geologic and geomorphic maps of the lunar north and south poles: Houston, Lunar and Planetary Institute, Lunar and Planetary Science Conference XXXVIII, CD-ROM, abstract 1842.

Mest, S.C., 2008, Geologic mapping of the lunar south pole: Geological Society of America Abstracts with Programs, v. 40, no. 6, p. 519.

Mest, S.C., and Van Arsdall, L.E., 2008, Geologic mapping of the Schrödinger basin area, lunar south pole, *in* National Aeronautics and Space Administration (NASA) Lunar Science Institute Lunar Science Conference I Abstracts: Moffett Field, California, NASA Ames Research Center, abstract 2089.

Moore, H.J., Hodges, C.A., and Scott, D.H., 1974, Multi-ringed basins—Illustrated by Orientale and associated features: Houston, Lunar and Planetary Institute, Lunar and Planetary Science Conference V, p. 71–100.

Neukum, G., König, B., and Arkani-Hamed, J., 1975, A study of lunar impact crater size-distributions: The Moon, v. 12, p. 201–229, doi:10.1007/BF00577878.

Neukum, G., Ivanov, B.A., and Hartmann, W.K., 2001, Cratering records in the inner solar system in relation to the lunar reference system: Space Science Reviews, v. 96, p. 55–86, doi:10.1023/A:1011989004263.

Nozette, S., Rustan, P., Pleasance, L.P., Kordas, J.F., Lewis, I.T., Park, H.S., Priest, R.E., Horan, D.M., Regeon, P., Lichtenberg, C.L., Shoemaker, E.M., Eliason, E.M., McEwen, A.S., Robinson, M.S., Spudis, P.D., Acton, C.H., Buratti, B.J., Duxbury, T.C., Baker, D.N., Jakosky, B.M., Blamont, J.E., Corson, M.P., Resnick, J.H., Rollins, C.J., Davies, M.E., Lucey, P.G., Malaret, E., Massie, M.A., Pieters, C.M., Reisse, R.A., Simpson, R.A., Smith, D.E., Sorenson, T.C., Vorder Breugge, R.W., and Zuber, M.T., 1994, The *Clementine* mission to the Moon: Scientific overview: Science, v. 266, p. 1835–1839, doi:10.1126/science.266.5192.1835.

Pieters, C.M., Staid, M.I., Fischer, E.M., Tompkins, S., and He, G., 1994, A sharper view of impact craters from *Clementine* data: Science, v. 266, p. 1844–1848, doi:10.1126/science.266.5192.1844.

Pieters, C.M., Tompkins, S., Head, J.W., and Hess, P.C., 1997, Mineralogy of the mafic anomaly in the South Pole–Aitken basin: Implications for excavation of the lunar mantle: Geophysical Research Letters, v. 24, p. 1903–1906, doi:10.1029/97GL01718.

Pieters, C.M., Head, J.W., Gaddis, L., Jolliff, B., and Duke, M., 2001, Rock types of South Pole–Aitken basin and extent of basaltic volcanism: Journal of Geophysical Research, v. 106, no. E11, p. 28,001–28,022, doi:10.1029/2000JE001414.

Robinson, M.C., Brylow, S.M., Tschimmel, M., Humm, D., Lawrence, S.J., Thomas, P.C., Denevi, B.W., Bowman-Cisneros, E., Zerr, J., Ravine, M.A., Caplinger, M.A., Ghaemi, F.T., Schaffner, J.A., Malin, M.C., Mahanti, P., Bartels, A., Anderson, J., Tran, T.N., Eliason, E.M., McEwen, A.S., Turtle, E., Jolliff, B.L., and Hiesinger, H., 2010a, *Lunar Reconnaissance Orbiter* Camera (LROC) instrument overview: Space Science Reviews, v. 150, p. 81–124, doi:10.1007/s11214-010-9634-2.

Robinson, M.S., Eliason, E.M., Hiesinger, H., Jolliff, B.L., McEwen, A.S., Malin, M.C., Ravine, M.A., Thomas, P.C., Turtle, E.P., Bowman-Cisneros, E., and the LROC Team, 2010b, *Lunar Reconnaissance Orbiter* Camera: First results: Houston, Texas, Lunar and Planetary Institute, Lunar and Planetary Science Conference XLI, CD-ROM, abstract 1874.

Schultz, P.H., 1972, Moon Morphology: Austin, University of Texas Press, 626 p.

Schultz, P.H., 1976, Floor-fractured lunar craters: The Moon, v. 15, p. 241–273, doi:10.1007/BF00562240.

Shankar, B., Osinski, G., Antonenko, I., Stooke, P.J., and Mest, S., 2010, Multispectral study of the Schrödinger impact basin: Houston, Texas, Lunar and Planetary Institute, Lunar and Planetary Science Conference XLI, CD-ROM, abstract 2542.

Shoemaker, E.M., Robinson, M.S., and Eliason, E.M., 1994, The south pole region of the Moon as seen by *Clementine*: Science, v. 266, p. 1851–1854, doi:10.1126/science.266.5192.1851.

Smith, D.E., Zuber, M.T., Jackson, G.B., Cavanaugh, J.F., Neumann, G.A., Riris, H., Sun, X., Zellar, R.S., Coltharp, C., Connelly, J., Katz, R.B., Kleyner, I., Liiva, P., Matuszeski, A., Mazarico, E.M., McGarry, J.F., Novo-Gradac, A.-M., Ott, M.N., Peters, C., Ramos-Izquierdo, L.A., Ramsey, L., Rowlands, D.D., Schmidt, S., Scott, V.S., III, Shaw, G.B., Smith, J.C., Swinski, J.-P., Torrence, M.H., Unger, G., Yu, A.W., and Zagwodzki, T.W., 2010a, The *Lunar Orbiter* Laser Altimeter investigation

on the *Lunar Reconnaissance Orbiter* mission: Space Science Reviews, v. 150, p. 209–241, doi:10.1007/s11214-009-9512-y.

Smith, D.E., Zuber, M.T., Neumann, G.A., Lemoine, F.G., Mazarico, E., Torrence, M.H., Duxbury, T.H., Head, J., III, Aharonson, O., and the LOLA Science and Instrument Team, 2010b, LOLA observations of the Moon: Houston, Texas, Lunar and Planetary Institute, Lunar and Planetary Science Conference XLI, CD-ROM, abstract 1993.

Spudis, P.D., 1993, The Geology of Multi-Ring Impact Basins: The Moon and Other Planets: New York, Cambridge University Press, 263 p.

Spudis, P.D., Reisse, R.A., and Gillis, J.J., 1994, Ancient multiring basins on the Moon revealed by *Clementine* laser altimetry: Science, v. 266, p. 1848–1851, doi:10.1126/science.266.5192.1848.

Spudis, P.D., Plescia, J., Bussey, B., Josset, J.-L., Beauvivre, S., and the AMIE team, 2008, The geology of the south pole of the Moon and the age of Shackleton crater: Houston, Lunar and Planetary Institute, Lunar and Planetary Science Conference XXXIX, CD-ROM, abstract 1626.

Stöffler, D., and Ryder, G., 2001, Stratigraphy and isotope ages of lunar geologic units: Chronological standard for the inner solar system, *in* Kallenbach, R., Geiss, J., and Hartmann, W.K., eds., Chronology and Evolution of Mars: Space Sciences Series of International Space Science Institute, v. 12, Dordrecht, Kluwer Academic Publishers, p. 9–54.

Stöffler, D., Ryder, G., Ivanov, B.A., Artemieva, N.A., Cintala M.J., and Grieve, R.F., 2006, Cratering history and lunar chronology, *in* Jolliff, B.L., Wieczorek, M.A., Shearer, C.K., and Neal, C.R., eds., New Views of the Moon: Chantilly, Virginia, The Mineralogical Society of America, p. 519–596.

Stuart-Alexander, D.E., 1978, Geologic Map of the Rheita Quadrangle of the Moon: U.S. Geological Survey Miscellaneous Geologic Investigations Series Map I-694, scale 1:1,000,000.

Tanaka, K.L., 1994, The Venus Geologic Mappers Handbook: U.S. Geological Survey Open-File Report 94-438, 66 p.

Van Arsdall, L.E., and Mest, S.C., 2008, Geologic mapping of the Schrödinger Basin area, lunar south pole: Houston, Texas, Lunar and Planetary Institute, Lunar and Planetary Science Conference XXXIX, CD-ROM, abstract 1706.

Weisbin, C.R., Clark, P., Adumitroaie, V., Mrozinski, J., Shelton, K., Hua, H., Smith, J.H., Elfes, A., Lincoln, W., and Silberg, R., 2010, Formulation, modeling and analysis of a mission to the Moon's Schrodinger crater: Houston, Texas, Lunar and Planetary Institute, Lunar and Planetary Science Conference XLI, CD-ROM, abstract 1473.

Wieczorek, M.A., Jolliff, B.L., Khan, A., Pritchard, M.E., Weiss, B.P., Williams, J.G., Hood, L.L., Righter, K., Neal, C.R., Shearer, C.K., McCallum, I.S., Thompkins, S., Hawke, B.R., Peterson, C., Gillis, J.J., and Bussey, B., 2006, The constitution and structure of the lunar interior, *in* Jolliff, B.L., Wieczorek, M.A., Shearer, C.K., and Neal, C.R., eds., New Views of the Moon: Mineralogical Society of America, Reviews in Mineralogy and Geochemistry, v. 60, p. 221–364.

Wilhelms, D.E., 1972, Geologic Mapping of the Second Planet: U.S. Geological Survey Interagency Report: Astrogeology, v. 55, 36 p.

Wilhelms, D.E., 1987, The Geologic History of the Moon: U.S. Geological Survey Professional Paper 1348, 302 p.

Wilhelms, D.E., 1990, Geologic mapping, *in* Greeley, R., and Batson, R.M., eds., Planetary Mapping: Cambridge, UK, Cambridge University Press, p. 208–260.

Wilhelms, D.E., Howard, K.A., and Wilshire, H.G., 1979, Geologic Map of the South Side of the Moon: U.S. Geological Survey Miscellaneous Geologic Investigations Series Map I-1162, scale 1:5,000,000.

Wood, C.A., and Andersson, L., 1978, New morphometric data for fresh lunar craters: Houston, Lunar and Planetary Institute, Lunar and Planetary Science Conference IX, CD-ROM, p. 3669–3689.

Manuscript Accepted by the Society 26 August 2010

Printed in the USA

The Geological Society of America
Special Paper 477
2011

Calibrating several key lunar stratigraphic units representing 4 b.y. of lunar history within Schrödinger basin

Katie M. O'Sullivan
Department of Civil Engineering and Geological Sciences, University of Notre Dame, Notre Dame, Indiana 46556, USA

Tomas Kohout
Department of Physics, University of Helsinki, P.O. Box 64, 00014 Helsinki University, Finland, and *Institute of Geology, Academy of Sciences of the Czech Republic v.v.i. Rozvojova 269, 16500 Prague, Czech Republic*

Kevin G. Thaisen
Planetary Geosciences Institute, University of Tennessee, Knoxville, Tennessee 37996, USA

David A. Kring
Center for Lunar Science and Exploration, Universities Space Research Association Lunar and Planetary Institute, 3600 Bay Area Blvd., Houston, Texas 77058, USA,
and *National Aeronautics and Space Administration Lunar Science Institute*

ABSTRACT

To test the lunar cataclysm hypothesis and anchor the beginning of the basin-forming epoch on the Moon, which are high science priorities for lunar exploration, we evaluated potential landing sites within Schrödinger basin. This impact site is the second youngest basin-forming event and lies within the South Pole–Aitken basin, which is the oldest and largest impact basin on the Moon. Thus, landing sites within Schrödinger should provide access to impact lithologies with ages of each event, providing a bracket of the entire basin-forming epoch and resolving both of the leading science priorities. Additionally, the floor of Schrödinger basin has been partially covered by younger mare and pyroclastic units. The volcanic materials, as well as impact-excavated and uplifted units, will provide chemical and lithologic samples of the lunar crust and potentially the upper mantle. Collectively, the impact and volcanic lithologies will provide calibration points to the entire lunar stratigraphic column.

O'Sullivan, K.M., Kohout, T., Thaisen, K.G., and Kring, D.A., 2011, Calibrating several key lunar stratigraphic units representing 4 b.y. of lunar history within Schrödinger basin, *in* Ambrose, W.A., and Williams, D.A., eds., Recent Advances and Current Research Issues in Lunar Stratigraphy: Geological Society of America Special Paper 477, p. 117–127, doi:10.1130/2011.2477(05).

INTRODUCTION

The earliest phases of the Moon's evolution are marked by planetary differentiation, solidification of its crust (Smith et al., 1970), and an intense period of impact bombardment (Turner et al., 1973; Tera et al., 1974), which produced dozens of basins several hundreds of kilometers in diameter (Baldwin, 1949; Hartmann and Wood, 1971; Wilhelms et al., 1987). Flood basalts subsequently filled many of those basins (Hackman and Mason, 1961; Shoemaker and Hackman, 1962; Quaide, 1965) before significant magmatic activity appears to have ceased. Impact cratering continued to modify the Moon up to, and including, the present time.

These events echo the geologic processes that shaped Earth, but the Moon also provides a window into eras that are masked on Earth. While more than 97% of the lunar surface is composed of rocks greater than 3 b.y. old, only ~3% of the rocks on the surface of Earth are older than 3 b.y. (Chamberlain et al., 1972). Thus, the lunar surface provides an opportunity to study far more ancient events than those revealed on the surface of Earth.

The dominant process that affected the surface of the ancient Moon was impact cratering. Thus far, 44 impact basins with diameters ranging from 300 to 2500 km have been mapped (e.g., Wilhelms et al., 1987; Spudis, 1993). It is generally agreed that the basin-forming epoch was limited to the first ~700 m.y. of lunar history. A large number of those basins may have been produced in a brief period of time ca. 3.9–4.0 Ga, in what has been called the lunar cataclysm (Tera et al., 1974). This event may have affected the entire inner solar system (Bogard, 1995; Kring and Cohen, 2002; Strom et al., 2005). Not only do variations in the impact flux affect stratigraphic assessments of lunar history, it may affect our calibration of geologic processes on every planetary surface in the solar system. Thus, testing the lunar cataclysm hypothesis is the highest science priority for lunar exploration (NRC, 2007).

The largest of those impact basins, the South Pole–Aitken basin, is still recognizable as an ~13-km-deep topographic low. Because South Pole–Aitken anchors the basin-forming epoch, determining its age is the second highest priority for lunar exploration (NRC, 2007). As the United States prepares to return to the Moon (Bush, 2004; ESAS, 2005), landing sites and exploration targets will likely include old impact basins where these chronologic and stratigraphic issues can be resolved (e.g., Kring, 2008, 2009).

The Schrödinger basin is a compelling candidate for lunar surface operations. Based on crater counting (e.g., Shoemaker et al., 1994), it is one of the youngest and therefore best-preserved impact basins. It is also associated with the South Pole–Aitken basin, so a single mission could be designed to potentially study both of these features. The purpose of this paper is to explore these options.

As noted already, the Moon continued to evolve after the basin-forming epoch. Interestingly, Schrödinger basin is also a site where several stages of volcanism occurred that are younger (late Imbrian or Eratosthenian) than the mare units sampled by the *Apollo* missions (Shoemaker et al., 1994). Samples of these materials will expand our ability to calibrate the timing of other geologic events on the Moon. The National Research Council (2007) outlined 35 science goals to be addressed by future missions to the Moon. The highest-priority goals include: (1) test the cataclysm hypothesis by determining the ages of lunar basins, (2) determine the age of the oldest lunar basin (South Pole–Aitken basin), (3) establish a precise absolute lunar chronology, and (4) determine the age and distribution of a variety of lunar rocks. Thus, this paper also explores the possibility of landing in a geologically complex region within Schrödinger basin where several high-priority science issues (NRC, 2007) can be addressed simultaneously. Using the geologic maps of Shoemaker et al. (1994) and *Clementine* images, we outline an example set of sortie missions that will address high-priority science questions.

LUNAR STRATIGRAPHY

The U.S. Geological Survey (USGS) developed a stratigraphic framework for the Moon during the *Apollo* era (Shoemaker, 1962; Shoemaker and Hackman, 1962). The chronologic system that they developed is based on relative superposition techniques, crater counting, and surface morphology. Periods and epochs were defined by large complex cratering events and immense basin-forming impact events that modified large areas on the Moon's surface and broadly distributed ejecta blankets. For example, the Nectarian Period (ca. 3.9–3.8 Ga) begins with the formation of the Nectaris basin and ends with the formation of the Imbrium basin (Fig. 1). The Imbrian Period (ca. 3.8–3.2 Ga) begins with the formation of the Imbrium basin and ends with the formation of Orientale basin, which was the last of the basin-forming impact events. The subsequent Eratosthenian (ca. 3.2–1.1 Ga) and Copernican Periods (ca. 1.1 Ga to present) reflect lower cratering rates and are characterized by two representative craters (Eratosthenes and Copernicus). Eratosthenian craters are postbasin features, and yet are old enough to be space-weathered, and they usually have no visible rays and have relatively dark (mature) albedos. Copernican craters, on the other hand, are young enough to have bright albedos and extensive ray systems, which are so brilliant that those on the nearside are easily seen from Earth.

This stratigraphic system was partially calibrated with samples recovered by the *Apollo* Program. Those analyses revealed that much of the basin-forming activity occurred ca. 3.9–4.0 Ga during a possible lunar cataclysm (Turner et al., 1973; Tera et al., 1974; Ryder, 1990), but precise ages of some of the defining basins (e.g., Nectaris) are still debated, and the ages of pre-Nectarian basins are completely unknown. As described in more detail herein, the Schrödinger basin may harbor samples with ages of both the beginning and end of the basin-forming epoch.

The lunar surface was also affected by volcanic processes, some of which created continent-size flood basalt provinces

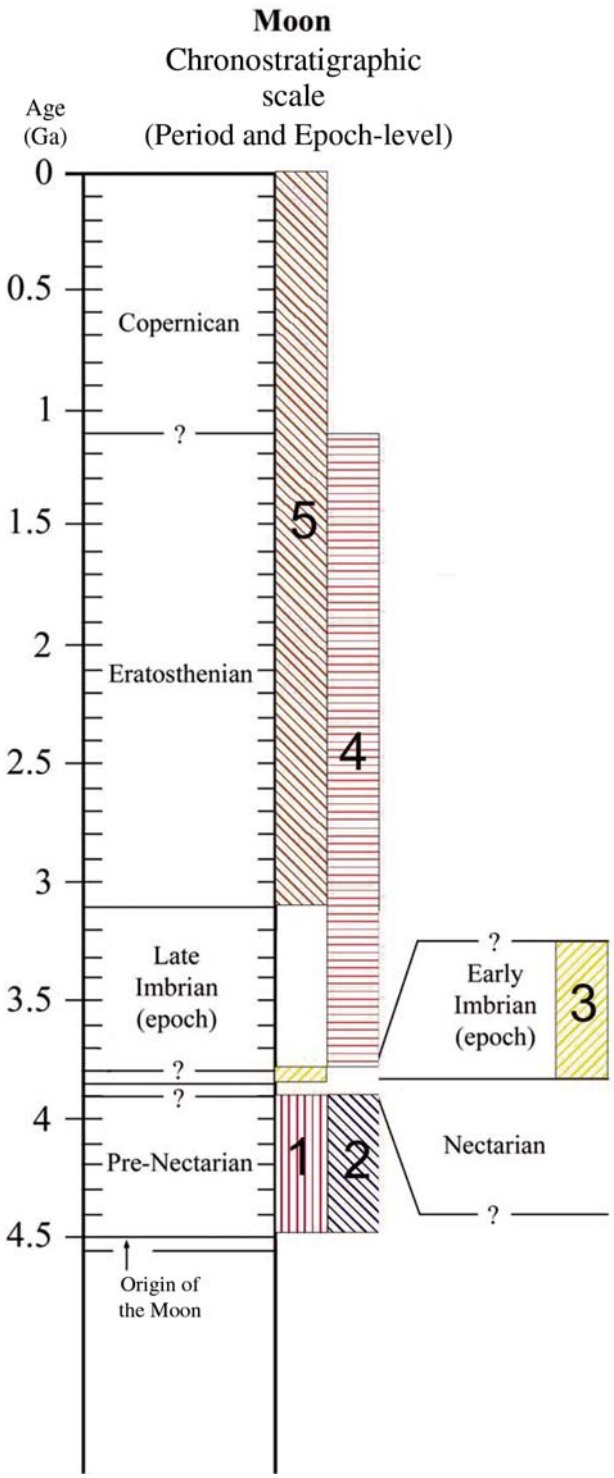

Figure 1. Lunar stratigraphic column and the relative ages of various geological events and materials within Schrödinger basin. 1—South Pole–Aitken impact, 2—Amundsen-Ganswindt impact, 3—Schrödinger impact, 4—mare-type volcanism, and 5—pyroclastic volcanism.

within basin interiors such as Mare Imbrium (e.g., Schaber, 1973). Extensive mare sheets cover ~17% of the lunar surface (Head, 1976), most of which occur on the nearside of the Moon. Analyses of *Apollo* samples suggest that much of that activity occurred after the basin-forming epoch and continued until ca. 3 Ga. In spite of this, younger magmatic activity is suspected but needs to be tested with appropriate samples. Crater counting suggests that most mare volcanism took place between ca. 4 Ga and ca. 2 Ga (Hiesinger et al., 2000), with some areas as young as 1.2 Ga (Hiesinger et al., 2003; this issue). The Schrödinger basin may contain some of these younger volcanic deposits (Shoemaker et al., 1994). Thus, the Schrödinger basin provides access to several geologic units that can provide calibration points for all lunar periods (Fig. 1).

SCHRÖDINGER BASIN DESCRIPTION

Schrödinger basin lies on the farside of the Moon near the south pole and is centered at 75°S, 132.4°E (dashed line, Fig. 2). Schrödinger is a complex impact structure with a 320-km-diameter rim and a 150-km-diameter inner peak ring (Pike and Spudis, 1987). The basin floor is 2–3 km below the main topographic rim, and the inner peak ring rises half a kilometer above the basin floor (Spudis et al., 1994).

Basins like Schrödinger provide benchmarks in evaluations of the lunar impact flux. They also provide crucial information

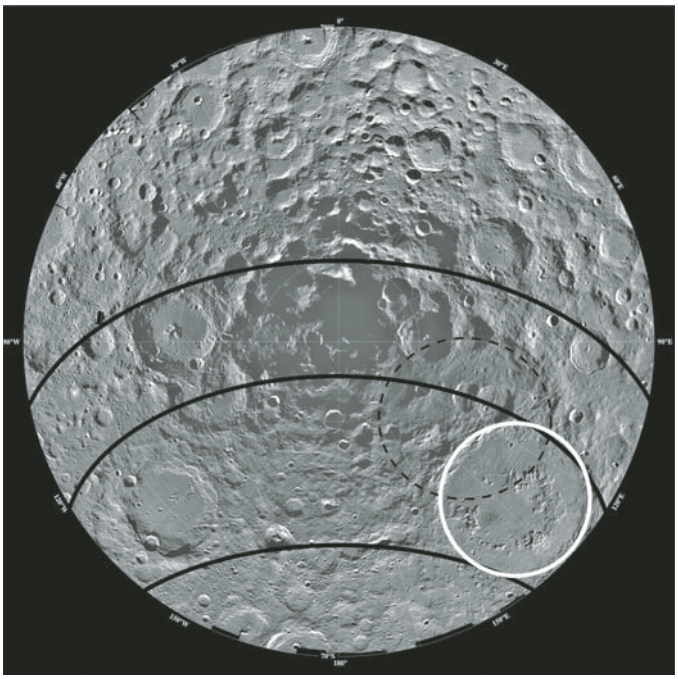

Figure 2. View of the lunar south pole with the relative locations of Schrödinger (white), Amundsen-Ganswindt (dotted black), and South Pole–Aitken (solid black lines, middle ring is the main ring). In this projection, the lunar nearside is in the top half of the figure.

about the lunar interior. Normal faults along the basin margins expose up to 3 km of the crust in cross section. In addition, a basin-forming event of this size is thought to excavate material from depths of ~10–30 km (Cintala and Grieve, 1998; Ivanov, 2005; Kring, 2005). This material is redistributed in a variety of breccias within the basin and beyond its rim as ejecta deposits. Collectively, the exposed crust in the peak ring, basin margins, and fragments within breccias should provide a substantial cross section of the south polar crust.

Schrödinger was initially identified as Nectarian in age by Wilhelms et al. (1979) based on the number of craters superposed on the basin and its corresponding ejecta blanket. It was later reassigned as early Imbrian by Wilhelms et al. (1987) and confirmed with crater counting (Shoemaker et al., 1994) using *Clementine* imagery. Because Schrödinger is the second youngest basin, it has been only slightly eroded from subsequent cratering and crater ejecta, and geologic features are still intact and prominent (Fig. 3). However, the northeastern part of the main rim has been subjected to massive landslides due to the intersection with the pre-Nectarian basin Amundsen-Ganswindt. These landslides are associated with preexisting fractures related to the main ring of Amundsen-Ganswindt (Shoemaker et al., 1994). *Clementine* imagery reveals that both Schrödinger and Amundsen-Ganswindt basins lie within the main topographic ring of South Pole–Aitken. It is apparent that Schrödinger potentially includes units that span a wide time scale, from pre-Nectarian (South Pole–Aitken material) to late Imbrian (Schrödinger) units.

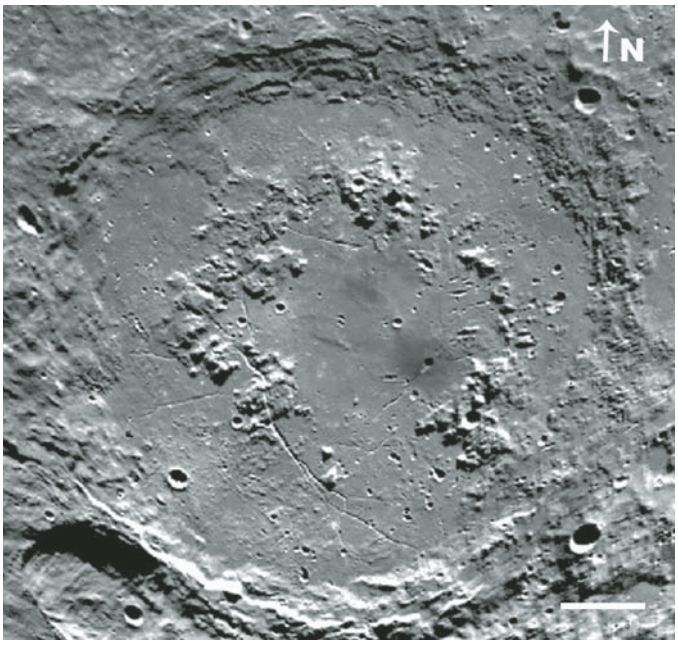

Figure 3. *Clementine* mosaic image of Schrödinger basin. White bar is 50 km long. Main ring is 320 km in diameter; inner ring is 150 km in diameter.

KEY FEATURES WITHIN THE INNER PEAK RING OF SCHRÖDINGER BASIN

The following features make Schrödinger basin an ideal candidate to address high-priority science objectives as outlined by the NRC (2007) and calibrate several key points on the Moon's chronologic scale.

Schrödinger Impact Melt Material

Large impact cratering events produce considerable volumes of impact melt and melt-bearing breccias. In a large basin like Schrödinger, an extensive melt sheet is deposited on the basin floor (Cintala and Grieve, 1998). Based on observations at large terrestrial craters (e.g., Kring, 2005), these central melt sheets are blanketed by a sequence of breccias. Both types of lithologies are deposited far above the Ar-Ar degassing temperatures and take sufficiently long to cool that their radiometric age is reset. Thus, analyses of basin impact melts and breccias can be used to determine the age of the basin-forming impact.

Based on relative chronology, Schrödinger is younger than Imbrium and older than Orientale (e.g., Shoemaker et al., 1994). Imbrium has an estimated age of 3.85 ± 0.02 Ga to 3.77 ± 0.02 Ga (Stöffler and Ryder, 2001) based on repeated analyses of the Fra Mauro Formation, which is interpreted to be a thick unit of impact ejecta that was sampled at *Apollo* sites; *Apollo 15* samples reflect the unit on the margin of the basin, while *Apollo 14* and *16* samples reflect regions of the unit emplaced 550 km and 1045 km, respectively, from the basin margins. The age of Orientale is also uncertain. Rough estimates ranging from 3.80 Ga to 3.85 Ga have been proposed (e.g., Hiesinger et al., 2000), but the timing of the final basin-forming event is still unclear. Determining the age of Schrödinger basin will greatly improve estimates for the cratering flux during this final stage of the basin-forming epoch.

Schrödinger impact melt and melt-bearing breccias are concentrated within the inner peak ring and are well exposed due to the lack of substantial overprinting by ejecta from younger impact events or extensive volcanism. These melts and breccias can be distinguished from localized volcanic deposits in the basin based on macroscopic textures and location. Once collected and returned to Earth, an impact origin can be further confirmed by their chemical composition, inclusions of shock-metamorphosed material, and the possible presence of projectile remnants.

South Pole–Aitken Impact Melt Material

The South Pole–Aitken basin is the oldest of the ~28 pre-Nectarian basins mapped thus far (Wilhelms et al., 1987) and so large (~2500 km diameter) that it melted lower-crustal material and potentially upper-mantle material (e.g., Lucey et al., 1998; Jolliff et al., 2000; Potter et al., 2010). The interior of South Pole–Aitken is chemically distinct from the surrounding lunar highlands (Pieters et al., 2001), which suggests that its unique

melt composition (reflecting very deep crustal and possibly mantle melting) has been preserved. The South Pole–Aitken impact material can be found in a number of locations both inside and outside of the main topographic rim. However, due to ~4 b.y. of subsequent cratering and gardening of the lunar surface, finding and correctly identifying such material on the surface is difficult.

Schrödinger basin lies just within the southwest portion of the main topographic ring of the South Pole–Aitken basin (Fig. 2) (e.g., Wilhelms et al., 1987; Hiesinger and Head, 2003). Complex craters have peak rings that are composed of material originating from below the surface. Based on crater modeling, estimates for the depth of origin of the inner ring of a basin of Schrödinger's size are ~10–30 km (Cintala and Grieve, 1998; Ivanov, 2005; Kring, 2005). Petro and Pieters (2008) estimated cumulative ejecta from all major basins greater than 300 km in diameter (excluding South Pole–Aitken) to be on the order of hundreds of meters thick in the Schrödinger area. The peak ring of Schrödinger should be composed of material that is deep enough to surpass regolith and impact ejecta, and sample material created during the South Pole–Aitken impact event. The inner peak ring of Schrödinger is well exposed and rises steeply from the basin floor; therefore, uplifted samples of South Pole–Aitken impact melt and melt breccias can be collected from talus at the base of cliffs and recovered for chronologic analyses. This would provide a stratigraphic benchmark for the oldest event in the basin-forming epoch.

Volcanism

Two types of volcanism occurred within the inner peak ring of Schrödinger long after the basin formed. Mare-type volcanism is represented by a few localized basaltic flows in the northern part of the inner ring, while pyroclastic volcanism is represented by a single unit in the south (Figs. 3 and 4). Pyroclastic deposits, in the form of volcanic glass beads, are considered to be derived from a distinct and deeper source within the lunar mantle relative to mare basalt flows (e.g., Delano and Livi, 1981; Delano, 1986; Longhi, 1992).

The mare-type volcanic units are estimated to be late Imbrian or Eratosthenian in age based on crater counting (Shoemaker et al., 1994). If these units were confirmed to be this age, they would be millions of years younger than the extensive mare units sampled by the *Apollo* and *Luna* missions on the nearside of the Moon. Such material would be readily accessible for sampling on the surface of the basin floor.

The pyroclastic unit is represented by an area of dark albedo in the southern part of the basin. Crater counting estimates date this event to be Eratosthenian to Copernican in age (Shoemaker et al., 1994). If the volcano were found to be Copernican in age, it would represent one of the youngest volcanic events on the Moon and thus provide volcanic samples millions of years younger than those represented in the *Apollo* and *Luna* collections. Sampling of the mare and pyroclastic deposits would yield the first snapshot of the farside lunar mantle during a time period distinct from that represented by samples from the nearside.

Amundsen-Ganswindt Impact Melt Material

The Amundsen-Ganswindt basin is a highly eroded pre-Nectarian basin (Wilhelms et al., 1987) that intersects the southern side of Schrödinger (Fig. 2). Landslides and fault scarps on the southern rim of Schrödinger may expose impact material created by the Amundsen-Ganswindt event. If so, lunar surface-based imagery will provide much insight into melt sheet differentiation of basins that are similar in size to Amundsen-Ganswindt. Samples produced by the Amundsen-Ganswindt impact may be found on the surface, but they may not be easily collectable due to the large distance from an inner-ring landing site.

Ghost Craters

Ghost craters form during a basin-forming event as debris ejected upon impact falls back into the basin cavity to create a small crater. Concurrently, the central melt sheet is created and splashes up to coat the sides of the basin. The small craters are then partially filled by the central melt sheet as it flows back into the center of the basin. Ghost craters are only formed when the melt sheet is relatively thin; otherwise they would be completely flooded and covered. Ghost craters can therefore be used to determine a maximum thickness of the central melt sheet of a basin.

Shoemaker et al. (1994) identified ghost craters in the inner ring of Schrödinger on both the smooth and rough plains units. Field study of ghost crater geology and morphology in Schrödinger basin will provide constraints on flooding mechanisms and serve as a calibration for central melt sheet thickness.

Secondary Craters

Secondary impact craters are formed when a large impact ejects material massive enough to create a crater upon impact. Secondary craters often have a distinct morphology and can be identified from images because they are elongate, shallow, and have a low rim when compared to primary craters (Shoemaker, 1960). Shoemaker et al. (1994) identified secondary craters within the inner ring of Schrödinger associated with Antoniadi crater, Orientale basin, and Humboldt crater (crater rims outlined in blue in Fig. 4). These impact structures lie 386 km, 1760 km, and 3000 km away from Schrodinger, respectively. Three sets of secondary craters with varying source crater distances will provide insight into the relationship of secondary crater morphology and source crater distance.

Secondary crater impactors have velocities less than the escape velocity of the Moon (2.4 km/s), which is far slower than the velocities of impacting asteroids and comets. For that reason, a significant fraction of the impacting material may survive, which means that we may be able to sample material excavated from the lunar crust beneath Antoniadi, Orientale, and Humboldt

craters by proxy. Because of this redistribution of material, a traverse in Schrödinger may provide samples of the ancient highlands (excavated from Orientale and Humboldt) and South Pole–Aitken regolith (excavated from Antoniadi). This greatly expands the potential sampling area to include the farside polar region (Antoniadi), the western equatorial limb (Orientale), and the southeastern nearside limb (Humboldt).

SURFACE SCENARIO OPTIONS

At the time of our final edits (April 2010), NASA's Constellation Program to develop human-crewed launch vehicles for a return to the Moon has been cancelled by the Obama administration, although the cancellation has yet to be approved by the U.S. Congress. Whether this cancellation decision is implemented or not, we expect that the architecture developed for a human return to the lunar surface will likely involve some version of the Constellation Program elements described herein. Indeed, NASA projects are continuing to plan for operations within the South Pole–Aitken basin, including the elements needed for exploration of Schrödinger basin.

First, an *Ares V* rocket will carry an Earth Departure Stage (EDS) and Lunar Surface Access Module (LSAM) into Earth orbit. An *Ares I* rocket will carry the *Orion* crew vehicle with

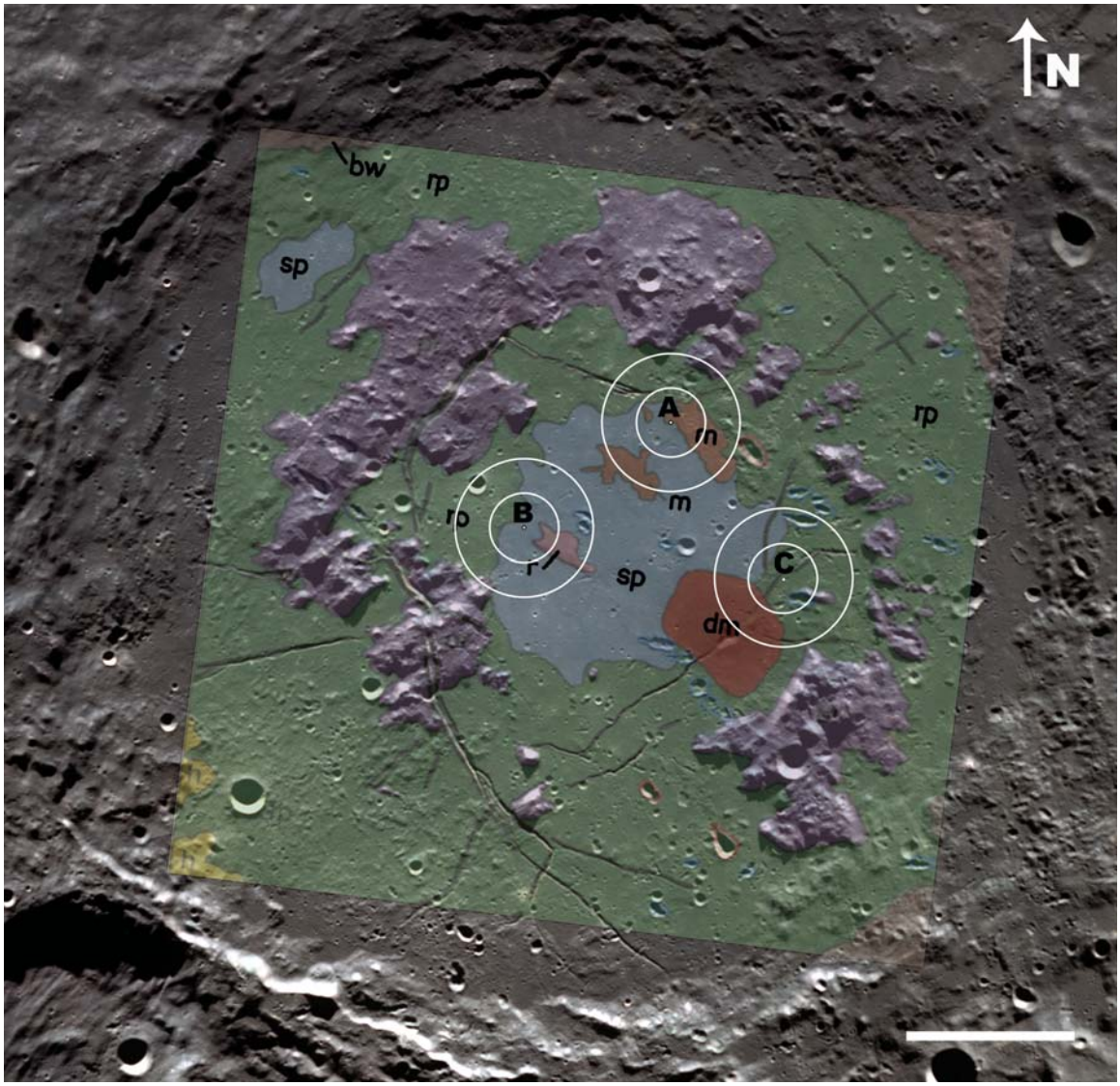

Figure 4. *Clementine* image of the Schrödinger basin with superimposed geological map by Shoemaker et al. (1994). White bar is 50 km long, white dots are landing sites, and white circles are 10 and 20 km radii. The main units are smooth plains material (sp), rough plains material (rp), basin wall material (bw), mare material (m), dark explosive volcanic material (dm), and ridged terrain (r). The sp unit is interpreted to be Schrödinger impact melt, and the rp unit is interpreted to be Schrödinger impact melt breccia.

a crew of four into orbit, where they will dock with the EDS. The EDS will then propel *Orion* to the Moon. Once in lunar orbit, the EDS will jettison, and the crew will transfer from *Orion* to the LSAM, called *Altair*. During the *Apollo* Program, crews were split at this point in the operation. One crew member remained in orbit, while two landed on the lunar surface. In the Constellation Program, all four astronauts will land using the *Altair* vehicle. Several mobility options are still being considered, but traverses will involve at least two crew members in some type of rover. Trade studies are being conducted to determine which activities will occur using an unpressurized roving platform (akin to the *Apollo Lunar Roving Vehicle*; Harrison et al., 2008) or pressurized rovers like the *Lunar Exploration Rover* (e.g., Garry et al., 2009).

Surface operations may be conducted in a sortie format, in which crew land, conduct activities, and return to Earth during a single sunlit period (equivalent to 14 d on Earth). This model is similar to the *Apollo* mode of operations, where the longest extravehicular activity (EVA) time was limited to a maximum of 22 h (*Apollo 17*). This allows the crew to avoid the complications of lunar night and loss of solar power. However, there may also be longer-duration sortie missions and eventually an outpost from which multiple-month-long activities are coordinated.

At present, NASA is considering four surface campaigns over an 11 yr period. One involves an outpost at the lunar south pole and roving capability to a distance of 500 km. The second involves the same outpost and a roving capability to a distance of 1000 km. Both of those campaigns can reach Schrödinger basin. The third and fourth campaigns also involve a south pole outpost and sortie opportunities to three and five sites, respectively. In both of these latter cases, roving capability to 500 km is also planned, which allows Schrödinger to be a target of study for all of the campaigns currently being considered.

Long-distance traverse excursions from an outpost at Shackleton crater and the lunar south pole are being considered (Clark et al., 2009). In these campaigns, additional science stations can be distributed on the basin ejecta blanket and basin rim before, ideally, a route to the basin floor is identified. Once on the basin floor, many of the stations identified in our shorter-duration sortie mission will be good science targets.

Initially, traverses will probably be limited to distances within 10 km of *Altair*, so that crew can safely walk back to the lander in the event of rover failure. Options that extend this limit to 20 km are being considered when two rovers are deployed. Both limits will be examined at potential landing sites within Schrödinger basin.

TRAVERSE OPTIONS

Based on geological mapping (Shoemaker et al., 1994) and *Clementine* images, we chose three landing sites (Figs. 4 and 5) where NRC (2007) objectives can be addressed at each location, summarized in Tables 1 and 2.

Site A

For site A (Fig. 5A), landing and take-off would take place upon the central melt sheet, because it provides a relatively smooth surface. Access to the central melt sheet ("sp" unit), melt breccia ("rp" unit), two mare-type basalt outcrops ("m" units), and a series of faults and fractures is available within a 10 km radius. Craters, as well as the deep fracture within the central melt sheet, can provide excellent outcrops to view and sample central melt sheet differentiation. In a 20 km radius, a third basaltic outcrop, peak-ring material (South Pole–Aitken material), and an Orientale secondary crater are available for study. Reaching the Orientale secondary crater will require a path either across or around the "m" unit, either of which will provide many areas for study along the way.

Site B

Site B (Fig. 5B) is located in the western part of the inner ring. Again, landing would be on the smooth central melt sheet. Central melt sheet, melt breccia, and "r" unit (interpreted to be either a viscous eruption or a buckling of the central melt sheet; Shoemaker et al., 1994) are all within 5 km of the landing site. Within a 20 km radius, ghost craters, Antoniadi secondary craters, and peak-ring material (South Pole–Aitken material) are available for study, with most of the traverse taking place upon the smooth central melt sheet.

Site C

Site C (Fig. 5C) landing would take place on the impact melt breccia, possibly making landing and traversing more difficult than the previous two sites. However, the explosive volcano is only 8 km away. Peak-ring material, central melt sheet, and Antoniadi secondary craters are within 10 km. Further exploration of the volcano and additional secondary craters are within a 20 km radius. This site features abundant faults and fractures, which would make observations similar to *Apollo 15* Hadley Rille.

DATA REQUIREMENTS NEEDED PRIOR TO SPECIFIC SITE SELECTION

Better imagery, elevation, and geophysical data will optimize a future mission to Schrödinger basin.

High-Resolution Imaging

The standard resolution of the *Clementine* High-Resolution Imaging (HIRES) camera (images within this paper) is ~100–360 m/pixel. High-resolution images are 20–60 m/pixel, and are only available in narrow strips, providing incomplete coverage (Robinson et al., 1997). Full high-resolution coverage of our proposed landing sites is needed in order to optimize surface activities.

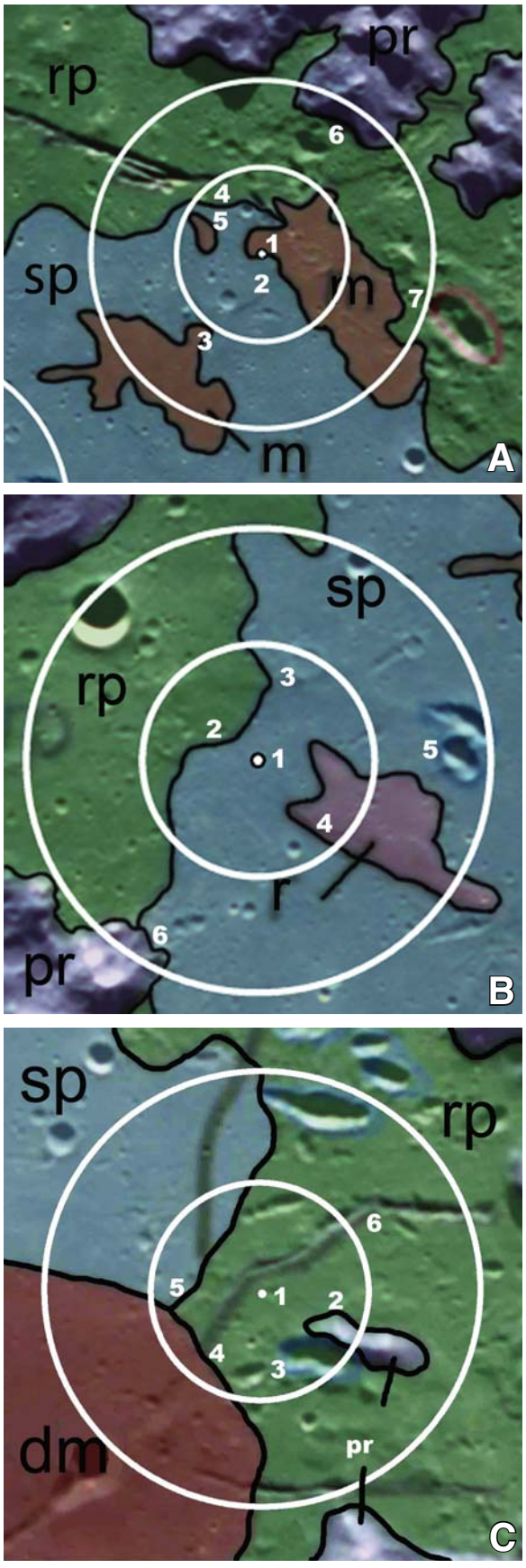

Current missions such as the *Lunar Reconnaissance Orbiter* (LRO) can fulfill this requirement. The *Lunar Reconnaissance Orbiter* Camera (LROC) (Chin et al., 2007) can obtain additional images to further evaluate the traverses proposed here. The entire basin should be canvassed by the wide-angle camera, which will generate images of 59.6 km^2 with a resolution of 74.3 m/pixel. We recommend several higher-resolution images of the landing and traverse sites outlined in the previous section to be captured by the narrow-angle camera (NAC). Because these images will have a resolution of 0.5 m/pixel, the accessibility of traverse stations proposed here can be verified. Because NAC images are 5 × 25 km in size, two to four parallel strips may be needed to define each landing site.

Topography

The *Clementine* laser altimetry coverage of the polar areas is incomplete, and Schrödinger basin lies partially in this uncovered region. High-resolution altimetry is needed in order to determine the topography on a scale that would be required for mission planning. *Chang'e 1*, *Chandrayaan-1*, and *Selene/Kaguya* spaceprobes were equipped with laser altimeter instruments. However, only *Kaguya* data are currently available, and the released grid has 0.25° resolution over Schrödinger area (Araki et al., 2009). The laser altimetry instrument onboard *Lunar Reconnaissance Orbiter* will provide a global digital elevation model of the Moon with 10 cm vertical resolution, 1 m vertical resolution, and 50–100 m horizontal resolution, with 1 km average cross-track sampling at the equator (Chin et al., 2007). These data will greatly improve our current data sets and will make detailed traverse planning possible.

Geophysical Probing of the Subsurface

Knowledge of the basin subsurface structure is essential in order to estimate the thickness, stratification, and lateral extent of various geological units (i.e., central melt sheet, basalt units). Orbital geophysical sounding using low-frequency radar may reveal the global subsurface structure of Schrödinger basin with resolution on the order of 10 m (approximately equal to the wavelength of the electromagnetic signal). Additionally, more

Figure 5. Proposed landing site (white dot) with 10 and 20 km radii (in white) and station numbers (in white). For description of geologic units, see Figure 4. The main units are smooth plains material (sp), rough plains material (rp), and mare material (m). (A) Site A stations: 1—basaltic unit, 2—Schrödinger central impact melt sheet, 3—second basaltic unit, 4—deep fracture, 5—impact melt breccia, 6—peak-ring material (pr), 7—Orientale secondary crater. (B) Site B stations: 1—central melt sheet, 2—Schrödinger impact melt breccia, 3—ghost craters, 4—ridged material ("r unit," see text for discussion), 5—Antoniadi secondary craters, 6—peak-ring material. (C) Site C stations: 1—impact melt breccia, 2—peak-ring material, 3—Antoniadi secondary craters, 4—explosive volcano, 5—central melt sheet, and 6—deep fracture.

TABLE 1. PRIORITIZED SCIENTIFIC CONCEPTS AND GOALS AS IDENTIFIED BY THE NATIONAL RESEARCH COUNCIL (NRC, 2007)

NRC priority	Scientific concept description
1	The bombardment history of the inner solar system is uniquely revealed on the Moon.
2	The structure and composition of the lunar interior provide fundamental information on the evolution of a differentiated planetary body.
3	Key planetary processes are manifested in the diversity of lunar crustal rocks.
4	The lunar poles are special environments that may bear witness to the volatile flux over the latter part of solar system history.
5	Lunar volcanism provides a window into the thermal and compositional evolution of the Moon.
6	The Moon is an accessible laboratory for studying the impact process on planetary scales.
7	The Moon is a natural laboratory for regolith processes and weathering on anhydrous airless bodies.
8	Processes involved with the atmosphere and dust environment of the Moon are accessible for scientific study while the environment remains in a pristine state.

detailed seismic (both refraction and reflection), gravity, and electromagnetic surveys conducted on the surface using mobile platforms (both robotic and human-operated) can provide higher-resolution data. Recently the Lunar Radar Sounder (LRS) experiment onboard *Selene/Kaguya* spacecraft, working with 5 MHz frequency (or 60 m wavelength), provided subsurface sounding data with resolutions of up to several kilometers in depth (Ono et al., 2009). If sections covering the Schrödinger area are released, it would greatly improve the data set.

Imagery can be used within a Geographic Information System (GIS) to identify locations of interest. In addition, GIS can be used to map and describe potential routes to maximize hazard avoidance by characterizing surface parameters such as slope angle, slope aspect, roughness, and composition prior to surface operations (e.g., Thaisen et al., 2008).

Precursor Robotic Reconnaissance

A precursor robotic rover can reduce the risk, requirements, and cost of human exploration (e.g., Kohout et al., 2008; Kring, 2007). In addition, a precursor rover could provide site characterization to enhance the efficiency of human exploration by identifying the highest priority traverse stations. A rover could also collect and deliver samples from remote areas to the human mission landing site or conduct complementary research after human mission departure (Kohout et al., 2008; Kring, 2007).

CONCLUSION

Schrödinger basin is a unique locality to study and sample a variety of materials ranging over a wide age span. Schrödinger basin is unique in that it is the only young basin within the main rim of the South Pole–Aitken basin, so it is well exposed and provides relatively fresh outcrops from which to sample. Sampling of the inner peak ring will be a reliable method of collecting South Pole–Aitken material. Schrödinger impact material will also be easily sampled within the inner peak ring. A landing site within Schrödinger provides a single location where one can sample both South Pole–Aitken and Schrödinger impact events, virtually bracketing the entire basin-forming epoch on the Moon, and addressing the highest-priority NRC goal.

Additionally, several young (Eratosthenian to Copernican) volcanic units are deposited on the floor of the inner peak ring of Schrödinger. Because the style of eruption varies (mare-type

TABLE 2. SUMMARY OF LANDING SITES WITH NATIONAL RESEARCH COUNCIL OBJECTIVES ADDRESSED AT EACH SITE

Site	Station	Feature	Distance from landing site (km)	NRC priority
A	1	First mare-type basaltic unit	0	3, 5, 7
	2	Central melt sheet	0	1, 6, 7
	3	Second mare-type basaltic unit	11	3, 5, 7
	4	Deep fracture	10	2, 6
	5	Third mare-type basaltic unit	7	3, 5, 7
	6	Peak-ring outcrop/South Pole–Aitken (SPA) material	17	1, 3, 6, 7
	7	Orientale secondary craters	20	1, 6
B	1	Central melt sheet	0	1, 6, 7
	2	Impact melt breccia	3	1, 6, 7
	3	Ghost craters	7	1, 3, 6
	4	“r” unit	4	3, 5
	5	Antoniadi secondary craters	16	1, 6
	6	Peak-ring outcrop/SPA material	18	1, 3, 6, 7
C	1	Impact melt breccia	0	1, 6, 7
	2	Peak-ring outcrop/SPA material	5	1, 3, 6, 7
	3	Antoniadi secondary craters	5	1, 6
	4	Explosive volcano	8	1, 2, 3, 5
	5	Central melt sheet	8	1, 6, 7
	6	Deep fracture	14	2, 6

to pyroclastic), the units may have tapped sources from different depths in the lunar interior. The volcanic deposits are also much younger than any unit sampled in the *Apollo* era and may be geochemically distinct from any unit yet sampled. Obtaining samples with these ages would address NRC goals 3 and 5 (Table 1).

Surface-based morphological studies of ghost and secondary craters within the inner peak ring will provide better understanding of such features and broaden our sample range to include areas from both the farside polar region and nearside equatorial limbs. Collection of samples with different ages and lithologies addresses NRC goals 3 and 7 (Table 1).

A landing site within the peak ring of Schrödinger will provide insight into the entire ancient basin-forming epoch, expose upper-crustal units in the walls of the basin, and allow sampling of deeper crustal units in the peak ring. A variety of samples will give an average chemical composition of the ancient crust (and potentially upper mantle) beneath the point of the Schrödinger impact. Igneous samples from several episodes of volcanic activity will offer a mineralogical and chemical window into subsurface magmatic processes. A similar mission with an extended traverse capability to the basin margins will provide access to additional samples of the lunar crust and an assessment of ejecta deposits around a basin.

ACKNOWLEDGMENTS

This manuscript benefited from a thoughtful review by W. Brent Garry. This project was initiated as part of the Lunar and Planetary Institute (LPI) Lunar Exploration Summer Intern Program, which was supported, in part, by the National Aeronautics and Space Administration (NASA) Lunar Science Institute. Additional support was provided by the LPI–Johnson Space Center for Lunar Science and Exploration, which is operated under a Cooperative Agreement with the NASA Lunar Science Institute (NNA09DB33A, principal investigator David A. Kring). The Institute of Geology is supported by Academy of Sciences of the Czech Republic Research Plan AV0Z 30130516. This is Lunar and Planetary Institute contribution 1550.

REFERENCES CITED

Araki, H., Tazawa, S., Noda, H., Ishihara, Y., Goossens, S., Sasaki, S., Kawano, N., Kamiya, I., Otake, H., Oberst, J., and Shum, C., 2009, Lunar global shape and polar topography derived from *Kaguya*-LALT laser altimetry: Science, v. 323, p. 897–900, doi:10.1126/science.1164146.

Baldwin, R.B., 1949, The Face of the Moon: Chicago, University of Chicago Press, 239 p.

Bogard, D.D., 1995, Impact ages of meteorites: A synthesis: Meteoritics, v. 30, p. 244–268.

Bush, G.W., 2004, A Renewed Spirit of Discovery: The President's Vision for U.S. Space Exploration: Washington, D.C., White House, U.S. Government, 9 p.

Chamberlain, J.W., Phinney, R.A., Adams, J.B., Coleman, P.J., Shoemaker, E.M., Toksoz, N.M., Walker, R.M., and Wasserburg, G.J., 1972, Post-*Apollo* Lunar Science: Houston, Texas, Lunar Science Institute, 104 p.

Chin, G., Brylow, S., Foote, M., Garvin, J., Kasper, J., Keller, J., Litvak, M., Mitrofanov, I., Paige, D., Raney, K., Robinson, M., Sanin, A., Smith, D., Spence, H., Spudis, P., Stern, S.A., and Zuber, M., 2007, *Lunar Reconnaissance Orbiter* overview: The instrument suite and mission: Space Science Reviews, v. 129, p. 391–419, doi:10.1007/s11214-007-9153-y.

Cintala, M.J., and Grieve, R.A., 1998, Scaling impact melting and crater dimensions: Implications for the lunar cratering record: Meteoritics & Planetary Science, v. 33, p. 889–912, doi:10.1111/j.1945-5100.1998.tb01695.x.

Clark, P.E., Bleacher, J., Mest, S., Petro, N., and Leshin, L., 2009, Lunar field exploration scenarios for a south pole outpost: Houston, Texas, Lunar and Planetary Institute, Lunar and Planetary Science Conference XXXX, CD-ROM, abstract 1135.

Delano, J.W., 1986, Pristine lunar glasses: Criteria, data, and implications: Journal of Geophysical Research, v. 91, p. D201–D213, doi:10.1029/JB091iB04p0D201.

Delano, J.W., and Livi, K., 1981, Lunar volcanic glasses and their constraints on mare petrogenesis: Geochimica et Cosmochimica Acta, v. 45, p. 2137–2149, doi:10.1016/0016-7037(81)90066-1.

ESAS (Exploration Systems Architecture Study), 2005, NASA's Exploration Systems Architecture Study: National Aeronautics and Space Administration Report NASA-TM-2005–214062, 752 p.

Garry, W.B., Hörz, F., Lofgren, G.E., Kring, D.A., Chapman, M.G., Eppler, D.B., Rice, J.W., Jr., Lee, P., Nelson, J., Gernhardt, M.L., and Walheim, R.J., 2009, Science operations for the 2008 NASA lunar analog field test at Black Point Lava Flow, Arizona: Houston, Texas, Lunar and Planetary Institute, Lunar and Planetary Science Conference XXXX, CD-ROM, abstract 1649.

Hackman, R.J., and Mason, A.C., 1961, Engineer Special Study of the Surface of the Moon: U.S. Geological Survey Map I-351, scale 1:3,800,000, 4 sheets.

Harrison, D.A., Ambrose, R., Bluethmann, B., and Junkin, L., 2008, Next Generation Rover for Lunar Exploration: Institute of Electrical and Electronics Engineers Transactions on Automatic Control (IEEEAC) Paper 1196, 13 p.

Hartmann, W.K., and Wood, C.A., 1971, Moon: Origin and evolution of multi-ring basins: The Moon, v. 3, p. 3–78.

Head, J.W., 1976, Lunar volcanism in space and time: Reviews of Geophysics and Space Physics, v. 14, p. 265–300, doi:10.1029/RG014i002p00265.

Hiesinger, H., and Head, J.W., III, 2003, Lunar South Pole–Aitken impact basin: *Clementine* topography and implications for the interpretation of basin structure and stratigraphy: Moscow, Vernadsky Institute/Brown University Microsymposium, v. 38, MS101.

Hiesinger, H., Jaumann, R., Neukum, G., and Head, J.W., III, 2000, Ages of mare basalts on the lunar nearside: Journal of Geophysical Research, v. 105, p. 29,239–29,275, doi:10.1029/2000JE001244.

Hiesinger, H., Head, J.W., III, Wolf, U., Jaumann, R., and Neukum, G., 2003, Ages and stratigraphy of mare basalts in Oceanus Procellarum, Mare Nubium, Mare Cognitum, and Mare Insularum: Journal of Geophysical Research, v. 108, p. 5065–5092.

Ivanov, B.A., 2005, Numerical modeling of the largest terrestrial meteorite craters: Solar System Research, v. 39, p. 381–409 (translated from Astronomicheskii Vestnik, v. 39, p. 426–456).

Jolliff, B.L., Gillis, J.J., Haslin, L.A., Korotev, R.L., and Wieczorek, M.A., 2000, Major lunar crustal terranes: Surface expressions and crust-mantle origins: Journal of Geophysical Research, v. 105, p. 4197–4216, doi:10.1029/1999JE001103.

Kohout, T., O'Sullivan, K.M., Losiak, A., Kring, D.A., Thaisen, K., and Weider, S., 2008, Robotic and human exploration of the Schrodinger basin: Houston, Texas, Lunar and Planetary Institute, Joint Annual Meeting of Lunar Exploration Analysis Group–International Lunar Exploration Working Group–Space Resources Roundtable 2008, abstract 4078.

Kring, D.A., 2005, Hypervelocity collisions into continental crust composed of sediments and an underlying crystalline basement: Comparing the Ries (~24 km) and Chicxulub (~180 km) impact craters: Chemie der Erde, v. 65, p. 1–46, doi:10.1016/j.chemer.2004.10.003.

Kring, D.A., 2007, Reducing the risk, requirements, and cost of the human exploration phase of the Constellation Program with robotic landers and rovers: Houston, Texas, Lunar and Planetary Institute, Lunar Exploration Analysis Group Workshop on Enabling Exploration: The Lunar Outpost and Beyond 2007, abstract 3037.

Kring, D.A., 2008, Deciphering the chronology and implications of impact cratering on the Moon: A high science priority for lunar exploration: Houston, Texas, Lunar and Planetary Institute, Lunar and Planetary Science Conference XXXIX, CD-ROM, abstract 1251.

Kring, D.A., 2009, Targeting complex craters and multi-ring basins to determine the tempo of impact bombardment while simultaneously probing

the lunar interior: Houston, Texas, Lunar and Planetary Institute, *Lunar Reconnaissance Orbiter* Science Targeting Meeting 2009, abstract 6037.

Kring, D.A., and Cohen, B.A., 2002, Cataclysmic bombardment throughout the inner solar system 3.9–4.0 Ga: Journal of Geophysical Research, v. 107, doi:10.1029/2001JE001529.

Longhi, J., 1992, Experimental petrology and petrogenesis of mare volcanics: Geochimica et Cosmochimica Acta, v. 56, p. 2235–2251, doi:10.1016/0016-7037(92)90186-M.

Lucey, P.G., Taylor, G.J., Hawke, B.R., and Spudis, P.D., 1998, FeO and TiO_2 concentrations in the South Pole–Aitken basin: Implications for mantle composition and basin formation: Journal of Geophysical Research, v. 103, p. 3701–3708, doi:10.1029/97JE03146.

National Research Council, 2007, The Scientific Context for Exploration of the Moon: Washington, D.C., National Research Council, 107 p.

Ono, T., Kumamoto, A., Nakagawa, H., Yamaguchi, Y., Oshigami, S., Yamaji, A., Kobayashi, T., Kasahara, Y., and Oya, H., 2009, Lunar Radar Sounder observations of subsurface layers under the nearside maria of the Moon: Science, v. 323, p. 909–912, doi:10.1126/science.1165988.

Petro, N.E., and Pieters, C.M., 2008, The lunar-wide effects of basin ejecta distribution on the early megaregolith: Meteoritics & Planetary Science, v. 43, p. 1517–1529, doi:10.1111/j.1945-5100.2008.tb01025.x.

Pieters, C.M., Head, J.W., Gaddis, L., Jolliff, B., and Duke, M., 2001, Rock types of South Pole–Aitken basin and extent of basaltic volcanism: Journal of Geophysical Research, v. 106, p. 28,001–28,022, doi:10.1029/2000JE001414.

Pike, R.J., and Spudis, P.D., 1987, Basin ring spacing on the Moon, Mercury, and Mars: Earth, Moon, and Planets, v. 39, p. 129–194, doi:10.1007/BF00054060.

Potter, R.W.K., Collins, G.S., Kring, D.A., Kiefer, W., and McGovern, P., 2010, Constraining the size of the South Pole–Aitken basin impact: Houston, Texas, Lunar and Planetary Institute, Lunar and Planetary Science Conference XXXXI, CD-ROM, abstract 1700.

Quaide, W.L., 1965, Rilles, ridges, and domes—Clues to maria history: Icarus, v. 4, p. 374–389, doi:10.1016/0019-1035(65)90041-2.

Robinson, M.S., Malaret, E., and White, T., 1997, *Clementine* HIRES calibration and mosaicking: Houston, Texas, Lunar and Planetary Institute, Lunar and Planetary Science Conference XXVII, CD-ROM, abstract 1717.

Ryder, G., 1990, Lunar samples, lunar accretion and the early bombardment of the Moon: Eos (Transactions, American Geophysical Union), v. 71, p. 313–323, doi:10.1029/90EO00086.

Schaber, G.G., 1973, Lava Flows in Mare Imbrium: Geologic evaluation from *Apollo* orbital photography: Houston, Texas, Lunar and Planetary Institute, Lunar and Planetary Science Conference IV, abstract 1245.

Shoemaker, E.M., 1960, Ballistics of the Copernican Ray System: Proceedings of Lunar and Planetary Colloquium, v. 2, 16 p.

Shoemaker, E.M., 1962, Exploration of the Moon's surface: American Scientist, v. 50, p. 99–130.

Shoemaker, E.M., and Hackman, R.J., 1962, Stratigraphic basis for a lunar time scale, *in* Kopal, Z., and Mikhailov, Z.K., eds., The Moon: London, Academic Press, p. 289–300.

Shoemaker, E.M., Robinson, M.S., and Eliason, E.M., 1994, The south pole region of the Moon as seen by *Clementine*: Science, v. 266, p. 1851–1854, doi:10.1126/science.266.5192.1851.

Smith, J.V., Anderson, A.T., Newton, R.C., Olsen, E.J., Wyllie, P.J., Crewe, A.V., Isaacson, M.S., and Johnson, D., 1970, Petrologic history of the Moon inferred from petrography, mineralogy, and petrogenesis of *Apollo 11* rocks: Proceedings of the *Apollo 11* Lunar Science Conference: Geochimica et Cosmochimica Acta, v. 1, suppl. 1, p. 897–925.

Spudis, P.D., 1993, The Geology of Multi-Ring Impact Basins—The Moon and Other Planets: Cambridge, UK, Cambridge University Press, 277 p.

Spudis, P.D., Reisse, R.A., and Gillis, J.J., 1994, Ancient multiring basins on the Moon revealed by *Clementine* laser altimetry: Science, v. 266, p. 1848–1851, doi:10.1126/science.266.5192.1848.

Stöffler, D., and Ryder, G., 2001, Stratigraphy and isotope ages of lunar geologic units: Chronological standard for the inner solar system: Space Science Reviews, v. 96, p. 9–54, doi:10.1023/A:1011937020193.

Strom, R.G., Malhotra, R., Ito, T., Yoshida, F., and Kring, D.A., 2005, The origin of planetary impactors in the inner solar system: Science, v. 309, p. 1847–1850.

Tera, F., Papanastassiou, D.A., and Wasserburg, G.J., 1974, Isotopic evidence for a terminal lunar cataclysm: Earth and Planetary Science Letters, v. 22, p. 1–21, doi:10.1016/0012-821X(74)90059-4.

Thaisen, K.G., Losiak, A., Kohout, T., O'Sullivan, K.M., Weider, S., and Kring, D.A., 2008, Geographic Information systems: An enabling tool for lunar exploration: Houston, Texas, Lunar and Planetary Institute, Joint Annual Meeting of Lunar Exploration Analysis Group–International Lunar Exploration Working Group–Space Resources Roundtable 2008, abstract 4098.

Turner, G., Cadogan, P.H., and Yonge, C.J., 1973, Argon selenochronology: Proceedings of the 4th Lunar Science Conference: Geochimica et Cosmochimica Acta, v. 2, suppl. 4, p. 1889–1914.

Wilhelms, D.E., Howard, K.A., and Wilshire, H.G., 1979, Geologic Map of the Far Side of the Moon: U.S. Geological Survey Map I-1162, scale 1:5,000,000.

Wilhelms, D.E., McCauley, J.F., and Trask, N.J., 1987, The Geologic History of the Moon: U.S. Geological Survey Professional Paper 1348, 8B, 302 p.

Manuscript Accepted by the Society 26 August 2010

Printed in the USA

The Geological Society of America
Special Paper 477
2011

Geomorphic terrains and evidence for ancient volcanism within northeastern South Pole–Aitken basin

Noah E. Petro*
National Aeronautics and Space Administration Goddard Space Flight Center, Code 698, Planetary Geodynamics Branch, Greenbelt, Maryland 20771, USA

Scott C. Mest
Planetary Science Institute, 1700 E. Ft. Lowell Road, Suite 106, Tucson, Arizona 85719-2395, USA, and *Planetary Geodynamics Laboratory (Code 698), National Aeronautics and Space Administration Goddard Space Flight Center, Building 33, Room F320, Greenbelt, Maryland 20771, USA*

Yaron Teich
Walter Johnson High School, 6400 Rock Spring Drive, Bethesda, Maryland 20814, USA

ABSTRACT

The interior of the enigmatic South Pole–Aitken basin has long been recognized as being compositionally distinct from its exterior. However, the source of the compositional anomaly has been subject to some debate. Is the source of the iron-enhancement due to lower-crustal/upper-mantle material being exposed at the surface, or was there some volume of ancient volcanism that covered portions of the basin interior? While several obvious mare basalt units are found within the basin and regions that appear to represent the original basin interior, there are several regions that appear to have an uncertain origin. Using a combination of *Clementine* and *Lunar Orbiter* images, several morphologic units are defined based on albedo, crater density, and surface roughness. An extensive unit of ancient mare basalt (cryptomare) is defined and, based on the number of superimposed craters, potentially represents the oldest volcanic materials within the basin. Thus, the overall iron-rich interior of the basin is not solely due to deeply derived crustal material, but is, in part due to the presence of ancient volcanic units.

INTRODUCTION

The South Pole–Aitken basin has been long been recognized as the oldest and largest impact basin on the Moon (e.g., Wilhelms, 1987; Spudis, 1993) that possesses clear basin attributes (e.g., a clearly defined topographic rim and a prominent gravity anomaly) (Garrick-Bethell and Zuber, 2009). The basin is unique in that it is the only location on the Moon that contains surficial exposures of material likely derived from the lower crust (e.g., Pieters et al., 2001; Lucey, 2004; Nakamura et al., 2009). However, because of the age of the basin, possibly greater than 4.1 Ga (e.g., Ryder, 2002), areas of the interior have

*Noah.E.Petro@nasa.gov

Petro, N.E., Mest, S.C., and Teich, Y., 2011, Geomorphic terrains and evidence for ancient volcanism within northeastern South Pole–Aitken basin, *in* Ambrose, W.A., and Williams, D.A., eds., Recent Advances and Current Research Issues in Lunar Stratigraphy: Geological Society of America Special Paper 477, p. 129–140, doi:10.1130/2011.2477(06).

been modified by both large impacts (e.g., the Apollo, Ingenii, and Schrödinger basins) and several volcanic eruptions (Yingst and Head, 1999). Additionally, the interior of the basin has been modified to a small degree by ejecta from basins external to South Pole–Aitken (Wilhelms, 1987; Haskin et al., 2003; Petro and Pieters, 2004, 2008). Unraveling the complex geologic history of the interior of the basin by way of geologic mapping and age dating of units will be central to understanding the evolution of this unique region of the Moon.

Lunar Orbiter images provided the first detailed views into the interior of the South Pole–Aitken basin and allowed geologic maps to be produced by Stuart-Alexander (1978) and Wilhelms et al. (1979). These maps identified numerous units across the South Pole–Aitken basin interior, the dominant terrain being either a pre-Nectarian– or Nectarian-age terra unit interpreted to represent highly degraded basin and crater ejecta. Wilhelms (1987) further grouped the ancient terrains together as "interior materials of the South Pole–Aitken basin," i.e., materials that likely represent the ancient, locally derived South Pole–Aitken materials (Haskin et al., 2003; Petro and Pieters, 2004). In addition to the ancient units inside South Pole–Aitken, several small plains units of Imbrian and/or Nectarian age were interpreted to represent impact-derived products from the Apollo and Ingenii basins (Stuart-Alexander, 1978). These plains units were observed to be relatively smooth with a higher density of craters than that found on nearby mare surfaces.

Here, we define several geomorphic terrains in the northeastern region of the South Pole–Aitken basin, a region that includes the Apollo basin and a large plains unit to the south (Figs. 1 and 2). In identifying units in the region, we redefine the extent of this plains unit and find that it is significantly larger than previously identified by Pieters et al. (2001) and is likely the most extensive cryptomare unit within South Pole–Aitken. We show, based on the cumulative number of craters within the plains unit, that the unit is older than other mare and plains units within South Pole–Aitken and is of a comparable age to a similar cryptomare deposit in the Schickard crater (Greeley et al., 1993).

INTERIOR OF THE SOUTH POLE–AITKEN BASIN

The interior of South Pole–Aitken basin contains a diversity of unique compositions that are found in few locations or are completely absent outside the basin (Pieters et al., 2001; Lucey, 2004). The unique lithologies found across the basin are the result of its enormous size and depth of excavation. The basin's large elliptical shape, roughly 2400 × 2050 km in diameter (Garrick-Bethell and Zuber, 2009), and enormous depth, –11 km at its deepest, imply that material from great depth in the lunar crust was exposed at the surface following South Pole–Aitken's formation (e.g., Jolliff et al., 2000; Pieters et al., 2001). The original floor of the basin was covered by an extensive impact melt deposit, which was largely derived from the middle to lower crust and perhaps upper mantle (Warren et al., 1996; Lucey et al., 1998; Pieters et al., 2001). This initial surface was then modified by subsequent impacts, some of basin scale, which redistributed materials across the basin and exposed additional material from below the original South Pole–Aitken floor (Nakamura et al., 2009).

Remote-sensing data from the *Galileo* and *Clementine* missions indicated that the central portion of the basin is enriched in iron relative to the basin's exterior (Pieters et al., 1993, 2001; Jolliff et al., 2000). Subsequently, *Lunar Prospector* gamma-ray data showed that the central iron-enhancement contains an iron abundance of at least 13.3 wt%, only 2 wt% less than mare basalts outside South Pole–Aitken (Gillis et al., 2004). The first spectral data of the basin, from *Galileo*'s flyby of the Moon, suggested that the interior of the basin contained a significant mafic signature relative to the exterior of the basin (Belton et al., 1992; Head et al., 1993; Pieters et al., 1993). Belton et al. (1992) presented three possible explanations for the observed mafic enhancement: (1) The formation of the enormous basin was excavated through the entire crust and exposed mantle material, (2) the South Pole–Aitken-forming event did not excavate to the mantle but post–South Pole–Aitken impacts within the basin excavated through the thinned crust and excavated and ejected mantle material, or (3) extensive ancient volcanism imparted much of the mafic signature and subsequent impacts, particularly the Orientale basin, masked the basalts with anorthositic ejecta. Yingst and Head (1999) postulated that an additional source of the mafic anomaly was the subsequent emplacement of smaller mare deposits within the South Pole–Aitken basin, deposits that have remained largely uncontaminated by anorthositic material. Volcanism within the basin is on a much smaller scale than that which occurred in nearside basins, is constrained to the interiors of basins and craters (Yingst and Head, 1997), and was limited to the Imbrian and Eratosthenian eras.

Pieters et al. (2001), using *Clementine* Ultraviolet-Visible (UVVIS) data, identified a range of lithologies across the basin, from the extensive low-Ca pyroxene-bearing (likely noritic in composition) "floor" of South Pole–Aitken to the relatively small exposures of mare and pyroclastic material. A few exposures of low-Fe bearing (anorthositic) and olivine-rich materials were also identified within South Pole–Aitken across the basin. Pieters et al. (2001) noted a number of small smooth plains regions, interpreted to be pre-Orientale mare basalts covered by a thin veneer of regionally derived material. Pieters et al. (2001) identified a plains unit located south of the Apollo basin as having a surface more iron-rich than basalts buried by Orientale ejecta in Oceanus Procellarum (Mustard and Head, 1996). Pieters et al. concluded that the material mantling the older mare was likely derived from the surrounding iron-rich noritic South Pole–Aitken floor material, and thus the plains unit not only retained the mafic signature of the basalts, it contains an iron signature from the locally derived material. Hartmann and Wood (1971) first noted that the small plains unit south of Apollo likely originated as mare subsequently covered by Orientale ejecta. Later, Stuart-Alexander (1978) and Wilhelms (1987)

described the unit as basin-derived plains of Imbrian-Nectarian age. Its origin as a volcanic unit could not be confirmed until multispectral data were obtained by *Clementine*. Pieters et al. (2001) showed that while the exposure of mare within South Pole–Aitken was limited, definitive cryptomare deposits, outside of the small plains unit south of Apollo, were almost nonexistent. Pieters et al. (2001) also showed that the general iron enhancement throughout the basin was largely due to the existence of low-Ca pyroxene-bearing materials (interpreted to be due to the presence of norite) across South Pole–Aitken's interior. In addition to this source of iron, the small plains unit south of Apollo was determined to be of volcanic origin based on its high-Ca pyroxene signature (Pieters et al., 2001). This ancient volcanism occurred outside of recognized basins and craters, implying a unique mode of occurrence for South Pole–Aitken basalts (Yingst and Head, 1997, 1999).

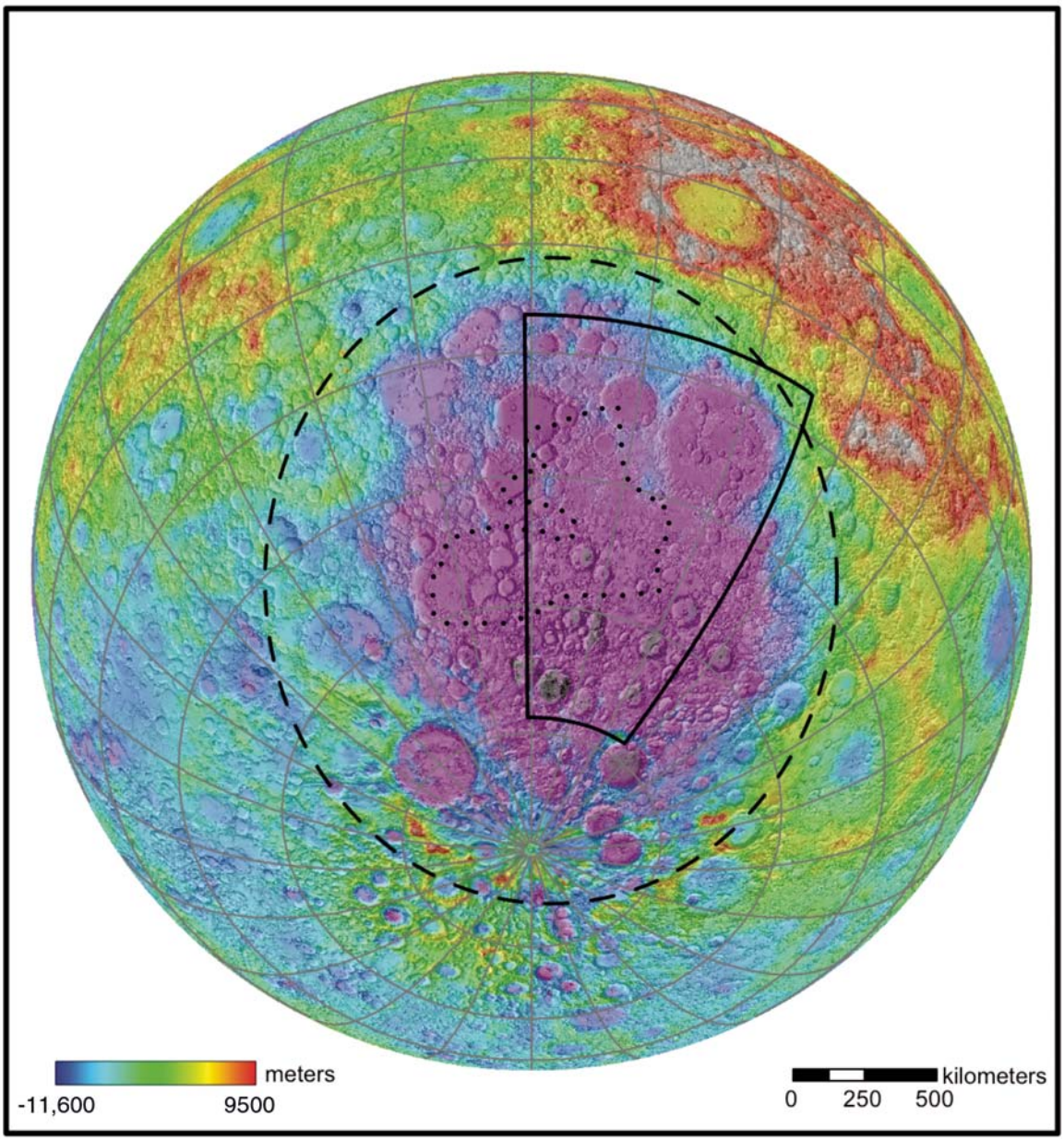

Figure 1. Orthographic projection of ULCN2005 topographic data over shaded relief map (U.S. Geological Survey) centered on South Pole–Aitken (56°S, 180°). Scale is referenced to the center of the basin. The approximate main topographic rim is denoted by black dashed line (Spudis, 1993). The region containing the plains south of the Apollo basin is outlined by the black box and is shown in more detail in Figures 2 and 3. The dotted line outlines the primary iron enhancement associated with the interior of the basin (Jolliff et al., 2000).

Geomorphic Terrains of South Pole–Aitken

In order to better investigate the plains south of Apollo, the basin interior was subdivided into geomorphic terrains (Fig. 3) that reflect the relative density of superposed impact craters, the albedo of the surface, and elemental abundances associated with each terrain. This section discusses of the methodology involved in identifying and mapping the geomorphic terrains, as well as a description of each terrain.

Mapping Methodology

The geomorphic map of the South Pole–Aitken region was produced in ArcGIS, the ease of use of which allows unit

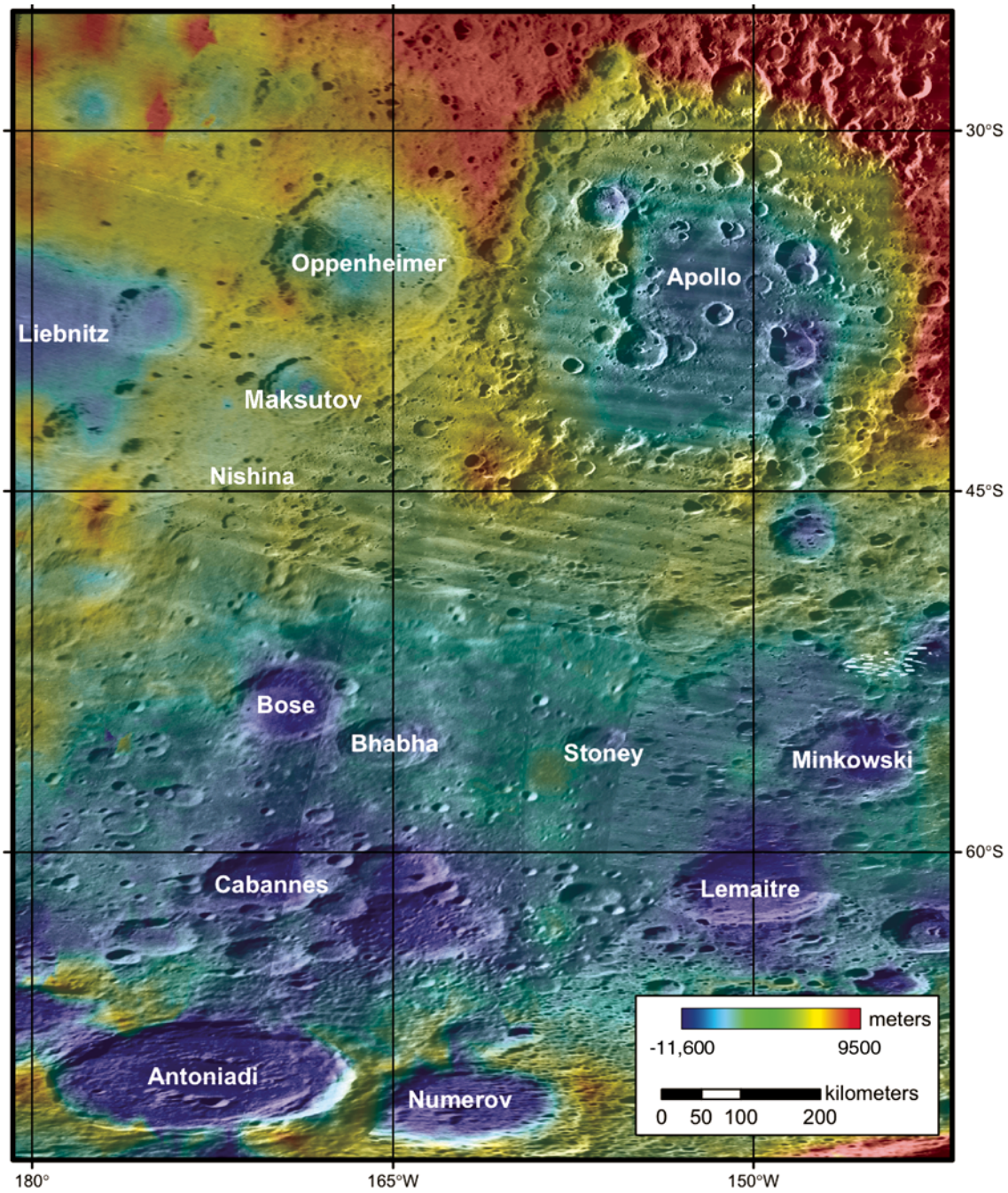

Figure 2. ULCN2005 topographic data over *Lunar Orbiter* photomosaic showing the plains south of the Apollo basin study area outlined in Figure 1. The names of several prominent moderate-sized impact craters are given. Projection is Plate Carrée.

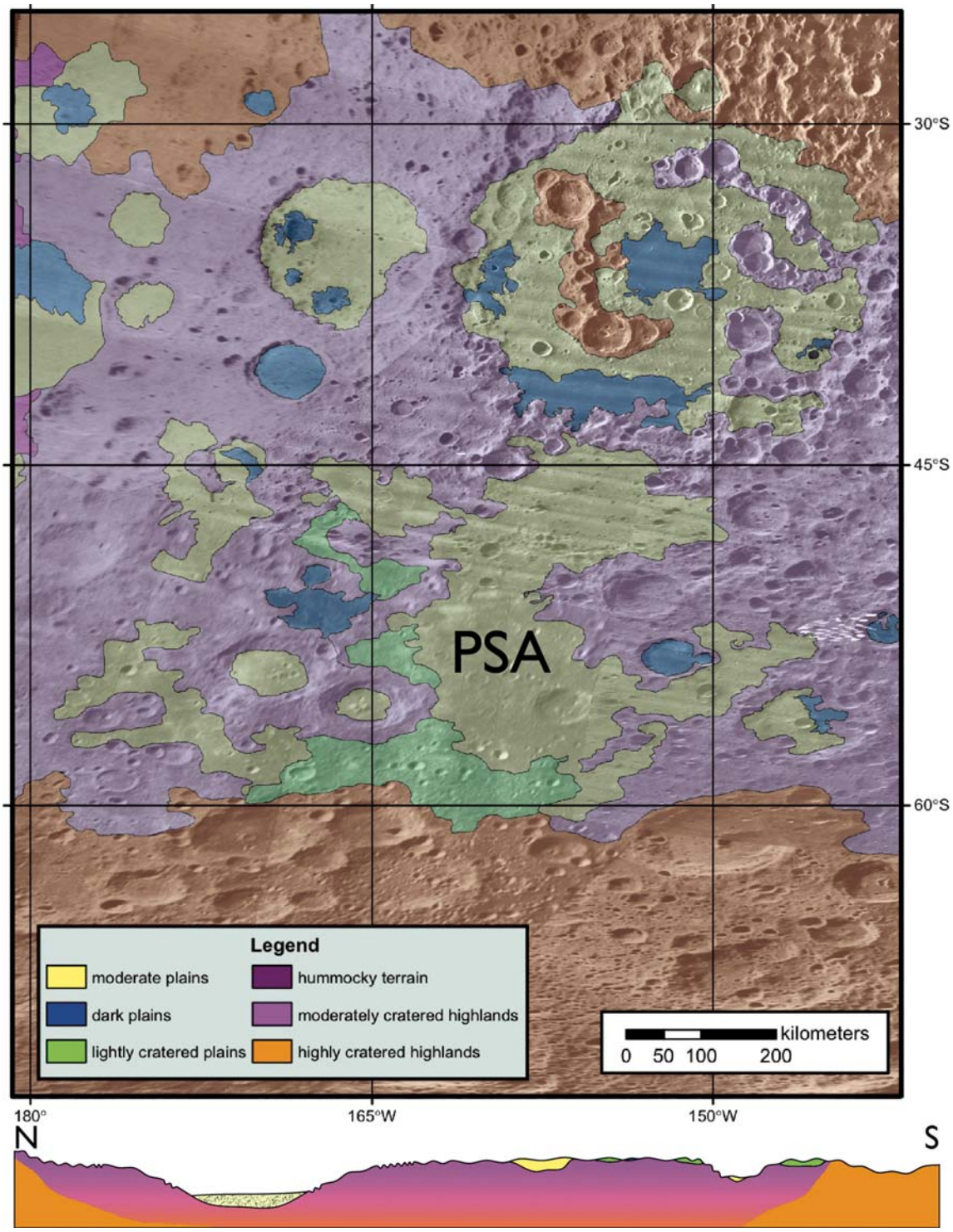

Figure 3. Geomorphic terrain map over *Lunar Orbiter* photomosaic showing the eastern South Pole–Aitken (SPA) study area outlined in Figure 1. Identification and characterization of these terrains are based on *Lunar Orbiter* and *Clementine* images, and topographic and geochemical data, and are described in the text. Projection is Plate Carrée. The extensive plains unit described in the text, the Plains South of Apollo (PSA), is labeled. At bottom, a schematic cross section through the study area, extending from north (left) to south (right) down the 165°W line of longitude, illustrates inferred stratigraphic relationships between the units. While the two highland terrains are morphologically similar to each other, the moderately cratered terrain (purple) has a higher iron content due to the presence of an abundance of deeply derived South Pole–Aitken impact melt breccia. The highly cratered highlands inside (in the south) and outside (in the north) of South Pole–Aitken certainly have distinct provenances, but are morphologically similar to one another.

characterizations and comparisons of data sets (e.g., imagery, topographic, spectral) to be made quickly. Identification of terrains was based primarily on analysis of several data sets, available from the U.S. Geological Survey (USGS) and the Planetary Data System, including the *Lunar Orbiter* (Becker et al., 2008) and *Clementine* 750 nm (100 m/pixel) (Eliason et al., 1999) global photomosaics, and *Clementine* UVVIS-derived color ratio maps (e.g., Pieters et al., 1994, 2001) and *Lunar Prospector* half-degree (15 km/pixel) gridded reduced gamma-ray spectrometer iron abundance data (e.g., Feldman et al., 2001; Elphic et al., 2000; Lawrence et al., 2003; Prettyman et al., 2006), which were used to characterize surface materials within the geomorphic terrains. The 2005 Unified Lunar Control Network (ULCN2005) (Archinal et al., 2006) was used to characterize the topographic expression of the surface.

Due to the regional scale of this map, high-spatial-resolution data sets were not required to identify geomorphic "contacts" between terrains. Many of the contacts defined in Figure 3, particularly the highlands contacts, represent subtle gradations, especially between the two highlands terrains. *Lunar Orbiter* images provide adequate low-sun-angle views that enable subtle topographic and morphologic features to be seen, especially impact craters, which were required to calculate the crater size-frequency distribution statistics (see following) for the Plains South of Apollo unit (Fig. 3). The plains units were most distinctive based on their relative albedos. The *Clementine* reflectance at 750 nm was used to define the albedo of each unit: The dark plains albedo is typically between 0.09 and 0.12, the moderate plains albedo is from 0.12 to 0.13, and the lightly cratered plains albedo is from 0.13 to 0.16. The dark plains units typically have sharper contacts with their neighboring units. Therefore, the *Lunar Orbiter* mosaic complemented the *Clementine* imagery, and together these data provided detailed views of the lunar surface suitable for mapping at this scale.

Geomorphic Terrain Identification

The geomorphic terrains mapped in Figure 3 are delineated by their relative density of superposed impact craters (Table 1; Fig. 4), relative albedo, and various chemical anomalies. Six primary geomorphic units were identified within the greater South Pole–Aitken area, and all are represented within the study area outlined in Figure 3. The units were divided into three subcategories—highlands, hummocky, and plains terrains, which are described in more detail later herein. The relative stratigraphic relationships between the units, where the plains and hummocky terrains are interpreted as mantling the older highlands units, are illustrated in a cross section at the bottom of Figure 3. The

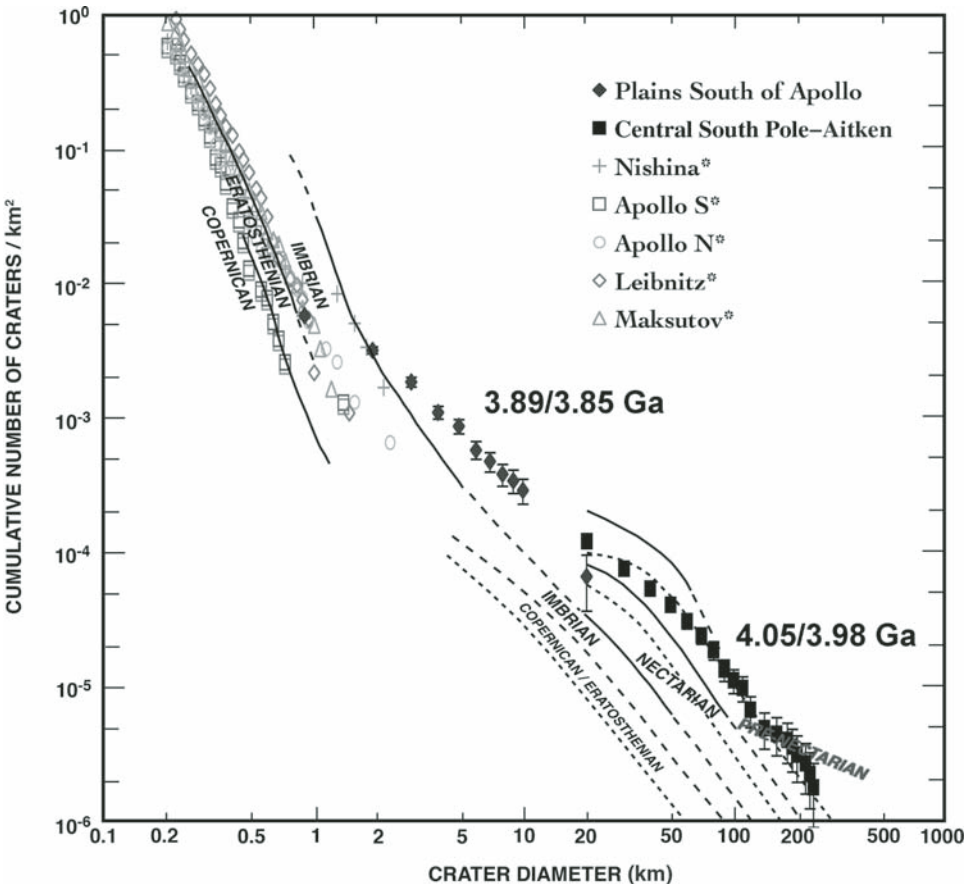

Figure 4. Cumulative crater counts for several regions in the South Pole–Aitken basin. The central South Pole–Aitken region corresponds to the most iron-enriched central portion of South Pole–Aitken, while the Plains South of Apollo (PSA) corresponds to the large plains unit illustrated in Figure 3. The Plains South of Apollo are interpreted to represent an expansive cryptomare unit representing ancient volcanism. Crater counts for four South Pole–Aitken mare basalts from Haruyama et al. (2009) are presented for comparison. The Plains South of Apollo are estimated to have an age between 3.89 and 3.85 Ga, while central South Pole–Aitken has an age of, at a minimum, between 4.05 and 3.98 Ga, using the empirically derived chronology of Neukum and Ivanov (1994). The South Pole–Aitken basalts investigated by Haruyama et al. (2009) and listed in Table 1 have ages from 2.44 to 3.85 Ga.

TABLE 1. MODEL AGES OF VARIOUS VOLCANIC UNITS

Region	Area (km^2)	*N*(1)	Age (Ga)*	Reference
Plains South of Apollo	76,675.4	0.0325	3.89	This study
		0.0245	3.85	This study
Central South Pole–Aitken Fe enrichment (See Fig. 1)	2,278,000	0.0876	4.05	This study
		0.0554	3.98	This study
Apollo basin north basalts†,§	1541.5	0.00209	2.49	Haruyama et al. (2009)
		0.00491	3.51	
Apollo basin south basalts†,§	7784	0.00205	2.44	Haruyama et al. (2009)
Apollo basin basalts	(Not reported)	0.0078	3.63	Greeley et al. (1993)
Apollo basin basalts	(Not reported)	0.00495–0.0109	3.57, 3.71	Williams et al. (1995)
Leibnitz†,§	926.0	0.00410	3.44	Haruyama et al. (2009)
		0.00473	3.50	
Antoniadi	592.7	0.00217	2.58	Haruyama et al. (2009)
Maksutov†,§	615.3	0.00311	3.27	Haruyama et al. (2009)
		0.00451	3.48	
Nishina†	596.7	0.00207	2.47	Haruyama et al. (2009)
		0.00282	3.16	
		0.02406	3.85	
Schickard Light Plains	(Not reported)	0.0233	3.84	Greeley et al. (1993)
Van de Graff Plains	1369	0.00804	3.64	Neukum et al. (1975)
Van de Graff mare unit	(Not reported)	0.0078	3.64	Greeley et al. (1993)

*Determined by the empirically derived chronology of Neukum and Ivanov (1994).
†For locations, see Figure 2.
§Cumulative crater curves are illustrated in Figure 4.

cross section extends from north to south (left to right), along the 165°W line of longitude.

Highland Terrains

The oldest terrains in the study region, the highlands terrains, generally exhibit relatively rugged surfaces, fairly constant albedos (typically greater than 0.16 in the *Clementine* 750 nm band), and are heavily cratered. Two geomorphic highland units were identified and include the moderately cratered highlands and the highly cratered highlands. These terrains roughly correlate to the Nbl (basin material, lineated) unit described by Wilhelms et al. (1979) and the pNt (cratered terra) and NpNt (irregular terra material) units of Stuart-Alexander (1978) and Wilhelms et al. (1979). While we refer to these terrains as being "highlands," it is important to note that they are compositionally distinct (containing higher abundances of both Fe and Th) relative to highlands outside of the South Pole–Aitken basin (e.g., Jolliff et al., 2000).

The highly cratered highlands consist of a large population of large (diameter [*D*] >50 km) degraded impact craters superposed by a large population of smaller (*D* <10 km) morphologically fresh craters. The high density of impact craters of all sizes and preservation states gives the highly cratered highlands a more rugged appearance compared to the moderately cratered highlands. Within the study area, the highly cratered highlands occur along the northern and southern edges (Fig. 3), whereas across the entire basin, the heavily cratered highlands were identified along the entire southern portion and along the rim of the South Pole–Aitken basin. Stuart-Alexander (1978) described the comparable NpNt and pNt units as being a mixture of local erosional debris and crater and basin ejecta, dominated by materials from craters of Nectarian and pre-Nectarian age. The highly cratered highlands defined here also likely contain a mixture of debris from several recent, nearby large craters and basins. In the northern exposure of this terrain, several secondary craters from Orientale pepper the landscape, while in the south and outside the study region, ejecta and secondary craters from the Imbrian-age Schrödinger basin and Antoniadi crater occur (Wilhelms et al., 1979). The contact between the two highlands units is interpreted to be diffuse, with the primary distinction between the two concerning the number of superposed fresh craters and not an inherent crustal difference.

The moderately cratered highlands unit forms ~50% of the study area, and in the greater South Pole–Aitken region, the moderately cratered highlands predominantly occupy the central part of the South Pole–Aitken basin floor. This central portion of South Pole–Aitken also corresponds to the primary iron enhancement associated with the basin (Fig. 1), with iron abundances generally greater than 9 wt%. The enhancement in iron associated with this terrain is possibly due to an abundance of iron-rich South Pole–Aitken–derived impact melt breccia. South Pole–Aitken impact melt is likely derived from the very deep crust and possibly upper mantle, which would impart a higher iron concentration to the melt (Warren et al., 1996). There is almost certainly South Pole–Aitken impact melt mixed in the highly cratered highlands terrain; however, this terrain has a lower average iron content (~5 wt%), suggesting that the impact melt is from a shallower portion of the crust. The moderately cratered highlands consist of fewer large craters than the highly cratered highlands, but the large craters and basins found within this unit (e.g., Apollo, Oppenheimer) display equivalently degraded morphologies (Fig. 3). In addition, the moderately

cratered highlands also contain fewer small-diameter, morphologically fresh craters superposed on the highlands between the larger basins and craters. This general lack of craters gives the moderately cratered highlands an overall less rugged appearance. Wilhelms et al. (1979) described a lineated basin material unit (Nbl), which roughly corresponds to the moderately cratered highlands terrain defined here. The Nbl unit was described as containing textured material on basin flanks but is also found far from basin rims. The moderately cratered terrain extends well beyond the flanks of the Apollo basin and contains material from the Oppenheimer crater (D = 208 km, Fig. 2), the Liebnitz crater (D = 245 km; Fig. 2), and several other large craters located west of the study area (e.g., Von Kármán, Von Kármán M).

Despite the apparent differences within the study area in the crater densities between the two highland terrains, differences attributable to the number of secondary craters from the Orientale and Schrödinger basins, both are interpreted to consist of South Pole–Aitken floor materials that underwent intense bombardment subsequent to the formation of the basin. Craters within both highland terrains have been noted as containing noritic compositions (Pieters et al., 2001; Nakamura et al., 2009), suggesting that South Pole–Aitken–derived impact melt is a component of both.

Hummocky Terrain

The hummocky terrain in South Pole–Aitken occurs as an exposure of ridges and furrows that surround Mare Ingenii and Van de Graaff crater. In our study area (Fig. 1), the unit is limited to a small exposure just north of Liebnitz crater (Figs. 2 and 3). This hummocky terrain coincides with the Imbrian grooves (Ig) unit defined by Stuart-Alexander (1978) that was noted to cover craters of pre-Nectarian to Imbrian age, as well as South Pole–Aitken interior material. The terrain has been noted to roughly coincide with the antipode of two large nearside basins, Serenitatis and Imbrium. This spatial relationship gave rise to a possible formation mechanism for the terrain—the convergence of shock waves and/or ejecta from the Imbrium and/or Serenitatis impact events substantially disrupting the existing South Pole–Aitken floor materials (Schultz and Gault, 1975; Wieczorek and Zuber, 2001; Hood and Artemieva, 2008). The larger hummocky terrain has also been noted as containing a distinctive localized thorium enhancement relative to the rest of the South Pole–Aitken basin and the nearby Feldspathic Highlands terrane (Jolliff et al., 2000). The enhancement has been cited as being caused by the addition of Th-bearing Imbrium/Serenitatis basin ejecta to the South Pole–Aitken regolith (Haskin, 1998; Wieczorek and Zuber, 2001). However, integrated analyses of the *Lunar Prospector* half-degree Th and *Clementine* UVVIS data by Garrick-Bethell and Zuber (2005) showed that the two highest Th enhancements are directly related to two Eratosthenian-age craters that excavated South Pole–Aitken–derived, Th-rich material, such that the overall compositional anomaly associated with South Pole–Aitken basin may be due to endogenous Th-rich material. Within the study area, there are larger terrains that are directly associated with local basins and large craters, and the properties of these terrains are described next.

Plains Terrains

The terrains identified as plains generally exhibit relatively flat surfaces, fairly constant albedos in the 750 nm band of *Clementine* image data, and tend to be sparsely cratered but peppered with small, fresh craters. Three geomorphic plains units were identified and include, in order of extent over the study area, the lightly cratered plains (LCP), dark plains (DP), and moderate plains (MP).

There are few exposures of the lightly cratered plains in the study area (Fig. 3), as well as within the greater South Pole–Aitken region. Exposures of lightly cratered plains occur at slightly higher elevations than the moderate and dark plains. These plains display higher albedo than the moderate plains, but they are similar in albedo to most of the adjacent highland terrains. The higher elevation and albedo difference allow them to be distinguished from the moderate plains. The lack of degraded craters and rugged surfaces within the lightly cratered plains also allow it to be distinguished from the adjacent highlands; however, the plains' similar albedo to the highlands suggests that the lightly cratered plains could be a less cratered extension of the highlands, possibly consisting of lightly cratered ejecta from local large craters (e.g., Bhabha; Fig. 2) mantling nearby intercrater highland terrains (Fig. 3).

The dark plains display flat surfaces and the lowest albedo relative to other surfaces in the study area and are associated with known mare basalt or pyroclastic deposits. Exposures of the dark plains occupy low-lying areas and appear to be embayed by adjacent terrains. The dark plains contain few impact craters, most of which are small (D <10 km) and fresh in appearance. Most exposures of the dark plains occur on the floors of the larger impact basins and craters, such as the Apollo basin, and the large craters Oppenheimer and Maksutov, craters that superpose the South Pole–Aitken basin floor materials. Some dark plains are surrounded by highlands terrain, apparently outside of craters, such as the unit northeast of Bose (Fig. 2). The low albedo and relatively smooth appearance of the dark plains suggest that these materials are composed of mare deposits that were erupted and emplaced following the formation of their host basins or craters (Schultz and Spudis, 1979; Head and Wilson, 1992).

The moderate plains include relatively flat surfaces that display a moderate albedo relative to other plains surfaces, particularly the dark plains, as well as the generally brighter highland terrains (Fig. 2). The moderate plains tend to occupy low-lying areas and display relatively flat to gently rolling surfaces with hundreds of meters of topography over several tens of kilometers. Most exposures of the moderate plains contain numerous impact craters that consist of both large, morphologically degraded craters and smaller, more fresh-appearing craters. The initial geologic maps of the South Pole–Aitken basin by Scott et al. (1977),

Stuart-Alexander (1978), and Wilhelms et al. (1979) identified plains deposits across much of the basin interior, with most mare units localized in the interiors of small craters. The previously mapped plains units were defined as commonly being associated with Imbrian- or Nectarian-age basin ejecta deposits and were not interpreted to be volcanic in origin.

Using *Clementine* UVVIS data, Pieters et al. (2001) further subdivided the plains units by identifying several units of volcanic plains material. The volcanic plains units were identified based on having a higher albedo and higher apparent cratering density than the mapped mare units. Additionally, small craters within the plains units identified by Pieters et al. contained the spectral signature of high-Ca pyroxene common in basaltic materials. These units were interpreted to represent ancient mare volcanism (i.e., cryptomare: Schultz and Spudis, 1979; Head and Wilson, 1992) covered by regionally derived mafic material and Orientale secondary craters. Of the plains units Pieters et al. (2001) mapped, the Plains South of Apollo (PSA) was the largest; however, we find that the extent of this unit as defined by Pieters et al. (2001) is roughly half the area of what we interpret for this unit (Fig. 3). Pieters et al. (2001) defined the Plains South of Apollo largely based on the plains units mapped using *Lunar Orbiter* data by Stuart-Alexander (1978). Other exposures of moderate plains in the west of the study area could be dark plains that are superposed by brighter impact ejecta.

AGES OF MATERIALS IN SOUTH POLE–AITKEN BASIN

While the ancient relative age of the South Pole–Aitken basin is accepted (Wilhelms 1987; Spudis, 1993; Ryder, 2002), the absolute ages of the basin and of specific units within the basin are poorly understood due to a lack of high-resolution imagery and therefore poorly defined crater frequency counts. *Apollo* spacecraft covered and subsequently photographed small portions of the northwest corner of the basin, and *Lunar Orbiter* took some oblique high-resolution images of the South Pole–Aitken interior. This lack of high-resolution photographic coverage has led to a paucity of crater counts of areas within the South Pole–Aitken basin (Neukum et al., 1975; Greeley et al., 1993; Williams et al., 1995; Haruyama et al., 2009).

Initial geologic mapping of the Plains South of Apollo region suggested that it was a plains unit (INp by Stuart-Alexander, 1978) or basin material (Nbl by Wilhelms et al., 1979) related to the Apollo basin and was classified as being Imbrian-Nectarian in age (Stuart-Alexander, 1978; Wilhelms et al., 1979). The INp unit was also identified inside the Apollo basin, but it is distinct from the Imbrian-age mare basalts also mapped inside the basin. However, the plains unit south of Apollo is a factor of three smaller in area than the large area we identify as moderate plains in Figure 3.

Recently, Haruyama et al. (2009), using high-resolution (10 m per pixel) Terrain Camera images from the Japanese *Kaguya* spacecraft, reported ages of farside mare deposits. They found that most farside mare deposits were late Imbrian in age, and few deposits were Eratosthenian in age (Table 1). The oldest volcanic deposits Haruyama et al. (2009) identified are in the crater Nishina (Fig. 2), which may be as old as 3.85 Ga or possibly as young as 2.47 Ga. Haruyama et al. suggested two possibilities for the range in ages. One is that the derived ages may be due to multiple eruptions within Nishina, suggesting that at least some of the basalts are possibly Nectarian in age. Another possible explanation for the range in ages is that the multiple cratering production functions (e.g., Neukum and Ivanov, 1994) can be fit to the crater-size frequency diagram. In discussing the age range of basalts in the north of the Apollo basin, Haruyama et al. point out that fitting a size-frequency diagram to craters >700 m in diameter yields an age of 3.51 Ga, whereas fitting craters <500 m in diameter yields a younger model age of 2.49 Ga (Table 1). In this case, they conclude that the 2.49 Ga age is the result of a younger, thinner eruption that did not obscure the larger, older craters.

Clementine 750 nm images of the basin have previously been utilized to perform crater counts and determine the ages of surfaces across the entire Moon (Craddock and Howard, 2000; Hirata and Nakamura, 2006); however, because of the spatial resolution (~100–200 m) and high sun angle associated with much of the *Clementine* data, identifying small craters (<1 km), and therefore age dating for small areas, is difficult (Hiesinger et al., 2003; Wilcox et al., 2005). *Clementine* images can be used to identify larger craters, and therefore they can be useful in determining the relative age of large areas (larger than hundreds of square kilometers). Additionally, the *Lunar Orbiter* global mosaic (Becker et al., 2008), with a resolution varying from 200 to 1000 m and generally low-sun-angle illumination, is useful for identifying and verifying the presence of larger craters within the Plains South of Apollo. The Plains South of Apollo unit identified previously (with an area of 76,675.4 km^2; Fig. 2) contains a sufficient number of craters larger than 1 km in diameter to determine a meaningful model age. One of the difficult aspects in determining a model age for the Plains South of Apollo region is that it is peppered with secondary craters from the Orientale basin. In identifying craters within the Plains South of Apollo, we do not include craters that have either been previously mapped as secondary craters of the Orientale basin (Wilhelms et al., 1979) or appear to have morphologies suggestive of secondary craters (Oberbeck and Morrison, 1974; McEwen and Bierhaus, 2006). In total, we identified 42 secondary craters within the Plains South of Apollo.

Our crater counting of the Plains South of Apollo (Fig. 3) suggests that the unit has a maximum model age of 3.89 Ga, making it Nectarian in age, assuming the empirically derived chronology of Neukum and Ivanov (1994) (Table 1; Fig. 4). Within the Plains South of Apollo, we identified 447 craters larger than 1 km in diameter and 22 larger than 10 km in diameter. The derived age is similar to the empirically determined age of 3.84 Ga (Table 1) for the Schickard light plains (Greeley et al., 1993), which may, like the Plains South of Apollo, be mantled by Orientale ejecta

(Blewett, et al., 1995). Additionally, as Pieters et al. (2001) indicated, the mantling material likely also contains regionally derived (i.e., within South Pole–Aitken) material that contributes to the overall low-albedo and mafic signature of the ancient volcanic material. We also performed crater counts across the iron enhancement of central South Pole–Aitken basin (Fig. 1), corresponding to the inner South Pole–Aitken terrane of Jolliff et al. (2000). This central region is likely to be the least modified by basins external to South Pole–Aitken (Petro and Pieters, 2004), contains several Upper Imbrian age mare deposits (Wilhelms, 1987; Yingst and Head, 1999), and has surfaces mapped as either Nectarian or pre-Nectarian Terra by Wilhelms et al. (1979) and Stuart-Alexander (1978). Despite the modification of portions of this region by volcanism, the derived model age of the iron enhancement is 4.05 Ga, with 272 craters with diameters >20 km in diameter (Table 1; Fig. 4). This age is certainly not an age of South Pole–Aitken formation, because there are likely a number of craters that have been obscured by volcanic flooding and erased by other impacts. However, this age does likely represent an upper limit that can be determined with currently available data for South Pole–Aitken.

CONCLUSIONS

The interior of the South Pole–Aitken basin contains a number of unique terrains, which, due to their location in the large and ancient basin, are unique for the entire Moon. The region south of the Apollo basin, in northeastern South Pole–Aitken basin (Fig. 1), contains a number of diverse terrain types, including heavily cratered ancient surfaces, mare deposits possibly as young as 2.44 Ga (Haruyama et al., 2009), and expansive cryptomare surfaces possibly as old as 3.89 Ga (Fig. 3). Hiesinger et al. (2003) identified 12 basalt units on the nearside of comparable early Imbrian age that are primarily distributed in Mare Tranquillitatis and Mare Australe.

The two identified highlands terrains in the region represent crustal material that has been significantly modified by the formation of the South Pole–Aitken basin and that contain an abundance of South Pole–Aitken–derived impact melt (Haskin et al., 2003; Petro and Pieters, 2004). The primary differences between the two highlands terrains are in the relative abundance of iron, with an iron enhancement (~5 wt% greater than the immediate surroundings) in the moderately cratered highlands, and the greater density of secondary craters from nearby basins in the highly cratered highlands. The iron enhancement in the moderately cratered highlands is likely due to the presence of impact melt material derived from deepest portions of the South Pole–Aitken transient cavity (Cintala and Grieve, 1998). While the surface expressions of the two highlands terrains are distinct, at depth the contact between the two is likely gradational (Fig. 3) due to the intense modification and mixing of the crust as a result of South Pole–Aitken's formation.

The three plains units in the region are purely surficial units, associated with topographic lows, typically crater and basin interiors (Fig. 3). The dark plains units are mare basalts or large pyroclastic deposits (Greeley et al., 1993; Yingst and Head, 1997, 1999; Gaddis et al., 2003), with the mare basalts in the region covering a range of ages from 2.44 to 3.85 Ga (Table 1; Greeley et al., 1993; Haruyama et al., 2009). The lightly cratered plains unit, covering a small portion of the study region, is likely dominated by ejecta from smaller, local craters (e.g., Bhabha). The third plains unit, the moderate plains, is associated with the interiors of large craters (Apollo and Oppenheimer; Fig. 2) and other larger topographic lows that are not directly related to obvious impact craters. One such unit, the Plains South of Apollo (PSA; Fig. 3), may represent the oldest and most widespread mare volcanic unit within the South Pole–Aitken basin and therefore represent an early stage of lunar volcanism. Additionally, the material mantling this volcanic unit is likely composed of anorthositic material from both the Orientale impact, as well as regionally derived iron-bearing material from the floor of the South Pole–Aitken basin (Pieters et al., 2001).

High-resolution images of the unit from orbiting spacecraft (i.e., the *Lunar Reconnaissance Orbiter* Camera–narrow-angle camera) will allow for improved crater age determinations, and hyperspectral data from the Moon Mineralogy Mapper (M^3) will improve our understanding of the composition of the unit.

ACKNOWLEDGMENTS

The authors would like to acknowledge the input of William Ambrose and an anonymous reviewer, input that significantly improved the quality of this manuscript. We would also like to acknowledge the support of the National Aeronautics and Space Administration (NASA) Postdoctoral Program (NEP). Special thanks go to William Ambrose and David Williams for organizing this Geological Society of America Special Paper.

REFERENCES CITED

Araki, H., Tazawa, S., Noda, H., Ishihara, Y., Goossens, S., Sasaki, S., Kawano, N., Kamiya, I., Otake, H., Oberst, J., and Shum, C., 2009, Lunar global shape and polar topography derived from *Kaguya*-LALT laser altimetry: Science, v. 323, p. 897–900, doi:10.1126/science.1164146.

Archinal, B.A., Rosiek, M.R., Kirk, R.L., and Redding, B.L., 2006, The Unified Lunar Control Network 2005: U.S. Geological Survey Open-File Report 2006-1367, available at http://pubs.usgs.gov/of/2006/1367/ (accessed 10 December 2010).

Becker, T.L., Weller, L., Gaddis, L., Cook, D., Archinal, B., Rosiek, M., Isbell, C., Hare, T., and Kirk, R., 2008, *Lunar Orbiter* mosaic of the Moon: Houston, Texas, Lunar and Planetary Institute, Lunar and Planetary Science Conference XXXIX, CD-ROM, abstract 2357.

Belton, M.J.S., Head, J.W., III, Pieters, C.M., Greeley, R., McEwen, A.S., Neukum, G., Klaasen, K.P., Anger, C.D., Carr, M.H., Chapman, C.R., Davies, M.E., Fanale, F.P., Gierasch, P.J., Greenberg, R., Ingersoll, A.P., Johnson, T., Paczkowski, B., Pilcher, C.B., and Veverka, J., 1992, Lunar impact basins and crustal heterogeneity: New western limb and farside data from *Galileo*: Science, v. 255, no. 5044, p. 570–576, doi:10.1126/science.255.5044.570.

Blewett, D.T., Hawke, B.R., Lucey, P.G., Taylor, G.J., Jauman, R., and Spudis, P.D., 1995, Remote sensing and geologic studies of the Schiller-Schickard region of the Moon: Journal of Geophysical Research, v. 100, no. E8, p. 16,959–16,977, doi:10.1029/95JE01409.

Cintala, M.J., and Grieve, R.A.F., 1998, Scaling impact melting and crater dimensions: Implications for the lunar cratering record: Meteoritics & Planetary Science, v. 33, p. 889–912, doi:10.1111/j.1945-5100.1998.tb01695.x.

Craddock, R.A., and Howard, A.D., 2000, Simulated degradation of lunar impact craters and a new method for age dating farside mare deposits: Journal of Geophysical Research, v. 105, no. E8, p. 20,387–20,401, doi:10.1029/1999JE001099.

Eliason, E., McEwen, A., Robinson, M., Lee, E., Becker, T., Gaddis, L., Weller, L., Isbell, C., Shinaman, J., Duxbury, T., and Malaret, E., 1999, Digital processing for a global multispectral map of the Moon from the *Clementine* UVVIS imaging instrument: Houston, Texas, Lunar and Planetary Institute, Lunar and Planetary Science Conference XXX, CD-ROM, abstract 1933.

Elphic, R.C., Lawrence, D.J., Feldman, W.C., Barraclough, B.L., Maurice, S., Binder, A.B., and Lucey, P.G., 2000, Lunar rare earth element distribution and ramifications for FeO and TiO: *Lunar Prospector* neutron spectrometer observations: Journal of Geophysical Research, v. 105, p. 20,333–20,345, doi:10.1029/1999JE001176.

Feldman, W.C., Maurice, S., Lawrence, D.J., Little, R.C., Lawson, S.L., Gasnault, O., Wiens, R.C., Barraclough, B.L., Elphic, R.C., Prettyman, T.H., Steinberg, J.T., and Binder, A.B., 2001, Evidence for water ice near the lunar poles: Journal of Geophysical Research, v. 106, p. 23,231–23,251, doi:10.1029/2000JE001444.

Gaddis, L.R., Staid, M.I., Tyburczy, J.A., Hawke, B.R., and Petro, N.E., 2003, Compositional analyses of lunar pyroclastic deposits: Icarus, v. 161, p. 262–280, doi:10.1016/S0019-1035(02)00036-2.

Garrick-Bethell, I., and Zuber, M., 2005, An indigenous origin for the South Pole–Aitken basin thorium anomaly: Geophysical Research Letters, v. 32, doi:10.1029/2005GL023142.

Garrick-Bethell, I., and Zuber, M., 2009, Elliptical structure of the lunar South Pole–Aitken basin: Icarus, v. 204, p. 399–408, doi:10.1016/j.icarus.2009.05.032.

Gillis, J.J., Jolliff, B.L., and Korotev, R.L., 2004, Lunar surface geochemistry: Global concentrations of Th, K, and FeO as derived from lunar prospector and *Clementine* data: Geochimica et Cosmochimica Acta, v. 68, p. 3791–3805, doi:10.1016/j.gca.2004.03.024

Greeley, R., Kadel, S.D., Williams, D.A., Gaddis, L.R., Head, J.W., McEwen, A.S., Murchie, S.L., Nagel, E., Neukum, G., Pieters, C.M., Sunshine, J.M., Wagner, R., and Belton, M.J.S., 1993, *Galileo* imaging observations of lunar maria and related deposits: Journal of Geophysical Research, v. 98, no. E9, p. 17,183–17,205.

Hartmann, W.K., and Wood, C.A., 1971, Moon: Origin and evolution of multiring basins: The Moon, v. 3, p. 3–78, doi:10.1007/BF00620390.

Haruyama, J., Ohtake, M., Matsunaga, T., Morota, T., Honda, C., Yokota, Y., Abe, M., Ogawa, Y., Miyamoto, H., Iwasaki, A., Pieters, C.M., Asada, N., Demura, H., Hirata, N., Terazono, J., Sasaki, S., Saiki, K., Yamaji, A., Torii, M., and Josset, J.-L., 2009, Long-lived volcanism on the lunar farside revealed by *SELENE* terrain camera: Science, v. 323, p. 905–908, doi:10.1126/science.1163382.

Haskin, L.A., 1998, The Imbrium impact event and the thorium distribution at the lunar highlands surface: Journal of Geophysical Research–Planets, v. 103, no. E1, p. 1679–1689, doi:10.1029/97JE03035.

Haskin, L.A., Gillis, J.J., Jolliff, B.L., and Korotev, R.L., 2003, Regolith in the South Pole–Aitken basin is mainly indigenous material: Houston, Texas, Lunar and Planetary Institute, Lunar and Planetary Science Conference XXXIV, CD-ROM, abstract 1434.

Head, J.W., III, and Wilson, L., 1992, Lunar mare volcanism: Stratigraphy, eruption conditions, and the evolution of secondary crusts: Geochimica et Cosmochimica Acta, v. 56, p. 2155–2175, doi:10.1016/0016-7037(92)90183-J.

Head, J.W., Murchie, S., Mustard, J.F., Pieters, C.M., Neukum, G., McEwen, A., Greeley, R., Nagel, E., and Belton, M.S., 1993, Lunar impact basins: New data for the western limb and far side (Orientale and South Pole–Aitken basins) from the first *Galileo* flyby: Journal of Geophysical Research, v. 98, p. 17,149–17,181, doi:10.1029/93JE01278.

Hiesinger, H., Head, J., Wolf, U., Jaumann, R., and Neukum, G., 2003, Ages and stratigraphy of mare basalts in Oceanus Procellarum, Mare Nubium, Mare Cognitum, and Mare Insularum: Journal of Geophysical Research, v. 108, no. E7, doi:10.1029/2002JE001985.

Hirata, N., and Nakamura, A.M., 2006, Secondary craters of Tycho: Size-frequency distributions and estimated fragment size-velocity relationships: Journal of Geophysical Research, v. 111, doi:10.1029/2005JE002484.

Hood, L.L., and Artemieva, N.A., 2008, Antipodal effects of lunar basin-forming impacts: Initial 3-D simulations and comparisons with observations: Icarus, v. 193, p. 485–502, doi:10.1016/j.icarus.2007.08.023.

Jolliff, B.L., Gillis, J.J., Haskin, L.A., Korotev, R.L., and Wieczorek, M.A., 2000, Major lunar crustal terranes: Surface expressions and crust-mantle origins: Journal of Geophysical Research, v. 105, no. E2, p. 4197–4216.

Lawrence, D.J., Elphic, R.C., Feldman, W.C., Gasnault, O., Genetay, I., Maurice, S., and Prettyman, T.H., 2003, Small-area thorium features on the lunar surface: Journal of Geophysical Research, v. 108, doi:10.1029/2003JE002050.

Lucey, P.G., 2004, Mineral maps of the Moon: Geophysical Research Letters, v. 31, doi:10.1029/2003GL019406.

Lucey, P.G., Taylor, J., Hawke, B.R., and Spudis, P.D., 1998, FeO and TiO_2 concentrations in the South Pole–Aitken basin: Implications for mantle composition and basin formation: Journal of Geophysical Research, v. 103, no. E2, p. 3701–3708, doi:10.1029/97JE03146.

McEwen, A.S., and Bierhaus, E.B., 2006, The importance of secondary cratering to age constraints on planetary surfaces: Annual Review of Earth and Planetary Sciences, v. 34, p. 535–567, doi:10.1146/annurev.earth.34.031405.125018.

Mustard, J.F., and Head, J.W., 1996, Buried stratigraphic relationships along the southwestern shores of Oceanus Procellarum: Implications for early lunar volcanism: Journal of Geophysical Research–Planets, v. 101, no. E8, p. 18,913–18,926, doi:10.1029:96JE01826.

Nakamura, R., Matsunaga, T., Ogawa, Y., Yamamoto, S., Hiroi, T., Saiki, K., Hirata, N., Arai, T., Kitazato, K., Takeda, H., Sugihara, T., Kodama, S., Ohtake, M., Haruyama, J., and Yokota, Y., 2009, Ultramafic impact melt sheet beneath the South Pole–Aitken basin on the Moon: Geophysical Research Letters, v. 36, doi:10.1029/2009GL040765.

Neukum, G., and Ivanov, B.A., 1994, Crater size distributions and impact probabilities on Earth from lunar, terrestrial-planet, and asteroid cratering data, *in* Gehrels, T., ed., Hazards Due to Comets and Asteroids: Tucson, University of Arizona Press, p. 359–416.

Neukum, G., König, B., Fechtig, H., and Storzer, D., 1975, Cratering in the Earth-Moon system: Consequences for age determination by crater counting: Proceedings of the Lunar and Planetary Science Conference VI: New York, Pergamon Press, p. 2597–2620.

Oberbeck, V.R., and Morrison, R.H., 1974, Laboratory simulation of the herringbone pattern associated with lunar secondary crater chains: The Moon, v. 9, p. 415–455, doi:10.1007/BF00562581.

Petro, N.E., and Pieters, C.M., 2004, Surviving the heavy bombardment: Ancient material at the surface of South Pole–Aitken basin: Journal of Geophysical Research–Planets, v. 109, no. E6, E06004, doi:06010.01029/02003JE002182.

Petro, N.E., and Pieters, C.M., 2008, The lunar-wide effects of basin ejecta distribution on the early megaregolith: Meteoritics & Planetary Science, v. 43, no. 9, p. 1517–1529, doi:10.1111/j.1945-5100.2008.tb01025.x.

Pieters, C.M., Head, J.W., Sunshine, J.M., Fischer, E.M., Murchie, S.L., Belton, M., McEwen, A., Gaddis, L., Greeley, R., Neukum, G., Jaumann, R., and Hoffmann, H., 1993, Crustal diversity of the Moon: Compositional analysis of *Galileo* solid state imaging data: Journal of Geophysical Research, v. 98, no. E9, p. 17,127–17,148, doi:10.1029/93JE01221.

Pieters, C.M., Staid, M.I., Fischer, E.M., Tompkins, S., and He, G., 1994, A sharper view of impact craters from *Clementine* data: Science, v. 266, p. 1844–1848, doi:10.1126/science.266.5192.1844.

Pieters, C.M., Head, J.W., Gaddis, L., Jolliff, B., and Duke, M., 2001, Rock types of South Pole–Aitken basin and extent of basaltic volcanism: Journal of Geophysical Research, v. 106, no. E11, p. 28,001–28,022, doi:10.1029/2000JE001414.

Prettyman, T.H., Hagerty, J.J., Elphic, R.C., Feldman, W.C., Lawrence, D.J., McKinney, G.W., and Vaniman, D.T., 2006, Elemental composition of the lunar surface: Analysis of gamma ray spectroscopy data from *Lunar Prospector*: Journal of Geophysical Research, v. 111, doi:10.1029/2005JE002656.

Ryder, G., 2002, Mass flux in the ancient Earth-Moon system and benign implications for the origin of life on Earth: Journal of Geophysical Research–Planets, v. 107, no. E4, 5022, doi:10.1029/2001JE001583.

Scott, D.H., McCauley, J.F., and West, M.N., 1977, Geologic Map of the West Side of the Moon: U.S. Geologic Survey Map I-1034, scale 1:5,000,000.

Schultz, P.H., and Gault, D.E., 1975, Seismic effects from major basin formations on the Moon and Mercury: The Moon, v. 12, p. 159–177, doi:10.1007/BF00577875.

Schultz, P.H., and Spudis, P.D., 1979, Evidence for ancient mare volcanism: Houston, Lunar and Planetary Institute, Lunar and Planetary Science Conference XX, p. 2899–2918.

Spudis, P.D., 1993, The Geology of Multi-Ring Impact Basins: New York, Cambridge University Press, 263 p.

Stuart-Alexander, D.E., 1978, Geologic Map of the Central Far Side of the Moon: U.S. Geologic Survey Map I-1047, scale 1:5,000,000.

Warren, P.H., Claeys, P., and Cedillo-Pardo, E., 1996, Mega-impact melt petrology (Chicxulub, Sudbury, and the Moon): Effects of scale and other factors on potential for fractional crystallization and development of cumulates, *in* Ryder, G., Fastovsky, D., and Gartner, S., eds., The Cretaceous-Tertiary Event and Other Catastrophes in Earth History: Geological Society of America Special Paper 307, p. 105–124.

Wieczorek, M.A., and Zuber, M.T., 2001, A Serenitatis origin for the Imbrian grooves and South Pole–Aitken thorium anomaly: Journal of Geophysical Research–Planets, v. 106, no. E11, p. 27,853–27,864, doi:10.1029/2000JE001384.

Wilcox, B.B., Robinson, M.S., Thomas, P.C., and Hawke, B.R., 2005, Constraints on the depth and variability of the lunar regolith: Meteoritics & Planetary Science, v. 40, p. 695–710, doi:10.1111/j.1945-5100.2005.tb00974.x.

Wilhelms, D., 1987, The Geologic History of the Moon: U.S. Geological Survey Professional Paper 1348, 302 p.

Wilhelms, D.E., Howard, K.A., and Wilshire, H.G., 1979, Geologic Map of the South Side of the Moon: U.S. Geological Survey Miscellaneous Investigation Series I-1162, scale 1:5,000,000.

Williams, D.A., Greeley, R., Neukum, G., Wagner, R., and Kadel, S.D., 1995, Multispectral studies of western limb and farside maria from *Galileo* Earth-Moon Encounter 1: Journal of Geophysical Research, v. 100, no. E11, p. 23,291–23,299, doi:10.1029/94JE01863.

Yingst, R.A., and Head, J., 1997, Volumes of lunar lava ponds in South Pole–Aitken and Orientale basins: Implications for eruption conditions, transport mechanisms, and magma source regions: Journal of Geophysical Research, v. 102, no. E5, p. 10,909–10,931, doi:10.1029/97JE00717.

Yingst, R.A., and Head, J., 1999, Geology of mare deposits in South Pole–Aitken basin as seen by *Clementine* UV/VIS data: Journal of Geophysical Research, v. 104, no. E8, p. 18,957–18,979, doi:10.1029/1999JE900016.

Manuscript Accepted by the Society 26 August 2010

Printed in the USA

The Geological Society of America
Special Paper 477
2011

Origin of nearside structural and geochemical anomalies on the Moon

Peter H. Schultz*
Department of Geological Sciences, Brown University, Providence, Rhode Island 02912-1846, USA

David A. Crawford
Sandia National Laboratories, Albuquerque, New Mexico 87185, USA

ABSTRACT

Mare basalts cover much of the Earth-facing side of the Moon. The underlying cause for this distribution has been attributed to an ancient nearside megabasin, asymmetric accretion, and differential tidal effects. While each hypothesis is plausible, the hypothesis for a megabasin also accounts for a subconcentric and radial system of graben and ridges that centers on a region southwest of Imbrium basin. Moreover, such a nearside megabasin could account for the distribution of nearside geochemical anomalies related to localized igneous intrusions. The farside South Pole–Aitken basin, however, is a well-established impact megabasin exceeding 2200 km in diameter. Here, we propose an oblique collision scenario for this basin on the farside that would have created the initial conditions for localized deep-seated and long-lasting weaknesses on the nearside. Laboratory and computational experiments demonstrate that a large oblique collision generates asymmetric shock waves that converge in a region offset from the basin-center antipode. The resulting damage would have provided pathways for deep magma to reach shallow reservoirs.

INTRODUCTION

In 1981, Whitaker proposed that a large and ancient impact basin was responsible for a system of radial and concentric ridges and graben, as well as the distribution of mare basalts of Oceanus Procellarum (Whitaker, 1981; Byrne, 2007) as illustrated in Figure 1A. This basin (called the "Procellarum basin") has been frequently cited to account for the localization of high-Th values with enhanced concentrations of KREEP (i.e., potassium, K; rare earth elements, REE; and phosphorus, P) on the lunar surface (e.g., Wilhelms, 1987; Haskin, 1998; Korotev, 2000). Preserved geophysical evidence for such a large impact, however, appears to be absent, perhaps due to subsequent isostatic adjustment (Neumann et al., 1996). Nevertheless, models of the derived gravity field reveal that there is a pronounced linear gravity anomaly extending southeastward from near the Aristarchus Plateau (Konopliv et al., 1998; Namiki et al., 2009). The Airy model described by Konopliv et al. (1998) concluded that significant lateral variations in density (Pratt model) were needed in order to account for the anomaly.

The absence of tectonic systems (e.g., graben) and widespread maria on the lunar farside is as enigmatic as is their presence on the nearside. The underlying cause for the widespread localization of maria, structural patterns, and geochemical

*Peter_Schultz@Brown.edu

Schultz, P.H., and Crawford, D.A., 2011, Origin of nearside structural and geochemical anomalies on the Moon, *in* Ambrose, W.A., and Williams, D.A., eds., Recent Advances and Current Research Issues in Lunar Stratigraphy: Geological Society of America Special Paper 477, p. 141–159, doi:10.1130/2011.2477(07).

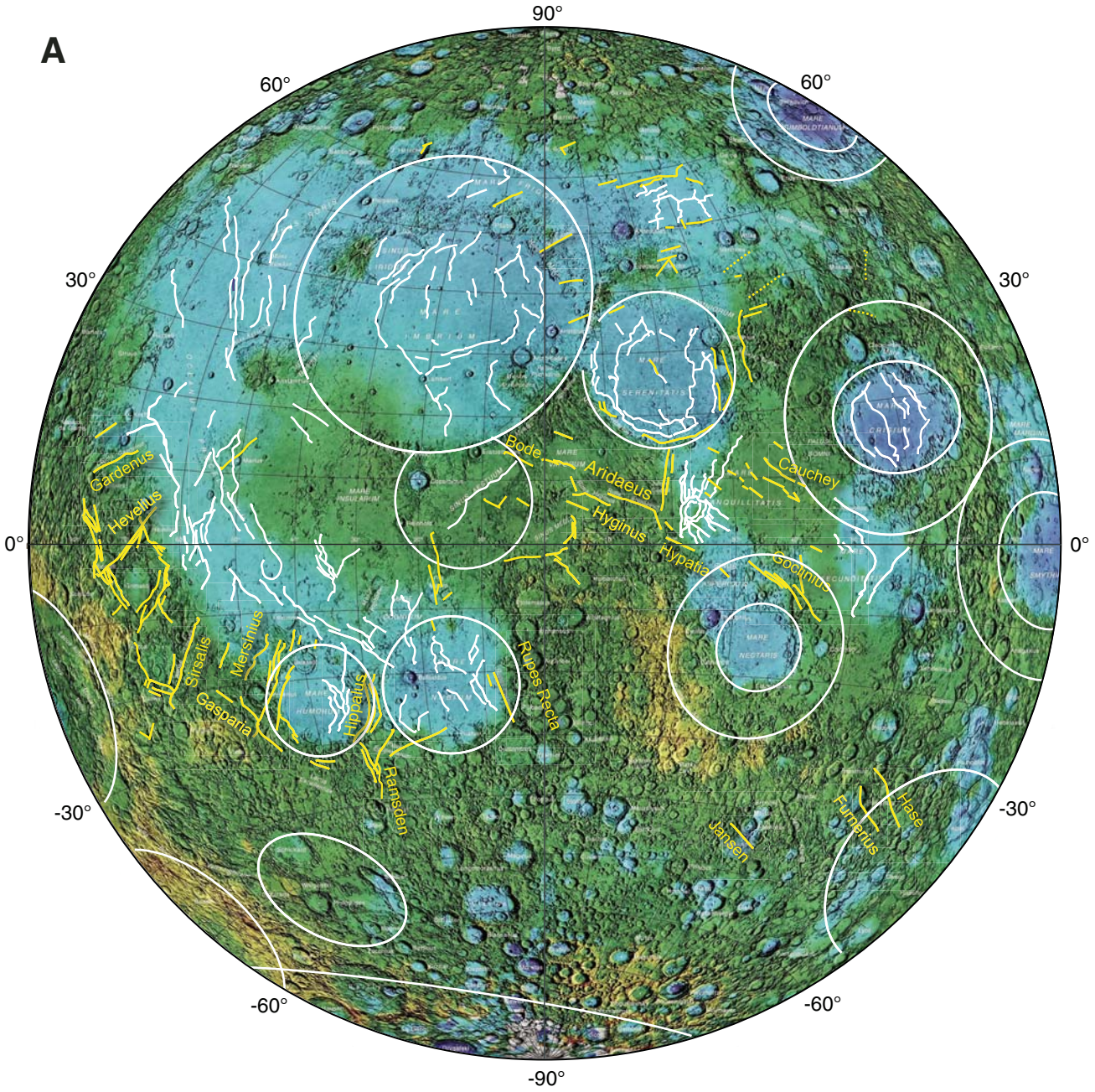

Figure 1 (*Continued on following page*). (A) Major ridges (white) and nonsinuous rilles (yellow) on the Moon superposed on a physiographic and topographic map (stereographic projection). (B) Distribution of nearside ridges (blue) and rilles (red) along with major nearside basins (blue) mapped on a Lambert azimuthal-equal-area projection of the lunar nearside. Great circles indicate general trends delineated by rilles and ridges, converging in an area southwest of Imbrium. The antipode (solid triangle) to the geometric center of the South Pole–Aitken (SPA) basin is northeast of the Imbrium basin. The southern rim of South Pole–Aitken extends into the lunar nearside along the southern limb. The colored contours approximate concentrations of high-Th regions determined from gamma-ray spectrometer data from the *Lunar Prospector* mission (Gillis et al., 2004), where yellow contours indicate concentrations >9 ppm and orange is >10 ppm.

anomalies on the lunar nearside remains debated. This contribution offers a new hypothesis that can be tested by future geophysical data, geologic studies, and mapping. We first review the evidence for an arcuate system of graben and ridges in Oceanus Procellarum. Next, we consider the hypothesis that this system could have been initiated by the formation of the South Pole–Aitken basin by an oblique impact on the farside. Last, discussion centers on the implications of this hypothesis for lunar evolution.

BACKGROUND

The Procellarum System

The concentration of maria on the lunar nearside was first attributed to a pre-Nectarian megabasin (Cardogan, 1974). Whitaker (1981) later recognized an annular system of faults on the lunar nearside (along with arcuate mare borders) and attributed this distribution to an ancient "Procellarum basin." The existence of such a basin seemed to be necessary in order to account for geochemical anomalies generally restricted to the nearside (e.g., Wilhelms, 1987; Haskin, 1998).

The basic observations made by Whitaker are not in question; neither is the need for a cause for the observed nearside concentration of maria and the geochemical anomalies indicating shallow magma reservoirs. Rather, we suggest that the pattern of subconcentric and radial ridges and graben in Procellarum should be described as a "system" rather than be called a basin. Although subtle, this is an important distinction, because the label "basin" on the Moon implicitly connotes an impact origin.

Figure 1 highlights the major structural features expressed (wrinkle ridges and graben) on the lunar nearside superposed on topography (Fig. 1A) and major basins (Fig. 1B). The Procellarum system (PS) of graben and ridges is centered on a region south of the Aristarchus Plateau. Graben in the highlands cross (but are accentuated and deflected by) old basins where they coincide with extensional stresses created by later basalt loading (e.g., Humorum and Grimaldi). Well-known nonsinuous rilles (Rima Sirsalis, Rima Hyginus, Rima Bode, and Rima Aridaeus) appear to follow a tectonic pattern unassociated with nearby large basins. Moreover, sites of recent gas release occur near the intersections of these graben (Schultz et al., 2006). Non-basin–related sinuous rille source vents (e.g., near Letronne and Marius Hills)

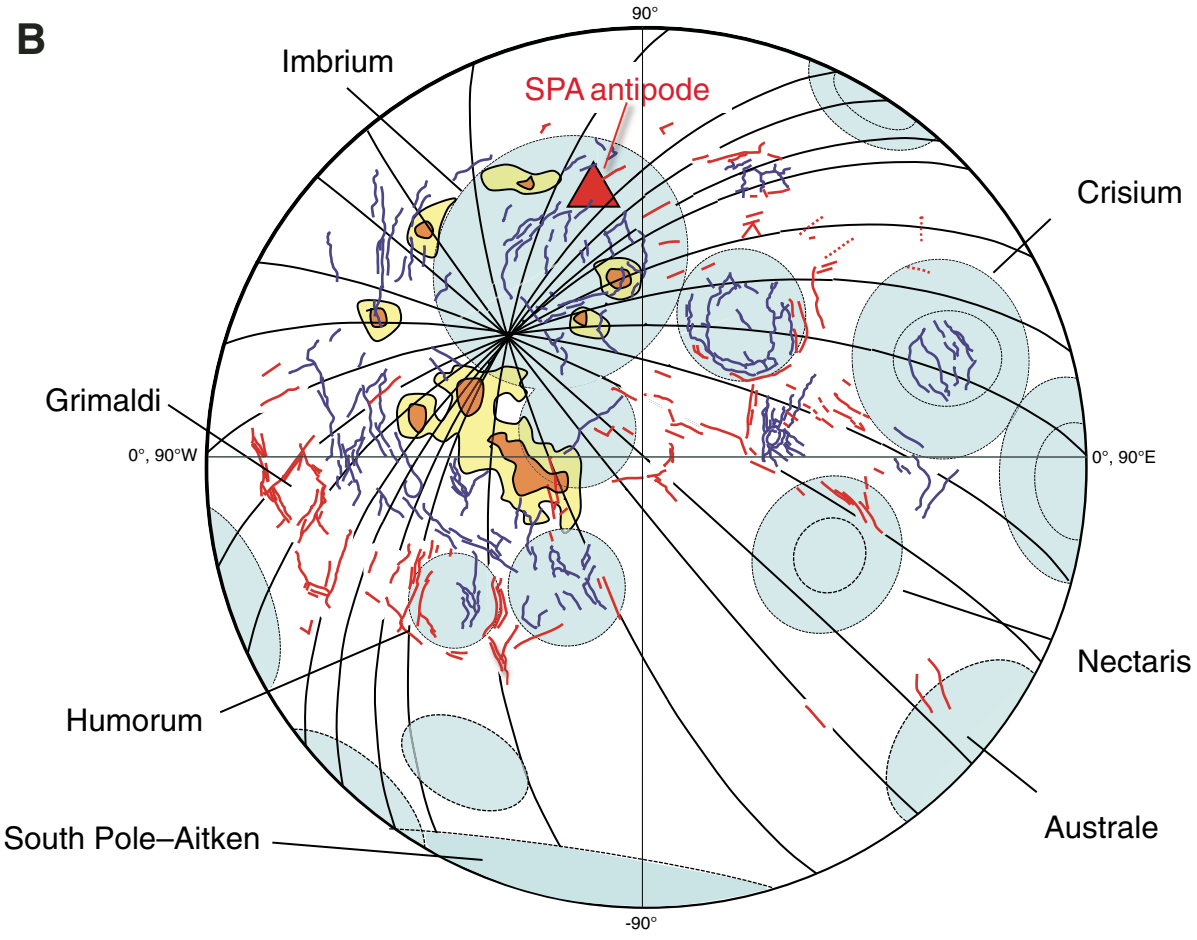

Figure 1 (*Continued*).

also occur along wrinkle ridges within this system (e.g., Guest and Murray, 1976; Wilhelms, 1987). It should be noted that loading by basin-centered mascons does not exclusively control the distribution of wrinkle ridge systems, since they are known to extend well into the highlands (Schultz, 1976a; Binder, 1985; Watters et al., 2010).

Several working hypotheses can be considered for the origin of the Procellarum system. First, an ancient nearside impact did form but has now been completely isostatically adjusted and overprinted, i.e., the hypothesis by Whitaker (1981). Second, the nearside concentration of the maria (and subsequent expressions of crustal strain and geochemical anomalies) may be inherited from the earliest stages of accretion and differentiation localized on the nearside through tidal effects (Zhong et al., 2000). Third, the geochemical anomalies may represent a long-lasting expression of antipodal effects induced by the well-established South Pole–Aitken basin (e.g., Garrick-Bethell and Zuber, 2005). The convergence of radial and concentric structural elements, however, is more than 800 km away from the antipodal point (Fig. 2) on the nearside (referenced to the South Pole–Aitken center). New impact oblique-impact experiments using spherical targets (Schultz, 2007) produce damage, which is offset from the antipode, thereby allowing this hypothesis. Consequently, the next section explores the possible consequences and expressions of an oblique trajectory for the South Pole–Aitken basin.

South Pole–Aitken Basin

The diameter of the South Pole–Aitken basin exceeds the lunar radius (1738 km) and contains the deepest terrains on the

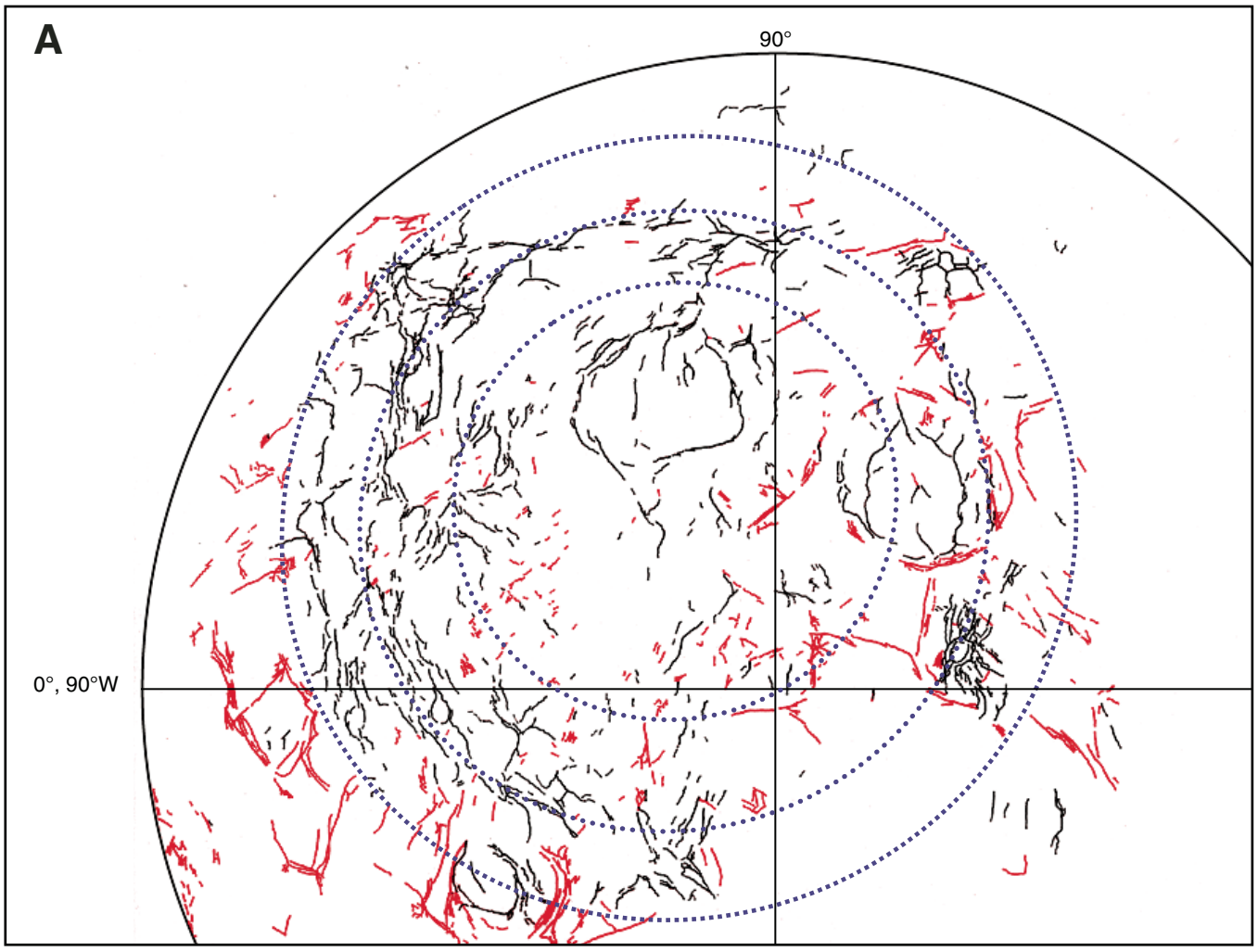

Figure 2 (*Continued on following page*). (A) Distribution of graben (red) and wrinkle ridges (black) and the outline of the proposed Procellarum basin rings (blue dotted circles) following Wilhelms (1987). (B) Reprojection of system of ridges and rilles (Fig. 1) with a center near southern Imbrium. Ridges and graben form a subconcentric structural system covering much of the western lunar nearside, with a center along the southwestern edge of the Imbrium basin. Sites for recent gas release (Schultz et al., 2006) are identified: Ina (D-caldera), intersection of Hyginus rilles, and south of the crater Arago. HM—Harbinger Mountains; MH—Marius Hills.

Moon (>12 km). It was discovered from *Lunar Orbiter* images (Schultz, 1976a; Stuart-Alexander, 1978) based on a system of high massifs and low-lying plains. Petro and Pieters (2004) examined the distribution of ancient materials within this basin, which is believed to be pre-Nectarian in age (Wilhelms, 1987). Mare basalts do occur within superposed basins and craters inside the South Pole–Aitken basin rim, but mare basalts do not fill this basin, in contrast to most other impact basins on the lunar nearside. The enormity of the South Pole–Aitken basin should have destroyed the Moon were it not for the binding force of the Moon's own gravity. Regardless, the consequences for lunar evolution should have been significant and long-lasting.

Possible surface expressions of disruption antipodal to a major impact on the Moon (opposite Imbrium and Orientale) and Mercury (opposite Caloris) include disrupted (hilly and lineated) terrains and basaltic eruptions (Schultz and Gault, 1975). Early hydrocodes tested this hypothesis and concluded that the initial estimates may have been too conservative (Hughes et al., 1977). Since then, convergent antipodal shock and seismic waves have been applied to the Moon (Hood and Artemieva, 2006), Mars (Williams and Greeley, 1994), icy bodies (Bruesch and Asphaug, 2004), and other objects (Richardson et al., 2005). Antipodal effects from South Pole–Aitken, however, have not been assessed fully. We used two strategies to explore the consequences of a large impact on a small body: experimental and computational. While experiments allow assessment of modes of failure, hydrocode models reveal controlling processes and allow scaling to a differentiated body with self-gravity over much longer time scales.

CONSEQUENCES OF THE SOUTH POLE–AITKEN IMPACT

Experimental Studies

Impacts into spherical targets generate intersecting shocks and rarefactions reflected off the free surface and induce multiple failure planes deep inside the target on the opposite side. Oblique impacts, however, produce asymmetries in the peak shock pressure (Dahl and Schultz, 2001; Pierazzo and Melosh, 2000), distribution of ejecta (Gault and Wedekind, 1978; Anderson et al., 2003, 2004), crater shape (Gault and Wedekind, 1978), and crater structure (Schultz, 1992; Schultz and Anderson, 1996). The consequences

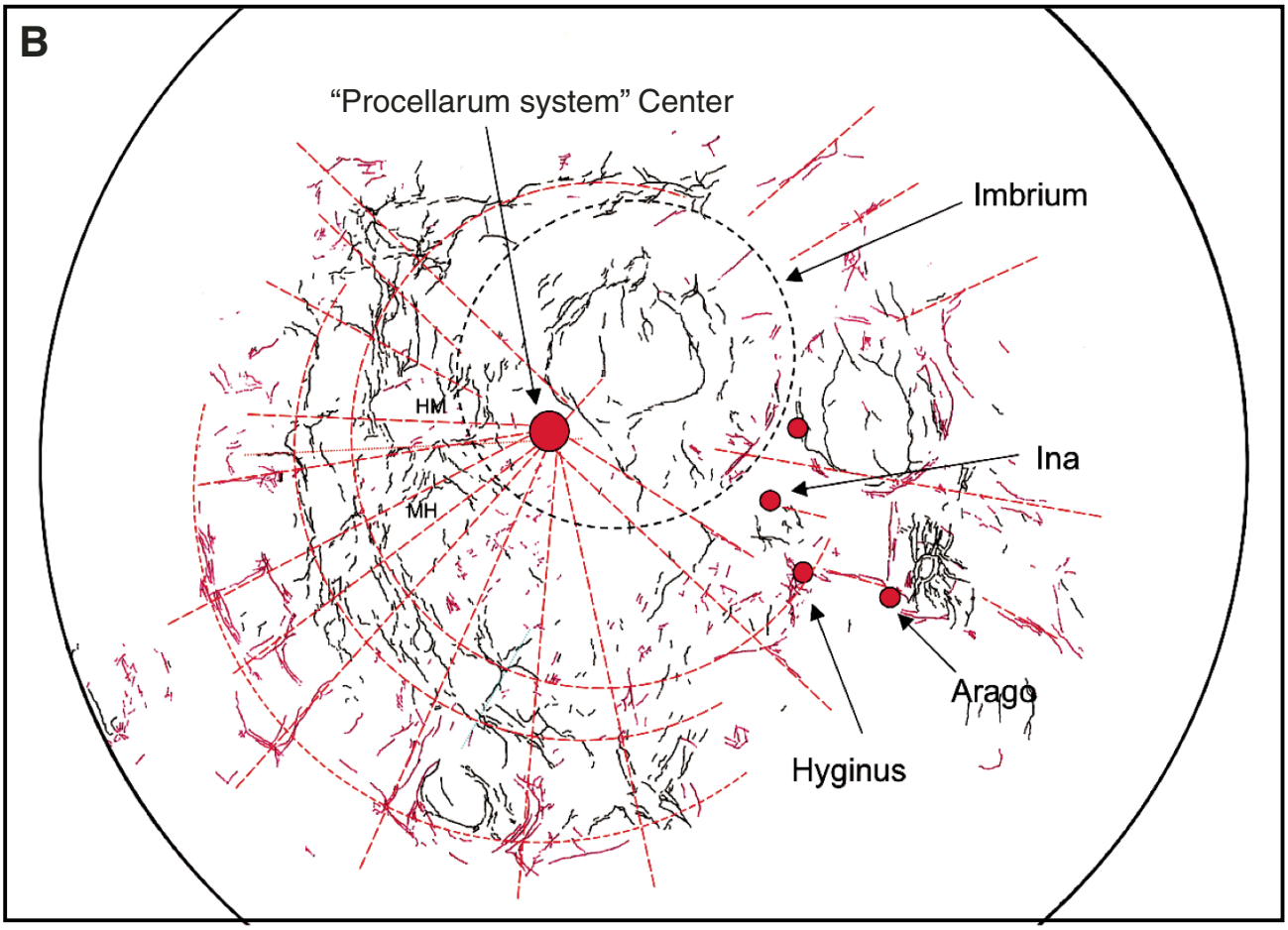

Figure 2 (*Continued*). The unlabeled dot (above Ina) is a possible site of gas release near the Sulpicius Gallus Rilles.

of an oblique impact into a spherical body have not been fully explored. While various studies have assessed the effect of trajectory on survival of small bodies (e.g., Marinova et al., 2008), the focus here is the degree and distribution of damage within these bodies well before reaching conditions leading to disruption.

In an oblique impact, the maximum peak pressures are enhanced downrange (Dahl and Schultz, 2001; Pierazzo and Melosh, 2000). Maximum coupling, however, controls crater diameter and occurs as the impactor penetrates farther into the target. For the present study, hypervelocity impact experiments were performed at the National Aeronautics and Space Administration (NASA) Ames Vertical Gun Range (AVGR) using spherical projectiles and clear polymethylmethacrylate (PMMA) spherical targets. This strategy revealed the evolution of impact asymmetries and documented the propagation and convergence of the impact-generated shock waves for different impact angles (Fig. 3).

Above a critical value for the specific energy (but well below catastrophic disruption), shocks reflect off the curved free surface and converge antipodal to the impact (Fig. 4). Five key features characterize this damage. First, there is a haze of microcracks (star-like discs) below the surface, downrange from the impact. Second, maximum antipodal surface damage (concentric and radial extensional cracks) occurs antipodal to the crater. Third, a distinctive tree-like structure emerges deep within the sphere, emanating from a region near (but offset from) the impact antipode. Fourth, the sphere remains undamaged uprange from the impact (and the antipode). Fifth, total target damage strongly depends on impact angle.

These observations document a downrange-directed shockwave that reflects and reinforces off a curved free surface. Damage increases downrange below the surface, even though the peak pressures decrease. As the free surface becomes less oblique to the shock front, shock rarefactions converge and exceed the material strength limit. The impact does not couple its energy and momentum instantly but evolves as the projectile penetrates deeper into the target. The initial contact does, however, create the greatest peak pressures, with most of the energy and momentum directed downrange, as illustrated in planar impacts (Dahl and Schultz, 2001; Stickle et al., 2009).

New high-speed imaging available at the AVGR (up to 10^6 frames per second) allows documentation of the damage sequence within the spheres (Fig. 4). The first appearance of damage

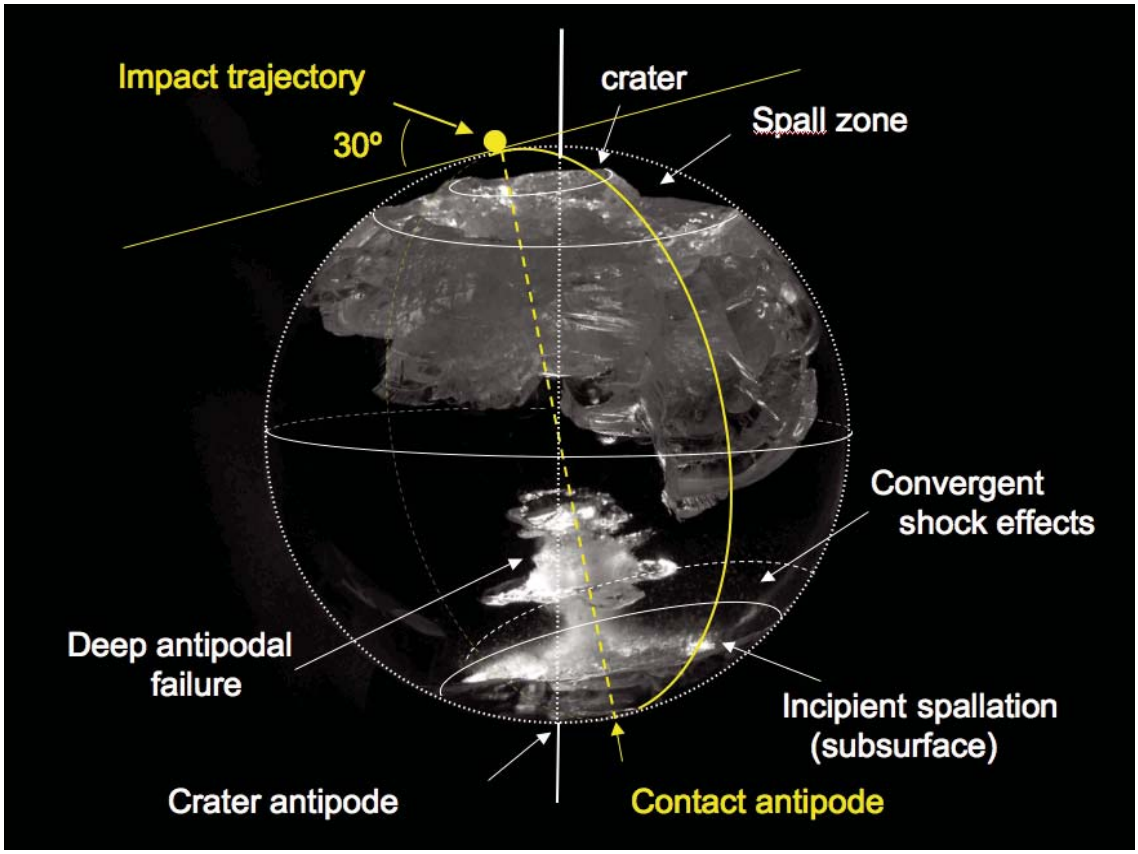

Figure 3. Oblique impact into acrylic sphere (45°) at 5.4 km/s. Oblique trajectory results in higher peak pressures downrange (yellow line). Failure is initiated at the center and progresses toward antipode. Antipodal deformation is offset from the crater but coincides more closely with the first contact. Incipient spallation below the surface is further offset back toward the crater.

(beyond the crater) emerges behind the downrange-directed shock front, ~90° from the point of first contact. This damage migrates and increases as the shock progresses downrange along the interior curved surface where the front becomes less oblique. Below a limiting specific energy, there is no surface spallation, only damage below the surface. The resulting "haze" of microcracks is offset from the antipodal point referenced to the final crater. Deep inside the sphere, damage initiates near the center and grows downward toward the antipodal surface. The "tree-like" appearance develops as cracks propagate outward along specific planes. The overall pattern, however, remains offset from the antipodal point to the crater. Rather, it is offset with respect to the first point of contact by the impactor. A separate contribution details this evolution and includes comparisons with hydrocode models (Stickle et al., 2009).

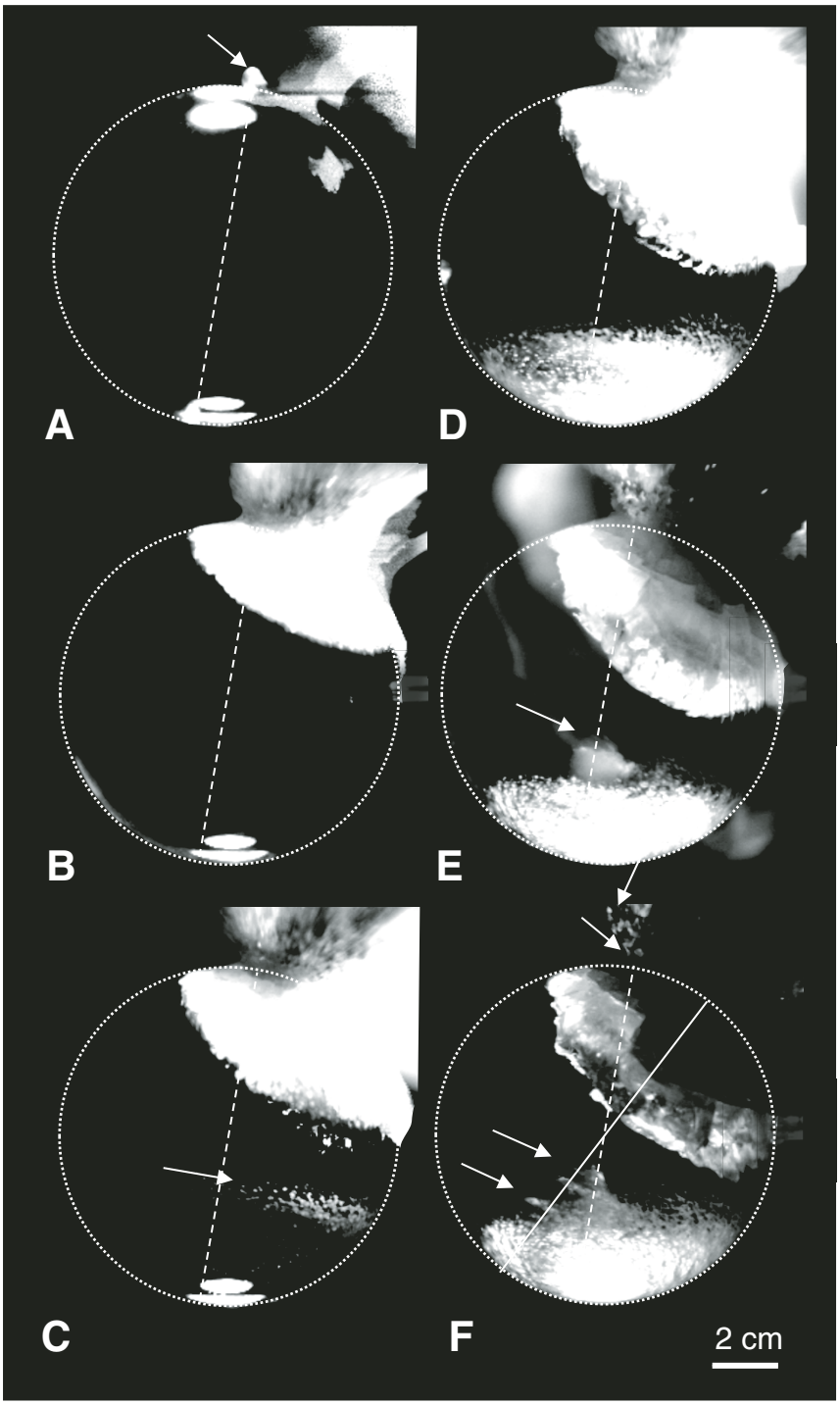

Figure 4. Time sequence for an oblique (30°) impact by a 0.635 cm Pyrex sphere into a clear polymethylmethacrylate (PMMA) sphere (10.2 cm diameter). The first frame (A) shows the moment just after first contact, where the dashed line indicates the first-contact antipode line. The bright ovals (top and bottom) are reflections from the illumination sources. The next image (B) shows the disruption behind advancing shock 24 µs after first contact. A near-surface haze develops 32 µs after impact (C). Small disc-shaped damage centers (below the surface) comprise this haze. As the reflected shock waves reflect off the curved free surface, they converge and induce shear damage below the surface (Stickle et al., 2009). The greatest damage occurs farther downrange 40 µs after impact, as the expanding shock becomes more normal to the surface of the sphere (D). Soon after, the convergent shocks in the center of the sphere induce tensile failure near the center of the sphere (E), which grows with time (64 µs). Horizontal failure planes extend from the central damage zone, 98 µs after impact (F). Most of the damage occurs offset (uprange) from the point directly opposite to the final crater (solid line).

The reduction in damage correlates with reduced penetration depths for impacts into curved surfaces (Schultz, 1997). This process is illustrated geometrically in Figure 5, and it can be shown that the limiting impact angle (θ), where a fraction "*k*" of a projectile (of radius *r*) decouples from an impacted sphere (of radius *R*) and misses further interaction with the surface downrange. This geometry is given by:

$$\cos\theta = R/(R + kr).$$

The decoupled mass fraction (m) relative to the initial impactor mass (M) can given by:

$$m/M = (k')^2(3/4 - k'/4),$$

where k' is defined as the decoupled fraction of impactor (50% when $k' = 1$).

Impacts into aluminum cylindrical targets result in significantly shallower penetration relative to impacts into planar targets for the same initial conditions (Fig. 6). The shallow depth is attributed to decoupling of the projectile during impact (Schultz and Gault, 1990; Schultz, 1997) and simple shear (Schultz and Crawford, 2007). Consequently, reduced peak pressures due to the oblique trajectory only partially account for the reduced damage in the PMMA spheres. Hydrocode models at much larger scales further demonstrate this process.

Hydrocode Simulations

Three-dimensional hydrocode computations allow us to test extrapolations and parametric studies inferred from the experiments. An improved version of the CTH (McGlaun et al., 1990) hydrocode includes self-gravity based on a parallel implementation of the Barnes and Hut (1986) algorithm and adaptive mesh refinement (Crawford et al., 2006). For the computations, undifferentiated dunite bodies with diameters from 140 to 700 km collided with the Moon at 20 km/s and angles of 30°, 45°, 60°, and 90° (from the impact tangent plane at first contact). The selection of a dunite composition provides a reasonable match for an asteroid of mafic composition. The calculations used ANEOS (i.e., Analytic Equations Of State) (Thompson and Lauson, 1972) for the dunite, the lunar mantle, and the 350-km-radius molten iron core. The Moon was initialized in hydrostatic equilibrium with pressure and temperature profiles at the time of impact based on theoretical models (Wieczorek and Phillips, 1999). The impactor was initialized with a constant temperature and radial lithostatic pressure appropriate for hydrostatic equilibrium. Numerical resolution of 40 km for the finest mesh was adequate to capture shock compression, release, and tensile fracture (spall) in the bulk of the Moon. The combination of experiments and modeling reveals

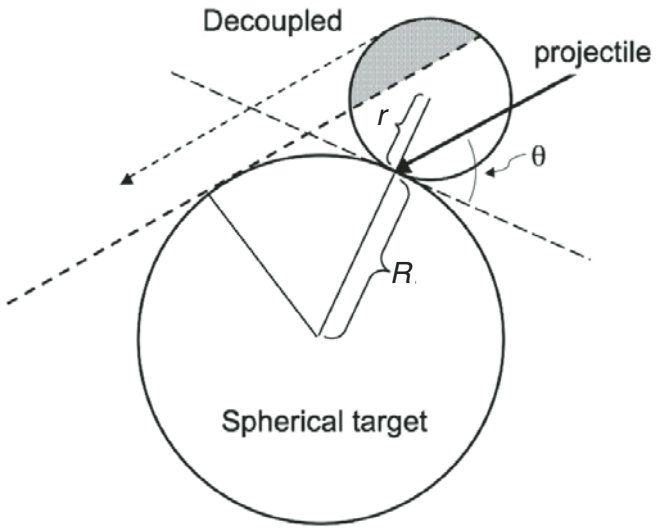

Figure 5. Diagram illustrating decoupling of the projectile from the impact process through simple shear and spallation of the back of the projectile. As the projectile diameter approaches 10% of the target diameter, the top of the projectile is removed from crater excavation after the initial shock.

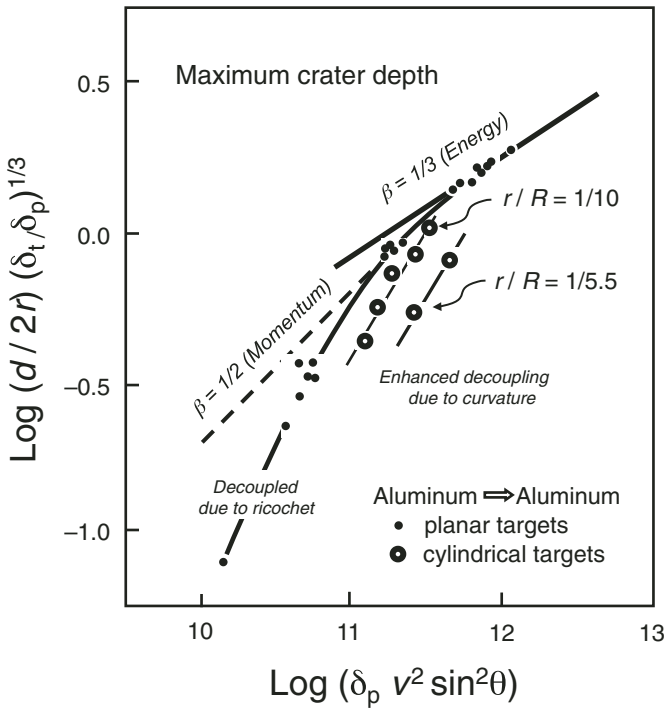

Figure 6. The maximum crater depth (penetration) for aluminum spheres impacting aluminum blocks (planar targets) and cylinders. As the vertical component of impact velocity (*v*) increases, penetration depth (*d*) for impacts into blocks transitions from momentum to energy scaling. Spherical aluminum projectiles (radius, *r*) impacting aluminum cylinders (radius, *R*), however, exhibit reduced crater depth as the radius of the projectile exceeds ~5% of the target radius. This is due to projectile decapitation and decoupling as illustrated geometrically in Figure 5. Other variables include δ_t for target density, δ_p for projectile density, θ for impact angle (referenced from the surface tangent to the trajectory), and β for the exponent (corresponding to momentum or energy scaling).

the controlling process for failure. For the largest-energy events, the impact kinetic energy (KE) represents a significant fraction (up to ~30%) of the total gravitational potential (binding) energy of the Moon.

For reference, Figure 7 illustrates the effect of changing the projectile mass for a given speed (10 km/s) for a vertical impact (90°). Objects larger than 400 km in diameter at this speed induce damage affecting more than 50% of the total lunar mass (7.35×10^{22} kg). In this case, the impact kinetic energy (KE) represents ~0.3% of the total gravitational potential energy of the Moon. Converging shocks at the antipode become strong enough to overcome the lithostatic overburden at depth.

The effect of impact angle (90°, 60°, 45°, and 30°) on internal failure (tensile stress >250 MPa) for a South Pole–Aitken–scale collision is shown in Figure 8. Coupled energy is kept nearly constant in order to produce the same-sized crater with an impact speed of 20 km/s. Impactor diameters and angles correspond to: 260 km at 90° (A); 300 km at 60° (B); 380 km at 45° (C); and 700 km at 30° (D). Total damage to the Moon is kept nearly constant (~65%) for the different impact angles in order to assess the effect on the interior. The crust is considered fractured when stress locally exceeds the lithostatic load by 250 MPa, which is estimated to be the fracture strength appropriate for gabbroic anorthosite (Ai and Ahrens, 2004). A 260-km-diameter asteroid colliding vertically (90°) at 20 km/s (9.2×10^{21} ergs) would induce the same amount of damage as a 700-km-diameter asteroid at 30° (1.8×10^{23} kg). This damage, however, is distributed very differently, as illustrated in Figure 8. Even though the 30° impact angle (from the surface tangent) has ~20 times more kinetic energy than the vertical impact, the amount of failure remains the same as the vertical impact. This lost energy reflects decapitation (decoupling) of the impactor from the target (e.g., Fig. 6).

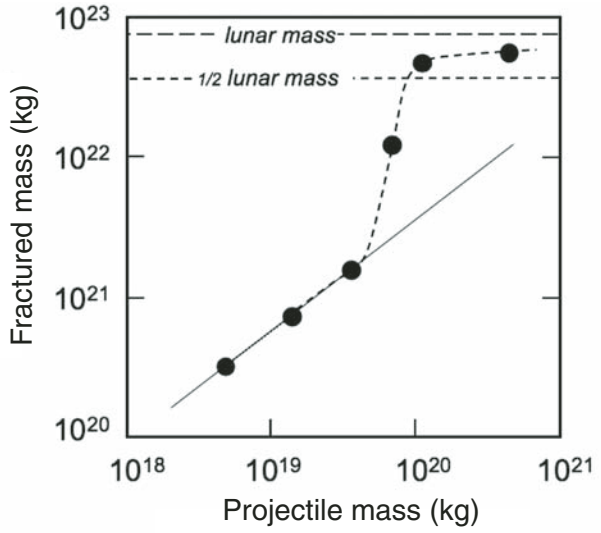

Figure 7. Objects larger than 400 km in diameter (10 km/s) fracture more than 50% of the total lunar mass (7.35×10^{22} kg). Converging shocks at the antipode become strong enough to overcome the lithostatic overburden at depth and induce fracturing where/when the tensile stress exceeds 250 MPa. In this calculation, all impacts are vertical, and individual sizes of projectiles include 140, 200, 274, 340, 400, and 634 km in diameter (left to right).

Both computational and laboratory experiments exhibit the same basic failure patterns within the body, even for very different material properties and overpressures (Fig. 9A). Specifically, the greatest antipodal damage is offset toward the incoming trajectory due to the convergence of shock rarefactions near the first-contact antipode. This should be expected because of the three-dimensional (3-D) geometry and the shock asymmetry. The code and experiments also reveal that different styles of failure evolve and overlap. The computation demonstrates, however, that a South Pole–Aitken–scale impact generates stresses that exceed the fracture strength of rocks at depth (lithostatic burden) throughout more than half of the lunar volume over a time exceeding 15 min. Furthermore, the deepest region of fracturing is antipodal to the point of first projectile contact, not the center of the crater. Depending on impact angle, this leads to a significant offset of fracture-associated features from the antipode to the transient crater.

Cumulative damage at depths of 400 km and 800 km (halfway to the core-mantle boundary) is shown in Figure 9B (middle). Because such deep disruption may be expressed by later igneous activity on the surface above, the damage is projected onto the surface (Fig. 9B, right). along with the locations of the antipode from the first-contact and excavation crater for South Pole–Aitken. Figure 9B reveals that failure would have extended to great depths from near South Pole–Aitken to beyond the direct antipode. Detailed models comparing laboratory and hydrocode experiments further indicate that shear damage may be as important as extensional damage (Stickle et al., 2009).

In summary, both experiments and computational models demonstrate that oblique impacts by very large objects should have had a profound effect on the lunar interior. Moreover, these effects include asymmetric internal damage.

DISCUSSION

The South Pole–Aitken basin does not exhibit obvious evidence for an oblique impact, in part because of its preservation state. In this section, we first consider expectations for an oblique megacollision on the Moon. We then briefly examine possible evidence for the trajectory based on the relict shape of the South Pole–Aitken basin revealed by different criteria. Next, we assess the trajectory necessary to account for Oceanus Procellarum. Last, we consider the implications for nearside-farside dichotomy.

Expectations from Experiments and Hydrocodes

Results show that a large oblique impact on the Moon could produce a megabasin without destroying it. Maximum damage occurs along the trajectory downrange but reaches its greatest depth antipodal to the first point of contact. Shock damage induced within (and on the other side of) the Moon would actually exceed the damage around and below the transient basin of

South Pole–Aitken itself (Fig. 9A). Relict melts deep in the cooling Moon (800 km) could have found pathways into the lower crust (200 km) through this damaged interior (Fig. 9B). Radioactive heat–producing elements concentrated within with these melts would later create magma reservoirs (e.g., KREEP-rich magmas) closer to the surface on the nearside. Fracturing closer to the surface also would provide secondary pathways through subsequent impact basins (e.g., Imbrium) as the Moon thermally expanded due to delayed radiogenic decay. Pathways through the brecciated floors of smaller craters could have contributed to the concentration of floor-fractured craters along the western "shores" of Oceanus Procellarum (Schultz, 1976b; Wichman and Schultz, 1995). While there are other floor-fractured craters peripheral to mare-filled impact basins (e.g., Serenitatis, Procellarum, and Smythii), the western edge of Oceanus Procellarum has one of the greatest concentrations.

The primary goal of this study is to demonstrate that an oblique impact for South Pole–Aitken could account for the absence of evidence directly opposite, northeast of Imbrium. While it is possible that Imbrium overprinted (buried) such effects, an oblique impact for South Pole–Aitken would not only accommodate this enigma but also provide an alternative explanation for the nearside distribution of volcanism and tectonism. For this hypothesis to apply, however, the trajectory for a South Pole–Aitken impactor would have to have been generally from the NW to the SE in order to induce maximum damage in the area of

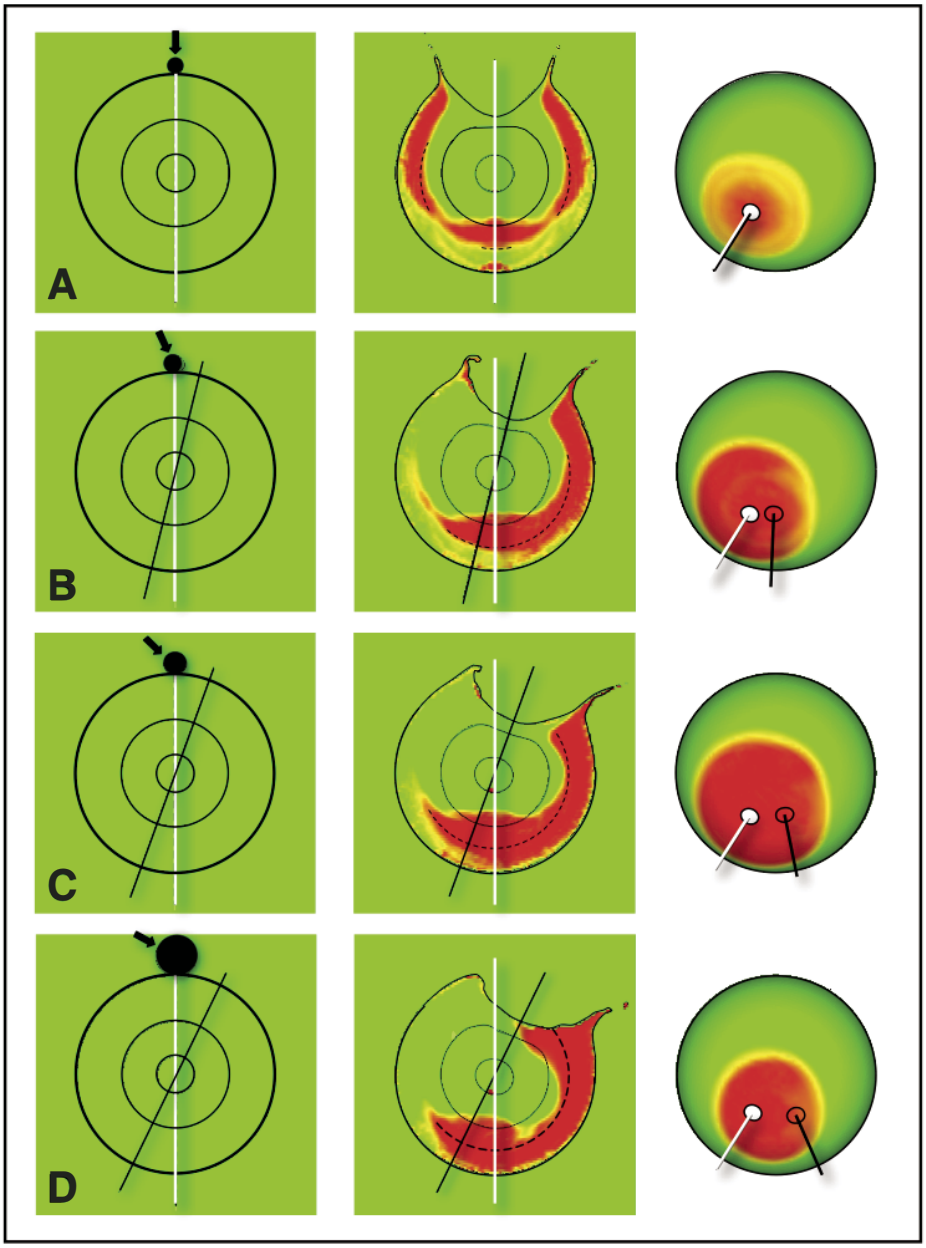

Figure 8. Effect of impact angle on disruption of the lunar interior. Total damage to the Moon is kept nearly constant (~65%) for the different impact angles. Even though the 30° impact has ~20 times more kinetic energy than the vertical impact, the amount of failure remains the same as the vertical impact. Coupled energy is kept nearly constant in order to produce the same-sized crater with an impact speed of 20 km/s. Impactor diameters and angles correspond to: 260 km at 90° (A); 300 km at 60° (B); 380 km at 45° (C); and 700 km at 30° (D). The crust is considered fractured when stress locally exceeds the estimated tensile fracture stress of 250 MPa (yellow region) appropriate for gabbroic anorthosite (Ai and Ahrens, 2004). The 800-km-depth contour (about halfway to the core-mantle boundary) and core-mantle boundary are indicated; dashed line corresponds to 400 km depth (middle). Global maps (right) indicate fractured rock at 800 km depth as well as the first-contact antipode (white line) and final-crater antipode (black line). Fracturing at 200 km exhibits an even greater offset toward the downrange crater rim.

Oceanus Procellarum. Next, we briefly consider the South Pole–Aitken basin itself and the possible evidence, first for an oblique impact and second for this trajectory.

Proposed South Pole–Aitken Basin Impactor Trajectory

Data from the *Clementine* mission revealed that the South Pole–Aitken basin contains the deepest point on the Moon (Smith et al., 1997). Such a deep basin contrasts with all other (and much smaller) basins in which the floors are filled with mare basalts or light plains. Two possible explanations include an absence of magma sources on the farside or a thicker farside crust. The difficulty with both explanations is that mare basalts do fill the adjacent Australe basin as well as the numerous craters and basins within South Pole–Aitken itself. An oblique trajectory could account for the absence of this postbasin fill for the following reasons.

First, a large impactor (~20% the diameter of the Moon) would decapitate when it hit a curved surface obliquely and decouple a sizeable fraction of the energy/momentum away from the Moon. Impactor decoupling would result in decreased penetration depths. The crustal response to reduced penetration depth should be expressed by reduced uplift of the basin floor as

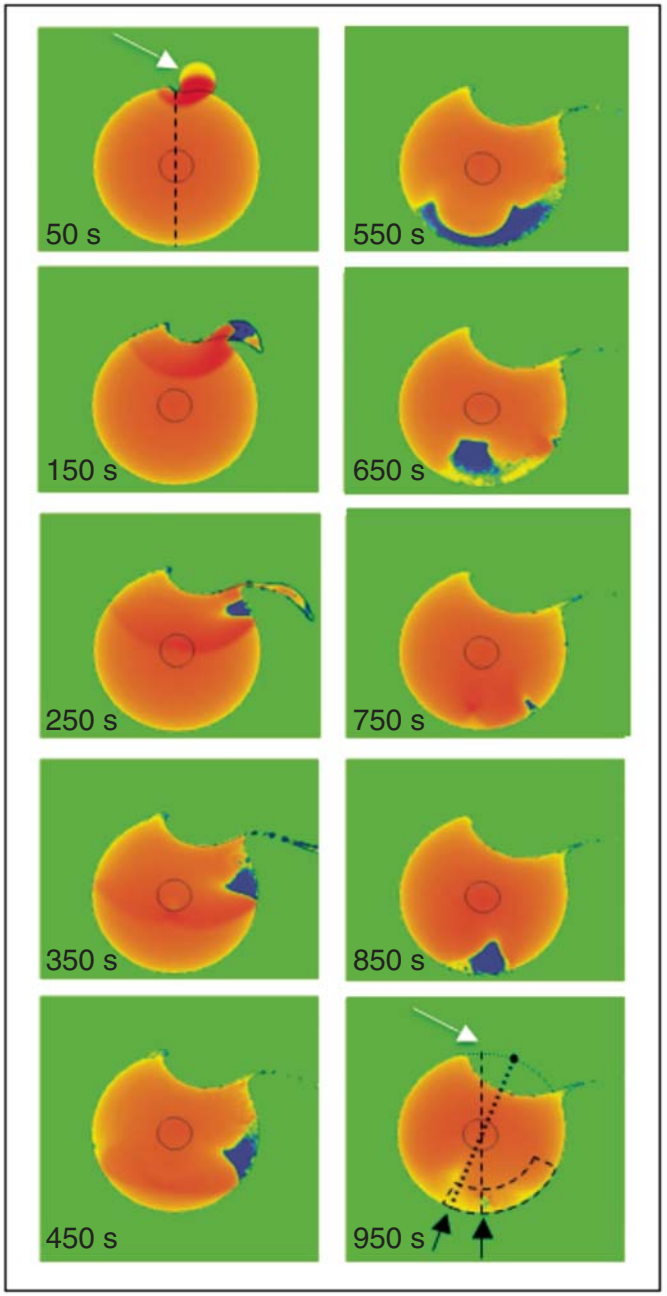

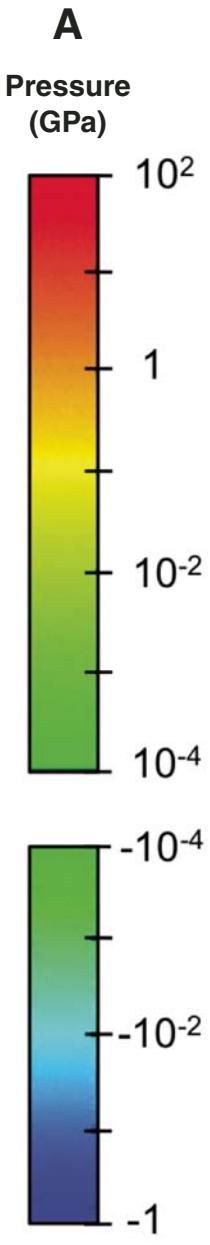

Figure 9 (*Continued on following page*). (A) Evolution of the shock created by a 700-km-diameter asteroid hitting the Moon at an angle of 30° from a surface tangent at different times after impact from 50 s (upper left) to 950 s (lower right). Red regions indicate compression and track the overpressure created by the shock. The blue regions denote extension (beyond local lithostatic overpressure). The greatest cumulative damage occurs opposite to the point of first contact and not the basin center (dashed region at 950 s after impact). Conditions of the Moon correspond to published models of thermal evolution models during pre-Nectarian time. (B) Cumulative damage at different depths produced by the South Pole–Aitken impact (left panel) and as projected onto the surface in a three-dimensional view (right). Yellow indicates regions subjected to tensile stress exceeding 250 MPa tension (including lithostatic overpressure). Conditions and failure criteria are the same as in Figures 7 and 8. Failure at depth is offset toward the impact direction (first contact). This figure reveals that the greatest depth (800 km, top figure) of extensive failure is offset from the antipodal point (black labels) and corresponds more closely to the first-contact antipode (white labels). At shallower depths (200 km, bottom figure), antipodal failure extends from near the basin to beyond the South Pole–Aitken antipode.

observed for South Pole–Aitken. Even though the upper half of the impactor would decouple, its footprint would set a minimum diameter of South Pole–Aitken.

Second, relict high-relief massifs (reflecting structural uplift) can be used to trace the outer South Pole–Aitken rim (Schultz, 1976a; Wilhelms, 1987; Garrick-Bethell and Zuber, 2009). Such massifs are typically lost around pre-Nectarian impact basins due to collapse of the transient crater. For example, an outer boundary scarp delineates portions of the outer rim (e.g., the Cordilleras of Orientale, and the Altai Scarp of Nectaris). The preserved rim uplift expressed by South Pole–Aitken massifs indicates that the impact conditions did not induce the same degree of collapse characterizing smaller basins.

Figure 10A shows a map of individual massifs based on images (*Lunar Orbiter*, *Apollo*, and *Clementine*) and topography from *Clementine* (Smith et al., 1997) and *Kaguya* (Namiki et al., 2009). It also includes post–South Pole–Aitken basins and craters as well as major transitions in elevation based on topographic maps and visible scarps. Significant local relief (from topography) or actual features characterize individual massifs. This map reveals that the massifs extend farther to the northwest than the typically identified South Pole–Aitken boundaries (e.g., Wilhelms, 1987; Garrick-Bethell and Zuber, 2009).

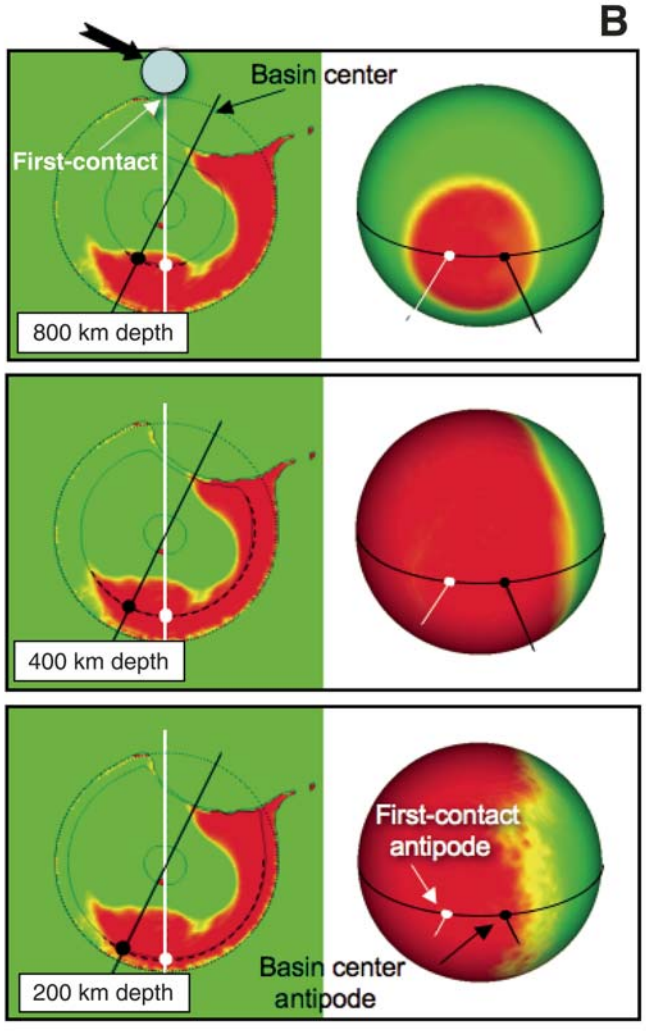

Figure 9 (*Continued*).

Large adjacent impact basins partially disrupt the continuity of the South Pole–Aitken basin rim. The Australe basin, in particular, disrupts the massif ring to the southwest (in the context of Fig. 10A). South Pole–Aitken massifs, however, appear to extend across the interior of Australe. These massifs and the preservation state of Australe basin contrast with the South Pole–Aitken basin and raise a question concerning its age, i.e., a pre– rather than post–South Pole–Aitken age. Moreover, it appears that Australe basin approaches the size of South Pole–Aitken basin based on boundary scarps, elevations, and the distribution of mare-filled craters.

Although not compelling, the distribution of massifs and transitions in elevations indicate a NW-SE elongation, even though the general topographic shape indicates a more NNW-NNE trend (Garrick-Bethell and Zuber, 2009). Petro and Pieters (2004) remapped original South Pole–Aitken materials (identified by Wilhelms, 1987) that also follow a NW-SE elongation (Fig. 10A). The difference between the map shown here and prior studies is attributed to differences in approach (inclusion of morphological features here), new high-resolution topographic data from JAXA, and recognition of the effect of overlapping large basins that may mask the initial shape.

The most obvious oblique multiring impact basins on the Moon are Crisium (e.g., Wilhelms, 1987; Wichman and Schultz, 1994), Orientale (McCauley, 1977; Scott et al., 1977; Schultz, 1996), and Imbrium (Schultz and Spudis, 1985). Only the Crisium massifs trace an obvious oblong shape, although the inner massif rings of the Imbrium and Orientale basins are also oblong or breached, respectively. The outer rings of these basins are not immediately obvious due to rim collapse (Wichman and Schultz, 1994). Nevertheless, the Bouguer gravity high within Imbrium correlates with its oblong inner massif ring and is offset uprange from an arc fitted to the Apennines/Carpathians (southern uplifted rim). The gravity high within Orientale is also offset uprange relative to its geometric center (Schultz, 1996). For South Pole–Aitken, the vertical gravity anomaly (relative to a perfect sphere with removal of lunar oblateness) and greater "Airy depth" also cover the northwestern portion of South Pole–Aitken, although the maximum Airy depth is nearly central (Konopliv et al., 1998).

As crater size increases, excavation efficiency for gravity-controlled growth decreases significantly, decreasing even more for oblique impacts (Schultz, 1992). The transient crater size relative to projectile size for a large oblique impact basin approaches laboratory-scale, strength-controlled impacts. Projectile failure and re-impact events downrange contribute to the elongation (Schultz and Gault, 1990). As a result, it would seem that oblique trajectories should become more obvious for an oblique megabasin. A factor offsetting this effect, however, is the consequence

of projectile decoupling due to surface curvature, preventing the failed impactor from re-impacting downrange within or directly adjacent to the basin. Consequently, the excavation crater shape for South Pole–Aitken actually becomes less elongate for an oblique impact because trajectories of the failed (and decoupled) impactor would have re-impacted farther downrange, e.g., scouring the pre-Procellarum crust.

The slightly elongated outline of the South Pole–Aitken massifs, original South Pole–Aitken materials, and elevation transitions are consistent with a NW-SE impact trajectory. Figure 10B shows the approximate distribution of high-Th regions within South Pole–Aitken (Garrick-Bethell and Zuber [2005] based on data from Lawrence et al. [2007]). Haskin (1998) proposed that high-Th ballistic ejecta from Imbrium converged in this antipodal region, whereas Wieczorek and Zuber (2001) attributed the South Pole–Aitken anomaly to convergent antipodal ejecta from Serenitatis. Garrick-Bethell and Zuber (2005), however, argued the distribution of high-Th materials in the northwest edge of South

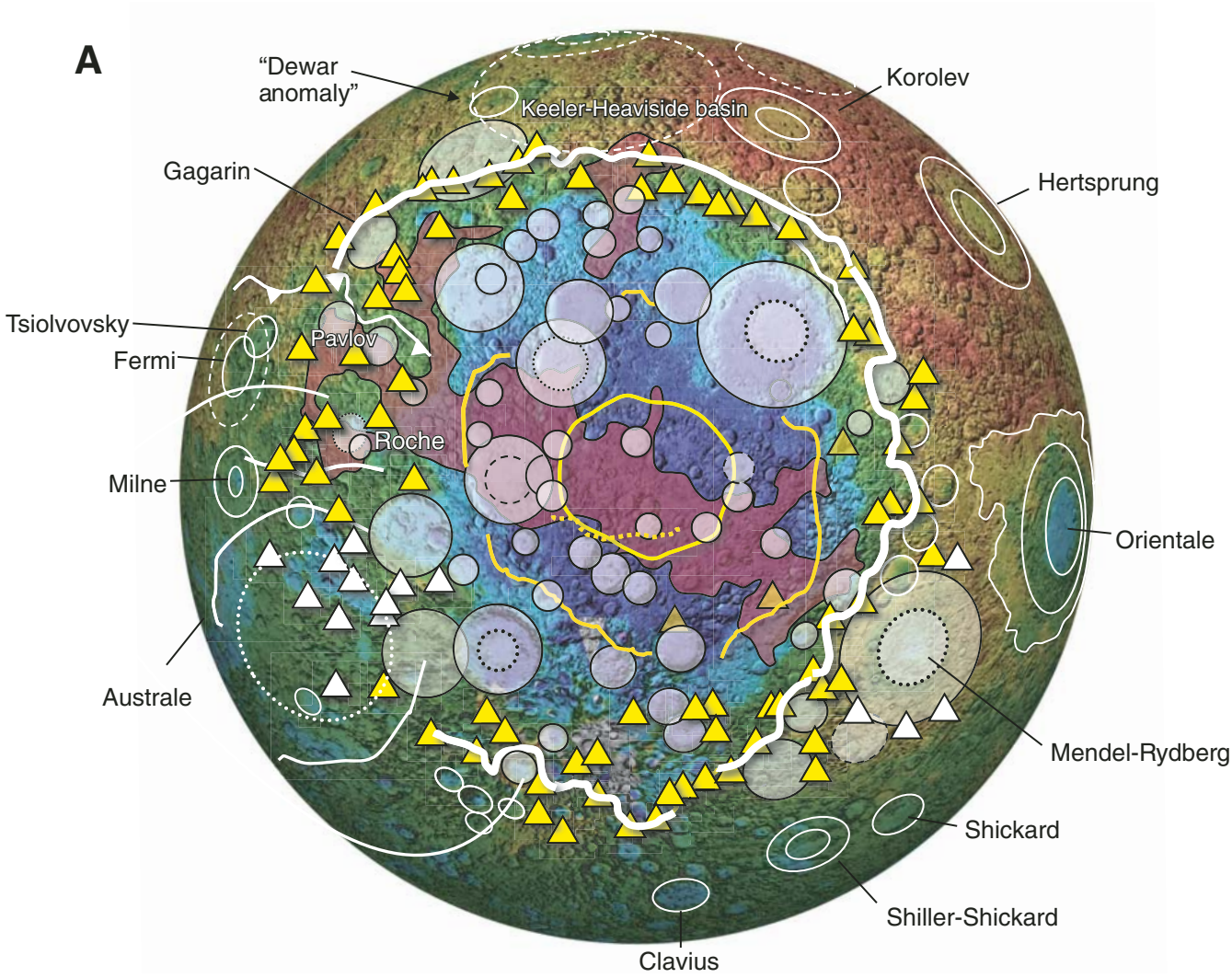

Figure 10 (*Continued on following page*). (A) Distribution of massifs associated with the South Pole–Aitken basin (yellow triangles) based on imaging and topographic maps. Interior topographic transitions form a NW-SE–elongate depression coincident with the mapped distribution of interior South Pole–Aitken materials (Wilhelms, 1987) shown in purple. White triangles indicate massifs affected by adjacent basins (Mendel-Rydberg and Australe). The Australe basin disrupts a significant portion of the southwest rim of South Pole–Aitken basin. Large massifs occur on the eastern side of Australe coincident with South Pole–Aitken massif ring. This requires that either they survived Australe or that South Pole–Aitken postdates Australe. More likely, the Australe predates South Pole–Aitken but was reactivated when mare basalts filled later craters. (B) Effect of craters and basins on the structure and expression of the South Pole–Aitken basin. Black circles correspond to the primary rim for each basin or crater, with dashed and dotted lines indicating interior rings. Colored regions indicate high-Th regions (from Garrick-Bethell and Zuber [2005] based on data from Lawrence et al. [2007]); yellow indicates values above 2 μg/g, orange indicates values above 2.5 μg/g, and red indicates values above 3 μg/g. These orthographic projections are both centered on latitude –59° S and longitude 166° W.

Pole–Aitken likely represents indigenous materials exposed by smaller craters (Garrick-Bethell and Zuber, 2009).

As endogenous materials, the high-Th anomaly in South Pole–Aitken represents the uplifted material from deepest displacement within the transient crater, which occurs near the region of initial coupling (Schultz, 1992; Schultz and Anderson, 1996). In a recent detailed study of topographic and geochemical data of South Pole–Aitken, Garrick-Bethell and Zuber (2005, 2009) found that two 50–80-km-diameter craters correlate with the high-Th materials in South Pole–Aitken; consequently, greatest uplift within the basin may have occurred to the north of the center. Alternatively, several much larger (>200 km) basins (Ingenii, Poincare, Leibnitz, and Von Karman) in the northwest interior of South Pole–Aitken excavated deeper materials and were subsequently reexposed by these "smaller" craters. The largest basin (Apollo) within South Pole–Aitken on the northeastern floor of South Pole–Aitken, however, did not expose these high-Th materials; nor did the adjacent Australe impact.

If the higher concentrations of Th-rich material in northwest South Pole–Aitken is due to uplift (exposed by later impacts), then this offset seems to be consistent with a trajectory from the northwest. If the Th enrichment is instead due to antipodal convergence of ejecta from Imbrium (or Serenitatis), then an oblique trajectory for South Pole–Aitken is necessary in order to account for the absence of uplifted KREEP-rich mantle material. A clue for its trajectory, then, could come from internal damage expressed on the surface.

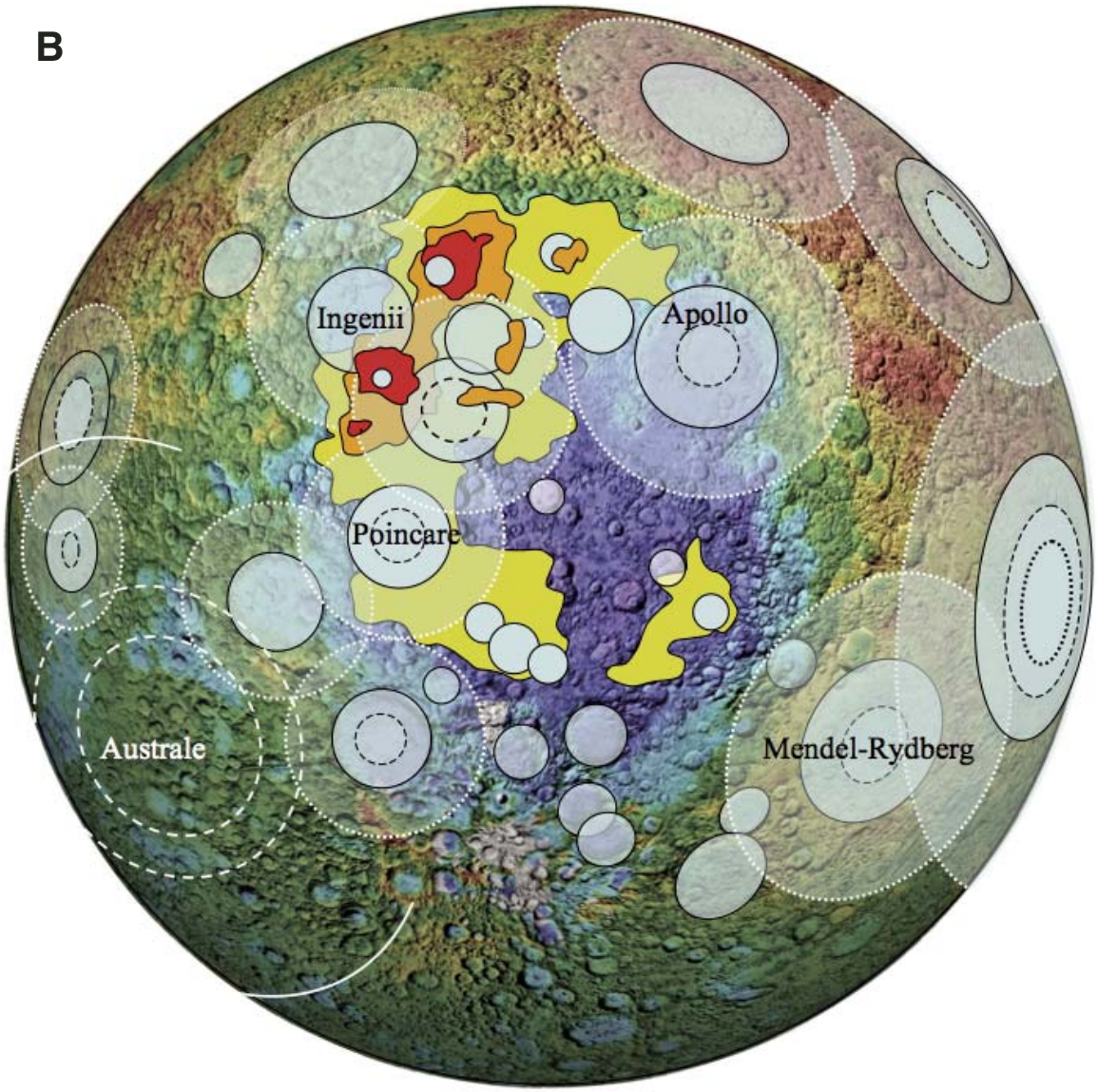

Figure 10 (*Continued*).

IMPLICATIONS

The South Pole–Aitken–forming impact should have damaged much of the lunar interior, regardless of impact angle (Fig. 8). A vertical impact (Fig. 8A) localizes damage below the crust surrounding the impact and deep in the mantle. An oblique impact (Fig. 8D), however, generates greater internal damage for the same size excavation crater that is offset back toward the impact. For an oblique trajectory by the South Pole–Aitken impactor, the offset between first contact and transient crater center should exceed 500–800 km, mirrored by a similar offset in antipodal damage. Figure 11 proposes a trajectory for South Pole–Aitken that would accommodate the offset between both the basin-center antipode and the Procellarum system center (Fig. 1B).

Figure 11 also includes the distribution ejecta from the South Pole–Aitken impact for the proposed trajectory. The earliest stages of coupling between the impacting body and the target comprise a larger fraction of the excavation process. For the oblique trajectory of South Pole–Aitken, the downrange ejecta component (plus surviving decapitated impactor debris) would have scoured the Procellarum region, thereafter leaving the Moon at speeds near (or greater than) escape velocity. The uprange-directed ejecta component, however, would have had minimal ejecta and result in a zone of avoidance, consistent with the survival of the adjacent Australe basin just uprange. Consequently, downrange ejecta for this proposed scenario may not have contributed to an identifiable ejecta deposit. Some ejecta (and impactor remains) returned to the Moon and would have added to crater populations interpreted as part of the Late Heavy Bombardment flux (Schultz and Crawford, 2008). Thicknesses of near-rim ejecta (late-stage, lower-speed ejecta) would be greatest transverse to the original trajectory, contributing to the farside elevated terrains and the Southern Highlands (Fig. 11). This provides an alternative to the Procellarum mega-impact as the cause of the lunar farside elevated terrains (Byrne, 2007).

The damaged lunar interior antipodal to an oblique South Pole–Aitken impact should have created extended pathways for deep-seated magma (middle mantle to the lower crust). Basalts may not have immediately erupted over the antipodal surface following the impact. Rather, it is suggested that the early internal plumbing below the nearside was initially established by the South Pole–Aitken collision. In this case, the absence of similar pathways across the lunar farside would be consistent with reduced shock-induced failure uprange. Conversely, a basin the size of the proposed Procellarum impact should have induced extensive failure and igneous pathways on the lunar farside, both of which are absent.

The proposed effects from the South Pole–Aitken impact may provide a new mechanism for the enigmatic distribution

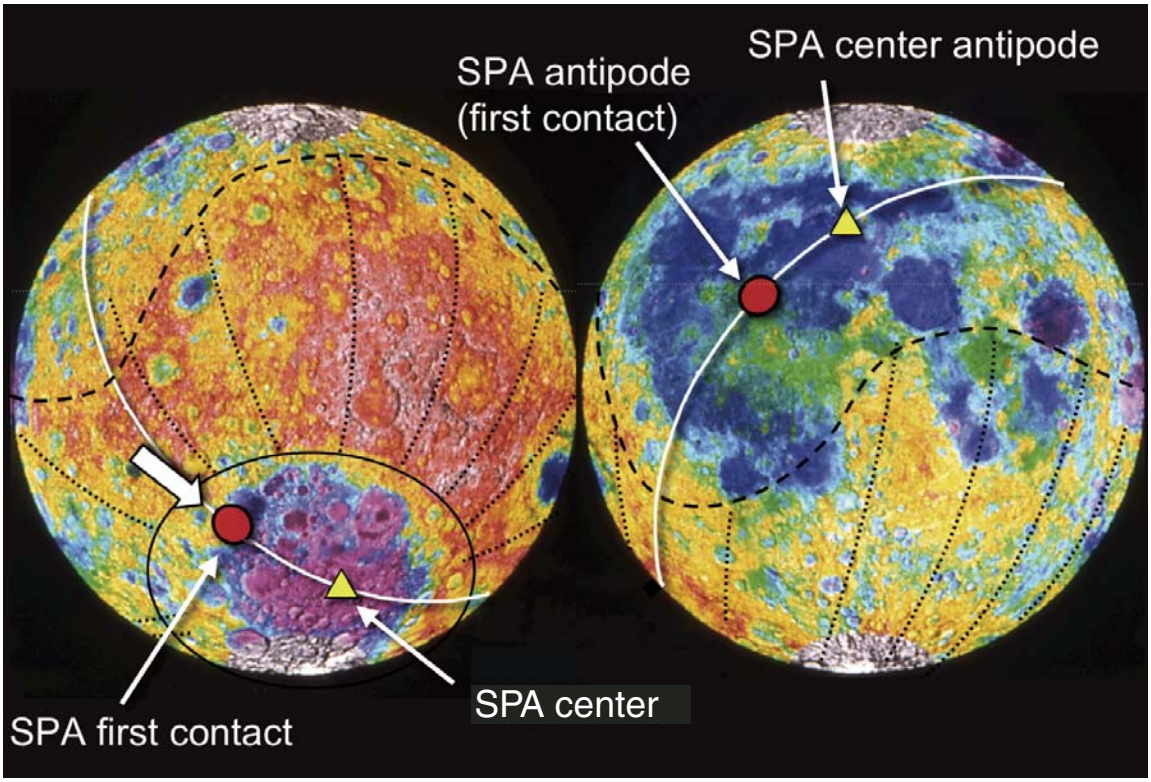

Figure 11. Proposed trajectory for the South Pole–Aitken (SPA) impact in order to produce the Procellarum system. The nearside and farside uplands may correspond to ejecta from South Pole–Aitken (depicted by lineations).

of PKT ("Procellarum Kreep terrane") materials and the widespread basaltic maria on the nearside. Offset antipodal fracturing from the South Pole–Aitken impact would have localized progenitor (radiogenic) magmas responsible for the high-Th "great lunar hot spot," extending vertically a few tens of kilometers and laterally hundreds of kilometers on the nearside (Haskin, 1998). Wieczorek and Phillips (2000) argued that KREEP magmas were established early and continued for a few billion years, whereas Hess and Parmentier (2001, p. 28,030) thought it is more likely that there was "…local thickening of the liquid layer under the PKT and concomitant thinning in the SPA [South Pole–Aitken] part of the crust.…" The South Pole–Aitken impact would establish the latter two conditions.

Because the Imbrium impact occurred northeast of the offset South Pole–Aitken antipode, it would have excavated partially differentiated remnants of these intrusions and contributed to the Th-rich Fra-Mauro ejecta (Haskin, 1998; Garrick-Bethell and Zuber, 2005, 2009). This asymmetry is more clearly revealed in further processing of *Lunar Prospector* data (Lawrence et al., 2007) and is evidence that the Imbrium impact excavated a northeast extension of the Th-rich layer. Other impact basins did not excavate significant KREEP-rich materials because the source magma (or mantle) remained inaccessible (too deep) or was not present.

The South Pole–Aitken impact should have induced failure extending well into the lower mantle of the Moon. This disruption would have acted as a pump: opening and closing pathways over tens of minutes in response to the convergent shock rarefactions (Fig. 9B). The greatest depths disrupted the mantle to depths exceeding 800 km and approaching the core-mantle boundary. This region is projected onto the surface in Figure 12 in order to illustrate the approximate boundary of deeply tapped materials in response to a South Pole–Aitken impact (Fig. 9B). Perhaps KREEP-rich magmas (with associated heat-producing elements) were localized in the upper mantle and lower crust on the lunar nearside. This correlates with mapped structural features and geochemical anomalies, such as the nearside PKT (e.g., Jolliff et al., 2000). A very large impact basin adjacent to the South Pole–Aitken antipodal zone of disruption northeast of Imbrium (e.g., the Humboldtianum basin), however, still could have resulted in outliers, e.g., the high-Th anomalies near Compton-Belkovich (Gillis et al., 2002; Lawrence et al., 2007).

The ridges and sinuous-rille source regions visible today reflect igneous centers controlled by the South Pole–Aitken antipode magmas, whereas the graben reflect peripheral extension in response to their load. The KREEP materials would have remained largely hidden, except for the subsequent excavation by the Imbrium basin impact and localized eruptions of basalts (Wieczorek and Phillips, 2000). Regardless, the shattered nearside continued to provide the pathways to the surface for the last stages of lunar volcanism (<0.8 Ga) correlated with high-Ti basalts in Procellarum (Schultz and Spudis, 1983).

The impact producing the Imbrium basin occurred when radiogenic decay increased thermal expansion of the Moon. Thermal expansion favored basaltic eruptions through the fractured regions beneath old (e.g., Smythii, Nectaris) and new (e.g., Imbrium, Serenitatis) basins and craters. Because the resulting radial and concentric fractures comprising the Procellarum system are deep seated, they typically cut tectonic features around later-produced basins, including Imbrium. Possible sites of recent pulses of degassing (Fig. 2B) all appear to occur near intersections between Procellarum system– and Imbrium-related graben (Schultz et al., 2006). Such locations would be consistent with gas following pathways created by South Pole–Aitken, released during continued cooling at depth. *Lunar Prospector* data from the Alpha Particle Spectrometer experiment (Lawson et al., 2005) further documented degassing indicated by enhanced ^{222}Rn in Procellarum, the greatest levels associated with recent Procellarum craters, Aristarchus and Kepler.

CONCLUSIONS

The formation of the South Pole–Aitken basin dominates the lunar farside; it also profoundly affected the evolution of the lunar nearside. Offset-antipodal shocks generated by the South Pole–Aitken impact converged on the nearside and created conditions leading to mafic magma networks localized in the lower crust, later excavated by the Imbrium impact. This proposed scenario would provide an alternative explanation for the Procellarum impact basin, which, up to now, has been widely cited as the underlying cause for nearside geochemical anomalies. The following is a summary of evidence for the proposed oblique trajectory:

(1) retained depth of the South Pole–Aitken basin, which is consistent with reduced disruption at depth and decoupling of large fractions of the impactor (e.g., Figs. 5, 6, and 9A);

(2) the absence of extensive (and unavoidable) convergent shock effects directly opposite to South Pole–Aitken as predicted (Fig. 8);

(3) the presence of an extensive system of radial and concentric structural weaknesses (graben, wrinkle ridges) on the lunar nearside accommodated by the proposed oblique trajectory (Fig. 2B);

(4) widespread mare basalts on the western lunar nearside consistent with shock effects offset from the South Pole–Aitken antipode and related to long-lasting pathways at depth (Fig. 1A);

(5) localization of high-Th materials (re-excavated by Imbrium) on the lunar nearside in a region predicted to have maximum offset-antipodal disruption at depth (Fig. 12); and

(6) localization of the youngest, high-Ti basalts within Procellarum.

In addition, there are several observations that are consistent with the proposed trajectory, including: the pattern of relict massifs (Fig. 10A); offset high-Th regions within the South Pole–Aitken basin (Fig. 10B); and the distribution of elevated terrains, including the Southern Highlands and farside highlands (Fig. 11).

Future lunar missions and models will allow the proposed trajectory for South Pole–Aitken and its consequences to be tested through much higher resolution topographic,

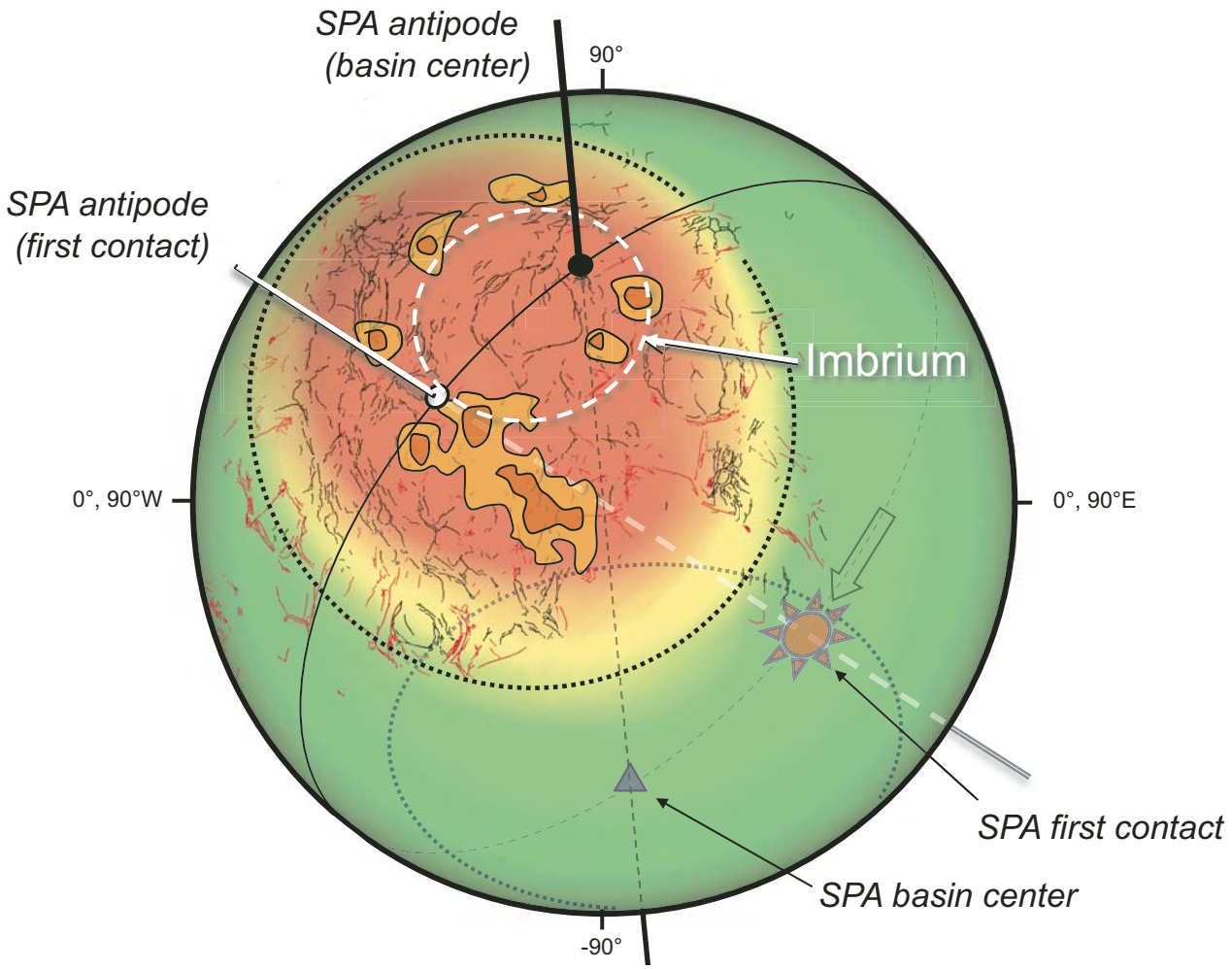

Figure 12. Implications of offset antipodal effects due to the formation of South Pole–Aitken (SPA) basin on the farside of the Moon. Calculated effects of the farside South Pole–Aitken basin on the nearside are superimposed on a system of radial and concentric ridges and rilles that comprise the Procellarum system. The background color indicates offset antipodal failure (>250 MPa) at a depth of 800 km (800 s after impact) predicted for a 30° impact angle from the northwest to southeast (first contact at 155°E longitude, 15°S latitude) responsible for the South Pole–Aitken basin as indicated in Figure 11. Failure limits approximately correspond to boundary of the Procellarum graben system. Regions with high-Th (and K) values are also shown (see Fig. 1B). This Lambert azimuthal-equal-area projection of the nearside matches Figure 1B.

geophysical, and geochemical data. Specific measurements include the following:

(1) updated mapping of the nearside structural system and non-basin-related volcanic vents;

(2) seismic networks that would identify a network of intrusions beneath Procellarum, rather than a relict basin structure;

(3) anisotropy, scattering, and shear splitting related to deep-seated intrusions related to offset antipodal effects;

(4) resolved gravity of the South Pole–Aitken basin that provides a better distribution of its structure;

(5) seismic networks that identify the nature, source, and distribution of deep and shallow moonquakes; and

(6) thermal and petrologic models placing limits on the contrast in thermal evolution between the lunar nearside and farside crust.

ACKNOWLEDGMENTS

Schultz acknowledges a grant from the National Aeronautics and Space Administration (NASA) Planetary Geology and Geophysics Program (NASA Grant No. NNX08AM45G); Crawford acknowledges that Sandia National Laboratories is a multiprogram laboratory operated by Sandia Corporation, a Lockheed Martin Company, for the U.S. Department of Energy under

contract DE-AC04-94AL85000. The authors appreciate the constructive comments by J.G. Taylor and an anonymous reviewer.

REFERENCES CITED

Ai, H., and Ahrens, T.J., 2004, Dynamic tensile strength of terrestrial rocks and application to impact cratering: Meteoritics & Planetary Science, v. 39, no. 2, p. 233–246, doi:10.1111/j.1945-5100.2004.tb00338.x.

Anderson, J.L.B., Schultz, P.H., and Heineck, J.T., 2003, Asymmetry of ejecta flow during oblique impacts using three-dimensional particle image velocimetry: Journal of Geophysical Research, v. 108, no. E8, p. 5094, doi:10.1029/2003JE002075.

Anderson, J.L.B., Schultz, P.H., and Heineck, J.T., 2004, Experimental ejection angles: Implications for the subsurface flow field during oblique impacts: Meteoritics & Planetary Science, v. 39, p. 303–320, doi:10.1111/j.1945-5100.2004.tb00342.x.

Barnes, J.E., and Hut, P., 1986, A hierarchical O(N Log N) force calculation algorithm: Nature, v. 324, no. 4, p. 446–449, doi:10.1038/324446a0.

Binder, A.B., 1982, Post-Imbrian global lunar tectonism: Evidence for an initially totally molten Moon: Earth, Moon and Planets, v. 26, p. 117–133.

Bruesch, L.S., and Asphaug, E., 2004, Modeling global impact effects on middle-sized icy bodies: Applications to Saturn's moons: Icarus, v. 168, p. 457–466, doi:10.1016/j.icarus.2003.11.007.

Byrne, C.J., 2007, A large basin on the near side of the Moon: Earth, Moon, and Planets, v. 101, p. 153–188, doi:10.1007/s11038-007-9225-8.

Cadogan, P.H., 1974, Oldest and largest lunar basin?: Nature, v. 250, no. 5464, p. 315–316, doi:10.1038/250315a0.

Crawford, D.A., Taylor, P.A., Bell, R.L., and Hertel, E.S., 2006, Adaptive mesh refinement in the CTH shock physics hydrocode: The Russian Journal of Physical Chemistry B, v. 25, no. 9, p. 85–90.

Dahl, J.M., and Schultz, P.H., 2001, Measurement of stress wave asymmetries in hypervelocity projectile impact experiments: Proceedings of the 2000 Hypervelocity Impact Symposium (HVIS): International Journal of Impact Engineering, v. 26, p. 145–155, doi:10.1016/S0734-743X(01)00077-X.

Garrick-Bethell, I., and Zuber, M.T., 2005, Endogenous origin for the South Pole–Aitken basin thorium anomaly: Geophysical Research Letters, v. 32, p. L13203, doi:10.1029/2005GL023142.

Garrick-Bethell, I., and Zuber, M.T., 2009, Elliptical structure of the South Pole–Aitken basin: Icarus, v. 204, p. 399–408, doi:10.1016/j.icarus.2009.05.032.

Gault, D.E., and Wedekind, J.A., 1978, Experimental studies of oblique impact, *in* Proceedings of the Ninth Lunar and Planetary Science Conference: New York, Pergamon Press, p. 3843–3875.

Gillis, J.J., Jolliff, B.L., Lawrence, D.J., Lawson, S.L., and Prettyman, T.H., 2002, The Compton-Belkovich region of the Moon: Remotely sensed observations and lunar sample association: Houston, Texas, Lunar and Planetary Institute, Lunar and Planetary Science Conference XXX, CD-ROM, abstract 1967.

Gillis, J.J., Jolliff, B.L., and Korotev, R.L., 2004, Lunar surface geochemistry: Global concentrations of Th, K, and FeO as derived from *Lunar Prospector* and *Clementine* data: Geochimica et Cosmochimica Acta, v. 68, p. 3791–3805, doi:10.1016/j.gca.2004.03.024.

Guest, J.E., and Murray, J.B., 1976, Volcanic features of the nearside equatorial lunar maria: Journal of the Geological Society of London, v. 132, p. 251–258, doi:10.1144/gsjgs.132.3.0251.

Haskin, L.A., 1998, The Imbrium impact event and the thorium distribution at the lunar highlands surface: Journal of Geophysical Research, v. 103, p. 1679–1689, doi:10.1029/97JE03035.

Hess, P.C., and Parmentier, E.M., 2001, Thermal evolution of a thicker KREEP liquid layer: Journal of Geophysical Research, v. 106, no. E11, p. 28,023–28,032.

Hood, L.L., and Artemieva, N.A., 2006, Formation of magnetic anomalies antipodal to lunar impact basins: Improved numerical and analytic analysis: Houston, Texas, Lunar and Planetary Institute, Lunar and Planetary Science Conference XXXVII, CD-ROM, abstract 2137.

Hughes, H.G., App, F.N., and McGetchin, T.R., 1977, Global seismic effects of basin-forming impacts: Physics of the Earth and Planetary Interiors, v. 15, p. 251–263, doi:10.1016/0031-9201(77)90034-6.

Jolliff, B.L., Gillis, J.J., Haskin, L.A., Korotev, R.L., and Wieczorek, M.A., 2000, Major lunar crustal terranes: Surface expressions and crust-mantle origins: Journal of Geophysical Research, v. 105, p. 4197–4216, doi:10.1029/1999JE001103.

Konopliv, A.S., Kucinskas, A.B., and Sjogren, W.L., 1998, Improved gravity field of the Moon from *Lunar Prospector*: Science, v. 281, p. 1476–1480, doi:10.1126/science.281.5382.1476.

Korotev, R.L., 2000, The great lunar hot spot and the composition and origin of the *Apollo* mafic "LKFM" impact melt breccias: Journal of Geophysical Research, v. 105, no. E5, p. 4317–4345, doi:10.1029/1999JE001063.

Lawrence, D.J., Puetter, R.C., Elphic, R.C., Feldman, W.C., Hagerty, J.J., Prettyman, T.H., and Spudis, P.D., 2007, Global spatial deconvolution of *Lunar Prospector* Th abundances: Geophysical Letters, v. 34, p. L03201, doi:10.1029/2006GL028530.

Lawson, S.L., Feldman, W.C., Lawrence, D.J., Moore, K.R., Elphic, R.C., Belian, R.D., and Maurice, S., 2005, Recent outgassing from the lunar surface: The *Lunar Prospector* Alpha Particle Spectrometer: Journal of Geophysical Research, v. 110, E09009, doi:10.1029/2005JE002433.

Marinova, M.M., Aharonson, O., and Asphaug, E., 2008, Crustal consequences of planetary-scale impacts: Large Meteorite Impacts and Planetary Evolution IV, August 17–21, 2008: Vredefort Dome, South Africa, Lunar Planetary Institute Contribution No. 1423, CD-ROM, abstract 3097.

McCauley, J.F., 1977, Orientale and Caloris: Physics of the Earth and Planetary Interiors, v. 15, no. 2–3, p. 220–250, doi:10.1016/0031-9201(77)90033-4.

McGlaun, J.M., Thompson, S.L., and Elrick, M.G., 1990, CTH: A three-dimensional shock wave physics code: International Journal of Impact Engineering, v. 10, p. 351–360, doi:10.1016/0734-743X(90)90071-3.

Namiki, N., Iwata, T., Matsumoto, K., Hanada, H., Noda, H., Goossens, S., Ogawa, M., Kawano, N., Asari, K., Tsuruta, S.-I., Ishihara, Y., Liu, Q., Kikuchi, F., Ishikawa, T., Sasaki, S., Aoshima, C., Kurosawa, K., Sugita, S., and Takano, T., 2009, Farside gravity field of the Moon from four-way Doppler measurements of *Selene* (*Kaguya*): Science, v. 323, p. 900, doi:10.1126/science.1168029.

Neumann, G.A., Zuber, M.T., Smith, D.E., and Lemoine, F.G., 1996, The lunar crust: Global structure and signature of major basins: Journal of Geophysical Research, v. 101, p. 16,841–16,843.

Petro, N.E., and Pieters, C.M., 2004, Surviving the heavy bombardment: Ancient material at the surface of South Pole–Aitken basin: Journal of Geophysical Research, v. 109, E06004, doi:10.1029/2003JE002182.

Pierazzo, E., and Melosh, H.J., 2000, Hydrocode modeling of oblique impacts: The fate of the projectile: Meteoritics & Planetary Science, v. 35, p. 117–130, doi:10.1111/j.1945-5100.2000.tb01979.x.

Richardson, J.E., Melosh, H.J., Greenberg, R.J., and O'Brien, D.P., 2005, The global effects of impact-induced seismic activity on fractured asteroid surface morphology: Icarus, v. 179, p. 325–349, doi:10.1016/j.icarus.2005.07.005.

Schultz, P.H., 1976a, Moon Morphology: Austin, Texas, University of Texas Press, 604 p.

Schultz, P.H., 1976b, Floor-fractured lunar craters: The Moon, v. 15, p. 241–273, doi:10.1007/BF00562240.

Schultz, P.H., 1992, Atmospheric effects on ejecta emplacement and crater formation on Venus from Magellan: Journal of Geophysical Research, v. 97, no. E10, p. 16,183–16,248.

Schultz, P.H., 1996, Nature of the Orientale and Crisium impacts: Houston, Texas, Lunar and Planetary Institute, Lunar and Planetary Science Conference XXVII, p. 1147–1148.

Schultz, P.H., 1997, Forming the South Pole–Aitken basin: The extreme games: Houston, Texas, Lunar and Planetary Institute, Lunar and Planetary Science Conference XXVIII, p. 1259–1260.

Schultz, P.H., 2007, Possible link between Procellarum and the South-Pole-Aitken Basin: Houston, Texas, Lunar and Planetary Institute, Lunar and Planetary Science Conference XXXVIII, CD-ROM, abstract 1839.

Schultz, P.H., and Anderson, R.A, 1996, Asymmetry of the Manson impact structure: Evidence for impact angle and direction, *in* Koeberl, C., and Anderson, R.R., eds., The Manson Impact Structure, Iowa: Anatomy of an Impact Crater: Geological Society of America Special Paper 302, p. 397–417.

Schultz, P.H., and Crawford, D.A., 2007, Comparing laboratory and hydrocode experiments for oblique impacts into spherical targets: Bridging the Gap II: Effect of Target Properties on the Impact Cratering Process, September 22–26, 2007: Saint-Hubert, Canada, Lunar and Planetary Institute Contribution No. 1360, CD-ROM, abstract 8049.

Schultz, P.H., and Crawford, D.A., 2008, Impactor survivors as additional sources for the Late Heavy Bombardment: Workshop on Early Solar

System Impact Bombardment, September 15–17, 2008: Houston, Texas, Lunar and Planetary Institute Contribution No. 1439, CD-ROM, abstract 3026.

Schultz, P.H., and Gault, D.E., 1975, Seismic effects from major basin formation on the Moon: The Moon, v. 12, p. 159–177, doi:10.1007/BF00577875.

Schultz, P.H., and Gault, D.E., 1990, Prolonged global catastrophes from oblique impacts, *in* Sharpton, V.L., and Ward, P.D., eds., Global Catastrophes in Earth History: An Interdisciplinary Conference on Impacts, Volcanism, and Mass Mortality: Geological Society of America Special Paper 247, p. 239–261.

Schultz, P.H., and Spudis, P.D., 1983, The beginning and end of lunar volcanism: Nature, v. 302, p. 233–236, doi:10.1038/302233a0.

Schultz, P.H., and Spudis, P.D., 1985, Procellarum basin: A major impact or the effect of Imbrium?: Houston, Texas, Lunar and Planetary Institute, Lunar and Planetary Science Conference XXVI, abstract, p. 746–747.

Schultz, P.H., Staid, M.L., and Pieters, C.M., 2006, Lunar activity from recent gas release: Nature, v. 444, no. 7116, p. 184–186, doi:10.1038/nature05303.

Scott, D.H., McCauley, J.F., and West, M.N., 1977, Geologic Map of the West Side of the Moon: U.S. Geological Survey Miscellaneous Investigations Series I-1034, scale 1:5,000,000.

Smith, D.E., Zuber, M.T., Neumann, G.A., and Lemoine, F.G., 1997, Topography of the Moon from the *Clementine* LIDAR: Journal of Geophysical Research, v. 102, p. 1591–1611, doi:10.1029/96JE02940.

Stickle, A., Schultz, P.H., and Crawford, D.A., 2009, The role of shear in oblique impacts: Houston, Texas, Lunar and Planetary Institute, Lunar and Planetary Science Conference XXXX, CD-ROM, abstract 2357.

Stuart-Alexander, D., 1978, Geologic Map of the Central Far Side of the Moon: U.S. Geological Survey Miscellaneous Investigations Series I-1047, scale 1:5,000,000.

Thompson, S.L., and Lauson, H.F., 1972, Improvement in the Chart D Radiation Hydrodynamic Code III: Revised Analytic Equation of State: Sandia National Laboratories Report SC-RR-71 0714, 15 p.

Watters, T.R., Robinson, M.S., Beyer, R.A., Banks, M.E., Bell, J.F., III, Pritchard, M.E., Hiesenger, H., van der Bogert, C.H., Thomas, P.C., Turtle, E.P., and Williams, N.R., 2010, Evidence of recent thrust faulting on the Moon revealed by the *Lunar Reconnaissance Orbiter* camera: Science, v. 329, no. 5994, p. 936–994.

Whitaker, E.A., 1981, The lunar Procellarum basin, *in* Schultz, P.H., and Merrill, R.B., eds., Multi-Ring Basins: Formation and Evolution: Proceedings of the Lunar and Planetary Science Conference: New York and Oxford, Pergamon Press, p. 105–111.

Wichman, R.W., and Schultz, P.H., 1994, The Crisium basin: Implications of an oblique impact for lithospheric failure and mare emplacement, *in* Dressler, B.O., Grieve, R.A.F., and Sharpton, V.L., eds., Large Meteorite Impacts and Planetary Evolution: Geological Society of America Special Paper 293, p. 61–72.

Wichman, R.W., and Schultz, P.H., 1995, Floor-fractured craters in Mare Smythii and west of Oceanus Procellarum: Implications of crater modification by viscous relaxation and igneous intrusion models: Journal of Geophysical Research, v. 100, no. E10, p. 21,201–21,218, doi:10.1029/95JE02297.

Wieczorek, M.A., and Phillips, R.J., 1999, Thermal modeling of mare volcanism and the Procellarum KREEP terrane: Houston, Texas, Lunar and Planetary Institute, Lunar and Planetary Science Conference XXX, CD-ROM, abstract 1547.

Wieczorek, M.A., and Phillips, R.J., 2000, The "Procellarum KREEP terrane": Implications for mare volcanism and lunar evolution: Journal of Geophysical Research, v. 105, no. E8, p. 20,417–20,430, doi:10.1029/1999JE001092.

Wieczorek, M.A., and Zuber, M.T., 2001, A Serenitatis origin for the Imbrium grooves and South Pole-Aitken thorium anomaly: Journal of Geophysical Research, v. 106, p. 27,825–27,840.

Wilhelms, D.E., 1987, Geologic History of the Moon: U.S. Geological Survey Professional Paper 1348, 302 p.

Williams, D.A., and Greeley, R., 1994, Assessment of antipodal-impact terrains on Mars: Icarus, v. 110, p. 196–202, doi:10.1006/icar.1994.1116.

Zhong, S., Parmentier, E.M., and Zuber, M.T., 2000, A dynamic origin for the global asymmetry of lunar mare basalts: Earth and Planetary Science Letters, v. 177, p. 131–140, doi:10.1016/S0012-821X(00)00041-8.

Manuscript Accepted by the Society 26 August 2010

Printed in the USA

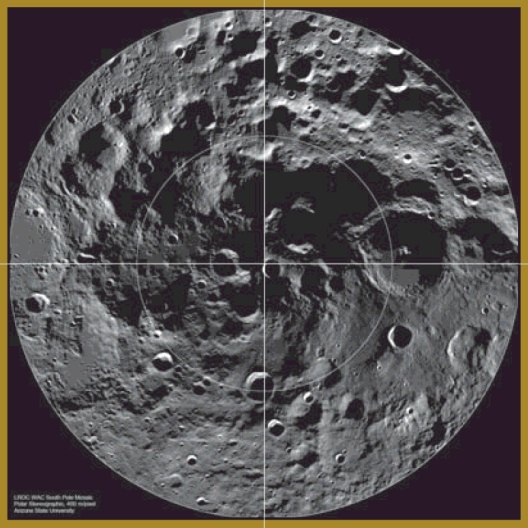

Contents

THE GEOLOGICAL SOCIETY OF AMERICA®

3300 Penrose Place • P.O. Box 9140
Boulder, CO 80301-9140, USA

ISBN 978-0-8137-2477-5